Characterization of Sulfonated Perfluorocyclobutane /Poly(Vinylidene Difluoride)-co-Hexafluoropropylene (PFCB/PVDF-HFP) Blends for Use as Proton Exchange Membranes

Katherine Augusta Finlay

Dissertation submitted to the faculty of the Virginia Polytechnic Institute and State University in partial fulfillment of the requirements for the degree of

DOCTOR OF PHILOSPHY
In
Macromolecular Science and Engineering

David A. Dillard, Co-Chair
Robert B. Moore, Co-Chair
Scott W. Case
Michael W. Ellis
James E. McGrath
Yeh-Hung Lai

November 28, 2012
Blacksburg, Virginia

Keywords: Perfluorocyclobutane, Polyvinylidene Difluoride, Polymer Blend, Proton Exchange Membrane, Fuel Cell, Viscoelasticity, Time Temperature Moisture Superposition, Constitutive Modeling, Membrane Morphology, Structure Property Relationships

Characterization of Sulfonated Perfluorocyclobutane /Poly(Vinylidene Difluoride)-co-Hexafluoropropylene (PFCB/PVDF-HFP) Blends for Use as Proton Exchange Membranes

Katherine Augusta Finlay

Abstract

The research herein focuses on the characterization of a PFCB/PVDF-HFP (70:30 wt:wt) blend fuel cell membrane including the constitutive and morphological properties, how these properties predict the stresses incurred under fuel cell operating conditions, and how these properties change over time under fuel cell operating conditions. Characterization was performed to mimic temperature and moisture conditions found in operating fuel cells to understand how these materials will behave in service. This included thermal and hygral expansion, mass uptake, and the stress relaxation modulus. These constitutive properties were chosen for characterization such that a model could be created to predict the stresses incurred during fuel cell operation, and examine how these stresses may change under different operating conditions and over time. Based on the results of this model, lifetime predictions were made resulting in recommendations to further extend the operating time of this membrane beyond the DOE 5000 hr requirement.

Stress predictions are useful, however if the material properties are changing over time under the fuel cell operating conditions, they may no longer be valid. Therefore, PFCB/PVDF-HFP membranes were conditioned for different amounts of time under conditions similar to those commonly found in operating fuel cells. These conditioned membranes were then characterized and compared with solvent exchanged membranes, the same materials used for previous material characterization. The properties examined included stress relaxation modulus, bi-axial strength, mass uptake, water diffusion, and proton conductivity. To further understand any changes noted in these properties after different environmental exposures,

morphological analysis was performed. This included small angle x-ray scattering, infrared spectroscopy, transmission electron microscopy, and differential scanning calorimetry.

It was initially found that the proton conductivity decreased severely when the material was immersed at high temperatures over short time periods. This was consistent with changes noted in other properties, and morphological analysis showed a decrease in the ionic network as well as an increase in the phase separation of the PFCB block copolymer as well as the PVDF-HFP crystallinity. These large morphological changes could be very detrimental while in service, resulting in early termination of the fuel cell. However, it was also noted that if these materials are annealed at high temperature (140°C), the negative property changes are abated. This abatement is again tied to the morphology of the material, as annealing the material at high temperature creates stronger physical crosslinks, and induces a small amount of chemical crosslinking via condensation of the sulfonic acid groups, thus allowing the stress predictions performed earlier to have greater validity. Therefore, it is important to not only understand the properties of a material during characterization, but also the underlying polymer structure, and how this structure can change over time, as all of these items control the long term material performance while in service.

Acknowledgements

I'd like to express my gratitude to Dr. Dillard and Dr. Moore for advising me throughout my graduate school career. The different insight provided by my engineering and chemistry advisors allowed me to become a better researcher and communicator as I learned how to tackle problems from both sides of the science. Dr. Ellis and Dr. Case also provided invaluable insight and assistance during project meetings, in the lab, and with data analysis. I'd also like to thank General Motors for not only financial support of my research, but also the time and knowledge they shared on at least a biweekly basis in addition to extra time spent over email and phone discussing data.

I would not have been successful in my work without all the great students in both the Dillard and Moore groups, as well as the ICTAS 420 lab. I'd especially like to thank all the students I've worked with on the GM project, including Jessica Wright, Chase Siuta, Ashley Gordon, Nathan May, Mingqiang Zhang, Angela Osborn, Kshitish Patankar, Lei Yan, and Timothy Gray. I would also like to recognize Amanda Neighbors for her assistance with the collection of IR data, Mingqiang Zhang for his assistance with the collection of SAXS data, Kathy Lowe and Daniel Dodge for their assistance with TEM imaging, Matt Green and Nancy Zhang for their assistance with the collection of mass uptake data, and Jianbo Hou for his assistance with pulsed-field gradient NMR. Fellow graduate students have been of great help, but I must also sincerely thank the undergraduate students who have helped me in the lab including Gina Cruz, James Malone, and Dawn Jackson. These undergraduates took on some of the less exciting work with gusto and allowed me to accomplish research tasks at a much faster pace.

Finally, I'd like to thank my parents Doris and Richard Finlay, John Hofmann, and my little dog too. My parents have always pushed me to be the best at what I do and without their support I may never have even considered graduate school. While my parents may have gotten me here, John and Broccoli got me through. John, I don't think I could have handled the stress if you hadn't been here with me to keep me calm and powering through, I love you and I can't wait for the next stage of our lives. Broccoli, your happy little smile and snuggles cheered me up on countless occasions and I'm so glad I had you here at school with me.

Table of Contents

Table of Figures

Table of Tables

Table of Schemes

Chapter 1 : Review of the Literature

1.1 Introduction

The durability of polymer electrolyte membranes or proton exchange membranes (PEM) is of key importance for the commercialization of fuel cells for portable, stationary, and transportation applications [1]. Cell assembly parameters such as MEA compression, gasket design, operating temperature and pressure, as well as relative humidity of the reactant gasses, can all have a significant effect on membrane lifetime [2]. Care must be taken during manufacturing as uneven contact pressure between the membrane electrode assembly (MEA) and bipolar plates can lead to accelerated membrane degradation. In addition, foreign particles can cause perforations, especially in areas where the membrane is subject to increased stresses such as reactant inlets, seals, and edges [3]. Beyond foreign particles, the catalyst particles can penetrate the membrane and create localized stresses again due to manufacturing problems such as misalignment of the catalyst transfer decal [3]. Additionally, membrane degradation can be caused due to chemical, electrochemical, mechanical, thermal, and other physical processes that interact and degrade performance during operation [4].

Within an operating fuel cell, the membrane is subjected to a harsh chemical environment with both reducing and oxidizing interactions. One common problem is the formation of radicals, specifically peroxy and hyperperoxy radicals, which will then attack and degrade the membrane. Most commonly, these radicals attack α-carbons of aromatic groups, ether linkages, branch points, and hydrogen containing terminal bonds. In addition to attacks from radicals, contamination due to trace metals is also a source of membrane failure. These metals can come from corrosion of stack components or impurities in the reactant gasses and humidifiers. Only 5% contamination is required to reduce the water flux in the system, which can increase the

concentration of peroxides, and thus accelerate degradation due to radical attacks [3]. To reduce membrane damage due to the formation of radicals, several researchers have suggested including radical scavengers or traps [3, 5]. These include cerium and manganese ions, cerium oxide nanoparticles, and rare earth oxide layers on either side of the membrane [5-7]. Radical scavengers have been shown to greatly improve membrane resistance to chemical degradation. In addition, the chemical structure of membrane materials has been altered to reduce radical attacks. Du Pont's Nafion® materials can be treated with fluorine gas to reduce the number of proton containing end groups; fluorination of the backbone of styrene sulfonic acid materials greatly reduces radical attack, and positioning the sulfonic acid on the meta position of the aromatic groups in sulfonated polyarylene ether membranes greatly increases stability to peroxide attack [5, 8, 9].

While significant progress has been made in reducing chemical degradation of membrane materials, mechanical degradation has only recently been recognized as an important area of research. Within a fuel cell, the membrane is at least partially constrained by the gasket and rigid gas diffusion layers, catalyst layers, and bipolar plates. It is well known that better proton conductivity is achieved at high water contents, however, PEM materials have been shown to expand due to moisture by at least 10%, and many by more than 20% in all three directions [10]. Due to the in-plane constraint created by the fuel cell system, varying in-plane compressive and tensile stresses are induced in the membrane as the PEM expands and contracts with changing temperature and humidity conditions [11]. Automotive applications are especially mechanically challenging due to the rapidly changing temperature and humidity conditions imposed to meet the needed power demands [12, 13].

It is believed that the repeated cycling of these induced hygrothermal mechanical stresses leads to a fatigue loading of the PEM, which over time contributes to delamination of the PEM and catalyst layers, as well as the formation and propagation of microcracks [14-16]. These and other defects or pinholes allow the reactant gasses to crossover and react on the catalyst surface. This reaction results in localized heating which can cause the membrane to soften or melt, thereby increasing degradation of the membrane, and allowing further gas crossover, creating a destructive cycle that ultimately causes failure of the fuel cell [2, 3, 15-19]. In addition, humidity cycle testing was performed by General Motors without the use of hydrogen or current draw, thereby eliminating chemical reactions and ensuring failure is solely due to mechanical stresses [12]. They showed failure in multiple perfluorosulfonic acid (PFSA) membranes, specifically with cracks perpendicular to the plane of the membrane in the channel region, suggesting these cracks were propagated via tensile stresses. Therefore, even in the absence of chemical degradation, mechanical durability is an important membrane failure mechanism, and thus it is essential to understand and characterize the constitutive properties of PEMs to accurately predict and improve the lifetime durability of a fuel cell.

1.2 Constitutive Property Characterization of PEM Materials

1.2.1 Constitutive Property Characterization of Nafion® Materials

The mechanical properties that affect membrane durability have recently attracted significant attention including Young's modulus, yield stress and strain, stress and strain at break, stress relaxation, creep, and fracture energy. Many authors have investigated the tensile properties of various forms of Nafion® under different temperature and moisture conditions. These authors all concluded that the Young's modulus and strengths at yield and break decrease, while the strains at yield and break increase, with increasing temperature and membrane

moisture content [20-28]. The decrease in modulus and yield strength with increasing moisture level has been explained as a weakening of the ionic interactions as water is sorbed into the sulfonic acid clusters, therefore reducing the mechanical stability of the membrane [21]. The temperature-driven softening of Nafion® is thought to be due to the increased mobility of polymer chains due to the increased expansion at higher temperatures [29]. In addition, the stress-strain profile developed from tensile testing has a clear bilinear shape with an identifiable yield point for dry and humidified Nafion® membranes. However, once the sample is immersed, the stress-strain curve takes on a power law shape with no distinct yield region and the material displays characteristic features of an elastomer [23, 29]. Several authors also note that temperature appears to have a greater effect than moisture content on the tensile properties of Nafion® materials, noting larger changes in the tensile properties with changes in temperature than with changes in the moisture level [21, 23, 30]. For example, a 20°C change in temperature results in a 31% change in the yield stress, while a 25% change in relative humidity results in an 11% change in the yield stress [23].

Additional tensile testing of Nafion® performed at different strain rates shows little effect on the Young's modulus, but an increase in the yield strength and a decrease in the strain at break with increasing strain rate were observed [20, 28, 31]. Yielding occurs when the polymer chains disentangle, and as the strain rate is increased, the polymer chains have less time to reorient. Therefore less free volume is created and the linear stress-strain region can be taken to higher stresses and strains, resulting in higher yield points with increasing strain rates.

Tensile testing was also performed on samples that had been aged at least 72 hours in an operating fuel cell and compared with a new membrane. The results showed the Young's modulus and yield strength decreased by about a factor of two after aging, implying the fuel cell

environment is quite harsh on the mechanical properties of the membrane [25]. An additional study examined aged membrane electrode assemblies in an operating fuel cell at 90°C and 30% RH under open circuit voltage conditions. These authors found a large decrease in the stress and strain at break after aging, indicating a severe reduction in the ductility of the membranes [32]. This reduction in ductility was thought to be caused by a decrease in the molecular weight of the membrane. Shorter polymer chains can escape entanglements more easily, and even shorter chains are unable to form entanglements, both of which would reduce the material's resistance to deformation, resulting in embrittlement and loss of ductility. Another aging study conditioned the samples at 70, 80, or 90°C in an operating fuel cell and noted a decrease in the Young's modulus and the strain at break with increasing operating temperature [33]. This is again in agreement with the observation that temperature has a large impact on Nafion® materials, and also indicates that Nafion® should only be used in low temperature operating fuel cells due to the deterioration of mechanical properties at higher temperatures. However, it is believed that the hydrogen or oxygen gasses alone do not cause Nafion® deterioration because after 1000 hrs of exposure to either gas, unconstrained, at room temperature, showed no change in the tensile strength remains the same, indicating the stability of Nafion® under typical atmospheric gasses in an operating fuel cell [34].

Researchers have also investigated time dependent mechanical properties, such as storage and loss modulus from dynamic testing, stress relaxation and creep. Some of the earliest work characterizing the viscoelastic properties of Nafion® examined the loss tangent [35, 36]. Additional dynamic mechanical studies have noted a decrease in the storage and loss modulus with an increase in water content [20, 25, 37]. Similar conclusions were reached with stress relaxation tests performed over multiple temperature and water conditions, noting lower

relaxation moduli and faster relaxations with increasing temperature and moisture content [30, 36, 38]. Stress relaxation testing performed on samples immersed in water showed a strain dependent relaxation response. In addition, amorphous Nafion® relaxed much faster than semi-crystalline Nafion® while immersed, and samples annealed in 70°C water for three days slows the relaxation process as compared with non-annealed samples [29, 35]. It is likely chain mobility is reduced in the semi-crystalline Nafion® due to the presence of crystalline regions which would immobilize backbone segments in addition to the reduced mobility created by the electrostatic interactions of the ionic aggregates [35]. Therefore, an amorphous Nafion® with only electrostatic interactions should be expected to relax faster than a semi-crystalline Nafion®.

In contrast to these multiple authors' findings, Satterfield and Benziger found that the relaxation time increased with increasing moisture content, but did observe a decrease in the modulus [39]. While previous authors explained the decrease in relaxation time as a result of increased free volume and chain mobility, Satterfield and Benziger suggest that ordering of the microphase structure in Nafion® is the cause of the increased relaxation times. They claim that as the moisture content is increased, microphase separation is increased as water is attracted to the sulfonic acid groups, but repelled by the polytetrafluoroethylene backbone. Therefore, as more water is added to the membrane, the hydrophilic domains have greater mobility, resulting in a driving force for order in the hydrophilic domains, and thusly increasing the time necessary for relaxation.

Similar to tensile testing, the effect of initial strain rate on stress relaxation was examined. The authors found no stress relaxation dependence on strain rate when the material was stretched to a maximum of 3% strain. However when the membrane was stretched to a maximum of 50% strain, the relaxation modulus was found to decrease with increasing initial

strain rate while the relaxation time remained the same [31]. The authors believe this occurs because polymer chain disentanglement is the key relaxation mechanism after the material has yielded based on their bundle-cluster morphology model. In addition, the effect of total strain level on relaxation time was investigated [39]. It was again noted that higher strain levels resulted in lower relaxation moduli, however the authors also noted that as the total strain was increased, the relaxation time also increased. This material behavior is thought to be due to strain induced microphase separation, similar to the effects of increased temperature and moisture.

A limited number of experiments have also been performed examining the creep behavior of Nafion® membranes. Creep experiments performed over multiple temperatures and relative humidity levels showed an increase in creep strain with an increase in temperature at a constant water activity [40]. However, the authors show that adding a small amount of water stiffens the membrane, resulting in a lower creep strain, and once the temperature reaches 90°C and above, water is seen to again stiffen the membrane. This is in agreement with studies performed under tensile testing, dynamic mechanical analysis, and stress relaxation [30, 37, 39, 41].

The first phenomenon, in which a small amount of water, less than 5% RH, stiffens the membrane is discussed as antiplasticization and thought to be caused by water bridging [37, 39, 41]. At low water activities one water molecule can hydrogen bond with multiple sulfonic acid groups, acting to create a bridge between them. This bridging creates a stronger physical crosslink between sulfonic acid groups, effectively stiffening the material. However, after a certain threshold water activity, excess water molecules will increase the number of possible hydrogen bonding sites, creating a dynamic network with rapidly exchanging bonds. This effectively decreases the number of discrete junction points, weakening the overall effectiveness

of restricting polymer chain dynamics, resulting in the standard plasticization effect of water on Nafion®.

The second phenomenon, in which the addition of any water above 90°C stiffens the membrane, is discussed in terms of microphase separation [39, 40]. The authors believe that at zero water content, the size of a sulfonic acid group is approximately the same as the size of a perfluoroether side chain, and as such microphase separation is minimized, resulting in a lamellar structure. However, as water is sorbed by the sulfonic acid groups, their effective diameter is increased while the perfluoroether side chain remains unchanged. Therefore, as the size of the sulfonic acid group increases, the preferred packing changes such that curvature around the sulfonic acids occurs, resulting in a rod-like structure. This model is also consistent with domain spacing measured via scattering, although the authors admit this is not proof that this structure truly exists. The authors believe it is this proposed transition from a lamellar structure to a rod-like structure that causes an increase in stiffness above 90°C when water is sorbed by Nafion®.

An additional creep study examined the effect of degradation on creep strain. Membrane electrode assemblies were exposed to 90°C 30% RH open circuit voltage conditions in an operating fuel cell [32]. The authors found that aged membranes underwent less creep strain than non-aged membranes, indicative of a stiffer material in contrast to the results obtained via tensile testing. The authors believe this is because the molecular weight was reduced, causing the material to become brittle and less tough. As the membrane is subjected to small deformations, such as the creep experiments performed, the material will undergo local rupture to relieve the applied stress, rather than chain slippage which would be expected at larger deformations.

Stress relaxation and creep data taken over multiple temperatures and moisture levels were used successfully to create master curves using the Time Temperature Superposition Principle (TTSP) [31, 35, 36, 40, 41], or Time Temperature Moisture Superposition Principle (TTMSP) [15, 30] both of which will be discussed in more detail in **Sections 1.4.1** and **1.4.3.2**. It was initially thought the addition of moisture to Nafion® would create a microphase separated structure and TTSP would no longer be applicable [36]. However, success using the TTSP has been found at constant moisture levels for Nafion®, and success using the TTMSP has also been found combining multiple TTSP curves at constant RH levels, and it is thusly thought initial testing was flawed such as by poor moisture control. Long term validation taken under different test modes was also compared with the TTMSP master curve and showed excellent agreement, implying that the TTMSP is valid for Nafion® materials [30]. In addition, the thermal and hygral shift factors also show that temperature has a greater effect on Nafion® properties than moisture, as the thermal shift factors cover 6 decades and the hygral shift factors only cover 2. It is believed that temperature has a larger effect because near and above the α-transition, the polymer chains have enough mobility due to the higher fraction of free volume, and additional moisture does not provide significant additional free volume for chain mobility [30].

It should be noted that TTMSP was only successful for data taken at relative humidities greater than 5%. Below this level, the antiplasticization of Nafion® did not allow lower humidity levels to align with the master curve. In addition, at dry conditions the material appears to have a fundamentally different relaxation behavior, appearing to relax more quickly than humidified materials, as noted by Patankar et al., and Satterfield et al. [30, 39]. It has been observed that physical aging occurs under dry conditions by Patankar et al. and Kundu et al. [25, 30]. Subsequent relaxation tests on the same sample showed a stiffening behavior, but after

raising the material above its α-transition, the Nafion® modulus returned to its original value, corresponding with rejuvenation. Therefore, if the material is becoming denser over time, it would not be expected that the dry master curve would be correct, or align with the humidified data.

During fuel cell operation it is possible for impurities in reactant gasses as well as corrosion of fittings or tubing to cause contamination via cation exchange with the membrane. These cation contaminants likely decrease fuel cell performance, and also are thought to accelerate mechanical degradation. Therefore, several authors have investigated the mechanical properties of membranes neutralized with different cations to gain understanding of the contaminant impact on mechanical durability. Eisenberg and Yeo were one of the first to examine the effect of cations, and found that neutralizing with potassium cations resulted in a broadening of the distribution of relaxation times, causing an increase in the relaxation time, as compared with an acid form membrane [36]. Kyu and Eisenberg also analyzed the effect of sodium and barium cations on stress relaxation immersed in water [35]. These authors found that the relaxation behavior was very similar for the acid and neutralized forms, however the neutralized forms were slightly stiffer. It is believed this increase in stiffness is due to the lower hygral expansion of the neutralized forms, and thus lower water sorption and less chain mobility, resulting in a stiffer material. Immersed tensile testing was performed on neutralized Nafion® by Kundu et al. and under humidified conditions by Jia et al., noting a linear increase in the Young's modulus and yield strength with increasing cation radius size [25, 26]. Cations with larger radii can likely interact with multiple sulfonic acid groups, resulting in stronger physical crosslinks with increasing cation radius, reducing chain mobility, and thereby increasing the stiffness and strength of the material. It was also determined that the size of the cation has a

larger impact than the charge of the cation, as similarly sized mono- and divalent cations resulted in similar changes in the modulus and yield strength of the material. In conclusion, cation contamination can result in stiffer membranes, which could lead to early fuel cell failure.

Additional mechanical characterization examined the fracture properties of cast and extruded Nafion® membranes as well as the effect of platinum contamination. Two different fracture tests are employed in the literature, a knife slit test, and a trouser tear test. Cast and extruded Nafion® membranes were examined utilizing a knife slit test over multiple temperatures and humidities [42, 43]. For all membranes it was noted that the fracture energy decreases with increasing temperature and moisture condition, and increases with increasing cutting rate. The decreased fracture energy with increased moisture content is believed to be caused by the presence of excessive water weakening the electrostatic network of the membrane. It was shown that cast Nafion® had significantly higher crack propagation rates than the other three membranes, suggesting reduced resistance to fracture and perhaps reduced durability. In addition, it was shown that fracture data collected over multiple temperature and moisture levels follows the TTMSP, implying the time dependence of membrane fracture properties.

Trouser tear testing was performed on cast Nafion® that had been ion exchanged or contained a catalyst platinum dispersion to examine the effects of contamination on the fracture properties of the material [26, 44]. The authors noted that cation contamination reduces the tearing force by a factor of two, indicating the severely reduced fracture properties of contaminated membranes. It is suggested this reduction in fracture resistance is due to the increased stiffness of the material caused by the incorporation of the cations, as discussed previously. In addition, the tearing energy was decreased gradually with increasing platinum concentration, up to about 50% platinum to PFSA mass ratio. Based on SEM images, the

authors note that cracks initiated and propagated easily along the platinum aggregates, rather than the polymer matrix. Therefore contaminants, such as platinum or cations, incurred during fuel cell operation can severely reduce the fracture resistance of a membrane, potentially resulting in early failure of the membrane and thus the fuel cell.

RH cycle testing allows for the mechanical durability of a membrane to be examined under typical fuel cell operating conditions without any chemical reactions. Therefore, failure, as measured by air crossover, is purely based on hygrothermal cycling and the constraint of the fuel cell system. Using this test set-up, cast and extruded Nafion® were compared using RH cycles from 0-150% at 80°C every two minutes [15]. It should be noted that 150% RH refers to 1.5 times the amount of water for saturation of air at a given temperature. This was achieved by supplying supersaturated water at the inlet using humidifiers set for a 90°C dew point in the 80°C test. In this test, the cast Nafion® failed prior to 5000 cycles, whereas the extruded Nafion® lasted for 20000 cycles. Therefore the extruded Nafion® displays better mechanical durability than the more commonly used cast Nafion® with higher proton conductivities.

1.2.2. Constitutive Property Characterization of Filled Nafion® Materials

Efforts to reduce mechanical failures in Nafion® membranes during fuel cell operation have been undertaken by incorporating filler materials. These filler materials have the potential to reduce fracture propagation, increase the α-transition allowing for higher operating temperatures, and increase dimensional stability such that stresses incurred during RH and temperature cycling are reduced due to the decrease in expansion. Fillers investigated include organic materials such as polytetrafluoroethylene (PTFE), polyphenylsulfone, and polyethylene polysulfone [45-47], and inorganic materials such as zirconium phosphate, zirconium hydrogen

phosphate, titania, silica, organically modified silica, alumina, quartz, microglass fiber, silicon oxide, and ionic liquids [27, 47-54].

1.2.2.1. Constitutive Property Characterization of Nafion® with Organic Fillers

Organic fillers are typically incorporated as reinforcing mats into which Nafion® is impregnated. These fillers are hydrophobic and believed to reduce water uptake and thus swelling of the PFSA membrane. A reduction in swelling could in turn reduce hygothermal stresses developed during RH cycling, and therefore extend membrane lifetime by reducing mechanical degradation. Commercially available Nafion® membranes reinforced with expanded polytetrafluoroethylene mats are produced by W. L. Gore & Associates Inc.. Tensile testing under multiple temperature and relative humidity conditions of a GORE-SELECT™ membrane was performed by Tang et al. [55]. These authors noted that the Young's modulus, yield strength, and ultimate strength all decrease with increasing temperature and humidity conditions, while the strain at break increases, in agreement with previously discussed work. In addition, the authors note a large increase in the Young's modulus, yield strength, and ultimate strength of the GORE-SELECT™ material, while the strain at break is approximately half that of the unreinforced Nafion®. Therefore, the reinforced Nafion® is stiffer and less ductile than unreinforced Nafion®, however, with about 100% strain at break, this material should be sufficiently ductile to withstand the strains incurred in an operating fuel cell. In addition, the authors also note that hygral expansion is only about 2% for the GORE-SELECT™ material, whereas unreinforced Nafion® was around 10%. Thus, it is possible the stresses incurred by the reinforced material would be much lower, as they are a direct result of constraining the membrane against hygrothermal swelling and deswelling.

Despite the observed changes during tensile testing, stress relaxation performed by Patankar et al. over multiple temperature and humidity conditions of Gore-Select® 57 showed a similar relaxation modulus to Nafion®, as well as similar temperature and moisture dependence [56]. Therefore, if the time dependent modulus is considered, rather than the Young's modulus, Gore membrane materials may be quite similar to unreinforced Nafion® and with lower hygral expansion could have increased mechanical durability. An additional commercial PFSA membrane reinforced with mats of PTFE developed by Johnson Matthey Fuel Cells was examined by Ralph et al. [47]. Fuel cell testing in a 30 cell stack showed failure after 1400 and 1800 hrs of operation, whereas the unreinforced membrane failed after less than 500 hrs of operation. Furthermore, RH cycling from 0-150% RH at 80°C showed Gore-Select® 57 membranes failing after approximately 7500 cycles, whereas the unreinforced cast Nafion® failed after less than 5000 cycles [15]. This is in good agreement with the proposed conclusion that the added PTFE reinforcement decreases the induced hygrothermal stresses during operation, resulting in increased mechanical durability.

An alternative to the expanded PTFE reinforcement mat has been explored by Ballengee et al., creating dual-nanofiber electrospun mats [46]. These authors created two membranes by simultaneously electrospinning Nafion® and polyphenylsulfone from two separate spinnerets, and softening one component to fill the interfiber voids of the other component. Therefore, a Nafion® membrane reinforced by a web of nanofiber polyphenylsulfone was produced by annealing the sample at 150°C for 2 hrs, and a a polyphenylsulfone membrane reinforced by a web of nanofiber Nafion® was created by exposing the samples to choloroform vapor followed by thermal compression at 70°C. The proton conductivity of these two membranes is effectively indistinguishable based on Nafion® content. In addition, the nanofiber composite membranes

both have greater Young's moduli and yield strengths than unreinforced Nafion®, and as the volume fraction of polyphenylsulfone is increased, the Young's modulus and yield strength increase further. The polypheylsulfone membrane reinforced with Nafion® nanofibers has a greater Young's modulus and yield strength than the inverse morphology. This likely occurs because of greater connectivity of the polyphenylsulfone which has a three times greater Young's modulus in the neat state than Nafion® as measured at 30°C, 20% RH, and 0.1000 N/m force ramp rate. Finally, membrane durability was examined via open-circuit voltage cycling RH from 0 to 100% at 80°C every 2 min. Based on this experiment, the Nafion® membrane reinforced by polyphenylsulfone outlasted the neat Nafion® by about 300 hrs. This again implies that fiber mat reinforced Nafion® has better mechanical durability under fuel cell operating conditions than unreinforced Nafion® materials.

The fracture properties of organic mat reinforced Nafion® have also been examined. It was again noted that the fracture energy decreases with increasing temperature and moisture condition, and increases with increasing cutting rate. Based on a knife-slit test, the reinforced perfluorosulfonic acid Gore™ Gore-Select® 57 membrane appeared to have the lowest crack propagation rates [42, 57]. In addition, trouser tear testing was performed by Ralph et al. noting that the tear propagation was seven times larger for the PTFE reinforced PFSA material versus the non-reinforced PFSA membrane [47]. It is believed this increase in fracture resistance is due to the PTFE reinforcement layer which provides resistance to crack propagation and fracture.

1.2.2.2. Constitutive Property Charcterization of Nafion® with Inorganic Fillers

Although organic reinforcement mats have shown improved mechanical properties, inorganic particulate fillers are believed to add both thermal and mechanical stability to Nafion®. These inorganic fillers may allow operation at temperatures up to 150°C, as well as

increased proton conductivity and moisture sorption at these high temperatures. Bauer et al. investigated the properties of zirconium-phosphate filled Nafion® and determined that the storage modulus increased with increasing zirconium-phosphate content, up to an order of magnitude greater than pure Nafion® [58]. In addition the α-relaxation of the material was increased up to 125°C at 24.4% filler content, and the decrease in the storage modulus was less than a quarter of a decade over this transition, indicating this material maintains mechanical stability at temperatures much greater than pure Nafion®. The authors also investigated the effect of moisture on the storage modulus at 75°C, noting an order of magnitude decrease from dry to 100% RH conditions, resulting in a modulus similar to pure Nafion® at high levels of hydration [59]. Finally, the authors noted an increase in water uptake, but a large decrease in the expansion of the filled Nafion®, implying the material would have better proton conductivity while inducing lower hygrothermal stresses during cycling. Therefore, it is possible this membrane would maintain mechanical integrity at temperatures greater than the α-transition of pure Nafion®, allowing for fuel cell operation at higher temperatures, and thus reduced operating costs.

An alternative heavy metal oxide filler, titania, was investigated by Satterfield et al. examining the tensile and creep properties under multiple temperatures and water contents [27]. The authors noted that the Young's modulus and yield strength and strain were very similar between the composite membrane and unfilled Nafion®, contrary to the findings of Bauer et al. with zirconium phosphate. In addition, they noted a decrease in the Young's modulus and yield strength with increasing temperature and moisture content, for both the composite and pure Nafion® similar to results discussed previously. Furthermore, these authors showed that increased water content had a larger effect on the Young's modulus of the unfilled Nafion® vs.

the filled memebrane, a larger effect on the plastic modulus of the filled Nafion® vs. the unfilled membrane, and that temperature had an equivalent effect on both membranes. Therefore, the composite membrane had a higher stiffness at higher water contents, but after yielding had reduced strain hardening compared with the pure Nafion®. Creep data showed that the filled membrane was stiffer than the pure Nafion®, resulting in less total creep under dry and 100% RH conditions. A decrease in plastic deformation and creep could allow for greater recovery of the material during hygrothermal cycling, resulting in a greater mechanical lifetime of the titania filled Nafion® under fuel cell operating conditions.

Yuan et al. investigated the effect of incorporating hollow silica spheres functionalized with sulfonic acid groups into Nafion® membranes, showing an increase in the Young's modulus, and a small decrease in the stress and strain at break with incorporation of the silica spheres [60]. Additional silica Nafion® hybrids were investigated by Deng et al. and Young et al., examining the properties of silica, dimethylsiloxane, and organically modified silicate created *in situ* via sol-gel reactions [61-63]. The authors note increases in tensile strength and storage modulus, and decreases in ductility over a variety of different monomers used to create the organically modified silicate, of which almost all showed greater strength than pure Nafion®. It is believed these mechanical properties are the result of constraints of the Nafion® perfluoroether side chains due to entanglements created by the organically modified silicate nanostructures.

A final composite membrane discussed here is Nafion® filled with Na^{+}-montmorillonite clay [64, 65]. Based on SAXS data, the membranes consist of polymeric aggregates oriented parallel to the membrane induced by the two-dimensional nature of the clay which also tends to align parallel to the surface of the membrane. With increasing clay content, the storage modulus

increases, by a decade with 20% clay loading. In addition, the α-transition is delayed to much higher temperatures with the incorporation of clay, up to 215°C at 20% loading. The increase in the α-transition is advantageous for use in higher temperature fuel cells, while the stiffer membrane would allow for thinner materials to be used, decreasing resistance, resulting in increased conductivity and reduced material needs. However, tensile testing shows a severe decrease in the strain at break with increased clay loading, less than 20% strain at 20% clay loading, compared to over 220% for pure Nafion®. Therefore it is unlikely these composite materials could withstand the hygrothermal stresses induced by RH cycling.

1.2.3. Constitutive Property Characterization of Aromatic Hydrocarbon Based Membranes

Although Nafion® membranes have excellent proton conductivity and decent mechanical properties below their α-transition, these materials are difficult to process and as such are quite costly. In addition, it would be useful to operate fuel cells at temperatures greater than the α-transition of Nafion® to increase catalyst reactivity and thus reduce the amount of catalyst required, and ease heat and water management. While inorganic reinforced Nafion® membranes allow operation at higher temperature, the cost of production of these materials is still quite high. Therefore, alternative membranes, namely aromatic hydrocarbons, have been investigated for possible use in proton exchange fuel cells. These include fluorinated styrenic membranes, sulfonated poly(arylene ether)s such as poly(ether ether ketone) and poly(arylene ether sulfone), poly(imide)s, polybenzimidazoles, polyphosphazenes, and other high performance polymeric backbones [66].

Styrenic-based membranes have been examined due to their wide availability and ease of modification, as well as their simpler processing requirements. However, these membranes have

been shown to be unstable due to their poor oxidative stability, and also have poor mechanical properties due to being within the glassy region of the material. Saga et al. examined the properties of a sulfonated polystyrene membrane with fullerene incorporated based on reports that fullerene reduces thermo-oxidative degradation [67]. The addition of 0.57% and 1.4% fullerene decreased the Young's modulus and stress at break, and increased the strain at break to just over 15% as compared with less than 5% strain for pure polystyrene membranes, implying the fullerene added some ductility to the membrane. However, at higher loadings, the Young's modulus and stress at break continued to decline, and the strain at break also reverted back to that of pure polystyrene. Based on TEM images, the authors believe this decrease in mechanical properties at 2.8% fullerene loading occurred due to the formation of micro-scaled agglomerates, whereas at lower loadings the fullerene was dispersed more evenly throughout the membrane. Despite the slight increase in ductility from the fullerene, the mechanical properties of styrene based membranes are incredibly poor as compared with PFSA materials, which show ductilities up to 250%. Therefore it is unlikely these materials would survive the harsh mechanical environment of a fuel cell, making them unlikely candidates for replacement of Nafion® regardless of the decreased cost and ease of processing.

Sulfonated polyimides have been investigated, and five-membered ring polyimides were shown to quickly degrade under fuel cell conditions, whereas six-membered ring polyimides have shown some stability. Hydrolytic stability based on mechanical property degradation at 80°C immersed in water was shown to be improved by decreasing the degree of sulfonation, and utilizing random copolymers rather than block or sequenced copolymers [66]. Four co-polyimides were investigated by Rabiee et al. who noted based on SEM and x-ray diffraction data that the membranes appeared amorphous and homogenous, and separation into hydrophobic

and hydrophilic domains did not occur [68]. All four membranes showed a large increase in the Young's modlus and strength as compared with Nafion®, however the strain at break ranged between 15 and 40%, significantly lower than Nafion® materials. Miyatake et al. also noted extremely poor mechanical properties in their polyimide fuel cell membranes despite increased hydrolytic stability with the addition of an aliphatic component [69]. Therefore, while these materials offer higher operating temperatures, their poor mechanical properties limit application in operating fuel cells.

Phosphoric acid-doped sulfonated polybenzimidazoles have shown promise as fuel cell membranes for use at high operating temperatures, as they maintain high proton conductivity up to 200°C with low water content. In addition, these materials have shown low reactant permeability, high fuel impurity tolerance, good thermal and oxidative stability, and almost zero water drag coefficient [70]. However, the intensive processing of these materials makes them unlikely candidates to replace Nafion®, as polybenzimidazoles would likely cost more to produce. To help overcome the difficult processing requirements of these materials, Qian et al. incorporated perfluorocyclobutane into the backbone of polybenzimdazole, allowing for improved solubility and flexibility [70]. Typical sulfonated polybenzimidazoles with large levels of phosphoric acid doping produce membranes with very poor mechanical properties that cannot be fabricated into membrane electrode assemblies. However, with the addition of the perfluorocyclobutane group, the tensile strength was measured at 0.35 MPa and the strain at break was 130%, resulting in materials that could be used in membrane electrode assemblies. These membranes dissolved in phosphoric acid at 140°C, limiting the operation temperature range, and the mechanical properties are still reduced in comparison to Nafion® materials, therefore this material is still not a likely candidate for fuel cell applications.

Sulfonated poly(arylene ether)s are attractive alternative fuel cell membranes due to their hydrolytic and oxidative stability, as well as processability, and multiple chemical compositions, including partial fluorination, that can be created. One popular form is sulfonated poly(ether ether ketone) (PEEK), due to its high proton conductivity and thermal stability. Increasing the degree of sulfonation decreases the yield strength from non-sulfonated PEEK, however the yield strength is still approximately 6 times greater than that of Nafion®, and greatly increases the elongation at break up to 95% at 83% degree of sulfonation [71]. These authors believe this change in tensile properties occurs because PEEK is semicrystalline in its unmodified form, however once it is sulfonated it becomes amorphous, allowing for greater ductility. In addition, increased moisture and temperature decrease the Young's modulus and yield strength, and increase the strain at break, similar to behavior noted for Nafion®-type materials.

Sgreccia et al. examined the effect of thermal annealing at elevated temperatures on the mechanical properties of sulfonated PEEK [72]. The authors noted an increase in the tensile properties, including Young's modulus, yield strength, and yield strain, with an increase in the annealing temperature and time, however the ductility does decrease to less than 10% strain at break. In addition, the storage modulus shows a large delay in the onset of the α-transition when the materials are thermally annealed at elevated temperatures, from 105°C to 205°C. This large increase in the α-transition is consistent with the change in tensile properties, and corresponds to crosslinking of the polymer chains at high annealing temperatures. The crosslinking does lead to a decrease in the degree of sulfonation, which in turn reduces proton conductivity. Thus, while the thermal treatment does improve the mechanical properties allowing fuel cell operation at higher temperatures, the severely reduced ductility and proton conductivity suggest annealing sulfonated PEEK would not improve fuel cell efficiency and lifetime.

Tensile testing of sulfonated PEEK samples aged in an operating fuel cell was performed by Marrony et al. to examine the effects of operation on the mechanical properties of the material [33]. After aging at temperatures between 70 and 90°C, the sulfonated PEEK materials showed a larger Young's modulus and stress at break, and a smaller strain at break, as compared with aged Nafion®. In addition a large decrease in mechanical tensile properties was noted for Nafion® samples aged at 90°C with strain at break decreasing more than 90%, and stress at break decreasing by approximately one third. Whereas the sulfonated PEEK materials only showed a decrease of approximately 40% in the strain at break, and about 33% decrease in the stress at beak with aging at 90°C. Therefore, based on aging under fuel cell operating conditions, the sulfonated PEEK appears to maintain better mechanical properties than Nafion® materials.

In an effort to improve conductivity without significantly impacting the mechanical properties, Reyna-Valencia et al. added boron orthophosphate filler to the sulfonated PEEK matrix [71]. However, the authors note that with increasing filler content the tensile properties severely degrade, in that the Young's modulus decreases, and the material no longer yields and thus undergoes brittle fracture. Adding moisture to the system does increase ductility, however the yield strength, Young's modulus, and stress and strain at break are all decreased from unfilled sulfonated PEEK. The authors believe these poor mechanical properties are induced due to poor adhesion between the matrix and the filler, resulting in stress concentrations and interfacial failures that create weakened materials. Consequently, although the proton conductivity was improved, it is not beneficial to incorporate a filler material unless further compatibilization between the filler and matrix is performed to improve the mechanical stability of these materials.

An alternative poly(arylene ether) to PEEK is poly(arylene ether sulfone) (PAES). Comparing tensile testing of 40% sulfonated biphenyl sulfone PAES with Nafion® under dry conditions showed the PAES had an approximately 6 times greater yield strength, 3 times greater ultimate strength, and about half the ductility of Nafion® [73]. Under immersed conditions the PAES behaved almost identically to dry Nafion®, although the ductility was still reduced about 25%. The excellent toughness of these materials both wet and dry makes them good candidates for fuel cell use, although the reduced ductility in the dry state could prove problematic under the high tensile stresses incurred during hygrothermal cycling.

Tensile testing performed on 35% sulfonated biphenyl sulfone PAES at ambient conditions showed that with increasing strain rate the strain at break decreased from 80 to 30% and the stress at break increased from 27 to 32 MPa [31]. These values can be compared with the 250% elongation and 36 MPa ultimate strength of Nafion® [31]. The authors also noted large amounts of yielding and necking in the PAES as compared with Nafion®. Stress relaxation moduli are very similar between the PAES and Nafion®, however the Nafion® relaxes at a slightly higher rate. As the total strain level is increased above the yield strain, the relaxation of the PAES is much slower than at lower strain levels, and the total relaxation is also reduced. Similar behavior is noted in Nafion® however, the degree of relaxation reductions is larger for the PAES. This could be problematic in an operating fuel cell as the PAES may not be able to relax high stresses, resulting in decreased mechanical lifetime.

In addition, as the molecular weight of PAES was increased the Young's modulus, yield strength, and stress and strain at break also increased. This increase in mechanical properties of the PAES with increased molecular weight is likely due to an increase in the number of polymer chain entanglements [31]. An increased number of entanglements would restrict polymer chain

motion, resulting in a higher modulus, and greater ductility as the chains require higher stresses to disentangle. It was also shown that, for random copolymer PAESs consisting of two sulfonated blocks, increases in molecular weight and block lengths had little effect on the storage modulus or onset of the α-transition [74]. This behavior is assumed to occur because the molecular weights tested were above the threshold values at which molecular weight has an effect on material properties. In addition, these multiblock copolymers consisting of two sulfonated blocks were two brittle at the lowest molecular weight to form a freestanding film, and only the largest molecular weight and block length withstood a dynamic temperature sweep. Therefore mechanical properties increase with increasing molecular weight and block length, however, random copolymers appear to have better mechanical properties and would likely survive the operating fuel cell environment much longer.

The effect of thermal annealing at 170°C on the tensile properties of sulfonated poly(phenyl sulfone) was shown to increase the storage modulus and delay the onset of the α-relaxation, due to the formation of crosslinks between polymer chains [72]. In addition, the effect of 2% zirconium phenylphosphonate on the tensile properties of 40%sulfonated biphenyl sulfone PAES at ambient conditions was examined [31]. The author showed that with the addition of the inorganic filler, the yield strength, and stress and strain at break increased as compared with the non-reinforced PAES. This increase in mechanical properties was believed to occur because the zirconium phenylphosphonate interacts strongly with the sulfonic acid moieties. Therefore more dispersed hydrophilic/hydrophobic phases are formed, resulting in an increase in chain entanglements, which is beneficial as discussed previously.

One of the benefits of poly(arylene ether)s is the ability to partially fluorinate the material. This can be accomplished by reacting a fluorinated oligomer with a non-fluorinated

oligomer, resulting in a random or multi-block copolymer with hydrophobic and hydrophilic blocks. Fan et al. examined the effects of molecular weight and block length on the storage modulus of partially fluorinated biphenyl sulfone PAES multi-block copolymers [75]. Contrary to the study completed by Badami with two hydrophilic blocks, these multi-block copolymers easily formed free standing films for testing. Dynamic mechanical results show a decrease in the glassy storage modulus and an increase in the onset temperature of the α-transition with increasing molecular weight and block length. Therefore, a shorter block length increases the glassy modulus, while a longer block length delays the onset of the α-relaxation. Additionally, the rubbery modulus appears to be the same for all block lengths. Tensile testing of a similar partially fluorinated biphenyl sulfone PAES examined the effect of the degree of sulfonation on the mechanical properties [76]. An increase in the degree of sulfonation results in a decrease in the Young's modulus, an increase in the strain at break, and effectively no change in the tensile strength. Therefore the PAES begins to behave as a more rubbery material with increasing sulfonic acid content. Finally, the storage modulus of another similar partially fluorinated biphenyl sulfone PAES was examined with respect to the effects of thermal annealing [77]. It was shown that the glassy storage modulus greatly increased when the material was annealed at 195°C vs. 110°C, however the α-transition still occurred at the same temperature, and the rubbery modulus was decreased slightly when annealed at a higher temperature. The authors believe that annealing at a temperature above the glass transition of the fluorinated block, creates a preferred co-continuous nanophase-separated morphology, resulting in the changes noted in the storage modulus.

The mechanical properties of PAES materials appear to make them a good candidate as an alternative fuel cell membrane. However, although not discussed herein, the water uptake of

these materials can range from 50-300% depending on the degree of sulfonation, block length, and thermal treatment. These water uptake values are significantly higher than those of Nafion® and could result in very large induced hygrothermal stresses during RH cycling. Therefore, while these membranes maintain excellent mechanical properties, the water sorption and swelling behavior needs to be examined further to ensure the material can withstand fuel cell operating conditions.

1.2.4. Constitutive Property Characterization of Blend Membranes

Some of these alternative membranes, such as PAESs are very promising for use in fuel cells, however, as compared with Nafion®, the mechanical properties and/or mechanical stability of these aromatic hydrocarbon materials may not withstand the harsh operating conditions of a fuel cell. Therefore, to help improve mechanical durability but still maintain low production costs, researchers have begun investigating blend membranes. Blending provides a simpler and less expensive process for material design than creating and synthesizing new molecules. In addition, it is easier to tailor material and morphological properties by adjusting the blend component ratios. In recent years multiple blend membranes have been studied for use in fuel cells typically blending one acidic and one basic material [78-80], one sulfonated and one hydrocarbon material [81, 82], two sulfonated materials [83-86], or one sulfonated and one fluorinated material [87-100].

Gourdoupi et al. investigated alternative hydrocarbon membranes, blending a polyether containing pyridine units with a co-polyether containing pyridine units [81]. The copolyether was chosen because it exhibits a high glass transition temperature, and good thermal and oxidative stability. Because the copolyether is not easily doped with phosphoric acid, used to increase proton conductivity, the copolyether was blended with the homo-polyether due to its

excellent acid uptake properties. Due to the similarity of these molecules the authors hoped a miscible blend would be created, and decided this had occurred after observing a singular glass transition between the two blend component glass transitions. Increasing the amount of the homo-polyether such that it is the major blend component, results in a delay in the onset of the α-transition, whereas the glassy storage modulus of about 1000 MPa does not appear to be affected by blend composition. When these blends are doped with phosphoric acid, the storage modulus is decreased by two orders of magnitude to 10 MPa at low temperatures, and the modulus declines more quickly, resulting in the α-transition moving to ~135°, as opposed to the 250°C noted for non-doped membranes. This large decrease in mechanical properties with acid doping may not make it suitable for the harsh conditions encountered in an operating fuel cell.

Polysulfones are typically amorphous, high glass transition, high stiffness materials that are difficult to manufacture into the thin films necessary for fuel cell membranes. Therefore, Linares et al. created multiple binary and ternary blends with polysulfone using two thermoplastic elastomers, ethylene-propylene-diene terpolymer and hydrogenated poly(butadiene-styrene), as well as polyphenylsulfone. The authors note from DSC and DMA measurements that all glass transitions of the components were retained in each blend, and thus all blends are considered incompatible. In addition all blended membranes showed a decrease in the glassy storage modulus as compared with the component storage moduli, consistent with a phase separated material. The storage modulus reported at room temperature, above the α-transition for almost all blends, ranged from 350-1200 MPa, however the storage modulus at higher temperatures was not reported. The authors note excellent proton conductivity for all blends and the mechanical properties at ambient conditions are excellent. However, it is highly likely that these incompatible blends will phase separate at higher temperatures, resulting in

possible failure at the interfaces between the blend components. Therefore, it is likely these blends are non-mechanically robust materials and likely would not work well in fuel cell applications.

Sulfonated PEEK blends have been investigated by Arigonda et al. and Sgreccia et al. to improve the mechanical properties under hydrated conditions while maintaining or improving the proton conductivity. Arigonda et al. examined blends of sulfonated PEEK with poly(ether sulfone) because chemical groups of both polymers are identical, and thus expected to blend well together [83]. The blend was declared miscible based on the existence of only one transition located between the two component transitions, as measured by both DSC and DMA. The storage modulus of the dry and hydrated blend membranes is almost identical to that of dry sulfonated PEEK. Tensile testing also showed an increase in the yield and ultimate strength of the blends as compared with pure sulfonated PEEK, while the ductility of the blend membranes is reduced by 50-80%. In addition, the Young's modulus decreases with increasing poly(ether sulfone) content under dry conditions, and increases with increasing poly(ether sulfone) content under immersed conditions. The authors believe the improved properties of the blend under hydrated conditions, as compared with pure sulfonated PEEK, is due to the addition of the poly(ether sulfone). This is possibly because the non-ionic poly(ether sulfone) interacts with the non-ionic portion of sulfonated PEEK inducing a better channel morphology for sulfonic acid interaction, water uptake, and proton conductivity.

A different sulfonated PEEK blend was investigated by Sgreccia et al., who incorporated a small amount of sulfonated and/or silylated poly(phenyl sulfone) with the sulfonated PEEK [84]. The addition of pure sulfonated poly(phenyl sulfone) decreased the Young's modulus and ultimate strength of the blended material, however the addition of silanol greatly increased the

Young's modulus and ultimate strength of the blended material. The authors believe this occurs because the silanol groups strongly interact with the sulfonic acid groups of the sulfonated PEEK, and the large phenyl-silanol side chains provide additional stiffening. Despite the increased mechanical properties, these blends show a severe reduction in ductility to less than 5% strain, making them unlikely candidates for use in fuel cells.

To improve the mechanical stability of sulfonated poly(styrene-ethylene-butylene-styrene) (SEBS) hydrocarbon membranes, Bhavani et al. incorporated sulfonated polysulfone. Based on x-ray diffraction data, the authors believe a compatible blend was created by the lack of crystalline peaks in the blended materials, implying a strong association of the sulfonated polysulfone with the sulfonated SEBS, resulting in the prevention of crystallite formation. The tensile strength was observed to double with 10% sulfonated polysulfone content. This was believed to occur based on a shift in the OH-stretching band of the blended material, implying interactions occur between the sulfonic acid groups of the sulfonated SEBS and the sulfonated polysulfone. Therefore, the incorporation of the high tensile strength sulfonated polysulfone even at low loading levels, greatly improves the mechanical properties of the blended membrane, however the highest tensile strength reported, just above 8 MPa, is still quite a bit lower than Nafion® at values reported of approximately 30 MPa.

As noted previously, one of the only drawbacks to sulfonated PAESs is the large degree of swelling that occurs upon hydration. Therefore, in an effort to reduce swelling but maintain excellent mechanical properties and proton conductivity, Bi et al. examined blends of crosslinked sulfonated PAESs and sulfonated polyimides [86]. Based on optical clarity under both dry and hydrated conditions, the authors believe this blend system to be miscible. With the incorporation of the sulfonated polyimide, in-plane swelling at 30 and 80°C showed a marked reduction as

compared with pure sulfonated PAESs, and has values consistent with those of Nafion®. In addition, the yield strength, as well as stress and strain at break were greatly increased in the blended systems, showing ductilities greater than 100% strain. Therefore it is highly likely this blended membrane system would have excellent mechanical durability under operating fuel cell conditions, and should be considered as a cheaper, easier to produce, proton conducting fuel cell membrane.

Multiple authors have also investigated blending sulfonated hydrocarbon polymers with fluorinated polymers, such as poly(vinylidene difluoride) (PVDF) and poly(vinyilidene difluoride-co-hexafluoro propylene) (PVDF-HFP) to create materials similar to perfluorinated Nafion®. Utilizing PVDF rather than another hydrocarbon material, allows for the incorporation of a material with high chemical resistance, mechanical toughness, excellent oxidative and electrochemical stability, and is commercially available at a low cost [91, 93]. Recently, Arkema began producing a commercially available hydrocarbon-based membrane blended with PVDF [93]. Mechanical durability was measured using RH cycling from 0 to 150% every 2 min at 80°C. The blend membrane showed minimal air crossover, and lasted the full 20,000 cycles, whereas cast Nafion® failed after approximately 7500 cycles. Thus, this blend membrane has excellent mechanical durability, as well as electrochemical properties and should be considered as a low cost alternative to Nafion® for fuel cell usage.

The extremely poor mechanical properties of sulfonated styrenic-based membranes makes them ideal for blending with a rubbery PVDF component, as performed by Piboonsatsanasakul et al. [92]. However, it is unlikely that a miscible blend would be formed between these two components, and as such the authors incorporated a compatibilizer, polystyrene-poly(methyl methacrylate) block copolymer. The poly(methyl methacrylate) is

known to be miscible with PVDF, while the polystyrene block should interact with sulfonated styrene. A homogenous blend was formed with the addition of the compatibilizer, and the tensile strength increased to 12 MPa, and the elongation to 5%. While these are improvements over the pure sulfonated styrene membranes, the authors point out that these mechanical properties are still not sufficient for use within a fuel cell.

Inan et al. investigated the effect of the type, PVDF or PVDF-HFP, and molecular weight of PVDF incorporated into sulfonated PEEK blends [87]. Based on SEM, TEM, and elemental dispersive analysis, the authors note that sulfonated PEEK appeared homogenously blended with PVDF, however the PVDF-HFP showed phase separation. The authors noted a decrease in Young's modulus, and stress and strain at break for all blend materials, as compared with pure sulfonated PEEK. In addition, incorporation of PVDF at levels greater than 10 wt% resulted in a further decrease in the elongation. Therefore, the mechanical properties of sulfonated PEEK were decreased by the addition of all types of PVDF, but could be improved if the system were compatibilized.

Multiple authors have investigated the blending of sulfonated SEBS with PVDF in an effort to increase the mechanical durability of the highly rubbery membrane material. Bhavani et al. noted minimal change in the glassy storage modulus and α-relaxation of the blend with PVDF content up to 15%, as compared with pure sulfonated SEBS [85]. To improve the homogeneity of the sulfonated SEBS/PVDF blend, compatibilizers were explored. Seeponkai et al. examined the effect of a polystyrene-poly(methyl methacrylate) block copolymer compatibilizer for use in sulfonated SEBS/PVDF blends [95]. The addition of 5 wt% compatibilizer did increase the tensile strength and elongation of all blend compositions, however these mechanical properties were far below those of Nafion®, and as such are not viable for use in fuel cells. Mokrini et al.

added as little as 2% methyl methacrylate-butyl acrylate-methyl methacrylate (MMA-BA-MMA) compatibilizer and noted the formation of a dispersed morphology with reduced domain sizes, indicating a decrease in the interfacial tension between the two blend components [94]. The authors also showed an increase in the Young's modulus with the addition of MMA-BA-MMA compatibilizer, measuring moduli greater than Nafion® for all blend ratios. In addition, the MMA-BA-MMA compatibilizer greatly increased the strain at break with increasing PVDF content, noting elongations up to 500%. Whereas the polystyrene-poly(methyl methacrylate) block copolymer compatibilized blend examined by Seeponkai et al. did not show a vast improvement in mechanical properties, this MMA-BA-MMA-compatibilized blend membrane shows excellent mechanical properties and may be a candidate as an alternative fuel cell membrane depending on proton conductivity and hygrothermal swelling properties.

The fracture properties have also been investigated for two hydrocarbon/PVDF blend membranes. The commercial membrane produced by Arkema was shown to have more than twice the tear strength of extruded Nafion® at the given testing condition (not provided) [91]. A more in-depth study at multiple temperatures and humidities was performed via knife slit on a perfluorocyclobutane/PVDF-HFP (PFCB/PVDF-HFP) blend by Gordon et al. [96, 97]. The authors found a decrease in fracture energy with an increase in cutting rate and temperature, similar to Nafion® and Gore-Select™ membranes, however the trend with increasing humidity is unclear. In addition, the fracture energy of the blend membrane is greater than that of Nafion® at all conditions analyzed, and is similar to or better than Gore-Select™ 57 membranes. The increased fracture energy of this blend material implies it is more resistant to fracture than even the PTFE-reinforced membranes, which could result in greater resistance to the formation of pinholes and thus greater mechanical durability in an operating fuel cell.

1.2.5. Biaxial Constitutive Property Characterization of Fuel Cell Membranes

Up to this point, discussion has focused on uniaxial property characterization. However, in a fuel cell, the membrane is constrained biaxially, and it is thus useful to also understand the biaxial mechanical properties of a membrane. The biaxial stress and strain of numerous membranes have been examined utilizing a pressure loaded blister or bulge test [26, 44, 100-104]. Membranes investigated using pressurized air include cast Nafion®, extruded Nafion®, PTFE reinforced PFSA Gore™ Gore-Select® 57, and the blend membrane PFCB/PVDF-HFP (70/30 wt:wt). Ramp to burst testing shows the burst strengths at 80°C and 0% RH for the extruded Nafion® and PTFE reinforced Gore™ Gore-Select® 57 are superior to cast Nafion®. Additional fatigue to leak testing was performed at multiple temperatures for cast Nafion® showing a decrease in the stress at leak with increased temperature. Comparison of fatigue to leak results for cast Nafion®, extruded Nafion®, and PTFE reinforced Gore™ Gore-Select® 57 measured at 90°C and 2% RH shows the extruded Nafion® has the longest lifetime and maintains higher stresses under load, while the PTFE reinforced Gore™ Gore-Select® 57 has longer lifetimes than cast Nafion®. Cast Nafion® likely underperforms the other two membranes due to its larger hygral expansion and lower resistance to fatigue and creep damage.

Blister testing of PFCB/PVDF-HFP (70/30 wt:wt) before and after annealing the membrane at 100°C and 0% RH shows an increase in the biaxial modulus and yield strength of the material with annealing [100]. These membranes appeared to have undergone crosslinking during the annealing process, and furthermore, additional crystalline order was seen in small angle x-ray scans of the material. Therefore, it appears the material has undergone chemical and physical changes during the annealing process, contributing to the increased biaxial modulus and yield strength.

Biaxial blister testing was also performed on acrylic polyelectrolyte/PVDF blends [89, 90, 105]. Rather than using air to pressurize the material, these authors created an in-house instrument equipped with a small hemi-spherical probe and a sample holder attached to a motor. To examine the biaxial properties of the membrane, the sample holder was moved in contact with the probe and as the material was pressed onto the probe further, a load cell recorded the force applied to deform the membrane under axisymmetric biaxial conditions. The test set-up was such that the authors could probe multiple points on the same membrane and gain spatial information. This is particularly useful for membranes that have been thermally or hygrally treated, or even tested previously in RH cycling or fuel cell test stands. The authors initially examined a semi-interpenetrating network acrylic polyelectrolyte membrane blended with different types and molecular weights of PVDF. The authors noted the highest biaxial moduli and ultimate strength for samples prepared with PVDF homopolymers as compared to the PVDF-HFP copolymer. It is believed this occurs due to the added flexibility of the HFP side chains in the copolymer. The measured mechanical properties exceed those of Nafion® at multiple blend compositions, and to attempt to improve these further the authors investigated the same membranes filled with different zirconium inorganic particles. The authors found a small increase in the modulus of materials with 0.5% or 1% particle loading, but the toughness of the material was reduced, similar to other reinforced membranes discussed previously. In addition, particle loadings above 1% were found to form large aggregates rather than disperse in the membrane matrix, and as such all mechanical properties were severely reduced.

Water pressurized blisters were utilized to examine the effects of contamination from cations and catalyst platinum dispersion, as well as the effects of cracks in the catalyst layer, on the biaxial mechanical properties of membranes [26, 44, 104]. The authors noted an increase in

the biaxial modulus with increasing cation size and a decrease with increasing temperature, similar to the results reported for other test modes of contaminated or neutralized Nafion®. The authors again note that the increased cation radius would interact with multiple sulfonic acid groups, resulting in a stiffer membrane as observed during testing. In addition, as the platinum content is increased, the biaxial modulus increases, but the stress and strain at break both decrease significantly. This reduction in properties is explained after examination of SEM images that show cracks initiating preferentially at platinum aggregates, and propagating through regions with platinum distributions. Therefore, contaminant materials severely reduce the biaxial strength of a membrane, likely leading to early failure within an operating fuel cell.

Additional biaxial characterization of Nafion® has been performed using a cruciform shaped sample with four dual actuators to create an equal biaxial stress in the center of the membrane, and with bimaterial curvature measurements [11, 106, 107]. Utilizing the cruciform sample, the authors note that the biaxial modulus and yield strength are both greater than their uniaxial counterparts. The biaxial modulus is expected to be greater than the uniaxial modulus, however the yield strengths should be equal based on a von Mises or Tresca yield theory. This disparity from yield theory is thought to be caused by a non-homogenous biaxial stress strain field in the center of the sample, and the difficulty in identifying the beginning of yielding due to the lack of a clear bilinear curve shape. Thus the data obtained using a cruciform specimen may not be entirely accurate, and the simpler blister form may be more useful for characterizing biaxial mechanical properties. In addition, to understand the biaxial stresses developed during hygrothermal cycling, a bilayer speciman was created. As the sample is hydrated the bimaterial strip curves away from the membrane but as the sample is dehydrated the induced stress is relaxed by 80% RH, and a residual stress begins to develop due to the constraint of the

membrane. Monitoring the curvature of the specimen through multiple RH cycles may provide insight into the biaxial stresses developed during fuel cell operation, as well as predicted ratcheting of the tensile stress over time.

1.3 Constitutive Modeling of PEM Materials

1.3.1 1-D Numerical Model of Fuel Cell Membranes

Using these measured mechanical properties, researchers have begun developing models to calculate the hygrothermal stresses incurred in a fuel cell stack, and the resulting effects on the lifetime of a PEM. The first model to incorporate membrane stress calculations was created by Weber and Newman [18]. In addition, this model accounts for hygral expansion, unlike previous macroscopic models which assumed a constant membrane thickness, generally equal to the liquid equilibrated thickness. This one-dimensional model also included terms for the plasticization effect of water on membranes, as well as a term to describe the degree of constraint. The authors found their model predicted the membrane was not fully constrained, rather only approximately 50%, due to the fuel cell stack and calculated a 13 MPa stress at 30°C for a fully vapor equilibrated membrane, and 3.5 MPa stress at 80°C. Although a simplified analysis, this model points out the importance of including the moisture dependence of the membrane in all modeling efforts due to the differences in water flux with changing membrane dimensions as well as the large stresses incurred by the membrane.

1.3.2 2-D Numerical Modeling of Fuel Cell Membranes

Huang et al. further advanced Weber and Newman's model by creating a 2-dimensional elastic-plastic numerical model in a finite element program to examine the internal strain distribution of an MEA under a constrained configuration due to changes in temperature and humidity [22]. They found a maximum tensile strain of 2.6% when decreasing the RH from 75%

to 0%. Solasi et al. further developed Huang's elastic-plastic model constraining the membrane on all four edges and neglecting out of plane deformations, performing plane stress simulations [23]. Just as in Huang's model, Solasi's model is based on changes in moisture and temperature as the only driving forces for the creation of stress in the plane of the membrane. They noted that cycling moisture conditions have a far greater effect than temperature, and when applying a gradient of moisture across the membrane surface the largest strains are seen at the most hydrated edge of the material. Finally, the authors also modeled the stresses around a circular hole in the membrane, noting that stresses exceeded the ultimate strength of the material and therefore cracks are likely initiated at the edges of pinholes.

A similar 2-dimensional linear elastic model was created by Tang et al. [108, 109]. However these authors incorporated the land channel geometry of a fuel cell stack, as well as all material properties for the membrane, gas diffusion layer, and bipolar plates to capture the property mismatch. The authors apply a temperature gradient across the membrane, but a uniform moisture profile, and assume the hygrothermoelasticity theory in which the additional changes in temperature brought about by changes in strain are neglected. Using finite element software, two different bipolar plate alignments are examined, lands aligned and alternating, as well as three different membrane thicknesses, and two different clamping methods in which either a fixed load is applied or a fixed displacement. In all cases the in-plane stresses are always dominant when the RH is increased from 35 to 100%. Compressive stresses are highest between the two lands in the aligned land plate configuration, and at the edge of the land and channel in the alternating plate configuration, with the aligned plates generally having higher compressive stresses than the alternating configuration. In addition, a fixed displacement clamping mode induced much larger stresses than a fixed load clamping mode in all cases. Finally, it was noted

that the larger the membrane thickness, the larger the induced compressive stresses when the humidity is increased.

Kusoglu et. al extended the model created by Tang et al. to examine the mechanical stresses incurred in the membrane when considered as an elastic-plastic material similar to Huang and Solasi [110]. The model increased the humidity from ambient conditions to 100% RH at 85°C, and then returned to ambient conditions, simulating a simplified duty cycle. The authors again note that in-plane stresses are significantly higher than out-of-plane stresses. In addition, at the simulated operating conditions, the compressive stresses are greater than the yield strength of the membrane, and when the cell is cycled back to ambient conditions tensile stresses are developed. Kusoglu utilized the same model to analyze gradients in temperature and moisture across the membrane, as well as the effect of multiple loading cycles from ambient to operating conditions [111]. The authors noted a large stress gradient across the membrane with a moisture gradient, such that swelling was much higher on the cathode side and almost negligible on the anode side. With each cycle from ambient to operating conditions, on the cathode side the membrane cycled from tensile to compressive stresses, both exceeding the yield strength of the material. This large stress gradient could easily lead to bending of the MEA, while the cyclic loading could lead to thinning and the formation of pinholes, all contributing to the accelerated failure of the fuel.

This same elastic-plastic model with a moisture gradient across the membrane and cyclic loading was utilized by Tang et al. to examine the differences in stress incurred by a Nafion® material and a similar PFSA material containing a PTFE reinforcement layer [55]. The reinforced PFSA material has a lower in-plane swelling and higher yield strength than non-reinforced Nafion®, resulting in lower in-plane stresses and increased mechanical lifetime. This

is consistent with other studies that conclude that a reduction in the in-plane swelling of a material will significantly reduce the stresses incurred by the membrane, whereas out-of-plane swelling can be large in comparison with negligible effect on the membrane stresses [111].

To further capture the effects of moisture on a constrained membrane, Kusoglu et al. modified their previous 2-dimensional elastic-plastic numerical model to include both swelling induced stresses and water uptake via diffusion including mechanisms such as electro-osmotic drag [112]. When the membrane is constrained due to the bi-polar plates, the water distribution is altered, resulting in the accumulation of water at the cathode and less water at the anode than in a non-constrained membrane. Thus, this simulation is similar to their previous work and all results agree well in that the large stresses are mostly confined to the cathode region corresponding with observed localized deformation of MEAs after operation.

Bograchev et al. and Martemniov et al. used the model developed by Kusoglu modified to account for edge effects near seal joints by modeling all channels and joints, as well as more realistic clamping effects utilizing two fastening elements to emulate bolts rather than a constant displacement or constant applied stress [113, 114]. The authors note a large discontinuity in the stress distribution at the interface between the seal joint and the GDL, resulting in a sharp increase in the normal stresses, as well as all other components of the stress tensor. It is believed this singularity in the stress arises due to bending of the bipolar plates caused by the bolt fasteners, as well as the difference in stiffness between the GDL and the seal material. This large stress formed at the edges as compared with the center of the membrane implies failure is more likely to occur around the seal. Bograchev et al. also use their model to examine the stresses developed during start-up of a fuel cell, prior to cell equilibration [115]. They note that the stresses change drastically in the first 100s, but stabilize quickly thereafter, with plasticity

occurring around 70s at the seal joint with a corresponding large discontinuity in the normal stresses in the same location. In addition, Martemniov et al. used the same model to examine the stresses created by assembly of the fuel cell [116]. Again, it was noted that a large stress discontinuity arises at the seal joint, however in this case the authors point out it is prior to any thermal or humidity cycling has occurred and is purely due to the pressure distribution created by the bolts. Finally, it was determined that a bolt torque of 15.8 Nm is necessary to cause plastic deformation without any temperature or moisture effects.

1.3.3 Comprehensive Fluid Dynamics Fuel Cell Models Used to Examine Mechanical Durability

Up to this point, all models have been simplified 1- or 2-dimensional set-ups. However Al-Baghdadi et al. created a full 3-dimensional model multiphase, elastic-plastic, non-isothermal PEM fuel cell model utilizing comprehensive fluid dynamics (CFD) incorporating thermal strains to examine the mechanical behavior of the membrane [117]. This full 3-dimensional model also provides a prediction of the local current density distribution, leading to a higher accuracy prediction of the temperature distribution and thus thermal stresses in the membrane. The authors show the highest strains are developed at the highest temperatures, which occur at the cathode side implying major heat generation occurs here. They also point out that the distribution of strains will induce bending which is likely to lead to delamination of the membrane from the GDL. In addition, local hot spots can be generated when the GDL thickness, porosity and thermal conductivity are decreased, as well as wider gas channels and thicker membranes. These hot spots will likely lead to localized bending and decreased fuel cell lifetime.

Al-Baghdadi et al. extended their model to account for hygral expansion and water management including gas and liquid phase moisture in the same domain and examined the effect of operating conditions [118]. The authors determined that higher operating temperatures reduce the temperature gradient, but increases the Mises stresses, while an increased pressure and stoichiometric flow ratio both decrease the temperature gradient and the Mises stresses. Finally, Al-Baghdadi altered this model to be used with air-breathing membranes, in which the cathode side of the cell is directly exposed to ambient conditions, and came to the same conclusions as in their earlier publications [119].

An additional 2-dimensional linear-elastic non-isothermal CFD model was created by Serincan and Pasaogullari, combining it with a structural mechanics model [120]. The authors examine various effects of water in the system, noting that due to electro-osmotic drag the cathode has more moisture than the anode as back diffusion is unable to overcome these effects. Therefore a gradient always exists across the membrane despite equal moisture levels in gas inlets. Therefore, the membrane on the cathode side is under compression due to expansion from moisture, while on the anode side the membrane undergoes tension as it dries out. These stresses were shown to exceed the membrane yield limit, implying plastic deformation can occur under normal operating conditions.

1.3.4 Constitutive Modeling of Fuel Cell Membranes

While numerical modeling has been a main focus of the literature, Kusoglu also developed a constitutive equation and corresponding phenomenological model to describe elastic-plastic behavior in the membranes at different temperature and moisture conditions [24]. This model is based on the G'Sell-Jonas approach in which stress is expressed in terms of

equivalent strain and strain rate. The modified equation that accounts for both temperature and humidity is given as:

$$\sigma(\varepsilon, T, H) = K_0 e^{-(\alpha T + \beta H)} \left(1 - e^{-W_0(1-\varpi H)\varepsilon}\right) e^{h_0(1+h_1 H)\varepsilon^2} \quad \textbf{[1.1]}$$

where the first term accounts for the change in the proportional limit due to temperature and moisture changes, the second term accounts for the nonlinear stiffness and its dependence on moisture, and the third term accounts for strain hardening and its relationship to moisture. This modeling approach describes the decrease in the yield strength with increasing temperature and humidity conditions, as well as the strain hardening behavior up to about 30% strain. However, above 30% strain the model overpredicts the stresses in the material because the viscoelastic behavior of the membrane is not accounted for and as such the relaxation of the membrane stresses is not incorporated in the model.

Kusoglu noted that the above constitutive model describes humidified PFSA membranes, however immersed membranes appear to behave as elastomers and can thusly be described by rubber constitutive equations [29]. Specifically, the authors investigated Moony-Rivlin and Ogden formulations. They note that both models capture the rubber like uniaxial deformation of the PFSA, however the Ogden formulation provides a better fit of the experimental data. Thus the authors propose that the G'Sell-Jonas constitutive model be used at low water contents to describe PFSA deformation, and the Ogden rubber model be used at water contents greater than 40%.

While the models discussed thus far provide good insight into material behavior in an operating fuel cell, they do not capture the time dependence or viscoelastic behavior of PEM

materials. Therefore, to more accurately describe the stress state of the PEM, Lai et al [12, 15, 16] proposed a one-dimensional linear viscoelastic constitutive model in the form of:

$$\sigma_x(\varepsilon,t,T,\lambda) \approx \int_0^t E(t-\xi)\frac{d[\varepsilon_x(\xi)-\alpha\cdot T(\xi)-\beta\cdot\lambda(\xi)]}{d\xi}d\xi \qquad \textbf{[1.2]}$$

where σ is the uniaxial stress, t is time, $T(\xi)$ is the change in temperature from a reference condition, $\lambda(\xi)$ is the change in the moles of water molecules per mole of sulfonic acid group in the membrane from a reference condition, E is the uniaxial relaxation modulus, ξ is the time parameter, ε is the strain, α is the linear coefficient of thermal expansion, and β is the linear coefficient of hygral expansion. To account for a time dependent modulus, the authors utilized the time temperature moisture superposition principle, creating a master curve and corresponding hygral and thermal shift factors. Multiple RH cycles were applied as input to the model at constant temperature, and the changes in strain over the hydration and dehydration of the membrane were examined. It was noted that compressive stresses formed during hydration and reached a maximum at the highest level of moisture, and then relaxed toward a zero stress state. Tensile stresses were induced during dehydration, reaching a maximum at the lowest moisture level, and then relaxing toward a zero stress state. However it was also noted that with subsequent cycles, the tensile stresses increased, implying that further cycling could cause the tensile stresses to exceed the strength of the material resulting in failure of the fuel cell. Finally, the authors note that a larger humidity swing or a faster hydration and dehydration rate result in larger stresses in the membrane. Thus for design purposes, if a fuel cell could be operated with better system control, better membrane lifetime could be achieved.

More recently, Khattra et al. extended Kusoglu et al.'s linear-elastic plastic models to include time dependence, creating a constitutive model to describe the hygrothermal mechanical

time-dependent response of the membrane [121]. The authors adapted a two layer viscoelastic-plastic model to include strain rate dependence, and incorporated the model into commercial finite element software defining material temperature and moisture dependence based upon tensile testing and stress relaxation data. Predictions of the tensile and stress relaxation data are very good, and as such the authors created a model consisting of half a land/channel fuel cell geometry, and cycled the humidity from dry to about 100% RH at 80°C over various time scales. The authors note that longer hold times at humidified conditions result in larger tensile stresses under dry conditions due to the longer relaxation times under the humid compressive state. In addition, if a moisture gradient is applied across the membrane, to account for cathode flooding and electro-osmotic drag, the stresses in the membrane are reduced than if the water content is the same at both the anode and cathode. Finally, the stresses developed using their time-dependent model are larger than those predicted previously when time dependence was ignored, emphasizing the importance of incorporating time dependence to better understand the stresses developed during operation, and corresponding membrane lifetimes.

1.3.5. Non-linear Modeling of Fuel Cell Membranes

While the previous 1-dimensional constitutive models account for material time dependence, it does not account for non-linear behavior of the membrane. Due to the large strains developed by PEMs due to hygral expansion, it is likely plastic deformation occurs during fuel cell operation, and as such, including plasticity as well as time dependence in a stress model is important for capturing true material behavior. The first viscoplastic model was created by Solasi et al. as a two-dissipative mechanisms model with parameters dependent on temperature and moisture content [122]. This model can be represented as an elastic-plastic network in parallel with an elastic-viscous network, allowing for the separation of the rate-dependent and

rate-independent behavior of the material. The model accurately captures the over stress and observed strain rate dependence, as well as strain-hardening. However, while it predicts the small strain relaxation behavior as well as the correct relaxation times, it over predicts the final relaxation values.

Improving upon Solasi et al.'s viscoplastic model, Silberstein and Boyce created a three-dimensional elastic-viscoplastic model also accounting for the moisture and temperature dependence of the membrane [20]. Similar to Solasi, Silberstein and Boyce have split the stress response of the membrane into two mechanisms, an intermolecular deformation mechanism acting in parallel with a nonlinear molecular network alignment mechanism. This simple elastic-viscoplastic model captures the linear-elastic response, the rate-dependent yield phenomenon, nonlinear strain hardening, as well as the temperature and moisture dependence of the elastic modulus and yield stress. However, it fails to capture nonlinear unloading behavior seen under cyclic loading conditions. Therefore, the authors modified the model to include a backstress in the intermolecular mechanism, assuming the membrane develops a local back stress around plastically deformed regions that assists in reverse deformation during unloading. Including this additional term allows the model to accurately capture both uniaxial loading and unloading as well as temperature and moisture dependence of the membrane.

1.3.6. Biaxial Stress Modeling of Fuel Cell Membranes

While the previously discussed models capture uniaxial behavior well, a more accurate model could be created by considering the biaxial constraint of a membrane in an operating fuel cell. Silberstein and Boyce collected biaxial stress data on Nafion® utilizing a cruiciform specimen and applied their previous elastic-viscoplastic model to a biaxially deformed membrane [107]. Although no parameters were changed to fit the biaxial stress data, the model

predicts the initial stiffness, yield behavior, and post-yield behavior all during the loading of the sample. However, it over predicts the forward and reverse plastic deformation, and under predicts the strain recovery of a specimen in the buckled state. This model is not entirely accurate but does predict multiple biaxial cyclic loadings of the membrane well. Based on the success of this model, Silberstein and Boyce used it further combined with a nonlinear finite method to predict the bimaterial curvature of a membrane bonded to a GDL when hydrated and dehydrated [106]. The model shows excellent qualitative and quantitative agreement with experimental data. Therefore, the authors applied the model to a membrane in a fuel cell land channel set-up, similar to Kusoglu and Tang [24, 55, 108-112]. This fuel cell model similarly predicts compressive stresses during hydration, and tensile stresses during dehydration. Strains are largest within the channel where the membrane is not constrained by the bipolar plates. Finally, the development of plastic strains and tensile stresses upon cycling is in good agreement with mechanically driven failures observed experimentally.

1.3.7. Models Utilized to Examine Effects of Sub-Freezing Temperatures on Fuel Cell Membrane Stresses

Recently, membrane models have been utilized to examine material behavior cycling from sub-freezing temperatures to operating conditions. He et al. created a 1-dimensional model to describe the water migration and formation of an ice lens between the Nafion® and catalyst layer based on porous media flow and soil frost heave mechanisms [123]. This model helps explain the origin of holes in the GDL after freeze-thaw cycles, as well as delamination of the membrane from the GDL. Sun and Zhou used a thermal linear elastic 3-dimensional numerical model to examine the effects of start-up, braking, and collisions on the mechanical durability of a fuel cell undergoing freeze cycling [124]. As discussed previously, a linear elastic model will

not truly describe the material properties, but it provides a basis for looking at the effects of inertial loading on membranes. The authors conclude that by incorporating a heat insulator start up can be completed within three minutes from sub-freezing conditions prior to beginning the electrochemical reaction, thereby reducing hotspots and early degradation of the material. Similarly, the heat insulator would allow heat to be maintained within 1 week of shut off, keeping the membrane from going below freezing, preventing ice lens formation. Finally, they note that acceleration, braking, and collisions all result in large deformations of the membrane, sufficient enough to reduce lifetime or even cause failure. Kusoglu et al. also applied their model to examine the mechanical response of a membrane at sub-freezing temperatures [112]. Upon cooling below freezing, the magnitude of the in-plane stresses increases, and the maximum tensile stresses are much higher than those obtained via cycling at from ambient conditions and above. It is believed this occurs due to the increased stiffness of the material at low temperatures. These large stresses observed by multiple authors could be detrimental to mechanical durability, and it is important to understand the impact of freeze-thaw cycles on membranes.

1.3.8. Mesoscale Modeling to Examine the Effects of Morphology on Mechanical Properties of Fuel Cells

Beyond moisture and temperature effects, other authors have begun to realize the importance of morphology in not only proton conductivity and chemical stability, but also mechanical durability. Qi and Lai created a mesoscale model to examine the influence of two different morphologies on the mechanical properties of membrane materials to to understand why extruded membranes show a 10x longer lifetime than cast membrane [125]. A spherical morphology was used to represent cast membranes, and a cylindrical morphology for extruded

membranes. A finite element method was used to apply a displacement to volume cubes of each morphology, assuming linear-elastic behavior. Water is incorporated into the mesoscale model of each morphology, and the dry material is assumed to be isotropic, such that anisotropic properties that arise due to hydration are a direct result of the morphologies. In both morphologies the peak stress is located at the water/polymer smeared interface, with increasing stresses at higher water contents. In addition, the peak stress is always lower in the cylindrical morphology, by as much as 30% at low water contents due to the sharper interface found in the spherical morphology. Therefore, the increased lifetime of extruded membranes as compared with cast could be attributed to the cylindrical morphology of the material. Based on these results the authors recommend a cylindrical morphology that is oriented through the plane, rather than parallel as observed with extrusion, to both increase mechanical durability and proton conductivity.

1.4. Time Temperature Superposition

1.4.1 Time Temperature Superposition Principle

As previously mentioned, the time dependent modulus can be incorporated into constitutive modeling to capture the viscoelastic behavior of fuel cell membranes. This is frequently done by using a Prony series fit of a master curve created using the Time Temperature Superposition Principle (TTSP). The TTSP states that a change in temperature is equivalent to a shift along the logarithmic time or frequency scale, if the relaxations in a material all have the same temperature dependence. This Principle allows for data to be taken over a short time scale and many temperatures, and then shifted to form a single master curve at a reference condition over a larger time scale. Therefore material behavior can be predicted at times too short to be

measured experimentally, and at times longer than economically feasible to continue experiments.

This principle was initially developed for, and is most directly applicable to thermorheologically simple materials, meaning that the viscoelastic behavior of a material at one temperature, can be related to that at another temperature by a change in the time scale alone. [126, 127] In addition, the molecular processes that occur in a thermorheologically simple material will be the same at different temperatures, such that all processes are accelerated by the same amount at a given temperature. However, a thermorheologically complex material is likely to have molecular processes with differing temperature dependences, for example, the temperature dependence of the motions associated with the alpha relaxation would be different than for the motions associated with the beta relaxation. Additionally, thermorheologically complex materials could have molecular events and conformations that occur at a temperature, T_1, that do not occur at a different temperature T_2, such as changing morphologies with heat treatments [128]. Although having less basis, TTSP has been extended to thermorheologically complex materials, especially over narrow time windows where a single mechanism dominates [129, 130]. Beyond thermorheological simplicity time temperature superposition is considered applicable when three conditions are met; the matching of shapes of adjacent curves is obtained, the thermal shift factors are the same value for all viscoelastic functions, and the temperature dependence of the thermal shift factor has a reasonable form [131]. It is important to note that the form of the shift factors is developed empirically from the data and then later fit with an appropriate expression. In addition, TTSP is only applicable if the material remains morphologically and chemically the same over the temperature range examined.

Although the TTSP was originally developed empirically, it can be shown to be mathematically true based on the kinetic theory of polymers [132, 133]. The definition of the stress relaxation modulus is known to be dependent on both time and temperature as follows:

$$E(t,T) = \int_0^\infty H[\tau(T),T]e^{\frac{-t}{\tau}}d\tau \qquad \textbf{[1.3]}$$

where $H[\tau(T),T]$ is defined as the relaxation spectrum, a continuous distribution function of relaxation times, t is time, and τ is a discrete relaxation time [132]. The Rouse theory of polymer molecular motions suggests that $H(\tau(T),T)$ is not explicitly dependent on temperature, rather the temperature dependence is implicit in the relaxation time. Therefore, the stress relaxation can be rewritten as such:

$$E(t,T) = \rho T\int_0^\infty h[\tau]e^{\frac{-t}{\tau}}d\tau \qquad \textbf{[1.4]}$$

where $h[\tau]$ has no explicit temperature dependence, and ρ is the density of the polymer at temperature T [132]. The kinetic theory of polymers shows the ratio of relaxation times at two different temperatures can be expressed as a shift factor:

$$a_T = \frac{\tau}{\tau_o} = \left(\frac{\eta}{\eta_o}\right)\frac{\rho_o T_o}{\rho T} \qquad \textbf{[1.5]}$$

here η is the viscosity of the polymer. Multiplying the stress relaxation function by the shift factor gives the following:

$$\left(\frac{\rho_o T_o}{\rho T}\right)E(t,T) = \rho_o T_o\int_0^\infty h[\tau]e^{\frac{-t}{\tau}}d\tau \qquad \textbf{[1.6]}$$

And using the shift factor, this can be rewritten with an alternative time scale:

$$E(t',T) = \rho_o T_o \int_0^\infty h[\tau] e^{\frac{-t'}{\tau}} d\tau \quad \textbf{[1.7]}$$

where *t'* is:

$$t' = \frac{t}{a_T} \quad \textbf{[1.8]}$$

Therefore, the modulus can be expressed as a function of reduced time, *t'*, and temperature:

$$E(t,T) = \left(\frac{\rho T}{\rho_o T_o}\right) E\left(t' = \frac{t}{a_T}, T_o\right) \quad \textbf{[1.9]}$$

showing the modulus at one temperature is equivalent to the modulus at another temperature after modifying the time scale with a shift factor. This is a formal mathematical statement of the TTSP as applied to the relaxation modulus, but it is also true of other viscoelastic constitutive functions such as creep, storage modulus, and loss modulus.

It is common to define $\left(\frac{\rho T}{\rho_o T_o}\right)$ as b_T, a vertical shift factor. This vertical shift was developed as a correction factor for the modulus based on the theory of rubber elasticity, in which the modulus is proportional to the absolute temperature. However, the application of this shift factor has received some debate. If the major chain response mechanism is dominated by entropy, such as coiling and uncoiling, to an applied deformation, then rubber elasticity would be an appropriate description for the material. Conversely, if the response mechanism is straining of bond angles and lengths as in the glassy region for materials, or chain slippage as in the terminal region, rubber elasticity is not an appropriate description [134]. In addition, the correction b_T provides is typically small, and as such is often ignored.

As defined previously the horizontal shift factor for relaxation moduli is the ratio of a given relaxation time to a relaxation time at a reference condition. This can be redefined as:

$$a_T = \frac{t_T}{t_{T_o}} \qquad \textbf{[1.10]}$$

where t_T is the time necessary to reach a given response at a particular temperature, T, and t_{To} is the time necessary to reach the same response at the reference temperature, T_o. Therefore, temperature does not affect the shape of the master curve, only the position. At temperatures above T_o the material has a shorter relaxation time or a faster response to an imposed deformation, and therefore log a_T is less than 1. The opposite is true of temperatures below T_o, and at T_o log a_T is equal to 1 [134].

1.4.1.1. Arrhenius Shift Factor Fit

The horizontal shift factors automatically developed during the shifting process are typically examined and fitted with an appropriate expression. One of the first models developed for shift factor fitting is based on the Arrhenius form of the activation energy, and was established from the Site Model Theory [135]. This theory describes two sites, separated by an equilibrium free energy. For a polymer, these two sites on a molecular level could represent two chain conformations, gauche and trans. During a mechanical relaxation process, the applied stress causes a change in the energy separating the two sites, thus creating a change in the population of the two sites. The frequency of molecular jumps between the two conformations, ν, is given by:

$$\nu = \frac{A'}{2\pi}\exp\left(\frac{-\Delta G}{RT}\right) \qquad \textbf{[1.11]}$$

where A' is a constant, R is the universal gas constant, and ΔG is the free energy barrier height between the two equilibrium conformational states. This equation can be rewritten as:

$$\nu = \frac{A''}{2\pi}\exp\left(\frac{\Delta S}{R}\right)\exp\left(\frac{-\Delta H}{RT}\right) = \nu_o \exp\left(\frac{-\Delta H}{RT}\right) \quad \textbf{[1.12]}$$

where *A"* is a constant, *ΔS* is the change in entropy, and *ΔH* is the activation energy, which is truly an enthalpy, however it will be referred to as an energy. The activation energy for the molecular jump process can be approximated as:

$$\Delta H = -R\left[\frac{\partial(\ln \nu)}{\partial\left(\frac{1}{T}\right)}\right] \quad \textbf{[1.13]}$$

which is known as the Arrhenius equation because Arrhenius first showed this equation to describe the influence of temperature on the speed of chemical reactions. To show the application of the Arrhenius equation to shift factors, consider a tan δ curve at two different temperatures, T_1 and T_2, the peaks of which occur at two different frequencies, ν_1 and ν_2. If the tan δ curve at T_2 is used as the reference temperature, and the other tan δ curve is shifted to create a master curve, a shift factor would be obtained as follows:

$$a_T = \frac{\nu_1}{\nu_2} = \frac{\exp\left(\frac{-\Delta H}{RT_1}\right)}{\exp\left(\frac{-\Delta H}{RT_2}\right)} \quad \textbf{[1.14]}$$

$$\log a_T = \frac{\log \nu_1}{\log \nu_2} = \frac{\Delta H}{2.303R}\left\{\frac{1}{T_2} - \frac{1}{T_1}\right\} \quad \textbf{[1.15]}$$

A more general form of the Arrhenius shift factor is given by:

$$\log a_T = \frac{\Delta H}{2.303R}\left\{\frac{1}{T} - \frac{1}{T_o}\right\} \quad \textbf{[1.16]}$$

It is important to note that the site model, and therefore Arrhenius equation, is only applicable to relaxation processes that maintain a constant activation energy, such as localized motions in an amorphous region of a semi-crystalline polymer below its melting temperature or an amorphous polymer below its glass transition temperature. The large temperature dependence of a polymer glass transition does not have a constant activation energy, and therefore this region and above should be fit with more applicable models.

An interesting application of the Arrhenius model to shift factors was performed by Seitz and Balazs on highly crystalline ethylene-butene copolymers.[136] They chose to employ the Arrhenius fit because for highly crystalline polymers below their melt temperatures, the amorphous region between crystals is too small to have motions that could be described by other models such as free volume, but the molecular motions occurring still have a temperature dependence. The authors performed stress relaxation tests at 0.5% strain for 30 and 100 minutes, and then created a master curve that extends to 10000 hours. The authors verified that predicted behavior from the master curve is valid by performing stress relaxation tests for 1000 hours and comparing the data sets. The predicted behavior and the real behavior match exactly and the shift factors have a reasonable form, following Arrhenius behavior, implying the TTSP is applicable for this highly crystalline material above its glass transition.

1.4.1.2 Free Volume Shift Factor Fit

1.4.1.2.1 Doolittle Shift Factor Fit

An alternative approach to fitting shift factors for master curves of an amorphous material is based on the concept of free volume. Free volume represents the unoccupied space within a polymeric material. This could be thought of as holes or voids on the molecular scale between polymer molecules due to packing irregularities [131]. Free volume is approximately a constant fraction of the total volume below the glass transition; however it can decrease further below the glass transition due to physical aging. Physical aging occurs in materials that are not in thermodynamic equilibrium, resulting in the slow rearrangement of polymer chains until equilibrium is reached. In addition it is believed the occupied volume increases at the same rate above and below the glass transition. Therefore, the additional volume gained above the glass transition is attributed to excess free volume [135].

The transition state model developed by Bueche states that a polymer unit cell cannot move until the local fractional free volume exceeds some critical value [135]. Therefore, polymer chain mobility at any temperature is primarily dependent upon the amount of free volume present in the material. If this concept is believed, then relaxations could be expressed in terms of free volume rather than temperature. This relationship between free volume and chain mobility, or viscosity, is logarithmic in nature as shown by Doolittle [137]. This expression, known as the Doolittle equation is shown below:

$$\eta = Ae^{\left(B \Big/ \frac{v_f}{v_o}\right)} \qquad \textbf{[1.17]}$$

$$\ln \eta = B\left(\frac{v_o}{v_f}\right) + \ln A \qquad \textbf{[1.18]}$$

where A and B are constants for a specific material, and $\frac{v_f}{v_o}$ is the fractional free volume of the system, which will be referred to as f from here on out. A thermal shift factor with a Doolittle form can be defined by comparing the viscosity, η, of a system at a temperature T, to the viscosity, η_o, at a reference temperature, T_o:

$$\ln a_T = \frac{\ln \eta}{\ln \eta_o} = \frac{\ln A + B\left(\frac{1}{f}\right)}{\ln A + B\left(\frac{1}{f_o}\right)} \qquad \textbf{[1.19]}$$

$$\ln a_T = B\left(\frac{1}{f} - \frac{1}{f_o}\right) \qquad \textbf{[1.20]}$$

$$\log a_T = \frac{B}{2.303}\left(\frac{1}{f} - \frac{1}{f_o}\right) \qquad \textbf{[1.21]}$$

Kovacs et al. collected dynamic shear data on poly(vinyl acetate) in the glass transition region to test if the relaxation times in this region were controlled by free volume as hypothesized.[138] Therefore the authors calculated shift factors using the Doolittle equation with B set to unity, f_o equal to 0.0225 based on the equilibrium free volume at 35°C, and f determined from the coefficient of thermal expansion of free volume and isothermal contraction measurements. These shift factors were then applied to the storage and loss modulus data and

while the storage modulus shifts well to multiple temperatures, the loss modulus does not. The authors believe the poor shifting of the loss modulus is also due to free volume, as vertical shifting brings these curves into alignment. When the vertical shifts are plotted against the fractional free volume, a single curve is formed, indicating the initial poor shifting is directly related to free volume, however no further explanation is provided. In addition, the authors empirically shifted tan δ data and compared the empirical shift factors with the calculated shift factors from the storage and loss modulus. These shift factors match well, and only deviate from the Doolittle equation at very small free volumes, implying that the molecular motions are governed by free volume, and the Doolittle equation is a good fit for this data. Similar testing was performed on poly(n-butyl methacrylate) by Meyer et al. and the same conclusions were reached for this material [139].

1.4.1.2.2 Williams-Landel-Ferry Shift Factor Fit

In practice, many people use a modified version of the Doolittle equation to fit the shift factors from the glass transition to 100°C above the glass transition [131, 140]. The fractional free volume is assumed to increase linearly with temperature as follows:

$$f = f_o + \alpha_f (T - T_0) \qquad \textbf{[1.22]}$$

where α_f is the coefficient of thermal expansion of free volume for a material. This expression can then be substituted into the Doolittle thermal shift factor equation, developing the following expression:

$$\log a_T = \frac{B}{2.303}\left(\frac{1}{f_o + \alpha_f (T - T_o)} - \frac{1}{f_o}\right) \qquad \textbf{[1.23]}$$

$$\log a_T = \frac{B}{2.303}\left(\frac{-\alpha_f (T - T_o)}{f_o{}^2 + f_o \alpha_f (T - T_o)}\right) \quad \textbf{[1.24]}$$

$$\log a_T = \frac{\left[\frac{-B}{2.303 f_o}\right](T - T_o)}{\left[\frac{f_o}{\alpha_f}\right] + (T - T_o)} \quad \textbf{[1.25]}$$

$$\log a_T = \frac{-C_1 (T - T_o)}{C_2 + T - T_o} \quad \textbf{[1.26]}$$

where C_1 and C_2 are constants used to fit data, and are frequently known as universal constants. These universal constants were determined from fitting data on several polymer systems, and are defined as follows:

$$C_1 = \frac{-B}{2.303 f_o} \approx -17.4 \quad \textbf{[1.27]}$$

$$C_2 = \frac{f_o}{\alpha_f} \approx 51.6^o C \quad \textbf{[1.28]}$$

however, in practice these constants are typically dependent on the polymer system [131, 140]. If the reference condition is selected as the glass transition temperature, then the fractional free volume has been found to be 0.025 ± 0.005 for many polymeric systems and therefore the system variation of C_1 and C_2 are due to B and α_f, although α_f should be on the order of 10^{-4} /°C [131]. The variation in B is thought to be associated with the different hole sizes required for local segmental motions in different polymers, while the variation in α_f is due to the direct dependence on the local motions of the polymer backbone and side chains [131]. Therefore, it is suggested

that C_1 and C_2 be determined empirically for different systems, using the universal values when no other option is available.

This form of the horizontal shift factor (**Eqn [1.26])** is known as the Williams-Landel-Ferry equation (or WLF). The equation was initially developed for 17 different polymers including concentrated solutions and gels. It was initially thought that each material would have a unique shift factor:temperature relationship, however, the results showed the temperature dependence was universal and not based on the chemical structure over the temperature range from the glass transition to 100^{o}C above the glass transition [141]. This universal function implies that the nature of the free volume change and molecular rearrangements is effectively the same in all supercooled organic and inorganic liquids, polymer, and non-polymeric systems, completely independent of the molecular structure.[140] Therefore, these systems show a dependence on temperature primarily through free volume, and are independent of the time dependence of mechanical properties, applying equally to narrow and broad relaxation distributions.

The WLF equation is not typically applicable below the glass transition because of its basis in free volume, unless a sample has undergone physical aging. As the temperature is decreased the free volume decreases as molecules become more tightly packed and molecular motions slow. This reduction in free volume correlates with a discontinuity in the slope of the specific volume at the glass transition which also corresponds to a discontinuity in the coefficient of thermal expansion [132]. The WLF equation predicts a monotonic increase in the shift factors with decreasing temperature, however, the inflection in the slope of the specific volume and coefficient of thermal expansion results in an inflection in the shift factor plot [131].

Therefore the shift factors increase less rapidly with decreasing temperature than the WLF equation predicts, as demonstrated by Brinson [132, 133].

Brinson characterized the creep properties of Hysol 4290, an epoxy. The glass transition temperature was measured via changes in the coefficient of linear expansion and extended to a volumetric measurement. Knowing that the WLF equation was not applicable to data collected below this 90°C glass transition, Brinson empirically shifted the creep data to form a master curve. The shift factors were then plotted against the WLF equation with C_1 and C_2 equal to the universal constants, as shown in **Figure 1.1**. The creep shift factors match the WLF equation well above the glass transition, but below 90°C it is clear that the shift factors increase less rapidly than the WLF equation predicts, as expected.

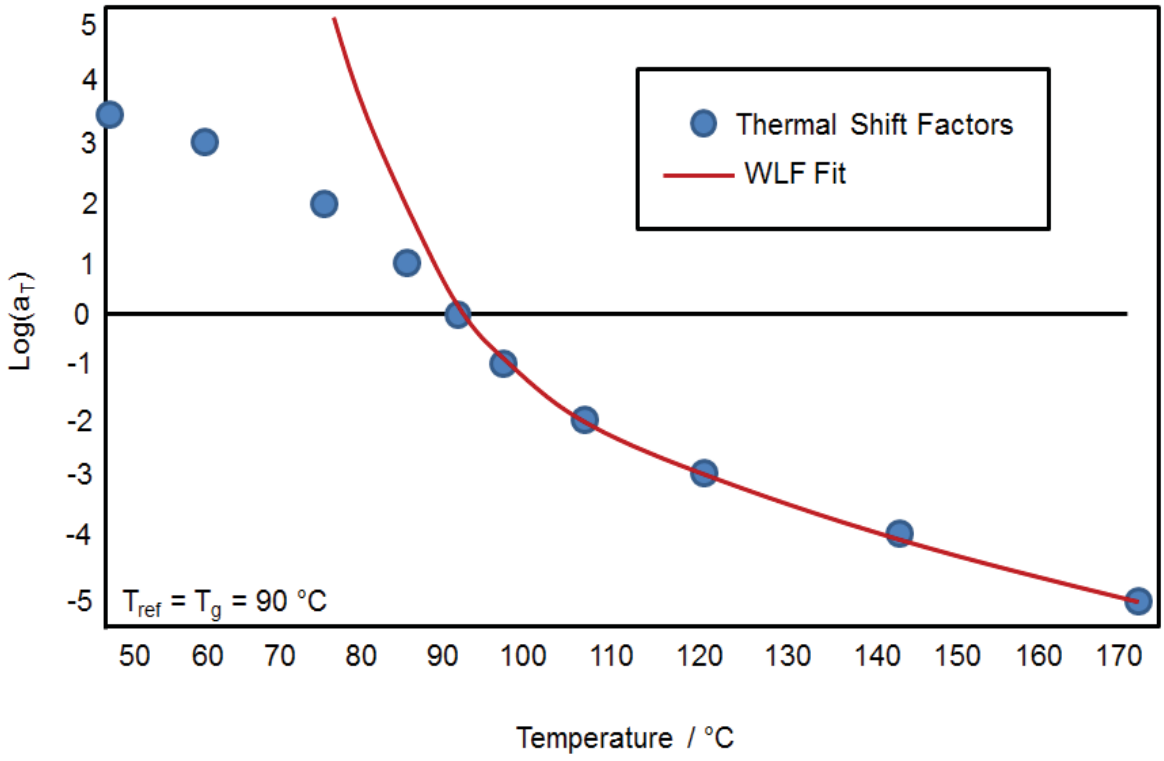

Figure 1.1. Schematic comparing empirical shift factors with the WLF equation, showing the disagreement below the glass transition.

Due to the inapplicability of the WLF equation below the glass transition, often times an Arrhenius fit is used to fit shift factors below the glass transition, and the WLF equation applied above. This fitting procedure was followed by Ishisaka and Kawagoe on an as-cured epoxy, Cape2002, as shown in **Figure 1.2** [142]. It is clear that the dual fit works well to describe the behavior of this epoxy system, whereas only one of the fitting procedures would only partially describe the system.

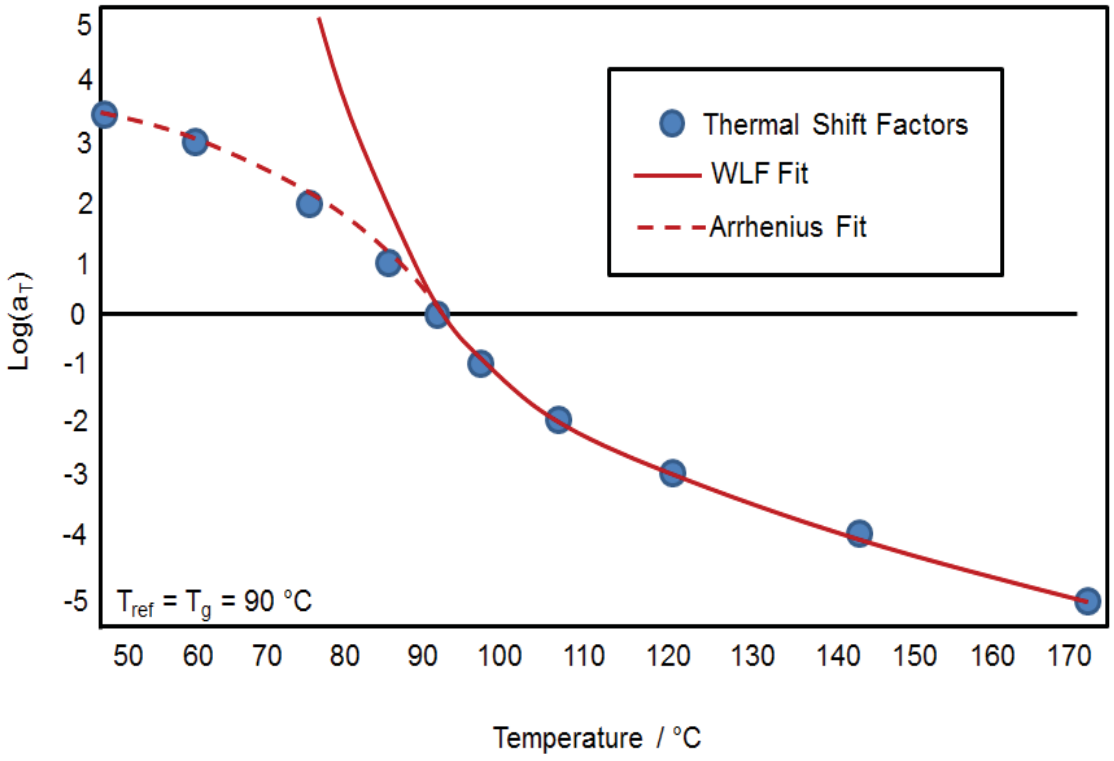

Figure 1.2. Schematic of a dual shift factor fit utilizing an Arrhenius fit below the glass transition, and the WLF fit above.

The WLF equation is not believed to apply above 100°C beyond the glass transition. This is because well above the glass transition of polymers, or the freezing point of liquids, the viscosity varies widely and is dependent upon the molecular structure of the material. This

difference can be seen in **Figure 1.3** where two different polymer systems are compared, and deviations in the high temperature behavior are noted between the two curves [140]. Due to the limited temperature range of the WLF equation many researchers have examined alternative equations to fit a wider range of data.

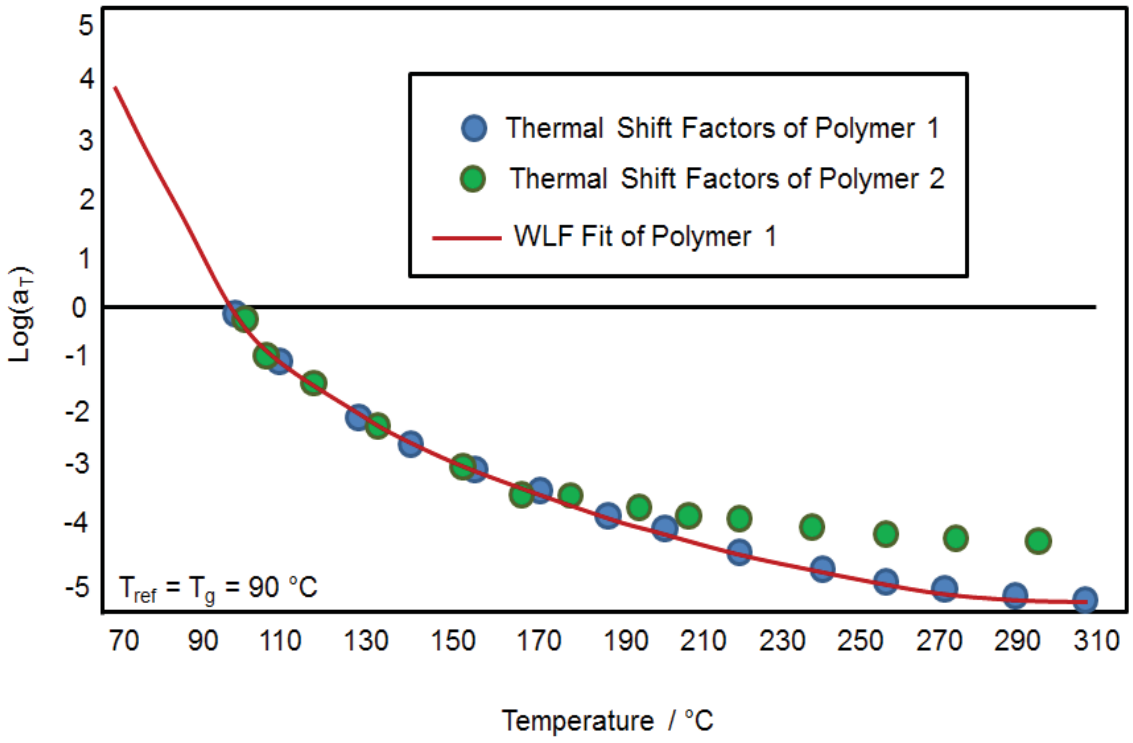

Figure 1.3. Schematic comparing the thermal shift factors of two different polymers, displaying deviations at high temperatures from the WLF equation.

1.4.1.2.3. Vogel-Fulcher-Tamman-Hesse Shift Factor Fit

An alternative to the WLF equation is the Vogel-Fulcher-Tamman-Hesse equation (VFTH), which is also based on free volume and will be shown to be of the same form as the WLF equation. The VFTH shift factor fit as originally proposed empirically by Vogel is as follows:

$$\log a_T = c_1^{\,o} \frac{[T - T_o]}{[T - T_\infty]} \qquad \textbf{[1.29]}$$

where T_∞ is known as the Vogel temperature, or the temperature at which the viscosity becomes infinite, and is typically approximately 50°C below the glass transition.[131, 143] An empirical equation to fit viscosity data was later developed independently by Fulcher, and Tamman and Hesse of the same form as Vogel, and utilizing the Vogel temperature. The VFTH equation is however equal to the WLF equation if C_1 is set equal to $c_1^o(T\text{-}T_\infty)$ and C_2 is set equal to $(T_o\text{-}T_\infty)$. In addition, the VFTH equation has the same temperature limitations as the WLF equation, and choosing one form over the other typically depends upon the ease of use with other analyses being performed on the same data set, rather than a material dependence.

1.4.1.2.4 Alternative Free Volume Fits

Kenner et al. investigated the shear compliance of a two-part rubber-filled adhesive, FM-73 using an in-house creep torsiometer above and below the glass transition region [144]. The authors were able to successfully shift all of the data to form a single master curve, using both vertical and horizontal shift factors. The horizontal shift factors contain a discontinuity around the glass transition. The authors were expecting this behavior based on the free volume theories previously discussed. Therefore, to fit the entirety of the shift factors, the authors performed two separate WLF fits, one above the glass transition, and one below. The dual WLF fit appears to fit the shift factors well, however for modeling purposes many researchers prefer to use a single equation.

1.4.1.2.4.1 Brostow Shift Factor Fit

Thus, Brostow created a shift factor equation based on free volume with continuity through the glass transition [145]. The author argues that the glass transition does not represent a discontinuity in the volume because the glass transition is known to occur over a narrow temperature region, rather than at a specific temperature as commonly defined. In addition, Brostow believes that because Kovacs showed continuous volume curves for multiple polymers that a discontinuous glass transition does not exist. Using the Doolittle equation, Brostow defines a thermal shift factor based on the reduced volume, $\tilde{v}$, a ratio of the specific volume to the occupied volume:

$$\ln a_T = A + \frac{B}{\tilde{v} - 1} \qquad \textbf{[1.30]}$$

where A and B are both constants. Brostow later defines the reduced volume as a function of the reduced temperature, $\tilde{T}$, a ratio of the test temperature to the reference temperature, creating a final shift factor function of the form:

$$\ln a_T = A - \frac{B}{\rho'}\left[\frac{1 + \rho'\left(1 - \tilde{T}\right) - p'\left(1 - \tilde{T}\right)^{\frac{1}{3}}}{\left(1 - \tilde{T}\right) - \left(1 - \tilde{T}\right)^{\frac{1}{3}}}\right] \qquad \textbf{[1.31]}$$

where ρ' is a material specific constant. As frequently done with the Doolittle equation, B is set to unity, leaving two unknowns to solve for, A and ρ'. Using the same data as presented by Kenner et al., Brostow uses his shift factor equation to describe the entire set of shift factors. It is seen that Brostow's shift factor fit describes the data set well, better than the WLF fit for temperatures below the glass transition. Some deviation does occur from the shift factors above the glass transition, however the overall fit is quite decent proving that one equation can be used to fit shift factors over a wide temperature range.

1.4.1.2.4.2. Magill and Li Shift Factor Fit

Magill and Li also suggest a shift factor fit based on free volume and a temperature ratio, similar to Brostow, rather than the temperature difference used in the Doolittle and WLF equations:

$$a_T = \frac{\eta}{\eta_o} = f\left(\frac{T - T_g}{\phi T_g}\right) = g\left(\frac{T}{T_g}\right) \qquad \textbf{[1.32]}$$

where ϕ was found to be 0.24 to provide a good fit for all materials [146]. The authors plotted the ratio of the viscosities against the ratio of the temperatures for tri-α-naphthylbenzene, 1:2 diphenylbenzene, α-phenyl-o-cresol, selenium, polybutadiene, polystyrene, and polydimethylsiloxane. The Magill-Li fit matches all the data sets well covering 16 orders of magnitude above and below the glass transition for organic liquids, metals, and polymers, whereas the WLF fit deviates from the data after about 3 decades. Therefore, the authors argue that their shift factor equation is a universal function for all materials, and can be determined if the glass transition and viscosity at a given temperature are known.

1.4.1.2.4.3 Litt Shift Factor Fit

The previous shift factor models all require the determination of at least two unknowns, however Litt introduces a shift factor fit with only one unknown [147]. Litt contends that the linear dependence of free volume on temperature as used by Doolittle and WLF is purely empirical and invalid. Based on experimental data, this dependence should instead be of $T^{3/2}$ as derived by Gee, Bueche, and Simha and Weil. In addition, this shift factor is based on an effective free volume, rather than the total free volume. This is reasoned because only the fraction of free volume, or holes, that have a large enough radius for a polymer segment to move

from one low energy position to another one, will contribute to segmental motion and local relaxation processes. The final form of Litt's shift factor is:

$$a_T = \frac{\ln \eta}{\ln \eta_o} = \frac{\pi^{\frac{1}{2}}}{\left[\frac{\alpha_\ell \Delta T}{1.5 - \alpha_\ell} \cdot \frac{\pi^{\frac{1}{2}}}{\Delta T^{\frac{3}{2}}}\right] T^{*\frac{3}{2}}} \left(\frac{T^*}{\Delta T}\right)^{\frac{3}{2}} \left(1 + \frac{T^*}{\Delta T}\right)^{-1} \exp\left(\frac{T^*}{\Delta T}\right) \qquad \textbf{[1.33]}$$

where α_l is the coefficient of linear thermal expansion, and T^* is a characteristic temperature that is proportional to the energy necessary to generate a hole with a large enough radius for segmental motion to occur. Although this equation appears to be more complicated than shift factor fits previously presented, it only requires fitting one parameter, T^*.

Litt compares his fit to that of WLF for many materials and overall it appears fairly similar, although it fits data up to 200°C above the glass transition and is better in some cases, like that of Polystyrene. Despite being similar in fit, Litt believes this form of the equation is superior for two reasons. First, the WLF equation predicts an infinite viscosity at a temperature approximately 50°C below the glass transition due to the definition of free volume used during development. The Litt equation avoids this problem because the effective free space reaches zero at 0K. Second, this theory reconciles the different free volume predictions of Doolittle and Williams-Landel-Ferry, and Simha-Boyer and Litt-Tobolosky. The former stated that there is 2.5% free volume at the glass transition, and the latter found 5-15%. Therefore, the effective free volume defined by Litt corresponds to the 2.5% of Doolittle and Willams-Landel-Ferry, and the total free volume corresponds to the Simha-Boyer and Litt-Tobolosky findings. Thus, the Litt theory more comprehensively accounts for molecular behavior, but he does note that if a

material free volume does not follow the $T^{3/2}$ relationship then the shift factor fit may not work well.

1.4.1.2.4.4. Plazek Shift Factor Fit

Plazek also thought the choice of linear dependence between free volume and temperature by Doolittle was arbitrary, and caused fits based on free volume to not work well over a large temperature range of a material.[148] Although Litt chose to make a theoretically accurate model, Plazek chose to create a simpler form, by modifying the VFTH equation:

$$\ln a_T = \ln A + \frac{C}{(T - T_\infty)^n} \qquad \textbf{[1.34]}$$

where the exponent *n* is fit along with the constants *A* and C. The VFTH equation was chosen over the WLF form because adherence to a straight line can be checked visually. By allowing the free volume dependence on temperature to vary from unity, a much better fit over a much larger temperature range is obtained for polystyrene and polyvinylacetate. However, Plazek notes that while this fit works very well, changing the exponent on the fractional free volume is purely empirical and likely does not have a theoretical or physical significance, as the exponent can be greater or less than one.

1.4.1.3. Applicability of TTSP

An example of a polymer that follows the TTSP well with WLF-form shift factors is shown via storage compliance data taken on poly(n-octyl methacrylate) at 24 different temperatures over approximately 3 decades [131]. This data was empirically shifted until each curve overlaped at a reference temperature of 100°C and the shift factors obtained follow a WLF behavior. The same shift factors were used to successfully create a master curve for loss

compliance data collected on the same material. Therefore, all three criteria for the applicability of time temperature superposition, and thermorheological simplicity, have been met. However, not all materials meet these requirements.

Poly(n-octyl methacrylate) is an amorphous polymer, and while the master curve ranges from the glassy to the rubbery region, the material physical structure remains the same – only the rate of molecular rearrangement is increased [149]. As described previously, the glassy region may not shift well with the transition region due to different types of molecular motions creating the relaxations in both of these regions. Within the glassy region viscoelastic responses occur due to local backbone and side chain motions. In addition, highly crystalline materials also have different molecular mechanisms with different temperature dependences, such as uncoordinated motions in the crystal lattice or deformation in the amorphous regions between crystallites. As stated previously, the morphology must remain the same for the TTSP to be applicable, and often with crystalline materials this is not the case, as the degree of crystallinity changes with temperature [131].

Furthermore, Ngai and Plazek contend that most materials do *not* follow the TTSP because they do not have the same molecular motions and therefore relaxation mechanisms over an entire temperature range [126]. They believe that the underlying conjecture of free volume or configurational entropy may describe properties well as a mean field approximation, but likely oversimplify or completely miss intermolecular cooperative dynamics. Molecular motions on short length scales have been proven to be dependent on the chemical structure of a material such as in the glassy or terminal regions of a material. However, over the softening zone, or the transition from glassy to rubbery, molecules are moving through long range cooperation, and these motions are independent of the chemical structure. This difference may indicate the

temperature dependence of the short length scales and long range cooperative motions are quite different, and could signify the breakdown of thermorheological simplicity.

For this reason, Ngai and Plazek suggest that data used with the TTSP should be collected over more than three decades of time or frequency, otherwise superposition may appear to be possible, when in fact it is not. The only way to truly establish thermorheological simplicity is to capture the temperature dependences of the different molecular motions over a common temperature range. An example of the importance of taking data over a large time range is provided with poly(isobutylene). Tan δ data was collected at different temperatures over 5-7 decades using a combination of creep and dynamic measurements. As the temperature is increased a shoulder on the right side of the main peak appears. This is attributed to the torsional motions along the chain of units smaller than the submolecule, whereas the main peak is attributed to the modified Rouse modes. However, when tan δ data was determined from creep compliance data collected over 5 decades, from -74 – 27^{o}C, and shifted using TTSP, a smooth master curve was obtained, however, it does not have the shoulder that was present in the data collected over a larger temperature and frequency range. Therefore, the master curve collected over a smaller temperature and frequency range obscures the true viscoelastic nature of polyisobutylene, and it becomes clear that data must be taken over large temperature and frequency ranges to obtain the true material behavior.

Ngai and Plazek also provide examples of TTSP failure and thermorheological complexity in high molecular weight entangled polymers in both the softening and terminal regions, as well as low molecular weight polymers. The failure of the high molecular weight materials in the softening and terminal zones is again attributed to the different molecular motions and the corresponding different temperature dependences that occur within the softening or terminal

zones versus the glassy or rubbery regions. The failure of the low molecular weight material is due to a loss of molecular modes, associated with chain backbone motions, as the temperature is decreased. Polymers that have shown similar behavior at high and low molecular weights include polystyrene, polyisobutylene, poly(vinyl acetate), atactic polypropylene, poly(methyl methacrylate), and poly(cyclohexyl methacrylate).

1.4.2. Time Temperature Superposition of Polymer Blends

As stated in the previous section, the TTSP is typically inapplicable to materials with molecular motions that have different temperature dependences. Therefore most applications of the TTSP are primarily performed on homopolymers, and as previously pointed out can even fail for these materials. However, recently, the TTSP has been applied to polymer blends including miscible,[143, 150-166] immiscible,[154, 167-171] and compatibilized blends.[167-169] The literature has reported both the failure [151, 153, 157-161, 163-166, 171] and success [143, 162, 166, 168, 172-175] of TTSP for all three types of blends, and is often contradictory. For example, the miscible polymer blend of poly(ethylene oxide) and poly(methyl methacrylate) was reported to obey TTSP by Wu, and fail TTSP by Colby [159, 168].

Multiple explanations exist for the failure of TTSP for miscible blends. Miscible blends are typically defined as such based on the existence of a single glass transition, however, this assumption is not always accurate. Frequently, a single glass transition is measured for a polymer blend, however the transition is typically much broader than the transitions measured for the individual components [176]. This same broadening is not observed in low molecular weight solution glasses or random copolymers, making the behavior unique to polymer blends. These glass transition measurements are usually performed with a differential scanning calorimeter (DSC), however a DSC cannot resolve phases smaller than 50nm in size, and thus

microheterogenities may exist in the blended system [168]. In fact, it is unlikely a homogenous blend would not have any microheterogeneities due to the intramolecular chain connectivity of each blend component. This creates a self-concentration of each component on the segmental length scale resulting in the retention of component intrinsic characteristics [150, 155]. Therefore, each component will relax in a local environment that is compositionally different from the macroscopic blend [151]. It is these differing local segmental relaxation times that result in the broadening of the measured glass transition [150, 151, 155]. Several explanations have been offered to describe the compositional heterogeneities frequently found in blended systems that result in the observed broadened relaxations.

1.4.2.1. Concentration Fluctuations and Dynamic Heterogeneities in Polymer Blends

The first explanation is that of a concentration fluctuation and dynamic heterogeneity referring to the vacillations of component concentrations and chain dynamics over various length scales [126, 150, 155, 159]. Concentration fluctuations arise due to the local composition varying about its average value. Blends with very small enthalpic interactions, where the interaction parameter χ is near zero, will have large concentration fluctuations. If the correlation length of the concentration fluctuation is on the same size scale as the Doi-Edwards tube diameter each polymer chain will see a very heterogeneous environment [159]. An alternative, yet complimentary idea to the concentration fluctuation is the dynamic heterogeneity. This refers to the different chain dynamics or intrinsic chain mobilities of the blend components, and how they change with different local compositions within the blend. Two similar definitions for a dynamic heterogeneity exist, the first refers to only the heterogeneity that broadens the segmental relaxation of the blended system, and the second more general definition refers to a transient spatial nonuniformity of concentration on any length scale that vanishes when

averaging over a sufficiently long time. The effects of a dynamic heterogeneity are temperature and blend composition dependent and are often enhanced at low temperatures and when the blend components have widely separated glass transitions [126, 150, 155, 160, 161].

1.4.2.1.1. Coupling Model to Describe Blend Material Behavior

Three theoretical models exist to describe the concentration fluctuations or dynamic heterogeneities found in blended polymer systems. The first is that of Roland and Ngai in which they extended their coupling model for homopolymers to miscible binary blends [126, 153, 160, 161, 163, 177]. The coupling model for homopolymers states that a primitive species, such as a polymer chain, is coupled to its environment and other primitive species' via molecular, ionic, electronic, or other interactions. Therefore, relaxation of a primitive species requires cooperative motion by both the environment and the primitive species' itself. These intrachain transitions acquire time dependence when the interactions with neighboring chains build up sufficiently to impede the relaxation. Thus, the mechanical relaxation, *E(t)*, is described by:

$$E(t) = E(0)\exp\left[-\left(\frac{t}{\tau^*}\right)^{1-n}\right] \qquad \textbf{[1.35]}$$

where *E(0)* is the initial relaxation, τ^* is the apparent relaxation time, and *n* is the coupling parameter. The apparent relaxation time and the coupling parameter are related via:

$$\tau^* = \left(\left[1-n\right]\omega_c^n \tau_o\right)^{\frac{1}{1-n}} \qquad \textbf{[1.36]}$$

where ω_c^{-1} is a characteristic time for the intermolecular couplings to manifest, for relaxations involving Van der Waals interactions ω_c^{-1} is on the order of 10^{-10} s. In addition, τ_o is one of the two primitive relaxation times in the Hall Helfand function. However, as previously stated, the degree of cooperativity in a material is not only dependent on the neighboring molecules, but

also on the local environment. In a polymer blend the local environment fluctuates and thus the interchain interactions and correlations will also fluctuate with the local compositional heterogeneities. A higher degree of compositional heterogeneity will result in a distribution of coupling parameters and consequently a distribution of relaxation times, as observed in the broadened transitions of blended systems. The mechanical relaxation can be rewritten in the case of polymer blends to account for this distribution of relaxation times:

$$E(t)_{blend} = \sum_i E_i(t) = \sum_i E_i(0) \int_0^1 \exp\left[-a_i\left(n_i - n^2\right)\right] \times \exp\left[-\left(\frac{t}{\tau_i^*\left(\tau_{i0}, n\right)}\right)^{1-n}\right] dn \qquad \textbf{[1.37]}$$

where the sum is over all chemical species comprising the blend, ie $i = 2$ for a binary blend, $E_i(0)$ scales with the concentration of the i^{th} component, and τ_i^* is an effective relaxation time for individual segments of all components that contribute to the measured relaxation response in their local environments as described by n_i and τ_{i0}. Although the heterogeneity of relaxations described above implies the TTSP is not applicable, it can typically be applied over a limited frequency or time span empirically. The shift factors would then be described by:

$$a_{i,n,T} \equiv \frac{\tau_i^*(n,T)}{\tau_i^*(n,T_o)} \qquad \textbf{[1.38]}$$

in which a broader relaxation is described by a larger coupling parameter, n, and should thusly exhibit a stronger temperature dependence. This increased temperature dependence with increased coupling can be observed through the use of fragility plots in which the shift factors are plotted against the normalized glass transition, T_g/T. For a poly(vinyl methyl ether) and polystyrene blend the curves show increased temperature dependence for an increased polystyrene component in the blend. This implys the addition of polystyrene requires greater coupling or intermolecular cooperativity than in pure poly(vinyl methyl ether). This supports the

theory in that pure polystyrene has less mobility and a higher capacity for coupling than pure poly(vinyl methyl ether). Therefore polystyrene will create a larger hindrance to intermolecular motion of poly(vinyl methyl ether) in a blend, creating an increased coupling parameter with increased polystyrene content.

Alegria et al used the coupling model to explain the failure of TTS for the miscible polymer blend of poly(vinyl ethylene) and polyisoprene [160]. The authors noted an asymmetric broadening toward lower frequencies of the dielectric loss and shear mechanical loss peaks, and that the asymmetry and broadening both increase with poly(vinyl ethylene) content. The poly(vinyl ethylene) has less mobility and a higher coupling capacity than the polyisoprene. Therefore, at low frequencies, the loss spectrums are broadened due to the increased distribution of relaxations caused by the increased coupling of the polyisoprene with the poly(vinyl ethylene), supporting the coupling theory. Similar results were obtained via NMR studies by Chung et al for the same polymer blend system [161].

1.4.2.1.2. Double Reptation Model to Describe Blend Material Behavior

A related idea of the coupling model is that of double reptation as proposed independently by des Cloizeaux and Tsenoglou [178-180]. This theory accounts for the effects of surrounding chains on chain dynamics, or constraint-release effects not initially included in the Doi-Edwards tube model. des Cloizeaux describes the relaxation of a stress point, or entanglement, as a two body process:

$$\frac{G(t)}{G_o} = \left[\sum \varphi_A p_A(t)\right]^2 \qquad \textbf{[1.39]}$$

where ϕ_A is the volume fraction of polymer *A* and $p_A(t)$ is the corresponding average fraction of the tube conserved after a time, *t*. Alternatively, the probability of two polymers, *A* and *B*, being entangled at time *t* is $p_A(t)\ p_B(t)$. The entanglement will be relaxed when either chain reptates away via diffusion or sliding. Therefore the stress state of the material is described by the fraction of original entanglements that remain intact, resulting in a time dependent diffusion equation for entanglement release. This theory therefore accounts for the broadening of transitions observed in polymer blends, and has been used to confirm the failure of TTSP [164].

Zetsche and Fischer created a quantitative model based on the free energy of mixing and the concentration fluctuations to describe the broadening of the glass transition and the asymmetric broadening of relaxation functions [181, 182]. The authors claim that the presence of concentration fluctuations will create fluctuations of concentration-dependent properties of the mixture, resulting in a broadening that corresponds to the distribution of the concentration. To investigate this theory, the authors divided the blend into subcells of size *V*, corresponding to a cooperatively rearranging region, each with a concentration ϕ_i, due to the existence of the concentration fluctuations. Each volume then has a unique glass transition and therefore relaxation time, creating a distribution of relaxations over the entire blend, resulting in the observed broadened transitions. A model was therefore created based on a Gaussian distribution of subvolumes with different concentrations, which was then used to calculate glass transition and subsequently relaxation distributions. Inherent to the model is the assumption that the relaxation of the concentration fluctuation is much longer than the relaxation time of the glass transition process and thus remains stationary. The authors also note that the volumes have radii between 3 and 6 nm, large enough to have their own temperature dependence which must be accounted for in modeling. With these assumptions, the Zetsche-Fischer model describes the

relaxation behavior of poly(vinyl methyl ether) blended with polystyrene and poly(cyclo-hexyl acrylate-*stat*-butyl methacrylate) blended with polystyrene very well. In addition, the model can be used to calculate the size of concentration fluctuations in a given blend using the second derivative of the free energy of mixing, and the structure factor if the volume is small compared with structural lengths in the blend.

Kumar et al. recognized that the Zetsche-Fischer concentration fluctuation model depended only on the average composition of the blend and temperature, resulting in the examination of concentration fluctuations at fixed length scales relative to the control volume. However, because of the self-concentration effect, each local composition has a unique local glass transition, and thus each local composition defines a local cooperative volume. Therefore, it makes more sense to define each cooperative volume self-consistently based on the local composition, rather than a single volume defined by the overall blend composition [183]. The cooperative volume is then defined by:

$$V = \frac{(bd)^3 T_\infty{}^2}{(T - T_\infty)} \qquad \textbf{[1.40]}$$

where b is the monomer size, d is a material specific constant, and T_∞ is the Vogel temperature. The size of the cooperative volume is now a function of the local blend composition, if the components have different Vogel temperatures. For example, regions rich in the low Vogel temperature component will have smaller cooperative volumes. Now, however, the distribution of concentration fluctuations is no longer symmetric about the mean blend composition:

$$P(\phi) \sim \exp\left[\frac{-(\phi - \tilde{\phi})^2 b^2 d^3 T_\infty{}^2}{24\xi^2 \tilde{\phi}(1-\tilde{\phi})(T - T_\infty)^2}\right] \qquad \textbf{[1.41]}$$

where $\widetilde{\phi}$ is the mean blend composition, and ξ is the correlation length of the concentration fluctuations. This function can now have two local maxima depending on the blend composition, one at the mean blend composition, and the other corresponding to fluctuations rich in the low Vogel temperature component, maximizing the temperature differential in the denominator. The authors assert that this is a more accurate description of blend composition as it accounts for blends with a component well above its glass transition. For example, a blend of polystyrene and poly(methyl phenyl siloxane) shows two distinct peaks. The first is centered about the mean blend composition, and has a cooperative volume size of approximately 50 nm. The second is associated with regions rich in poly(methyl phenyl siloxane), resulting in a cooperative volume of about 3 nm. This formulation also describes unimodal distributions, as the Vogel temperatures and glass transition temperatures of the two components become close, a single Gaussian distribution is again obtained.[143, 183-186]

Pathak et al. use the Kumar dynamic scaling model to explain the applicability of the TTSP for polymer blends.[143] First, the TTSP is applicable if the blend components have strong interactions, suppressing concentration fluctuations, which leads to cooperative volumes with the same concentrations. Therefore the distribution of segmental relaxation times is unimodal. Second, if the blend components have dynamic symmetry the TTSP will be applicable. This means that the components have glass transitions and Vogel temperatures that differ by less than 30K, causing each fluctuation to have the same local chain dynamics. This results in a symmetric Gaussian function for which the TTSP is always valid, regardless of the concentration fluctuation sizes. Finally, at temperatures much greater than the Vogel temperature the concentration fluctuation sizes are very small and the differences in chain dynamics are reduced, and thus the TTSP is applicable as long as the blend remains in a single-

phase state. The authors use many examples to explain these criteria, but focus mainly on a blend of styrene acrylonitrile and poly(methyl methacrylate) which shows dynamic symmetry and the successful application of the TTSP.

In addition, Pathak et al. used the Zetsche-Fischer concentration fluctuation model to create a so called phase diagram for miscible blends with weak energetic interactions that can be used to predict if the blend is thermorheologically complex. Using other references from the literature, the authors plotted blends reported to follow the TTSP, and blends that did not. They then constructed a phase boundary line using the inequality:

$$\frac{d\frac{\tau_a}{\tau_b}}{dT} < a \qquad \textbf{[1.42]}$$

where τ_a and τ_b are the relaxation times of the low- and high-glass transition components, and the parameter a is equal to 0.05 K^{-1} based on experimental data. This inequality was applied to a hypothetical 50/50 blend with an interaction parameter of zero, where both components have the same universal WLF constants. The low glass transition was kept constant while varying the high glass transition, and the concentration fluctuation volumes are estimated based on the poly(isoprene) and poly(vinyl ethylene). The blend systems which follow TTSP plotted up and to the left of the phase boundary line, while the blend systems for which TTSP failed plotted down and to the right, creating a correlative model that predicts the application of TTSP very well. The authors note that the phase boundary would be better represented as a broad band rather than a discrete boundary, inside of which TTSP works nearly as well for blends as for homopolymers.

1.4.2.1.3. Self-Concentration Model to Describe Blend Material Behavior

The final theoretical model refers back to the self-concentration effect, in which the local region around one blend component will always be somewhat enriched in the same component due to chain connectivity as mentioned previously. This self-concentration creates a bias in the mean concentration of a local environment experienced by each component. Lodge and McLeish noted that the Zetsche-Fischer model and Kumar model both use cooperative length scales 10 nm or larger near the glass transition, whereas other measures of the cooperative length suggest this value should be around 2 nm [187]. Therefore, the authors suggest that the relevant length scale for determining the local composition is the Kuhn length, and as such the relaxation is taken to correspond to the fastest Rouse mode and is only influenced by the concentration of monomers within a volume of the cubed Kuhn length. This volume is only weakly dependent on temperature, in contrast to the previously described coupling and dynamic scaling models in which the cooperative volume is of such size to be dependent on temperature, causing divergence at the Vogel temperature. Within this volume, centered on one of the two blend components, will always have, on average, an excess of that blend component due to chain connectivity effects. Thus, the effective local concentration (ϕ_{eff}) felt by one of the two components, on average, is described by:

$$\phi_{eff} = \phi_s + (1-\phi_s)\phi \qquad \textbf{[1.43]}$$

where ϕ_s the self-concentration, defined as the volume actually occupied by a Kuhn length's worth of monomers, divided by the cubed Kuhn lenth. This definition assumes athermal mixing, and that local concentrations will only be defined based on the statistics of random packing of connected objects. The authors believe this to be a reasonable simplification because previously reported dynamic effects appear to have no clear correlation to the sign or magnitude of the

interaction parameter, χ. In addition, the small interaction parameters typically found in miscible blends should not affect the local packing significantly.

Although this model emphasizes the average composition experienced by a chain segment rather than the distribution of compositions utilized in other models, it does successfully describe several key features of miscible blend relaxations. The first is the broader glass transition of a blend than its pure components, and the typical asymmetry of blend relaxation curves as described by a 25:75 blend having a broader glass transition than a 75:25 blend, for the lower glass transition component listed first. This result is explained by the flexible component having a higher self-concentration, due to the smaller Kuhn length and therefore smaller associated volume. Larger concentration fluctuations would be seen within this smaller volume, resulting in a larger distribution of relaxation times. In addition, a larger self-concentration will have average dynamics of that component that are similar to the dynamics in the pure component. Thus, larger self-concentrations lead to the breakdown of TTS in blends whose components have large glass transition differences.

Leroy et al. show quantitative agreement of the Lodge-McLeish self-concentration model using differential scanning calorimetry and thermally stimulated depolarization current on poly(vinyl methyl ether)/poly(styrene), poly(styrene)/poly(*o*-chlorostyrene), and poly(vinyl methyl ether)/poly(*o*-chlorostyrene) blends.[188] In addition, Hirose et al. show the validity of the two length scale model, as defined by the two separate cooperative volumes described by the Kuhn length of each blend component, as compared with the single length scale employed previously by Zetsche and Fischer, and Kumar using poly(isoprene)/poly(vinyl ethylene) blends.[166] The Lodge-McLeish self-concentration model is also used to explain the failure of TTSP for poly(isoprene)/poly(vinyl ethylene) blends near the glass transition. The temperature

and composition dependence of the segmental and terminal dynamics was shown to be essentially the same in the blend for both components. Therefore, the failure of TTSP is attributed solely to local effects due to the self-concentration of the blend components, causing each component to retain distinct and separate temperature dependences [151, 165, 166].

The resulting effects of the local environmental differences seen by the blend components, is a nonuniform frictional environment, assuming a Rouse model is used to describe the chain dynamics [150, 151, 153, 155]. This effect could also be described as a nonuniform viscous environment, however the discussion will typically refer to friction rather than viscosity. For the following discussion, a blend with two components, one fast one slow, will be considered. If the concentration of the slow moving component is slightly larger than its overlap concentration, and the average end-to-end distance of the global chain relaxation of the fast component is slightly larger than the global relaxation of the slow component, and the fast and slow components have widely separated glass transitions, then it is highly unlikely that the fast component can achieve the same degree of chain overlap as the slow component. This results in a nonuniform frictional environment that changes with temperature for the global relaxation of the fast chains. Therefore some of the fast chains would see a higher friction during the relaxation process compared with other fast chains. It is consequently thought that the blend therefore behaves as a thermorheologically complex material, and that time temperature superposition no longer holds [150].

Another way of explaining the thermorheological complexity that arises from a frictional nonuniformity deals again with a blend consisting of a fast and slow component. In this system the slow component acts as an antiplasticizer, or obstacle to motion, for the fast component due to its larger segmental friction factor. However, due to the concentration fluctuations throughout

the system, the fast component will see different distributions of the slow component. Therefore, the relaxation process of some of the faster chains will be slowed due to immobile obstacles, while others will not see a reduced friction state, and relax normally. This again creates a nonuniform frictional environment, leading to thermorheologically complex behavior and the breakdown of time temperature superposition [155].

Despite the existence of these heterogeneities, research has shown that miscible, and some immiscible, blends do follow time temperature superposition. For example, if the blend components have a broad molecular weight distribution, it is possible to apply TTSP successfully. This is because the individual characteristics of each blend component become smeared, whereas components with narrow molecular weight distributions retain their individual characteristics. This results in the failure of TTSP, because of the highly defined properties of each component, such as the relaxation time. However, when the properties of each component, such as the relaxation time, become smeared, they are described by a broad distribution allowing TTSP to be successful [158, 159, 168].

Another common example for the successful application of TTSP to polymer blends (miscible or immiscible) is the use of intermolecular interactions between the two components. If the components of a polymer blend do not have specific interactions, TTSP will typically fail if the glass transitions of the components differ by more than 25^{o}C [156]. However, if the components are interacting through hydrogen bonding, ionic bonding, or strong exothermic interactions such as complexation, TTSP is typically successful no matter the difference between the glass transitions [156, 159, 167, 168]. It is thought this occurs because the effects of dynamic heterogeneities and concentration fluctuations are reduced, and that the relaxation of either component is now tied to the other in the case of complexation. Finally, if the shift factors

for the two individual components can be described by the same WLF equation, then TTSP may be successfully applied to the blend due to the similar temperature dependence of the relaxing polymers [189]. However, this method does not guarantee successful application of TTSP, as demonstrated by Colby and Roovers for two different miscible polymer blends [158, 159].

1.4.2.3. Plotting Techniques to Examine TTSP Applicability for Polymer Blends

1.4.2.3.1. van Gurp Plot to Examine TTSP Applicability for Polymer Blends

Several plotting methods are commonly used to determine if TTSP is truly applicable to a blended polymer system. These include the van Gurp plot,[154, 169, 190-194] the Cole-Cole plot, the Han plot, and shifting of loss modulus data. Each plotting technique allows for the observation of temperature dependence that may not be seen in empirically shifted storage modulus data. The van Gurp plot graphs the phase angle, δ, vs. the absolute value of the complex modulus, $|G^*|$.[154] If the different isotherms used to create the master curve will superpose without any time scale shifting, showing temperature independence, then it is assumed that TTSP is applicable, although a viscoelastic explanation for this phenomenon is not currently understood. For example empirical shifting of both the storage and loss modulus of a long chain branched EPDM works well, however in the Van Gurp plot temperature dependence exists, therefore showing that TTSP is not applicable to this system.

Carrot et al. and Li et al. relate typical shapes of van Gurp plots to different polymer morphologies [190, 192]. For neat linear polymers the plots show a plateau at the phase angle of 90^o in low frequency zones, and then monotonically decrease with increasing frequency or modulus. Furthermore, neither the average molecular weight nor polydispersity have an effect on the shape of these curves, while the chemical structure only has a slight influence. Branched

polymers show a minimum that becomes more pronounced with an increasing degree of branching. Blended polymers generally show a decrease in the phase angle compared with the neat components reflecting the general increase in elasticity. In addition, if the blends have a droplet/matrix morphology a minimum and maximum in the phase angle are observed due to the low frequency relaxation that arises due to interfacial effects.

An excellent experimental use of the van Gurp plot is shown by Macaúbas and Demarquette with two immiscible blended polymer systems [169]. The first immiscible blend is of polypropylene and polystyrene (PP/PS), and the second immiscible blend is of a different polypropylene and high density polyethylene (PP/HDPE). Empirical shifting of the PP/PS and PP/HDPE storage modulus works well, resulting in what appears to be a temperature independent master curve. However, the van Gurp plots show temperature independence for the PP/HDPE blend, but not for the PP/PS blend.

The authors then added a block copolymer compatibilizer to the PP/PS immiscible blend and regraphed the van Gurp plot. Their results show temperature independence for the now compatibilized blend. It is believed that the PP/HDPE immiscible blend showed temperature independence without compatibilization because the activation energies of the two components were very similar, 32 kJ/mol and 31 kJ/mol respectively. Whereas the activation energies of the PP/PS immiscible blend were very different, at 53 kJ/mol and 120 kJ/mol, thereby requiring a compatibilizer to overcome the effects of dynamic heterogeneities.

1.4.2.3.2. Cole-Cole Plot to Examine TTSP Applicability for Polymer Blends

An alternative to the van Gurp plot is the Cole-Cole plot, which was originally developed to easily analyze the departure from the expected behavior of dielectric liquids and solids [195].

A complex plane locus is utilized, plotting the imaginary part of the complex dielectric constant against the real part, with each point corresponding to a specific frequency. It was seen that although dispersion theory predicts a perfect semi-circle, both dielectric liquids and solids are more aptly described by circular arcs. The Cole-Cole plot has since been extended to describe thermorheological complexity in polymer blends [192]. The definition of a Cole-Cole plot has been extended from the complex dielectric constant, to plotting the imaginary part of any complex property against the real part, such as the viscosity or modulus. For homogenous blends only one circular arc will appear in a Cole-Cole plot, however, if a second circular arc appears in the right hand side, this indicates a second relaxation mechanism is occurring, corresponding to a second phase in the blend. Therefore, it is assumed that if anything more than a singular arc is obtained in a Cole-Cole plot that the material is thermorheologically complex and TTSP is not applicable.

1.4.2.3.3. Han Plot to Examine TTSP Applicability for Polymer Blends

Very similar to the Cole-Cole plot qualitatively is the Han plot, which charts the log of the storage modulus vs. the log of the loss modulus [196-202]. Therefore, at first glance the Han plot appears to merely be a modification of the Cole-Cole plot, simply minimizing the temperature dependence seen in the Cole-Cole plot, as shown in **Figure 1.4**. Also, similar to the van Gurp plot, the Han plot is used to test for temperature independence in a blend if each temperature isotherm falls on a single line without employing any shifting.

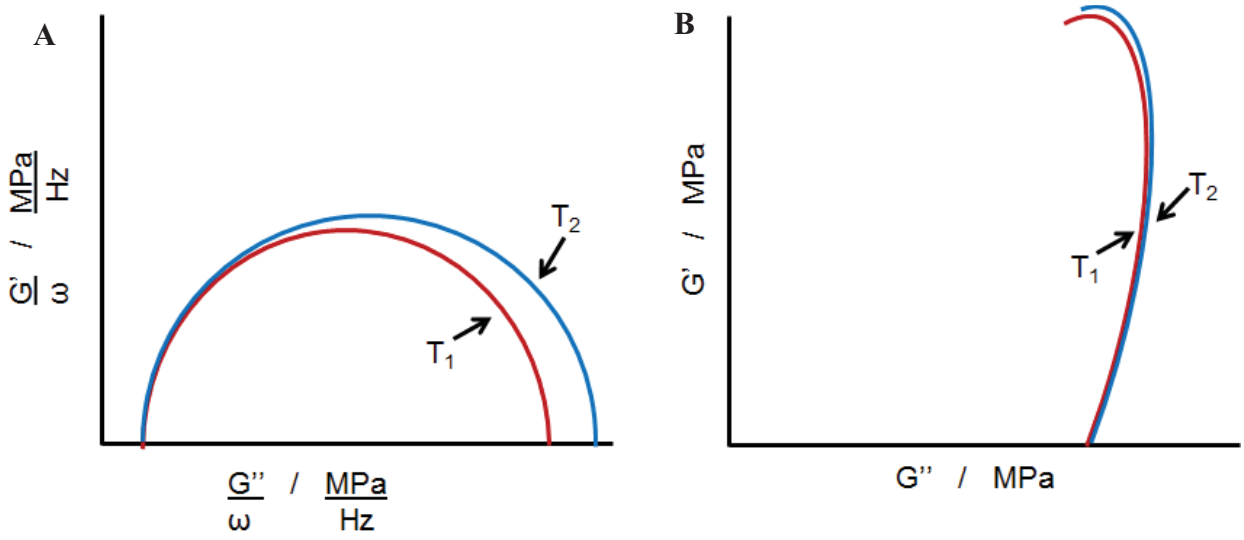

Figure 1.4. Schematics of **(A)** Cole-Cole plot and **(B)** Han plot of a polymer system at two different temperatures.

Han initially qualitatively developed this plotting technique for polymer fluids under shear in the terminal region, noting that plotting the first normal stress difference against the shear stress was temperature independent. He then noted that these stress variables were similar to the loss modulus and storage modulus, and the same qualitative temperature independence could be observed. Therefore, qualitatively, the ratio of the energy dissipated is not very sensitive to variations in temperature, implying the temperature coefficient of the energy dissipated is approximately the same as that of the energy stored in the polymeric system. Han and Jhon later develop a more quantitative explanation based on the Doi-Edwards viscoelastic theory, resulting in the following two equations:

$$\text{For } M < M_e \quad \log G' = 2\log G'' - \log\left(\frac{\rho RT}{M}\right) + \log\left(\frac{\pi^2}{8}\right) \qquad \textbf{[1.44]}$$

$$\text{For M} > \text{M}_\text{e} \quad \log G' = 2\log G'' - \log\left(\frac{\rho RT}{M_e}\right) + \log\left(\frac{\pi^2}{8}\right) \qquad \textbf{[1.45]}$$

where M is the molecular weight and M_e is the entanglement molecular weight. Based on these equations the it can be seen that an increase in temperature from T_1 to T_2 will result in a shift in log G' by the log of (T_1/T_2). However, if, for example, the temperature was increased from 180 to 240°C the value of log G' will only be shifted b 0.054, a value so insignificant that it would barely be noticeable in a Han plot. Therefore, Han modified previous observations to state that log G' vs. log G'' plots give rise to a correlation that becomes virtually independent of temperature.

Han later explains in another publication qualitative aspects of his plot that indicate the failure of a material's temperature independence. He first shows a plot for a polystyrene homopolymer, which shows temperature independence on a nearly straight line with a slope of 2 in the terminal region, with the slope of 2 coming from **Eqns [1.44]** and **[1.45]** as previously developed. He then compares this with an immiscible multiphase blend of polystyrene and poly(methyl methacrylate) (30/70) which shows temperature independence, however there is now a strong kink in the data set. According to Han, this kink indicates the failure of thermorheological simplicity and therefore TTSP failure. He further does not advocate the use of his plots for known multiphase systems. Finally, he compares both plots with that of a miscible polymer blend of polystyrene and polyvinyl methyl ether (75/25). Miscibility for this blend was determined by a single transition seen in a DSC scan; however the Han plot shows clear temperature dependence and Han therefore suggests that this polymer blend system has microheterogeneities that the DSC cannot discern, and thus TTSP does not apply.

1.4.2.3.4. Loss Modulus Shifting to Examine TTSP Applicability for Polymer Blends

It is common for researchers to attempt to construct master curves for both the storage and loss modulus data for their polymer blend systems. It is assumed if one or the other does not empirically shift well into a master curve that TTSP does not apply to the system, despite their relation by Kramers-Kronig. For example the storage modulus of a polyethylene oxide and polymethyl methacrylate blend (35/65) shifted well, however the loss modulus did not [154]. It is believed that the loss modulus did not shift well because this signal is more sensitive to the slow relaxations or viscous interactions than the storage modulus which is dominated by the elastic reponse of the components. Therefore, plotting the loss modulus can provide insight into the existence of nonuniform viscous interactions that occur in a blended system, which cannot be seen in DSC or the storage modulus.

1.4.2.3.5. Tan δ Shifting to Examine TTSP Applicability for Polymer Blends

Lastly, it has been suggested that rather than empirically shifting the storage and loss moduli, that the tan δ is more useful for determining the applicability of TTSP [143]. This is because vertical shifts do not affect the tan δ since it is a ratio of the storage and loss modulus, resulting in the cancelling of the vertical shift. Therefore, the minima and maxima of the tan δ are not changed through the application of TTSP. In addition, when testing utilizing shear rheological measurements, the error in tan δ is approximately ±0.5%, whereas it is ±5% in the storage and loss modulus due to sample loading reproducibility [143].

1.4.3. Extensions of the TTSP

Over the years, the TTSP has been extended to account for the time equivalence of other material properties such as stress [203, 204], drying time[205], filler content [206, 207], and moisture [142, 204, 206, 208-223], across the polymer, biopolymer, agriculture, and composite industries. Again, most of these extensions are based upon Doolittle's free volume theory, and as such it should be noted that any variable that alters the free volume has the potential for predicting long term behavior of a material.

Temperature happens to be the variable most frequently used, however Williams shifted Nylon 6,6 data for applied stress rather than temperature, and Brostow later introduced the derivation of a time-stress shift factor [203]:

$$\ln a_\sigma = \ln\left[\frac{v(\sigma)}{v_{ref}}\right] + B\left[(\tilde{v}-1)^{-1} - (\tilde{v}_{ref}-1)^{-1}\right] + C(\sigma - \sigma_{ref}) \qquad \textbf{[1.46]}$$

where $v(\sigma)$ is the free volume at a given stress level, v_{ref} is the free volume at a given reference condition and is a function of temperature and stress, B is the Doolittle constant, $\tilde{v}$ is the reduced volume as defined previously, C is a constant that represents the effects of varying stress on chain conformations and structures of the material. This shift factor can now be used to describe the long-term behavior of materials using experiments at multiple stress levels, analogous to shifting performed with experiments performed at multiple temperature levels.

Akinay and Brostow applied their concept of stress shifting to a polymer liquid crystal comprised of poly(ethylene terephthalate) and *p*-hydroxybenzoic acid [224]. Data was taken

under a creep mode, over 10-50 J/cm^3 stress levels at 20^{o}C, however it was noted that these stress levels do enter the non-linear viscoelastic regime of the material. Despite this, the authors successfully shifted the data empirically to form a master curve with stress shift factors. The empirical stress shift factors are compared with values calculated using **Eqn [1.46]** and are in good agreement. This implies that the time-stress-correspondence can be used to predict long time behaviors of a material similar to that of temperature.

Perhaps one of the most innovative extensions of the TTSP is to the drying time of tomato slices, in which Khazaei et al. created a doubly shifted moisture content master curve using temperature and tomato slice thickness shift factors [205]. The authors were interested in the time to dry tomatoes to less than 15 wt% moisture content, because dried tomatoes are a common component in pizza sauces and various vegetable dishes. However the long drying treatments currently used cause the tomatoes to lose many of their vitamins and minerals. The authors therefore monitored the moisture content and drying time of tomato slice thicknesses from 3-11mm, at temperatures from 60-120^{o}C. The authors initially created slice thickness master curves for each temperature, and then shifted each of these curves to a reference temperature of 100^{o}C and 7mm thickness to form a doubly shifted master curve. This master curve was used to estimate the moisture ratio of tomato slices over the test conditions examined using a logarithmic fit of the data. The authors provide a plot of the temperature shift factors and a table of the slice thickness shift factors. It is important to note that these shift factors do not take on a reasonable form as necessary for the true application of the superposition principle. Therefore the shifting represents a purely phenomenological behavior, with no physical basis. This does however provide the authors with predictive capabilities for modeling purposes over

the test conditions. Other agricultural applications of the TTSP include the stress relaxation behavior of yellow-dent kernel corn and sea buckthorn berries [225, 226].

Diamant and Folman also create a doubly-shifted master curve for both temperature and filler content of carboxy terminated poly(butadiene) filled with spherical aluminum powder via uniaxial tensile testing.[206] The authors define the filler shift factor based on the WLF equation:

$$\log a_{\phi} = \frac{B_1(\phi - \phi_o)}{B_2 + \phi - \phi_o} \qquad \textbf{[1.47]}$$

where B_1 and B_2 are constants similar to those used in the WLF equation, ϕ is the filler volume fraction, and ϕ_o is the filler volume fraction at a given reference condition. The negative sign from the WLF equation was omitted for this shift factor because filler content has the inverse effect on the material properties, namely that an increase in filler content makes a material stiffer, similar to lowering the temperature. The authors initially shift the data using the WLF equation to form thermal master curves at constant filler contents referenced to -25^{o}C, creating a family of curves for maximum stress. They then shift each of these curves to a reference of 0% filler content to form the doubly shifted master curve.

The authors note that they were able to form doubly shifted master curves for both the maximum stress and strain energy at failure. However, they were not successful in creating a doubly shifted curve for the initial modulus using the same filler content shift factors, rather higher values of a_{ϕ} were required to form this master curve. This is because the initial modulus was measured at the beginning of the test when the degree of dewetting of the filler from the polymer matrix was almost zero, whereas the ultimate properties were measured when the dewetting was at a maximum. Therefore the influence of the filler will be much greater at the

beginning of a test than at the end, and thus properties taken at the beginning will require larger shift factors. This shifting method not only provides a long-term prediction of the material behavior, but also allows for a measurement of the energy associated with the dewetting process by comparing the apparent activation energies of the shift factors needed for the beginning of the test and the end.

Sumita et al. also created doubly shifted master curves of the yield stress of Nylon 6 filled with ultrafine and micron sized silica and glass particles, using both temperature and filler content [207]. However, the authors note the thermal shift factors are fit well with an Arrhenius equation, and the filler content shift factors are proportional to the filler volume fraction. The authors utilize a simple relationship to describe the shift factors:

$$\log a_{\phi} = K'\phi^{x} \qquad \textbf{[1.48]}$$

where *K'* is a proportionality constant, and *x* is a polymer species' dependence upon the filler volume fraction. While quite simplified, the equation does work well to describe the filler content shift factors for the system studied.

1.4.3.1. Time Moisture Superposition

The most common alternative of the TTSP is the time moisture superposition principle (TMSP). It has been noted that the same stress relaxation modulus can be achieved by placing a sample in a chamber with a high humidity level for a short time, or in a chamber with a low humidity level for a long time. It was also observed that increased water sorption in a material decreases the modulus, which could occur via two mechanisms.[215, 221] The first is the scission of interchain bonds, and the second is a plasticizing effect in which molecules penetrate interchain spaces, thereby increasing the interchain distances. Therefore, absorbed moisture in a

material has an analogous effect to temperature by increasing free volume, and can be used instead of temperature for shifting to create master curves of creep,[213-215] stress relaxation,[212] and dynamic mechanical properties [142, 220].

The TMSP was confirmed by Onogi et al with both poly(vinyl acetate) and Nylon 6 [212]. The authors were able to successfully shift moisture curves from 0 – 82% RH at 25^{o}C to form hygral master curves for both materials utilizing only horizontal shifts. The poly(vinyl acetate) stress relaxation master curve was compared with data taken directly without the use of superposition on the same material. Despite differences in the test methods and material samples, the two data sets agree quite well, indicating the validity of the time moisture superposition principle. Onogi also notes the importance of plotting the hygral shift factors against water sorption rather than relative humidity. Testing was performed on poly(vinyl acetate) with two different degrees of polymerization, and when these shift factors are plotted together against relative humidity the plots are different, despite similar master curves. However, when the shift factors of both are plotted against the water content of the material, they fall on the same curve, and can be represented by two straight lines. Therefore, it is more appropriate to plot hygral shift factors against water content than relative humidity to represent the material behavior because the same materials chemically with different degrees of polymerization or crystallization may sorb different amounts of water at the same RH level.

Ishisaka and Kawagoe also confirmed the validity of the TMSP for nylon 6, as well as an epoxy [142]. The authors performed both time temperature superposition and time moisture superposition over -150-200^{o}C and 29-92% RH for the storage modulus of both materials. The two master curves created via time temperature and time moisture superposition should in principle match at the same reference conditions if the material is truly thermorheologically

simple. Therefore, the master curves are compared and show good agreement at short times and slight deviations at longer times. The authors suspect the deviation in the Nylon 6 curves is due to an increase in crystallinity caused by the presence of moisture, and the deviation in the epoxy curves is due to degradation at hot wet conditions. Additionally, Emri and Pavsek show exact agreement between master curves created via TTSP and TMSP for poly(vinyl acetate), further indicating the validity of TMSP for polymeric material [222].

Many authors have noted the WLF-like behavior of the moisture shift factors for nylon materials [142, 212, 220]. It is believed this behavior is reasonable if the first water molecules specifically absorbed will have the greatest impact on the free volume and therefore mechanical properties of the material. More specifically to nylon materials, the initial water sorbed will sever the stiff hydrogen bonds in the amorphous regions, whereas the water sorbed at higher humidity levels only contributes to increasing the free volume. Therefore, a greater response from a small amount of sorbed water is seen in nylon, and the addition of further water has a much smaller impact on the material properties.

Other applications of the TMSP include glass fiber reinforced polymer composites,[214] polyester resin used as a cementless polymer concrete binder,[213] and plasticized starch films used for food packaging [218]. Yao and Ziegmann showed that measured creep strength results matched well with the predicted values from the TMSP for glass fiber reinforced polymer composites, further validating the equivalence of moisture and time. Plushchik and Anskevich compare the time temperature and time moisture equivalence of the polyester resin, and show that the effect of 1.64% sorbed moisture is approximately equivalent to a 20% change in temperature on the creep strain, showing the equivalence of temperature and moisture effects on the material. Finally, Chaleat et al. plot the yield strength vs. the strain rate of plasticized starch

films, creating two thermal master curves at 23 and 50^{o}C over 6.5-14.9% moisture content, using the same shift factors for both curves. This wide range of applications shows the ubiquity of the TMSP.

1.4.3.2. Time Temperature Moisture Superposition

Several authors have further extended the moisture equivalency of many materials to form a doubly shifted master curve of both temperature and moisture, because the basic mechanics underlying both responses are the same, creating a time temperature moisture superposition principle (TTMSP).[209, 211, 216, 221] This shifting procedure is analogous to the doubly shifted master curves created based on time and filler content presented earlier, only now the filler is water. In principle the diluent could be any solvent, such as methanol as shown by Fujita and Kishimoto on poly(vinyl acetate) and poly(methyl acrylate).[221] This TTMSP was confirmed by Dunell and Quistwater using nylon 6,6, shortly after the introduction of the WLF form of the TTSP.[220] They show the shift factors for both the storage and loss moduli referenced to two different temperatures all fall on the same curve. This implies that the molecular relaxation processes have the same dependence on moisture content and temperature, confirming the equivalence of moisture and temperature with time.

Fujita and Kishimoto also examined poly(vinyl acetate) and poly (methyl acrylate) with different water concentrations, and developed a concentration shift factor based on the free volume concept, to be used in conjunction with a temperature shift factor.[221] As discussed earlier, the Doolittle equation shows viscosity is dependent on the free volume, which in turn is dependent on temperature. Fujita and Kishimoto propose that for polymers swollen with a

diluent that the free volume is now dependent on both the temperature and the diluent concentration, C:

$$\ln \eta = \ln B + \frac{1}{f(T,C)} \quad \textbf{[1.49]}$$

This leads to a concentration shift factor of:

$$\log a_C = \frac{B}{2.303}\left[\frac{1}{f(T,C)} - \frac{1}{f(T,0)}\right] \quad \textbf{[1.50]}$$

where $f(T,0)$ is the free volume of the unswollen polymer and is further defined as:

$$f(T,0) = f\left(T_g{}^o,0\right) + \alpha\left(T - T_g{}^o\right) \quad \textbf{[1.51]}$$

The authors then further assume that the free volume increases linearly with the diluent concentration at sufficiently low concentrations resulting in:

$$f(T,C) = f(T,0) + \beta C \quad \textbf{[1.52]}$$

where β is a variable representing the contribution of a given diluent to the increase in free volume in a material. The authors believe β should be independent of the diluent concentration, but will have a dependence on the diluent polymer physical and chemical interactions. They show this to be true with numerous polymer diluent pairs where different β values are obtained for the same polymer swollen with different diluents. The authors also show the applicability of their shift factor equation to describe the shift factors for poly(vinyl acetate) and poly(methyl acrylate) swollen with water and methanol.

Zhou et al. contend that the assumption of a linear dependence of free volume on moisture content is invalid for certain polymer systems, and a better definition of the free volume dependent on both temperature and moisture content is given by:

$$f(T, X_{RH}) = f(T_g{}^o, 0) + \alpha(T - T_g(X_{RH})) + k(X_{RH} - X_{RH}{}^o) + k'(X_{RH} - X_{RH}{}^o)^2 \quad \textbf{[1.53]}$$

where X_{RH} is the relative humidity of a sample, $X_{RH}{}^o$ is the relative humidity at a given reference state, and k and k' are material specific constants [216]. It was noted previously that a more accurate representation of material behavior is obtained when the shift factor is expressed in terms of moisture content of a sample rather than the relative humidity. However, the authors contend that sorbed water molecules could contribute differently to mechanical properties depending on their location such as in the amorphous region vs. the inner regions of crystallites. Therefore, they believe it difficult to describe the different contributions of sorbed water, and that even if **Eqn [1.53]** is altered for water content the results would not change much.

The authors examined the temperature and moisture dependence of nylon 6, nylon 6,6, poly(vinyl alcohol), ethylene-vinyl alcohol copolymers, and regenerated cellulose. They found similar results for nylon 6 and nylon 6,6 as previously reported, although a hygrothermal master curve was created for both. They also found that the shift factors for both of these materials could be described reasonably well by the equation developed by Fujita and Kishimoto. However, when they examined poly(vinyl alcohol), ethylene-vinyl alcohol copolymers, and regenerated cellulose this was not the case. All three of these materials have a higher water uptake than nylon 6 or nylon 6,6 and as such the square term in Zhou's free volume equation is necessary to describe these materials' shift factors. In addition, as the hydrophobic ethylene content of the ethylene-vinyl alcohol is increased, the nonlinear dependence of the hygral shift factor decreases, approaching linearity similar to those of nylon 6 and nylon 6,6. All the hygral shift factors for these polymeric systems are plotted together, and it is seen that materials with greater hydrophilicity display a larger dependence on the RH, as marked by a greater curvature.

Therefore, the authors believe their free volume definition is more accurate as it describes multiple polymer systems from crystalline to amorphous, and hydrophilic to hydrophobic.

An interesting application of the TTMSP is to carbon and graphite fiber reinforced polymer composites whose applications to airplanes and spacecraft show dependence on both temperature and moisture [208, 209, 223]. Fujieda et al. were able to successfully create hygrothermal master curves of flexural strength at constant strain rate, for composites comprised of 53 vol% carbon fiber and an epoxy resin over 0-2% RH and 25-120^{o}C. Shifting was first performed for each moisture level, creating thermal master curves referenced to 25^{o}C. Each thermal master curve was then shifted horizontally to a dry reference condition, creating a hygrothermal master curve allowing for the prediction of long time material behavior of the composite material to be made. Similarly, Daniel et al. were able to create hygrothermal master curves for the tensile strength and ultimate tensile strength transverse to the fiber direction for graphite fiber reinforced epoxy composites plotted against the strain rate rather than time. Data taken parallel to the fiber direction showed little dependence on moisture or temperature, as these properties are dominated by the fiber, whereas the transverse properties are more dependent on the matrix material. These hygrothermal master curves are significantly more noisy than those presented by other authors for neat polymer systems, however this kind of testing inherently has more scatter than stress relaxation, creep, or dynamic properties. Therefore, these curves are accurate within expected experimental error. The material property dependence on the strain rate is important for composites used in airplane propellers which need to be able to withstand foreign object impacts such as birds. These master curves therefore provide a prediction of the material strength with different impact times, as dictated by the application.

Up to this point authors have defined a separate hygral or concentration shift factor from the temperature shift factor, although the hygral or concentration shift factor is also dependent on temperature. This implies that the temperature and moisture content are not completely separable variables and the fractional free volume should instead be defined as the sum of the fractional free volume due to temperature and moisture changes. Thus the hygrothermal shift factor is not merely a product of a hygral and a thermal shift factor, and shifting is not simply the sum of the moisture and temperature shifts, but dependent on both inseparably. This idea agrees well with empirical shifting performed by Maksimov et al. on polyester as well as empirical shifting performed by Flaggs and Crossman for a fiber reinforced polymer [211, 223].

Some authors have even extended the TTMSP to include strain,[210] creating a triply shifted master curve. Harper et al. collected stress relaxation data on Kapton-type 300H film from 25-90^{o}C, 10-95% RH, and 1-3% applied strain. The authors propose that the modulus can be shifted for all three variables at once, creating a time temperature moisture strain superposition. However, they note that the fundamental difference in shape of data taken at 1% and 2 and 3% strain makes it impossible to apply this idea. The authors then instead vertically shift for moisture, and horizontally shift for strain and temperature, stating that the horizontal shift is independent of moisture content, creating a master curve. However it should be noted that vertical shifting is usually applied to account for density changes over changing test temperatures, as developed from the theory of rubber elasticity. In the case of moisture content in Kapton the vertical shifts are much larger than normally obtained in other polymeric systems. Therefore, it is questioned whether this is truly a valid form of shifting this data, especially when it appears a horizontal shift could easily be applied for time and moisture at each strain level. Based on the unshifted data presented by the authors, it is believed that this data crosses from the

linear to the nonlinear regime of the material, and it should not be expected that these data sets would shift together well. It is possible the 2 and 3% strain data would triply shift to form a hygrothermal strain master curve, but it is unlikely that all three strain levels could be combined, as noted by the authors.

1.5 References

[1] O.o.B.E.S. US Department of Energy, in: U. DOE (Ed.), Washington DC, 2004.
[2] W. Liu, K. Ruth, R. Greg, Journal of New Materials for Electrochemical Systems, 4 (2001) 227-231.
[3] A. Collier, H. Wang, X.Z. Yuan, J. Zhang, D. Wilkinson, P., International Journal of Hydrogen Energy, 31 (2006) 1838-1854.
[4] K. Reifsnider, X. Huang, Fuel Cell Technology, (2006) 53-68.
[5] R. Borup, J. Meyers, B. Pivovar, Y.S. Kim, R. Mukundan, N. Garland, D. Myers, M. Wilson, F. Garzon, D. Wood, P. Zelenay, K. More, K. Stroh, T. Zawodzinski, J. Boncella, J.E. McGrath, M. Inaba, K. Miyatake, M. Hori, K. Ota, Z. Ogumi, S. Miyata, A. Nishikata, Z. Siroma, Y. Uchimoto, K. Yasuda, K.-i. Kimijima, N. Iwashita, Chemical Reviews, 107 (2007) 3904-3951.
[6] F.D. Coms, H. Liu, J.E. Owejan, ECS Transactions, 16 (2008) 1735-1747.
[7] P. Trogadas, J. Parrondo, V. Ramani, ECS Transactions, 16 (2008) 1725-1733.
[8] D.E. Curtin, R.D. Lousenberg, T.J. Henry, P.C. Tangeman, M.E. Tisack, Journal of Power Sources, 131 (2004) 41-48.
[9] D. Xing, J. Kerres, Polymers for Advanced Technologies, 17 (2006) 591-597.
[10] R. O'Hayre, S.-W. Cha, W. Colella, F.B. Prinz, Fuel Cell Fundamentals, 2nd ed., Wiley, New York, NY, 2009.
[11] Y. Li, D.A. Dillard, Y.-H. Lai, S. Case, W., M.W. Ellis, M.K. Budinski, C.S. Gittleman, Journal of the Electrochemical Society, 159 (2012) B173-B184.
[12] Y.-H. Lai, D.A. Dillard, Mechanical Durability Characterization and Modeling of Ionomeric Membranes, in: W. Vielstich, H. Yokokawa, H. Gasteiger, A. (Eds.) Handbook of Fuel Cells - Fundamentals, Technology and Applications, John Wiley & Sons, New York, 2009.
[13] W.K. Liu, S.J.C. Cleghorn, B.E. Delaney, M. Crum, Chemical and Mechanical Membrane Degradation, in: W. Vielstich, H. Yokokawa, H. Gasteiger, A. (Eds.) Handbook of Fuel Cells - Fundamentals, Technology and Applications, John Wiley & Sons Ltd., New York, 2009, pp. 385-402.
[14] C.S. Gittleman, Y.-H. Lai, C. Lewis, D.P. Miller, in: AIChE, Cincinnati, OH, 2005.
[15] Y.-H. Lai, C.K. Mittelsteadt, C.S. Gittleman, Journal of Fuel Cell Science and Technology, 6 (2009) 021002/021001-021002/021013.
[16] Y.-H. Lai, C.K. Mittelsteadt, C.S. Gittleman, D.A. Dillard, in: Third International Conference on Fuel Cell Science, Engineering and Technology, Ypsilanti, Michigan, 2005.
[17] V. Stanic, in: 4th International Symposium on Proton Conducting Membrane Fuel Cells, 2004.
[18] A.Z. Weber, J. Newman, AIChE Journal, 50 (2004) 3215-3226.
[19] D. Liu, S. Case, Journal of Power Sources, 162 (2006) 521-531.

[20] M.N. Silberstein, M.C. Boyce, Journal of Power Sources, 195 (2010) 5692-5706.
[21] Y. Tang, A.M. Karlsson, M.H. Santare, M. Gilbert, S. Cleghorn, W.B. Johnson, Materials Science & Engineering, A: Structural Materials: Properties, Microstructure, and Processing, A425 (2006) 297-304.
[22] X. Huang, R. Solasi, Y. Zou, M. Feshler, K. Reifsnider, D. Condit, S. Burlatsky, T. Medden, Journal of Polymer Science, Part B: Polymer Physics, 44 (2006) 2346-2357.
[23] R. Solasi, Y. Zou, X. Huang, K. Reifsnider, D. Condit, Journal of Power Sources, 167 (2007) 366-377.
[24] A. Kusoglu, Y. Tang, M.H. Santare, A.M. Karlsson, S. Cleghorn, W.B. Johnson, Journal of Fuel Cell Science and Technology, 6 (2009) 011012-011011-011012-011018.
[25] S. Kundu, L.C. Simon, M. Fowler, S. Grot, Polymer, 46 (2005) 11707-11715.
[26] R. Jia, B. Han, K. Levi, T. Hasegawa, J. Ye, R.H. Dauskardt, Journal of Power Sources, 196 (2011) 3803-3809.
[27] M. Satterfield, Barclay, P. Majsztrik, W., H. Ota, J. Benziger, B., A.B. Bocarsly, Journal of Polymer Science, Part B: Polymer Physics, 44 (2006) 2327-2345.
[28] Z. Lu, M. Lugo, M.H. Santare, A.M. Karlsson, C.F. Busby, P. Walsh, Journal of Power Sources, 214 (2012) 130-136.
[29] A. Kusoglu, Y. Tang, M. Lugo, A. Karlsson, M., M. Santare, H., S. Cleghorn, W. Johnson, B., Journal of Power Sources, 195 (2010) 483-492.
[30] K.A. Patankar, D.A. Dillard, S.W. Case, M.W. Ellis, Y.-H. Lai, M.K. Budinski, C.S. Gittleman, Fuel Cells, (Accepted).
[31] D. Liu, S. Kyriakides, S. Case, W., J. Lesko, J., Y. Li, J. McGrath, E., Journal of Polymer Science, Part B: Polymer Physics, 44 (2006) 1453-1465.
[32] Y.P. Patil, W.L. Jarett, K.A. Mauritz, Journal of Membrane Science, 356 (2010) 7-13.
[33] M. Marrony, R. Barrera, S. Quenet, S. Ginoccio, L. Montelatici, A. Alsanides, Journal of Power Sources, 182 (2008) 469-475.
[34] H. Tang, S. Peiking, S.P. Jiang, F. Wang, M. Pan, Journal of Power Sources, 170 (2007) 85-92.
[35] T. Kyu, A. Eisenberg, Journal of Polymer Science, Symposia, 71 (1984) 203-219.
[36] S.C. Yeo, A. Eisenberg, Journal of Macromolecular Science, Physics, B13 (1977) 441-484.
[37] F. Bauer, S. Denneler, M. Willert-Porada, Journal of Polymer Science, Part B: Polymer Physics, 43 (2005) 786-795.
[38] D. Liu, M. Hickner, A., S. Case, W., J. Lesko, J., Journal of Engineering Materials and Technology, 128 (2006) 503-508.
[39] M.B. Satterfield, J.B. Benziger, Journal of Polymer Science, Part B: Polymer Physics, 47 (2008) 11-24.
[40] P.W. Majsztrik, A.B. Bocarsly, J.B. Benziger, Macromolecules, 41 (2008) 9849-9862.
[41] G.M. Divoux, K.A. Finlay, J.K. Park, J.-M. Song, B. Yan, M. Zhang, D. Dillard, A., R. Moore, B., ECS Transactions, 41 (2011) 87.
[42] Y. Li, J. Quincy, D.A. Dillard, S.W. Case, M.W. Ellis, Y.-H. Lai, M.K. Budinski, C.S. Gittleman, in: 4th International Conference on uel Cell Science, Engineering and Technology, Irvine, CA, 2006.
[43] K.A. Patankar, D.A. Dillard, S. Case, M.W. Ellis, Y. Li, Y.-H. Lai, M.K. Budinski, C.S. Gittleman, Journal of Polymer Science Part B: Polymer Chemistry, 48 (2010) 333-343.
[44] R. Jia, B. Han, K. Levi, T. Hasegawa, J. Ye, R.H. Dauskardt, Journal of Power Sources, 196 (2011) 8234-8240.

[45] F. Liu, B. Yi, D. Xing, J. Yu, H. Zhang, Journal of Membrane Science, 212 (2003) 213-223.
[46] J.B. Ballengee, P.N. Pintauro, Macromolecules, 44 (2011) 7307-7314.
[47] T.R. Ralph, D.E. Barnwell, P.J. Bouwman, A.J. Hodgkinson, M.I. Petch, M. Pollington, Journal of the Electrochemical Society, 155 (2008) B411-B422.
[48] K.T. Adjemian, S.J. Lee, S. Srinivasan, J.B. Benziger, A.B. Bocarsly, Journal of the Electrochemical Society, 149 (2002) A256-A261.
[49] P.L. Antonucci, A. Arico, S., P. Creti, E. Ramunni, V. Antonucci, Solid State Ionics, 125 (1999) 431-437.
[50] M. Doyle, S.K. Choi, P. Grant, Journal of the Electrochemical Society, 147 (2000) 34-37.
[51] N. Miyake, J.S. Wainright, R.F. Savinell, Journal of the Electrochemical Society, 148 (2001) A905-A909.
[52] N. Miyake, J.S. Wainright, R.F. Savinell, Journal of the Electrochemical Society, 148 (2001) A898-A904.
[53] S. Haufe, U. Stimming, Journal of Membrane Science, 185 (2001) 95-103.
[54] M.L. Hill, Y.S. Kim, B.R. Einsla, J.E. McGrath, Journal of Membrane Science, 283 (2006) 102-108.
[55] Y. Tang, A. Kusoglu, A.M. Karlsson, M.H. Santare, S. Cleghorn, W.B. Johnson, Journal of Power Sources, 175 (2008) 817-825.
[56] K.A. Patankar, D.A. Dillard, S.W. Case, M.W. Ellis, Y.-H. Lai, M.K. Budinski, C.S. Gittleman, Mechanics of Time-Dependent Materials, 12 (2008) 221-236.
[57] K.A. Patankar, D.A. Dillard, S.W. Case, M.W. Ellis, Y. Li, Y.-H. Lai, M.K. Budinski, C.S. Gittleman, Journal of Polymer Science, Part B: Polymer Physics, 48 (2010) 333-343.
[58] F. Bauer, M. Willert-Porada, Journal of Membrane Science, 233 (2004) 141-149.
[59] F. Bauer, M. Willert-Porada, Solid State Ionics, 177 (2006) 2391-2396.
[60] J. Yuan, H. Pu, Z. Yang, Journal of Polymer Science: Part A: Polymer Chemistry, 47 (2009) 2647-2655.
[61] Q. Deng, R.B. Moore, K.A. Mauritz, Journal of Applied Polymer Science, 68 (1998) 747-763.
[62] S.K. Young, K.A. Mauritz, Journal of Polymer Science, Part B: Polymer Physics, 39 (2001) 1282-1295.
[63] S.K. Young, K.A. Mauritz, Journal of Polymer Science Part B: Polymer Physics, 40 (2002) 2237-2247.
[64] R.H. Alonso, L. Estevez, H. Lian, A. Kelarakis, E.P. Giannelis, Polymer, 50 (2009) 2402-2410.
[65] E. Burgaz, H. Lian, R.H. Alonso, L. Estevez, A. Kelarakis, E.P. Giannelis, Polymer, 50 (2009) 2384-2392.
[66] M.A. Hickner, H. Ghassemi, Y.S. Kim, B.R. Einsla, J.E. McGrath, Chemical Reviews, 104 (2004) 4587-4612.
[67] S. Saga, H. Matsumoto, K. Saito, M. Minagawa, A. Tanioka, Journal of Power Sources, 176 (2008) 16.
[68] A. Rabiee, Mehdipour-Ataei, e-Polymers, 110 (2009) 1-10.
[69] K. Miyatake, M. Watanabe, Journal of Materials Chemistry, 16 (2006) 4465-4467.
[70] G. Qian, D.J. Smith, B.C. Benicewicz, Polymer, 50 (2009) 3911-3916.
[71] A. Reyna-Valencia, S. Kaliaguine, M. Bousmina, Journal of Applied Polymer Science, 98 (2005) 2380-2393.

[72] E. Sgreccia, J.-F. Chailan, M. Khadhraoui, M.L. Di Vona, P. Knauth, Journal of Power Sources, 195 (2010) 7770-7775.
[73] W.L. Harrison, M.A. Hickner, Y.S. Kim, J.E. McGrath, Fuel Cells, 5 (2005) 201-212.
[74] A.S. Badami, H.-S. Lee, Y. Li, A. Roy, H. Wang, J.E. McGrath, Molecular Weight Effects on Poly(Arylene Ether Sulfone)-Based Random and Multiblock Copolymers Characteristics for Fuel Cells, in: A. Herring (Ed.) Fuel Cell Chemistry and Operation, American Chemical Society, Washington DC, 2010.
[75] Y. Fan, M. Zhang, R.B. Moore, H.-S. Lee, J.E. McGrath, C.J. Cornelius, Polymer, 52 (2011) 3963-3969.
[76] X. Yu, A. Roy, S. Dunn, A.S. Badami, J. Yang, A.S. Good, J.E. McGrath, Journal of Polymer Science Part A: Polymer Chemistry, 47 (2009) 1038-1051.
[77] Y. Chen, R. Guo, C.H. Lee, M. Lee, J.E. McGrath, International Journal of Hydrogen Energy, 37 (2012) 6132-6139.
[78] J. Kerres, W. Cui, M. Junginger, Journal of Membrane Science, 139 (1998) 227-241.
[79] J. Kerres, A. Ullrich, T. Haring, M. Baldauf, U. Gebhardt, W. Preidel, Journal of New Materials for Electrochemical Systems, 3 (2000) 229-239.
[80] J. Kerres, A. Ullrich, F. Meier, T. Haring, Solid State Ionics, 125 (1999) 243-249.
[81] N. Gourdoupi, J.K. Kallitsis, S. Neophytides, Journal of Power Sources, 195 (2010) 170-174.
[82] A. Linares, J.L. Acosta, S. Rodriguez, Journal of Applied Polymer Science, 100 (2006) 3473-3482.
[83] M. Arigonda, A.P. Deshpande, S. Varughese, Journal of Applied Polymer Science, (2012).
[84] E. Sgreccia, M. Khadhraoui, C. de Bonis, S. Licoccia, M.L. Di Vona, P. Knauth, Journal of Power Sources, 178 (2008) 667-670.
[85] P. Bhavani, D. Sangeetha, Journal of Polymer Research, 19 (2012) 1-10.
[86] H. Bi, J. Wang, S. Chen, Z. Hu, Z. Gao, L. Wang, K.-i. Okamoto, journal of Membrane Science, 350 (2010) 109-116.
[87] T. Inan, H. Dogan, E.E. Unveren, E. Eker, International Journal of Energy and Environment, 35 (2010) 12038-11053.
[88] P. Zapata, P. Basak, J.C. Meredith, Electrochimica Acta, 54 (2009) 3899-3909.
[89] P. Zapata, J.-H. Lee, J.C. Meredith, Journal of Applied Polymer Science, 124 (2012) E241-E250.
[90] P. Zapata, D. Mountz, J.C. Meredith, Macromolecules, 43 (2010) 7625-7636.
[91] T. Zhang, W. He, J. Goldbach, D. Mountz, J. Yi, Journal of Power Sources, 196 (2011) 1687.
[92] P. Piboonsatsanasakul, J. Wootthikanokkhan, S. Thanawan, Journal of Applied Polymer Science, 107 (2008) 1325-1336.
[93] P. Bhavani, D. Sangeetha, Chinese Journal of Polymer Science, 30 (2012) 548-560.
[94] A. Mokrini, M.A. Huneault, Journal of Power Sources, 154 (2006) 51-58.
[95] N. Seeponkai, J. Wootthikanokkhan, Journal of Applied Polymer Science, 117 (2010) 393-399.
[96] A.R. Gordon, M.W. Ellis, D.A. Dillard, S.W. Case, R.B. Moore, Y. Li, Y.-H. Lai, C.S. Gittleman, in: ASME 6th International Conference on Energy Sustainability & 10th Fuel Cell Science, ASME, San Diego, CA, 2012.
[97] A.R. Gordon, M.W. Ellis, D.A. Dillard, S.W. Case, R.B. Moore, Y. Li, Y.-H. Lai, C.S. Gittleman, (In Preparation).

[98] A.M. Osborn, in: Macromolecular Science and Engineering, Virginia Polytechnic Institute and State University, Blacksburg, VA, 2010, pp. 501.
[99] A.M. Osborn, R.B. Moore, D.A. Dillard, S.W. Case, M.W. Ellis, T.J. Fuller, S.M. MacKinnon, C.S. Gittleman, Y.-H. Lai, in: 239th National American Chemical Society Meeting and Exposition, American Chemical Society, San Francisco, CA, 2010, pp. 55-56.
[100] C.M. Siuta, in: Engineering Science and Mechanics, Virginia Polytechnic Institute and State University, 2011, pp. 73.
[101] D.A. Dillard, Y. Li, J.R. Grohs, S.W. Case, M.W. Ellis, Y.-H. Lai, M.K. Budinski, C.S. Gittleman, Journal of Fuel Cell Science and Technology, 6 (2009) 031014/031011-021014/031018.
[102] J.R. Grohs, Y. Li, D.A. Dillard, S.W. Case, M.W. Ellis, Y.-H. Lai, C.S. Gittleman, Journal of Power Sources, 195 (2010) 527-531.
[103] Y. Li, D. Dillard, A., S. Case, W., M. Ellis, W., Y.-H. Lai, C. Gittleman, S., D.P. Miller, Journal of Power Sources, 194 (2009) 873-879.
[104] M. Pestrak, Y. Li, S. Case, D.A. Dillard, M.W. Ellis, Y.-H. Lai, C.S. Gittleman, Journal of Fuel Cell Science and Technology, 7 (2010) 041009-041001 - 041009-041010.
[105] J.-L. Sormana, S. Chattopadhyay, J.C. Meredith, Review of Scientific Instruments, 76 (2005) 062214-062211 - 062214-062219.
[106] M.N. Silberstein, M.C. Boyce, Journal of Power Sources, 196 (2011) 3452-3460.
[107] M.N. Silberstein, P.V. Pillai, M.C. Boyce, Polymer, 52 (2011) 529-539.
[108] Y. Tang, M.H. Sanatare, A.M. Karlsson, in: The 3rd International Conference on Fuel Cell Science, Engineering, and Technology, Ypsilanti, MI, 2005.
[109] Y. Tang, M.H. Santare, A.M. Karlsson, S. Cleghorn, W.B. Johnson, Journal of Fuel Cell Science and Technology, 3 (2006) 119-124.
[110] A. Kusoglu, A. Karlsson, M., M. Sanatare, H., S. Cleghorn, W. Johnson, B., Journal of Power Sources, 161 (2006) 987-996.
[111] A. Kusoglu, A. Karlsson, M., M. Santare, H., S. Cleghorn, W. Johnson, B., Journal of Power Sources, 170 (2007) 345-358.
[112] A. Kusoglu, M.H. Santare, A.M. Karlsson, S. Cleghorn, W.B. Johnson, Journal of the Electrochemical Society, 157 (2010) B705-B713.
[113] D. Bograchev, M. Gueguen, J.-C. Grandidier, S. Martemianov, Journal of Power Sources, 180 (2008) 393-401.
[114] S. Martemianov, D. Bograchev, J.-C. Grandidier, J.-J. Kadjo, International Journal of Energy Research, 34 (2010) 635-642.
[115] D. Bograchev, M. Gueguen, J.-C. Grandidier, S. Martemianov, International Journal of Hydrogen Energy, 22 (2008) 5703-5717.
[116] S. Martemianov, M. Gueguen, J.-C. Grandidier, D. Bograchev, Journal of Applied Fluid Mechanics, 2 (2009) 49-54.
[117] M.A.R.S. Al-Baghdadi, H.A.K.S. Al-Janabi, Energy & Fuels, 21 (2007) 2258-2267.
[118] M.A.R.S. Al-Baghdadi, H.A.K.S. Al-Janabi, International Journal of Hydrogen Energy, 32 (2007) 4510-4522.
[119] M.A.R.S. Al-Baghdadi, International Journal of Energy and Environment, 2 (2011) 589-604.
[120] M.F. Serincan, U. Pasaogullari, Journal of Power Sources, 196 (2011) 1303-1313.
[121] N.S. Khattra, A.M. Karlsson, M.H. Santare, P. Walsh, C.F. Busby, Journal of Power Sources, 214 (2012) 365-376.

[122] R. Solasi, Y. Zou, X. Huang, K. Reifsnider, Mechanics of Time-Dependent Materials, 12 (2008) 15-30.
[123] S. He, M.M. Mench, ECS Transactions, 1 (2006) 415-434.
[124] P. Sun, S. Zhou, Journal of Fuel Cell Science and Technology, 8 (2011) 011010-011011-011010-011024.
[125] Y. Qi, Y.-H. Lai, Polymer, 52 (2011) 201-210.
[126] K. Ngai, L., D. Plazek, J., Rubber Chemistry and Technology, 78 (1995) 376-434.
[127] J. Dealy, D. Plazek, J., Rheology Bulletin, 78 (2009) 16-31.
[128] F. Schwarzl, A.J. Staverman, Journal of Applied Physics, 23 (1952) 838-843.
[129] L.C. Brinson, W.G. Knauss, Journal of the Mechanics and Physics of Solids, 39 (1991) 859-880.
[130] Y.S. Urzhumtsev, Mechanics of Composite Materials, 10 (1974) 180-185.
[131] J.D. Ferry, Viscoelastic Properties of Polymers, 3 ed., John Wiley and Sons, New York, 1980.
[132] H.F. Brinson, L.C. Brinson, Polymer Engineering Science and Viscoelasticity An Introduction, Springer Science+Business Media, LLC, New York, NY, 2008.
[133] H.F. Brinson, Experimental Mechanics, 8 (1968) 561-566.
[134] S.L. Rosen, Fundamental Principles of Polymeric Materials, 2nd ed., John Wiley & Sons, New York, NY, 1993.
[135] I.M. Ward, D.W. Hadley, An Introduction to the Mechanical Properties of Solid Polymers, John Wiley & Sons, West Sussex, England, 1993.
[136] J.T. Seitz, C.F. Balazs, Polymer Engineering and Science, 8 (1968) 151-160.
[137] A.K. Doolittle, Journal of Applied Physics, 22 (1951) 1471-1475.
[138] A.J. Kovacs, R.A. Stratton, J.D. Ferry, Journal of Physical Chemistry, 67 (1963) 152-161.
[139] H.H. Meyer, P.-M.F. Mangin, J.D. Ferry, Journal of Polymer Science: Part A, 3 (1965) 1785-1792.
[140] M. Williams, L., R. Landel, F., J. Ferry, D., Journal of the American Chemical Society, 77 (1955) 3701.
[141] J.D. Ferry, Journal of Polymer Science Part B: Polymer Physics, 37 (1999) 621-622.
[142] A. Ishisaka, M. Kawagoe, Journal of Applied Polymer Science, 93 (2004) 560-567.
[143] J. Pathak, A., R.H. Colby, S. Kamath, Y., S. Kumar, K., R. Stadler, Macromolecules, 31 (1998) 8988-8997.
[144] V. Kenner, H., W.G. Knauss, H. Chai, Experimental Mechanics, 22 (1982) 75-80.
[145] W. Brostow, Materials Chemistry and Physics, 13 (1985) 47-57.
[146] J.H. Magill, H.-M. Li, Journal of Polymer Science Part C: Polymer Letters, 11 (1973) 667-672.
[147] M.H. Litt, Transactions of the Society of Rheology, 20 (1976) 47-64.
[148] D. Plazek, J., Journal of Polymer Science Part B: Polymer Physics, 20 (1982) 729-742.
[149] W.W. Graessley, Viscoelasticity and Flow in Polymer Melts and Concentrated Solutions, in: Physical Properties of Polymers, United Book Press, Baltimore, MD, 1993, pp. 98-143.
[150] Q. Chen, Y. Masumiya, Y. Masabuchi, H. Watanabe, T. Inoue, Macromolecules, 41 (2008) 8964-8711.
[151] J. Haley, C., T. Lodge, P., Colloid and Polymer Science, 282 (2004) 793-801.
[152] E. Kopesky, T., T. Haddad, S., G. McKinley, H., R. Cohen, E., Polymer, 46 (2005) 4743-4752.
[153] C. Roland, M., K. Ngai, L., Macromolecules, 25 (1992) 363-367.

[154] M. van Gurp, J. Palmen, Rheology Bulletin, 67 (1998) 5-8.
[155] H. Watanabe, Y. Matsumiya, J. Takada, H. Sasaki, Y. Matsushima, A. Kuriyama, T. Inoue, K. Ahn, H., W. Yu, R. Krishnamoorti, Macromolecules, 40 (2007) 5389-5399.
[156] Z. Yang, C. Han, D., Macromolecules, 41 (2008) 2104-2118.
[157] J. Roovers, P. Toporowski, M., Macromolecules, 25 (1992) 1096-1102.
[158] J. Roovers, P. Toporowski, M., Macromolecules, 25 (1992) 3454-3461.
[159] R.H. Colby, Polymer, 30 (1989) 1275-1278.
[160] A. Alegria, J. Colmenero, K. Ngai, L., C. Roland, M., Macromolecules, 27 (1994) 4486-4492.
[161] G.-C. Chung, J.A. Kornfield, S.D. Smith, Macromolecules, 27 (1994) 5729-5741.
[162] C.B. Gell, R. Krishnamoorti, E. Kim, W. Graessley, W., L.J. Fetters, Rheologica Acta, 36 (1997) 217-228.
[163] C. Roland, M., K. Ngai, L., Journal of Rheology, 36 (1992) 1691-1706.
[164] J. Pathak, A., S. Kumar, K., R.H. Colby, Macromolecules, 37 (2004) 6994-7000.
[165] J. Haley, C., T. Lodge, P., Y. He, M.D. Ediger, E.D. von Meerwall, J. Mijovic, Macromolecules, 36 (2003) 6142-6151.
[166] Y. Hirose, O. Urakawa, K. Adachi, Macromolecules, 36 (2003) 3699-3708.
[167] C. Bazuin, G., A. Eisenberg, Journal of Polymer Science Part B: Polymer Physics, 24 (1986) 1021-1037.
[168] R. Hagen, R. Weiss, A., Polymer, 26 (1995) 4657-4664.
[169] P. Macaubas, H., P., N. Demarquette, R., Polymer Engineering and Science, 42 (2002) 1509-1519.
[170] D. Wu, Y. Zhang, M. Zhang, W. Zhou, European Polymer Journal, 44 (2008) 2171-2183.
[171] M. Wagner, H., W. Wu, Y. Liu, Q. Qian, Y. Zhang, W. Mielke, Journal of Applied Polymer Science, 110 (2008) 177-182.
[172] M.E. Romero-Guzman, A. Romo-Uribe, B.M. Zarate-Hernandez, R. Cruz-Silva, Rheologica Acta, 48 (2009) 641-652.
[173] E. Shivakumar, C.K. Das, E. Segal, M. Narkis, Polymer, 46 (2005) 3363-3371.
[174] S. Tabatabaei, H., P. Carreau, J., A. Ajji, Chemical Engineering Science, 64 (2009) 4719-4731.
[175] W. Zheng, G. McKenna, B., S. Simon, L., Polymer, 51 (2010) 4899-4906.
[176] S.-f. Lau, J. Pathak, B. Wunderlich, Macromolecules, 15 (1982) 1278-1283.
[177] K. Ngai, L., R. Rendell, W., A. Rajagopal, K., S. Teitler, Annals New York Academy of Sciences, 150-184.
[178] J. des Cloizeaux, Macromolecules, 23 (1990) 3992-4006.
[179] J. des Cloizeaux, Macromolecules, 23 (1990) 4678-4687.
[180] C. Tsenoglou, Macromolecules, 24 (1991) 1762-1767.
[181] G. Katana, E.W. Fischer, T. Hack, V. Abetz, F. Kremer, Macromolecules, 28 (1995) 2714-2722.
[182] A. Zetsche, E.W. Fischer, Acta Polymer, 45 (1994) 168-175.
[183] S. Kumar, K., R.H. Colby, S.H. Anastasiadis, G. Fytas, Journal of Chemical Physics, 105 (1996) 3777-3788.
[184] S. Kamath, Y., R.H. Colby, S. Kumar, K., K. Karatasos, G. Floudas, G. Fytas, J. Roovers, Journal of Chemical Physics, 111 (1999) 6121-6128.
[185] J. Pathak, A., R.H. Colby, G. Floudas, R. Jerome, Macromolecules, 32 (1999) 2553-2561.
[186] S. Salaniwal, R. Kant, R.H. Colby, S. Kumar, K., Macromolecules, 35 (2002) 9211-9218.

[187] T. Lodge, P., T. McLeish, C., Macromolecules, 33 (2000) 5278-5284.
[188] E. Leroy, A. Alegria, J. Colmenero, Macromolecules, 35 (2002) 5587-5590.
[189] D. Wu, Journal of Polymer Science Part B: Polymer Physics, 25 (1987) 557-566.
[190] C. Carrot, S. Mbarek, M. Jaziri, Y. Chalamet, C. Raveyre, F. Prochazka, Macromolecular Materials and Engineering, 292 (2007) 693-706.
[191] O. Delgadillo-Velazquez, S. Hatzikiriakos, G., M. Sentmanat, Rheologica Acta, 47 (2008) 19-31.
[192] R. Li, W. Yu, C. Zhou, Polymer Bulletin, 56 (2006) 455-466.
[193] M. Thunga, B. Satapathy, K., U. Staudinger, R. Weidisch, M. Abdel-Goad, A. Janke, K. Knoll, Journal of Polymer Science: Part B: Polymer Physics, 46 (2008) 329-343.
[194] O. Delgadillo-Velazquez, S. Hatzikiriakos, G., M. Sentmanat, Journal of Polymer Science Part B: Polymer Physics, 46 (2008) 1669-1683.
[195] K.S. Cole, R.H. Cole, Journal of Chemical Physics, 9 (1941) 341-351.
[196] C. Han, D., Journal of Applied Polymer Science, 35 (1988) 167-213.
[197] C. Han, D., M. Jhon, S., Journal of Applied Polymer Science, 32 (1986) 3809-3840.
[198] C. Han, D., J. Kim, Kon, Macromolecules, 22 (1989) 1914-1921.
[199] C. Han, D., J. Kim, K., Polymer, 34 (1993) 2533-2539.
[200] C. Han, D., K.-W. Lem, Polymer Engineering Reviews, 2 (1982) 136-165.
[201] C. Han, D., H.-H. Yang, Journal of Applied Polymer Science, 33 (1987) 1221-1229.
[202] C. Han, D., J. Kim, Kon, Macromolecules, 22 (1989) 4292-4302.
[203] W. Brostow, Materials Research Innovations, 3 (2000) 347-351.
[204] M. Williams, L., M.F. Bender, Journal of Applied Physics, 36 (1965) 3044-3049.
[205] J. Khazaei, G.-R. Chegini, M. Bakhshiani, Drying Technology, 26 (2008) 759.
[206] Y. Diamant, M. Folman, Polymer, 20 (1979) 1025-1033.
[207] M. Sumita, T. Shizuma, K. Miyasaka, K. Ishikawa, Journal of Macromolecular Science, Physics, B22 (1983) 599-6116.
[208] I. Daniel, M., G. Yaniv, G. Peimanidis, Journal of Engineering Materials and Technology, 110 (1988) 169-173.
[209] H. Fujieda, N. Sekine, M. Nakada, Y. Miyano, A. Kuraishi, S.W. Tsai, JSME International Journal, Series A: Solid Mechanics and Material Engineering, 46 (2003) 467-472.
[210] B. Harper, D., J. Rao, M., V. Kenner, H., C. Popelar, H., Journal of Electronic Materials, 26 (1997) 798-804.
[211] W.G. Knauss, V. Kenner, H., Journal of Applied Physics, 51 (1980) 5131-5136.
[212] S. Onogi, K. Sasaguri, T. Adachi, S. Ogihara, Journal of Polymer Science, 58 (1962) 1-17.
[213] O. Plushchik, A., A. Aniskevich, N., Mechanics of Composite Materials, 36 (2000) 233-240.
[214] J. Yao, G. Ziegmann, Polymer Testing, 25 (2006) 149-157.
[215] G. Zheng, Y. Kang, J. Sheng, Q. Qin, H. Wang, D. Fu, Science in China, Series E: Engineering & Materials Science, 47 (2004) 595-607.
[216] S.-M. Zhou, K. Tashio, T. Li, Journal of Polymer Science, Part B: Polymer Physics, 39 (2001) 1638-1650.
[217] E. Kristo, C.G. Biliaderis, Food Hydrocolloids, 20 (2006) 1057-1071.
[218] C.M. Chaleat, G. Michel-Amadry, P.J. Halley, R.W. Truss, Carbohydrate Polymers, 74 (2008) 366-371.
[219] E.W.S. Hagan, M.N. Charalambides, C.T. Young, T.J.S. Learner, S. Hackney, Mechanics of Time-Dependent Materials, 13 (2009) 149-161.

[220] B.A. Dunell, J.M.R. Quistwater, The Journal of Chemical Physics, 29 (1958) 450.
[221] H. Fujita, A. Kishimoto, Journal of Polymer Science, 28 (1958) 547-567.
[222] I. Emri, V. Pavsek, Materials Forum, 16 (1992) 123-131.
[223] D. Flaggs, L., F. Crossman, W., Journal of Composite Materials, 15 (1981) 21-40.
[224] A.E. Akinay, W. Brostow, Polymer, 42 (2001) 4527-4532.
[225] K.M. Waananen, M.R. Okos, in: ASAE, 1999, pp. 1249-1258.
[226] J. Khazaei, D.D. Mann, Agricultural Engineering International: The CIGR Journal of Scientific Research and Development, (2004) 03-014.

Chapter 2 : Constitutive Property Characterization of Sulfonated Perfluorocyclobutane/Poly(vinylidene Difluoride)-co-Hexafluoropropylene (PFCB/PVDF-HFP) Blends for use as Proton Exchange Membranes

2.1 Introduction

The durability of polymer electrolyte membranes or proton exchange membranes (PEM) is of key importance for the commercialization of fuel cells for portable, stationary, and transportation applications [1]. Automotive applications are especially mechanically challenging due to the rapidly changing temperature and humidity conditions imposed to meet the needed power demands [2, 3]. In a fuel cell, the PEM transports protons from the anode to the cathode while also acting as a barrier to the reactant gasses and electrons. Better proton transport is achieved at higher water contents, and PEM materials have been shown to expand due to moisture by at least 10%, and many by more than 20% in all three directions [4]. However, within a fuel cell stack the PEM layers are largely constrained between rigid bipolar plates and gas diffusion layers. This limitation to movement induces varying in-plane compressive and tensile stresses as the PEM attempts to expand and contract with changing temperature and humidity conditions [5]. It is believed that the repeated cycling of these induced hygrothermal mechanical stresses leads to a fatigue loading of the PEM, which over time contributes to the formation and propagation of microcracks [6-8]. These and other defects or pinholes can allow the reactant gasses to crossover, resulting in localized heating, failure of the membrane, and ultimately, failure of the fuel cell [7-12]. Because the defects are created due to mechanical loading, it is therefore important to understand and characterize the constitutive properties of PEMs to accurately predict and improve the lifetime durability of a fuel cell.

The mechanical properties that affect membrane durability have recently attracted significant attention. Some of the earliest work characterizing the viscoelastic properties of Nafion® examined the loss tangent as a function of water content and shear storage modulus as a function of water content. The authors noted a shift of loss tangent peaks to lower temperatures and a decrease in the shear storage modulus with increasing water content [13]. Further studies performed on Nafion® at different moisture conditions under dynamic, stress relaxation, and creep modes showed that water plasticized the material at low temperatures, but stiffened the membrane above 90^{o}C. It was suggested this occurs due to a stabilization of the network of hydrophilic clusters and the microphase separation of the sulfonic acid clusters from the PTFE backbone [14-16]. Additionally, Liu et al [17] conducted stress relaxation tests under both atmospheric and immersed conditions at 30^{o}C on Nafion® 117, and noted lower stresses and faster relaxations in the immersed samples. Tensile testing of Nafion® NRE 212 under monotonic and cyclic loading at different environmental conditions was performed by Silberstein et al, showing increased hydration decreases the elastic modulus and yield stress of the material [18]. In addition, partially constrained swelling experiments showed the existence of a small tensile stress upon drying due to compressive plastic deformation in the hydrated state [19]. More recently the effects, of cation contamination and platinum dispersion on the mechanical durability of Nafion® NRE 211 have been investigated, showing a reduction in the fracture resistance of the material with increasing cation size and platinum particle aggregation [20, 21].

Using these measured mechanical properties, researchers have begun developing models to calculate the hygrothermal stresses incurred in a fuel cell stack, and the resulting effects on the lifetime of a PEM. The first model was one-dimensional and only accounted for hygral expansion in stress calculations [11]. Additional models were based on linear elastic or linear

elastic-plastic finite element simulations and incorporated temperature and humidity dependent material parameters, as well as constraint in a land/channel configuration [22-28]. These studies showed that significant residual stresses in the constrained PEM developed as the cell was cycled from low to high temperature and humidity levels. However, none of these models captured the time dependence or viscoelastic behavior of PEM materials. Therefore, to more accurately describe the stress state of the PEM, Lai et al [2, 7, 8] proposed a one-dimensional linear viscoelastic constitutive model in the form of **Eqn [2.1]**:

$$\varepsilon_{ij}(\sigma,t,T,\lambda) \approx \frac{3}{2}\int_0^t J(t-\xi)s_{ij}(\xi)d\xi + \delta_{ij}\alpha\cdot\Delta T + \delta_{ij}\beta\cdot\Delta\lambda \qquad \textbf{[2.1]}$$

where ε_{ij} is the strain tensor, J is the shear creep compliance, α is the coefficient of thermal expansion (CTE), β is the coefficient of hygral expansion (CHE), δ is the Kronecker delta, s_{ij} is the deviatoric component of the applied stress tensor σ, T is the temperature, t is time, ξ is the reduced time variable, and λ is the water content of the membrane in terms of the number of water molecules per sulfonic acid group. Although, in principle, all constitutive properties could be considered time dependent, the CTE and CHE have been assumed time independent in this treatment. This assumption was made because it is difficult to determine the time dependence of the CTE and CHE and the characteristic times are likely much faster than those for J. An additional assumption inherent in this relationship is that the material is approximately an elastomer, and therefore the Poisson's ratio was taken to be 0.5. This also implies that a single viscoelastic property can be used to characterize the material. Recognizing that a constrained membrane is strain-controlled rather than stress-controlled, this constitutive model can be rewritten in terms of strain to create a more natural representation of the application, as shown in **Eqn [2.2]**, where E is the uniaxial relaxation modulus.

$$\sigma_x(\varepsilon,t,T,\lambda) \approx \int_0^t E(t-\xi)\frac{d[\varepsilon_x(\xi)-\alpha\cdot T(\xi)-\beta\cdot\lambda(\xi)]}{d\xi}d\xi \quad \textbf{[2.2]}$$

Therefore, *E(t), α,* and *β* are the material constitutive properties needed to create a one-dimensional linear viscoelastic constitutive model, assuming both *α* and *β* are time, temperature, and humidity independent.

As **Eqn [2.2]** requires a time dependent stress relaxation modulus input, it is useful to employ the Time Temperature Superposition Principle (TTSP) to describe a broader range of material behavior than a single stress relaxation test defines. The TTSP states that a change in temperature is equivalent to a shift along the logarithmic time or frequency scale. This principle was initially developed for and is most directly applicable for thermorheologically simple materials, meaning that the viscoelastic behavior of a material at one temperature can be related to that at another temperature by a change in the time scale alone [29, 30]. For this type of material, reduced time can be written as shown in **Eqn [2.3]**, where a_T is the temperature shift factor.

$$t' = \int_0^t \frac{d\xi}{a_T[T(\xi)]} \quad \textbf{[2.3]}$$

Over broad time scales all real materials are likely to have relaxation mechanisms that shift differently with temperature, and would thus be considered thermorheologically complex materials [30, 31]. Although having less basis, TTSP has been extended to thermorheologically complex materials, especially over narrow time windows where a single mechanism such as an *α* or *β* relaxation dominates [32, 33]. One of the earliest studies examining the applicability of TTSP on Nafion® was performed by Yeo and Eisenberg [34] in which they found that TTSP was applicable for the dry acid form, but broke down below 180°C for the acid and potassium salt form exposed to 0.5 H_2O/SO_3H. The authors concluded that this was indicative of two

relaxation mechanisms, one due to chain diffusion and the other to the presence of ionic clusters. However, later studies performed by the same authors showed success in shifting Nafion® neutralized by various counterions under immersed and dry conditions, and it is therefore thought that initial testing may have been flawed [35].

Other authors have found success in the application of the TTSP with Nafion® materials [15, 36, 37], however, given the high moisture sensitivity of PEMs, it is important to consider hygrothermorheological simplicity. In this instance, the viscoelastic behavior of a material at one temperature and moisture level can be related to that at another temperature and moisture level by a change in time scale alone [38]. For this type of material reduced time can be written as shown in **Eqn [2.4]**, where a_H is the hygral shift factor.

$$t' = \int_0^t \frac{d\xi}{a_H[\lambda(\xi)] \cdot a_T[T(\xi)]} \qquad \textbf{[2.4]}$$

A hygrothermal master curve can then be created using the Time Temperature Moisture Superposition Principle (TTMSP). TTMSP has been used to describe other polymeric systems including a semicrystalline poly(vinyl alcohol), poly(vinyl acetate), various polyamides, and the debonding of silicone sealants from various substrates [39-42]. Previous work has also been conducted on PEM materials employing both TTMSP and the linear viscoelastic constitutive equation provided in **Eqn [2.1]** [7, 8, 38, 43].

The first reported application of TTMSP to PEMs was by Lai et al using a dynamic mechanical analyzer (DMA) in a creep mode on Gore Primea, Nafion NR-111, and Nafion N111-IP [7, 8]. A similar analysis was completed by Patankar et al on Gore Primea and Nafion NRE 211 using the stress relaxation mode of the DMA, resulting in a series of relaxation master curves, as well as temperature and humidity shift factors for use in durability modeling [38, 43].

TTMSP has also been used to describe the biaxial strength and fracture energies of perfluorinated sulfonic acid (PFSA) PEM materials over a range of temperature and humidity conditions [44-49]. The shift factors of the same PEM material (e.g. Gore Primea™ membrane) found in DMA, biaxial strength, and fracture energy testing, are all in good agreement, suggesting the application of the TTMSP is valid and therefore the underlying molecular dynamics are very similar over the timeframe examined.

Previous TTMSP and mechanical durability characterizations have focused on PFSA PEM materials, however, PFSA PEM materials are costly, difficult to produce, and face performance problems, creating a need for an improved PEM material [6]. A recently developed material, perfluorocyclobutane (PFCB), shows significant potential as a fuel cell membrane due to its multiple processing routes, low dielectric constant, high thermal and oxidative stability, and chemical resistance [50, 51]. One example synthesized by Iacono had a maximum conductivity of 0.011 S cm^{-1} at 100% RH, the same as Nafion® at 40% RH. An additional two reported membranes, sulfonated poly(fluorenyl ether) and sulfonated poly(fluorine-co-sulfone)ether membranes, show proton conductivities equal to and greater than Nafion® 115, dependent on the level of sulfonation. None of these studies examined the mechanical properties of the membranes, however Mao showed a tensile breaking stress of about 30 MPa for a sulfonated perfluorocyclobutane membrane [51-55]. Additional PFCB polymers used for other applications have been characterized with a 4-9% strain at break and 1 GPA modulus [56-58]. While these studies did not conduct durability analyses, the reported polymers appear to be brittle and likely would not survive the harsh mechanical environment of a fuel cell.

Therefore, to improve the mechanical durability by reducing the brittleness, the PFCB ionomer has been blended with poly(vinylidene difluoride)-co-hexafluoropropylene (PVDF-

HFP). Polymer blending has proven instrumental in the production of materials with tunable properties suitable for a variety of applications including fuel cell membranes [59-64]. One such example is a blend of a hydrocarbon ionomer and PVDF which showed excellent mechanical durability and fuel cell operating lifetimes five times greater than Nafion® NRE 211 [64]. In an attempt to understand this greater lifetime, the research herein focuses on obtaining the constitutive properties required to create a stress analysis model as described by Eqn 2 for a sulfonated PFCB/PVDF-HFP (70:30 wt:wt) ionomeric blend (**Figure 2.1**). Specifically, the thermal and hygral expansion, and viscoelastic properties under dry and humidified conditions will be reported. These properties will also be compared with those of Nafion® NRE 211. Nafion® NRE 211 was chosen to compare with the PFCB/PVDF-HFP blended membrane material because Nafion® is a common material widely used for fuel cell membranes and a previous constitutive characterization was completed on Nafion® NRE 211 [38].

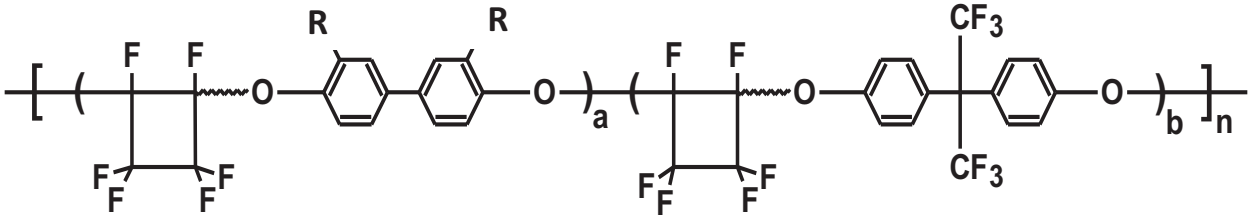

Perfluorocyclobutane Ionomer (PFCB)

+

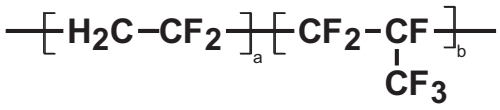

Polyvinylidene difluoride (PVDF) copolymer

Figure 2.1. Structure of PFCB ionomer family, where R represents a sulfonated substituent, and PVDF-HFP copolymer used in this study.

2.2 Experimental

2.2.1 Materials

Cast membranes, approximately 12 μm thick, of 70:30 wt:wt PFCB and PVDF-HFP (Kynar Flex® from Arkema) were received from the General Motors Electrochemical Energy Research Laboratory. The casting solution was created by dissolving 0.10000 kg of PFCB ionomer from Tetramer Technologies and 0.04286 kg of Kynar Flex® 2751 from Arkema in 0.7143 kg of *N,N*-dimethylacetamide (DMAc). The solution was roll milled for 1 week in a 1-L jar with a Teflon® screw cap, and pressure filtered through a 5-μm Mitex® Millipore filter. Several coating solutions were then combined and diluted with DMAc, resulting in a 15 wt% solids solution, in order to create smoother coatings.

The solution was then cast using a coating line consisting of a knife over roll, reverse roll coater onto a polypropylene coated blue paper backer. A coating width of 203 mm and a gap of 0.050 mm were utilized with varying speeds to obtain the targeted membrane coating thickness. After laying the solution down on the backing material, the solution was passed through a 24.4-m drier. The first 12.2 m utilized convection heating, and the second 12.4, IR heating both at temperatures less than 100°C. Rolls of membranes were created at the intended thickness of 14-16 μm, however the actual thickness after casting was ~12 μm as measured by a drop gauge micrometer.

A pre-test treatment was deemed necessary to remove excess DMAc as the excess solvent appeared to be creating a softer, lower modulus, and lower strength material [65]. Initially, a pretreatment consisting of a 12 h hold at 90°C and 10% RH was examined as it was

the procedure used for testing at both GM and Giner for previous Nafion® studies. This low RH level was chosen to allow the pores of the membrane to open and thus permit easier transport of DMAc and water. This pre-test treatment was examined utilizing a TA Instruments TGA Q5000 and observing the weight loss of a sample exposed to the pre-test treatment within a TA Instruments DMA Q800 equipped with a relative humidity accessory (DMA-RH). The sample treated in the DMA-RH was scanned in the TGA by ramping the temperature by 1°C per minute to 150°C under a nitrogen atmosphere. The weight loss occurring in the TGA up to ~100°C is assumed to be free water loss, and the weight loss occurring after 100°C is assumed to be bound water and DMAc loss.

The sample treated in the DMA-RH shows a greater percentage of weight loss due to free water loss (below 100°C) than the samples held isothermally in the TGA, implying the sample absorbed additional moisture in the 10% RH atmosphere. Additionally, the sample treated in the DMA-RH shows weight loss above 100°C, implying the sample did not expel a significant amount of DMAc during the 12 h treatment. Moreover, testing performed at GM with a TGA connected to a mass spectrometer showed a slow release of DMAc up to 200°C, implying that significant DMAc removal would be difficult unless the membrane was heated while immersed in liquid water. Therefore, all subsequent membranes received from GM underwent a solvent exchange in 50°C water for 1 h, while biaxially constrained in a 11.4 x 11.4 cm^2 polytetrafluoroethylene (PTFE) frame. The membranes were then stored in the PTFE frame overnight inside a desiccator to remove excess moisture.

As the membrane dries in the frame, it becomes taut, producing locked in stresses in the material. Alternative drying methods have been examined, but none produced satisfactory

cockle-free membranes for testing in the DMA and Instron. Therefore it became of interest to investigate how much stress is induced into the membrane during the drying process.

The membrane is taut enough to produce a sound when the frame is tapped, similar to a drumhead. Because the stress is related to the frequency of vibration, a test method was developed to record the vibration of the membrane in response to the agitation of the frame, such that the stress can then be calculated. **Figure 2.2** shows the output of the recorded frequency signal, as well as the taut membrane in the Teflon frame.

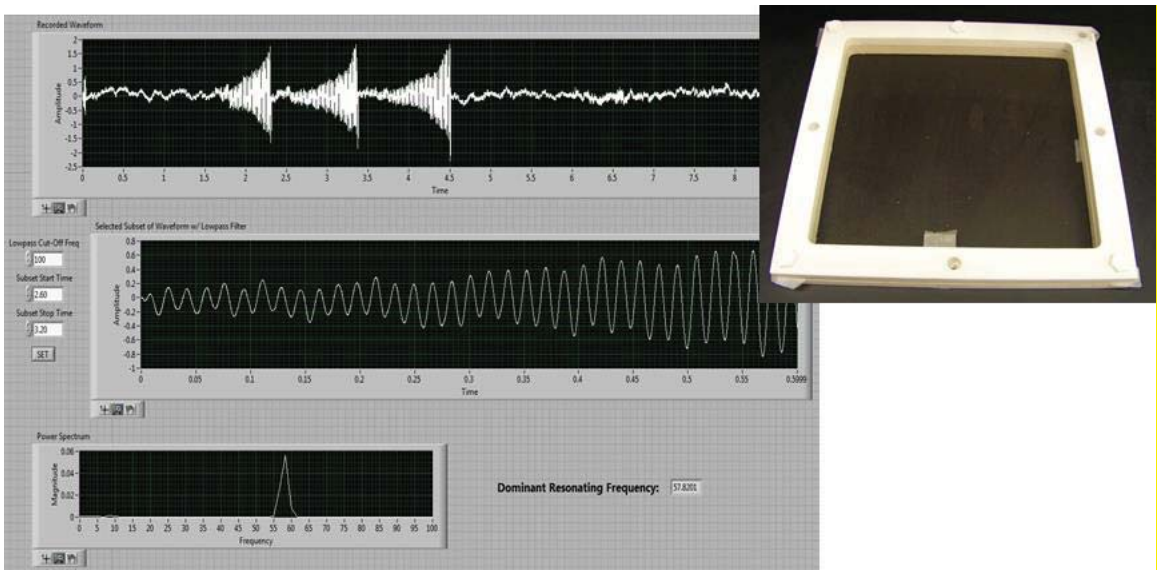

Figure 2.2. Recorded frequency signal after tapping a PTFE frame containing a taut dried membrane (shown at top right).

The dominant resonating frequency was found to be 58 Hz, and **Eqn [2.5]** was used to calculate the membrane surface tension, T, knowing the frequency of a vibrating rectangular membrane, f_{mn}, the areal density, ρ_a, the lengths of the sides of the rectangle, L_x and L_y, and setting the modes of vibration, m and n, to 1 [66].

$$f_{mn} = \frac{1}{2}\sqrt{\frac{T}{\rho_a}}\sqrt{\frac{m^2}{L_x{}^2} + \frac{n^2}{L_y{}^2}}$$

$$T = \frac{4 f_{mn}{}^2 \rho_a}{\frac{m^2}{L_x{}^2} + \frac{n^2}{L_y{}^2}} \qquad \textbf{[2.5]}$$

$$T = (58Hz) = 7.25N/m$$

Knowing that stress is equivalent to the membrane surface tension divided by the thickness, the residual stress in the membrane from the solvent exchange and drying process was determined to be 725 kPa. This test was performed approximately 1 week after the membrane was removed from the water bath, implying the stress was likely less than immediately after the membrane dried due to the relaxation process of the material. However, 725 kPa is still a large amount of induced stress in the membrane and shows the need for an additional pre-test treatment. Therefore, to remove the locked in strains formed during the solvent exchange process, immediately prior to testing and after removal from the PTFE frame, each membrane underwent a 100°C 2 h isotherm at 0% RH.

For comparison purposes Dupont™ Nafion® NRE 211 (NRE 211) membranes, approximately 25 μm thick, produced reportedly from a casting process, were also characterized. These membranes were not subjected to the one hour 50°C solvent exchange because it was not performed for prior characterization, but for consistency in membrane water content, samples were subjected to the two hour 100°C isotherm prior to testing.

2.2.2 Mass Uptake

Mass uptake measurements were performed by Matt Green, a student in Dr. Long's group, using a TA Instruments Q5000 SA Vapor Sorption Analysis instrument. Each test used approximately 1 mg of material cut into small pieces and began with a 1 h isotherm at 80°C and

0% RH to dry the material, 80°C was chosen because this is the temperature limit of the instrument. The sample was then cooled to the test temperature, 30, 40, 50, 60, or 70°C, and held for 2 h. The humidity was then increased by 5% every 2 h until reaching 95% RH. In addition, a step was included in the test protocol that allowed the instrument to increase the humidity if the sample weight percent changed by less than 0.01% over 5 min. At low humidity levels this override was used frequently, but at 60-80% RH each isotherm was held for approximately 1 hr, and 85-95% RH each isotherm was held for the full two hours. Lambda values were calculated using the equivalent weight as measured by Nathan May from titration experiments. Over four experiments he measured a range of equivalent weights from 802.62 – 1103.24 mmol/g, and the average value of 934.16 mmol/g was used for calculations.

2.2.3 In-Plane Thermal and Hygral Expansion

In-plane thermal and hygral expansion measurements of the PFCB/PVDF-HFP blend and NRE 211 were performed using a DMA-RH. Initially, all samples to be tested in the DMA were each hand cut using a razor blade. The width of each sample then had be measured under a microscope at the top, middle, and bottom to obtain an average width to acquire more accurate test results. However, this cutting method requires a very careful hand so as not to leave a serrated edge on the sample, or rip the membrane. In addition, it is very difficult to cut a parallel sample with the human eye, reducing the accuracy of the test results. This cutting and measuring process for a set of test samples required at least half a day to complete, and thus it was desirable to create a rule die so that all test specimens are cut evenly and efficiently. Moreover, a rule die would standardize the cutting process across the multiple labs that work with these membrane materials which in turn would reduce variability in the test results between labs.

The current rule die and sample design for the DMA can be seen in **Figure 2.3A**. The design of the slit samples increases the overall width of the sample in the DMA providing a stronger signal to noise ratio, but maintains the desired 5:1 aspect ratio which approximates a uniaxial stress state. The measurements given in Figure 5 for the rule die design are based on samples made and loaded in the DMA to see how well they fit. The bottom dimension, below the slit, is controlled by the location of the screw to close the bottom grip. The top is designed with extra length to ease the loading of the sample into the DMA. The grips are 9 mm wide, and therefore the sample could be made at most 9 mm wide and slit into three 3 mm sections as shown. The pressure distribution of the grips was determined to be uniform across the entire width of the clamp as deduced using pressure sensitive film **Figure 2.3B**.

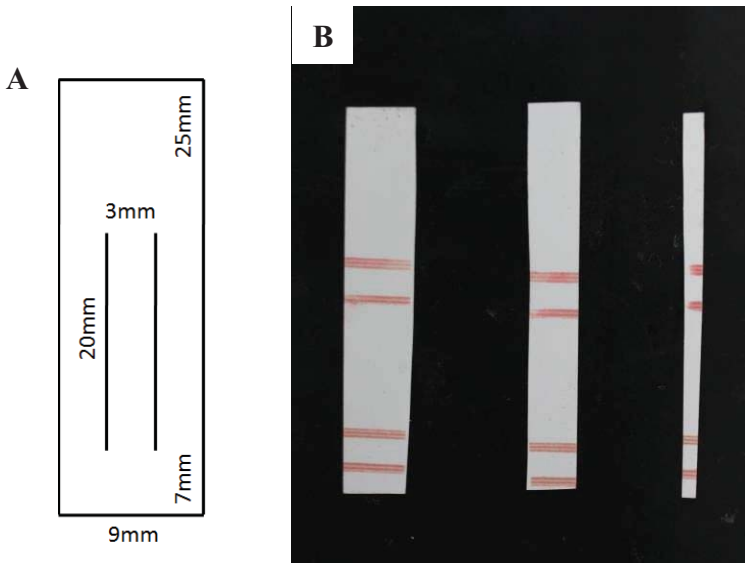

Figure 2.3. (A) Rule die and sample design of slitted sampled for use in the DMA. **(B)** Pressure paper after removal from DMA tension clamps, showing an even pressure distribution across the grips for 9, 6, and 3 mm wide samples respectively.

The DMA allows for a sequence of different runs to be completed, performing subsequent runs immediately after the completion of the first run. Therefore, the pre-test treatment to relax the locked in strains was separated into a different run from the data collection

test method. This was done so that the pre-test treatment could be performed under a creep mode to allow a small static force to be applied no matter the data collection test method. Within the creep method the static force was set at 3 mN and was applied for the entirety of the equilibration. The step normally used to apply creep to the sample was not employed, and only changes in temperature and humidity were used. Two tests were performed to examine possible creep occurring in this new test method for pre-test treatment. Each test equilibrated the sample at 100^{o}C, applied 30% RH for three hours, applied 0% RH for three hours, and then equilibrated the sample to 30^{o}C at 0% RH. This was done to examine the change in length with applied humidity, and it was thought that if the length after the removal of humidity was the same as or shorter than the initial length of the sample, then significant creep had not occurred. These tests were each performed using static applied forces of 1.5 or 3 mN to ensure that the magnitude of the applied static force did not cause significant creep. Both sets of data are shown as length vs. time in **Figure 2.4**.

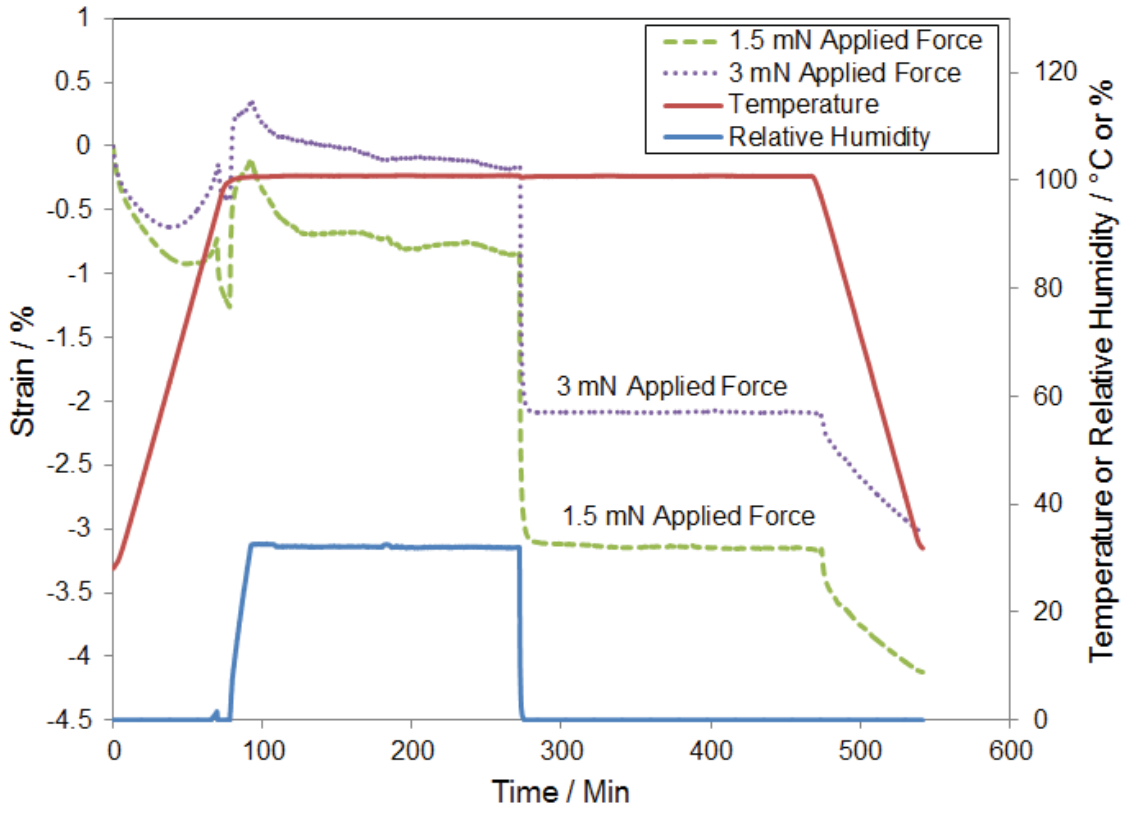

Figure 2.4. Length vs. time comparison of data taken under a static force load of 1.5 and 3 mN.

In both sets of data it can be seen that the length after the humidity is removed is shorter than the initial length of the sample; additionally, when the temperature is decreased to 30°C, the length of both samples decreases further. These results indicate that both force levels exhibited a negligible amount of creep. The sample exposed to a 1.5 mN load reached a maximum strain of ~ -0.2% strain and a minimum of ~ -4% strain. The sample exposed to a 3 mN load reached a maximum of ~ 0.3% and a minimum of ~ -3% strain. The minimum for both samples occurred when the temperature was reduced back to 30°C at the end of the test. The smaller minimum strain for the 3 mN sample is observed due to the higher applied load, which constrains the membrane from contracting a similar amount as the sample with the 1.5 mN applied load. However, the constraint the 3 mN load exhibits on the sample appears to not cause significant

creep, as any creep appears to be less than membrane shrinkage, as evidenced by the shorter final length of the sample. In addition, it is expected that the maximum strain would be higher for the sample with the 3 mN applied load, rather than the 1.5 mN applied load, however both maximum strains are very minimal and assumed to cause non-significant creep.

Because non-significant creep was found under a 3mN load, this force was applied during testing to hold the sample taut without causing significant creep in the sample. In addition this applied load was an order of magnitude larger than the lower force limits of the instrument, and therefore outside the noise range of the instrument. Thermal expansion characterization was performed by increasing the temperature from 30 – 120°C by 5°C increments every two hours, while maintaining a constant humidity level, and a different sample was used at subsequent humidity levels every 10% RH from 0-90% RH. Similarly, hygral expansion was performed by increasing the humidity from 0-95% by 5% RH steps every two hours, while maintaining a constant temperature every 10°C from 30-120°C, and a different sample was used at subsequent temperature levels. The length of the specimens, nominally loaded in uniaxial tension at very small stress levels, was measured at the completion of each two hour step, and the corresponding thermal or hygral expansion was calculated.

2.2.4 Characterization of the Blend α-Relaxation

The α-relaxation of the blend was characterized using the DMA with RHA, under the dynamic mode over 30-120°C with a temperature ramp rate of 0.1°C/min, from 0-90% RH in 10% RH increments. A constant relative humidity was used for each test, and the sample was equilibrated for 2 h prior to testing. This slow temperature ramp rate was found necessary to obtain clean data, as the instrument was unable to maintain a constant RH level if the

temperature were increased at a higher rate. The tan δ data were then examined to understand any changes in the α-relaxation with increasing moisture content.

2.2.5 Linear Viscoelastic Properties Characterization

2.2.5.1 Stress Relaxation Hygrothermal Master Curve Data Collection Method

A hygrothermal stress relaxation master curve was developed using data taken under the stress relaxation mode using 0.5% strain at 0, 2, 10, 30, 55, and 80% RH every 10°C from 30-120°C on samples cut parallel to the casting direction. For further information on method development, please see Appendix 1. One sample was used for each humidity level to minimize sample loading differences and equilibration times. Knowing the material requires more time to equilibrate for moisture content than temperature, the relative humidity was held constant and the temperature increased. In addition, the material was equilibrated for 2 h at each moisture level prior to testing. Each stress relaxation test was 17 minutes long, followed by a 60 min recovery period. The temperature was then raised 10°C, and held for an additional 60 min before the next stress relaxation test was performed allowing for 99% or greater recovery of the sample. To ensure significant recovery had occurred after each stress relaxation test, the 110°C data set measured on the sample used for 30% RH testing, was compared with an additional sample that was only tested at 110°C and 30% RH. As shown in **Figure 2.5** the agreement at times greater than 100s is very good between the single relaxation test and that taken after multiple relaxation tests, while at shorter times there is ~15% difference between the two samples. It is possible this difference at shorter times is due to a residual strain after multiple relaxation tests, but it is also possible it is due to differences in sample loading or the samples themselves. In addition, when the single relaxation test is shifted to align with the master curve, the difference in shift factors for both 110°C tests is less than 5%. Therefore, it is believed that recovery as observed during

testing of 99% or greater is sufficient, resulting in accurate measurement of the stress relaxation behavior of the PFCB/PVDF-HFP material. The stress relaxation data were then shifted for temperature and humidity simultaneously resulting in a hygrothermal master curve and hygrothermal shift factors.

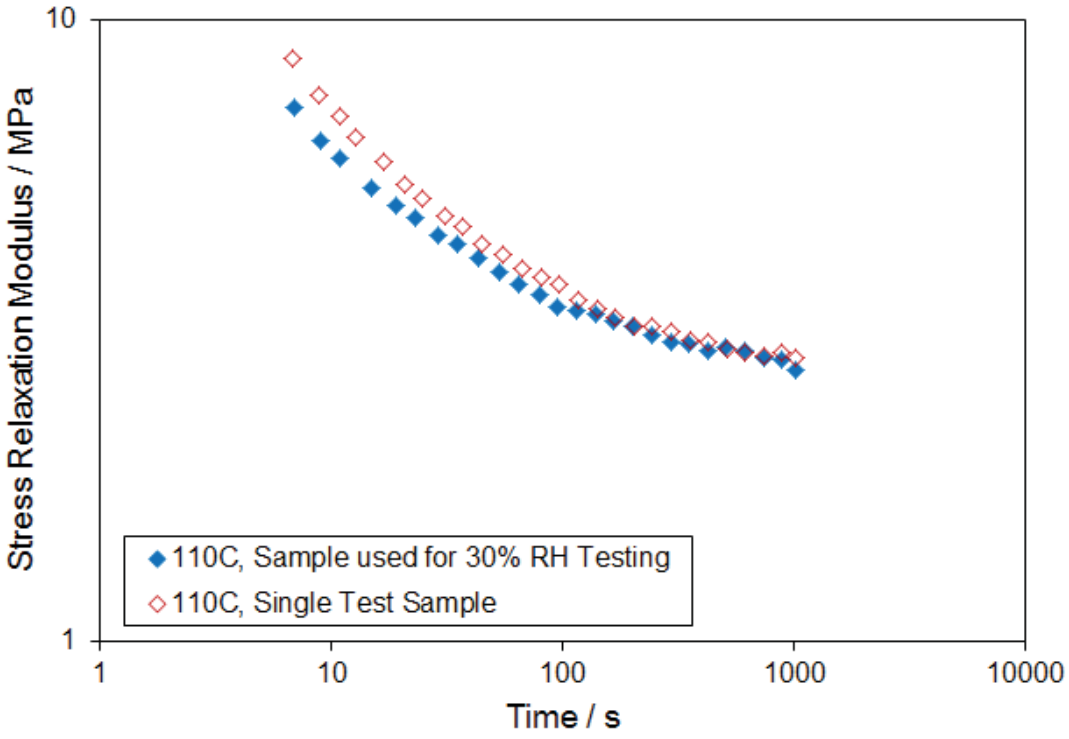

Figure 2.5. Comparison of the 110°C data set measured on the sample used for 30% RH testing, with an additional sample that was only tested at 110°C and 30% RH.

2.2.5.2 Long Term Creep Test Method

Long term creep data were also taken for validating the hygrothermal master curve utilizing a custom-built instrument, as shown in **Figure 2.6**. The fixture consists of a metal carousel housed within an oven. The carousel can hold up to 18 75-mL test tubes that are each individually capped with PTFE plugs, creating 18 small environments for testing within. A sample of length 90 mm and width 4.5 mm was clamped with an ~60 mm gage length, within each test tube, as shown in **Figure 2.7**, using ceramic magnetic grips coated in Permalite Sea

Goin'® Heavy Duty Poxy Putty, an epoxy designed for underwater use. This allows for testing to be performed under humid and immersed conditions at the oven temperature without the development of corrosion in the magnets. Because the samples were cut by hand, the true width of each sample was measured using the optical microscope by taking a measurement at the top, middle, and bottom, and an average value was used for calculations. A chosen stress was applied to each sample by adhering a small rubber block to the end of each sample. Each rubber block was massed to provide the appropriate stress level, and those used under immersed conditions were massed while hung in water to account for buoyancy effects. The change in length of each sample was measured using a traveling microscope with a resolution of 0.01mm over logarithmic time intervals.

The first successful run of the long term creep fixture utilized dry, 100% RH, and water immersed conditions under both 0.5 and 1 MPa stresses at 70°C for 98 days. The 100% RH condition was achieved by placing about 10 mL of DI water at the bottom of each test tube, such that a sample would not touch the water, but simply be enclosed with it. The water immersed condition was achieved by filling each test tube with DI water and submerging the sample inside. The 70°C temperature was chosen because this is where the hygrothermal master curves are referenced. The 0.5 and 1 MPa stresses were initially chosen because, based on the isochronal plots at 70°C and 30% RH shown in **Appendix 1**, both values were thought to be within the linear viscoelastic region. While the required mass for the 0.5 MPa piece was easily obtained with a small piece of rubber, the 1 MPa pieces had to be modified to reach the desired mass. Due to a large amount of buoyancy in the water immersed samples, both the 0.5 and 1 MPa pieces had to be modified. The increased mass was achieved by creating a small hole on the bottom of the rubber piece and depositing solder until the desired mass was reached. The solder

was then covered with an epoxy to reduce possible oxidation or hydrolysis problems during water exposure.

Each sample was placed in the magnetic grips and gently placed in the test tube which remained tilted on its side for approximately 12 hours until testing began. This allowed each sample to equilibrate with the water environment as necessary, and eased test start up as each sample merely needed to be carefully tipped upright and placed in the oven. However, the early time data is flawed in that samples were equilibrated at the respective moisture conditions at room temperature (about 28^{o}C). Therefore, when samples were placed in the 70^{o}C oven, each sample was equilibrating to the increased temperature. Equilibration could have taken quite a bit of time as the glass tube and the air or water inside the tube also had to equilibrate before the sample could fully equilibrate. In addition, the oven door was opened every 18 minutes to start a new sample over a six hour time frame, and thus while the temperature remained approximately 70^{o}C, it was not a constant value. Due to this temperature equilibration flaw in the early data, data analysis was performed only using data after 10,000s. This is just under three hours and should have allowed for the sample to fully equilibrate with the environment. In addition, samples in 100% RH and water immersed conditions showed significantly more creep than expected, resulting in the collection of data in the nonlinear viscoelastic regime of the material.

Therefore, to address the nonlinearity and temperature equilibration flaw, another long term creep test was prepared after modifying the test tube set up, and the applied stresses. Each test tube was equipped with a small acrylic disc platform adhered to a 2-mm diameter glass rod as shown in **Figure 2.7**. The rubber block rested on the acrylic disc platform, allowing the samples to equilibrate at the given moisture condition upright, in the oven, without any applied stress. When each test was begun, the glass rod that extended out of the top of each test tube was

pushed down through a small hole drilled in the top of the oven, allowing the stress to be applied easily, maintain a constant temperature, and obtain measurements within 30 seconds of the applied load. The applied loads were decreased to 0.25 and 0.5 MPa to obtain data in the linear viscoelastic region. Sixteen samples were tested, two 0.25 MPa 0% RH, two 0.5 MPa 0% RH, three 0.25 MPa 100% RH, two 0.5 MPa 100% RH, three 0.25 MPa immersed, and three 0.5 MPa immersed. The full 18 samples were not used because two 0% RH samples broke during loading, and one 100% RH sample platform fell prior to the start of the test. However, testing was continued for 218 days because at least one replicate existed for each condition.

Figure 2.6. Schematic of in-house long term creep fixture.

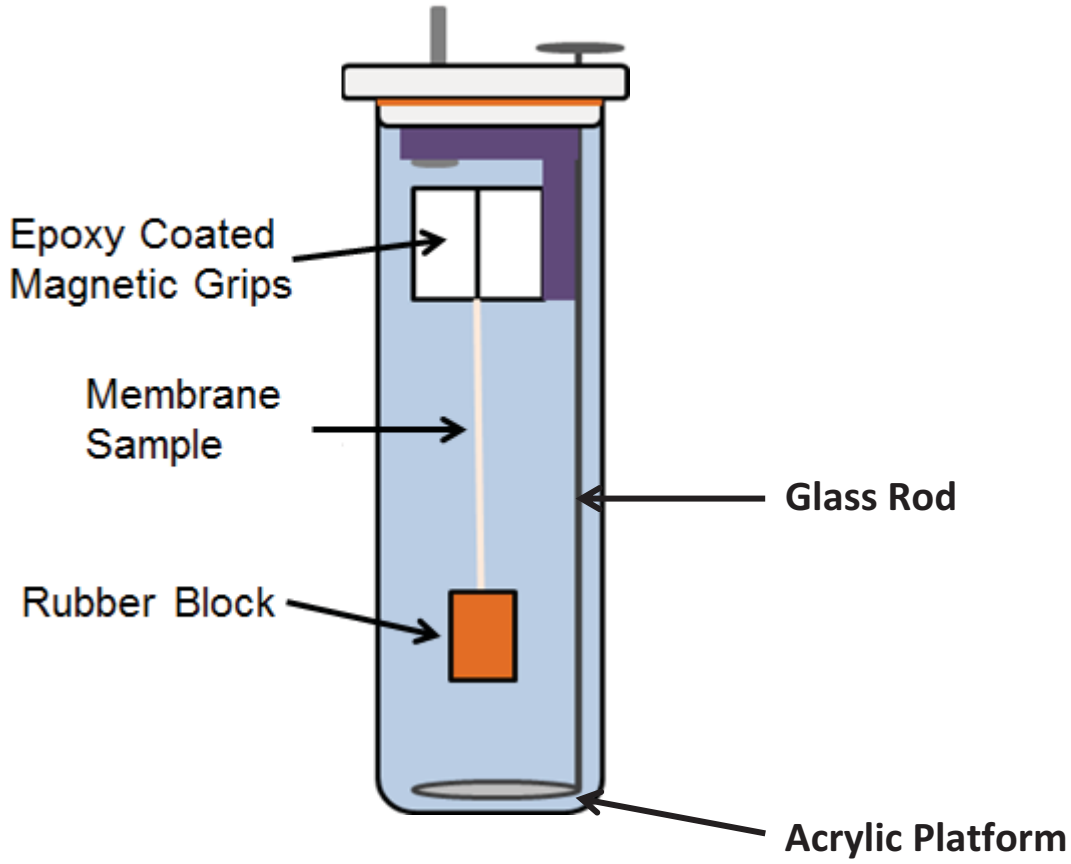

Figure 2.7. Schematic of sample gripped between two epoxy magnets with an applied stress via an adhered rubber block.

2.3 Results and Discussion

2.3.1 Mass Uptake

It is important to determine the water content, λ, defined as the moles of water per mole of sulfonic acid, of this ionomeric material, as other properties such as hygral expansion and modulus are dependent on the moisture level of the sample. Therefore, mass uptake measurements were performed on both PFCB/PVDF-HFP and NRE 211 (**Figure 2.8**), although NRE 211 measurements have been limited up to this point. Initially, measurements were performed from 30 - 70^{o}C on PFCB/PVDF-HFP that had been stored at ambient conditions. As seen in **Figure 2.8** by the solid symbols, the calculated λ values for PFCB/PDF-HFP show no

temperature dependence, indicating the material absorbs the same amount of moisture no matter the temperature. Therefore, the water uptake of PFCB/PVDF-HFP can be described by an empirical equation, **[2.6]**:

$$\lambda = 0.000013 * RH^3 - 0.001192 * RH^2 + 0.065369 * RH \quad \textbf{[2.6]}$$

It was previously believed that an empirical equation (**Eqn [2.7]**) developed based on Zawodzinski's Nafion® data would describe all other ionomeric materials because the water content is controlled by the sulfonic acid groups [67]. Therefore it was thought that all ionomeric materials would have similar sorption pathways.

$$\lambda = \left[1 + 0.2325RH^2\left(\frac{T-30}{30}\right)\right]\left(14.22RH^3 - 18.97RH^2 + 13.41RH\right) \quad \textbf{[2.7]}$$

This equation is plotted in **Figure 2.8** for comparison with the collected data. It is clear that the PFCB data does not match the behavior from **Eqn [2.7]**. Specifically, the initial mass uptake appears to be much lower than **Eqn [2.7]** predicts, causing the entirety of the curve to be lower than the equation prediction. However, this difference is not entirely unexpected, as the morphology of the PFCB/PVDF-HFP is likely quite different from that of Nafion® or PFSA materials. Thus, it should not be assumed that all ionomeric materials show similar water sorption pathways, because the morphology of different materials will play a key role.

To ensure the measured difference in PFCB/KF water uptake from the **Eqn [2.7]** prediction was real and not due to a higher level of initial moisture in the material, two additional tests were performed to see the effects of further drying the material prior to testing. First, PFCB/PVDF-HFP was held at 100^{o}C overnight in a vacuum oven, as shown by open pink squares in **Figure 2.8**. However, the corresponding lambda values decreased significantly from the PFCB stored at ambient conditions. It is presumed this occurred because the vacuum oven

removed such a high quantity of water from the material that the percolative channels collapsed. With collapsed channels, it was more difficult for water to be sorbed by the material, resulting in a significantly lower λ value. The second drying treatment was the same as performed prior to all DMA testing to ensure the locked in stresses from the water bath treatment are removed. Therefore, the PFCB material was held in an oven for 2 h at 100°C immediately prior to placing the material into the Sorption Analysis instrument. This sample is shown in Figure 2.8 as open blue squares, and while higher than the overnight annealed material, it is still lower than the material stored at ambient conditions. This behavior will be further discussed in **Chapter 4.3.1.2**.

Because concern was raised over the differences in the PFCB data and **Eqn [2.7]**, NRE 211 was also tested to see if this data could be matched with the lambda predictions and verify the testing method. Hysteresis type tests were used to examine NRE 211, increasing and decreasing the humidity twice on each sample. Two separate NRE 211 samples were tested, one with the 80°C, 0% RH 1 h drying step, and one held at the test temperature (30°C) and 0% RH for 30 min with no 80°C drying step prior to testing. Both samples were stored at ambient conditions prior to testing. The NRE 211 hysteresis tests are shown in **Figure 2.8** as dashed lines, short dashes for the first humidity cycle, and long dashes for the second humidity cycle. As seen, both NRE 211 samples match well implying independence of the drying temperature, however neither test matches the **Eqn [2.7]** predictions. Again, the initial mass uptake appears to be much less than the predicted value, causing the entire curve to be lower. In addition, the apparent hysteresis between increasing and decreasing the humidity is likely due to the test method, in which the sample was exposed to increasing humidity until held for 2 h at 95% RH, and then exposed to decreasing humidity which began with an additional 2 h isotherm at 95%

RH immediately after the completion of the increasing humidity test. This caused the sample to be exposed to the high RH level for an extended time, and therefore take up additional mass before reducing the RH level, resulting in an apparent hysteresis in samples.

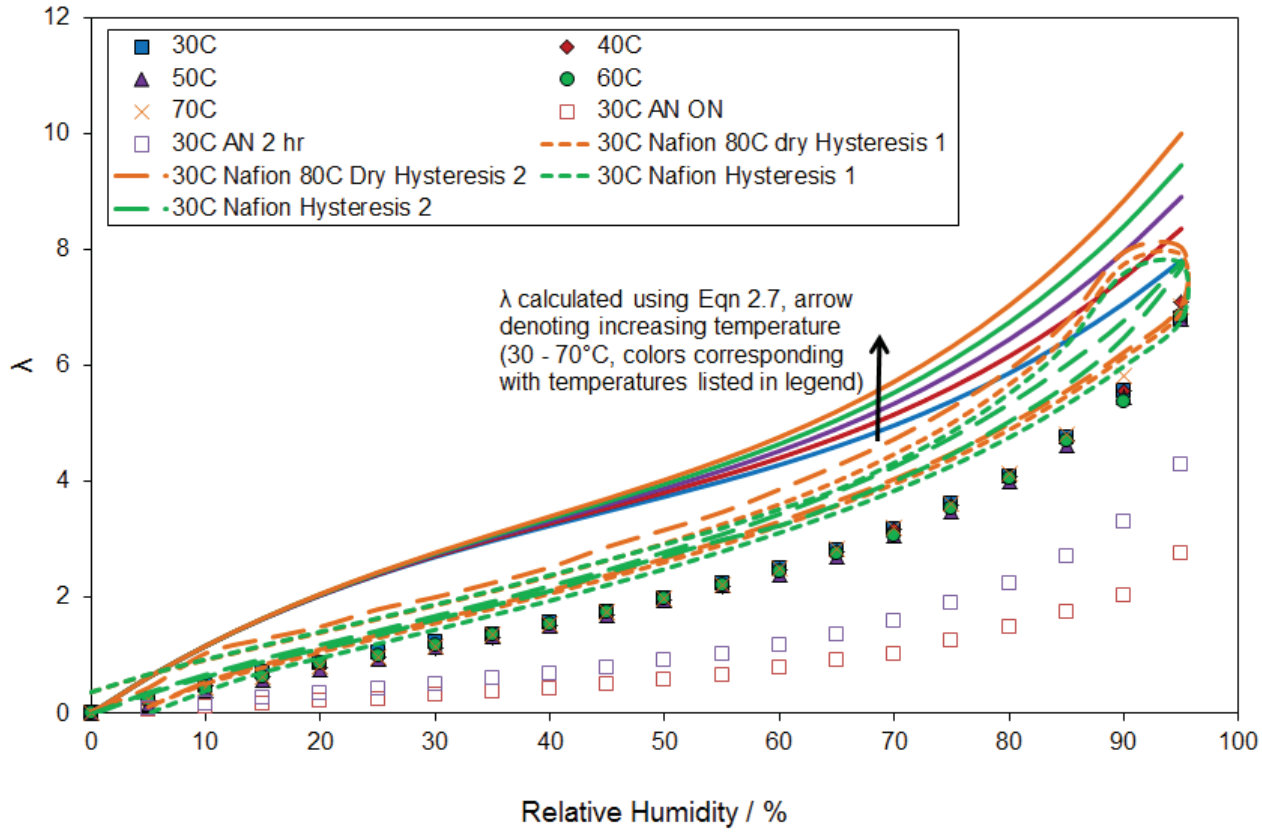

Figure 2.8. Comparison of lambda values measured for PFCB/PVDF-HFP stored at ambient conditions, PFCB stored overnight in a vacuum oven at 100°C, PFCB/PVDF-HFP heated in an oven at 100°C for two hours, and NRE 211, using a TA Instruments Q5000-SA sorption analysis instrument with **Eqn [2.7]**.

To further investigate the difference between the Nafion® data collected at Virginia Tech using the Sorption Analysis instrument and **Eqn [2.7]** predictions, published data and additional data taken gravimetrically at Virginia Tech were examined (**Figure 2.9**). The published data by Pushpa [68] and Zawodzinski [69] agree fairly well with the **Eqn [2.7]** prediction, shown as a solid green line in **Figure 2.9**. Although slightly different, they both show a large initial mass uptake, consistent with **Eqn [2.7]**. However, the data collected at Virginia Tech gravimetrically

matches better with the data taken at Virginia Tech using the Sorption Analysis instrument [70]. Again, the initial mass uptake is not as large as expected from **Eqn [2.7]** and the other published data. The data collected by Zawodzinski and Pushpa were both taken on non-chemically stable Nafion®, a fundamentally different material than NRE 211, and the differences between these data sets and those collected at Virginia Tech may be accounted for in this fashion. In addition, data collected by Maldonado et al. gravimetrically using NRE 211 over-predicts **Eqn [2.7]** [71]. Therefore it is possible that **Eqn [2.7]** does not universally describe ionomeric materials, or even PFSA materials, and water uptake measurements should be performed when characterizing and modeling new ionomers.

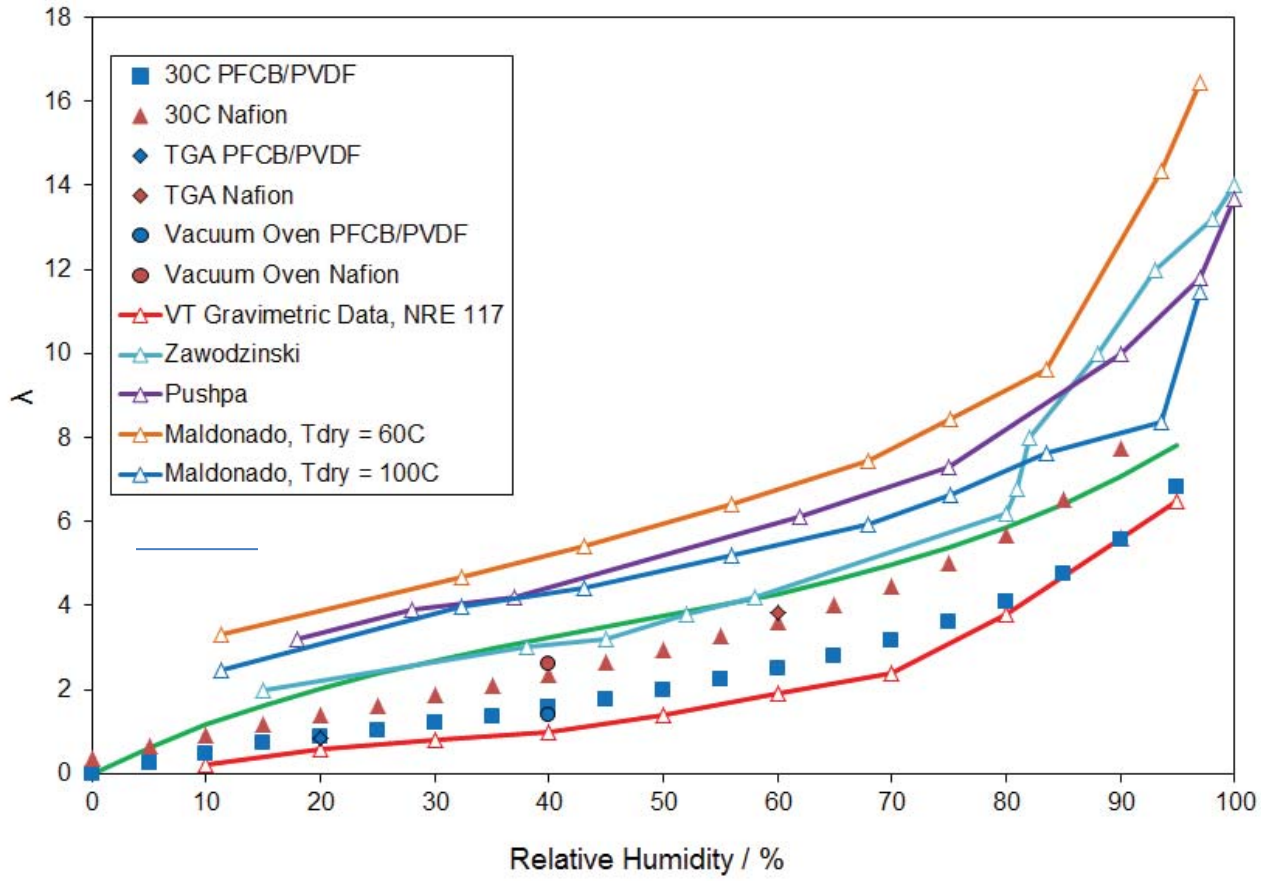

Figure 2.9. Comparison of mass uptake data for Nafion® taken gravimetrically at Virginia Tech, published data, and **Eqn [2.7]** [68-71].

Previous data collected by the Giner corporation on PFCB/PVDF-HFP and NRE 211 showed good agreement with **Eqn [2.7]**. The method utilized by Giner Corporation is similar to that of the TA Q5000-SA instrument. A 1 x 2 cm piece of membrane material is hung from a Rubotherm mass measurement device, within an RH chamber with temperature control. The sample is then dried for 1 hr at 80°C and 0% RH, followed by an increase the RH by 10% increments every half hour up to 90%, followed by an additional step at 95% RH. The measurements are then repeated stepping back down, with each RH level held for a half hour.

To investigate the differences in mass uptake between data taken at VT and at Giner Corporation further, two checks were performed, one utilizing a TGA Q5000 and the other utilizing a vacuum oven. The TGA test allows for monitoring of the mass change over the entirety of the test, utilizing less than a milligram of material. The vacuum oven allows for a bulk sample to be examined, however only the initial and final masses are available.

The TGA test was performed on a sample of PFCB/PVDF-HFP or NRE 211 that had been stored at ambient conditions. The sample was heated to 80°C and held for 12 hours, and the change in mass over this time was taken to be equivalent to the mass of water in the sample. Similarly, a larger sample was placed in a vacuum oven for 36 hours at 100°C, and was quickly massed on a scale after removal from the oven. The change in mass after the vacuum oven exposure was taken to be equal to the mass of water in the sample. Lambda for each sample was then calculated using **Eqn [2.8]** where EW is the equivalent weight of the membrane.

$$\lambda = \frac{g \text{ of } H_2O}{g \text{ of Membrane}} \cdot \frac{\left(\frac{mol \text{ of } H_2O}{18g \ H_2O}\right)}{\left(\frac{mol \text{ of Membrane}}{\text{EW of Membrane}}\right)} \qquad \textbf{[2.8]}$$

A summary of the data collected from the TGA and vacuum oven tests as compared with measured lambda values from the TGA Q5000-SA and **Eqn [2.7]** is provided in **Table 2.1**.

Table 2.1. Summary of lambda values from mass check testing, as well as mass uptake measurements and calculation from **Eqn [2.7]**.

	TGA Mass Check	Vacuum Oven Mass Check	TGA Q5000-SA Mass Uptake	Calculation from **Eqn [2.7]**
PFCB/PVDF-HFP (20% RH, 25°C)	0.848	---	0.8786 (20% RH, 30°C)	2.03
NRE 211 (60% RH, 23°C)	3.834	---	3.26 (60% RH, 30°C)	4.20
PFCB/PVDF-HFP (40% RH, 23°C)	---	1.38	1.57 (40% RH, 30°C)	3.21
NRE 211 (40% RH, 23°C)	---	2.63	2.107 (40% RH, 30°C)	3.21

*Ambient storage conditions provided below material
**Environmental condition used for comparison provided below TGA Q5000-SA mass uptake values

The mass checks performed on PFCB/PVDF-HFP from both the TGA and the vacuum oven match very well with the mass uptake data collected at Virginia Tech in the TGA Q5000-SA, rather than the predicted values from Eqn. **[2.7]**. In addition, the mass checks performed on NRE 211 both fall in between the measured mass uptake data from the TGA Q5000-SA at Virginia Tech, and Eqn. **[2.7]**. Therefore it is clear there is a difference between measurements taken at Virginia Tech and those taken at Giner Corporation. It is important to understand this discrepancy because the water uptake behavior of the material will have a large impact on the constitutive model. Further discussion on this difference and the impact on modeling is provided in **Appendix 2**.

2.3.2 Thermal and Hygral Expansion

2.3.2.1 In-Plane Thermal Expansion

The thermal expansion behavior of PFCB/PVDF-HFP and NRE 211 membranes is shown in **Figure 2.10** with CTE values provided in **Table 2.2**. Under the assumption that each data set could be fit linearly the CTE was calculated by performing a linear fit of each data set, of which the slope equaled the CTE. From 10-50% RH the CTE of PFCB/PVDF-HFP and NRE 211 shows little moisture dependence. However the average CTE from 10-50% RH of PFCB/PVDF-HFP of 1.46 x 10^{-4} $°C^{-1}$ is about double that of NRE 211 at 7.32 x 10^{-5} $°C^{-1}$, indicating the PFCB/PVDF-HFP membrane expands more with changes in temperature than NRE 211 over the lower humidity range. However, it is important to note that thermal expansion is 2-3 orders of magnitude smaller than hygral expansion, and thus the increased thermal expansion of PFCB/PVDF-HFP compared with NRE 211 is expected to have a very minimal effect on the stresses incurred in an operating fuel cell.

Above 50% RH the CTE begins to increase in both the PFCB/PVDF-HFP and the NRE 211. This behavior above 50% RH matches the in-plane hygral expansion curves. Therefore, the constant CTE measured below 50% RH may be more unexpected than the increase in CTE at high moisture contents. Based on FTIR studies of water in Nafion at different RH levels, a possible explanation for the constant CTE below 50% RH could be attributed to the distribution of water in the membrane [72]. As water enters a dry membrane it will begin to form aggregates with the sulfonic acid moieties, as the water content is increased, these aggregates will grow in size. At a threshold water content of about a λ of 5, the aggregates have grown so large the distance between sulfonic acid groups begins increasing. This results in a decrease in the

strength of the electrostatic network, and thus allows an increase in the thermal expansion of the material with further increased water content.

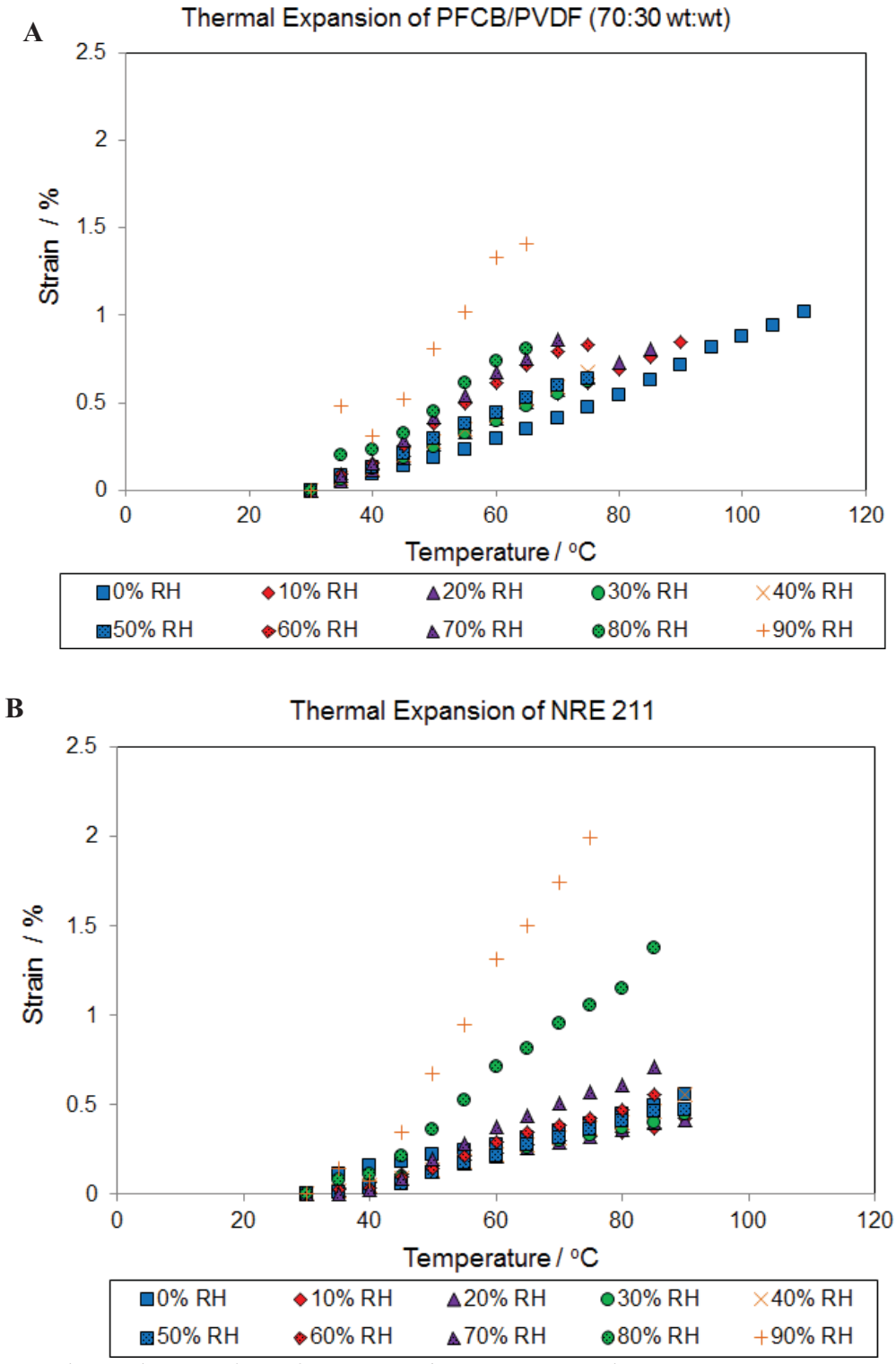

Figure 2.10. Thermal expansion of **(A)** PFCB/PVDF-HFP and **(B)** NRE 211.

Table 2.2. CTE of PFCB/PVDF-HFP and NRE 211 as measured from the slope of data taken over 30-120°C at different RH levels from 0 – 90% RH, by10% intervals.

	PFCB/PVDF-HFP ($x\ 10^5\ °C^{-1}$)	NRE 211 ($x\ 10^5\ °C^{-1}$)
0% RH	13.0	8.11
10% RH	14.2	6.97
20% RH	15.0	7.43
30% RH	13.9	7.57
40% RH	15.1	9.12
50% RH	14.7	8.75
60% RH	19.9	10.5
70% RH	22.6	14.0
80% RH	22.8	26.6
90% RH	39.3	47.8

2.3.2.2 In-Plane Hygral Expansion

Ionomeric materials often expand significantly more due to sorbed water than increases in temperature, underscoring the importance of characterizing the CHE of PFCB/PVDF-HFP membrane as well. To ensure the membrane sample did not undergo significant creep during testing, a sample was assessed at 40°C, increasing humidity from 0-95% RH, followed immediately by decreasing the humidity to 0% RH, by 5% RH steps. As can be seen in **Figure 2.11** the final strain returns to zero, verifying that the sample does not creep significantly and all expansion is apparently due to hygral swelling. It should be noted that the increasing and decreasing strains line up well at lower humidity levels, while they are some distance apart at higher humidity levels, indicating hysteresis. We currently believe this is not a true hysteresis; rather we hypothesize that the sample did not have enough time to fully equilibrate at the higher humidity levels. This is further evidenced by data taken at 60°C in which each humidity step was held for 5 hours, and the strains at high humidity levels were still not equilibrated. This indicates the PFCB/PVDF-HFP membrane requires more time to equilibrate hygral strains, in

contrast to the less than 60 minutes required for the PFCB/PVDF-HFP membrane to equilibrate strains with a change in temperature alone.

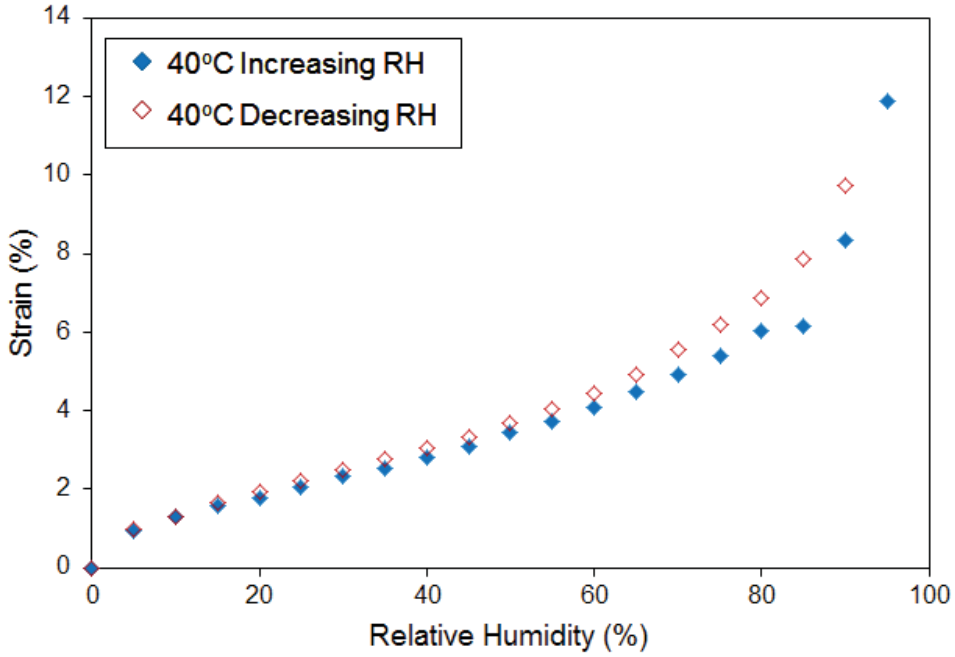

Figure 2.11. Strain of PFCB/PVDF-HFP at 40°C while increasing and decreasing the relative humidity from 0-95% under a 3 mN creep load.

Two hypotheses currently exist as to why it takes the material longer to equilibrate at higher humidities either due to diffusion-limited sorption or time dependent chain motions limiting sorption. Expanding upon the first hypothesis further, there are two possible explanations for this behavior in the material. First, water vapor can pass through the membrane easily after it is first exposed to a relative humidity environment. However, as liquid water begins to fill the membrane, the vapor cannot pass through as easily, thereby increasing the time needed for the membrane to sorb moisture. Second, water diffusion into the PFCB material may be kinetically limited, and at higher relative humidity levels there are a larger number of water molecules that need to diffuse into the material. This is shown in **Figure 2.12**, where the change in λ with a change in high relative humidity levels is larger than at changes in low relative

humidity levels. Therefore at higher relative humidity levels the material requires more time to equilibrate the hygral strains, indicating time dependence of hygral expansion.

The second hypothesis can be explained by examining the hydrophilic sulfonic acid groups in the PFCB material. These sulfonic acid groups therefore pull water into the membrane at low relative humidities due to the specific interactions. However, at higher relative humidity levels the sulfonic acid groups are already surrounded by water molecules, and the material has to find space and expand further via molecular rearrangements, to place the additional water molecules. This explanation indicates molecular motions which would be time dependent, indicating hygral expansion is also time dependent. While it is not known how water sorption is occurring, it is likely that a combination of all three explanations is key in the sorption of moisture in these PFCB materials.

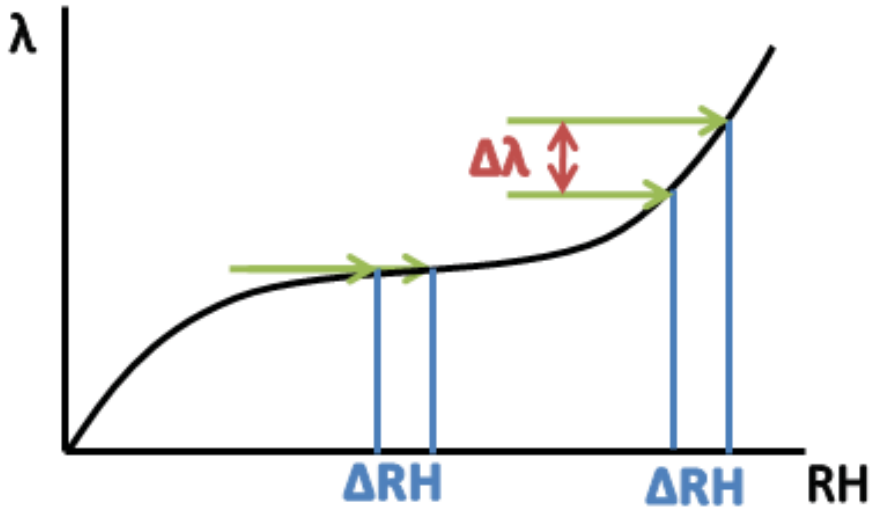

Figure 2.12. A change in moderate relative humidity levels results in little change in the lambda content, but a change in high relative humidity levels results in a large change in the lambda content.

Despite the increased equilibration time at higher humidity levels, testing was continued with 2 hour isotherms at each humidity step under the assumption that it is unlikely in a real fuel

cell that the membrane would spend over 2 hours at any given humidity state. It should be noted that the shape of the hygral expansion curve is sigmoidal, as shown in **Figure 2.13**, and as such it is uncommon to use the entire humidity range to calculate the CHE. Therefore, a limited range of interest is utilized from 35-90% RH, corresponding to a λ of about 1.4 – 6 for PFCB/PVDF-HFP and 3-7 for NRE 211, further justifying the use of a 2 hour equilibration time for each humidity step as the higher humidity levels are not included in the CHE calculation. This λ range is most commonly found in real fuel cell membranes, and it can be seen that the hygral expansion curve is approximately linear over this expanse. Similar to the CTE, the CHE is then taken as the slope of a linear fit performed over this region. To calculate λ for PFCB/PVDF-HFP **Eqn [2.6]** was utilized, while **Eqn [2.7]** was used for NRE 211 calculations.

In **Figure 2.13** and **Table 2.3** both the PFCB/PVDF-HFP and NRE 211 membrane CHEs are provided. There is little temperature dependence noted in both the PFCB/PVDF-HFP and NRE 211 hygral expansion data, and as such the CHE was taken as an average over all test temperatures. While the NRE 211 data has a slightly higher total strain than the PFCB/PVDF-HFP, the calculated slopes over the region of interest are very similar between the two materials at 1.32 ± 0.23 % / λ for PFCB/PVDF and 1.26 ± 0.2 % / λ for NRE 211, resulting in a slightly higher change in strain with changes in moisture for PFCB/PVDF-HFP. To ensure this limited range of fitting was valid, an additional linear fit was performed over the entire λ range, and the differences in the CHE were compared in the model described in **Chapter 3**. The differences were quite minimal, and the strain model outputs using the CHE calculated over a limited λ range are consistent with those measured experimentally, and as such it is believed that the CHE calculated over the limited λ range is acceptable to describe the material accurately.

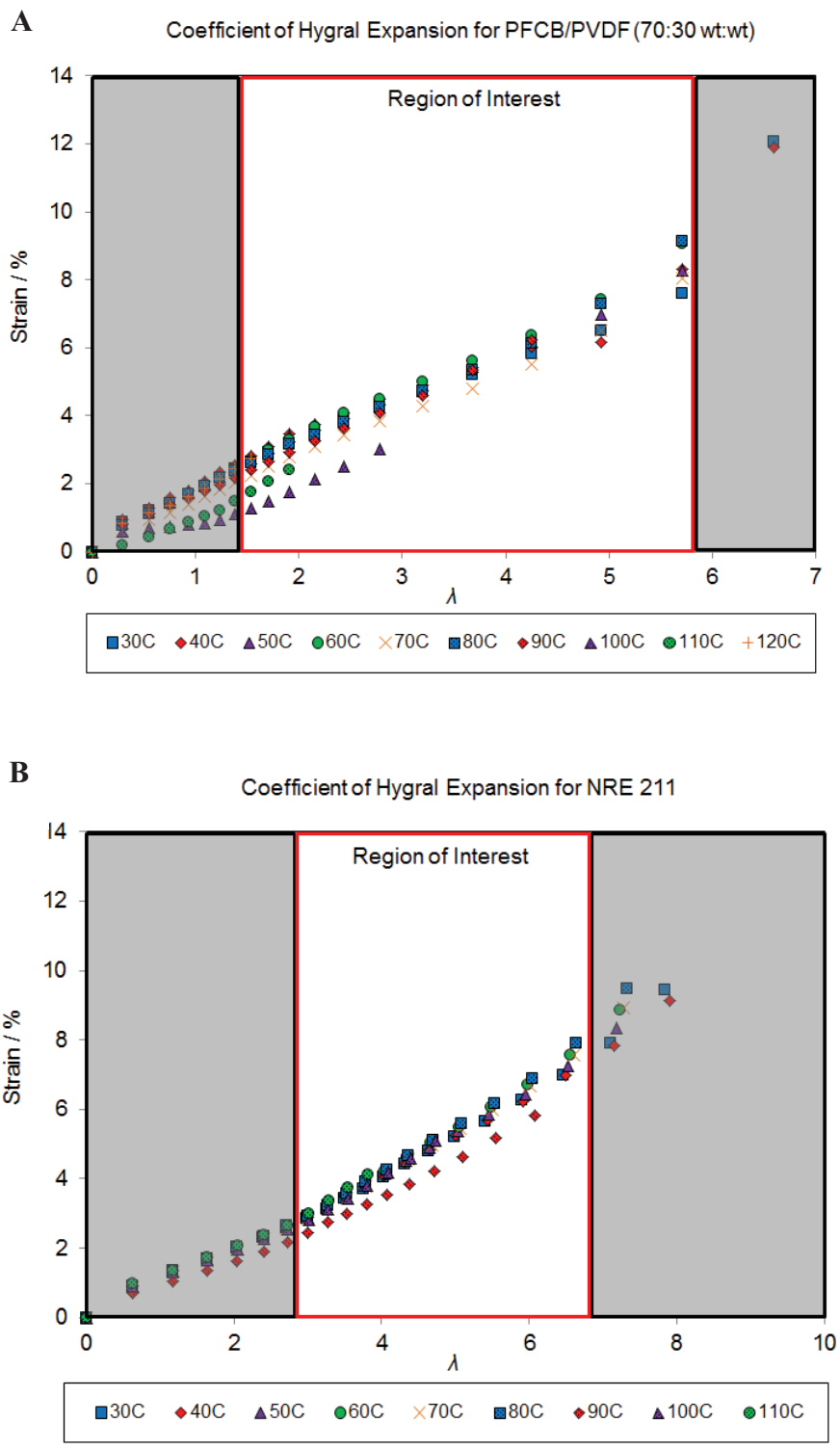

Figure 2.13. Hygral expansion of **(A)** PFCB/PVDF-HFP and **(B)** NRE 211.

Table 2.3. CHE of PFCB/PVDF and NRE 211 as measured from the slope of data taken over 35-90% RH from 30-110°C by 10°C intervals.

	PFCB/PVDF-HFP (x 10^2 λ^{-1})	NRE 211 (x 10^2 λ^{-1})
30°C	1.15	1.18
40°C	1.18	1.16
50°C	1.27	1.23
60°C	1.45	1.30
70°C	1.13	1.31
80°C	1.45	1.35
90°C	1.39	1.09
100°C	1.38	1.33
110°C	---	1.40

2.3.3 Characterization of the Blend α-Relaxation

The α-relaxation of the individual blend components was previously completed by Nathan May utilizing differential scanning calorimetry (DSC) [73]. He determined the α-relaxation of the PVDF-HFP was ~ -40°C, while that of the sulfonated PFCB was ~ 125°C. Attempts to measure the α-relaxation of the blend with the DSC were unsuccessful due to the hygroscopic nature of the PFCB/PVDF-HFP materials. Therefore, further attempts to understand the α-relaxation of the blend were performed utilizing the DMA with RHA, also allowing for the observation of how the α-relaxation may change with moisture content. The tan δ profiles for PFCB/PVDF-HFP at RH levels from 0-90 are provided in **Figure 2.14**. Although the peak of the tan δ profile cannot be observed with these scans due to the temperature limitations of the DMA with RHA, it is clear that as the relative humidity is increased, that the tan δ peak shifts towards lower temperatures. This would imply that with increasing moisture contents, the polymer chains have increased mobility and are able to relax at lower temperatures. Based on this data, it is difficult to provide actual α-relaxation temperatures, it is possible the α-

relaxation temperature of a dry sample could be obtained with a different DMA and then extrapolations of the humidified curves could be made. Further observation of this data indicates the α-relaxation of the PFCB/PVDF-HFP blend is closer to that of the pure sulfonated PFCB at dry conditions, and as the moisture content is increased, this value becomes more central between the two blend component α-relaxations. Finally, it should be noted that only one peak was observed in the DMA scan, implying good mixing between the PFCB and the PVDF-HFP.

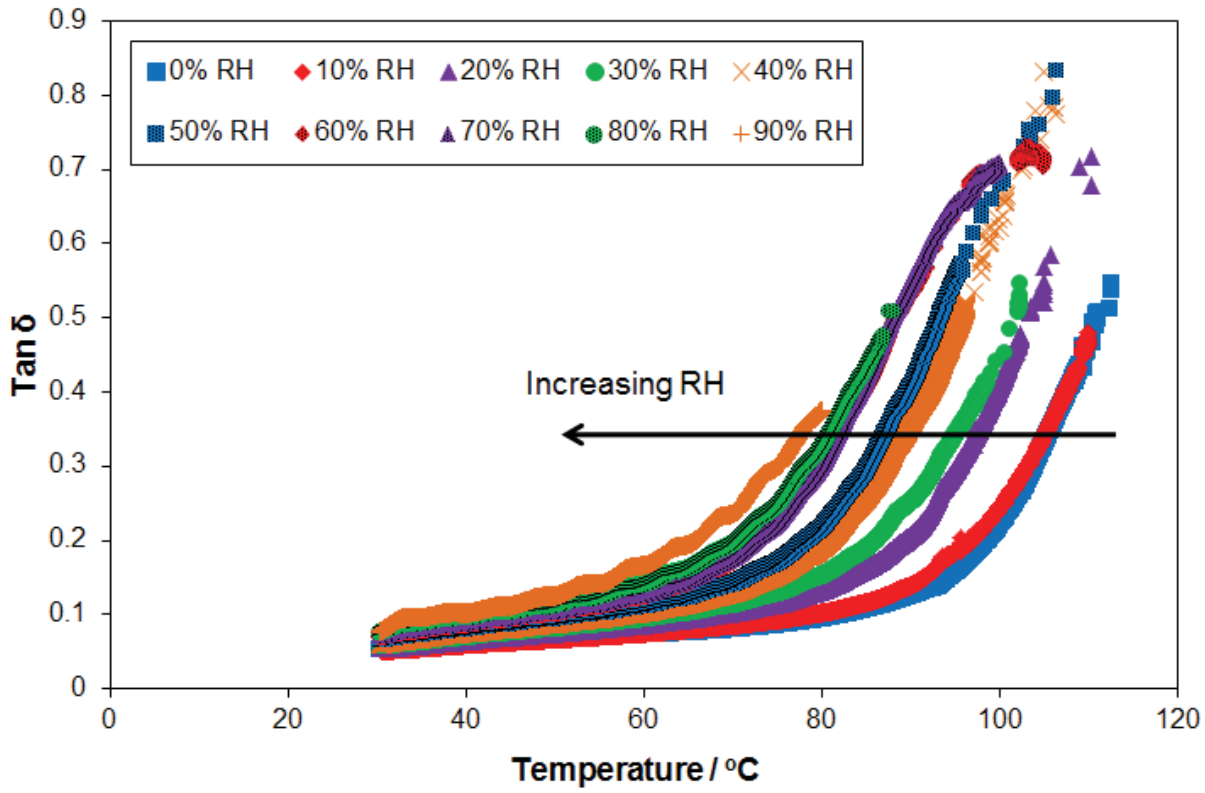

Figure 2.14. Tan δ temperature scans of PFCB/PVDF-HFP from 30-120°C over 0-90% RH.

2.3.4 Linear Viscoelastic Properties Characterization

2.3.4.1 Applicability of the TTSP to PFCB/PVDF-HFP

A polymer blend composed of two immiscible, phase-separated components with differing relaxation times would likely only follow the TTSP over a very limited time frame, let

alone TTMSP, whereas a molecularly mixed polymer blend likely would follow TTSP and possibly TTMSP. Because the PFCB/PVDF-HFP membrane system is a complex blend with a high glass transition (T_g) amorphous component, and a low T_g crystalline component, it is possible that TTMSP would not be applicable.

Three methods are commonly used to determine if TTSP is truly applicable to a blended polymer system. These include the van Gurp plot, the Han plot, and shifting of loss modulus data. Each plotting technique allows for the observation of temperature dependence that may not be seen in empirically shifted storage modulus data. The van Gurp plot graphs the phase angle, δ, vs. the absolute value of the complex modulus, $|G^*|$ [74]. If the different isotherms used to create the master curve will superpose without any time scale shifting, showing temperature independence, then it is assumed that TTSP is applicable, although a viscoelastic explanation for this phenomenon is not currently understood.

Similar to the van Gurp plot, the Han plot is used to test for temperature independence in a blend if each temperature isotherm falls on a single line without employing any shifting, when plotting the log of the storage modulus vs. the log of the loss modulus. [75, 76]. If we consider the Han plot purely in a qualitative state, it is very similar to the standard Cole-Cole plot, which charts the loss modulus against the storage modulus. Therefore, at first glance the Han plot appears to merely be a modification of the Cole-Cole plot, which minimizes the temperature dependence seen in the Cole-Cole plot.

Han initially qualitatively developed this plotting technique for polymer fluids under shear in the terminal region and later developed a more quantitative explanation based on the Doi-Edwards viscoelastic theory. Further examination of all published Han plots showed data taken at or near the terminal region of the material, all under rheometric methods, while van

Gurp plots often include lower temperature data. It is thusly believed that the Han plot can only be applied near the terminal region of a material. Therefore, the Han plot is not a valid analysis technique for NRE 211 and PFCB/PVDF-HFP data measured in a DMA, however if rheology data was collected, the Han plot could prove to be useful. Performing rheometric measurements is often difficult and very time consuming, and as the van Gurp plot and loss modulus shifting appear to be valid over the regions tested for these ionomeric materials, the Han plot will be disregarded for TTSP validity analysis.

Finally, it is common for researchers to attempt to construct master curves for both the storage and loss modulus data for their polymer blend systems. It is assumed if one or the other does not empirically shift well into a master curve that the TTSP does not apply to the system, despite their relation by Kramers-Kronig. Due to the need of determining the applicability of the TTSP to PFCB/PVDF-HFP, a van Gurp plot was created and loss modulus shifting was attempted.

A van Gurp plot of the dynamic data of PFCB is shown in **Figure 2.15A.** As can be seen, the high temperature (75-90^{o}C) and low frequency (0.1 – 10 Hz) data fall on the same curve (replotted in **Figure 2.15B**), whereas the low temperature and high frequency data show temperature dependence. Therefore, it is likely that the high temperature and low frequency data are thermorheologically simple, and TTSP does apply over this range.

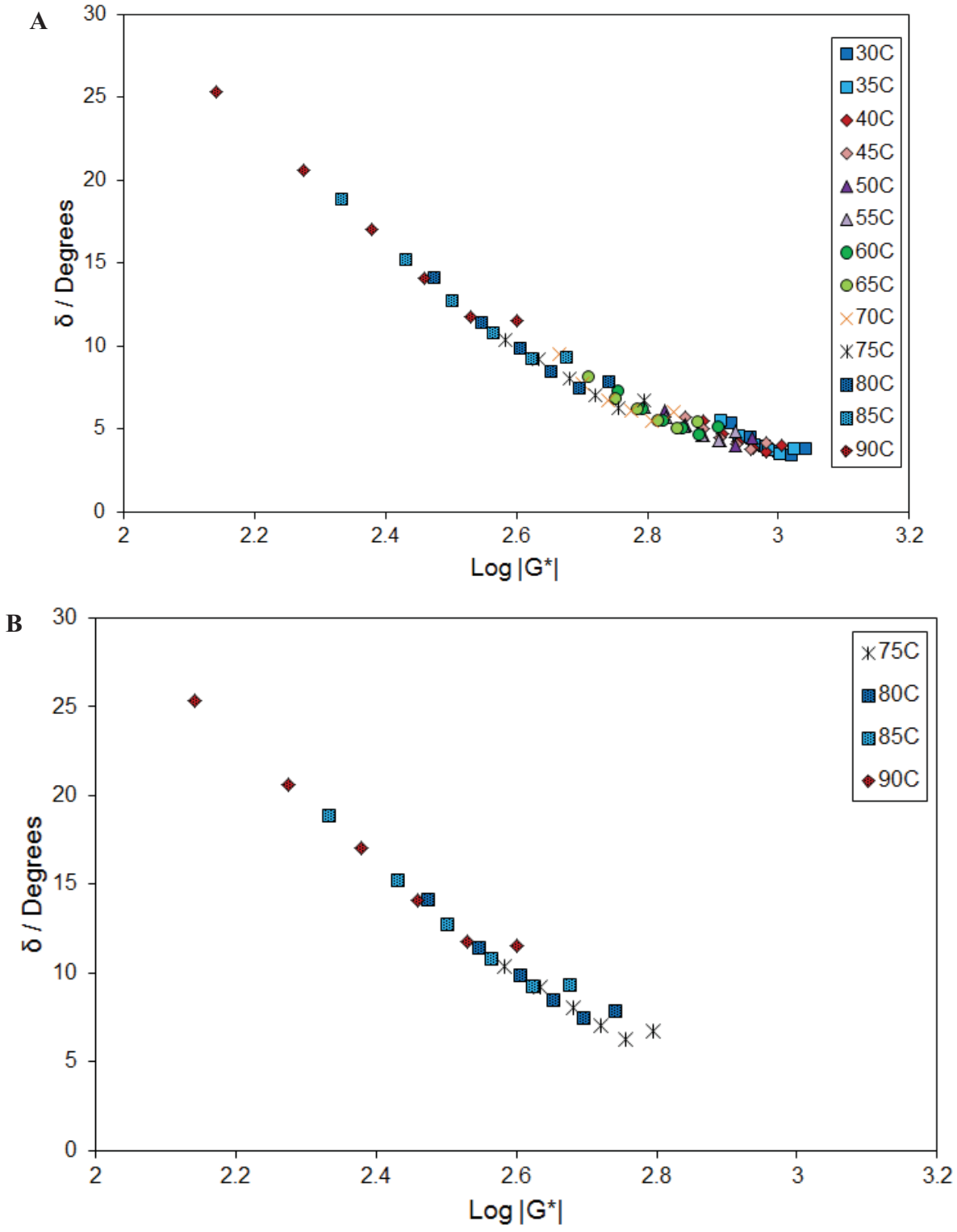

Figure 2.15. (A) van Gurp plot of PFCB with 30% KF at 30% RH. **(B)** van Gurp plot of high temperature and low frequency data for PFCB with 30% KF at 30% RH.

The loss modulus is first shifted using the 10% RH data, as shown in **Figure 2.16A**. The 10% RH data is provided to show the typical curve created via empirical shifting, as the 30% RH loss modulus shifts better than the other RH levels. Because Ferry states that shift factors should be applicable for multiple viscoelastic properties, the shift factors obtained from storage modulus shifting were applied to the loss modulus data [29]. This resulted in the plot shown in **Figure 2.16A**, in which none of the loss modulus curves overlap, implying a breakdown of TTSP. It should be noted, however, that Dow Corning has suggested that loss modulus shift factors are more sensitive than storage modulus shift factors, and as such loss modulus shift factors have successfully shifted the storage modulus, when the storage modulus shift factors do not successfully shift the loss modulus. Due to curiosity, empirical shifting of the loss modulus was then tried, as shown in **Figure 2.16B**, in which the high temperature and low frequency data appear to form a curve. This data was replotted without the low temperature or high frequency data, and is shown in **Figure 2.16C**. Therefore it again appears, at a different RH level, that TTSP is applicable over high temperature and low frequency ranges.

A

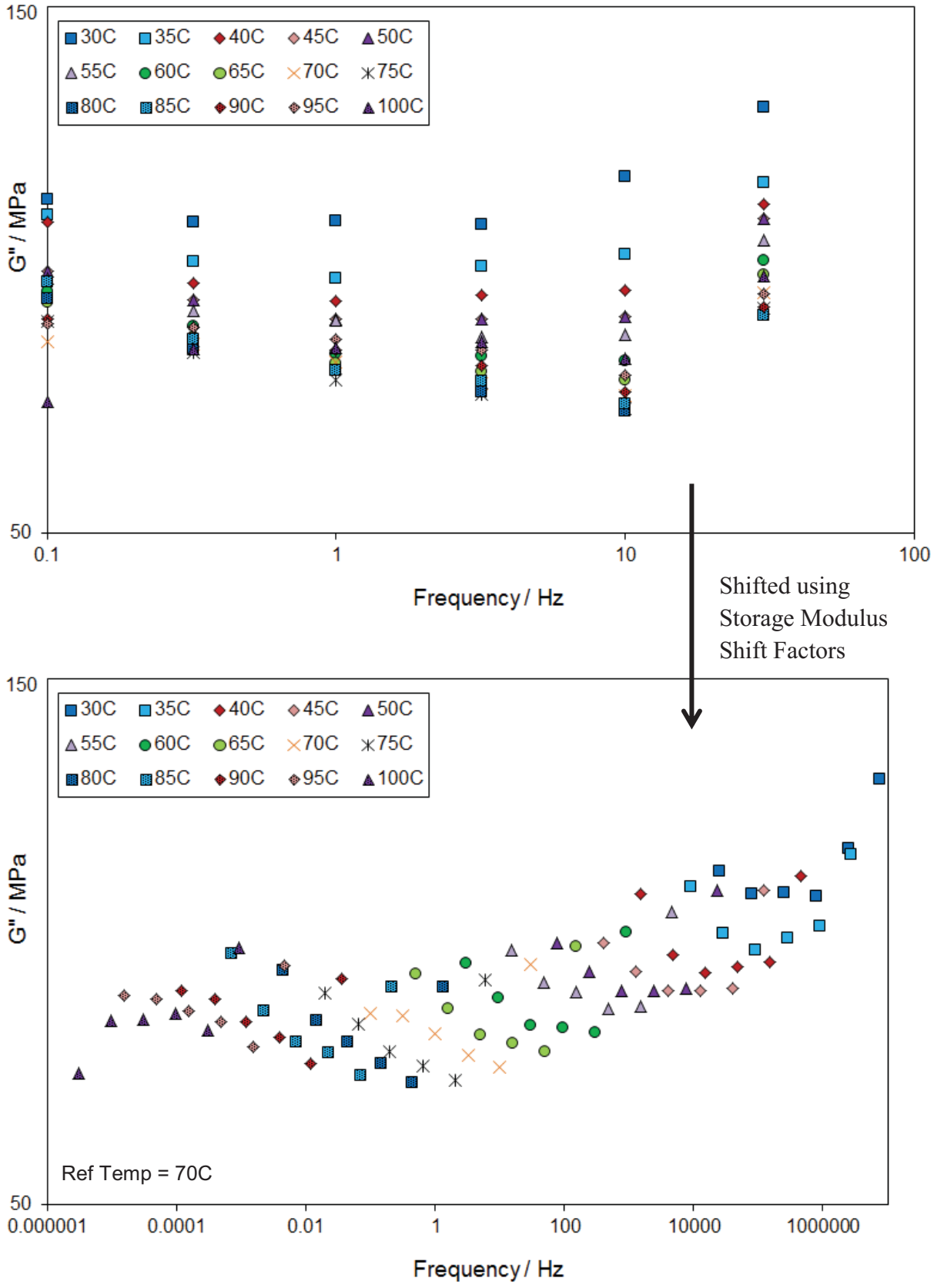
30C 35C 40C 45C 50C
55C 60C 65C 70C 75C
80C 85C 90C 95C 100C
G" / MPa
150
50
0.1
1
10
100
Frequency / Hz
Shifted using
Storage Modulus
Shift Factors
30C 35C 40C 45C 50C
55C 60C 65C 70C 75C
80C 85C 90C 95C 100C
G" / MPa
150
50
Ref Temp = 70C
0.000001
0.0001
0.01
1
100
10000
1000000
Frequency / Hz

B

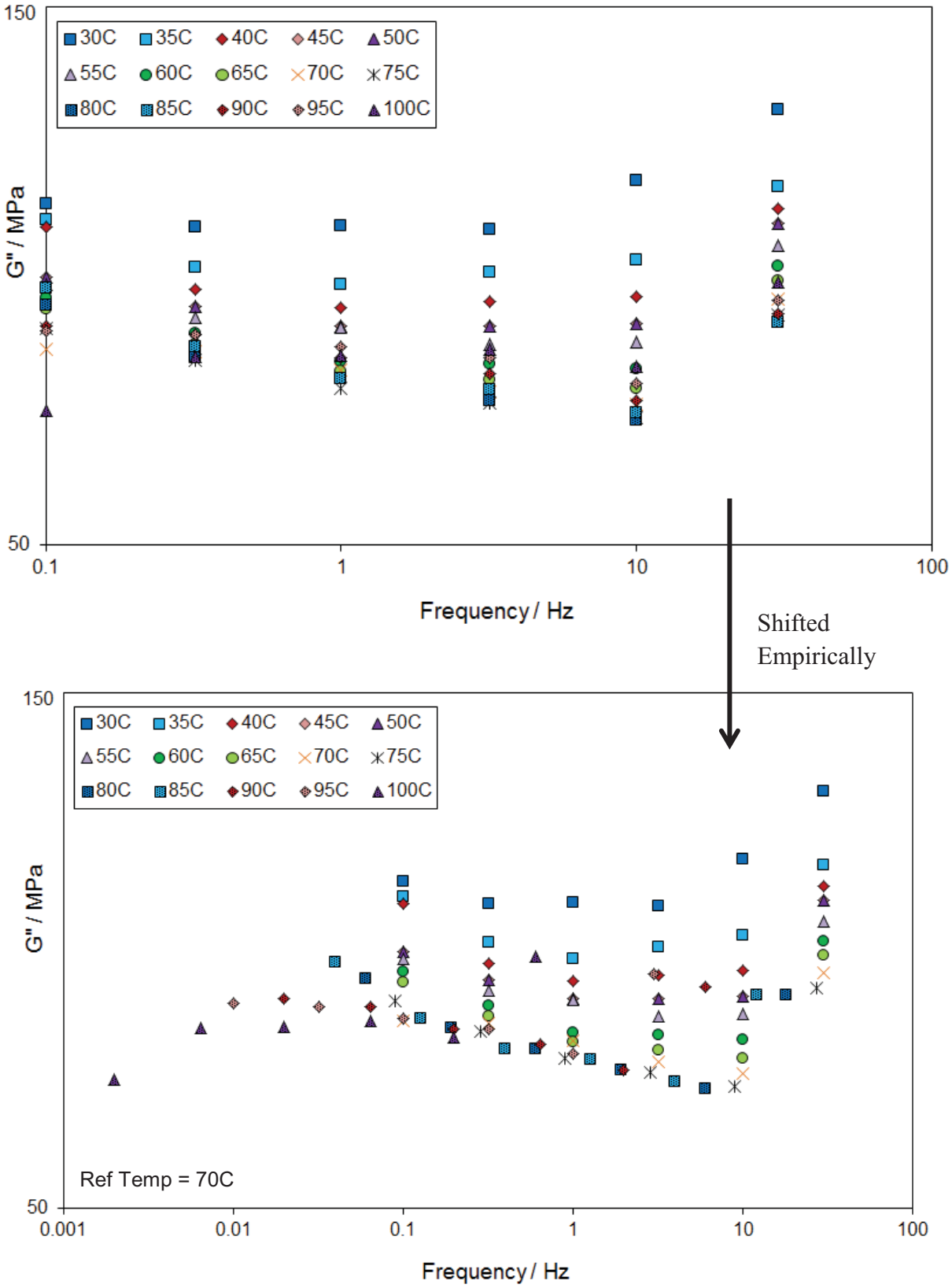
30C 35C 40C 45C 50C
55C 60C 65C 70C 75C
80C 85C 90C 95C 100C
G" / MPa
150
50
0.1
1
10
100
Frequency / Hz
Shifted
Empirically
30C 35C 40C 45C 50C
55C 60C 65C 70C 75C
80C 85C 90C 95C 100C
G" / MPa
150
50
0.001
0.01
0.1
1
10
100
Frequency / Hz
Ref Temp = 70C

C

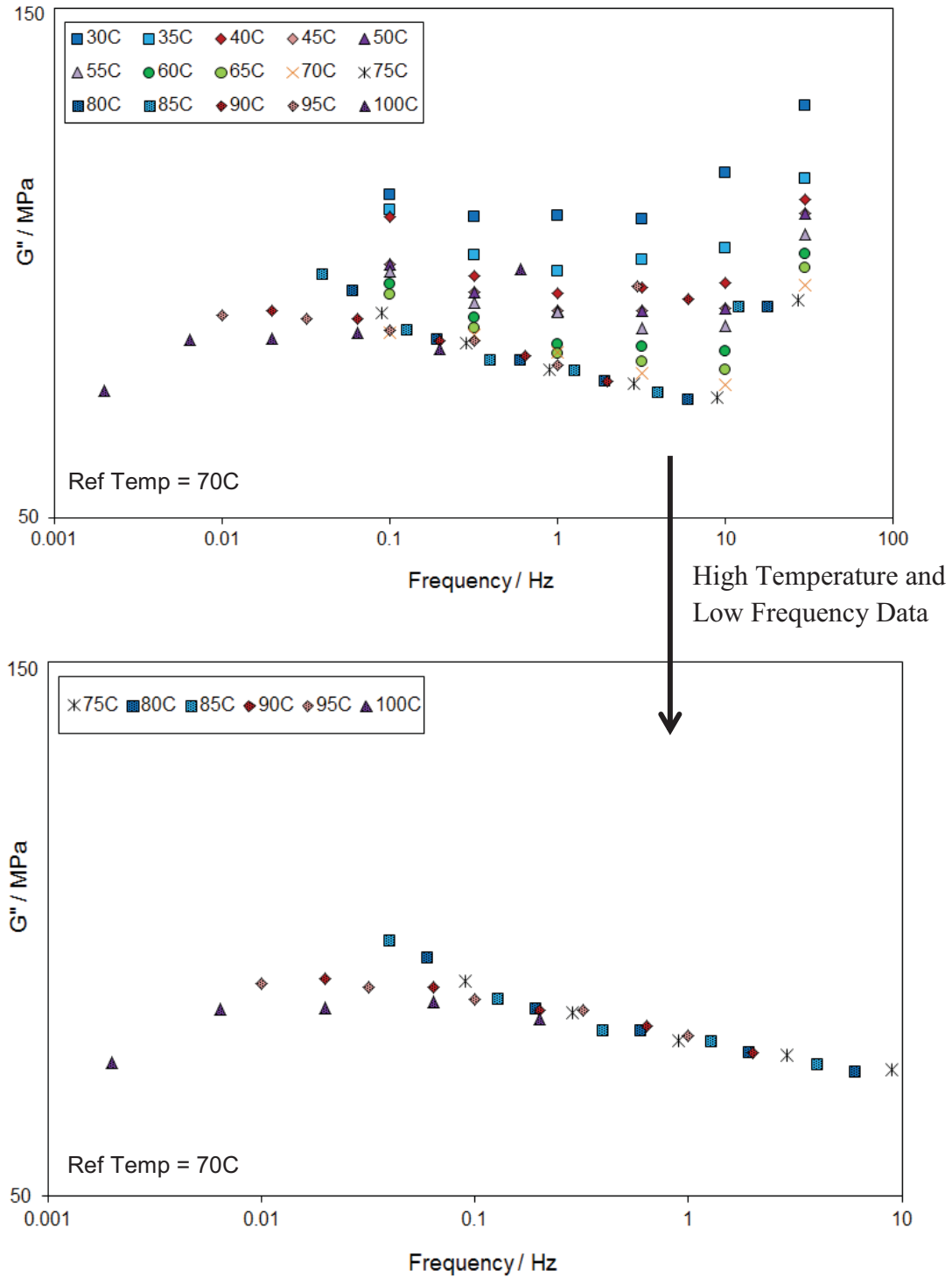

Figure 2.16. **(A)** Unshifted loss modulus data for PFCB/PVDF-HFP and shifted using storage modulus shift factors, **(B)** Unshifted loss modulus data for PFCB/PVDF-HFP and shifted empirically, **(C)** Loss modulus data shifted empirically for PFCB/PVDF-HFP and the high temperature and low frequency loss modulus data.

For comparison with **v**an Gurp plots, loss modulus data taken at 30% RH was also shifted empirically for PFCB/PVDF-HFP. As shown in **Figure 2.17**, the high temperature and low frequency data appears to fall on a single curve. In **Figure 2.17A** the high frequency data is circled, and **Figure 2.17B** is replotted without this high frequency data**. Figure 2.17B** then has the low temperature data circled, and **Figure 2.17C** is replotted without the high frequency and low temperature data. Therefore, at the 30% RH level, the data is internally consistent and TTSP appears to be applicable at high temperatures and low frequencies (75-95^{o}C, 0.1-10 Hz). While these van Gurp and loss modulus plots, according to the literature, imply that time temperature superposition is not applicable for this system over the entire temperature and frequency range, it is still possible that the obtained hygrothermal shift factors can be used in lifetime durability predictions. Therefore, long term creep and stress relaxation data will be used to determine the true applicability of time temperature superposition for this system.

A

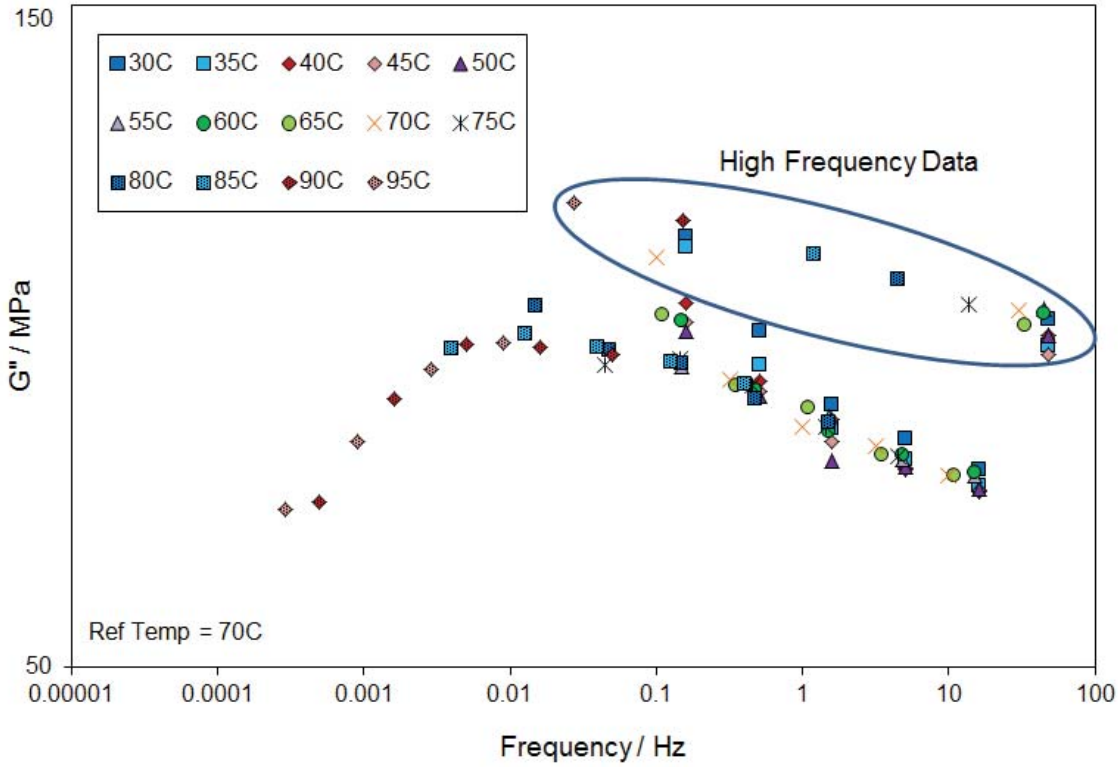
150
50
G" / MPa
30C 35C 40C 45C 50C
55C 60C 65C 70C 75C
80C 85C 90C 95C
High Frequency Data
Ref Temp = 70C
0.00001 0.0001 0.001 0.01 0.1 1 10 100
Frequency / Hz

B

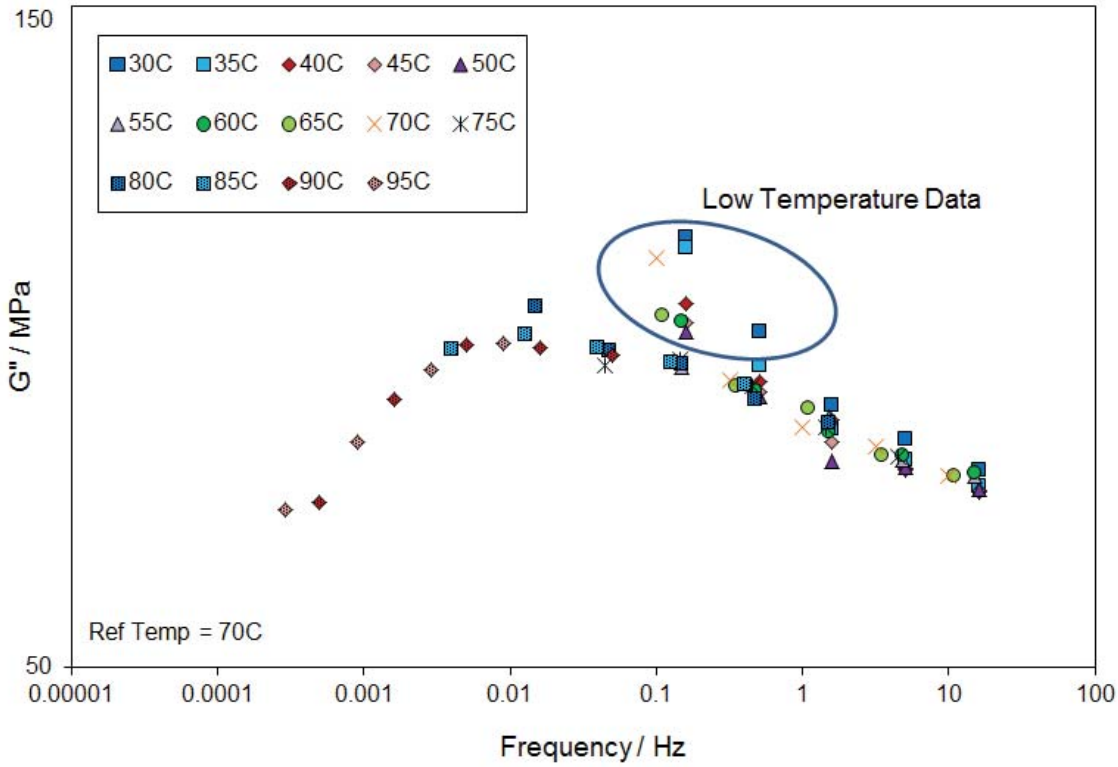
150
50
G" / MPa
30C 35C 40C 45C 50C
55C 60C 65C 70C 75C
80C 85C 90C 95C
Low Temperature Data
Ref Temp = 70C
0.00001 0.0001 0.001 0.01 0.1 1 10 100
Frequency / Hz

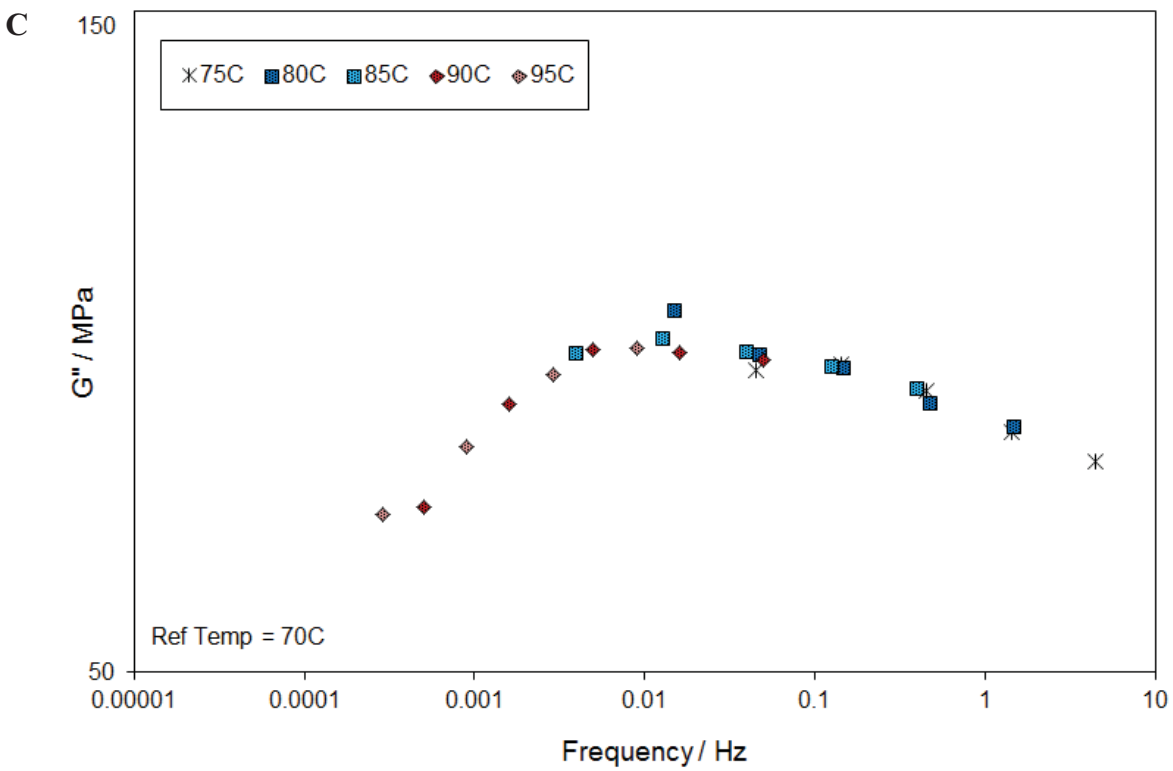

Figure 2.17. (A) Empirically shifted loss modulus data for PFCB with 30% KF at 30% RH. **(B)** Low frequency loss modulus data empirically shifted for PFCB with 30% KF at 30% RH. **(C)** Low frequency and high temperature loss modulus data empirically shifted for PFCB with 30% KF at 30% RH.

It is also of interest to apply these plots to another known ionomeric system to see if they predict thermorheological simplicity, knowing that TTSP is likely applicable based on based on consistent lifetime trends and shift factors between different testing methods as shown by Patankar et al. and Grohs et al [38, 46, 49]. Therefore, a van Gurp plot was created for NRE 211, as shown in **Figure 2.18**. As seen, this plot does show temperature dependence, implying Nafion® is a thermorheologically complex material and TTSP is not applicable. However, it is known that these plots do not work for known two phase systems, and as Nafion® is often considered a two phase system in the hydrated state, it may not be appropriate to apply these plots. This would also imply a two phase system would be present in the PFCB/PVDF-HFP

material upon hydration, and based on the poor results obtained for NRE 211 using the an Gurp plotting method, it may not be appropriate to apply this method to PFCB/PVDF-HFP materials, or any other ionomers.

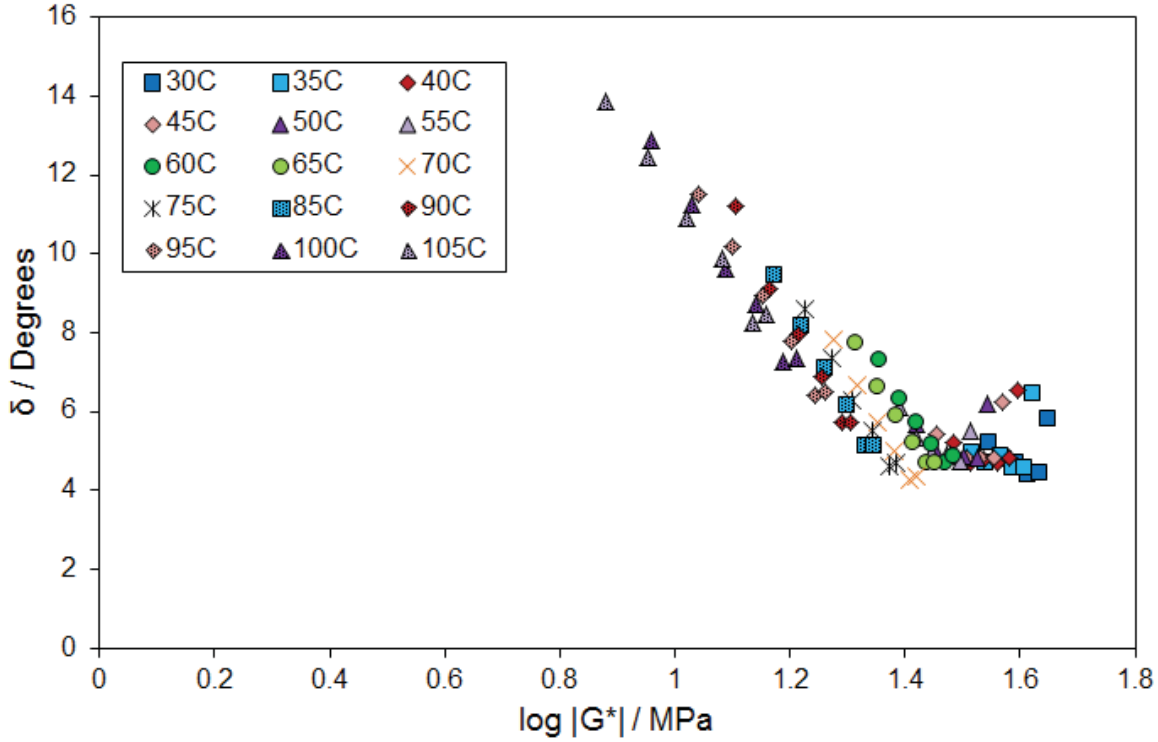

Figure 2.18. van Gurp plot for NRE 211 at 30% RH.

Thus far the literature has not covered an example of the application of the van Gurp or loss modulus plotting techniques for the detection of moisture dependence. Therefore, both plots were made for PFCB/PVDF-HFP using data taken at 2, 10, 30, and 55% RH as shown in **Figure 2.19**. While the van Gurp plot looks decent, the loss modulus plot shows clear moisture dependence, implying that TTMSP is not valid and the material is hygrothermorheologically complex. However, a hygrothermal mastercurve was previously created using dynamic data, producing reasonable shift factors, and as such long term data is needed to fully understand the validity of these plotting techniques as well as the true application of TTMSP for this material system.

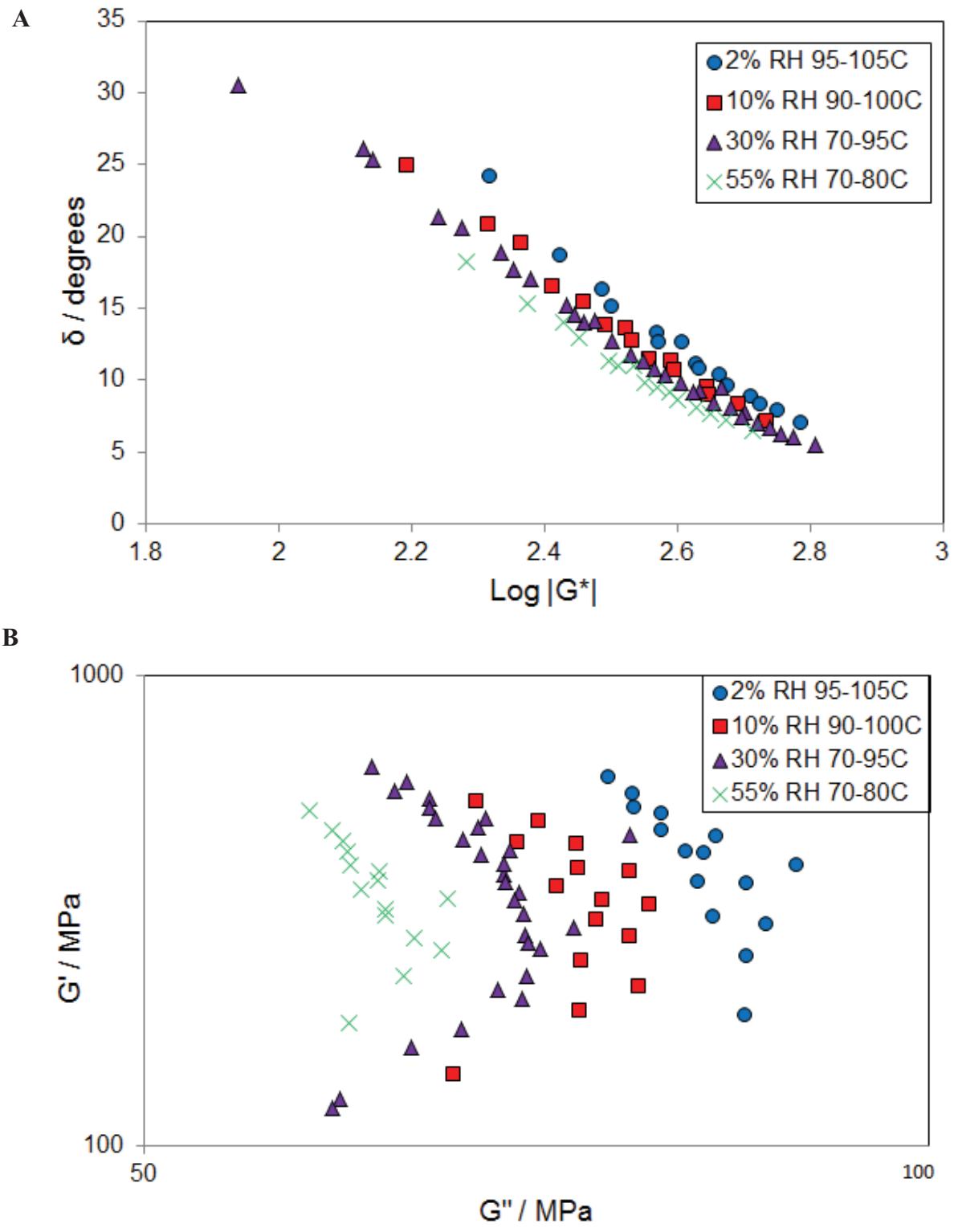

Figure 2.19. **(A)** van Gurp plot for PFCB/PVDF-HFP for different humidity levels. **(B)** Hygrothermal loss modulus plot for PFCB/PVDF-HFP for different humidity levels.

2.3.4.2 Hygrothermal Stress Relaxation Master Curve

Because the van Gurp plot appeared to imply that TTSP was not valid for NRE 211, despite the successful use of TTMSP across multiple testing techniques, it was thought the same could be true for PFCB/PVDF-HFP. Therefore, despite the results of the plotting techniques discussed above, a hygrothermal master curve was attempted and created successfully, using the stress relaxation data shown in **Figure 2.20.** Theoretically, there are three equivalent ways to create a doubly shifted hygrothermal master curve. Because data is taken at multiple temperatures and humidities, either multiple thermal master curves at different humidity levels, or multiple hygral master curves at different temperatures, could be created first as shown in **Figure 2.21**. Each of these thermal or hygral master curves could then be shifted a second time to form a hygrothermal master curve, as shown in **Figure 2.22**. Examination of **Figure 2.22** shows that both master curves appear to have shifting problems, implying that TTMSP would not be applicable. In both shifting methods the low temperature high humidity data does not align well with the master curve. However, it was assumed that the thermal and hygral shift factors were independent and separable, but upon further examination of the second set of shift factors, these are not independent of the other variable (temperature and humidity respectively). This has been pointed out previously by Patankar, when he shifted first for temperature and then for humidity [38]. Therefore it is believed that because these shift factors are not truly separable, that both temperature and humidity should be shifted simultaneously, as was done to create the hygrothermal master curve provided in **Figure 2.23.** Shifting for both temperature and humidity simultaneously creates a smooth master curve, implying the TTMSP is valid for this material system, contrary to first shifting for one variable and then the other. In addition, to further

validate this shifting approach, a round robin was performed with 3 other people, and the same master curve was produced via simultaneous shifting by all 3 participants. This is further proof that these variables are not separable, and shifting for multiple variables should be performed simultaneously to account for the interdependence of the variables.

Based on the hygrothermal master curve created via simultaneous shifting, it is likely the PFCB/PVDF-HFP membrane has enough phase mixing that the TTMSP is applicable. Previous work completed using tapping mode AFM, showed the phase domains in the PFCB/PVDF-HFP membrane are on the order of 25 nm [73]. The DMA is typically sensitive enough to measure differences between domain sizes greater than 5-10 nm and true molecular mixing [77]. Therefore, the PFCB/PVDF-HFP membrane phases are within the detection limits of the DMA, and phase-separated material behavior would likely be noticeable. However, the material appears to behave isotropically, suggesting a valid application of TTMSP [78]. A comparison of the hygrothermal stress relaxation modulus at 70^{o}C and 30% RH of the PFCB/PVDF-HFP membrane and NRE 211 is provided in **Figure 2.24**. The hygrothermal stress relaxation modulus of PFCB/PVDF-HFP material is stiffer than that of NRE 211, although both materials appear to be relaxing over the same time frame, while the increased stiffness of PFCB/PVDF-HFP causes it to relax about 2 decades later than NRE 211.

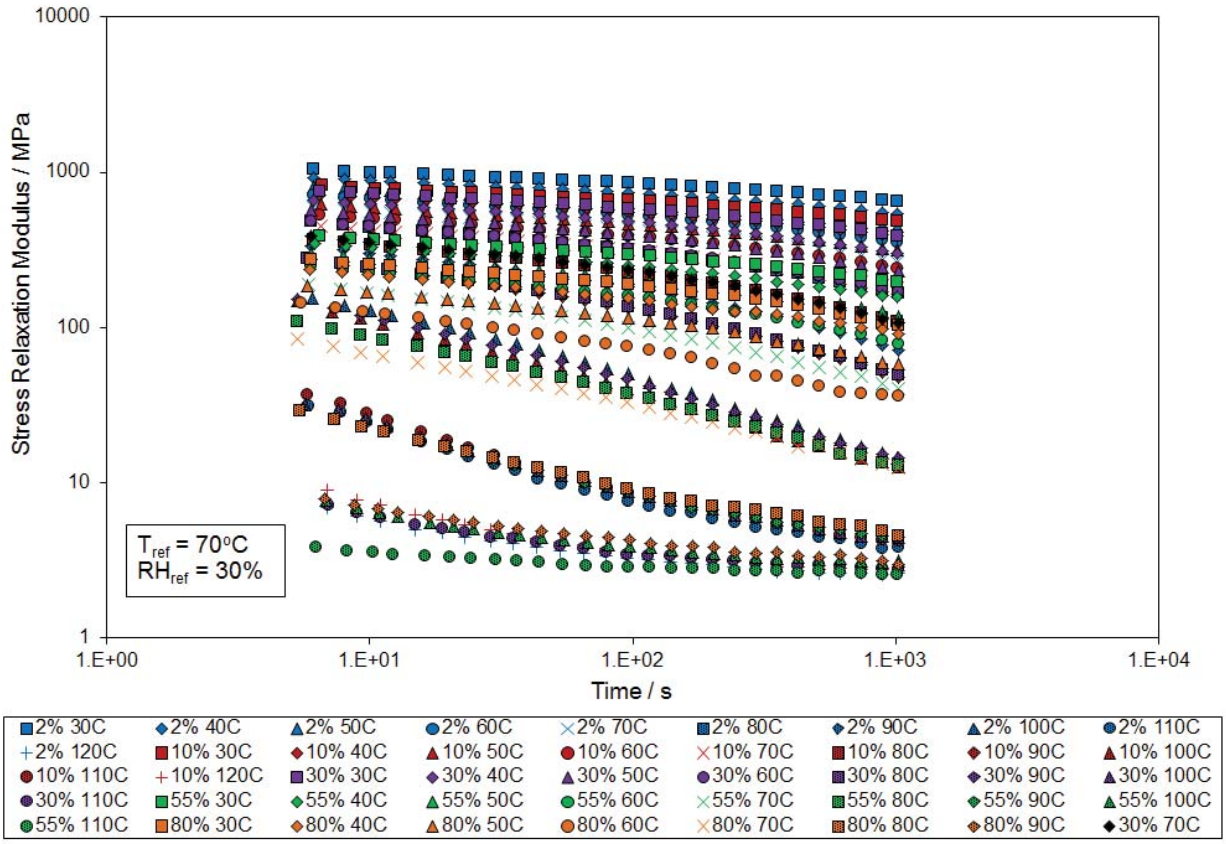

Figure 2.20. Unshifted stress relaxation modulus for PFCB/PVDF-HFP at multiple temperatures and RH levels.

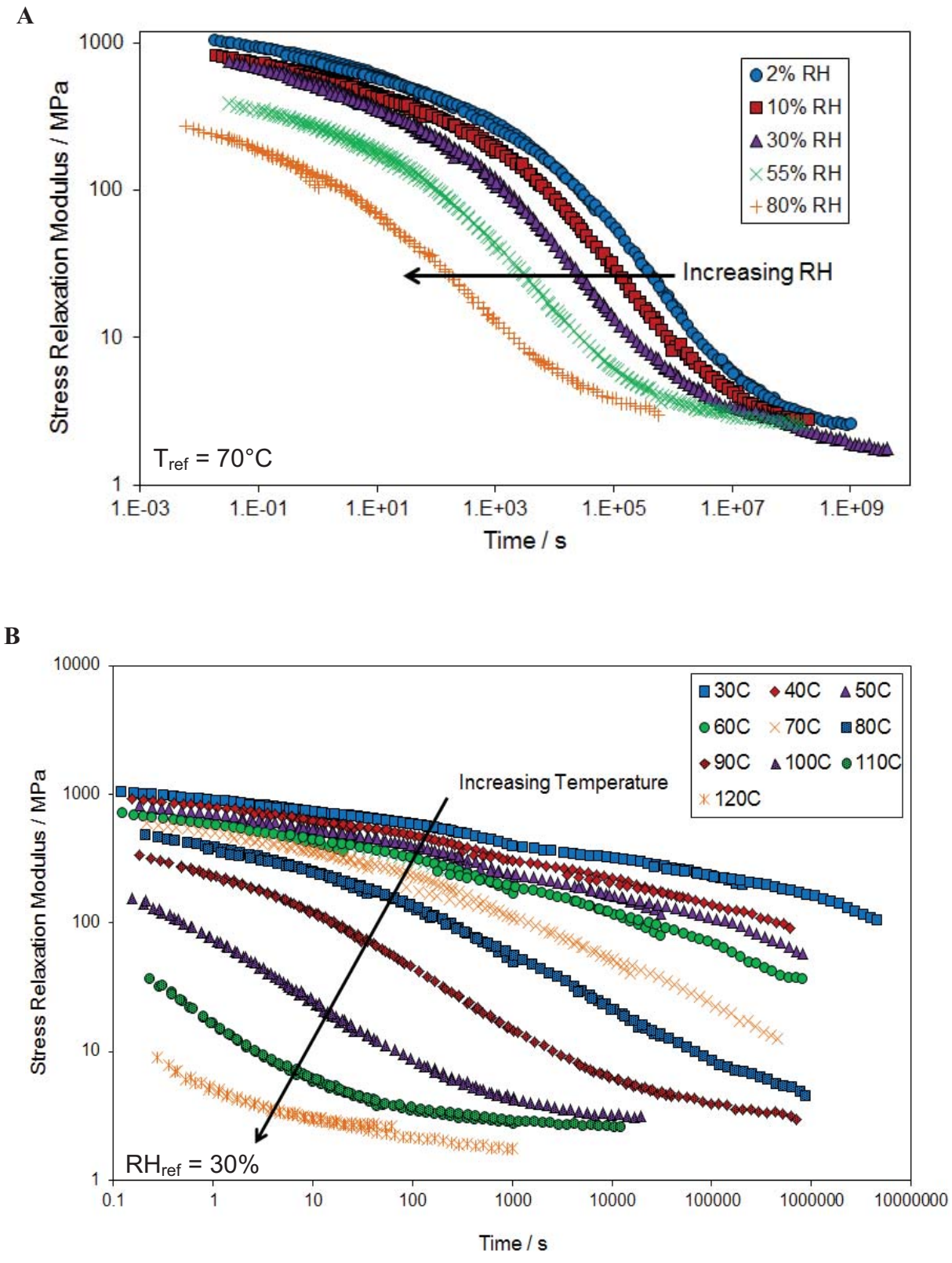

Figure 2.21. PFCB/PVDF-HFP **(A)** thermal master curves, and **(B)** hygral master curves.

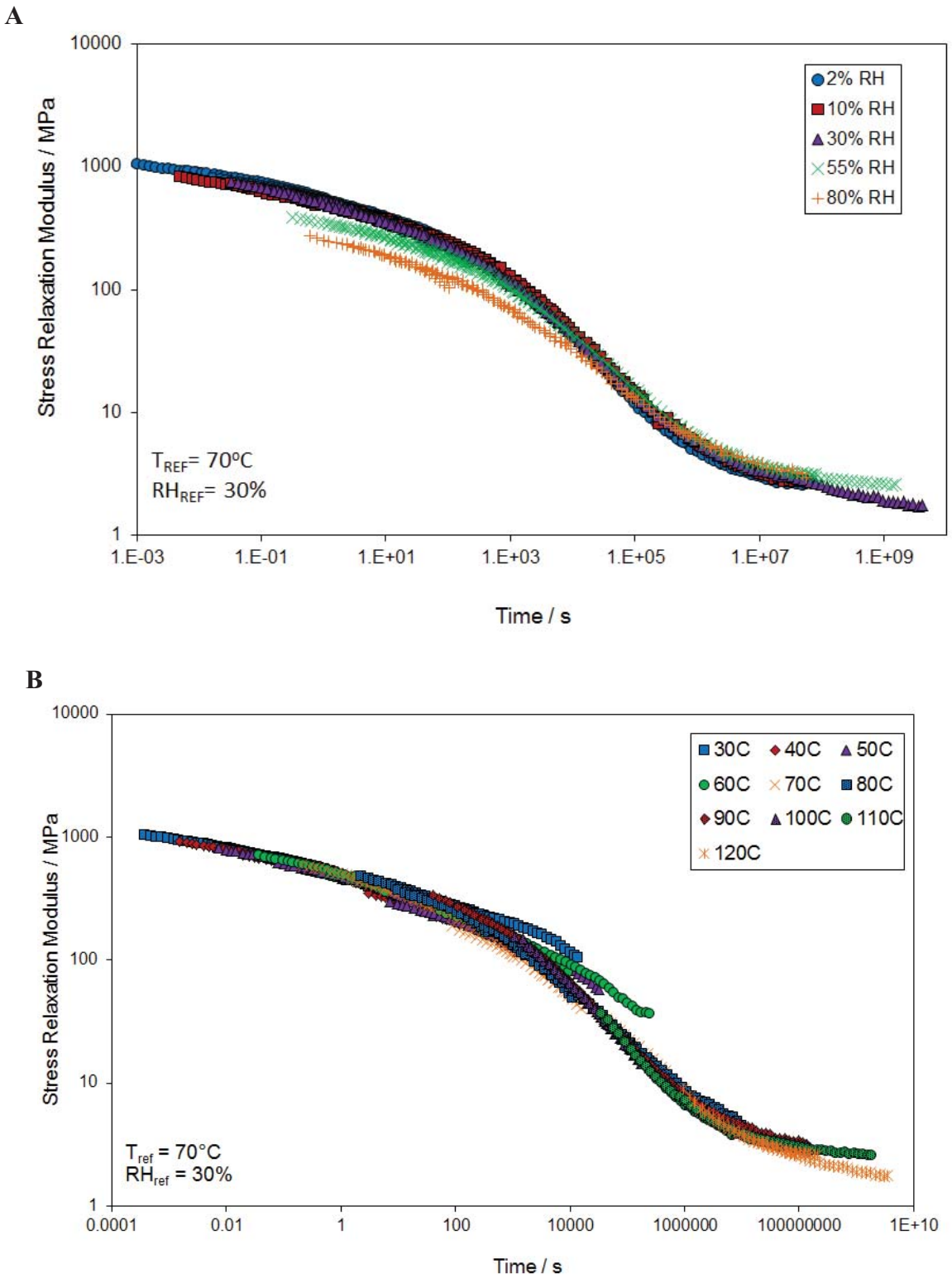

Figure 2.22. PFCB/PVDF-HFP hygrothermal master curve created by **(A)** first shifting for temperature then moisture, and **(B)** first shifting for moisture then temperature.

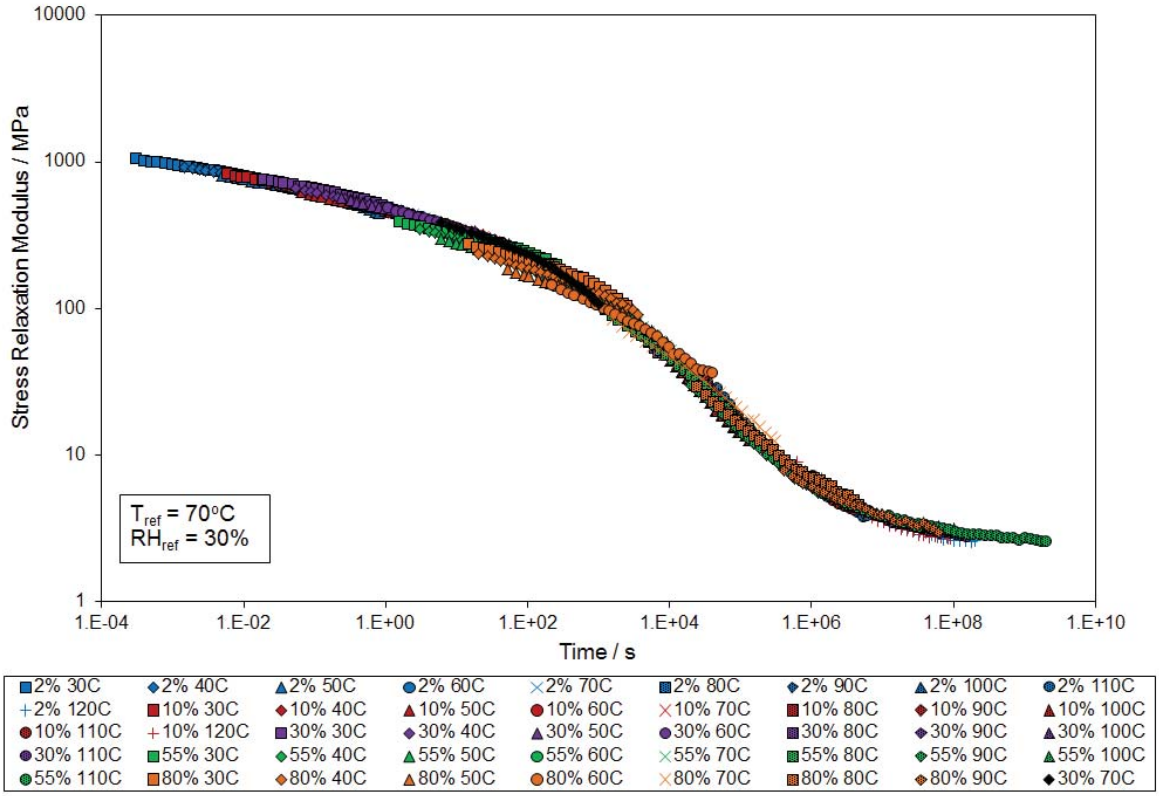

Figure 2.23. Stress relaxation modulus hygrothermal master curve for PFCB/PVDF-HFP at 30% RH referenced to 70°C.

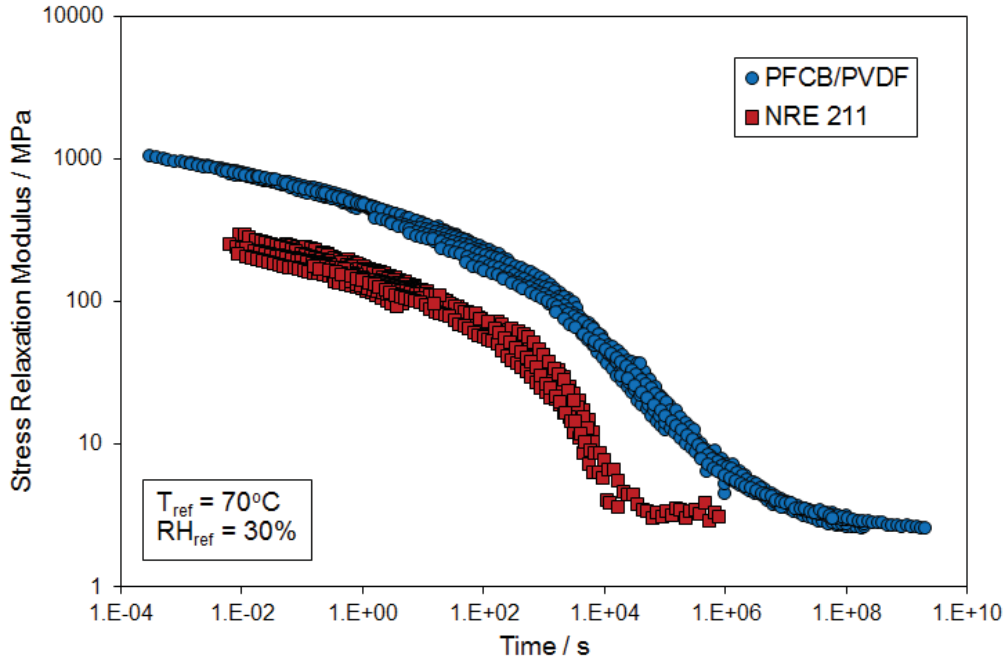

Figure 2.24. Comparison of PFCB/PVDF-HFP and NRE 211 stress relaxation hygrothermal master curves at 30% RH referenced to 70°C.

Similar to behavior noted in NRE 211, the 0% RH stress relaxation data could not be shifted to align well with the humidified stress relaxation data [38]. To examine the differences further, approximate thermal master curves were created by taking approximate hygral shift factors at the reference temperature of 70°C for each humidity level, and dividing each hygrothermal shift factor by the approximate hygral shift factor. As shown in **Figure 2.25**, the stress relaxation modulus at 0% RH is lower than the lightly hydrated 2% RH material for the entirety of the time scale shown, lower than the 10% RH thermal master curve below ~1000 s, lower than the moderately hydrated 30% RH material below ~10 s, while higher than that of the highly hydrated material at 55 and 80% RH for the entirety of the time scale shown. It should be noted that a change in temperature will change the time at which the 0% RH thermal master curve crosses the 10% and 30% RH thermal master curves, however the time scale for antiplasticization remains the same. This indicates that a low to moderate water content acts to antiplasticize the PFCB/PVDF-HFP membrane. This is consistent with behavior observed in NRE 211, although antiplasticization only occurs below ~5% RH [14, 16, 36].

We believe that the origin of the antiplasticization behavior observed in the PFCB/PVDF-HFP material is the same as that of Nafion, namely water bridging [36]. Hydrogen bonding will occur between the sulfonic acid moieties in the PFCB ionomer backbone and water molecules. One water molecule, at low water activities, can act to create a bridge between multiple sulfonic acid groups via hydrogen bonding. A stronger physical crosslink is then established between sulfonic acid moieties by this bridging, resulting in an effectively stiffer material, as seen with the 2% RH stress relaxation thermal master curve. However, excess water molecules will increase the number of possible hydrogen bonding sites. Therefore after a certain threshold water activity is reached, a dynamic network with rapidly exchanging bonds is created. The

number of discrete junction points is thus effectively decreased, resulting in a decreased effectiveness of restricting polymer chain dynamics. Consequently, the material appears to be softer, as seen with the 55 and 80% RH thermal master curves.

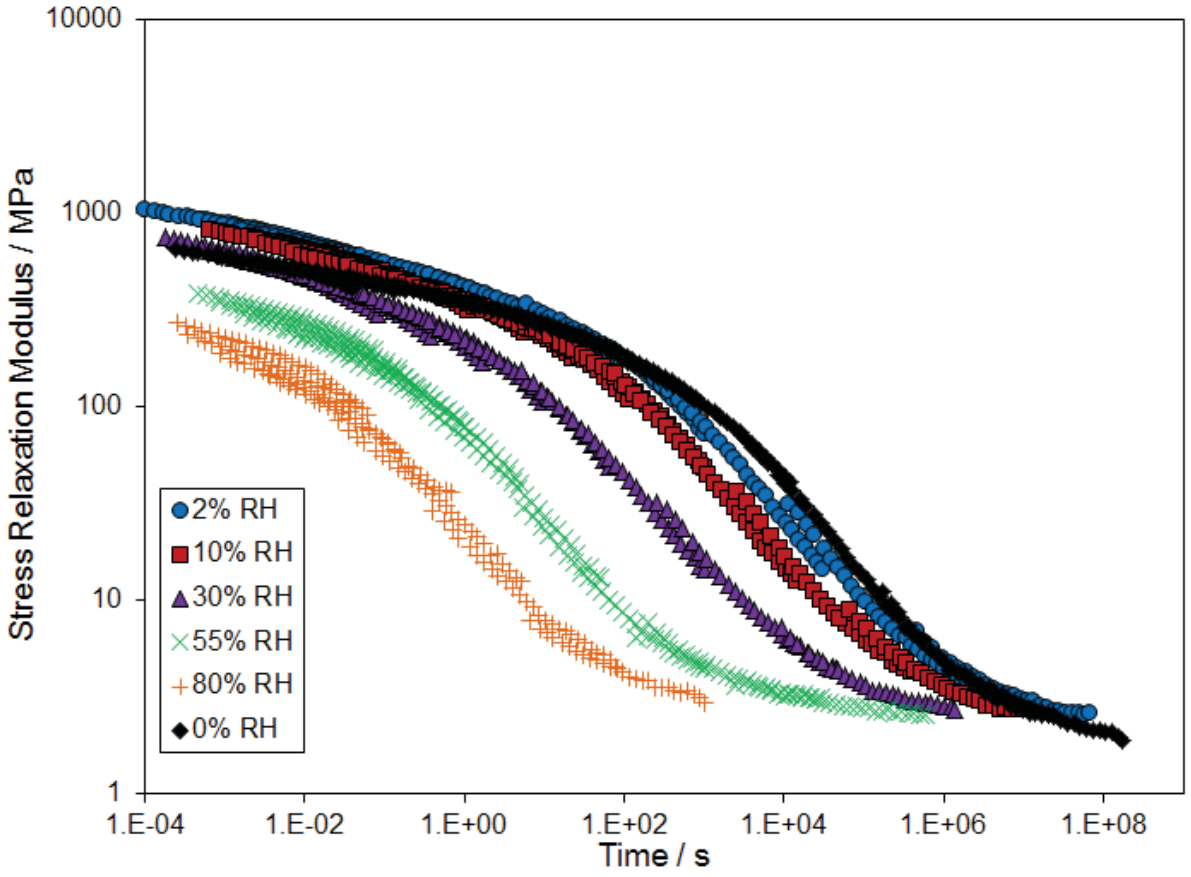

Figure 2.25. Approximate thermal master curves of PFCB/PVDF-HFP at various humidity levels, showing antiplasticization at low humidity levels.

2.3.4.3 Hygrothermal Shift Factors

Although the hygral and thermal shift factors are not completely separable, as discussed previously, the approximate hygral and thermal dependence of the material can be observed with the hygrothermal shift factors, provided in **Figure 2.26** for both PFCB/PVDF-HFP and NRE 211. The approximate thermal dependence can be taken as the vertical spread of all the shift

factor data sets, from a low to a high temperature. A comparison of the approximate thermal dependence of the PFCB/PVDF-HFP and NRE 211 shows about the same vertical spread of all the shift factor sets, about 6-7 decades from 40-100°C, indicating that PFCB/PVDF-HFP and NRE 211 moduli respond similarly to changes in temperature. This is in contrast to the approximate hygral dependence of both materials, which can be taken as the vertical spread of one of the shift factor sets. If the 80°C shift factor set is examined, for example, a comparison of the two materials shows that PFCB/PVDF-HFP has a vertical spread of about 4 decades over an RH range of 30-90%, corresponding to a λ range of 1.2-5.7, while NRE 211 has a vertical spread of about 1 decade over the corresponding λ range of 2.7-7.3, indicating the PFCB/PVDF-HFP membrane modulus undergoes larger deviations with changes in moisture than the NRE 211. This information has a considerable impact on the expected stresses in a PFCB/PVDF-HFP membrane versus those of NRE 211. It is possible that the larger shifts in modulus due to moisture exposure in the PFCB/PVDF-HFP membrane could create larger stresses in the material due to the constraint of the fuel cell stack. However, it is also possible that these larger shifts in modulus of the PFCB/PVDF-HFP membrane could provide faster relief from problematic high stresses often found in a fuel cell stack.

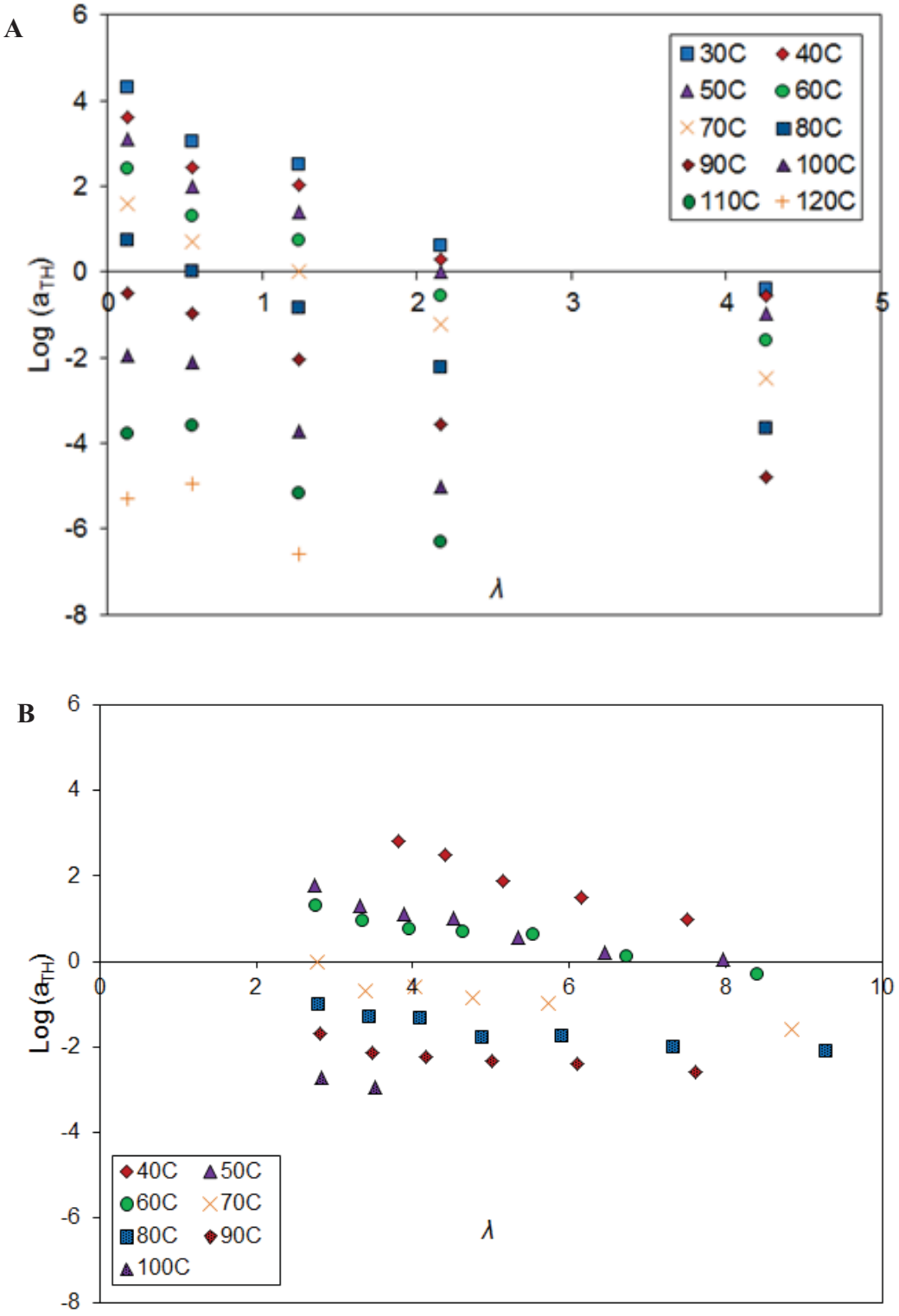

Figure 2.26. Hygrothermal shift factors for **(A)** PFCB/PVDF-HFP and **(B)** NRE 211 referenced to 30% RH and 70°C.

2.3.4.4 Long Term Creep Validation

Although a master curve was successfully created, it is important to realize this is only a prediction of the material behavior (for values outside the characterization conditions) and validation is needed to ensure the master curve is an accurate representation of the material response. Therefore, the long term creep data taken at 0.25 and 0.5 MPa, 0% RH, 100% RH, and immersed conditions at 70°C was compared with a stress relaxation master curve referenced to 70°C and 30% RH, or 0% RH respectively. The stress relaxation data was converted to creep compliance, *D(t)*, using an approximation provided by Ferry shown in Eqn. **[2.9]**:

$$D(t) = \frac{\sin(m\pi)}{m\pi E(t)} \qquad [2.9]$$

where *m* is the local slope of a doubly logarithmic plot of stress relaxation versus time.

The comparison of the 0% RH long term creep data with the 0% RH master curve referenced to 70°C is provided in **Figure 2.27**. As can be seen, there is a large amount of scatter in the 0% RH long term creep data, and it is difficult to make any true comparison of this data with the 0% RH master curve. It is currently believed this is not a resolution issue, as the precision of measurements is within ± 0.01mm, equivalent to ± 0.0015 MPa^{-1}. While resolution may not be the root cause of the large data scatter, fluctuations in humidity could be. Based on psychrometrics, if the room temperature RH is about 40%, at 70°C this would equate to about 3% rather than 0% RH. Because no attempt to control the RH was made in the "dry" samples, as the relative humidity in the lab changed, it also changed in the sample test tubes. Therefore it is possible the RH level the sample saw ranged from 0-5%, equivalent to ± ~ 0.4% strain, or ± ~0.016 MPa^{-1} accounting for the large spread in the measured data. To truly check this hypothesis the long term creep of dry samples should be measured at 80°C where the relative humidity is 0% and fluctuations in the room humidity should not have an effect on the data.

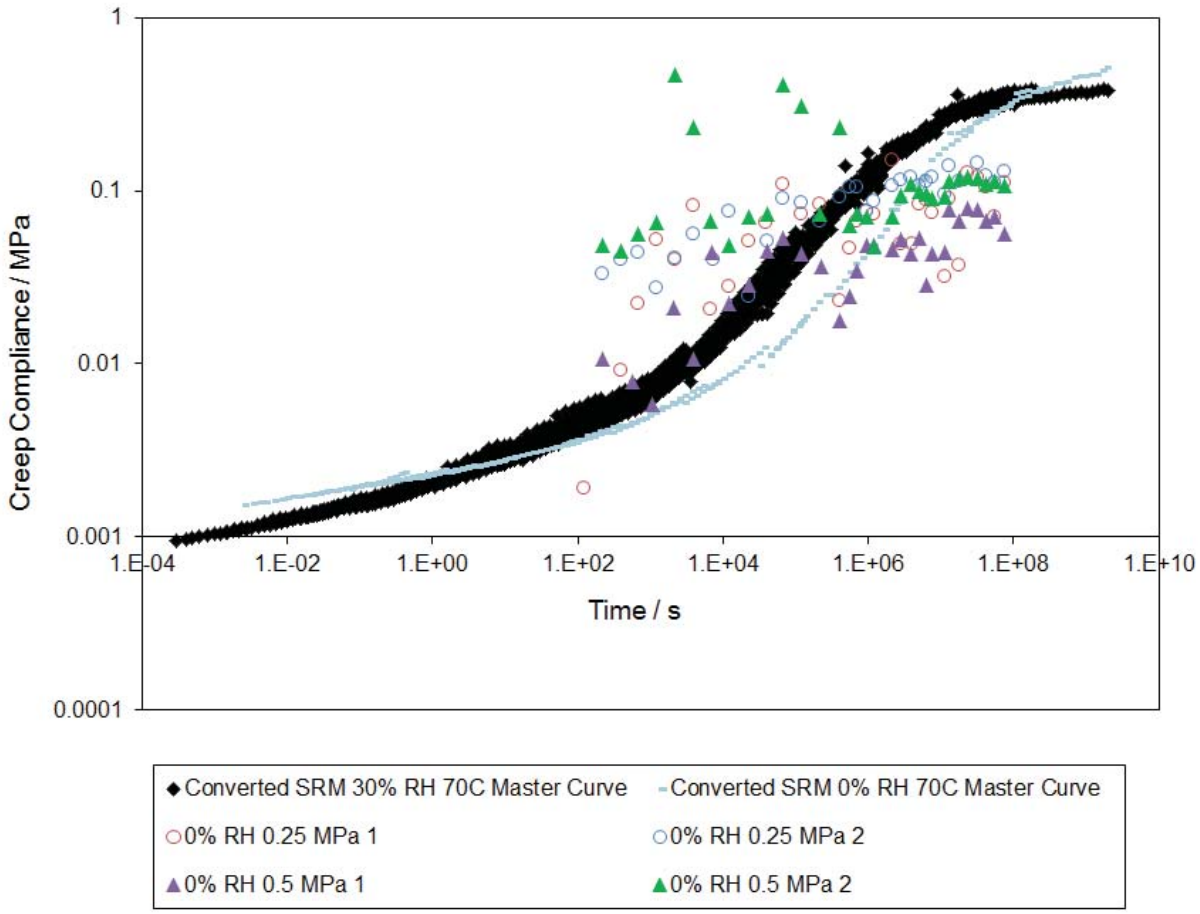

Figure 2.27. Comparison of stress relaxation master curve referenced to 70°C and 0% RH with long term creep data taken at 0.25 and 0.5 MPa, 0% RH, and 70°C.

To properly compare the 100% RH and immersed creep data with the 30% RH stress relaxation master curve, the creep data was shifted using the shift factor fit (discussed in Section 3.3.3.2) determined for the stress relaxation hygrothermal master curve shift factors. For 100% RH, corresponding to a λ of 7.6, the shift factor was calculated to be 9412, and for immersed conditions, corresponding to a λ of 14.2, the shift factor was calculated to be 281590. As shown in **Figure 2.28** and **Figure 2.29**, the agreement between the creep behavior predicted using the converted stress relaxation master curve and shift factors with the long term 100% RH and immersed creep data is very good, implying that the master curve is an accurate representation of the material behavior under humidified and immersed conditions.

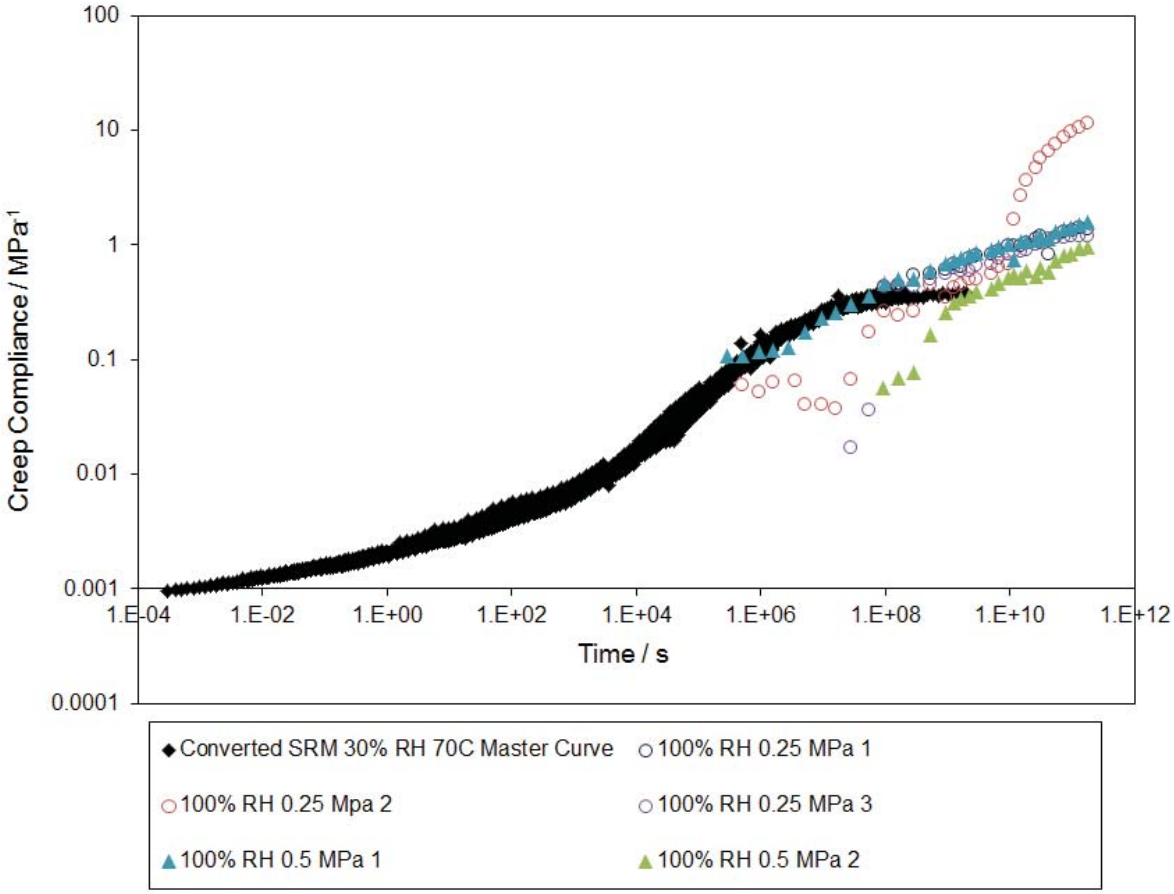

Figure 2.28. Comparison stress relaxation master curve referenced to 70°C and 30% RH with shifted long term creep data taken at 0.25 and 0.5 MPa, 100% RH, and 70°C.

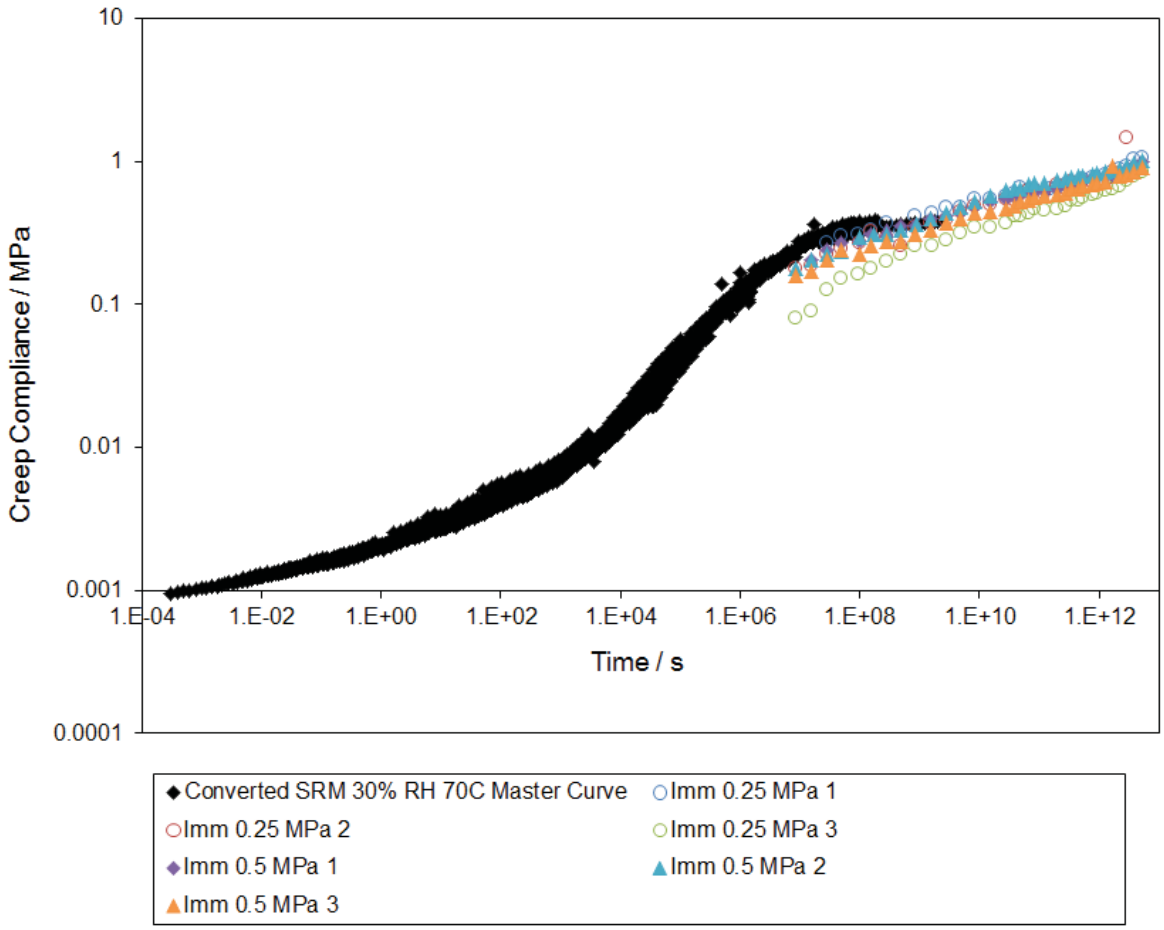

Figure 2.29. Comparison of stress relaxation master curve referenced to 70°C and 30% RH with shifted long term creep data taken at 0.25 and 0.5 MPa, immersed at 70°C.

The deviations at long times, 1E10 seconds and greater, could be due to entering the nonlinear viscoelastic region of the material. By this time, the samples have strained 25-30% for an applied stress of 0.25 MPa and 40-60% for an applied stress of 0.5 MPa. As shown in Appendix 1 the linear viscoelastic region of the material is about 2% strain and less, and so it may not be expected for these long term creep samples at very long times to match the linear viscoelastic stress relaxation curve. However, this long term nonlinear data may be more relevant to actual stresses incurred in an operating fuel cell, and provide useful nonlinear data for comparison with nonlinear viscoelastic modeling efforts.

Other possible errors in the long term creep data relate to the measured strain. Because a reference line was placed on each test tube, and each test tube was glued down, it is unlikely the length was measured improperly. However, deviations in what was taken to be the bottom of the sample each time could have occurred, and the resolution of the microscope is only 0.01mm. In addition, the large scatter in the dry data and the scatter in the 100% RH data could be avoided if a larger load was applied. However this cannot be done as previous testing indicates 1 MPa applied loads appear to be outside the linear viscoelastic region and there was still quite a bit of noise in these previous measurements. Therefore, it is likely a certain amount of noise will be inherent in data taken under this test method under dry and humidified conditions.

2.4 Conclusions

Thermal and hygral expansion, and stress relaxation measurements were taken to characterize the constitutive properties of a PFCB/PVDF-HFP (70:30 wt:wt) membrane material. Compared with Nafion® NRE 211, in-plane thermal expansion of the PFCB/PVDF-HFP is approximately twice as large over 0-50% RH and 30-120°C, although the two materials show similar thermal expansion at higher humidity levels as the CTE increases with increased humidity levels. Hygral expansion showed almost no temperature dependence for either material from 0-90% RH over 30-120°C, and both materials have CHE values that are approximately the same, although the PFCB/PVDF-HFP is slightly higher.

Stress relaxation measurements taken on the PFCB/PVDF-HFP over 30-120°C, at 0, 2, 10, 30, 55, and 80% RH were used to successfully create a hygrothermal master curve via simultaneous shifting for both temperature and humidity, implying the applicability of the time temperature moisture superposition principle over the timeframe examined. Comparing the hygrothermal master curve of the PFCB/PVDF-HFP with NRE 211 shows that PFCB/PVDF-

HFP material is stiffer, and both materials relax over a similar timeframe, although the PFCB/PVDF-HFP material relaxes approximately two decades after NRE 211 due to the increased stiffness. Also similar to NRE 211, PFCB/PVDF-HFP shows antiplasticization behavior at low moisture contents. The stress relaxation modulus thermal master curve at 2, 10, and 30% RH all show a higher stiffness than the stress relaxation modulus thermal master curve at 0% RH. It is believed this antiplasticization arises due to water bridging at low water contents. Finally, when the approximate hygral and thermal dependence of the hygrothermal shift factors used to create the hygrothermal master curves for both materials are examined, it is clear that both material moduli have approximately the same temperature dependence. However, PFCB/PVDF-HFP membranes have an approximately four times larger change in modulus with fluctuations in moisture than NRE 211. This increased moisture dependence could lead to higher incurred stresses under operating fuel cell conditions, but could also allow the PFCB/PVDF-HFP material to relax problematic high stresses more quickly, allowing for increased lifetime mechanical durability.

2.5 References

[1] O.o.B.E.S. US Department of Energy, in: U. DOE (Ed.), Washington DC, 2004.
[2] Y.-H. Lai, D.A. Dillard, Mechanical Durability Characterization and Modeling of Ionomeric Membranes, in: W. Vielstich, H. Yokokawa, H. Gasteiger, A. (Eds.) Handbook of Fuel Cells - Fundamentals, Technology and Applications, John Wiley & Sons, New York, 2009.
[3] W.K. Liu, S.J.C. Cleghorn, B.E. Delaney, M. Crum, Chemical and Mechanical Membrane Degradation, in: W. Vielstich, H. Yokokawa, H. Gasteiger, A. (Eds.) Handbook of Fuel Cells - Fundamentals, Technology and Applications, John Wiley & Sons Ltd., New York, 2009, pp. 385-402.
[4] R. O'Hayre, S.-W. Cha, W. Colella, F.B. Prinz, Fuel Cell Fundamentals, 2nd ed., Wiley, New York, NY, 2009.
[5] Y. Li, D.A. Dillard, Y.-H. Lai, S. Case, W., M.W. Ellis, M.K. Budinski, C.S. Gittleman, Journal of the Electrochemical Society, 159 (2012) B173-B184.
[6] C.S. Gittleman, Y.-H. Lai, C. Lewis, D.P. Miller, in: AIChE, Cincinnati, OH, 2005.
[7] Y.-H. Lai, C.K. Mittelsteadt, C.S. Gittleman, Journal of Fuel Cell Science and Technology, 6 (2009) 021002/021001-021002/021013.

[8] Y.-H. Lai, C.K. Mittelsteadt, C.S. Gittleman, D.A. Dillard, in: Third International Conference on Fuel Cell Science, Engineering and Technology, Ypsilanti, Michigan, 2005.
[9] W. Liu, K. Ruth, R. Greg, Journal of New Materials for Electrochemical Systems, 4 (2001) 227-231.
[10] V. Stanic, in: 4th International Symposium on Proton Conducting Membrane Fuel Cells, 2004.
[11] A.Z. Weber, J. Newman, AIChE Journal, 50 (2004) 3215-3226.
[12] D. Liu, S. Case, Journal of Power Sources, 162 (2006) 521-531.
[13] A. Eisenberg, M. King, Polymer Physics, A ed., Academic Press, New York, 1977.
[14] F. Bauer, S. Denneler, M. Willert-Porada, Journal of Polymer Science, Part B: Polymer Physics, 43 (2005) 786-795.
[15] P.W. Majsztrik, A.B. Bocarsly, J.B. Benziger, Macromolecules, 41 (2008) 9849-9862.
[16] M.B. Satterfield, J.B. Benziger, Journal of Polymer Science, Part B: Polymer Physics, 47 (2008) 11-24.
[17] D. Liu, M.A. Hickner, S.W. Case, J.J. Lesko, Journal of Engineering Materials and Technology, 128 (2006) 503-508.
[18] M.N. Silberstein, M.C. Boyce, Journal of Power Sources, 195 (2010) 5692-5706.
[19] M.N. Silberstein, M.C. Boyce, Journal of Power Sources, 196 (2011) 3452-3460.
[20] R. Jia, B. Han, K. Levi, T. Hasegawa, J. Ye, R.H. Dauskardt, Journal of Power Sources, 196 (2011) 8234-8240.
[21] R. Jia, B. Han, K. Levi, T. Hasegawa, J. Ye, R.H. Dauskardt, Journal of Power Sources, 196 (2011) 3803-3809.
[22] X. Huang, R. Solasi, Y. Zou, M. Feshler, K. Reifsnider, D. Condit, S. Burlatsky, T. Medden, Journal of Polymer Science, Part B: Polymer Physics, 44 (2006) 2346-2357.
[23] R. Solasi, Y. Zou, X. Huang, K. Reifsnider, D. Condit, in: The 4th International Conference on Fuel Cell Science, Engineering, and Technology, Irvine, CA, 2006.
[24] R. Solasi, Y. Zou, X. Huang, K. Reifsnider, D. Condit, Journal of Power Sources, 167 (2007) 366-377.
[25] Y. Tang, A.M. Karlsson, M.H. Santare, M. Gilbert, S. Cleghorn, W.B. Johnson, Materials Science & Engineering, A: Structural Materials: Properties, Microstructure, and Processing, A425 (2006) 297-304.
[26] Y. Tang, A. Kusoglu, A.M. Karlsson, M.H. Santare, S. Cleghorn, W.B. Johnson, Journal of Power Sources, 175 (2008) 817-825.
[27] Y. Tang, M.H. Sanatare, A.M. Karlsson, in: The 3rd International Conference on Fuel Cell Science, Engineering, and Technology, Ypsilanti, MI, 2005.
[28] Y. Tang, M.H. Santare, A.M. Karlsson, S. Cleghorn, W.B. Johnson, Journal of Fuel Cell Science and Technology, 3 (2006) 119-124.
[29] J.D. Ferry, Viscoelastic Properties of Polymers, 3 ed., John Wiley and Sons, New York, 1980.
[30] K. Ngai, L., D. Plazek, J., Rubber Chemistry and Technology, 78 (1995) 376-434.
[31] N.W. Tschoegl, W.G. Knauss, I. Emri, Mechanics of Time-Dependent Materials, 6 (2002) 53-99.
[32] L.C. Brinson, W.G. Knauss, Journal of the Mechanics and Physics of Solids, 39 (1991) 859-880.
[33] Y.S. Urzhumtsev, Mechanics of Composite Materials, 10 (1974) 180-185.
[34] S.C. Yeo, A. Eisenberg, Journal of Applied Polymer Science, 21 (1977) 875-898.

[35] T. Kyu, A. Eisenberg, Journal of Polymer Science, Symposia, 71 (1984) 203-219.
[36] G.M. Divoux, K.A. Finlay, J.K. Park, J.-M. Song, B. Yan, M. Zhang, D. Dillard, A., R. Moore, B., ECS Transactions, 41 (2011) 87.
[37] D. Liu, S. Kyriakides, S. Case, W., J. Lesko, J., Y. Li, J. McGrath, E., Journal of Polymer Science, Part B: Polymer Physics, 44 (2006) 1453-1465.
[38] K.A. Patankar, D.A. Dillard, S.W. Case, M.W. Ellis, Y.-H. Lai, M.K. Budinski, C.S. Gittleman, Fuel Cells, (Accepted).
[39] I. Emri, V. Pavsek, Materials Forum, 16 (1992) 123-131.
[40] M. Kohan, I., Nylon Plastics, 3rd ed., Wiley, New York, NY, 1973.
[41] S. Onogi, K. Sasaguri, T. Adachi, S. Ogihara, Journal of Polymer Science, 58 (1962) 1-17.
[42] N.E. Shepherd, in: Materials Science and Engineering, Virginia Tech, Blacksburg, VA, 1995.
[43] K.A. Patankar, D.A. Dillard, S.W. Case, M.W. Ellis, Y.-H. Lai, M.K. Budinski, C.S. Gittleman, Mechanics of Time-Dependent Materials, 12 (2008) 221-236.
[44] D.A. Dillard, Y.-H. Lai, M.K. Budinski, C.S. Gittleman, in: 3rd International Conference on Fuel Cell Science Engineering and Technology, Ypsilanti, MI, 2005.
[45] D.A. Dillard, Y. Li, J.R. Grohs, S.W. Case, M.W. Ellis, Y.-H. Lai, M.K. Budinski, C.S. Gittleman, Journal of Fuel Cell Science and Technology, 6 (2009) 031014/031011-021014/031018.
[46] J.R. Grohs, Y. Li, D.A. Dillard, S.W. Case, M.W. Ellis, Y.-H. Lai, C.S. Gittleman, Journal of Power Sources, 195 (2010) 527-531.
[47] Y. Li, J.K. Quincy, S.W. Case, M.W. Ellis, D.A. Dillard, Y.-H. Lai, M.K. Budinski, C.S. Gittleman, Journal of Power Sources, 185 (2008) 374-380.
[48] Y. Li, J. Quincy, D.A. Dillard, S.W. Case, M.W. Ellis, Y.-H. Lai, M.K. Budinski, C.S. Gittleman, in: 4th International Conference on uel Cell Science, Engineering and Technology, Irvine, CA, 2006.
[49] K.A. Patankar, D.A. Dillard, S.W. Case, M.W. Ellis, Y. Li, Y.-H. Lai, M.K. Budinski, C.S. Gittleman, Journal of Polymer Science, Part B: Polymer Physics, 48 (2010) 333-343.
[50] S.T. Iacono, S.M. Budy, J. Jin, D. Smith, Jr, Journal of Polymer Science Part A: Polymer Chemistry, 45 (2007) 5705-5721.
[51] S.T. Iacono, D. Ewald, A. Sankhe, A. Rettenbacher, D.W. Smith, Jr, High Performance polymers, 19 (2007) 581-591.
[52] B.-J. Chang, D.-J. Kim, J.-H. Kim, S.-B. Lee, H.-J. Joo, Journal of Membrane Science, 325 (2008) 989-996.
[53] DuPont, in, 2009, pp. 4.
[54] D.-J. Kim, B.-J. Chang, J.-H. Kim, S.-B. Lee, H.-J. Joo, Journal of Membrane Science, 325 (2008) 217-222.
[55] S.S. Mao, K.A. Lewinski, D.A. Ylitalo, in: U.S.P. Office (Ed.), 3M Innovative Properties Company, United States, 2003.
[56] D.A. Babb, B.R. Ezzell, K.S. Clement, W.F. Richey, A.P. Kennedy, Journal of Polymer Science Part A: Polymer Chemistry, 31 (1993) 3465-3477.
[57] A.P. Kennedy, L.D. Bratton, Z. Jezic, R.E. Lane, D.J. Perettie, W.F. Richey, D.A. Babb, K.S. Clement, in: U.S.P. Office (Ed.), The Dow Chemical Company, United States, 1995.
[58] H.-C. Liou, P.S. Ho, A. McKerrow, Journal of Polymer Science, Part B: Polymer Physics, 36 (1998) 1383-1392.

[59] N. Gourdoupi, J.K. Kallitsis, S. Neophytides, Journal of Power Sources, 195 (2010) 170-174.
[60] J. Kerres, W. Cui, R. Disson, W. Neubrand, Journal of Membrane Science, 139 (1998) 211-225.
[61] M. Lavorgna, G. Mensitieri, G. Scherillo, M.T. Shaw, S. Swier, R.A. Weiss, Journal of Polymer Science, Part B: Polymer Physics, 45 (2007) 395-404.
[62] L.M. Robeson, Polymer Blends: A Comprehensive Review, Hanser Gardner Publications, Cincinatti, OH, 2007.
[63] L.A. Utracki, Polymer Blends Handbook, Kluwer Academic Publishers, 2002.
[64] T. Zhang, W. He, J. Goldbach, D. Mountz, J. Yi, Journal of Power Sources, 196 (2011) 1687.
[65] Y. Li, in, 2010.
[66] A.E. Akinay, W. Brostow, Polymer, 42 (2001) 4527-4532.
[67] C.K. Mittelsteadt, H. Liu, Conductivity, Permeability, and Ohmic Shorting of Ionomeric Membranes, in: W. Vielstich, H. Gasteiger, A., H. Yokokawa (Eds.) Handbook of Fuel Cells: Fundametnals, Technology, and Applications, John Wiley & Sons, Ltd., New York, NY, 2009.
[68] K.K. Pushpa, D. Nandan, R.M. Iyer, Journal of the Chemical Society, Faraday Transactions 1: Physical Chemistry in Condensed Phases, 84 (1988) 2047-2056.
[69] T.A. Zawodzinski, Jr., T.E. Springer, J. Davey, J. Valerio, S. Gottesfeld, Batteries Fuel Cells, 91-10 (1991) 187-196.
[70] G.M. Divoux, in: Macromolecular Science and Engineering, Virginia Polytechnic Institute and State University, Blacksburg, VA, 2012.
[71] L. Maldonado, J.-C. Perrin, J. Dillet, O. Lottin, Journal of Membrane Science, 389 (2012) 43-56.
[72] M. Laporta, M. Pegoraro, L. Zanderighi, Physical Chemistry Chemical Physics, 1 (1999) 4619-4628.
[73] N. May, in: Materials Science and Engineering, Virginia Polytechnic Institute and State University, Blacksburg, VA, 2011, pp. 101.
[74] M. van Gurp, J. Palmen, Rheology Bulletin, 67 (1998) 5-8.
[75] C. Han, D., M. Jhon, S., Journal of Applied Polymer Science, 32 (1986) 3809-3840.
[76] C. Han, D., J. Kim, K., Polymer, 34 (1993) 2533-2539.
[77] A. Molnar, A. Eisenberg, Macromolecules, 25 (1992) 5774-5782.
[78] N. May, in: Materials Science and Engineering, Virginia Polytechnic Institute and State University, Blacksburg, VA, 2011, pp. 90.

Chapter 3 : Analytical and Numerical Stress Modeling of Perfluorocyclobutane/Poly(vinylidene Difluoride)-co-Hexafluoropropylene (PFCB/PVDF-HFP) Blends for Use as Fuel Cell Membranes

3.1 Introduction

The durability of polymer electrolyte membranes or proton exchange membranes (PEM) is of key importance for the commercialization of fuel cells for portable, stationary, and transportation applications [1]. Cell assembly parameters such as MEA compression, gasket design, operating temperature and pressure, as well as relative humidity of the reactant gasses can all have a significant effect on membrane lifetime [2]. Additionally, membrane degradation can be caused due to chemical, electrochemical, mechanical, thermal, and other physical processes that interact and degrade performance during operation [3]. Within an operating fuel cell, the membrane is subjected to a harsh chemical environment with both reducing and oxidizing interactions. One common problem is the formation of radicals, specifically peroxy and hyperperoxy radicals, which will then attack and degrade the membrane. To reduce membrane damage due to the formation of radicals, several researchers have suggested including radical scavengers or traps [4, 5]. These include cerium and manganese ions, cerium oxide nanoparticles, and rare earth oxide layers on either side of the membrane [4, 6, 7]. Radical scavengers have shown to greatly improve membrane resistance to chemical degradation.

While significant progress has been made in reducing chemical degradation of membrane materials, mechanical degradation has only recently been recognized as an important area of research. Within a fuel cell, the membrane is at least partially constrained by the gasket and rigid gas diffusion layers, catalyst layers, and bipolar plates. It is well known that better proton

conductivity is achieved at high water contents, however, PEM materials have been shown to expand due to moisture by at least 10%, and many by more than 20% in all three directions under high relative humidity or immersed conditions [8]. Due to the in-plane constraint created by the fuel cell system, varying in-plane compressive and tensile stresses are induced in the membrane as the PEM expands and contracts with changing temperature and humidity conditions [9]. Automotive applications are especially challenging mechanically due to the rapidly changing temperature and humidity conditions imposed to meet the needed power demands [10, 11].

It is believed that the repeated cycling of these induced hygrothermal mechanical stresses leads to a fatigue damage of the PEM, which over time contributes to delamination of the PEM and catalyst layers, as well as the formation and propagation of microcracks [12-14]. These and other defects or pinholes allow the reactant gasses to crossover and react on the catalyst surface. This reaction results in localized heating which can cause the membrane to soften or melt, thereby increasing degradation of the membrane, and allowing further gas crossover, creating a destructive cycle that ultimately causes failure of the fuel cell [2, 5, 13-17]. In addition, humidity cycle testing of a membrane constrained in a fuel cell set-up was performed by General Motors without the use of hydrogen or current draw, thereby eliminating chemical reactions and ensuring failure is solely due to mechanical stresses [10]. They showed failure in multiple perfluorosulfonic acid (PFSA) membranes, specifically with cracks perpendicular to the plane of the membrane in the channel region, suggesting these cracks were propagated via tensile stresses. Therefore even in the absence of chemical degradation, mechanical durability is an important membrane failure mechanism, and thus it is important to understand the stresses

incurred by a PEM during fuel cell operation to accurately predict and improve the lifetime durability of a fuel cell.

Due to the difficulty in measuring stresses in-situ in a fuel cell stack, as well as the extended experimental time required to examine membrane lifetime, researchers have begun developing models to calculate the hygrothermal stresses evolved by a PEM. The first model to incorporate membrane stress calculations was a 1-dimensional representation created by Weber and Newman [16]. Huang et al. further advanced Weber and Newman's model by creating a 2-dimensional elastic-plastic numerical model in a finite element program. Huang's model was used to examine the internal strain distribution within a constrained MEA due to changes in temperature and humidity [18]. Similar 2-dimensional linear elastic or elastic-plastic models were created and used by Tang et al. and Kusoglu et al. [19-25]. However these authors incorporated the land-channel geometry of a fuel cell stack, as well as all material properties for the membrane, gas diffusion layer, and bipolar plates to capture the property mismatch. Bograchev et al. and Martemniov et al. used the model developed by Kusoglu et al. but modified it to account for edge effects near seal joints. This was accomplished by modeling all channels and joints, as well as more realistic clamping effects utilizing two fastening elements to emulate bolts rather than a constant displacement or constant applied stress [26-29]. Up to this point, all models have been simplified 1- or 2-dimensional set-ups. However Al-Baghdadi et al. created a full 3-dimensional multiphase, elastic-plastic, non-isothermal PEM fuel cell model utilizing comprehensive fluid dynamics (CFD) incorporating thermal strains to examine the mechanical behavior of the membrane [30, 31]. An additional 2-dimensional linear-elastic non-isothermal CFD model was created by Serincan and Pasaogullari, combining it with a structural mechanics model [32]. While numerical modeling has been a main focus of the literature, Kusoglu also

developed a constitutive equation and corresponding phenomenological model to describe elastic-plastic behavior in the membranes at different temperature and moisture conditions using the G'Sell-Jonas approach [33].

While the models discussed thus far provide good insight into material behavior in an operating fuel cell, they do not capture the time dependence or viscoelastic behavior of PEM materials. Therefore, to more accurately describe the stress state of the PEM, Khattra et al. extended Kusoglu et al.'s linear-elastic plastic models to include time dependence, creating a constitutive model to describe the hygrothermal mechanical time-dependent response of the membrane [34]. The stresses developed using this time-dependent model are larger than those predicted previously when time dependence was ignored, emphasizing the importance of incorporating time dependence to better understand the stresses developed during operation, and corresponding membrane lifetimes.

An additional model incorporating membrane time dependence was proposed by Lai et al [10, 13, 14] as a one-dimensional linear viscoelastic constitutive model in the form of:

$$\sigma_x(\varepsilon,t,T,\lambda) \approx \int_0^t E(t-\xi)\frac{d[\varepsilon_x(\xi)-\alpha\cdot T(\xi)-\beta\cdot\lambda(\xi)]}{d\xi}d\xi \qquad \textbf{[3.1]}$$

where σ is the uniaxial stress, t is time, $T(\xi)$ is the change in temperature from a reference condition, $\lambda(\xi)$ is the change in the moles of water molecules per mole of sulfonic acid group in the membrane from a reference condition, E is the uniaxial relaxation modulus, ξ is the time parameter, ε is the strain, α is the linear coefficient of thermal expansion, and β is the linear coefficient of hygral expansion. This equation assumes that the membrane is stress-free at the reference condition and the approximation sign is utilized because α and β are assumed to be

time-independent. To account for a time dependent modulus, the authors utilized the time temperature moisture superposition principle, creating a master curve and corresponding hygral and thermal shift factors.

Previous modeling attempts have focused on PFSA PEM materials, however, PFSA PEM materials are costly, difficult to produce, and face performance problems, creating a need for an improved PEM material [12]. A recently developed material, perfluorocyclobutane (PFCB), shows significant potential as a fuel cell membrane due to its multiple processing routes, low dielectric constant, high thermal and oxidative stability, and chemical resistance [35, 36]. One example synthesized by Iacono had a maximum conductivity of 0.011 S cm^{-1} at 100% RH, the same as Nafion® at 40% RH. Two additional reported membranes, sulfonated poly(fluorenyl ether) and sulfonated poly(fluorine-co-sulfone)ether membranes, show proton conductivities equal to and greater than Nafion 115, dependent on the level of sulfonation. None of these studies examined the mechanical properties of the membranes, however Mao showed a tensile breaking stress of about 30 MPa for a sulfonated perfluorocyclobutane membrane [36-40]. Additional PFCB polymers used for other applications have been characterized with a 4-9% strain at break and 1 GPA modulus [41-43]. While these studies did not conduct durability analyses, the reported polymers appear to be brittle and likely would not survive the harsh mechanical environment of a fuel cell.

Therefore, to improve the mechanical durability by reducing the brittleness, the PFCB ionomer was blended with poly(vinylidene difluoride)-co-hexafluoropropylene (PVDF-HFP). Polymer blending has proven instrumental in the production of materials with tunable properties suitable for a variety of applications including fuel cell membranes [44-49]. One such example is a blend of a hydrocarbon ionomer and PVDF-HFP, which showed excellent mechanical

durability and fuel cell operating lifetimes five times greater than Nafion® NRE 211 [49]. In an attempt to understand this greater lifetime, the research herein focuses on creating a 1-dimensional linear viscoelastic model as described by Lai et al. [10, 13, 14], utilizing the constitutive properties previously presented in **Chapter 2** to analyze the stresses incurred during a fuel cell duty cycle as compared with those developed by Nafion® NRE 211.

3.2 Method

Due to the viscoelastic nature of the membrane, the time dependent uniaxial modulus should be considered when calculating the stresses. In addition, the strong hygrothermal dependence of the membrane should also be considered, as the induced hygrothermal stresses are created due to the biaxial constraint of the film during hygrothermal cycling. The time dependent uniaxial relaxation modulus, *E(t)*, is commonly represented by a Prony series:

$$E(t) = E_{\infty} + \sum_{n=1}^{N} E_n e^{-\frac{t}{\tau_n}} \qquad \textbf{[3.2]}$$

where E_{∞} is the long term modulus or rubbery plateau modulus, E_n is the Prony coefficient for the nth term, and τ is the corresponding relaxation time. Time dependent constitutive properties are frequently described by hereditary integrals, and the stress may be described as shown previously in **Eqn 3.1**.

For modeling purposes, the hereditary integral is often converted to a recursive form [50, 51]. First a Prony series representation of the time dependent modulus is substituted into the hereditary integral (**Eqn [3.1])** gives:

$$\sigma_x(\varepsilon,t,T,\lambda) \approx E_\infty(\varepsilon(t)-\alpha\Delta T(t)-\beta\Delta\lambda(t))+ \sum_{n=1}^{N} E(t)_n \left\{ \int_0^t e^{-(t-\zeta)/\tau} \frac{\partial[\varepsilon_x(\xi)-\alpha\cdot T(\xi)-\beta\cdot\lambda(\xi)]}{\partial\xi} d\xi \right\} \quad \textbf{[3.3]}$$

The integral in **Eqn [3.3]** can be described by piecewise integration, evaluating the integral to obtain the strain history, ε_i, at time t_i:

$$\varepsilon_i = \int_0^{t_{i-1}} e^{-(t-\zeta)/\tau_n} \frac{\partial[\varepsilon_x(\xi)-\alpha\cdot T(\xi)-\beta\cdot\lambda(\xi)]}{\partial\xi} d\xi + \int_{t_{i-1}}^{t_i} e^{-(t-\zeta)/\tau_n} \frac{\partial[\varepsilon_x(\xi)-\alpha\cdot T(\xi)-\beta\cdot\lambda(\xi)]}{\partial\xi} d\xi \quad \textbf{[3.4]}$$

The first integral may be rearranged as:

$$\begin{aligned} &\int_0^{t_{i-1}} e^{-(t-\zeta)/\tau_n} \frac{\partial[\varepsilon_x(\xi)-\alpha\cdot T(\xi)-\beta\cdot\lambda(\xi)]}{\partial\xi} d\xi \\ &= e^{-t_i/\tau_n} \int_0^{t_{i-1}} e^{\xi/\tau_n} \frac{\partial[\varepsilon_x(\xi)-\alpha\cdot T(\xi)-\beta\cdot\lambda(\xi)]}{\partial\xi} d\xi \\ &= e^{-(t_i-t_{i-1})/\tau_n} \int_0^{t_{i-1}} e^{-(t_{i-1}-\xi)/\tau_n} \frac{\partial[\varepsilon_x(\xi)-\alpha\cdot T(\xi)-\beta\cdot\lambda(\xi)]}{\partial\xi} d\xi \\ &= e^{-(t_i-t_{i-1})/\tau_n} \varepsilon(t_{i-1}) \end{aligned} \quad \textbf{[3.5]}$$

allowing the following recursive relationship to be developed:

$$\varepsilon(t_i) = e^{-(t_i-t_{i-1})/\tau} \varepsilon(t_{i-1}) + \Delta\varepsilon(t_i) \quad \textbf{[3.6]}$$

Because the incremental strain value is:

$$\Delta\varepsilon(t_i) = e^{-t_i/\tau} \int_{t_{i-1}}^{t_i} e^{\xi/\tau_n} \frac{\partial[\varepsilon_x(\xi)-\alpha\cdot T(\xi)-\beta\cdot\lambda(\xi)]}{\partial\xi} d\xi \quad \textbf{[3.7]}$$

the strain may be assumed constant over the incremental time interval, resulting in:

$$\Delta\varepsilon(t_i) \approx e^{-t_i/\tau} \frac{\left[\varepsilon(t_i) - \alpha\Delta T(t_i) - \beta\Delta\lambda(t_i)\right] - \left[\varepsilon(t_{i-1}) - \alpha\Delta T(t_{i-1}) - \beta\Delta\lambda(t_{i-1})\right]}{t_i - t_{i-1}} \int_{t_{i-1}}^{t_i} e^{\xi/\tau_n} d\xi \qquad \textbf{[3.8]}$$

Assuming the hygrothermal shift factor is constant over the incremental time interval, the strain history can be reduced to:

$$\Delta\varepsilon(t_i) \approx \frac{\left[\varepsilon(t_i) - \alpha\Delta T(t_i) - \beta\Delta\lambda(t_i)\right] - \left[\varepsilon(t_{i-1}) - \alpha\Delta T(t_{i-1}) - \beta\Delta\lambda(t_{i-1})\right]}{(t_i - t_{i-1})/a_{TH}} \tau\left[1 - e^{-(t_i - t_{i-1})/a_{TH}\tau_n}\right] \qquad \textbf{[3.9]}$$

Thus, the complete recursive relationship is:

$$\begin{aligned}\varepsilon(t_i) = {} & e^{-(t_i - t_{i-1})/a_{TH}\tau_n} \varepsilon(t_{i-1}) + \\ & \frac{\left[\varepsilon(t_i) - \alpha\Delta T(t_i) - \beta\Delta\lambda(t_i)\right] - \left[\varepsilon(t_{i-1}) - \alpha\Delta T(t_{i-1}) - \beta\Delta\lambda(t_{i-1})\right]}{(t_i - t_{i-1})/a_{TH}} \tau\left[1 - e^{-(t_i - t_{i-1})/a_{TH}\tau_n}\right]\end{aligned} \qquad \textbf{[3.10]}$$

and the final linear viscoelastic equation used to model the hygrothermal stresses incurred in an operating fuel cell membrane:

$$\begin{aligned}\sigma(t) = {} & E_\infty\left[\varepsilon(t) - \alpha\Delta T(t) - \beta\Delta\lambda(t)\right] + \\ & \sum_{n=1}^{N} E\left\{\begin{array}{l} e^{-(t_i - t_{i-1})/a_{TH}\tau_n}\left[\varepsilon(t_{i-1}) - \alpha\Delta T(t_{i-1}) - \beta\Delta\lambda(t_{i-1})\right] + \\ \dfrac{\left[\varepsilon(t_i) - \alpha\Delta T(t_i) - \beta\Delta\lambda(t_i)\right] - \left[\varepsilon(t_{i-1}) - \alpha\Delta T(t_{i-1}) - \beta\Delta\lambda(t_{i-1})\right]}{t_i - t_{i-1}} a_{TH}\tau_n\left[1 - e^{(-t_i + t_{i-1})/a_{TH}\tau_n}\right] \end{array}\right\}\end{aligned} \qquad \textbf{[3.11]}$$

Multiple assumptions were made in developing this constitutive model. First the Poisson's ratio of the PFCB/PVDF-HFP was assumed constant and thusly not time, temperature

or moisture dependent, however this only becomes important when this model is extended to a 2-dimensional case [10]. This is typically reasonable for temperatures above the moisture suppressed alpha transition of ionomers where fuel cells are often operated. However, if there is a large difference in the glassy and rubbery Poisson's ratios the model should be modified to account for this time and temperature dependent property. In addition, assuming the Poisson's ratio is constant, also assumes that a single viscoelastic constitutive property is sufficient to describe the material behavior. Second, the hygral and thermal expansion coefficients were also assumed to be time-independent, and while not strictly true, this assumption is usually applied to viscoelastic materials [10].

In addition, temperature is assumed uniform throughout the film, and water diffusion in and out of the membrane over changing moisture conditions is assumed to be instantaneous and symmetric throughout the film, such that there are no stress concentrations. Therefore, the gradient of moisture typically found across an operating fuel cell membrane as well as the time dependence of moisture sorption and desorption created by the viscoelastic chain rearrangements, are not accounted for in this model. A symmetric water content was assumed by Weber and Newman, Huang, Solasi, Tang, and Kusoglu in early models, and as such it is believed this is a good assumption to employ in the initial constitutive modeling of PFCB/PVDF-HFP presented here [16, 18-21, 52]. Finally, the film is assumed to be within the linear viscoelastic regime. This assumes that there is no plastic deformation in the film during hygrothermal cycling, however the high tensile stress incurred under low moisture conditions could likely exceed the linear viscoelastic region. Therefore, predictions made with this model will probably over predict these stresses, as plasticity and other non-linear effects are not accounted for.

3.3 Hygrothermal Shift Factor Fitting

To calculate the stresses incurred by changing hygrothermal conditions typically found in an operating fuel cell, the recursive equation includes a_{TH} terms, or the hygrothermal shift factors of the material. Therefore a fit of the corresponding hygrothermal shift factors was necessary to create the analytical model.

Previously, Patankar et al. created his hygrothermal master curves using a two-step process, initially shifting for temperature at a constant humidity level, and then shifting each thermal master curve for moisture content. This resulted in separated thermal and hygral shift factors, although temperature dependence was still noted in the hygral shift factors [53]. Therefore, the hygral and thermal shift factors are not completely separable variables, and artificial separation of the temperature and moisture dependence of the material can be avoided by shifting for both temperature and moisture content simultaneously. This results in the creation of hygrothermal shift factors, as shown in **Figure 3.1**.

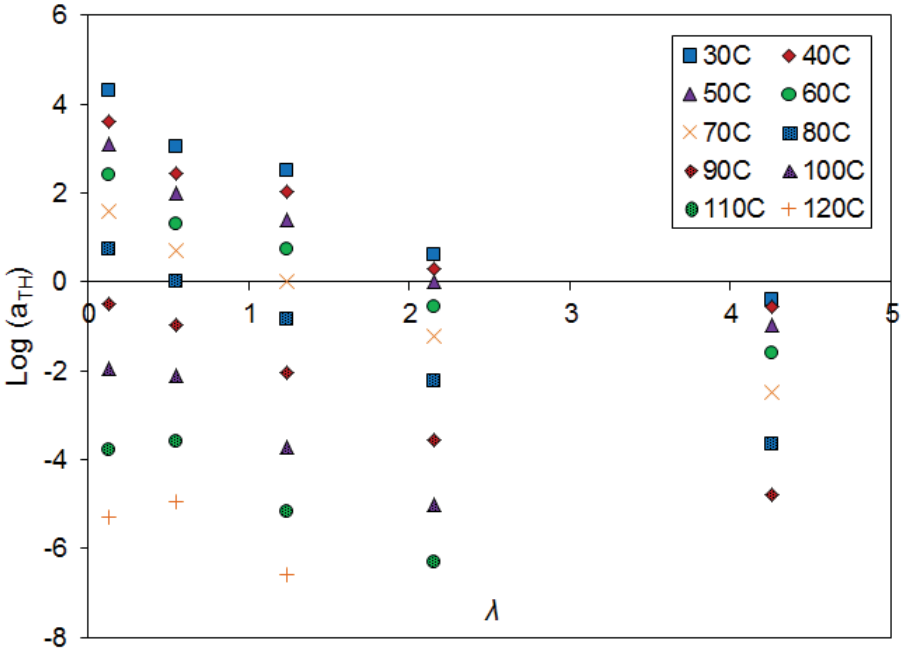

Figure 3.1. Hygrothermal shift factors for PFCB/PVDF-HFP for a 70°C 30% RH hygrothermal master curve.

3.3.1 Arrhenius Shift Factor Fit

Typical fitting techniques include an Arrhenius form to account for activated processes in the system, a Doolittle form or WLF form to account for changes in free volume in the polymeric system, and purely empirical fits which do not have any physical basis and cannot be used for predictive purposes outside the tested range. A general form of the Arrhenius shift factor is given by:

$$\log a_T = \frac{E_a}{2.303R}\left(\frac{1}{T} - \frac{1}{T_o}\right) \qquad \textbf{[3.12]}$$

where E_a is the activation energy, R is the universal gas constant, T is temperature, and T_o is the reference temperature. While this general form of the Arrhenius shift factor is well understood, extending this form to account for the moisture content is not. Fitting attempts resulted in the

inclusion of an apparent empirical term to account for moisture changes, and as such it is not believed a pure Arrhenius form shift factor is appropriate to describe hygrothermal shift factors.

3.3.2 Free Volume Shift Factor Fit

An alternative approach to fitting shift factors for master curves of an amorphous material is based on the concept of free volume. Free volume represents the unoccupied space within a polymeric material. This could be thought of as voids between polymer molecules due to packing irregularities [54]. Free volume is approximately a constant fraction of the total volume below the glass transition; however it can decrease further below the glass transition due to physical aging. Physical aging occurs in materials that are not in thermodynamic equilibrium, resulting in the slow rearrangement of polymer chains until equilibrium is reached. In addition it is believed the occupied volume increases at the same rate above and below the glass transition. Therefore, the additional volume gained above the glass transition is attributed to excess free volume [55]. The transition state model developed by Bueche states that a polymer unit cell cannot move until the local fractional free volume exceeds some critical value [55]. Therefore, polymer chain mobility at any temperature is primarily dependent upon the amount of free volume present in the material.

If this concept is believed, then relaxations could be expressed in terms of free volume rather than temperature. This relationship between free volume and chain mobility, or viscosity, is logarithmic in nature as shown by Doolittle [56]. A thermal shift factor with a Doolittle form can be defined as:

$$\log a_T = \frac{B}{2.303}\left(\frac{1}{f} - \frac{1}{f_o}\right) \qquad \textbf{[3.13]}$$

where B is a fitting constant, typically defined as unity in the literature, f is the fractional free volume, and f_o is the fractional free volume at a reference condition. The fractional free volume can be further defined by assuming a linear increase with temperature as follows:

$$f = f_o + \alpha_f (T - T_0) \quad \textbf{[3.14]}$$

where α_f is the thermal expansion coefficient of the free volume. This free volume definition can be expanded to also account for increases due to water uptake in the polymeric system:

$$f = f_o + \alpha_f (T - T_0) + \beta_f (\lambda - \lambda_o) \quad \textbf{[3.15]}$$

where β_f is the hygral expansion coefficient of the free volume. Substituting this definition of the free volume into the Doolittle equation, the following shift factor equation is developed:

$$\log a_{TH} = \frac{-\frac{B}{2.303}\alpha_f \Delta T - \frac{B}{2.303}\beta_f \Delta\lambda}{f_o^{\,2} + f_o \alpha_f \Delta T + f_o \beta_f \Delta\lambda} \quad \textbf{[3.16]}$$

A best fit was determined for the Doolittle free volume fit of the form described by **Eqn [3.16]** was attempted, as shown in **Figure 3.2** by setting B to unity as done previously in the literature to reduce the number of fitting parameters, and by assuming that α_f is approximately equal to α, or the coefficient of thermal expansion of the bulk material. Therefore the parameters used to determine the best fit were β_f, and f_o. Unlike α_f, β_f cannot be considered the approximately the same as its corresponding coefficient of expansion of the material because water molecules occupy volume, and the effects of water bridging in ionomers must also be considered [57-60]. Therefore, the free volume swelling efficiency of β_f would be expected to be considerably lower

than the coefficient of hygral expansion of the material. This pure free volume form fit describes the shift factors from 50-70°C well, however outside this temperature range, the fit no longer describes the material behavior sufficiently.

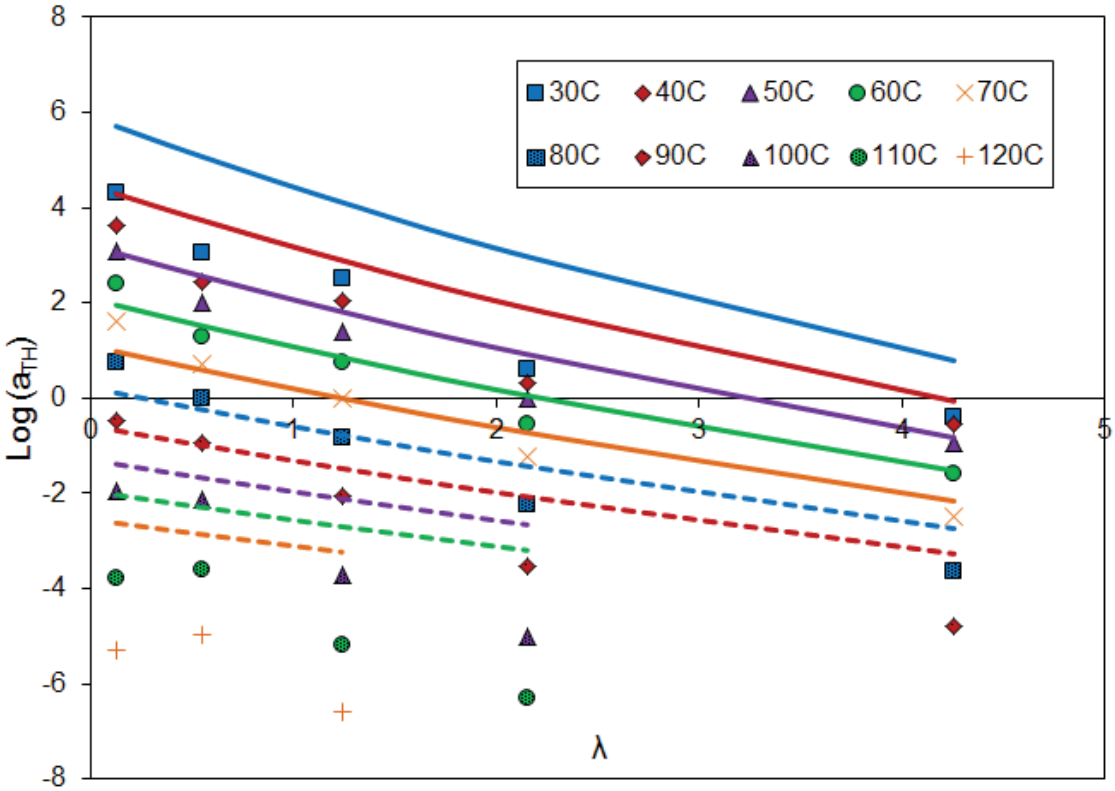

Figure 3.2. Free volume fit of the hygrothermal shift factors for the PFCB/PVDF-HFP system.

3.3.3 Combined Arrhenius and Free Volume Shift Factor Fit

Examination of the hygrothermal shift factors shows that neither a clear free volume nor Arrhenius behavior is observed, and thus could explain why neither fit describes the material behavior. However, if the hygrothermal shift factors are artificially separated into approximate

hygral and thermal shift factors (**Figure 3.3**), it appears the hygral shift factors have a shape that is reminiscent of WLF or free volume behavior, and the thermal shift factors have an approximate double Arrhenius behavior. It should be noted that this shift factor separation is artificial, and the values shown may not be exact, and therefore fitting was still performed utilizing the hygrothermal shift factors. However, based on the shapes obtained for the separated hygral and thermal shift factors it is thusly believed this system contains both a WLF, or cooperative motion, and Arrhenius, or activated motion, dependence. A combined fit with both free volume and Arrhenius forms was originally performed in 1965 to fit viscosity data, and has since been applied to other systems, especially within the agricultural field and to describe diffusion processes [61-67].

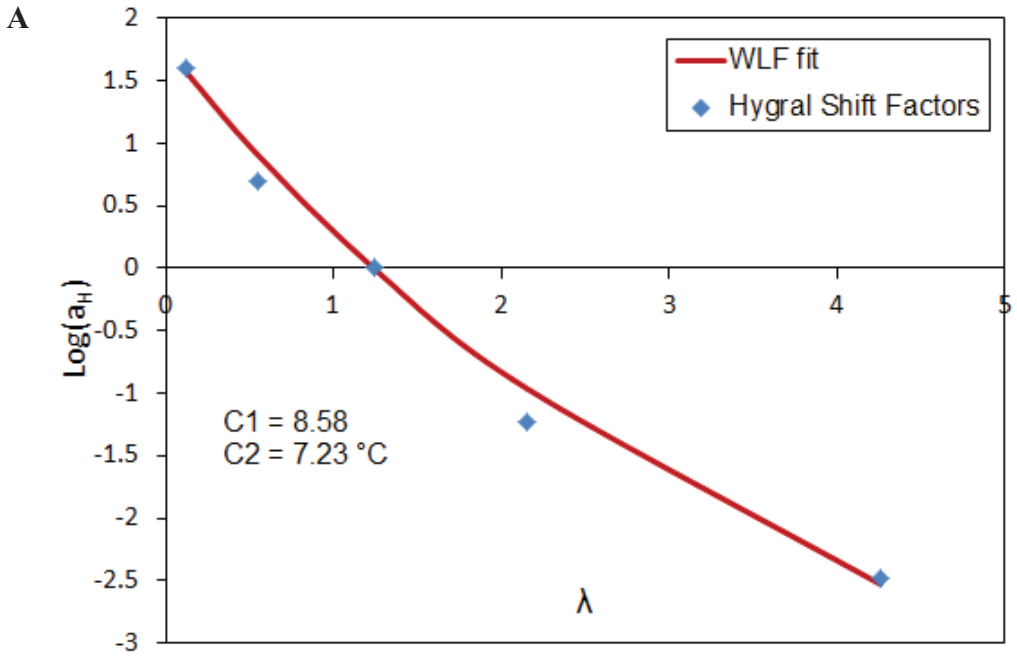

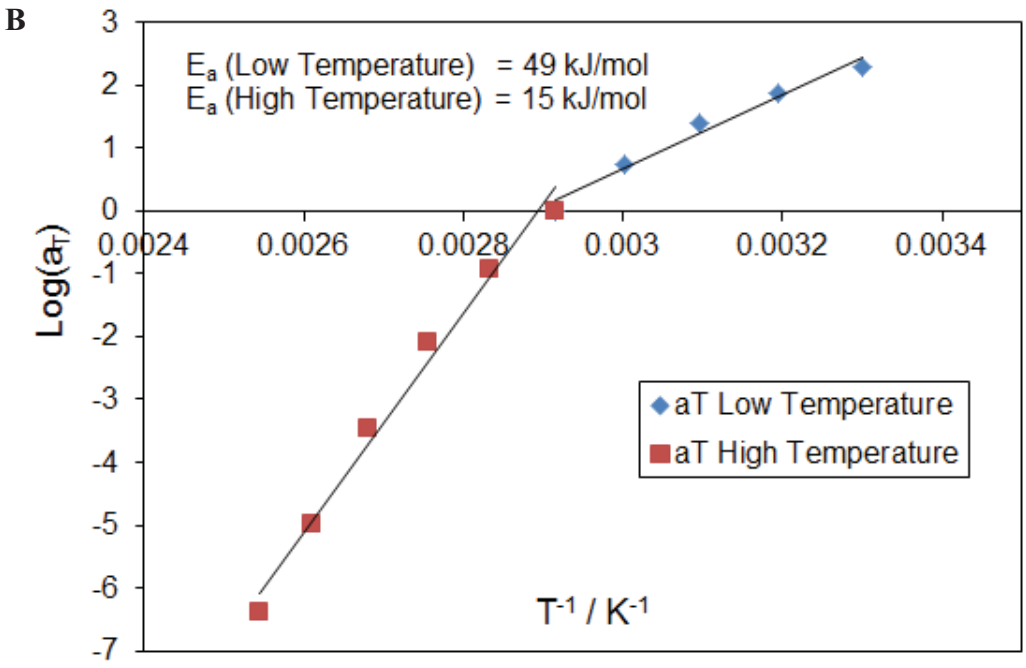

Figure 3.3. Approximate **(A)** hygral and **(B)** thermal shift factors for the PFCB/PVDF-HFP system.

Typically, free volume fits are applied to shift factors over the range from the glass transition to 100°C above the glass transition, and Arrhenius form fits are applied to shift factors below the glass transition. However, in this case the hygral shift factors appear to have an approximate WLF shape over the entire relative humidity, or λ, range, and the thermal shift factors appear to have a double Arrhenius form over the entire temperature range. Therefore, the combined free volume and Arrhenius fit will utilize both forms over the entire temperature and lambda range, rather than one or the other above and below the possible alpha transition at ~70°C. It is believed the Arrhenius form above 70°C may be necessary if this alpha transition is similar to that of Nafion® [68]. In Nafion®, at ~90°C, the sulfonic acid clusters begin to form a dynamic network which is related to a thermodynamic process, and as such would be described by Arrhenius behavior rather than free volume changes. Thus, if the sulfonic acid clusters in the

PFCB/PVDF-HFP system become a dynamic network above 70°C, the additional Arrhenius form dependence would be necessary to describe the material behavior. The combined free volume and Arrhenius form fit was created by coupling an Arrhenius term with the free volume fit described by **Eqn [3.17]**:

$$\log a_{TH} = \frac{-B\alpha_f \Delta T - B\beta_f \Delta\lambda}{f_o^{\,2} + f_o\alpha_f \Delta T + f_o\beta_f \Delta\lambda} - \frac{2.303R}{E_a}\Delta T \qquad \textbf{[3.17]}$$

3.3.3.1 Single Combined Arrhenius and Free Volume Fit

Using least squares regression, a best fit was determined for the combined shift factor fit, provided in **Figure 3.4**, by setting B to unity as done previously in the literature to reduce the number of fitting parameters, and by assuming that α_f is approximately equal to α, or the coefficient of thermal expansion of the bulk material. Therefore the parameters used to determine the best fit were β_f, f_o, and E_a. Unlike α_f, β_f cannot be considered the same as its corresponding coefficient of expansion of the material because water molecules occupy volume, and the effects of water bridging in ionomers must also be considered [57-60]. Therefore, the free volume swelling efficiency of β_f would be expected to be considerably lower than the coefficient of hygral expansion of the material. The best fit values determined were β_f = 0.007 λ^{-1} , f_o = 0.0532, and E_a = 0.26 kJ / K mol. However, as seen in **Figure 3.4**, this combined fit only describes the region over 60 – 90°C. Therefore, a single combined fit clearly does not describe the entire range of the shift factors.

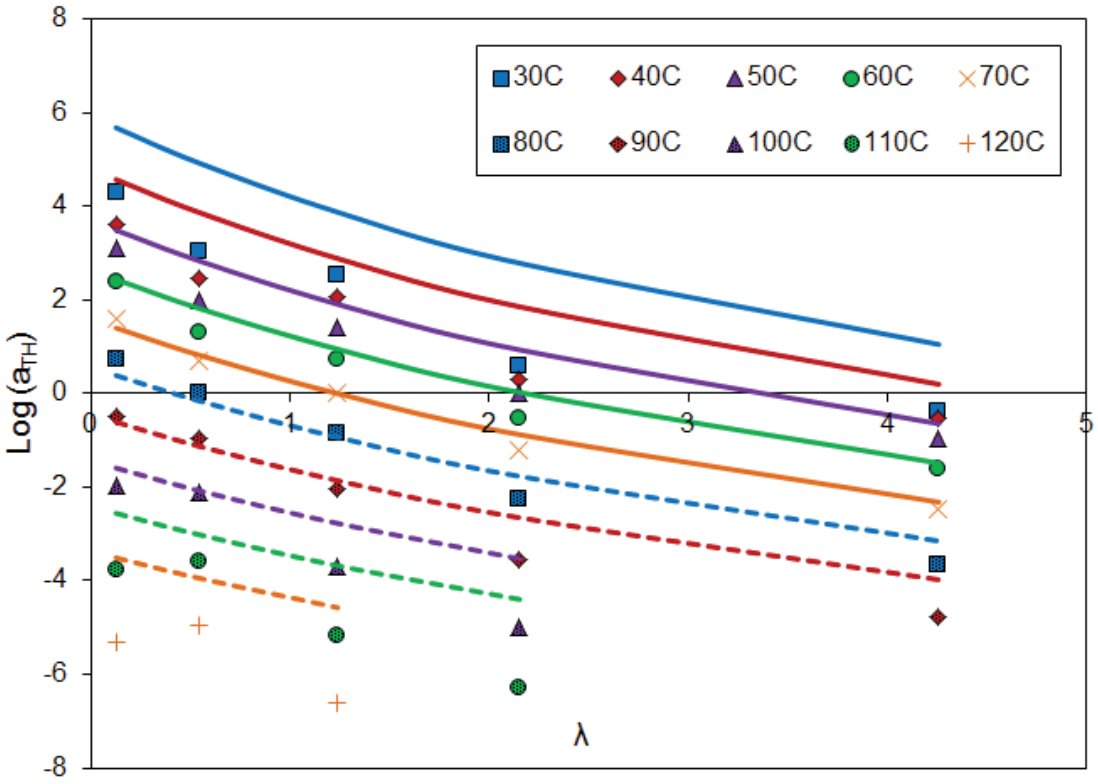

Figure 3.4. Combined free volume and Arrhenius form fit of hygrothermal shift factors for the PFCB/PVDF-HFP system.

3.3.3.2 Dual Combined Arrhenius and Free Volume Fit

Careful examination of the variables suggests that B, α_f, and f_o, should be constant over the entire temperature and moisture range examined. The variable B should be constant over the entire T and λ range, as B is a material constant, and is set to unity to reduce the number of fitting parameters. Furthermore, α_f should also be constant over the entire temperature and lambda range, as it should be approximately equal to the coefficient of thermal expansion of the material. It should be noted that in **Section 2.3.2.1**, α was shown to be dependent on the moisture content of the material above 50% RH. However, because α is very small and the increase of α with increased moisture content is also very small especially when compared with the magnitude of β,

it was assumed that any moisture dependence of α_f would result in negligible changes, and as such α_f was assumed constant over the entire T and λ range. Finally, the fractional free volume, f_o, should also be constant over the entire T and λ region, as this is the free volume at the reference temperature and the reference is kept constant throughout the fitting and modeling procedure.

Therefore, only two variables remain that could be changing over the temperature and moisture range of the shift factors, β_f and E_a. To examine this possibility further, the efficiency of swelling (**Figure 3.5**) as well as the approximate thermal shift factors (**Figure 3.3b**) of this material are reviewed further. The efficiency of swelling is defined as the degree of expansion of the membrane compared with the volume of water sorbed by the membrane. This efficiency of swelling can be examined by plotting the volume of water uptake vs. the volume of membrane expansion, and observing the slope. If perfect swelling were observed the slope would be equal to 1, as each water molecule would contribute to the expansion of the membrane. The volume of water uptake was calculated by dividing the mass measured via water uptake, by the density of water, taken to be 1 g/cm^3. The volume of membrane expansion was calculated by assuming isotropic swelling, and therefore multiplying the measured hygral expansion by 3. The efficiency of swelling shows a single linear behavior up to 90% RH, and the shift factors fitting only occurs up to 80% RH. Therefore, it is not appropriate to vary β_f over the moisture range examined. However, because the approximate thermal shift factors show what appears to be a doubly activated system with different activation energies above and below 70^{o}C, so too should E_a be different above and below 70^{o}C. Therefore the fitting parameters need to be modified to reflect one activation energy below 70^{o}C, and another above 70^{o}C, while all other fitting parameters remain constant over the entire temperature and moisture range. A pictorial summary

of the expected behavior of the combined fit variables over the T and λ range is provided in **Figure 3.6**.

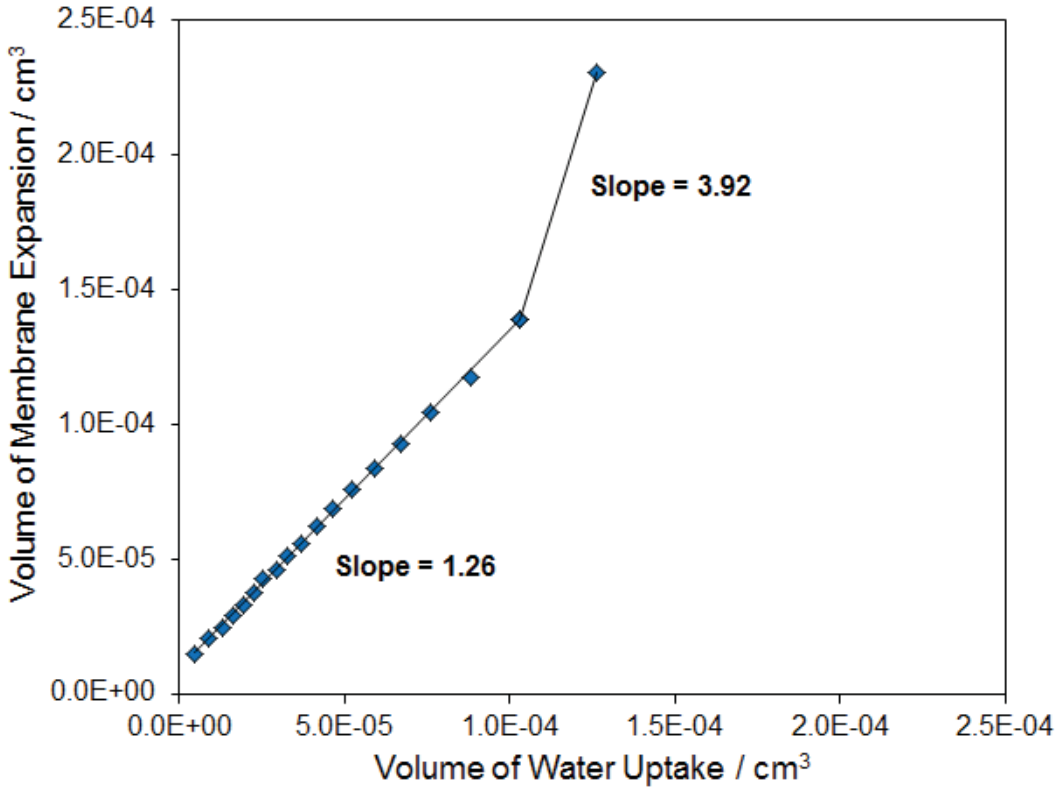

Figure 3.5. Efficiency of swelling of the PFCB/PVDF-HFP system.

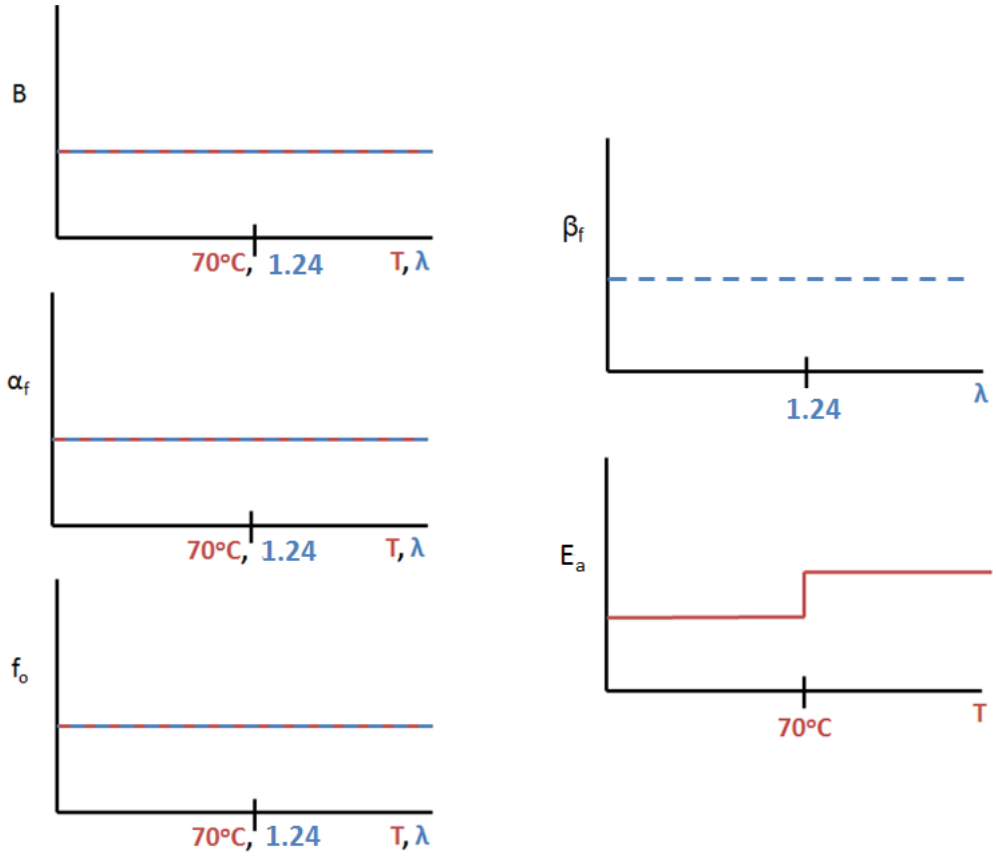

Figure 3.6. Changes in hygrothermal shift factor fitting parameters with temperature and water content.

To perform the fitting procedure, the least squares fitting analysis in Excel was utilized. It should be noted that because the shift factor equation being applied is in a $\log_{10}$ form, rather than the original natural log form, a factor of 2.303 must be accounted for, as shown with each B term. The fitting parameters used in the least squares procedure were therefore f_o, E_a, and β_f, resulting in the hygrothermal shift factor fits provided in **Figure 3.7**, and the corresponding equations provided in **Eqns [3.18]- [3.19**].

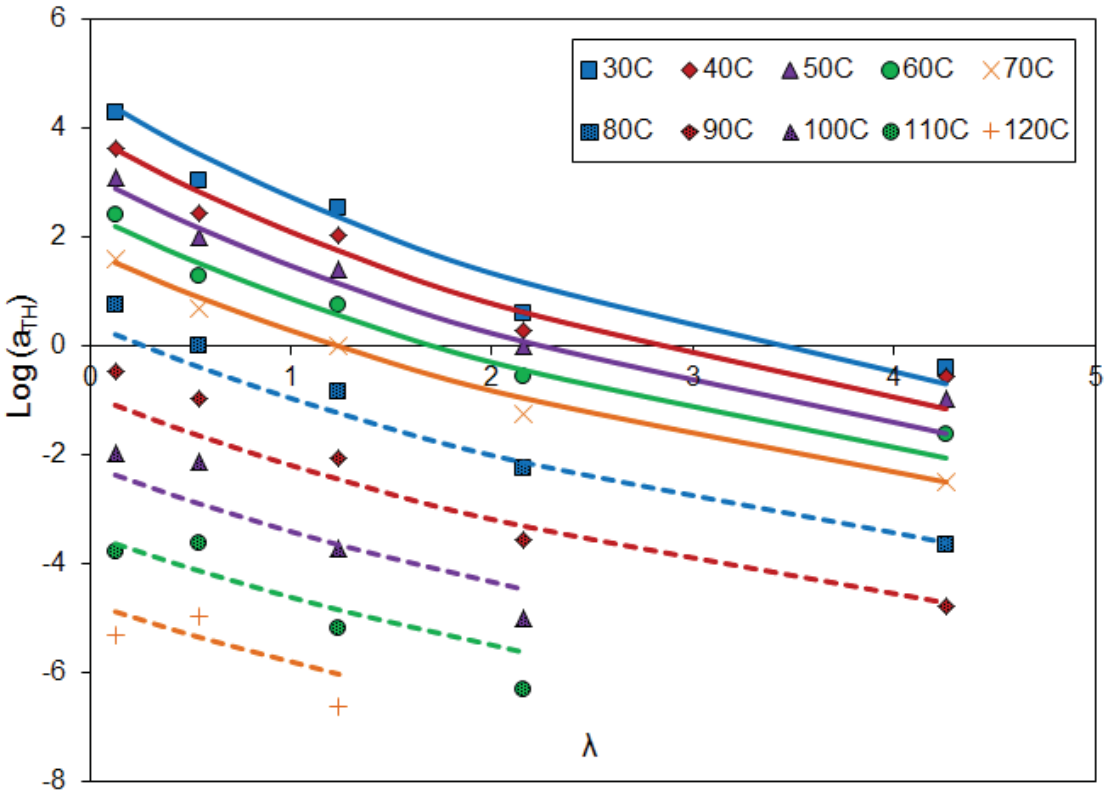

Figure 3.7. Hygrothermal shift factor fits based on combined Arrhenius and free volume fitting equations utilizing different variable values over different T and λ ranges.

$\alpha_f = 0.000145/^{\circ}\mathrm{C}, f_o = 0.051$

$\mathrm{T_{ref}} = 343K, \lambda_{ref} = 1.24$

$T \le 70^o C$:

$$\log a_{TH} = \frac{\frac{1}{2.303}\alpha_f \Delta T + \frac{1}{2.303}(0.007)\Delta\lambda}{0.051^2 + 0.051\alpha_f \Delta T + 0.051(0.007)\Delta\lambda} + 0.0319\Delta T \qquad \textbf{[3.18]}$$

$T > 70^o C$:

$$\log a_{TH} = \frac{\frac{1}{2.303}\alpha_f \Delta T + \frac{1}{2.303}(0.007)\Delta\lambda}{0.051^2 + 0.051\alpha_f \Delta T + 0.051(0.007)\Delta\lambda} + 0.0993\Delta T \qquad \textbf{[3.19]}$$

The fractional free volume, f_o, was found to be 0.051, or 5.1% at the reference temperature of 70°C. If the glass transition is used as the reference temperature, then f_o should be approximately 2.5%. If however 70°C is the alpha transition of the material, and not the true glass transition, it is plausible that the fractional free volume would be greater than 2.5% but still maintain the same order of magnitude, as is the case here. It is plausible 70°C could be considered an α-transition but not the glass transition, based on data reported for Nafion® materials [68, 69]. For Nafion®, the α-transition at 90°C corresponds to the onset of a dynamic ionic network, while the true glass transition occurs at the β-transition of the material. Therefore, a similar behavior could be occurring in the PFCB/PVDF-HFP material, however identification of the true glass transition has not been performed. Over the entire moisture range, β_f was found to be $0.007/\lambda$ which is equivalent to 50% of the coefficient of hygral expansion of the material. When compared with the slope of the swelling efficiency of 1.26, this low β_f may not be well understood, however it is not clear why the efficiency of swelling would be greater than 1. One possibility is that the material does not undergo isotropic swelling, and therefore volumetric swelling would be inaccurate, resulting in the determined slope. Therefore, rather than try to match the possibly inaccurate slope value determined from the efficiency of swelling, β_f was determined based on the knowledge that water molecules take up volume, as well as water bridging effects as discussed previously. Therefore, this low value of β_f corresponds well with these expectations and is thusly believed to be of the appropriate order of magnitude for this material.

These values obtained from the hygrothermal shift factor best fit can also be compared with the constants obtained from the WLF fit performed on the approximate hygral shift factors.

The WLF fit resulted in a C_1 value of 8.58, and a C_2 value of 7.23 °C. Because the WLF equation comes directly from the Doolittle free volume fit, the constants are defined as follows:

$$C_1 = \frac{B}{2.303 f_o} \quad \textbf{[3.20]}$$

$$C_2 = \frac{f_o}{\alpha_f} \quad \textbf{[3.21]}$$

However, because the WLF fit was applied to approximate hygral shift factors where the X-abscissa is λ rather than temperature, C_2 should be defined as:

$$C_2 = \frac{f_o}{\beta_f} \quad \textbf{[3.22]}$$

If B is again set to 1 to reduce the number of fitting parameters, f_o can be calculated using the definition of C_1, resulting in a value of 0.505. This is consistent with the hygrothermal shift factor best fit where f_o was found to be 0.51. With the free volume calculated from C_1, β_f can now be calculated using the definition of C_2, resulting in a value of 0.700. This is again consistent with the value obtained with the hygrothermal shift factor best fit. Therefore it is believed the values obtained from fitting the hygrothermal shift factors are reasonable and capture the free volume behavior of this material due to the sorption of moisture.

Finally, the additional temperature dependence described by the Arrhenius term in the dual fit resulted in an E_a of 0.60 kJ/ K·mol below 70°C, and above 70°C of 0.19 kJ/ K·mol. Unlike the good agreement seen with the WLF approximate hygral shift factor fitting parameters, these activation energies are much smaller than anticipated, as the activation energies determined from the approximate thermal shift factors were 49 and 145 kJ/ K·mol respectively. However, it

is plausible that much of this behavior has been partitioned to the free volume behavior due to the fitting procedure, resulting in much lower activation energies [54]. Therefore, it is believed this two-equation (**Eqn [3.18]-** [3.19]) fit describes the material behavior well and may show some physical relevance.

3.4 Modeling Results and Discussion

3.4.1 Prony Fit

The time dependent modulus is typically described by a Prony series in constitutive modeling. Therefore, a Prony series was fit to the hygrothermal relaxation modulus master curve of PFCB/PVDF-HFP referenced to 70°C and 30% RH, as shown in **Figure 3.8,** to be used in the stress model described by **Eqn [3.11]**. Due to the large time scale the hygrothermal master curve covers, it was thought at least 28 Prony terms were necessary, allowing for two terms per decade. However, it was discovered that additional terms were needed to fully describe the transition region from 10^5-10^7 seconds, requiring eight Prony terms over these two decades, rather than four. Therefore, the final Prony fit has 33 terms including an E_∞ term, as shown in **Table 3.1**Error! Reference source not found.. Temperature and moisture dependence were incorporated into the stress model by utilizing the two-equatioin fit of the hygrothermal shift factors for the a_{TH} term, over the corresponding temperature and moisture conditions. Finally, the thermal and hygral expansion were incorporated for α and β to allow for calculation of the induced strain, and thus stress, due to hygrothermal cycling. It should be noted that a constant value for α was used during modeling, despite the moisture dependence shown above 50% RH. Due to the small magnitude of α, it was assumed the changes due to moisture content were minimal, and would result in negligible changes in the calculated stress.

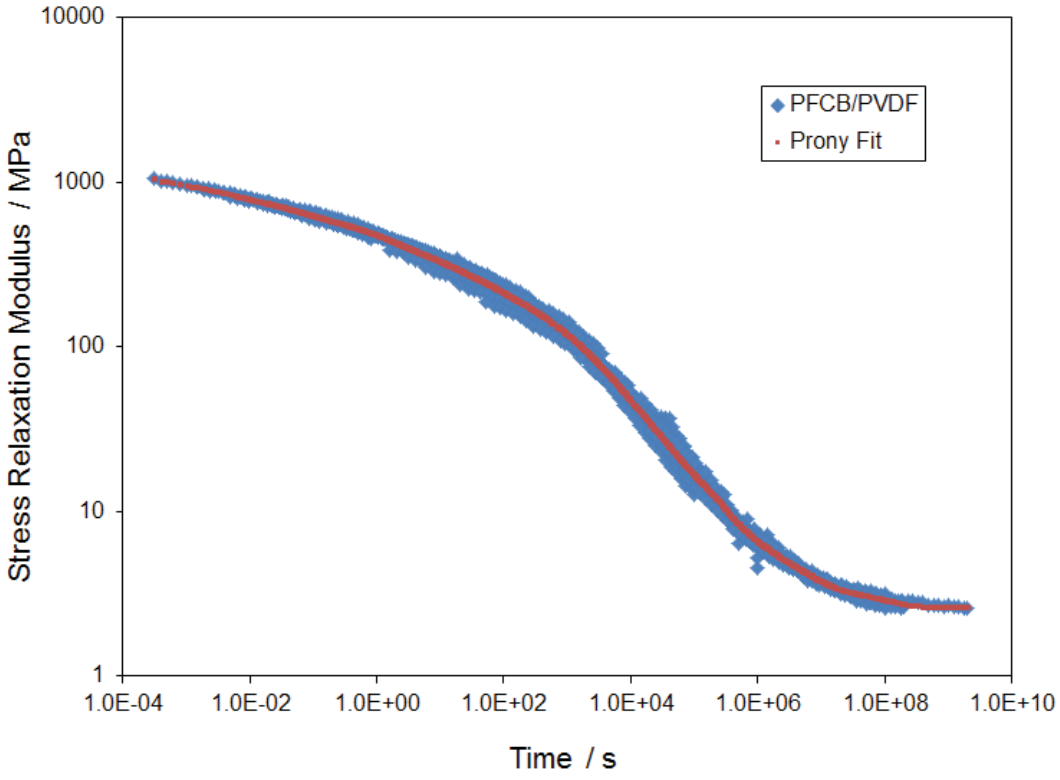

Figure 3.8. Prony series fit of PFCB/PVDF-HFP stress relaxation hygrothermal master curve.

Table 3.1. Prony series terms for PFCB/PVDF-HFP hygrothermal stress relaxation master curve.

τ	E’
0.00010	119.75
0.000316	163.37
0.0010	0.0493
0.00316	144.12
0.010	55.85
0.0316	90.13
0.10	92.76
0.316	40.93
1.0	107.41
3.16	68.18
10	70.44
31.6	57.82
100	59.21
316	42.1
1000	50.32
3160	45.25
10000	27.78
31600	19.48
100000	0.6673
177828	10.56
316000	1.317
562341	0.4051
1000000	2.70
1778279	0.29386
3162278	0.083798
5623413	1.67182
10000000	0.422956
31622777	0.102263
100000000	0.642588
316227766	0.0568843
1000000000	0.003114885
3162277660	0.0000351819
10000000000	0.0452862
E_∞	2.58

3.4.2 Model Validation

Both an analytical and numerical model were created using the model described by **Eqns [3.18]-** [3.19]. The analytical model was created using Excel, and the numerical model was written in Fortran so it could easily be interfaced with Simulia's Abaqus finite element modeling program. To ensure the models were working correctly before using either for stress predictions, a self-prediction of the hygrothermal master curve referenced to 70^{o}C and 30% RH was performed, with the analytical model shown as red dashes, and the numerical model as blue in **Figure 3.9**. Additional model validation was performed to observe if the model could correctly predict the approximate thermal master curves at 2, 10, 55, and 80% RH, as shown in black in **Figure 3.9**. Excellent agreement was noted for both models between the approximate thermal master curves and the predicted material behavior.

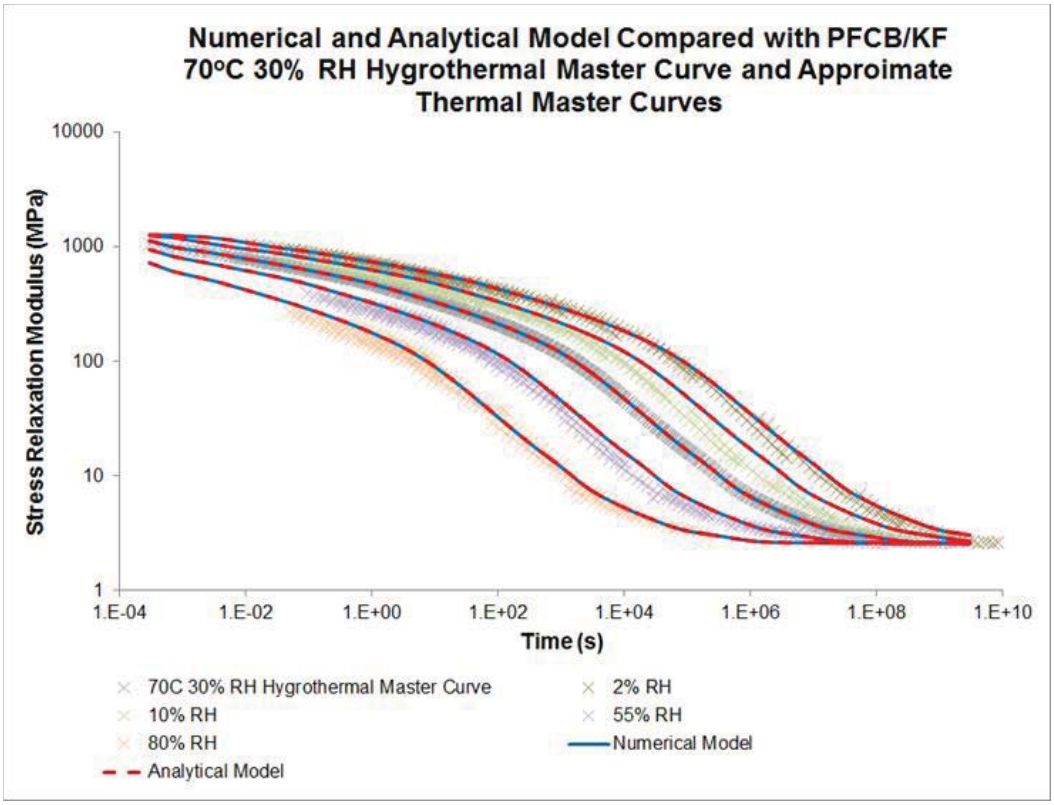

Figure 3.9. Model predictions of the 70°C 30% RH hygrothermal master curve and approximate thermal master curves referenced to 70°C.

3.4.3 Model Verification

Prior to using the models for stress predictions, model verification was performed by predicting strains induced by changes in the relative humidity. Strain data was taken using a TA Instruments DMA Q800 utilizing the creep mode, with a 9-mm wide sample, slit into three 3-mm sections, allowing for a stronger signal to noise ratio. The gage length was approximately 15 mm to maintain a 5:1 aspect ratio to approximate a uniaxial stress state. A small (3 mN) load was applied during testing to hold the sample taut without causing significant creep in the sample. This applied load was an order of magnitude larger than the lower force limits of the instrument, and therefore outside the noise range of the instrument. Four tests were completed, two at 80°C and two at 90°C. At each temperature two different humidity cycles were

performed. The first RH profile cycled from 80% RH to 0% RH four times, and the second RH profile cycled from 80% RH to 50% RH. For all tests the sample was initially equilibrated at 30% RH. The experimental data along with the model predictions is provided in **Figure 3.10**. As can be seen, the model predictz the tensile strains very well for the RH profiles at 80°C but under predicts the tensile strains at 90°C as well as the compressive strains for the 0-80% RH profiles at both temperatures. This under prediction of the tensile strain could be related to the applied load during testing. While the 3 mN applied load is not thought to cause significant creep, it does induce more creep at high moisture levels than smaller loads, as evidenced by **Figure 2.4**. Therefore, further verification testing should be completed with a lower applied creep load. This would ensure any differences at high RH levels are due to material properties rather than an applied stress that is not accounted for in modeling. The differences between the model and the compressive strain may be accounted for by considering that the relative humidity signal used for the λ profile in modeling is not a calibrated signal. TA Instruments states that this signal can be used to monitor the RH level, however the values may not be exact. In general, these values are very close to the expected numbers, however deviations at low RH levels are common, and as such the sensor may read a 0% RH, whereas the RH level has in fact not reached this dry state as of yet. In addition, in the model it was assumed that the sample instantaneously equilibrates with the surrounding atmosphere, and as such diffusion effects are not accounted for. As the material dries, it is likely it will continue to lose moisture over time, resulting in a continued increase in the compressive strains unlike the model which shows a flat line for the compressive strain at 0% RH.

A

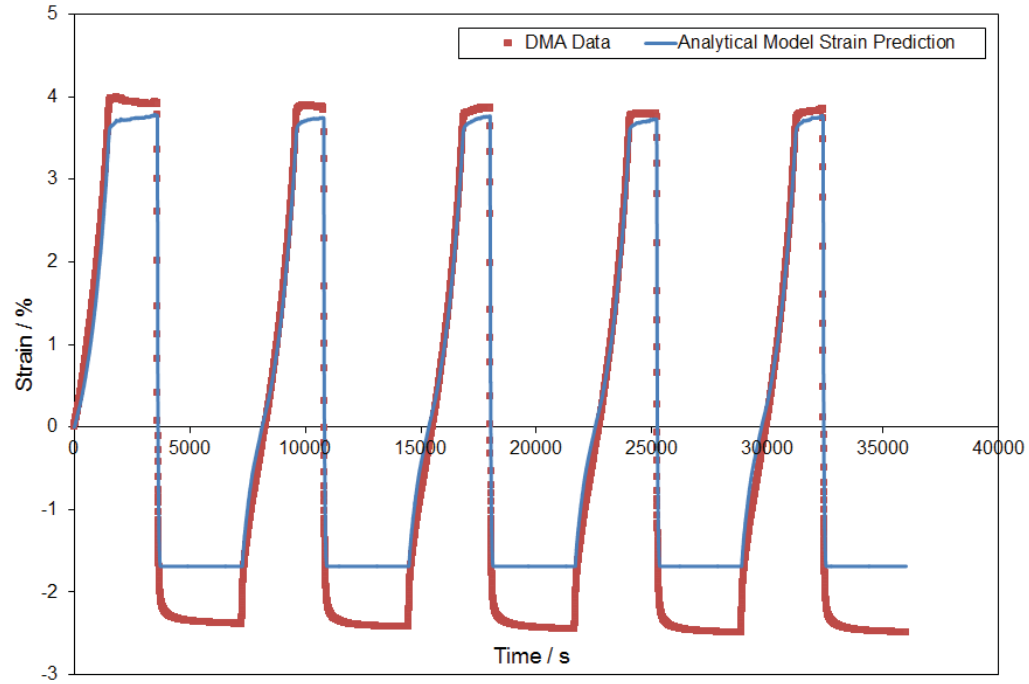
DMA Data
Analytical Model Strain Prediction
Strain / %
Time / s
5
4
3
2
1
0
-1
-2
-3
0
5000
10000
15000
20000
25000
30000
35000
40000

B

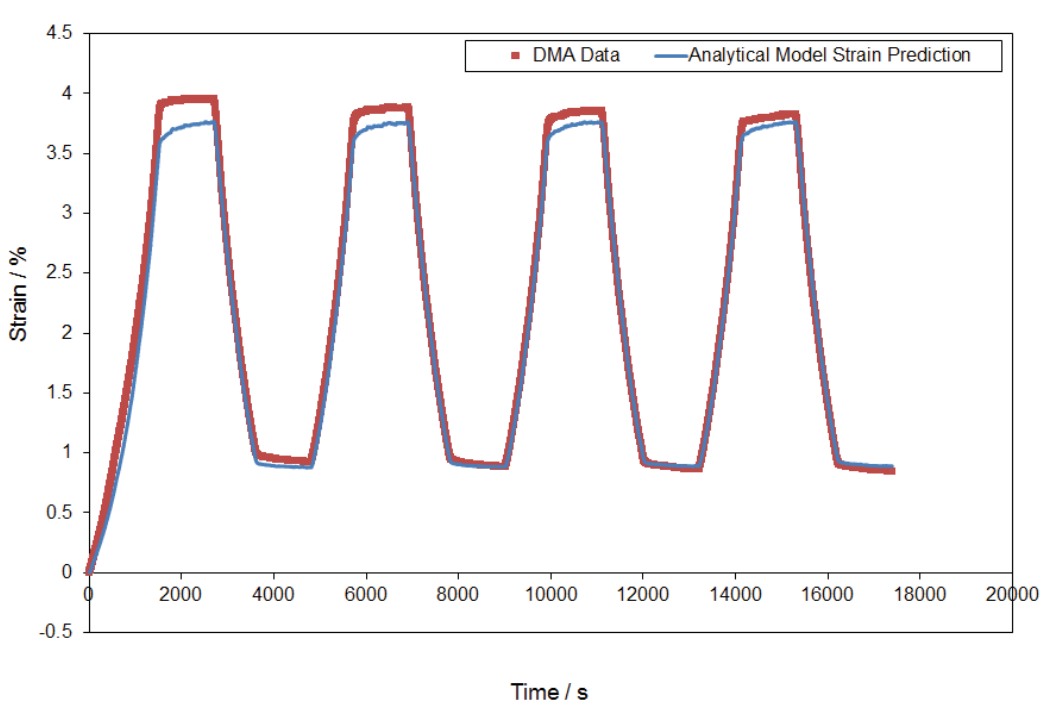
DMA Data
Analytical Model Strain Prediction
Strain / %
Time / s
4.5
4
3.5
3
2.5
2
1.5
1
0.5
0
-0.5
0
2000
4000
6000
8000
10000
12000
14000
16000
18000
20000

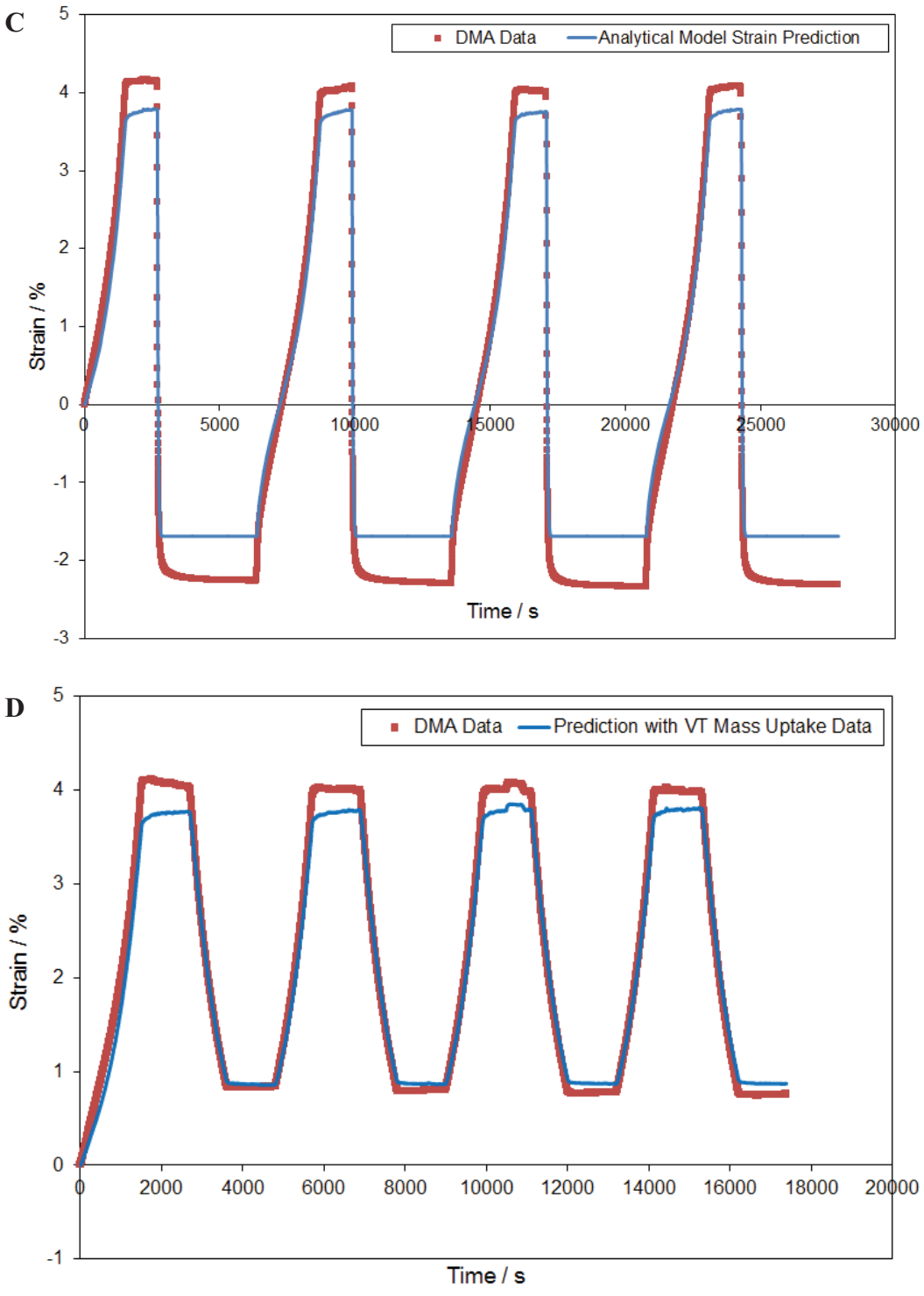

Figure 3.10. Analytical model strain predictions compared with strain data collected with a DMA Q800 for 4 different RH cycles, **(A)** 80°C 0-90% RH, **(B)** 80°C 50-90% RH, **(C)** 90°C 0-90% RH, **(D)** 90°C 50-90% RH.

3.4.4 RH Cycle Stress Predictions

Based on the good agreement between the models and the strain data, it is believed both models would provide a good representation of material behavior and thusly were used to predict the stresses incurred in an RH cycle at 80°C and compared with PTFE reinforced PFSA Gore™ Gore-Select® 57 over the same RH cycle (**Figure 3.11**) [10].

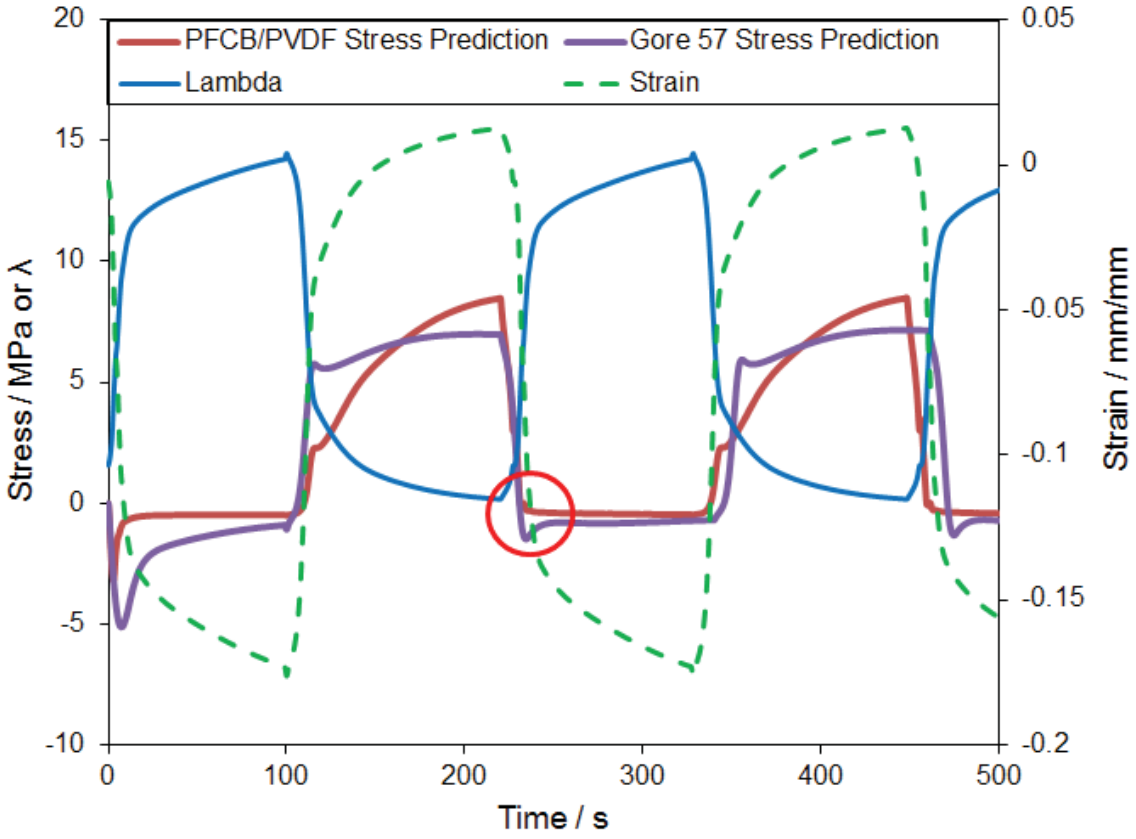

Figure 3.11. Membrane stress predictions of PFCB/PVDF-HFP and Gore 57 during an RH cycle at 80°C.

The predicted stresses of the PFCB/PVDF-HFP reach a maximum of approximately 7.3 MPa, whereas PTFE reinforced PFSA Gore™ Gore-Select® 57 reaches a maximum of

approximately 7 MPa. The slightly higher incurred stresses in PFCB/PVDF-HFP are likely due to the higher material stiffness as compared with PTFE reinforced PFSA Gore™ Gore-Select® 57. Additionally, it should be noted that the magnitude is likely over-predicted because this is a linear viscoelastic prediction, which does not account for nonlinear viscoelastic behavior or plasticity.

Furthermore, the compressive stress region has been highlighted in **Figure 3.11** to emphasize the nonexistence of a compressive stress during RH cycling in the PFCB/PVDF-HFP. In PFSA materials this compressive stress leads to ratcheting due to the incomplete rearrangement of polymer chains to relax the compressive stress, creating increased tensile stresses with time [13, 70, 71]. However, the increased moisture dependence of PFCB/PVDF-HFP results in a more than four times softer material at high moisture contents, as compared with PFSA materials (100% RH in this cycle). This allows the PFCB/PVDF-HFP to incur lower compressive stresses due to the lower modulus, and possibly relax these stresses completely due to viscoelastic rearrangement over the 2 minute time step. If this time step is shortened to 10 s, racheting is observed in the PFCB/PVDF-HFP material, although to a lesser degree than that of PFSA materials. If the time step is increased to 75 s or more, the racheting of PFCB/PVDF-HFP materials is removed, whereas time steps at least 5 min long are needed for the PFSA material. This implies the increased chain mobility of the PFCB/PVDF-HFP at high water contents as compared with PFSA materials allows for fast and complete relaxation of the imposed compressive stress. As ratcheting effects increase the tensile stresses in PFSA materials, it is likely these stresses will eventually exceed the ultimate tensile strength of the material. Therefore, the absence of ratcheting behavior in PFCB/PVDF-HFP could possibly explain the

similar lifetimes of PFCB/PVDF-HFP and PFSA materials, despite the increased stiffness of PFCB/PVDF-HFP at lower moisture contents.

Two alternative explanations for the similar lifetimes of PFCB/PVDF-HFP with PFSA materials again relate to the increased moisture dependence of the PFCB/PVDF-HFP material. It is possible that the PFCB/PVDF-HFP material modulus stiffens at a slower rate than the rate of stress increase as the moisture level is decreased. This would allow for viscoelastic rearrangement to relieve the tensile stress as it is building, which would again result in no racheting of the tensile stresses. Finally it is possible the PFCB/PVDF-HFP does not have a high enough stiffness at high moisture contents to allow buckling to occur. If buckling is reduced or removed, this would reduce the number of cracks formed in the catalyst layer. These cracks act as stress concentration points in the membrane, and ultimately lead to the formation of pinholes. A reduction in the number of stress concentrations could allow the PFCB/PVDF-HFP material to survive longer in an operating fuel cell, resulting in the similar lifetimes with PFSA materials. In reality, it is likely a combination of all three mechanisms is occurring in the PFCB/PVDF-HFP membrane material, showing how the increased moisture dependence of the material could result in similar lifetimes as PFSA materials.

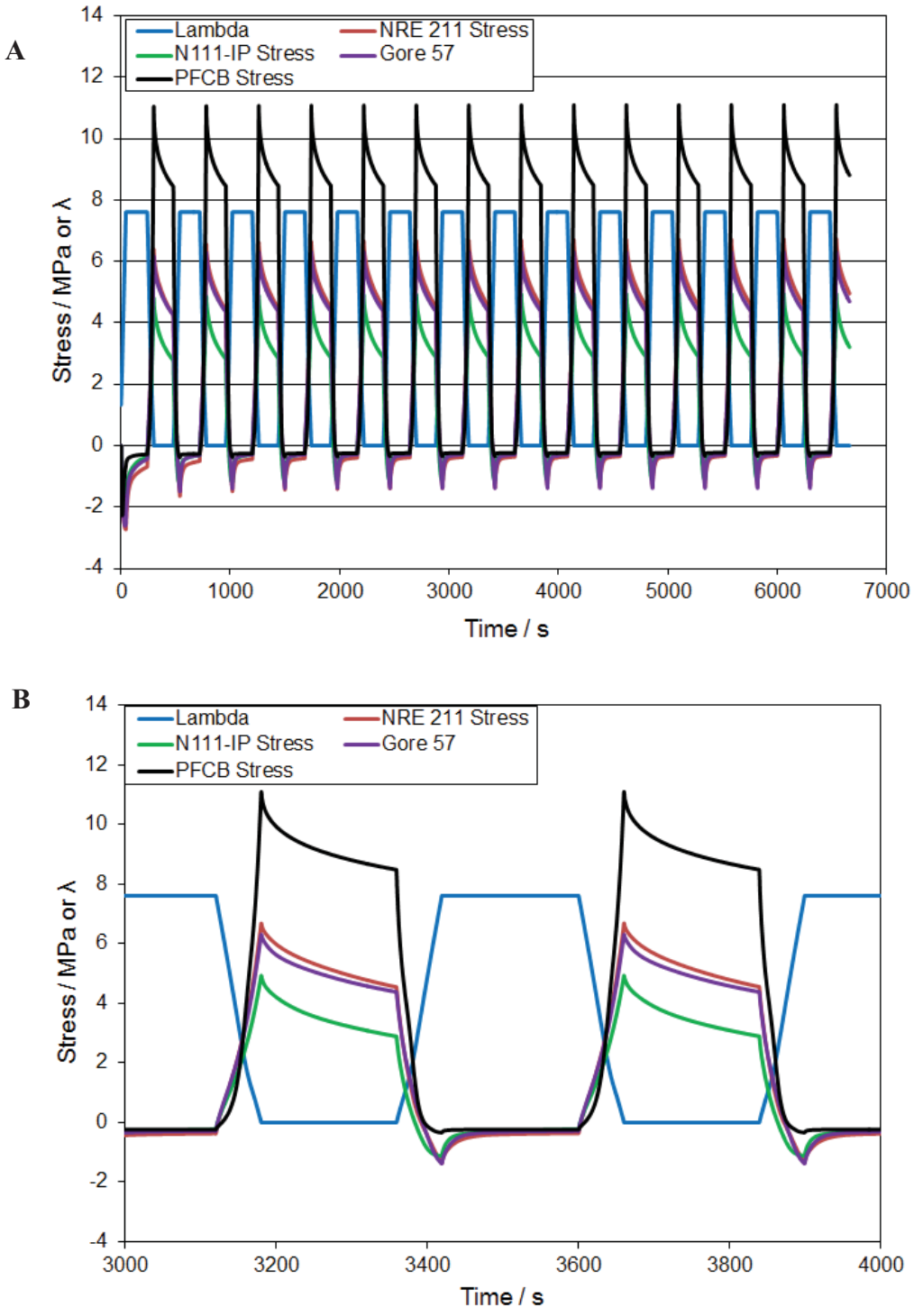

Figure 3.12. Comparison of PFCB/PVDF-HFP and PFSA membrane stresses during an RH cycle at 80°C **(A)** over a large time scale, and **(B)** zoomed in over two full RH cycles.

Further modeling was completed to compare the predicted stresses of NRE 211, N111-IP, PTFE reinforced PFSA Gore™ Primea 57, and PFCB/PVDF-HFP in a different RH cycle at 80^{o}C than shown above in **Figure 3.11**. As shown in **Figure 3.12**, in this RH cycle the PFCB/PVDF-HFP reaches a maximum stress of approximately 13.1 MPa, whereas NRE 211 and PTFE reinforced PFSA Gore™ Primea 57 reach a maximum of about 6.4 MPa, while N111-IP reaches a maximum of about 4.8 MPa. In addition, the compressive stresses in the PFSA membranes are again observed resulting in a ratcheting effect in the PFSA tensile stresses, but the compressive stresses are negligible for the PFCB/PVDF-HFP, and again no ratcheting is observed. Finally, tensile stresses appear to relax similarly in both PFCB/PVDF-HFP and NRE 211. The PFCB/PVDF-HFP relaxes from about 13.1 to 9.5 MPa, or approximately 27%, while the NRE 211 relaxes from about 6.4 to 4.2 MPa, approximately 32%, over the same time period. Therefore, the increased moisture dependence of the PFCB/PVDF-HFP as compared with PFSA materials does not appear to relax the high tensile stresses more quickly. However, as mentioned previously, the increased moisture dependence of PFCB/PVDF-HFP results in creating a softer material than PFSAs at high moisture contents. This allows the PFCB/PVDF-HFP to incur lower compressive stresses due to the lower modulus, and relax these stresses more quickly than PFSA materials, as shown, and again could help explain the similar lifetimes observed between PFSA and PFCB/PVDF-HFP in RH cycling, despite the increased stiffness of unhydrated PFCB/PVDF-HFP.

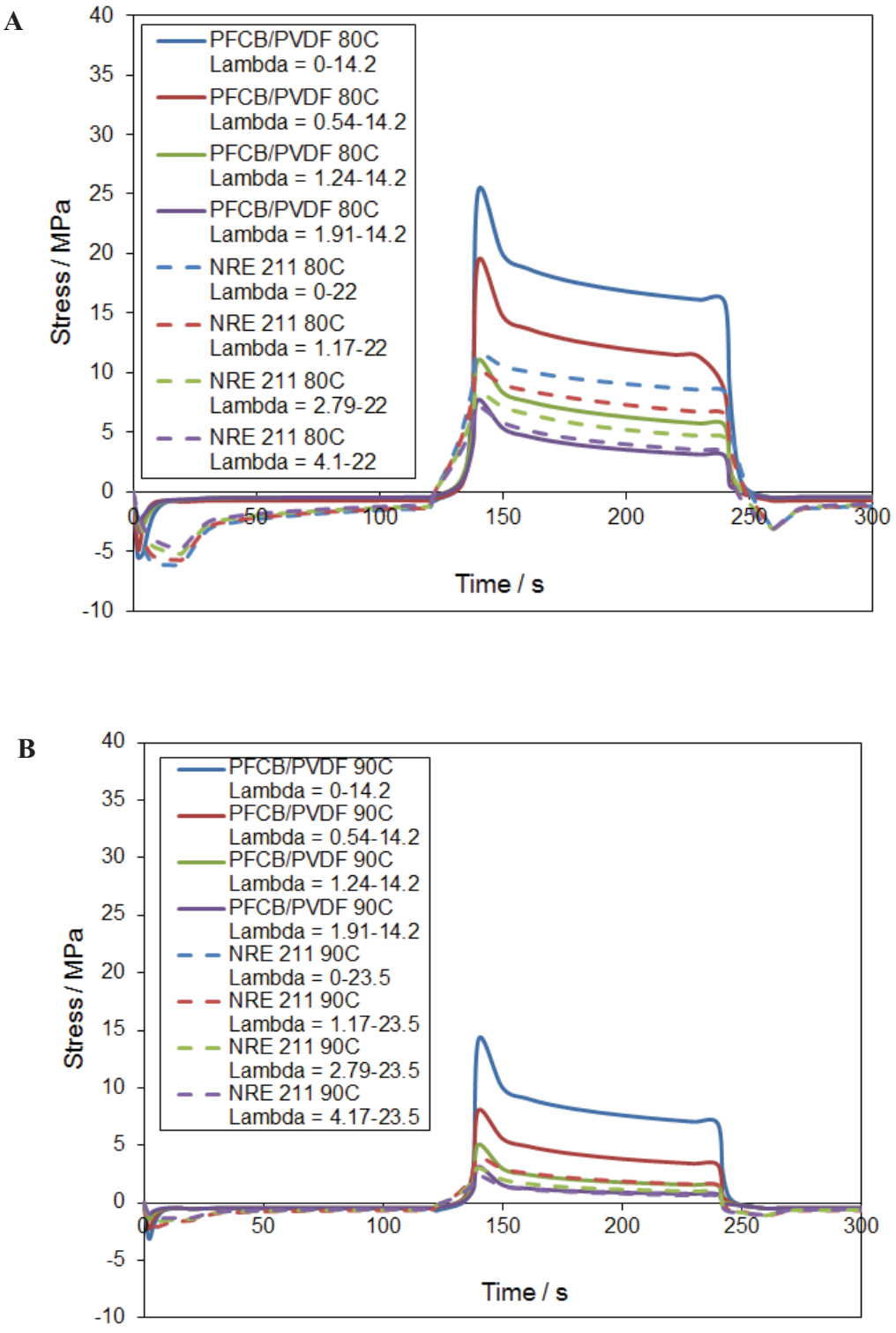

Figure 3.13. PFCB/PVDF-HFP and NRE 211 RH cycle stress predictions at **(A)** 80°C and **(B)** 90°C.

A final set of stress predictions was completed for both PFCB/PVDF-HFP and NRE 211 to examine how the induced hygrothermal stresses change dependent on the size of the RH swing used during RH cycling. Four different RH cycles at both 80 and 90°C were examined, 0% RH – immersed, 10% RH – immersed, 30% RH – immersed, and 50% RH – immersed. As shown in **Figure 3.13**A, the peak tensile stress in PFCB/PVDF-HFP is reduced by 60% when the lower RH level is increased from dry to 50%, whereas in NRE 211 it is only reduced by 39%. Both materials show an ~10% increase in the reduction of the peak stress when the temperature is increased to 90°C (**Figure 3.13**B), resulting in 69% and 51% reductions respectively. Therefore, increasing the temperature and decreasing the size of the RH swing will decrease the maximum tensile stress greatly for both materials, although to a greater degree in the PFCB/PVDF-HFP. This decrease in the maximum peak stress is in good agreement with modeling performed by Lai et al. on NRE 211, which also agrees well with experimental RH cycling data collected by General Motors [13]. It is believed the greater decrease in the maximum tensile stress of the PFCB/PVDF-HFP is due to the increased moisture dependence of the material modulus and shift factors. Thus the increased moisture dependence of PFCB/PVDF-HFP could decrease the maximum tensile stress observed during RH cycling when the RH swing is reduced. If it were possible during fuel cell operation to reduce the RH swing through better system control, it is likely the mechanical lifetime of the membrane would be increased, allowing for long term cost reduction as well as meeting or even possibly exceeding DOE requirements of a 5000 hour lifetime.

3.4.5 Stress Lifetime Predictions

Researchers at General Motors completed RH cycle testing on PFCB/PVDF-HFP at 80 and 88°C cycling from 10-150% RH, 30-150% RH, or 50-150% RH every two minutes as shown

in **Figure 3.14**. It should be noted that 150% RH refers to 1.5 times the amount of water for saturation of air at a given temperature. This was achieved by supplying supersaturated water at the inlet using humidifiers set for a 90°C dew point in the 80°C test. These RH cycles are similar to those previously discussed in **Section 3.4.4**, and the specific cycles used during testing are provided in **Figure 3.15.** It should be noted that these cycles differ from the idealized trapezoidal cycles employed previously, as these correspond to the measured water content of the membranes during RH cycling. Membrane failure was defined as when the crossover leak rate exceeded 10 sccm, by measuring the air flow rate across a membrane when 21 kPa of pressure was applied to one side [10]. Lifetime is then defined as the number of RH cycles required to exceed the 10 sccm crossover leak rate. To ensure failure occurred solely due to mechanical degradation, these tests were performed without hydrogen or current draw, eliminating chemical reactions and thus chemical degradation. The longest measured lifetimes occured for the 50-150% RH cycle, consistent with the lowest occurring tensile stress. Because the RH cycling test is performed on a biaxially constrained membrane, the predicted tensile stress values in **Figure 3.15** are given as biaxial stresses. This was accomplished based upon the relationship given in **[3.23]**:

$$\sigma_{Biaxial} = \frac{\sigma_{Uniaxial}}{1-\nu} \qquad \textbf{[3.23]}$$

where ν is the poisson's ratio, which was assumed to be 0.5 in these calculations.

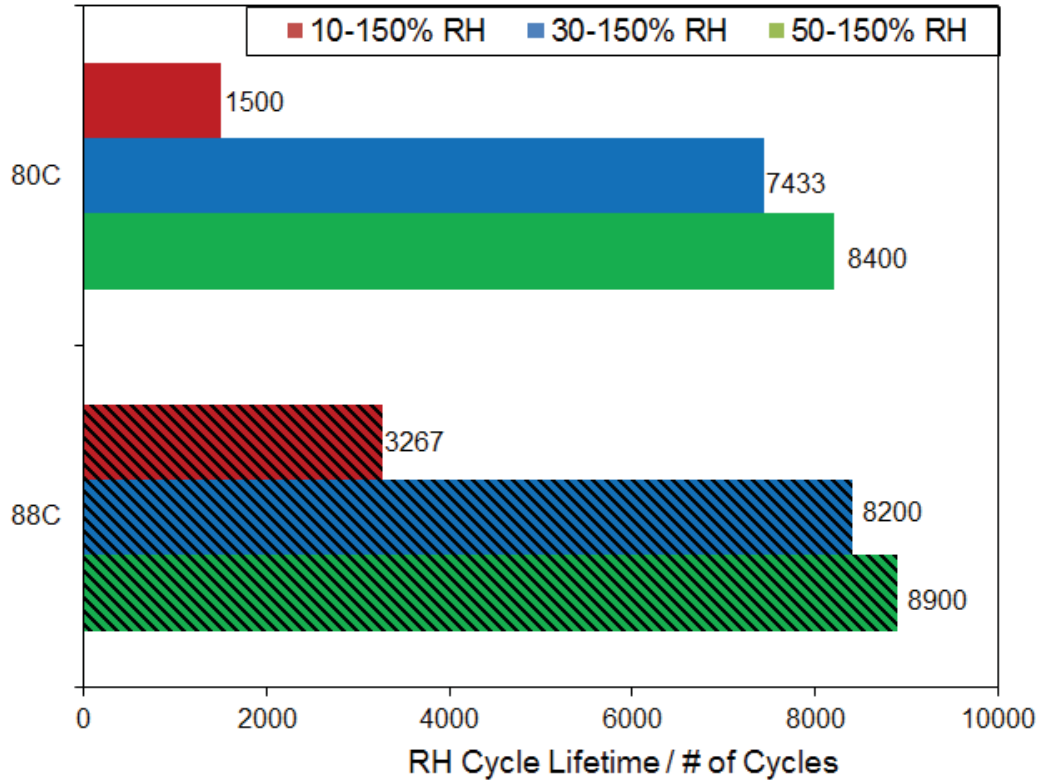

Figure 3.14. RH cycle lifetimes of PFCB/PVDF-HFP at 80 and 88°C.

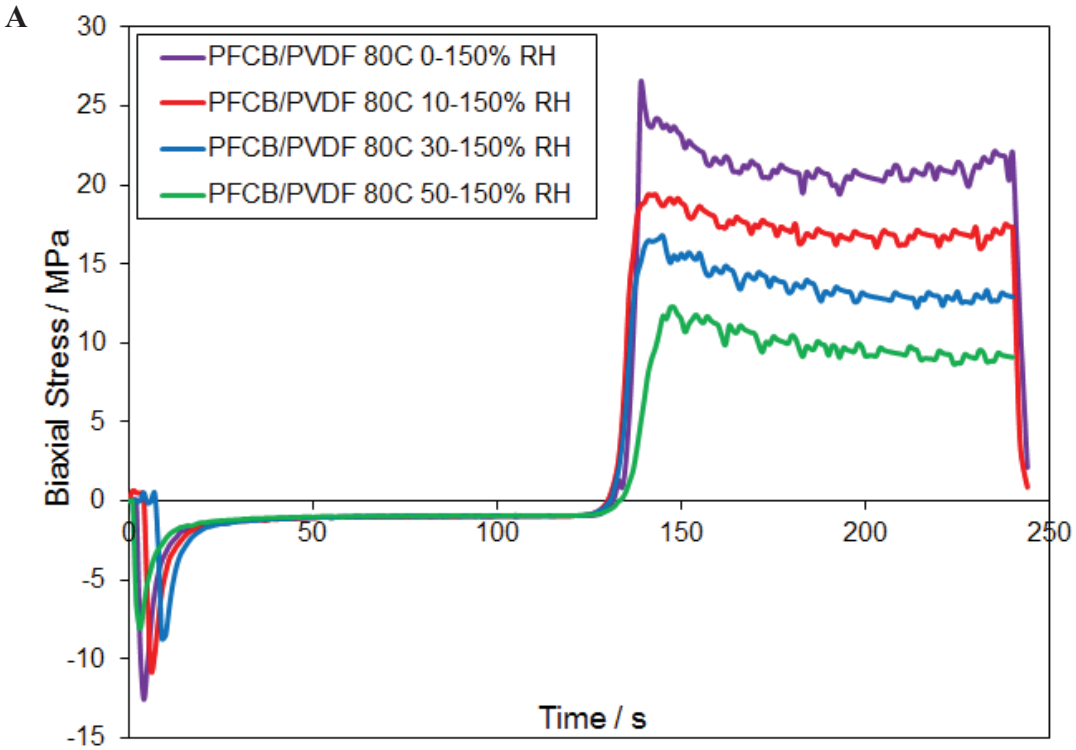

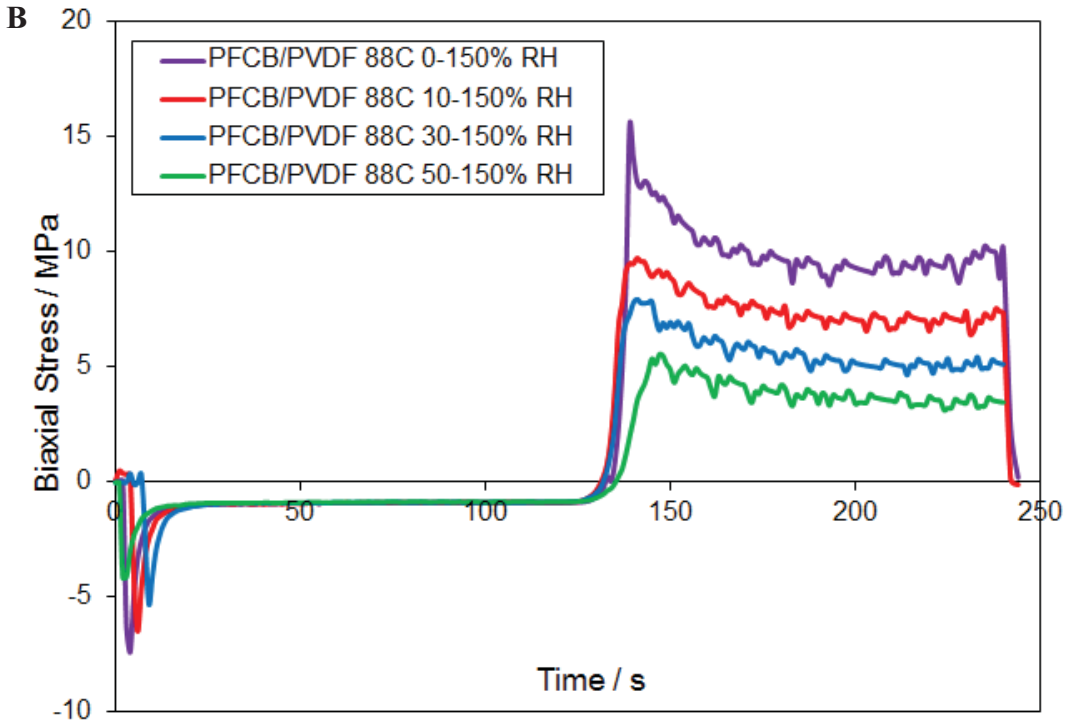

Figure 3.15. Predicted stress cycle profiles based on λ values measured during RH cycle testing, and corresponding to RH cycle lifetimes presented in **Figure 3.14** for **(A)** 80°C and **(B)** 88°C.

To examine the lifetime of a membrane at a given biaxial stress level, a biaxial stress lifetime plot was created. The stress was taken as the highest biaxial tensile stress the material sees during RH cycling, for example, ~5.5 MPa for a sample cycled from 50-150% RH at 88°C. The lifetime was taken as the number of cycles measured during RH cycling, as shown in **Figure 3.16**, multiplied by 120 seconds, the time the membrane is under a tensile load. Only the tensile loading is used for lifetime predictions because the compressive stresses are negligible in PFCB/PVDF-HFP membranes, and it is thusly believed it is the tensile stresses that lead to membrane failure. In addition, to create a stress lifetime master curve, the data points are shifted hygrothermally, as shown in **Figure 3.17**, using the shift factors provided in **Figure 3.7** and the corresponding fits provided by **Eqns [3.18]** and **[3.19**], and referenced to 80°C, 10% RH. The

RH levels chosen for shifting each data point correspond to the low humidity level utilized during RH cycling, thus either 10, 30 or 50% RH, where the maximum tensile stress occurs. This method of stress life analysis was previously employed for Gore-Select® 57 membranes with great success [10], and it is thusly believed this method is appropriate for other fuel cell membranes, including the PFCB/PVDF-HFP membrane studied here. The resulting stress lifetime master curve for PFCB/PVDF-HFP is provided in **Figure 3.18**. It is encouraging that the shift factors determined for stress relaxation data appear to shift the stress lifetime data well, implying the validity of TTMSP. Finally, the DOE requirement of a 5000 hr lifetime corresponds to 1.8 x 10^7 seconds. Therefore, if the fuel cell is operated at 80°C and the maximum biaxial tensile stresses are kept below ~10 MPa by decreasing the size of the RH swing, the PFCB/PVDF-HFP membrane is expected to not only meet, but exceed the DOE requirements. These results are consistent with the conclusions determined from the stress life analysis performed on Gore-Select® 57 membranes, and it is thus likely that decreasing the size of the RH swing would improve the lifetime of multiple fuel cell membranes.

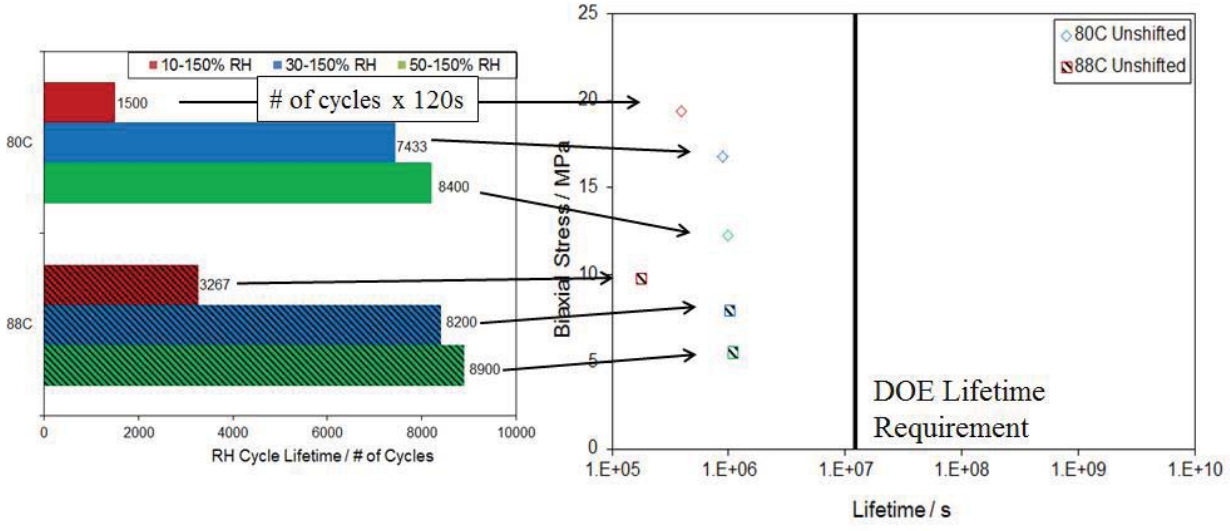

Figure 3.16. Biaxial stress lifetime values, based upon the number of cycles to failure for each RH profile.

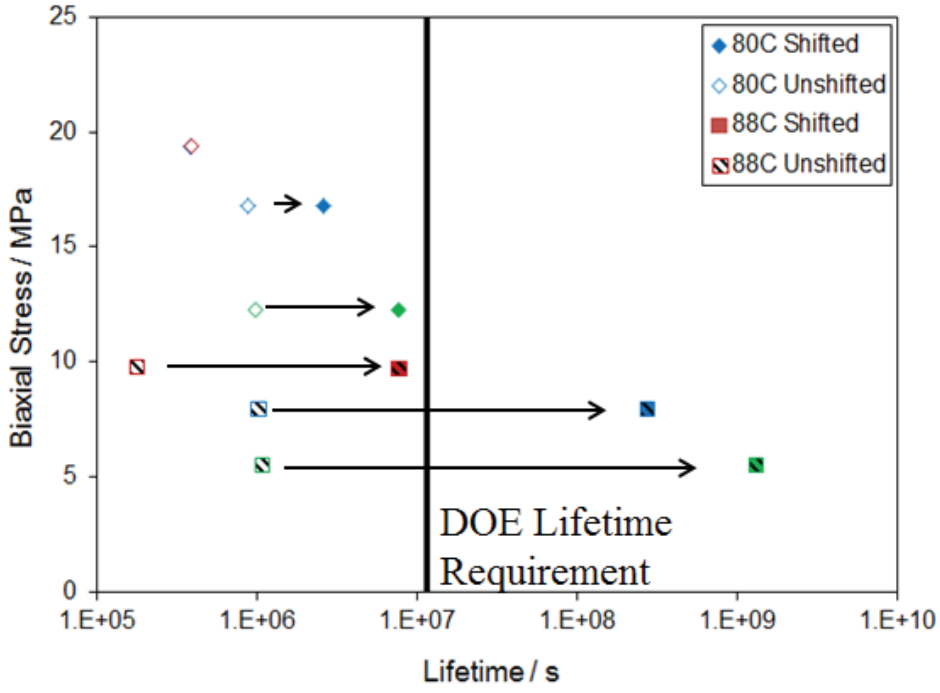

Figure 3.17. Biaxial stress lifetime predictions, displaying the use of hygrothermal shift factors to create a stress lifetime master curve, referenced to 80°C and 10% RH.

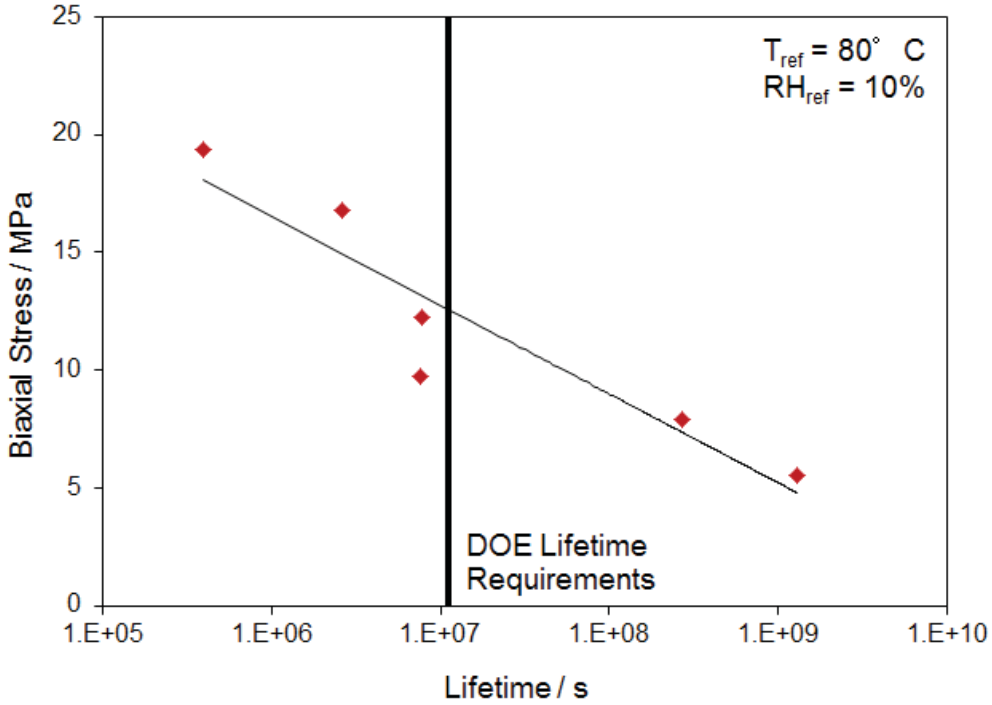

Figure 3.18. Biaxial stress lifetime predictions of PFCB/PVDF-HFP based on RH cycling failure times and maximum tensile stresses.

3.5 Conclusions

Analytical and numerical one-dimensional linear viscoelastic stress models were successfully created to describe the material behavior of PFCB/PVDF-HFP membranes. Time dependence was incorporated by utilizing a Prony series to describe the hygrothermal stress relaxation master curve. In addition, temperature and moisture dependence were incorporated by fitting the hygrothermal shift factors with a combined Arrhenius and free volume fit. The stress model was validated by predicting approximate thermal master curves, and verified by predicting the correct strain values over various RH cycles.

For a transient drying cycle the increased moisture dependence of the PFCB/PVDF-HFP modulus is easily noted when compared with PFSA materials. While the PFSA stress increases about 1 MPa over the drying cycle, the PFCB/PVDF-HFP stress increases about 6 MPa. In addition, while the maximum tensile stress differs between PFSA and PFCB/PVDF-HFP materials depending on the RH cycle employed, the PFCB/PVDF-HFP always shows a negligible compressive stress. Therefore the PFCB/PVDF-HFP membrane does not undergo ratcheting of the tensile stresses, allowing for longer material lifetimes despite the higher stiffness. In addition, if the low RH level during cycling is increased from 0, to 30 or 50% RH, the maximum tensile stress in PFCB/PVDF-HFP is significantly decreased, resulting in similar stresses in PFCB/PVDF-HFP materials and PFSA materials. Finally, this decrease in the maximum tensile stress results in an increase in the lifetime of the membrane. Therefore, for

fuel cells operated at 80°C with reduced RH swings, PFCB/PVDF-HFP membranes exceed the DOE requirements, making this a viable membrane for automotive applications.

3.6 References

[1] O.o.B.E.S. US Department of Energy, in: U. DOE (Ed.), Washington DC, 2004.
[2] W. Liu, K. Ruth, R. Greg, Journal of New Materials for Electrochemical Systems, 4 (2001) 227-231.
[3] K. Reifsnider, X. Huang, Fuel Cell Technology, (2006) 53-68.
[4] R. Borup, J. Meyers, B. Pivovar, Y.S. Kim, R. Mukundan, N. Garland, D. Myers, M. Wilson, F. Garzon, D. Wood, P. Zelenay, K. More, K. Stroh, T. Zawodzinski, J. Boncella, J.E. McGrath, M. Inaba, K. Miyatake, M. Hori, K. Ota, Z. Ogumi, S. Miyata, A. Nishikata, Z. Siroma, Y. Uchimoto, K. Yasuda, K.-i. Kimijima, N. Iwashita, Chemical Reviews, 107 (2007) 3904-3951.
[5] A. Collier, H. Wang, X.Z. Yuan, J. Zhang, D. Wilkinson, P., International Journal of Hydrogen Energy, 31 (2006) 1838-1854.
[6] F.D. Coms, H. Liu, J.E. Owejan, ECS Transactions, 16 (2008) 1735-1747.
[7] P. Trogadas, J. Parrondo, V. Ramani, ECS Transactions, 16 (2008) 1725-1733.
[8] R. O'Hayre, S.-W. Cha, W. Colella, F.B. Prinz, Fuel Cell Fundamentals, 2nd ed., Wiley, New York, NY, 2009.
[9] Y. Li, D.A. Dillard, Y.-H. Lai, S. Case, W., M.W. Ellis, M.K. Budinski, C.S. Gittleman, Journal of the Electrochemical Society, 159 (2012) B173-B184.
[10] Y.-H. Lai, D.A. Dillard, Mechanical Durability Characterization and Modeling of Ionomeric Membranes, in: W. Vielstich, H. Yokokawa, H. Gasteiger, A. (Eds.) Handbook of Fuel Cells - Fundamentals, Technology and Applications, John Wiley & Sons, New York, 2009.
[11] W.K. Liu, S.J.C. Cleghorn, B.E. Delaney, M. Crum, Chemical and Mechanical Membrane Degradation, in: W. Vielstich, H. Yokokawa, H. Gasteiger, A. (Eds.) Handbook of Fuel Cells - Fundamentals, Technology and Applications, John Wiley & Sons Ltd., New York, 2009, pp. 385-402.
[12] C.S. Gittleman, Y.-H. Lai, C. Lewis, D.P. Miller, in: AIChE, Cincinnati, OH, 2005.
[13] Y.-H. Lai, C.K. Mittelsteadt, C.S. Gittleman, Journal of Fuel Cell Science and Technology, 6 (2009) 021002/021001-021002/021013.
[14] Y.-H. Lai, C.K. Mittelsteadt, C.S. Gittleman, D.A. Dillard, in: Third International Conference on Fuel Cell Science, Engineering and Technology, Ypsilanti, Michigan, 2005.
[15] V. Stanic, in: 4th International Symposium on Proton Conducting Membrane Fuel Cells, 2004.
[16] A.Z. Weber, J. Newman, AIChE Journal, 50 (2004) 3215-3226.
[17] D. Liu, S. Case, Journal of Power Sources, 162 (2006) 521-531.
[18] X. Huang, R. Solasi, Y. Zou, M. Feshler, K. Reifsnider, D. Condit, S. Burlatsky, T. Medden, Journal of Polymer Science, Part B: Polymer Physics, 44 (2006) 2346-2357.
[19] Y. Tang, M.H. Sanatare, A.M. Karlsson, in: The 3rd International Conference on Fuel Cell Science, Engineering, and Technology, Ypsilanti, MI, 2005.
[20] Y. Tang, M.H. Santare, A.M. Karlsson, S. Cleghorn, W.B. Johnson, Journal of Fuel Cell Science and Technology, 3 (2006) 119-124.
[21] A. Kusoglu, A. Karlsson, M., M. Sanatare, H., S. Cleghorn, W. Johnson, B., Journal of Power Sources, 161 (2006) 987-996.

[22] A. Kusoglu, A. Karlsson, M., M. Santare, H., S. Cleghorn, W. Johnson, B., Journal of Power Sources, 170 (2007) 345-358.
[23] A. Kusoglu, M.H. Santare, A.M. Karlsson, S. Cleghorn, W.B. Johnson, Journal of the Electrochemical Society, 157 (2010) B705-B713.
[24] A. Kusoglu, Y. Tang, M.H. Santare, A.M. Karlsson, S. Cleghorn, W.B. Johnson, Journal of Fuel Cell Science and Technology, 6 (2009) 011012-011011-011012-011018.
[25] Y. Tang, A. Kusoglu, A.M. Karlsson, M.H. Santare, S. Cleghorn, W.B. Johnson, Journal of Power Sources, 175 (2008) 817-825.
[26] D. Bograchev, M. Gueguen, J.-C. Grandidier, S. Martemianov, International Journal of Hydrogen Energy, 22 (2008) 5703-5717.
[27] D. Bograchev, M. Gueguen, J.-C. Grandidier, S. Martemianov, Journal of Power Sources, 180 (2008) 393-401.
[28] S. Martemianov, D. Bograchev, J.-C. Grandidier, J.-J. Kadjo, International Journal of Energy Research, 34 (2010) 635-642.
[29] S. Martemianov, M. Gueguen, J.-C. Grandidier, D. Bograchev, Journal of Applied Fluid Mechanics, 2 (2009) 49-54.
[30] M.A.R.S. Al-Baghdadi, H.A.K.S. Al-Janabi, Energy & Fuels, 21 (2007) 2258-2267.
[31] M.A.R.S. Al-Baghdadi, H.A.K.S. Al-Janabi, International Journal of Hydrogen Energy, 32 (2007) 4510-4522.
[32] M.F. Serincan, U. Pasaogullari, Journal of Power Sources, 196 (2011) 1303-1313.
[33] A. Kusoglu, Y. Tang, M. Lugo, A. Karlsson, M., M. Santare, H., S. Cleghorn, W. Johnson, B., Journal of Power Sources, 195 (2010) 483-492.
[34] N.S. Khattra, A.M. Karlsson, M.H. Santare, P. Walsh, C.F. Busby, Journal of Power Sources, 214 (2012) 365-376.
[35] S.T. Iacono, S.M. Budy, J. Jin, D. Smith, Jr, Journal of Polymer Science Part A: Polymer Chemistry, 45 (2007) 5705-5721.
[36] S.T. Iacono, D. Ewald, A. Sankhe, A. Rettenbacher, D.W. Smith, Jr, High Performance polymers, 19 (2007) 581-591.
[37] B.-J. Chang, D.-J. Kim, J.-H. Kim, S.-B. Lee, H.-J. Joo, Journal of Membrane Science, 325 (2008) 989-996.
[38] DuPont, in, 2009, pp. 4.
[39] D.-J. Kim, B.-J. Chang, J.-H. Kim, S.-B. Lee, H.-J. Joo, Journal of Membrane Science, 325 (2008) 217-222.
[40] S.S. Mao, K.A. Lewinski, D.A. Ylitalo, in: U.S.P. Office (Ed.), 3M Innovative Properties Company, United States, 2003.
[41] D.A. Babb, B.R. Ezzell, K.S. Clement, W.F. Richey, A.P. Kennedy, Journal of Polymer Science Part A: Polymer Chemistry, 31 (1993) 3465-3477.
[42] A.P. Kennedy, L.D. Bratton, Z. Jezic, R.E. Lane, D.J. Perettie, W.F. Richey, D.A. Babb, K.S. Clement, in: U.S.P. Office (Ed.), The Dow Chemical Company, United States, 1995.
[43] H.-C. Liou, P.S. Ho, A. McKerrow, Journal of Polymer Science, Part B: Polymer Physics, 36 (1998) 1383-1392.
[44] N. Gourdoupi, J.K. Kallitsis, S. Neophytides, Journal of Power Sources, 195 (2010) 170-174.
[45] J. Kerres, W. Cui, R. Disson, W. Neubrand, Journal of Membrane Science, 139 (1998) 211-225.

[46] M. Lavorgna, G. Mensitieri, G. Scherillo, M.T. Shaw, S. Swier, R.A. Weiss, Journal of Polymer Science, Part B: Polymer Physics, 45 (2007) 395-404.
[47] L.M. Robeson, Polymer Blends: A Comprehensive Review, Hanser Gardner Publications, Cincinatti, OH, 2007.
[48] L.A. Utracki, Polymer Blends Handbook, Kluwer Academic Publishers, 2002.
[49] T. Zhang, W. He, J. Goldbach, D. Mountz, J. Yi, Journal of Power Sources, 196 (2011) 1687.
[50] C.F. Popelar, in, The University of Texas at Austin, Austin, TX, 1997.
[51] O.C. Zienkiewicz, M. Watson, I.P. King, International Journal of Mechanical Sciences, 10 (1968) 807-827.
[52] R. Solasi, Y. Zou, X. Huang, K. Reifsnider, D. Condit, Journal of Power Sources, 167 (2007) 366-377.
[53] K.A. Patankar, D.A. Dillard, S.W. Case, M.W. Ellis, Y.-H. Lai, M.K. Budinski, C.S. Gittleman, Fuel Cells, (Accepted).
[54] J.D. Ferry, Viscoelastic Properties of Polymers, 3 ed., John Wiley and Sons, New York, 1980.
[55] I.M. Ward, D.W. Hadley, An Introduction to the Mechanical Properties of Solid Polymers, John Wiley & Sons, West Sussex, England, 1993.
[56] A.K. Doolittle, Journal of Applied Physics, 22 (1951) 1471-1475.
[57] F. Bauer, S. Denneler, M. Willert-Porada, Journal of Polymer Science, Part B: Polymer Physics, 43 (2005) 786-795.
[58] M.B. Satterfield, J.B. Benziger, Journal of Polymer Science, Part B: Polymer Physics, 47 (2008) 11-24.
[59] T. Zawodzinski, A., Jr., C. Derouin, S. Radzinski, R. Sherman, J., V. Smith, T., T. Springer, E., S. Gottesfeld, Journal of the Electrochemical Society, 140 (1993) 1041-1047.
[60] G.M. Divoux, K.A. Finlay, J.K. Park, J.-M. Song, B. Yan, M. Zhang, D. Dillard, A., R. Moore, B., ECS Transactions, 41 (2011) 87.
[61] S. Kasapis, Food Hydrocolloids, 15 (2001) 239-245.
[62] H. Lin, B.D. Freeman, S. Kalakkunnath, D.S. Kalika, Journal of Membrane Science, 291 (2007) 131-139.
[63] P.B. Macedo, T.A. Litovitz, The Journal of Chemical Physics, 43 (1965) 245-256.
[64] A. Tsoga, S. Kasapis, R.K. Richardson, Biopolymers, 49 (1999) 267-275.
[65] J.S. Vrentas, J.L. Duda, Journal of Polymer Science, 15 (1977) 403-416.
[66] J.S. Vrentas, J.L. Duda, Journal of Polymer Science, 15 (1977) 417-439.
[67] J.S. Vrentas, J.L. Duda, Journal of Polymer Science, 15 (1977) 441-453.
[68] K. Page, A., K. Cable, M., R. Moore, B., Macromolecules, 38 (2005) 6472-6484.
[69] S. Osborn, J., M. Hassan, K., G. Divoux, M., D. Rhoades, W., K. Mauritz, A., R. Moore, B., Macromolecules, 40 (2007) 3886-3890.
[70] D.A. Dillard, S. Guo, B. Chen, J.-H. Yu, Mechanics of Time-Dependent Materials, 7 (2003) 21-39.
[71] R.G. Humfeld, D.A. Dillard, Journal of Adhesion, 65 (1998) 277-306.

Chapter 4 : Morphological and Constitutive Property Characterization of PFCB/PVDF-HFP Membranes Aged Under Operating Fuel Cell Conditions

4.1 Introduction

The durability of polymer electrolyte membranes or proton exchange membranes (PEM) is of key importance for the commercialization of fuel cells for portable, stationary, and transportation applications [1]. Automotive applications are especially mechanically challenging due to the rapidly changing temperature and humidity conditions imposed to meet the needed power demands [2, 3]. In a fuel cell, the PEM transports protons from the anode to the cathode while also acting as a barrier to the reactant gasses and electrons. Better proton transport is achieved at higher water contents, and PEM materials have been shown to expand due to moisture by at least 10%, and many by more than 20% in all three directions [4]. However, within a fuel cell stack the PEM layers are largely constrained between rigid bipolar plates and gas diffusion layers. This limitation to movement induces varying compressive and tensile stresses as the PEM attempts to expand and contract with changing temperature and humidity conditions [5]. It is believed that the repeated cycling of these induced hygrothermal mechanical stresses leads to a fatigue loading of the PEM, which over time contributes to the formation and propagation of microcracks [6-8]. These and other defects or pinholes allow the reactant gasses to crossover, resulting in localized heating, failure of the membrane, and ultimately, failure of the fuel cell [7-12]. Therefore, it is important to understand and characterize the constitutive properties of PEMs to accurately predict and improve the lifetime durability of a fuel cell.

While multiple authors have investigated the constitutive properties of new or pristine fuel cell membranes, few have examined the change in membrane properties after exposure to possible fuel cell operating conditions. Tensile testing performed on Nafion® samples that had been aged at least 72 hours in an operating fuel cell showed a decrease by a factor of two in the Young's modulus and yield strength [13]. Another aging study conditioned the samples at 70, 80, or 90°C in an operating fuel cell and noted a decrease in the Young's modulus and the strain at break with increasing operating temperature [14]. An additional study by Patil et al. examined aged membrane electrode assemblies in an operating fuel cell at 90°C and 30% RH under open circuit voltage conditions. These authors found a large decrease in the stress and strain at break after aging, indicating a severe reduction in the ductility of the membranes [15]. This reduction in ductility was thought to be caused by a decrease in the molecular weight of the membrane. Shorter polymer chains can escape entanglements more easily, and even shorter chains are unable to form entanglements, both of which would reduce the material's resistance to deformation, resulting in embrittlement and loss of ductility. This is again in agreement that temperature has a large impact on Nafion® materials, and also indicates that Nafion® should only be used in low temperature operating fuel cells due to the deterioration of mechanical properties at higher temperatures.

Contrary to the tensile testing results, Patil et al. noted that aged membranes underwent less creep strain than non-aged membranes, indicative of a stiffer material [15]. The authors believe this again is attributable to a reduction in the molecular weight. Because of the reduction in molecular weight, the material is now behaving as a brittle and less tough material, rather than a high molecular weight glassy material. Therefore, as the membrane is subjected to small deformations, such as the creep experiments performed, the material will undergo local rupture

rather than chain clippage to relieve the applied stress, consistent with a more brittle material as measured under uniaxial tensile testing. Stress relaxation testing performed immersed in water showed that annealing in 70°C water for three days slows the relaxation process as compared with non-annealed samples [16, 17]. It is likely that during the annealing period, chain mobility was increased, allowing for greater crystallinity to form in the Nafion®. The increase in crystalline regions would immobilize backbone segments in addition to the reduced mobility created by the electrostatic interactions of the ionic aggregates [16]. Based on these studies, it is clear the membrane undergoes at least physical changes and possibly additional chemical changes during fuel cell operation due to the high temperature and moisture levels employed.

Although Nafion® membranes have excellent proton conductivity and decent mechanical properties below their α-transition, these materials are difficult to process and as such are quite costly. Therefore, a need for an improved PEM material has resulted in the study of alternative hydrocarbon-based membranes. A recently developed material, perfluorocyclobutane (PFCB), shows significant potential as a fuel cell membrane due to its multiple processing routes, low dielectric constant, high thermal and oxidative stability, and chemical resistance [18, 19]. One example synthesized by Iacono had a maximum conductivity of 0.011 S cm^{-1} at 100% RH, the same as Nafion® at 40% RH. An additional two reported membranes, sulfonated poly(fluorenyl ether) and sulfonated poly(fluorine-co-sulfone)ether membranes show proton conductivities equal to and greater than Nafion 115, dependent on the level of sulfonation. None of these studies examined the mechanical properties of the membranes, however Mao showed a tensile breaking stress of about 30 MPa for a sulfonated perfluorocyclobutane membrane [19-23]. Additional PFCB polymers used for other applications have been characterized with a 4-9% strain at break and 1 GPA modulus [24-26]. While these studies did not conduct durability

analyses, the reported polymers appear to be brittle and likely would not survive the harsh mechanical environment of a fuel cell.

Therefore, to improve the mechanical durability by reducing the brittleness, the PFCB ionomer was blended with poly(vinylidene difluoride)-co-hexafluoropropylene (PVDF-HFP). Utilizing PVDF-HFP rather than another hydrocarbon material, allows for the incorporation of a material with high chemical resistance, mechanical toughness, excellent oxidative and electrochemical stability, and is commercially available at a low cost. Thus, blending provides a simpler and less expensive process for material design than creating and synthesizing new molecules. In addition, it is easier to tailor material and morphological properties by adjusting the blend component ratios. In recent years multiple blend membranes have been studied for use in fuel cells [27-29] [30, 31] [32-35] [36-49], one such example is a blend of a hydrocarbon ionomer and PVDF-HFP which showed excellent mechanical durability and fuel cell operating lifetimes five times greater than Nafion® NRE 211 [40].

Previously, the constitutive properties of new or pristine PFCB/PVDF-HFP (70/30 wt:wt) blend were investigated and discussed in Chapter 2. However, fuel cell operating conditions allow for a greater amount of free volume and thus chain mobility is increased, possibly resulting in increased crystallinity, microphase separation, and physical crosslinks. Therefore, understanding how these properties and the underlying morphological causes change over the operating lifetime is important, so that the development of poor mechanical, and/or electrochemical properties can be mitigated. The research herein focuses specifically on obtaining the material properties and morphological understanding of PFCB/PVDF-HFP (70:30 wt:wt) blend membranes including stress relaxation modulus, biaxial strength, water uptake,

differential scanning calorimetry, small angle X-ray scattering profiles, and TEM images for a new or pristine membrane compared with membranes aged under fuel cell operating conditions.

4.2. Experimental

4.2.1. Materials

Cast membranes, approximately 12 μm thick, of 70:30 wt:wt PFCB and PVDF-HFP (Kynar Flex® from Arkema) were received from the General Motors Electrochemical Energy Research Laboratory. The casting solution was created by dissolving 0.10000 kg of PFCB ionomer from Tetramer Technologies and 0.04286 kg of Kynar Flex® 2751 from Arkema in 0.7143 kg of *N,N*-dimethylacetamide (DMAc). The solution was roll milled for 1 week in a 1-L jar with a Teflon® screw cap, and pressure filtered through a 5-μm Mitex® Millipore filter. Several coating solutions were then combined and diluted with DMAc, resulting in a 15 wt% solids solution, in order to create smoother coatings.

The solution was then cast using a coating line consisting of a knife over roll, reverse roll coater onto a polypropylene coated blue paper backer. A coating width of 203 mm and a gap of 0.050 mm were utilized with varying speeds to obtain the targeted membrane coating thickness. After laying the solution down on the backing material, the solution was passed through a 24.4-m drier. The first 12.2 m utilized convection heating, and the second 12.4, IR heating both at temperatures less than 100°C. Rolls of membranes were created at the intended thickness of 14-16 μm, however the actual thickness after casting was ~12 μm as measured by a drop gauge micrometer.

A pre-test treatment was deemed necessary to remove excess DMAc as the excess solvent appeared to be creating a softer, lower modulus, and lower strength material [50]. Therefore, all membranes received from GM underwent a solvent exchange in 50°C water for 1 h, while biaxially constrained in a 11.4 x 11.4 cm^2 polytetrafluoroethylene (PTFE) frame. The membranes were then stored in the PTFE frame overnight inside a desiccator to remove excess moisture. As the membrane dries in the frame, it becomes taut, producing locked-in strains in the material. Therefore, immediately prior to testing and after removal from the PTFE frame, each membrane underwent a 100°C 2 h isotherm at 0% RH to remove the locked-in stresses.

For comparison purposes Dupont™ Nafion® NRE 211 (NRE 211) membranes, approximately 25 μm thick, produced reportedly from a casting process, were also characterized. These membranes were not subjected to the one hour 50°C solvent exchange because it was not performed for prior characterization, but for consistency in membrane water content, samples were subjected to the two hour 100°C isotherm prior to testing.

4.2.2. Linear Viscoelastic Constitutive Properties

Solvent-exchanged membranes were cut using a rule die into 50 x 9mm samples, with two 20mm slits creating three 3mm sections. The sample was mounted in a TA Instruments DMA Q800 in conjunction with a TA Instruments Relative Humidity Accessory, such that 15 mm of the slitted area was between the grips. This sample geometry was chosen to maintain a 5:1 aspect ratio approximating a uniaxial stress state, while also increasing the signal to noise ratio. Each test was performed at 30% RH, at temperatures from 30 to 120°C. After an initial 2 h equilibration at 30% RH and 30°C, stress relaxation testing began. Each stress relaxation test was 17 minutes long, followed by a 60 min recovery period. The temperature was then raised 10°C, and held for an additional 60 min before the next stress relaxation test was performed,

allowing for 99% or greater recovery of the sample. Data was then used to create a thermal stress relaxation master curve by applying the time temperature superposition principle (TTSP). The effects of different environmental exposures over time on the stress relaxation were compared with the stress relaxation of a solvent-exchanged membrane.

4.2.3. Biaxial Strength Measurements

Biaxial strength measurements were performed with air pressurized blisters, similar to work previously completed on Gore-Select™ membranes and Nafion® [49, 51-53]. Membrane samples were punched using a die into 2.54 cm diameter circles. Each sample was then placed in an oven at 80°C and ~20% humidity to equilibrate for 2 hours prior to testing. Humidity was controlled using a Fuel Cell Technology Humidification System and monitored with a Vaisala temperature and humidity probe. After equilibration, the sample was placed in the fixture shown in **Figure 4.1. F**, within the humidified oven, without the use of an adhesive. This fixture was designed by Ron Li at General Motors for use with digital image correlation (DIC). While DIC measurements were not performed herein, this fixture was employed due to ease of use. It consists of sandblasted polycarbonate, meant to diffuse light and ease DIC use, and is lined with Teflon® to help create a good seal and eliminate leaks, forcing the air to pressurize the blister. The blister hole radius is 9.525 mm, and the membrane was constrained in the fixture with three screws. The pressure input was placed on the side to create a uniform surface behind the blister and improve lighting for DIC use.

After the sample was mounted the air pressure was increased at 0.5 kPa/s, until the sample burst or the pressure reached 100 kPa. Pressure vs. time curves were collected using

LabVIEW, and the strength at failure was calculated using the quasi-elastic Hencky solution as shown in **[4.1]**:

$$\sigma_b = \frac{B_o}{4}\left(\frac{E(t_b)p(t_b)^2 a^2}{h^2}\right)^{1/3} \qquad [\mathbf{4.1}]$$

where B_o is a material constant, taken to be 1.77 assuming a constant Poisson's ratio of 0.4, $E(t_b)$ is the time dependent relaxation modulus taken at the time at burst, $p(t_b)$ is the pressure at the time at burst, a is the radius of the blister sample, and h is the thickness of the membrane [53]. Although the original Hencky solution was for linear elastic materials, the quasi-elastic solution can be created by using the time dependent modulus and assuming an initial zero strain state. Previous work has shown excellent applicability of the quasi-elastic solution for cast and extruded Nafion® and Gore-Select™ materials [53]. Therefore it is assumed to be an appropriate analysis for the PFCB/PVDF-HFP materials as well.

Figure 4.1. Fixture used for biaxial strength measurements, shown at left disassembled, and at right assembled with a pressurized blister.

4.2.4. Water Uptake (Preliminary Study Only)

Sorption tests were performed using a TA Instruments Q5000 SA Vapor Sorption Analysis instrument. Each test used approximately 1 mg of material cut into small pieces and began with a 1 h isotherm at 80°C and 0% RH to dry the material, where 80°C was chosen due to temperature limitations of the instrument. The sample was then cooled to 30°C and the humidity was increased by 5% every 2 h until reaching 95% RH. In addition, a step was included in the test protocol that allowed the instrument to increase the humidity if the sample weight percent changed by less than 0.01% over 5 min. At low humidity levels this over ride was used frequently, but at 60-80% RH each isotherm was held for approximately 1 hr, and 85-95% RH each isotherm was held for the full two hours. The moles of water molecules per moles of sulfonic acid groups, λ, were calculated using **Eqn [2.8]**:

$$\lambda = \frac{g \text{ of } H_2O}{g \text{ of Membrane}} \cdot \frac{\left(\frac{mol \text{ of } H_2O}{18g\ H_2O}\right)}{\left(\frac{mol \text{ of Membrane}}{\text{EW of Membrane}}\right)} \qquad [4.2]$$

where *EW* is the equivalent weight as measured by Nathan May from titration experiments. Over four experiments he measured a range of equivalent weights from 802.62 – 1103.24 mmol/g, and the average value of 934 mmol/g was used for calculations.

4.2.5. Pulsed-Field Gradient NMR (PFG-NMR) (Preliminary Study Only)

PFG-NMR experiments were performed using a 400 MHz Bruker Avance III WB NMR spectrometer, equipped with a single axis diffusion probe, from 25-55°C. Samples were created by stacking 100 6 x 6 mm squares of membrane to enhance the NMR signal. The sample stacks

were then dried at 40°C for 5 h, prior to being wrapped with polytetrafluoroethylene tape and soaked in H_2O for 24 h. The samples were then placed within a cylindrical Teflon® cell filled with H_2O and sealed with a piston cap to allow the sample to remain immersed for the entirety of the test. Therefore, the water content of the material was constant over the testing period. The free diffusion NMR signal attenuation is described by **Eqn [4.3]**:

$$I = I_0 e^{-D\gamma^2 g^2 \delta^2 \left(\Delta - \frac{\delta}{3}\right)} \quad \textbf{[4.3]}$$

where I is the spin-echo signal intensity, I_0 is the signal intensity at zero gradient, γ is the gyromagnetic ratio of the probe nucleus, δ is the duration of the field gradient pulse with magnitude g, D is the self-diffusion coefficient of water in the samples, and Δ is the time between the leading edges of the two gradient pulses [54]. The signal intensity is measured as a function of g to obtain the diffusion coefficient of water in the samples. In these experiments, Δ was 50 ms, giving a global diffusion constant, rather than one over a localized region.

4.2.6. Proton Conductivity

Proton conductivity was measured by two-probe electrochemical impedence spectroscopy (EIS) over 100 Hz-1 MHz using a proton conductivity cell developed at Virginia Tech, shown in **Figure 4.2**. The fixture is made of polytetrafluoroethylene with platinum wires. Two probe measurements were completed rather than four-probe because the two-probe scans provided cleaner Nyquist plots. EIS measurements were performed with a Solartron Analytical 2100A instrument, using Modulab software to analyze collected data. Using a Nyquist plot, the low frequency intercept on the real axis was extrapolated as many of the semi-circles did not

cross the real axis. The extrapolated value was taken to be equivalent to the membrane resistance, R, and the proton conductivity, σ, was calculated using **Eqn [4.4]**:

$$\sigma = \frac{d}{lwR} \qquad \textbf{[4.4]}$$

where d is 3.75mm, the distance between the two probes, l is 12 μm, the thickness of the membrane, and w is about 1 cm, the width of the sample.

All proton conductivity measurements were performed immersed in deionized water. The measured conductivity of the deionized water was 0.11 μS, and as such it was assumed that the water did not affect the conductivity measurements. The entire proton conductivity fixture was immersed in a 1000 mL beaker and placed on a Corning stirrer/hot plate. Three sets of conductivity measurements were performed. The first was measured from 30-95°C, and a measurement was performed every 5, 10, and 15 min at each temperature, to examine how the conductivity changes over short equilibration periods over a large temperature range. The second conductivity test measured conductivity at temperatures from 30-80°C, in 10°C increments, with 30 min equilibration times at each temperature, except 80°C when only a 5 min equilibration was employed, the reasons for which will be discussed in **Section 4.3.2.3**. Lastly, conductivity tests were performed over time, examining the change in conductivity at 60-90°C over 3 h time periods. These samples were then stored at ambient conditions overnight, and retested at the same temperature immersed in water the next day to see if the conductivity changed over the equivalent of an extended RH cycle.

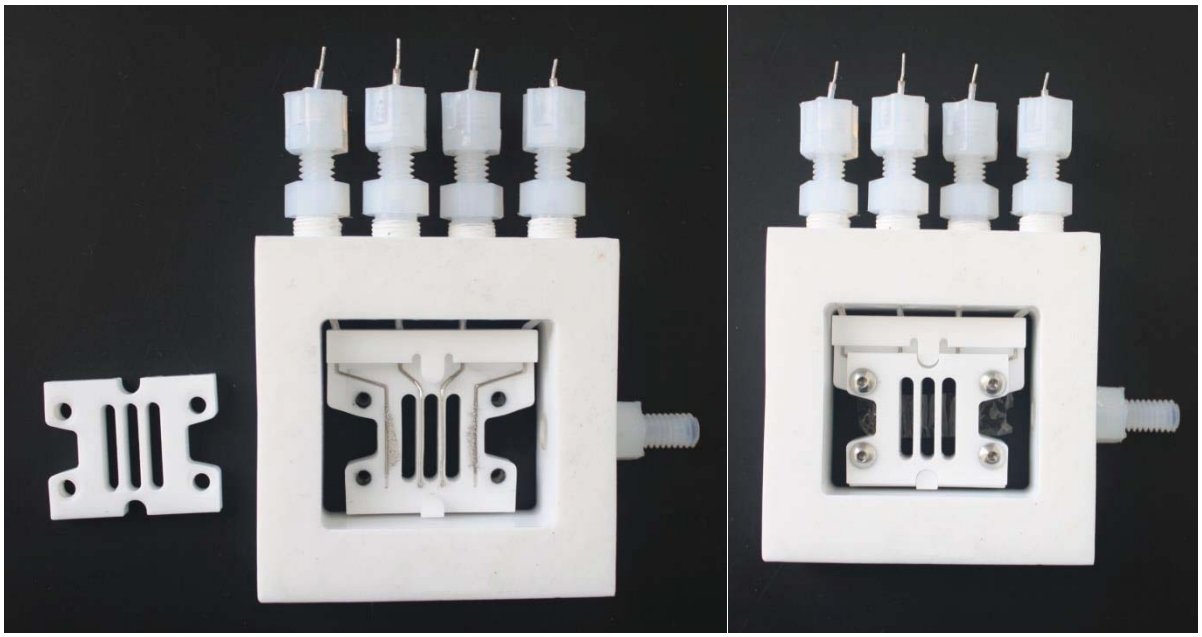

Figure 4.2. Proton conductivity cell, shown at left disassembled, and at right assembled with a membrane sample.

4.2.7. Small Angle X-Ray Scattering

Small angle X-ray scattering (SAXS) experiments were completed using a Rigaku S-Max 3000 3 pinhole SAXS system, equipped with a copper rotating anode emitting X-rays with a wavelength of 0.154 nm (Cu K_α). Two-dimensional SAXS patterns were obtained using a fully integrated 2D multiwire, proportional counting, gas-filled detector, with an exposure time of 1 hour. All SAXS data was analyzed using the SAXSGUI software package to obtain radially integrated intensity versus scattering vector q, where $q=(4\pi/\Lambda)\sin(\theta)$, θ is one half of the scattering angle, and Λ is the wavelength of the X-ray. For all scattering experiments, the sample-to-detector distance was either 1603 or 963.34 mm, and the q-range was calibrated using a silver behenate standard.

4.2.8. Fourier Transform Infrared Spectroscopy

Both transmission and attenuated total reflectance (ATR) infrared spectra were collected with a Varian 670-IR. ATR spectra were measured utilizing a Pike GladiATR variable Temperature ATR attachment. Each spectra was collected with 32 scans and a 4 cm^{-1} resolution. In addition, transmission spectra were collected under a nitrogen atmosphere, however ATR spectra were not as the sample chamber could not be closed with the Pike GladiATR attachment installed.

Additional ATR spectra were taken on immersed membrane samples. Membrane samples were initially immersed in room temperature DI water to ensure complete hydration had occurred, and then placed on the Pike GladiATR stage after the stage had reached the desired testing temperature. A piece of fritted glass was also immersed in water to ensure complete hydration had occurred, however the water temperature was equal to the test temperature. The fritted glass was then placed on top of the membrane at the beginning of the test, and the pin was lowered to ensure good contact between the membrane and the diamond, as shown in **Figure 4.3**. Water heated to the test temperature was added to the fritted glass every 3 min and the peaks corresponding to OH vibrations around 3000 Hz were monitored to ensure the sample stayed hydrated throughout the test. Three different test cycles were used with this ATR set-up to monitor possible changes in samples due to temperature and moisture exposure. The first test cycle held a membrane sample immersed at 80°C for 3 h, immersed at 30°C for 3 h, immersed at 80°C for 1 h, and a final step immersed at 30°C for 3 h. The second test cycle is similar to the first, however at 30°C the sample was dry, rather than remaining immersed. The third test cycle maintains the temperature at 80°C, beginning with immersion for 3 h, followed by a dry out for 1 h, immersion for 1 h, and a final dry out for 1 h.

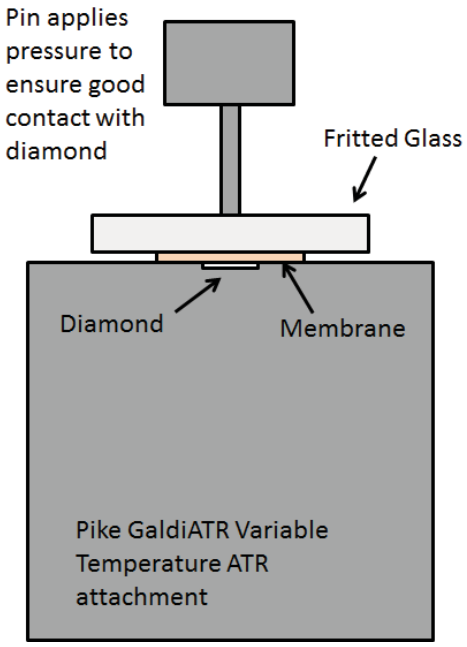

Figure 4.3. ATR-IR test set up for measuring samples under immersed conditions.

4.2.9. Differential Scanning Calorimetry (DSC)

DSC was performed using a TA Instruments Q2000 DSC equipped with an autosampler and refrigerated cooling system allowing temperatures to extend to -90°C without the use of liquid nitrogen. Membrane samples were cut into approximately 1 mm x 1 mm pieces and approximately 3 mg was loaded into non-hermetic sample pans. Non-hermetic pans were chosen to allow water to escape and thus not obscure the PVDF-HFP crystalline melting endotherm. The samples were equilibrated at -90°C, heated to 110°C with a ramp rate of 50°C/min and held for 5 min to ensure water was removed without disrupting crystallinity formed during different membrane treatments. The sample was then quenched to -90°C and heated to 200°C with a ramp rate of 20°C/min.

It was assumed that all crystallinity was formed by the PVDF-HFP component, and as such the percent crystallinity, X_c, was calculated using **Eqn [4.5]**:

$$X_c(\%) = \frac{\Delta H_f}{\Delta H_m^0} \times 100 \qquad \textbf{[4.5]}$$

where ΔH_f is the enthalpy of fusion of the PVDF-HFP calculated by integration of the crystalline melting endotherm, and ΔH_m^0 is the standard enthalpy of fusion of 100% crystalline PVDF. A typical accepted value of 104.7 J/g for PVDF materials was used for ΔH_m^0 [39, 55, 56].

4.2.10. Transmission Electron Microscope Imaging (TEM)

The ionic regions of the PFCB copolymer have the highest electron density in the blend, however the differences between the ionic regions and the non-ionic block of the PFCB as well as the PVDF-HFP are minimal, and thus it would be difficult to image these materials in their neat state. Therefore, to increase the electron density of the ionic regions, the membranes were stained with Ru(II) with two 2,2' bipyrdine ligands and one 2,3 (2-pyridyl)pyrazine ligand (**Figure 4.4**). This was completed by swelling 1 cm x 1 cm membrane squares in methanol at room temperature, adding an excess of the heavy metal complex, and shaking the samples for 24 hrs. As the membranes absorbed the heavy metal complex they turned bright orange and the solution became clear. These heavy metal complexes are known to associate with the ionic groups of the membrane, thereby increasing the electron density of these regions, allowing for a clear distinction between the ionic aggregates and the remaining material.

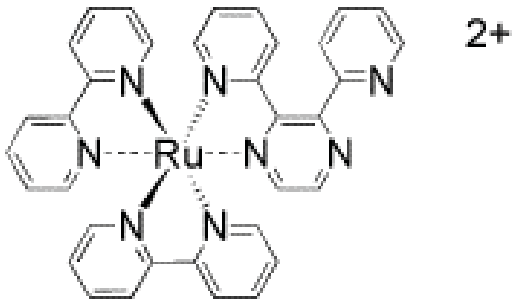

Figure 4.4. Chemical structure of Ru(II) with two 2,2' bipyridine ligands and one 2,3 (2-pyridyl)pyrazine ligand.

After staining the membrane samples with the heavy metal complex, each sample was embedded direction in Poly/Bed® 812 epoxy produced by Polysciences Inc., and placed in an oven for 24 h at 60 min to allow the epoxy to cure. After potting, a slice of membrane approximately 80-90 nm thick was cut using a microtome blade. TEM imaging was then performed with a JEOL JEM-1400 Electron Microscope equipped, with an 80V electron beam, and a Gatan ORIUS™ 2100A CCD Camera.

4.3 Results and Discussion

4.3.1. Preliminary Investigation of Post Processing Treatment Effects on the Mechanical and Morphological Properties of PFCB/PVDF-HFP Membranes

4.3.1.1 Exploration of Stress Relaxation Modulus Stiffening

Initially, a study was performed to determine the amount of time required to equilibrate a sample in the testing environment prior to collecting stress relaxation data. Therefore, an experiment was performed where the material was held at a specific condition for 25 h and each hour a 5 min stress relaxation test was performed, followed by a 55 min recovery, so that the

modulus could be observed after each hour of exposure time. Three different conditions were tested, 70°C with 55% RH, 30°C with 55% RH, and 30°C with 0% RH, as shown in **Figure 4.5**. It was expected that the modulus would decrease with increased exposure time until there were no further changes, indicating the sample was fully equilibrated. However, after each hour of exposure, a stiffening in the material was observed, as shown in **Figure 4.5**, implying another mechanism is occurring in the material during exposure.

This behavior is most notably seen in the 55% RH 70°C data set, as the spread in the data is decreased when the temperature is reduced to 30°C. The spread in the data is further reduced when the relative humidity is decreased. Data taken previously after a 3 h equilibration at 55% RH and 70°C was compared with that taken during this test, as shown in **Figure 4.5** by the solid black line. This previous data set agrees well with the data taken after 3 h at long times. However at short times it appears to agree better with the data taken after a 2 h exposure. It is likely this difference is due to some variation between samples, either in the material or from loading, and it is encouraging that the data sets do match over long times.

Three possible explanations for this stiffening behavior have been explored. The first is mechanical conditioning, similar to initial conditioning of filled composites. Filled composites are often subjected to a number of cycles prior to testing to break some of the bonds between the filler and the matrix. The material will then reach an apparently reduced modulus, with decreased time dependence as the bonds are no longer slowly giving way during testing [57]. Although the modulus was increasing with exposure time, the PFCB/KF data showed similar decreased time dependence with additional testing. Therefore a test was run such that the material was exposed to 70°C and 55% RH for 25 h. After 25 h a single 5 min stress relaxation test was performed, and the data was compared with the 70°C 55% RH 25 h exposure collected

after multiple stress relaxation tests, as shown by the purple line in **Figure 4.5**. As is seen in the Figure, the single stress relaxation test after a 25 h exposure has a higher modulus than the data taken after a 25 h exposure and multiple stress relaxation tests, consistent with a mechanical conditioning behavior. The lower time dependence in the 25 h single stress relaxation test may be due to sample or loading differences. The molecular origins of a mechanical conditioning phenomenon could be related to the physical crosslinks formed between the sulfonic acid groups. It is possible that multiple loadings break some of these physical crosslinks apart, resulting in a decreased modulus.

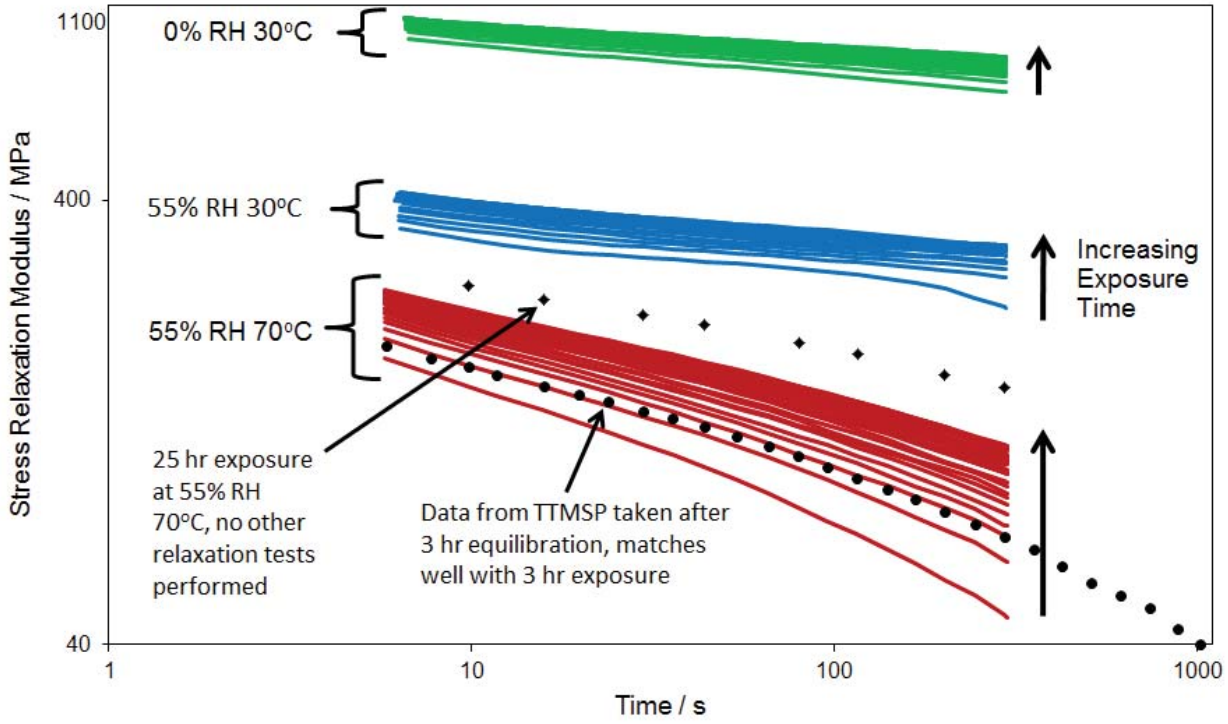

Figure 4.5. Increasing modulus with exposure time of PFCB/PVDF-HFP, compared with previously collected data.

The second explanation explored was the increased cross-sectional area with hygral expansion. During testing, a constant cross-sectional area is assumed, although the material is expanding due to moisture uptake. Therefore, the change in length measured during hygral expansion at 30^{o}C and 55% RH was fit with a logarithmic function, as shown in **Figure 4.6**. Assuming expansion occurs isotropically in the material, the calculated strain from the logarithmic function is applied to the cross-sectional area of the material, resulting in a greater cross-sectional area as time increases, up to a 0.4% increase. Using the modified cross-sectional area, each data set was replotted and compared with the original data set, as shown in **Figure 4.7**. The modified cross-sectional area data set does condense well as compared to the original data set, implying that hygral expansion may need to be accounted for during testing. However, for this to be accurate, the free water molecules in the material would need to be carrying a load, which is contrary to common physical beliefs. It is likely that the bound water in the material is carrying part of the load, but these molecules do not contribute as greatly to hygral expansion as the free water. Therefore, while the data indicates the changing cross-sectional area should be accounted for, the physics behind this explanation are not well understood at this point and alternative explanations are still being explored.

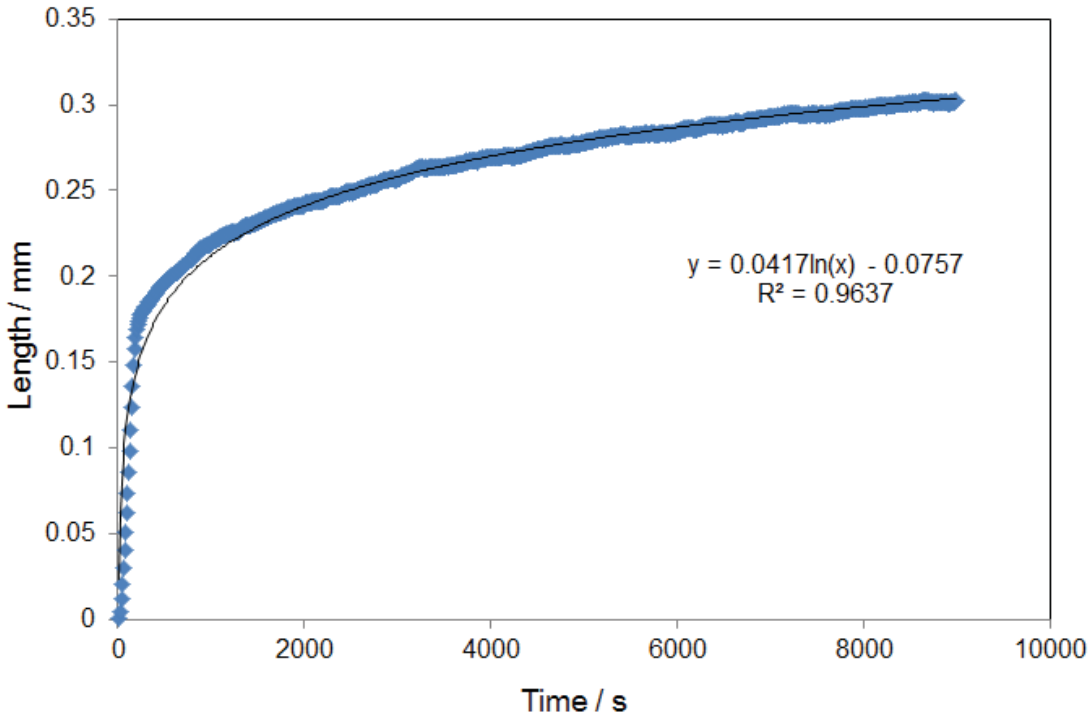

Figure 4.6. Hygral expansion step at 30°C for 55% RH, fit with a logarithmic function.

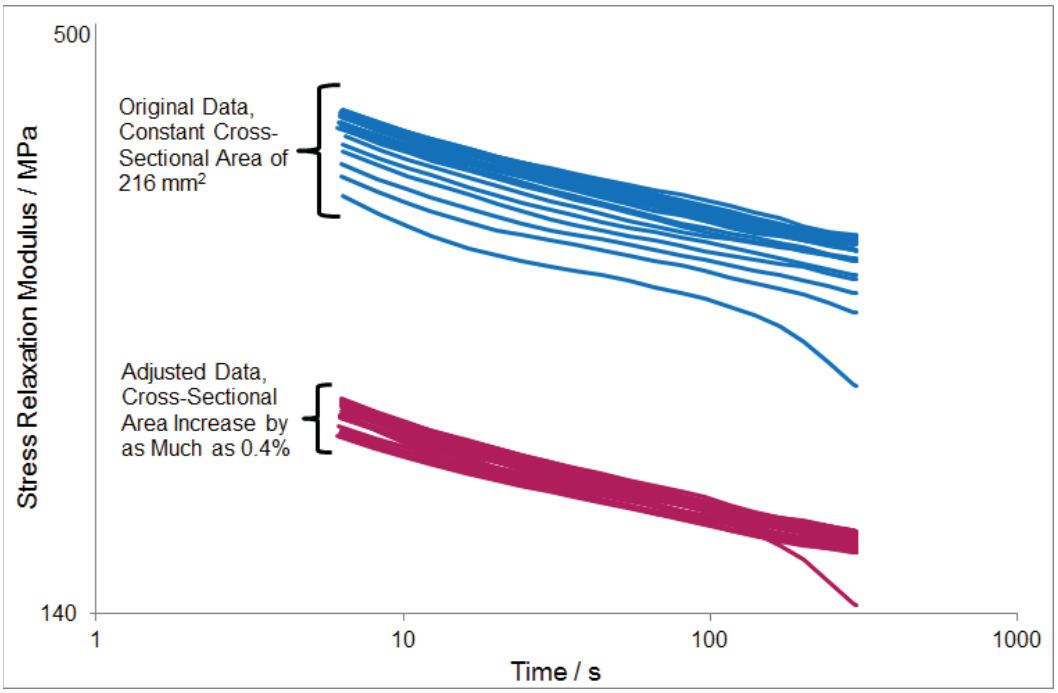

Figure 4.7. Adjusted stress relaxation modulus accounting for the change in cross sectional area due to hygral expansion.

The third possible explanation examined was physical aging in the material. Classically, physical aging corresponds to a densification of the material below the alpha transition. This would appear in stress relaxation testing as a stiffening as exposure time is increased, as observed in **Figure 4.5**. Therefore, a physical aging master curve was created, referenced to 3 h as previously collected data for the hygrothermal master curve had been taken after a 3 h exposure time. This allowed for simultaneous aging to be accounted and corrected for in the previously collected data. The physical aging master curve, created using Struik's method [58], and the corresponding shift factors appear in **Figure 4.8** and **Figure 4.9**. The slope of these shift factors is then used to correct the previously collected data for simultaneous aging. Although the physical aging master curve and shift factors look decent, the mechanism for aging in this material is not well understood and as such a rejuvenation experiment was performed to see if the material was truly undergoing physical aging. If physical aging is occurring, the material can be taken above its transition to erase the effects. Once the material is brought back below the transition temperature, the same aging effect should be observed, with the modulus beginning again at its softest point and stiffening with increased exposure time. Therefore, the same 25 h exposure time experiment was performed at 55% RH and 70^{o}C, followed by a 10 h isotherm at 110^{o}C with 55% RH, directly followed by another 25 h exposure experiment at 55% RH and 70^{o}C, as shown in **Figure 4.10**. As is clearly seen, after the 110^{o}C isotherm, the modulus begins again at its stiffest point and continues to stiffen further, contrary to physical aging theory. Therefore, despite the physical aging master curve, it is believed the material does not undergo physical aging, and further explanations for the stiffening behavior need to be explored.

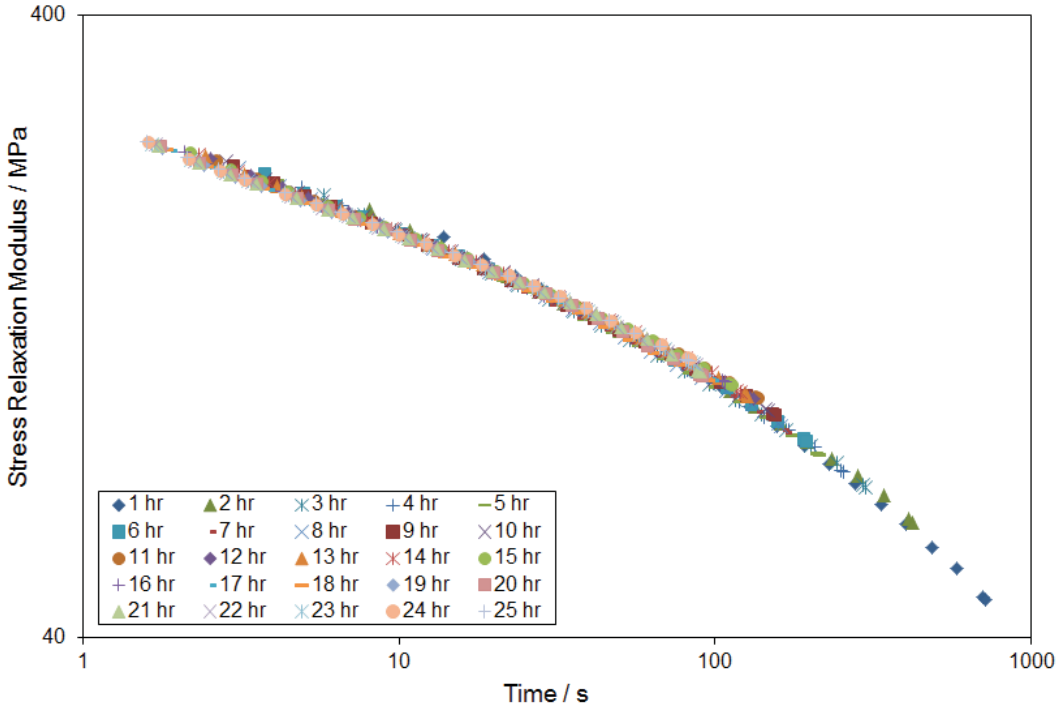

Figure 4.8. Physical aging master curve, created with data collected at 70°C and 55% RH for PFCB/PVDF-HFP.

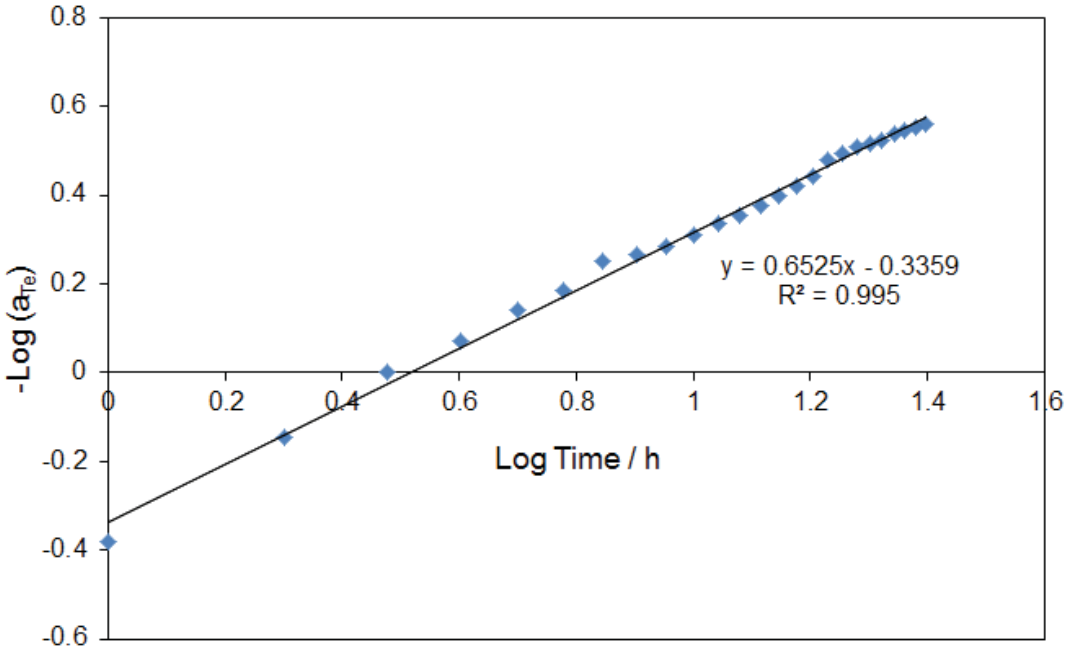

Figure 4.9. Physical aging shift factors corresponding to **Figure 4.8** for data collected at 70°C and 55% RH for PFCB/PVDF-HFP.

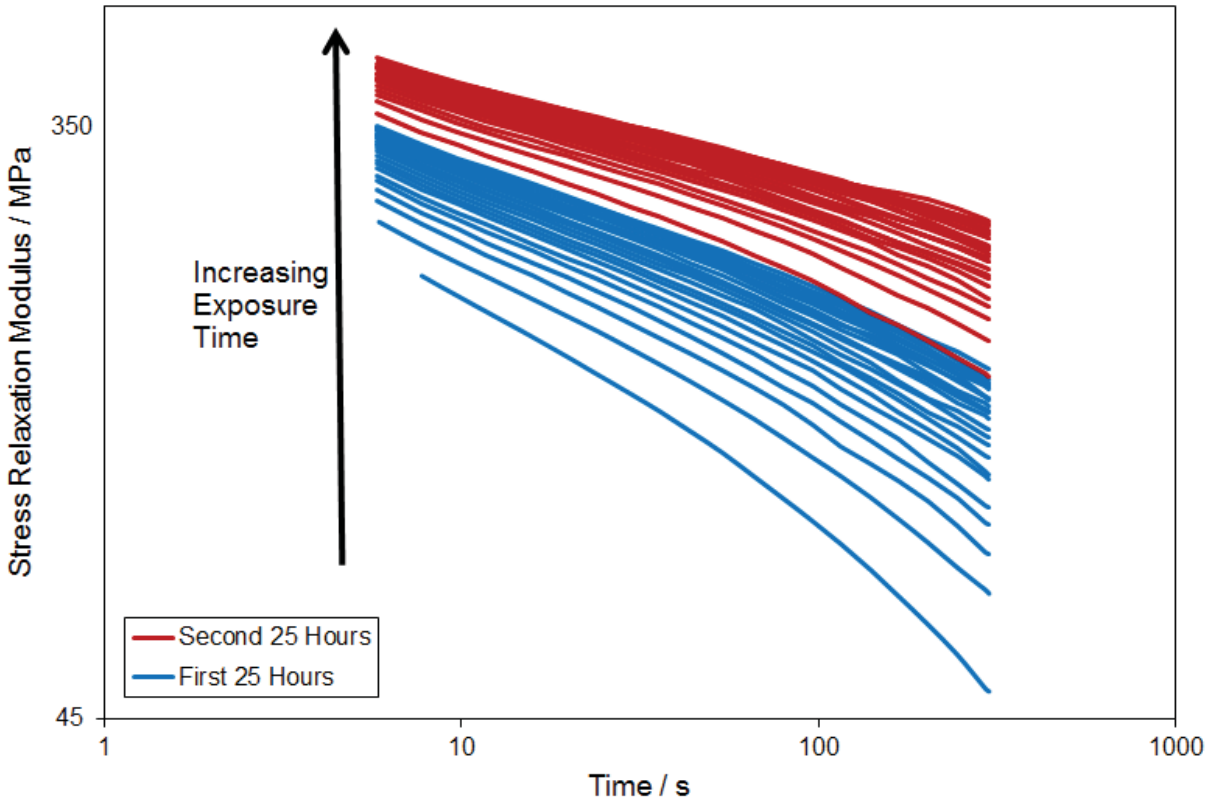

Figure 4.10. Rejuvenation plot for PFCB/PVDF-HFP exposed to 70°C, 55% RH conditions.

Therefore, to understand these observed changes further, a preliminary study was undertaken to examine the effects of two post processing treatments on constitutive properties, how this relates to the morphology of the system, and the impacts on fuel cell performance, as compared with the solvent exchanged PFCB/PVDF-HFP which was used as a baseline material. The two treatments chosen for initial study were a 2 h 100°C, 0% RH isotherm, and an initial exposure at 2 h 100°C, 0% RH followed by an additional exposure to a 24 h 70°C, 55% RH isotherm. The former was chosen to examine if any changes occur during the 2 h anneal that is employed for all samples to relax the locked-in strains from the solvent removal process. The latter was for initial study because it showed the greatest change over time in the initial

equilibration examination. In this study the stress relaxation modulus, mass uptake, and water diffusion were examined, as well as the morphology via small angle X-ray scattering (SAXS).

4.3.1.2. Linear Viscoelastic Constitutive Properties

Thermal stress relaxation master curves for solvent-exchanged and environmentally treated PFCB/PVDF-HFP 70:30 wt:wt referenced to 70°C at 30% RH and the corresponding shift factors are provided in **Figure 4.11** and **Figure 4.12.** It is clear there is either a stiffening or delay in the relaxation mechanism of the material with increased exposure time. The shift factors show a slight increase, approximately a half decade, in the temperature dependence of the second treatment. If the stress relaxation data is examined carefully, it appears that each curve could be overlaid if an additional time shift is applied, as shown in **Figure 4.13**. This additional shift was performed, by shifting to the 2 hr 100°C isotherm data, as this was used to create the hygrothermal master curve presented in Chapter 1. The log a_{TH} of the baseline material is 0.70, and for the material that underwent an additional 24 h at 70°C and 55% RH the log a_{TH} is -1.15. The relaxation and rubbery plateau line up almost perfectly between the three samples, whereas there are some differences in the glassy plateau region, although these may not be significant. This alignment that occurs with an additional time shift implies that while the observed differences in the stress relaxation moduli over a short time period appear as a stiffening, if the larger time scale is examined, a delay in the relaxation mechanism is the true material behavior. In addition, a shift of less than a decade as associated with the baseline material may not be a significant material change. However, a shift of more than a decade as associated with the material that underwent an additional 24 h exposure at 70°C and 55% RH, is significant, as this implies the material is relaxing on a much longer time scale. The impact on mechanical durability could be significant, as well as on fuel cell performance. Understanding how these

mechanical changes affect other constitutive properties, such as mass uptake and expansion, is important, as well as understanding the underlying morphological cause of these changes, towards building understanding of the impact on fuel cell performance.

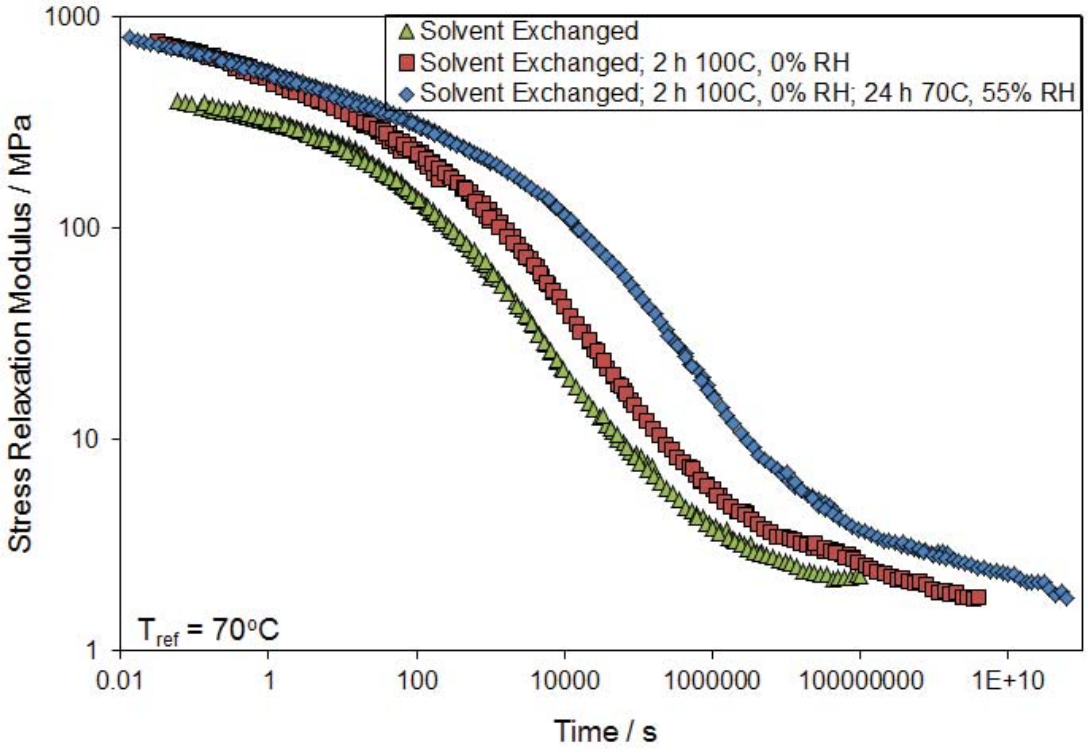

Figure 4.11. Thermal master curves referenced to 70°C taken at 30% RH of solvent exchanged membrane, solvent exchanged membrane plus 2 h at 100°C 0% RH, and solvent exchanged membrane plus 2 h at 100°C 0% RH and an additional 24 h 70°C 55% RH.

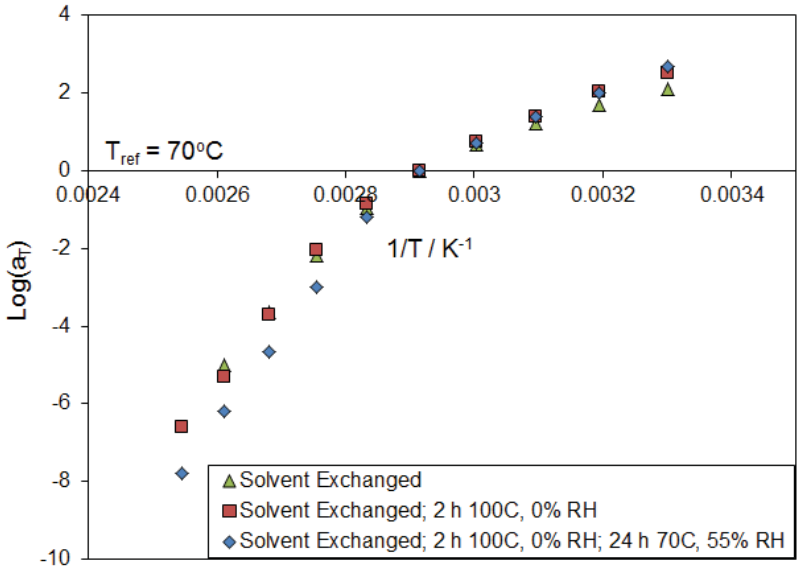

Figure 4.12. Thermal shift factors corresponding to the thermal master curves of **Figure 4.11** referenced to 70°C taken at 30% RH of solvent exchanged membrane, solvent exchanged membrane plus 2 h at 100°C 0% RH, and solvent exchanged membrane plus 2 h at 100°C 0% RH and an additional 24 h 70°C 55% RH.

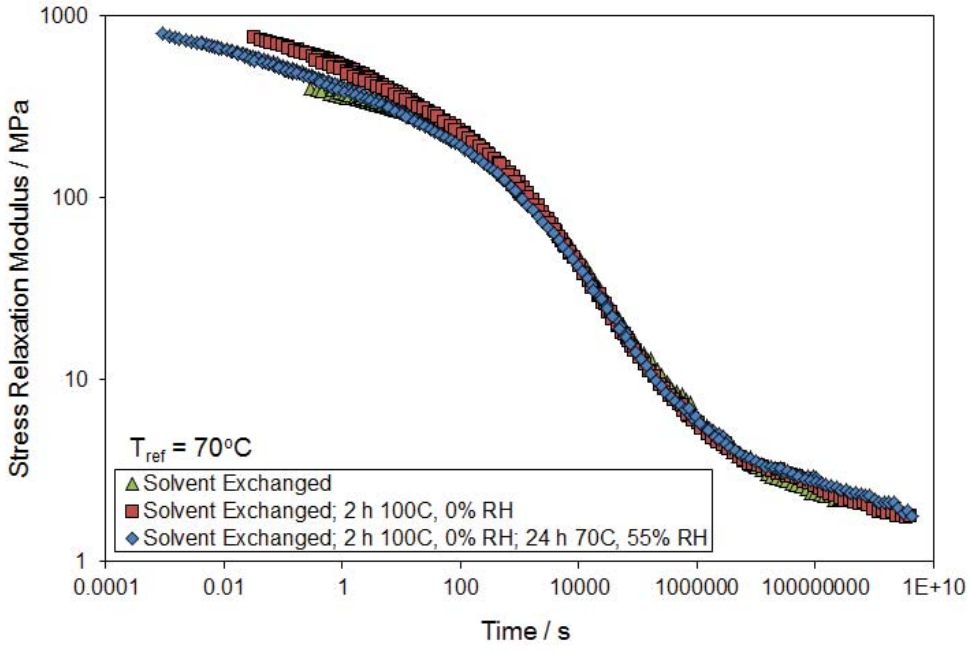

Figure 4.13. Shifted thermal master curves referenced to 70°C taken at 30% RH of solvent exchanged membrane, solvent exchanged membrane plus 2 h at 100°C 0% RH, and solvent exchanged membrane plus 2 h at 100°C 0% RH and an additional 24 h 70°C 55% RH.

4.3.1.3. Water Uptake

Sorption data is provided in **Figure 4.14** for solvent-exchanged and treated membranes. There is a significant difference between the solvent-exchanged material and the treated materials, however both the treated membranes show similar water uptake behavior. This is in contrast to the stress relaxation data, which showed increased stiffening with increased exposure time. It appears that the impact on water uptake with increasing exposure time is very minimal.

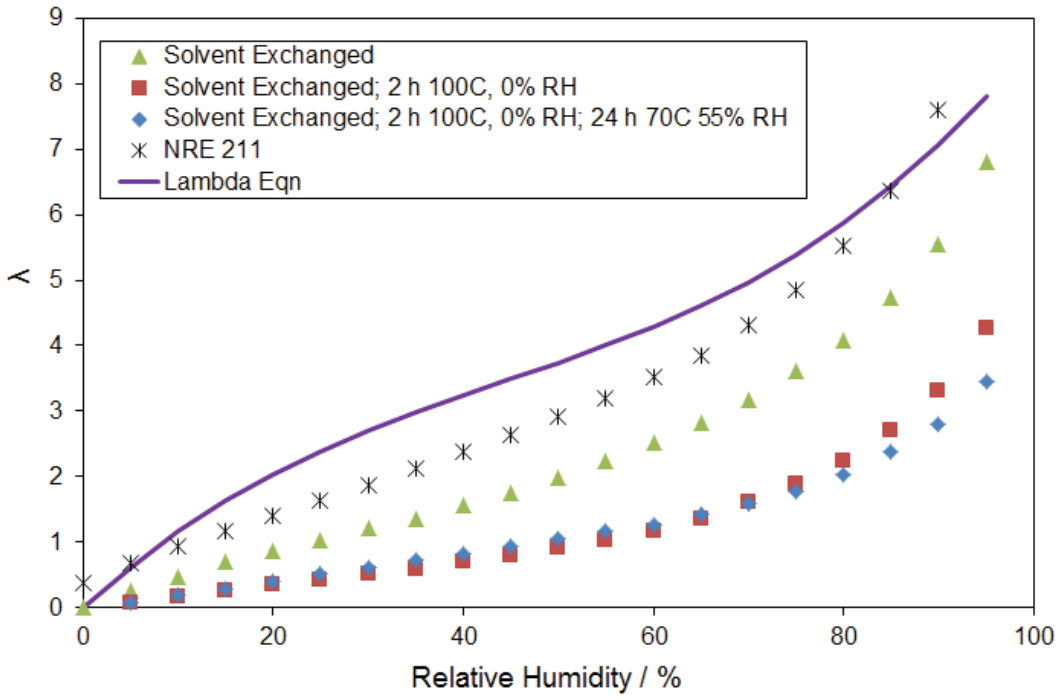

Figure 4.14. Comparison of mass uptake data taken on solvent exchanged membrane, solvent exchanged membrane plus 2 h at 100°C 0% RH, and solvent exchanged membrane plus 2 h at 100°C 0% RH and an additional 24 h 70°C 55% RH, NRE 211, and the lambda prediction equation.

4.3.1.4. PFG-NMR

To explore the effects on fuel cell performance further, water diffusion measurements were completed using PFG-NMR [59-61]. This technique allows the measurement of the displacement of water molecules over time. This is done using a pulse sequence applied with both radio frequency and magnetic gradient pulses. The gradient pulse is a variation in the magnetic field over the sample tube length. A homogenous magnetic field causes all the spins of the protons in the water molecules to flip equally, whereas a gradient field causes the spins to all flip differently. In the pulse sequence, the first gradient pulse is applied to encode a position, after which the water molecules move around the material, and a second gradient pulse is then applied to decode the position of the molecules. When the molecules move, a different signal is obtained and Fourier transforms are used to examine the signal attenuation. It should be noted that the exact path of the water molecules between the first and second gradient pulses cannot be determined. In addition, different length scales can be examined by probing different time scales. This technique can be used to examine the sub-micron region to tens of microns by probing for a few milliseconds to a few seconds of time.

Data is provided in **Figure 4.15** from 298-328K (25-55°C) and is also compared with data at 298K for NRE 212 [19]. Similar to the water uptake data, the water diffusion shows a large difference between the baseline and treated materials, however both treated materials appear to be similar. In addition, the diffusion of water is very similar between the baseline material and NRE 212. This behavior may not be expected as the materials are very different molecularly, NRE 212 is a PFSA material and PFCB/PVDF-HFP is a blended material of an ionomer (70%) and a rubbery PVDF-HFP (30%). However, if the similar IEC and proton conductivity are considered, the similarity in water diffusion is highly likely. Finally, a linear fit

of the PFCB data was performed to obtain the activation energy for diffusion in this material system before and after treatment. The activation energy for diffusion in the baseline material was calculated to be 11.6 kJ/mol, and decreased slightly for the treated materials to 9.4 kJ/mol. This is compared with the 205 kJ/mol activation energy for mechanical relaxation processes to occur over a similar temperature range. Therefore, the energy required for water diffusion is 16 times less than for mechanical relaxation processes.

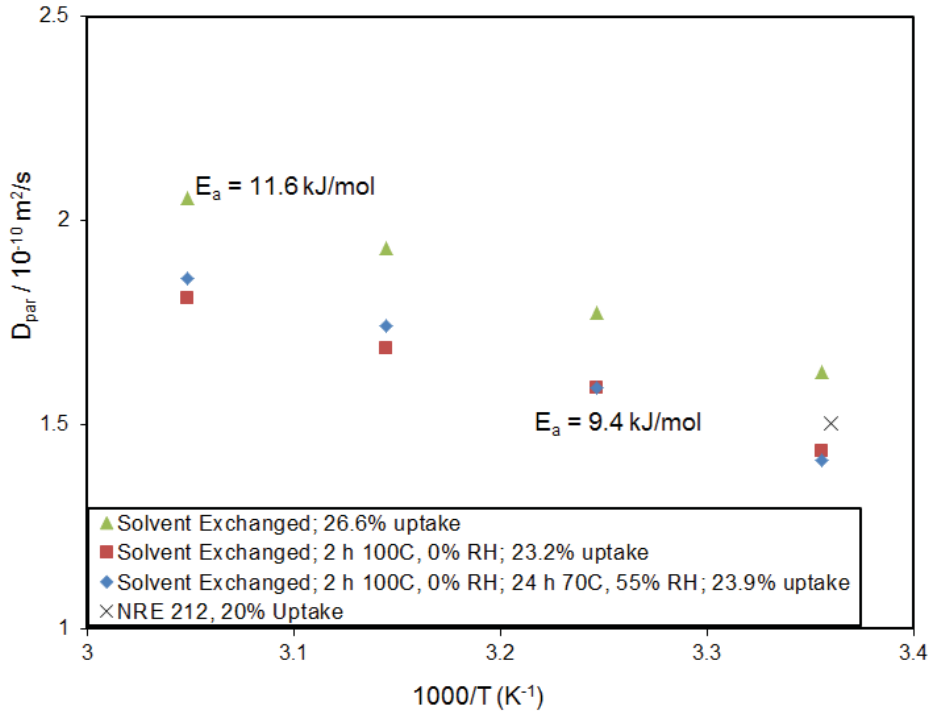

Figure 4.15. Diffusion of water in PFCB/PVDF-HFP and NRE 212 measured using PFG-NMR [59].

4.3.1.5. SAXS

To understand the underlying cause of the constitutive property changes, SAXS was performed to explore possible changes in the material morphology with treatment (**Figure 4.17** and **Figure 4.18**). SAXS is frequently used to measure dimensions of phase-separated domains

in block copolymers and the long period between lamellar stacks, and lamellar thickness in semicrystalline polymers. Typical angular dimensions are 2θ less than 5°, corresponding to structural dimensions from 1-100 nm. In a 2-D SAXS pattern, PFCB/KF has three characteristic peaks, as shown in **Figure 4.16** and determined originally by May with the assistance of Zhang [62, 63]. The first peak at ~0.24 nm^{-1} (0.28 nm^{-1} for Na^+ or Cs^+ forms) corresponds to the PFCB block copolymer phase separation resulting in approximately a 25-40 nm distance between block phases. The second peak at ~0.8 nm^{-1} (0.82 nm^{-1} for Na^+ or Cs^+ forms) corresponds to the PVDF-HFP crystalline order resulting in an approximately 8 nm distance between crystalline features. The third and final peak at ~1.3 nm^{-1} (2.8 nm^{-1} for Na^+ or Cs^+ forms) corresponds to the ionic aggregates, resulting in approximately 2.4 nm between aggregates.

The SAXS profile provided in **Figure 4.17** is plotted on a linear scale and highlights the change in the PFCB block copolymer peak between the solvent-exchanged membrane and the treated membranes. The peak has a higher intensity for both treatments, although there is not a discernible difference between the two treatments. The increase in intensity implies an increase in phase separation between the two blocks that make up the PFCB copolymer. The SAXS profile provided in **Figure 4.18** is plotted on a logarithmic scale and highlights the change in the PVDF-HFP crystalline order peak. Although subtle, the peak becomes more prominent with increasing exposure. This implies that the PVDF-HFP had enough mobility during the different exposures to crystallize a small amount. Therefore, with increasing exposure time the material shows phase separation and increased PVDF-HFP crystalline order. This is consistent with the stress relaxation data in that increased phase separation and crystalline order would likely decrease chain mobility, delaying the relaxation mechanism of the material. Phase separation of the blocks in the PFCB ionomer would act to create physical crosslinks pinning molecules in

different block regions, thereby decreasing chain mobility and delaying the relaxation mechanism. Further increases in crystalline order, as observed with increasing exposure time, will result in a further delay in the stress relaxation mechanism, as observed with the PFCB/PVDF-HFP with 24 h 70^{o}C 55% RH exposure. In addition, the change in the block copolymer peak is consistent with the mass uptake and diffusion data, in that increasing exposure time does not have a large impact on the material. It is likely the block copolymer phase has approached an equilibrium morphology which affects the water sorption paths, resulting in similar mass uptake for both treatments.

This preliminary study provides some insight into how the membrane changes in an operating fuel cell. Based on work completed on a similar material, it is possible that phase separation will negatively influence the proton conductivity [47, 48]. Therefore, further work was completed to understand the full impact of this phase separation and increased crystalline order under standard fuel cell operating conditions, as discussed in the following sections.

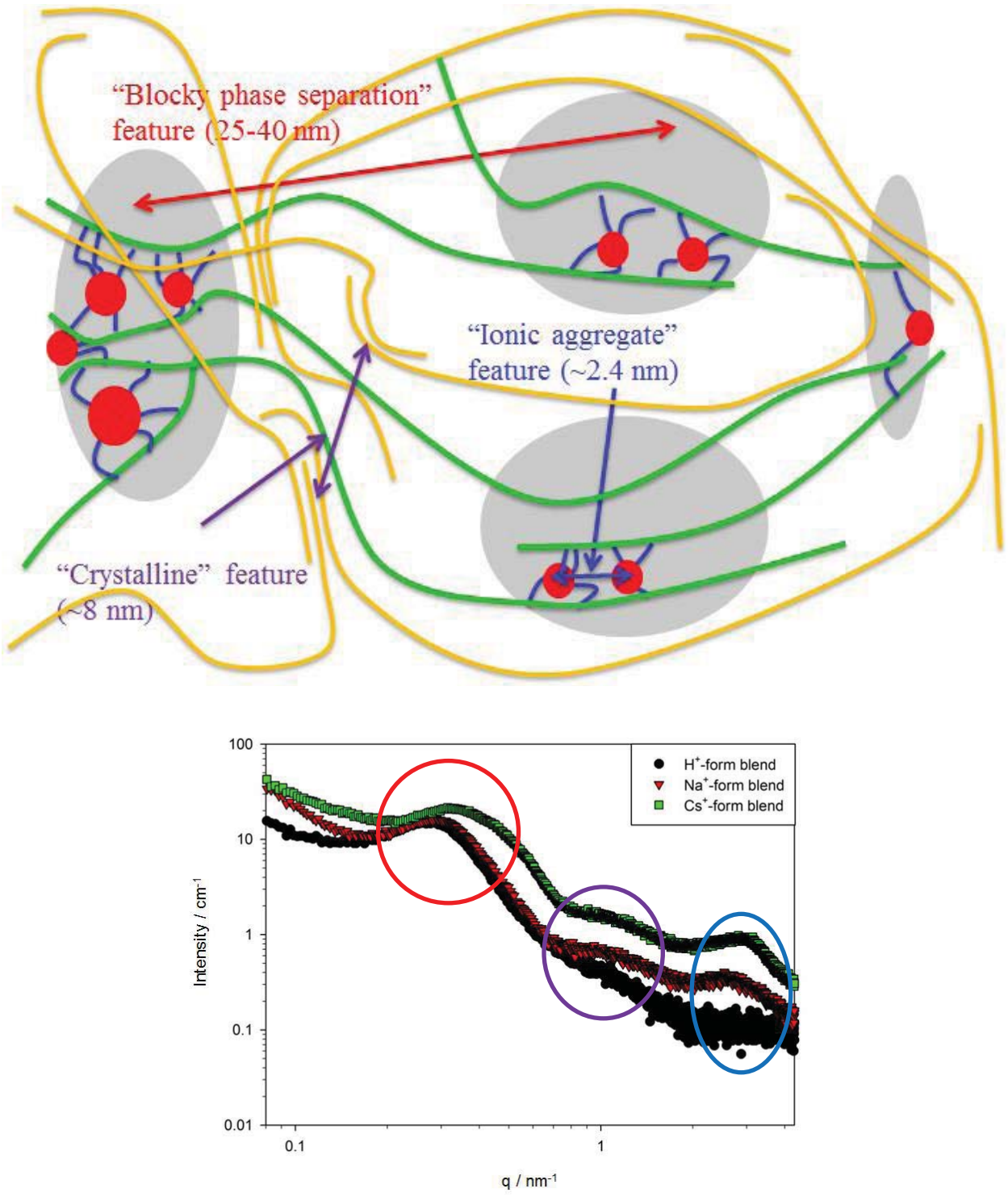

Figure 4.16. Schematic of possible PFCB/PVDF-HFP morphology, and corresponding SAXS profile [63].

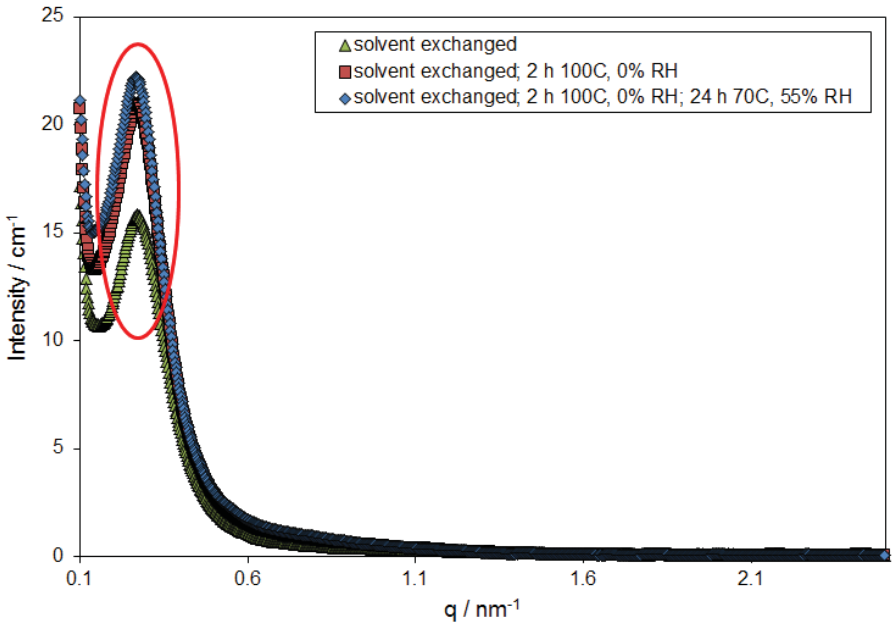

Figure 4.17. SAXS profiles of solvent exchanged membrane, a solvent exchanged membrane with a two hr isotherm at 100°C 0% RH, and a solvent exchanged membrane with a two hr isotherm at 100°C 0% RH with an additional 24 h 70°C 55% RH exposure, highlighting the PFCB copolymer phase peak.

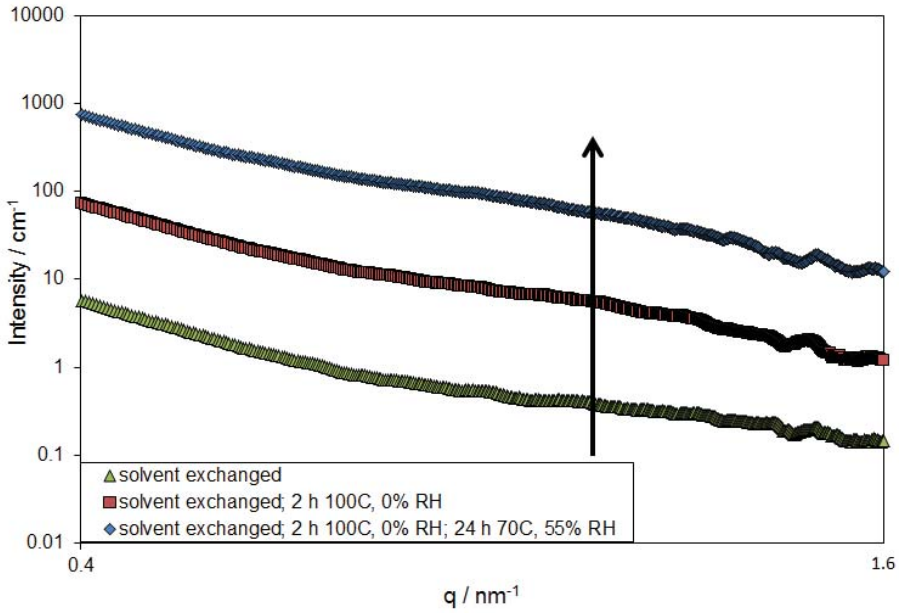

Figure 4.18. SAXS profiles of solvent exchanged membrane, a solvent exchanged membrane with a two hr isotherm at 100°C 0% RH, and a solvent exchanged membrane with a two hr isotherm at 100°C 0% RH with an additional 24 h 70°C 55% RH exposure, artificially shifted vertically, highlighting the Kynar Flex crystalline order peak.

4.3.2. Detailed Analysis of the Mechanical and Morphological Properties of PFCB/PVDF-HFP Membranes after Exposure to Fuel Cell Operating Conditions

Due to the implications of the preliminary analysis, a more in-depth study was completed. To emulate fuel cell operating conditions, two temperatures (30 and 80°C), four moisture levels (0, 5, 80% RH, and immersed in DI water) and three different lengths of time (1 hr, 24 hr, and 1 wk) were used to condition PFCB/PVDF-HFP samples. After conditioning, samples were stored in air and water tight containers until testing could be completed. All samples were conditioned in the form required for testing, e.g. DMA samples were cut using the rule die prior to conditioning, to reduce handling after environmental exposure. This was done because it has been noted previously that samples appear to become embrittled and difficult to handle after exposure at high temperature and moisture conditions.

4.3.2.1. Linear Viscoelastic Constitutive Properties.

Stress relaxation was measured for all conditioned samples and compared against a baseline material which had only been through the solvent exchange process. Thermal master curves referenced to 80°C and the corresponding shift factors for materials conditioned at 30°C are provided in **Figure 4.19** and for materials conditioned at 80°C in **Figure 4.20**. Materials conditioned at all RH levels at 30°C do not show any discernible difference from the baseline material, however the samples exposed to immersed conditions show a stiffening over a short time scale, but a delay in the relaxation mechanism over the larger time scale, similar to what was seen in **Figure 4.11**. In addition, the shift factors appear to agree well with the baseline material from about 50-100°C, but at lower and higher temperatures the shift factors begin to fan out. The change in shift factor at lower temperatures could be due to the release of wrinkles in samples, and therefore may not be real, while the change in shift factor at high temperatures

could be due to reaching instrument limitations, and thus may not be real. If only the shift factors from 50-100°C are considered, then all materials conditioned at 30°C may have the same modulus temperature dependence.

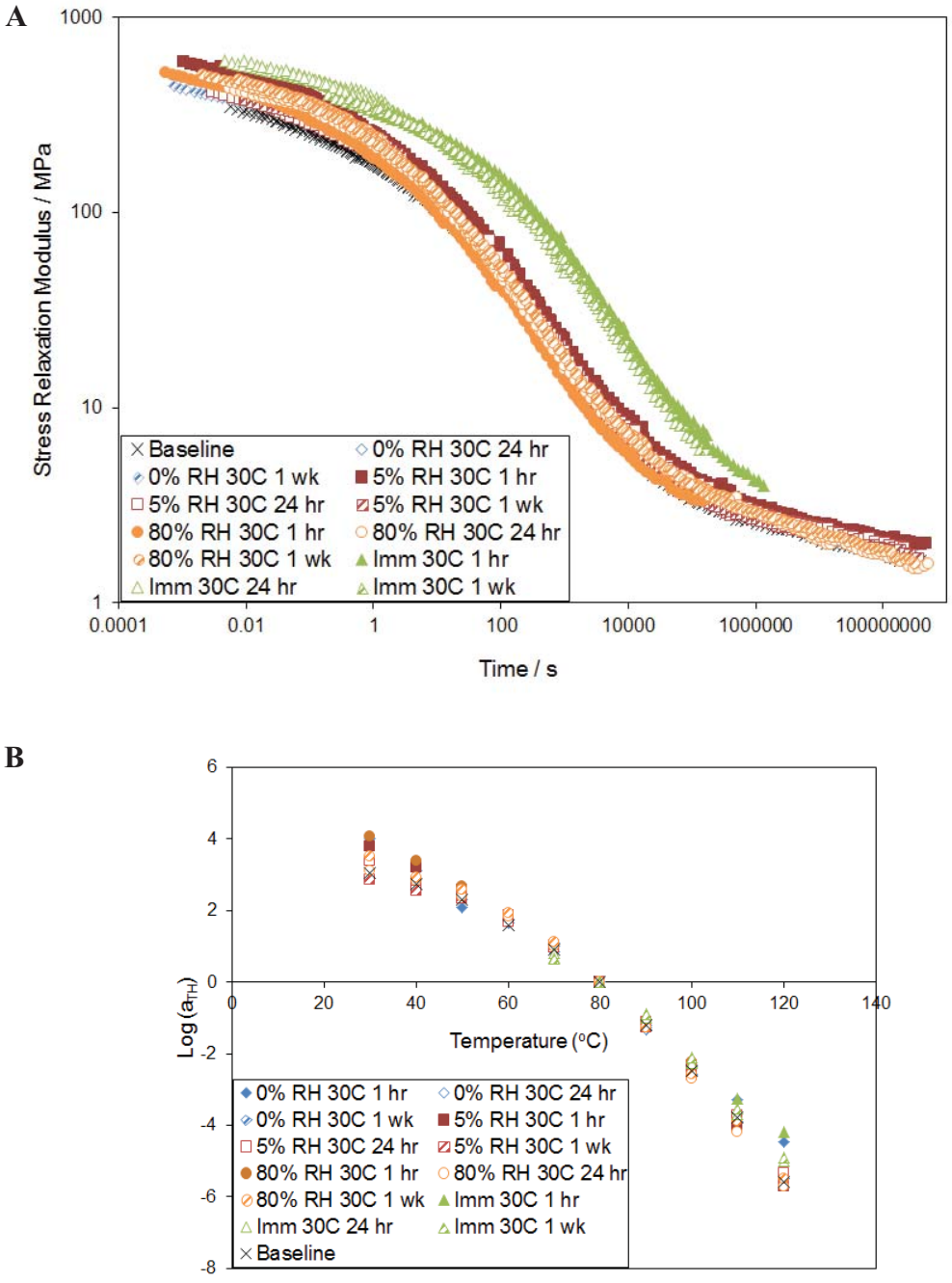

Figure 4.19. **(A)** Thermal stress relaxation master curves and **(B)** shift factors for PFCB/KF materials conditioned at 30°C.

It should be noted in **Figure 4.20** that the sample conditioned for 1 wk at 80°C immersed in DI water is not shown. This is because the immersed samples were wrinkled as well as delicate to handle; attempting to pull the wrinkles out prior to testing frequently resulted in breakage of these samples, and the sample conditioned for 1 wk never resulted in usable data. The materials conditioned at 0 and 5% RH align with the baseline material. The 80% RH and immersed samples begin to deviate with increased moisture and time of exposure. Therefore, as compared with the materials conditioned at 30°C, the higher temperature appears to increase the stiffness or delay the relaxation mechanism further for materials at high moisture conditions, implying the increased temperature and moisture condition allow for more polymer chain reorganization. Analysis of the shift factors shows good agreement between the baseline and all conditioned materials, except for the immersed samples, implying environmental conditioning does not change the temperature dependence of the moduli of the PFCB/PVDF-HFP material except when immersed. The immersed samples show a strikingly different shift factor pattern, and a large decrease in the temperature dependence of these materials. It is possible this change in the shift factors would indicate a change in the morphology of the material when immersed at 80°C and therefore rendering the TTMSP inapplicable for this material. However, long term creep data collected at 70°C and presented in **Section 2.3.3.4** shows excellent agreement with the TTMSP for immersed samples over 218 days. Therefore, it is more likely this large change in the shift factors is due to wrinkles in the sample convoluting the stress relaxation data. While it is expected for a delay to occur in the stress relaxation mechanism, a change in the shift factors is not, and it may not be possible to obtain valid stress relaxation data on samples immersed at 80°C. For discussion purposes, the delay in relaxation will be examined further in the following sections; despite the possibility the data may not be valid.

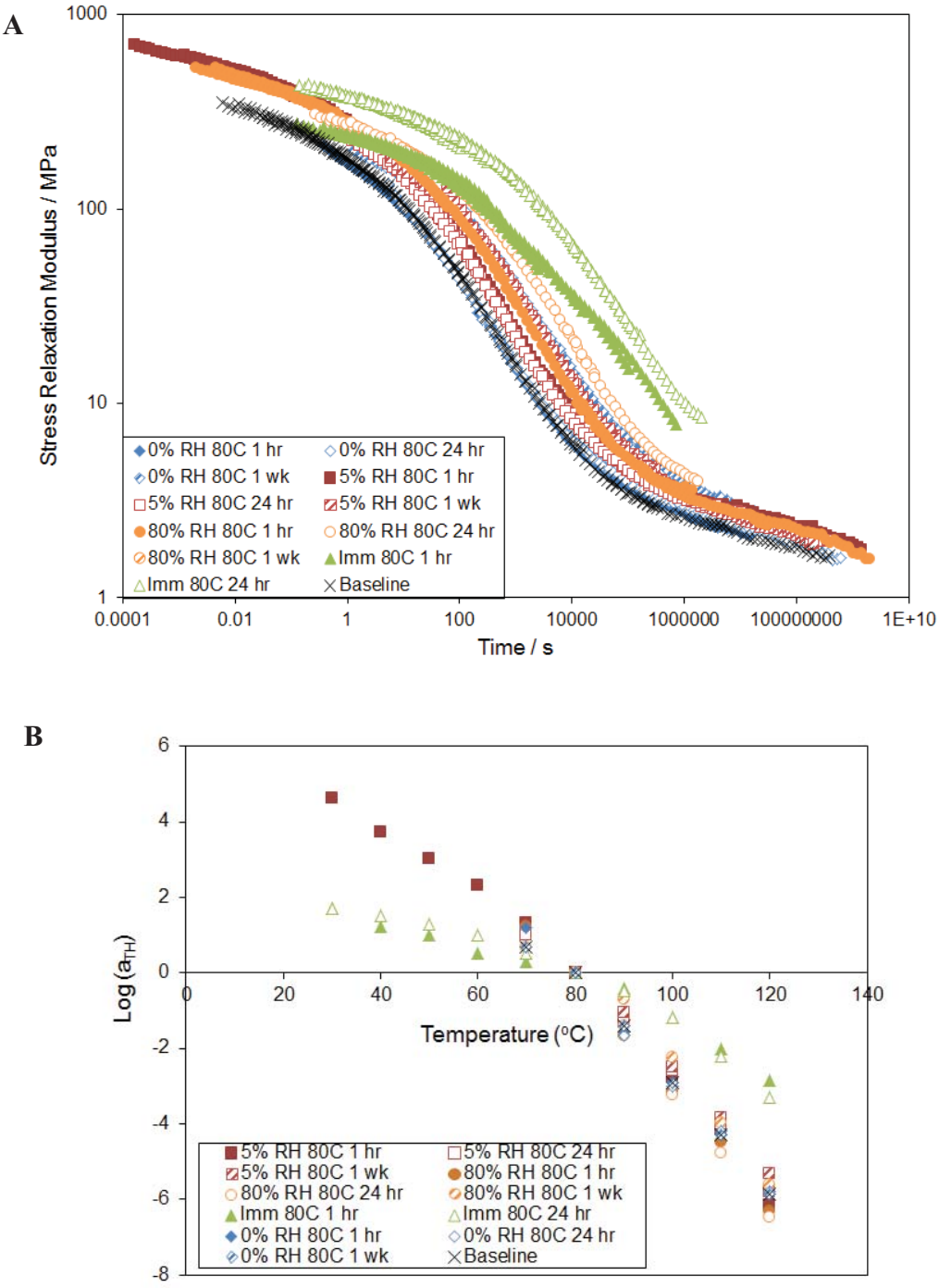

Figure 4.20. **(A)** Thermal stress relaxation master curves and **(B)** shift factors for PFCB/KF materials conditioned at 80°C.

4.3.2.2. Biaxial Strength

Pressure-loaded blister testing was performed for all conditioned samples and the strength at failure was compared with the baseline solvent exchanged material. Because a constant ramp rate was used during testing, despite the changes in modulus noted in **Section 4.3.2.1**., testing was completed with 0.1-5 kPa ramp rates to see if corrections would need to be applied to the strength at burst calculations. As seen in **Figure 4.21**, for both the pressure at burst and the strength at burst, there is a slight downward trend with decreasing ramp rates. However, this trend is not as severe as noted previously in NRE 211 [64]. This difference can be understood if the stress relaxation hygrothermal master curves are examined over the time frame used during blister testing, as shown in **Figure 4.22**, it is clear that the PFCB/PVDF-HFP material is further into the glassy plateau region compared to NRE 211. Therefore, we would not expect to see a very defined decreasing trend with decreasing ramp rates vs. time, as the modulus is barely changing over this time period. Thus, it was decided that a correction factor was unnecessary to modify the strength for differently conditioned materials.

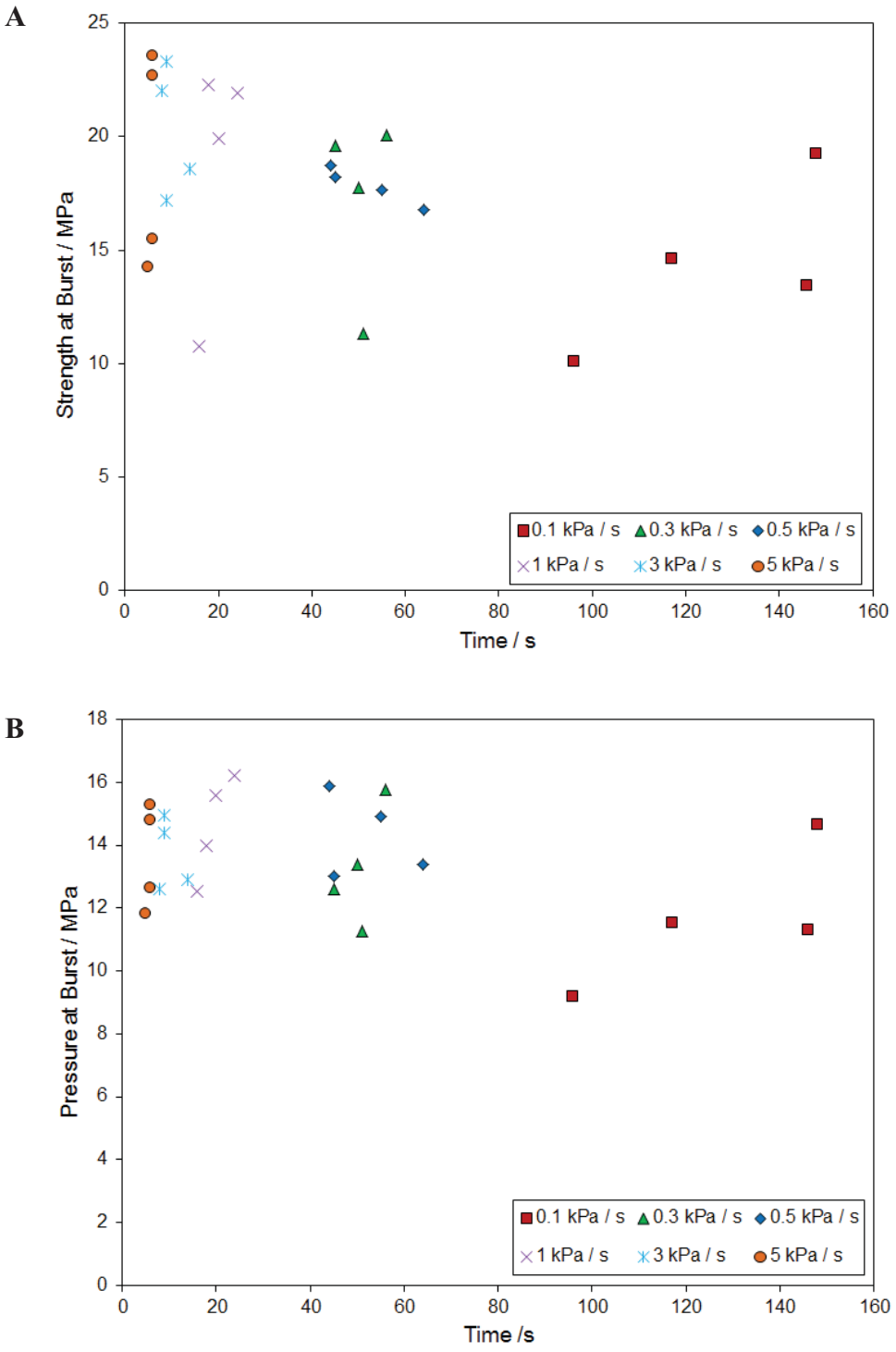

Figure 4.21. **(A)** Pressure and **(B)** strength at burst taken at different ramp rates for PFCB/PVDF-HFP solvent exchanged material.

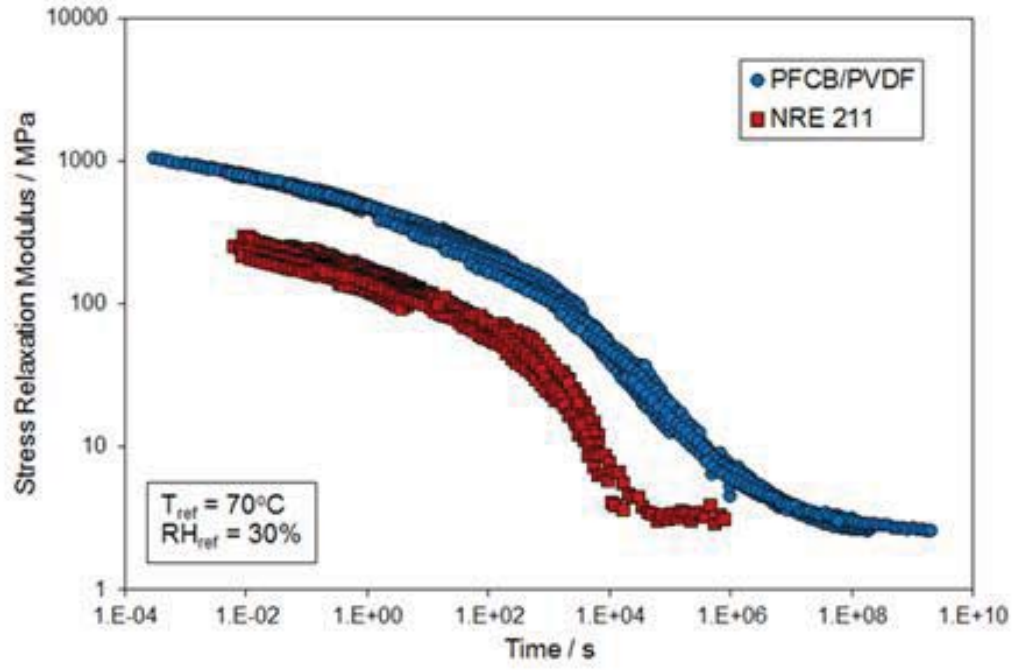

Figure 4.22. Stress relaxation hygrothermal master curves for PFCB/PVDF-HFP and NRE 211.

Typical pressure profiles for the pressure-loaded blisters are provided in **Figure 4.23** for the materials conditioned at 80% RH and 30°C. This condition was merely chosen as an example; all other environmental conditions show similar pressure profiles. It was noted that all samples failed via pinhole formation rather than blister rupture. If the pressure profile is examined, it appears the pressure was building for the initial 30 seconds, and shortly thereafter the pressure would peak and decrease. After approximately 75 seconds the pressure would begin to build again, likely because the pressure behind the blister overcame the pressure loss due to the pinhole formation. It is thusly assumed the pinhole formed at the maximum of the pressure profile, which was then taken as the failure of the blister, and t_b was therefore assigned the corresponding time at the maximum of the pressure profile.

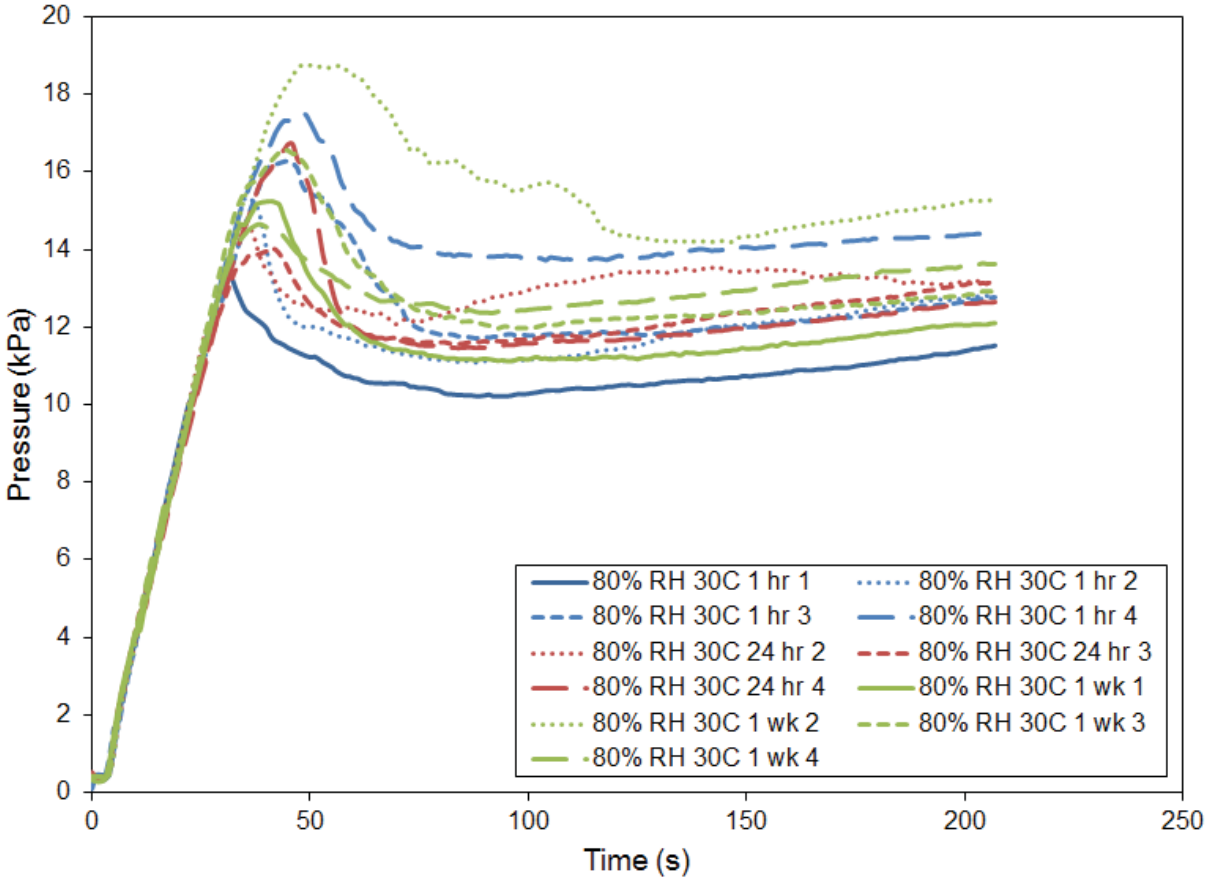

Figure 4.23. Typical blister pressure profiles for PFCB/PVDF-HFP, example shown for materials conditioned at 80% RH and 30°C.

The calculated strength at failure of all conditioned samples is provided in **Figure 4.24**, with the baseline shown as a gray line behind the data sets. Solid bars correspond to samples conditioned at 30°C, and crosshatched bars refer to samples conditioned at 80°C. The most notable deviations from the baseline are the immersed 30°C 24 hr and 1 wk samples, as well as all three immersed 80°C samples. The immersed samples at 30°C agree well with the baseline at 1 hr, but show an increase in strength at failure at longer times. In addition, the immersed samples at 80°C show much greater biaxial strength than the baseline at 1 and 24 hrs, but the

biaxial strength decreases significantly after 1 wk. The increase in burst strength of the immersed 30°C and 80°C samples could correspond well with the delay in the relaxation of the material seen in **Figure 4.19** and **Figure 4.20**. If the material is stiffer over the time at burst than the other conditioned materials, this could result in a higher strength at burst. In addition, it should be noted that the samples immersed at 80°C showed the least deformation during the blister test, implying the samples were indeed stiffer. However, the large decrease noted in the samples conditioned for 1 week at 80°C immersed in DI water implies the sample became brittle, rather than gaining strength from an increased modulus compared to the other conditioned samples. This behavior will be discussed further in reference to the SAXS data presented below.

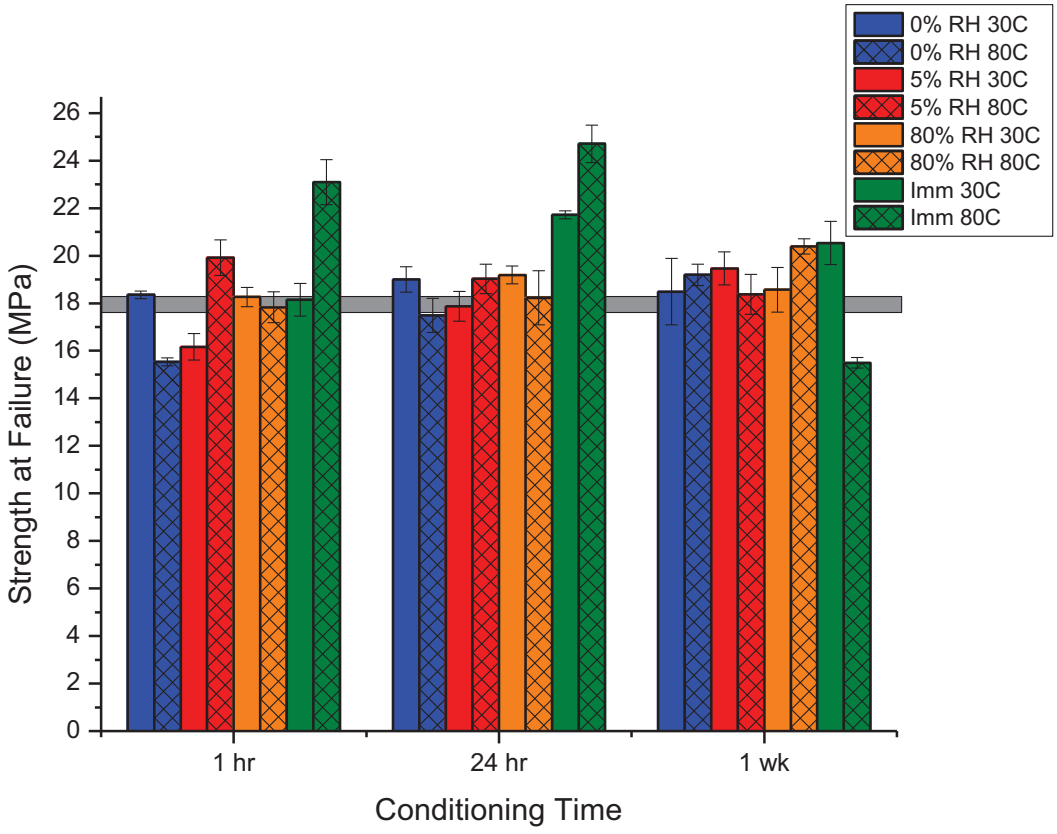

Figure 4.24. Strength at failure of PFCB/PVDF-HFP conditioned in multiple environments over different lengths of time.

Examination of the pinhole failures was performed to understand if failure was defect-driven or not. The optical micrographs provided in **Figure 4.25** for several pinholes shows a wide variety of failure sizes, but almost all formed as triangular shapes appearing to begin at the location of a defect in the membrane. These defects arose in the membrane during casting on polypropylene coated paper, as the membrane took on the texture of the casting substrate. The white portions seen in some of the images are due to light bouncing off of the membrane, and are not due to strain crystallization. In addition, it should be noted that these holes are quite large, much larger than would normally be classified as a pinhole. It is possible a small hole formed initially in a blister and as the pressure increased the hole grew in size over time. Many blisters also showed multiple failure points, implying a maximum pressure was reached at multiple defect points in the sample, resulting in simultaneous failure in multiple areas.

A couple of pinholes observed under optical microscopy appeared to be membrane failure rather than defect-driven failure (5% RH 80°C 1 wk, immersed at 80°C 24 hr, and 0.3 kPa ramp rate), therefore one defect-driven failure and one possible membrane failure were examined further under scanning electron microscopy (SEM). The two samples chosen for further examination were 80% RH at 30°C for 24 hr, and immersed at 80°C for 24 hrs, as shown in **Figure 4.26**. Although the sample immersed at 80°C for 24 hrs appears to be membrane failure under optical microscopy, there is clearly a defect on the surface under SEM. It can also be seen on the other side of the opening where the shape of the defect aligns, implying this too was a defect-driven failure. It is worth noting that in both samples the fracture edges are rough indicating ductile failure rather than brittle. Therefore, although the immersed at 80°C samples seem to be embrittled during handling, these materials still maintain toughness despite the

increased modulus. It is thusly possible that a defect free material would have a higher biaxial strength, as removing these stress concentrations would allow for a pure material failure.

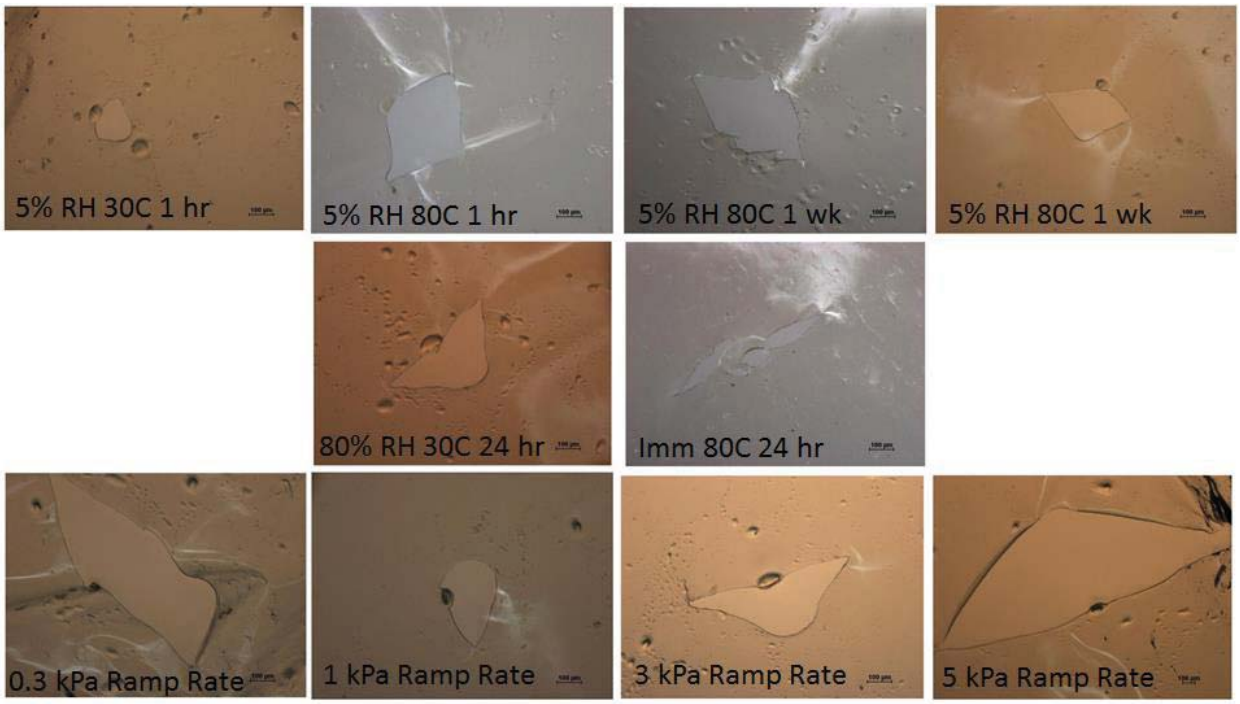

Figure 4.25. Optical micrographs of pinhole failures in blister samples, environmental or test conditions as labeled in the figure.

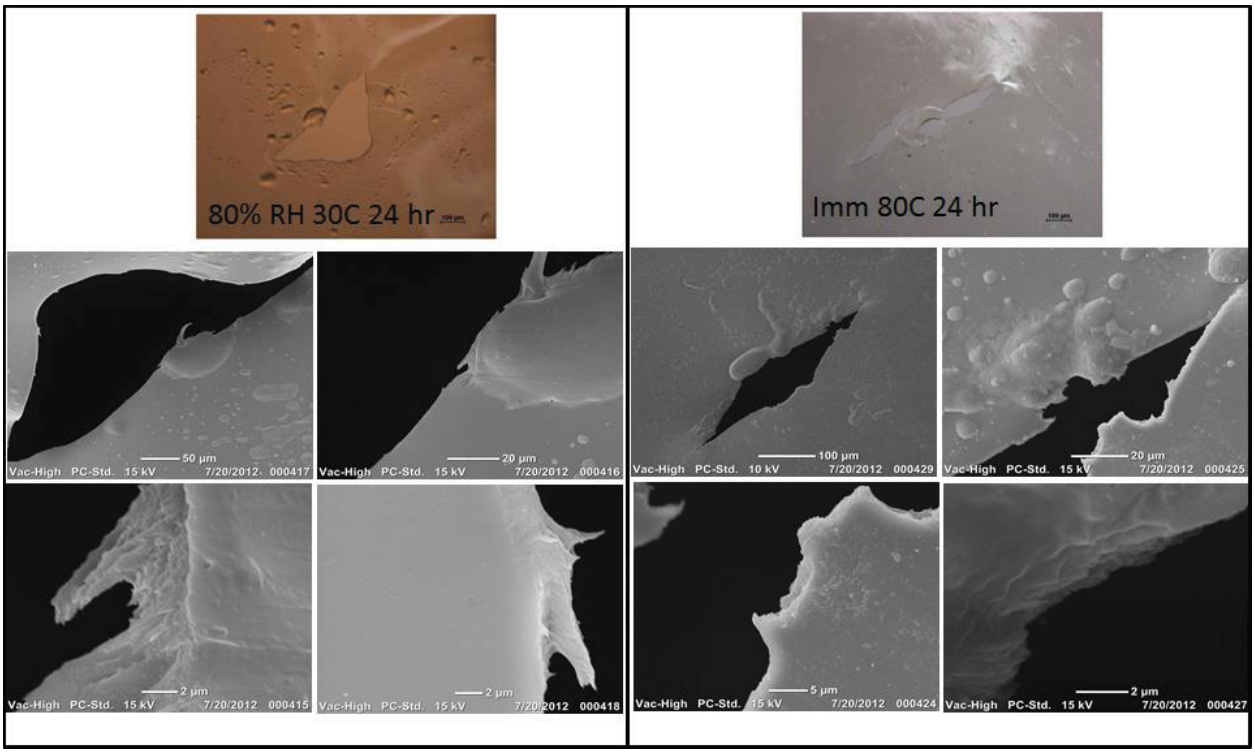

Figure 4.26. SEM images of blister pinhole failures, with sample conditioning as noted.

4.3.2.3. Proton Conductivity

To examine the required equilibration time at each temperature, proton conductivity measurements were performed at 5, 10, and 15 minutes from 30-95°C, as shown in **Figure 4.27**. It was noted that up to 70°C, the proton conductivity increases with increasing time and temperature, as observed with other proton conducting membranes. However, after 70°C the proton conductivity begins decreasing with increasing hold times and temperatures. Therefore, conductivity measurements were only performed to 80°C, and the sample was only equilibrated for 5 min at this temperature, as opposed to the 30 min used at lower temperatures. This reduction in conductivity noted at temperatures greater than 70°C will be investigated further in the detailed immersion study discussed in **Section 4.4**.

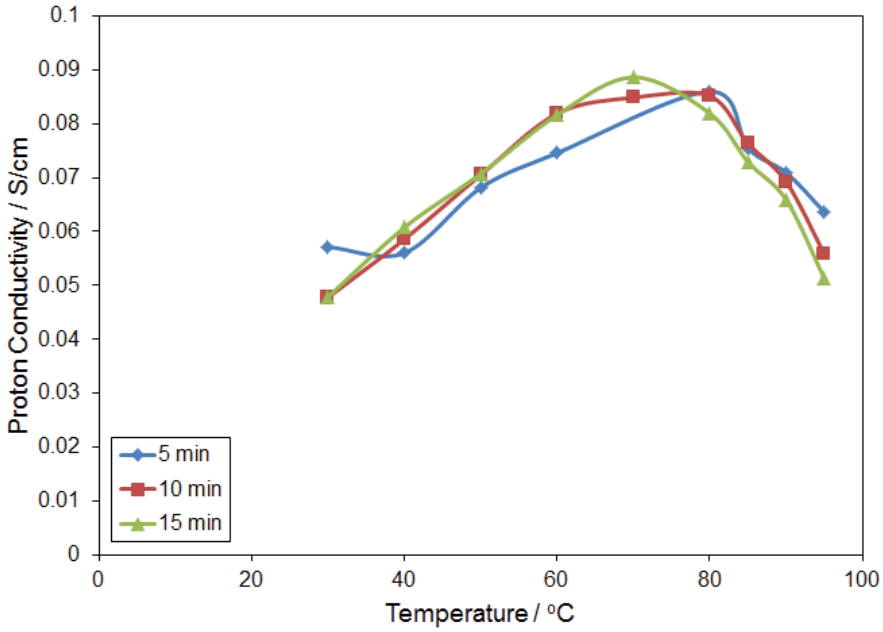

Figure 4.27. Proton conductivity measured at 5, 10, and 15 min from 30-95°C.

Proton conductivity measurements of PFCB/PVDF-HFP materials conditioned in different environments are provided in **Figure 4.28A-D.** The black stars represent the PFCB/PVDF-HFP solvent exchanged baseline measurement, and the black X's represent the NRE 211 measurement. It should be noted that NRE 211 is twice as thick as PFCB/PVDF-HFP, and therefore based on the thickness, these two materials do have similar proton conductivities, despite what appears to be a large difference in **Figure 4.28A-D**. The samples conditioned at 0% RH 30 and 80°C, 5% RH 30 and 80°C, and 80% RH 30°C generally agree well with the baseline conductivity measurement. Both the 0% and 5% RH 80°C 1 wk samples the conductivity decreased below the baseline over the entire temperature range. The 80% 80°C sample showed a decrease in conductivity at low temperatures. Finally, the samples conditioned immersed in DI water show a decrease in conductivity over the entire temperature range, and a severe reduction in conductivity when conditioned at 80°C, even after only one hour of conditioning. This severe

decrease with immersion at 80°C could be problematic during fuel cell operation, as the cathode is typically flooded due to electro-osmotic drag, and the membrane could easily see this environmental condition during operation.

A

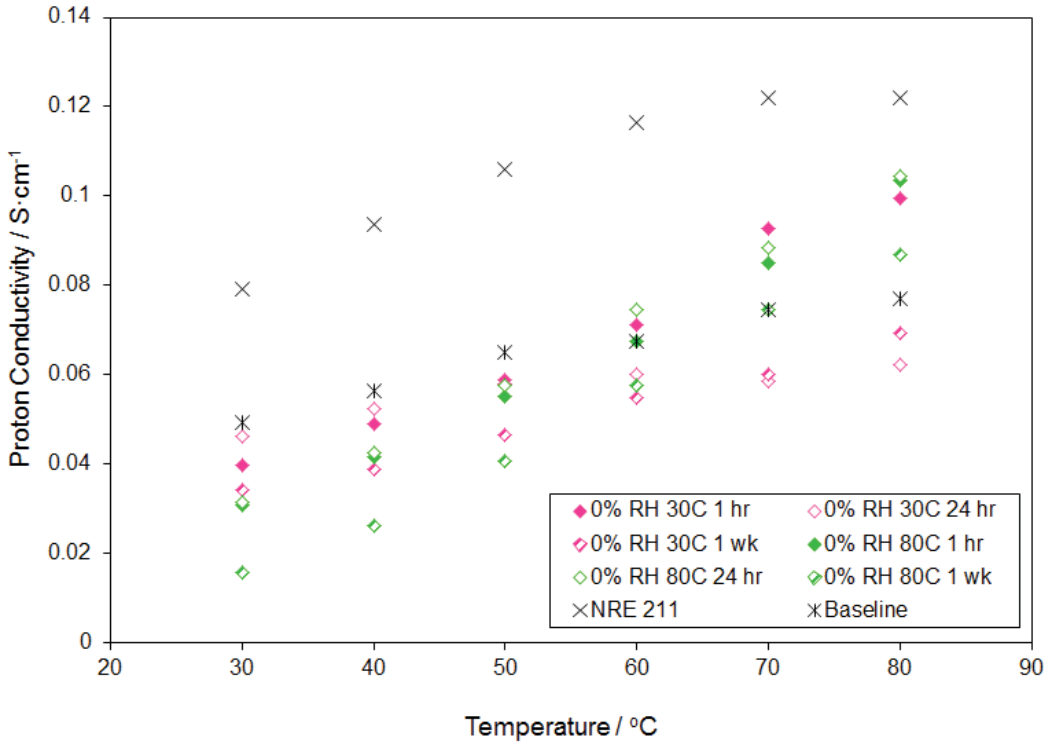
Proton Conductivity / S·cm-1
0.14
0.12
0.1
0.08
0.06
0.04
0.02
0
20
30
40
50
60
70
80
90
Temperature / °C
0% RH 30C 1 hr
0% RH 30C 24 hr
0% RH 30C 1 wk
0% RH 80C 1 hr
0% RH 80C 24 hr
0% RH 80C 1 wk
NRE 211
Baseline

B

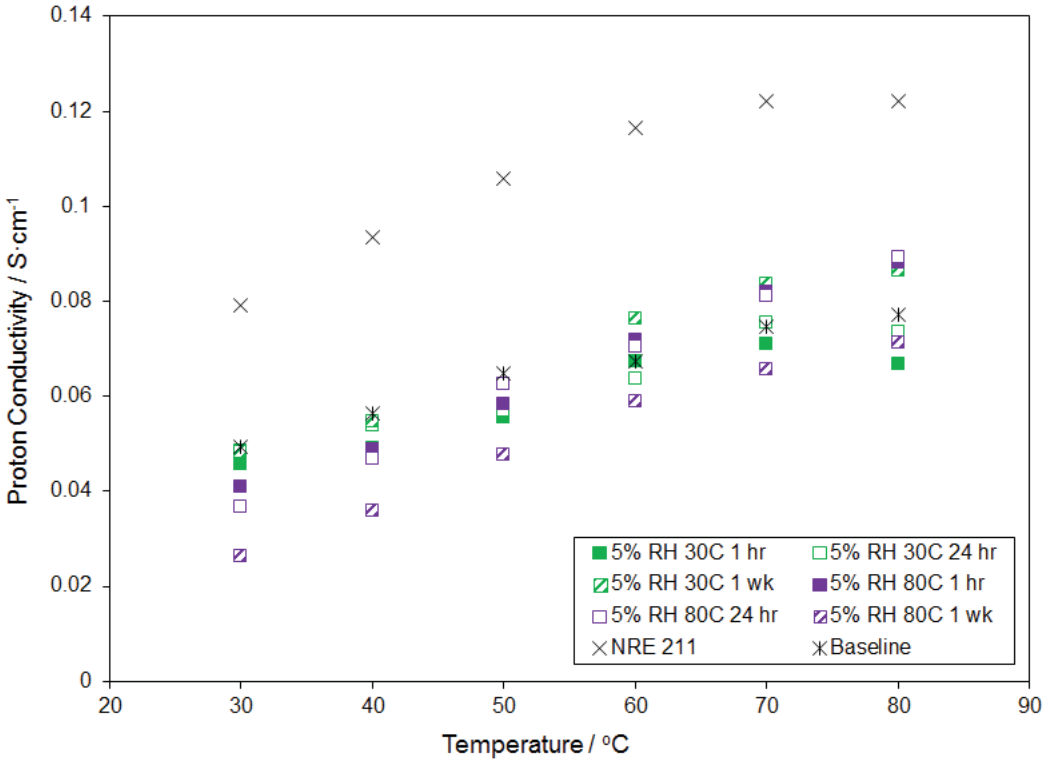
Proton Conductivity / S·cm-1
0.14
0.12
0.1
0.08
0.06
0.04
0.02
0
20
30
40
50
60
70
80
90
Temperature / °C
5% RH 30C 1 hr
5% RH 30C 24 hr
5% RH 30C 1 wk
5% RH 80C 1 hr
5% RH 80C 24 hr
5% RH 80C 1 wk
NRE 211
Baseline

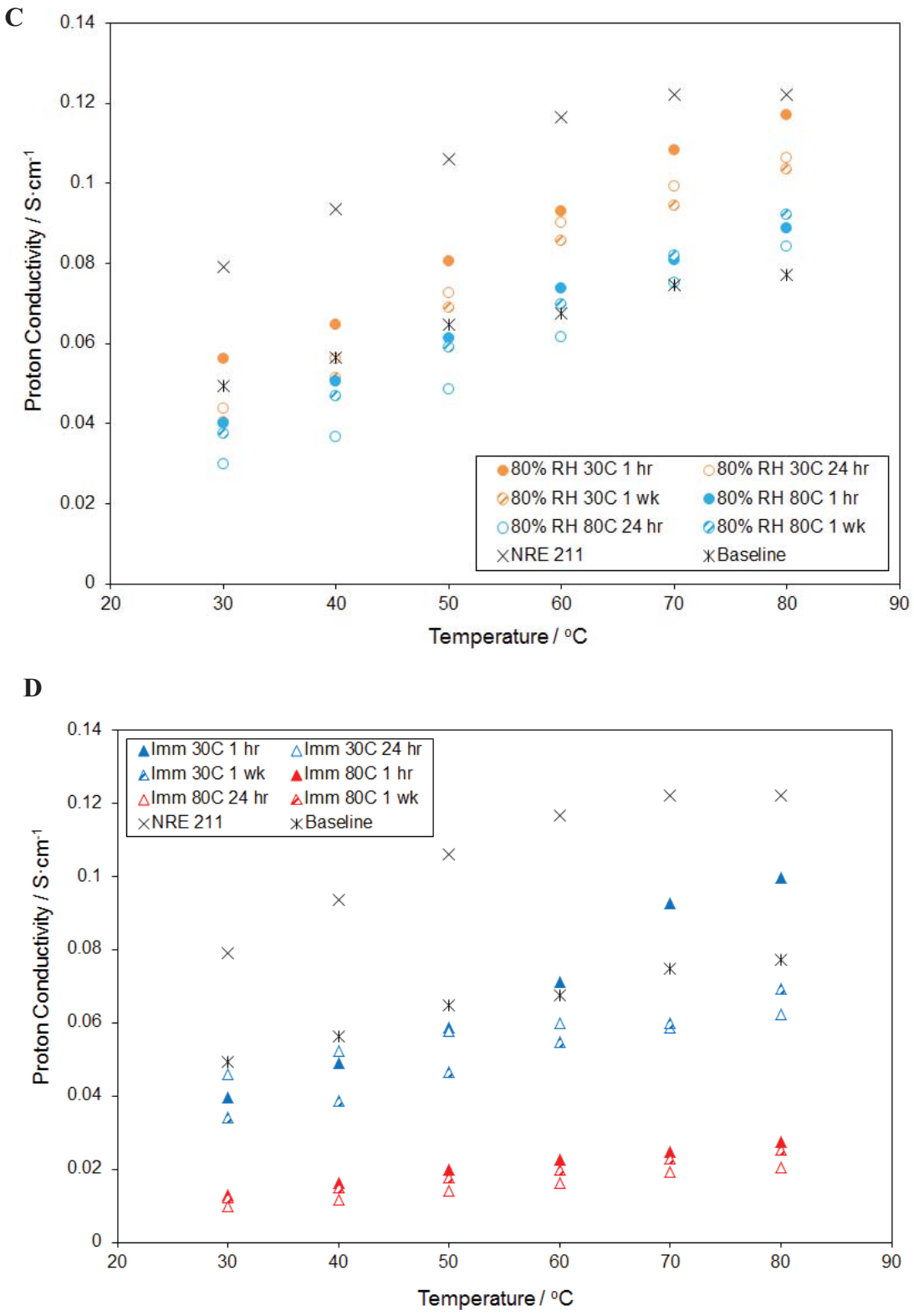

Figure 4.28. Proton conductivity of samples conditioned at **(A)** 0% RH, **(B)** 5% RH, **(C)** 80% RH, and **(D)** Immersed in DI water.

4.3.2.4. SAXS

To help gain understanding of why the relaxation modulus, biaxial strength, and proton conductivity change with environmental exposure, SAXS was performed. In this study, acid form PFCB/PVDF-HFP was used to examine the blocky phase separation of the PFCB block copolymer in conditioned samples (**Figure 4.29A** and **B**), while Na^+ form was used to examine the PVDF-HFP crystalline order and the PFCB ionic aggregates in conditioned samples (**Figure 4.30A** and **B**). The Na^+ form membrane was used because May had previously shown that contrast was increased as compared to the H^+ form, allowing for easier observation of the PVDF crystalline order and ionic aggregate peaks. Unfortunately the ionic peak is still difficult to observe in these scans, and as such discussion will focus on the block copolymer phase separation peak, and the PVDF crystalline order peak.

Comparing the block copolymer phase separation peak of samples conditioned at 30°C with the baseline shows no change. In addition, examination of the PVDF-HFP crystalline order peak for samples conditioned at 30°C also shows no change, indicating that even at very high water contents, the degree of phase separation an crystalline order does not change at low temperatures. However, when the block copolymer phase separation peak of samples conditioned at 80°C is examined, it is clear the peak shifts to lower q at 80% RH and immersed conditions. In addition, as the conditioning time is increased and the moisture content increased, the peak shifts to lower q. Furthermore, the PVDF-HFP crystalline order peak also shifts to lower q for samples conditioned at 80% RH and immersed in DI water, shifting further with increased conditioning time and moisture content. This indicates that at high temperature and water content the degree of phase separation of the block copolymer and crystalline order increases.

This is consistent with the stress relaxation data, in that increased block copolymer phase separation and increased crystalline order would pin molecules in different domains, causing restricted chain motion, resulting in a delay in the relaxation mechanism. This data could also be considered consistent with the biaxial strength data, as increased phase separation and crystalline order could result in higher strength materials. This would occur due to increased entanglements in the material, which would require higher forces to cause chain disentanglement corresponding with material failure. However, if the phase separation and crystalline order were increased further, as in the sample immersed at 80°C for 1 wk, it is plausible that chains would no longer easily disentangle, resulting in embrittlement of the material and a decrease in the material strength. Therefore, increased mobility at high temperatures and high water contents could eventually result in a decrease in material strength, and thus a reduction in the mechanical lifetime of the material.

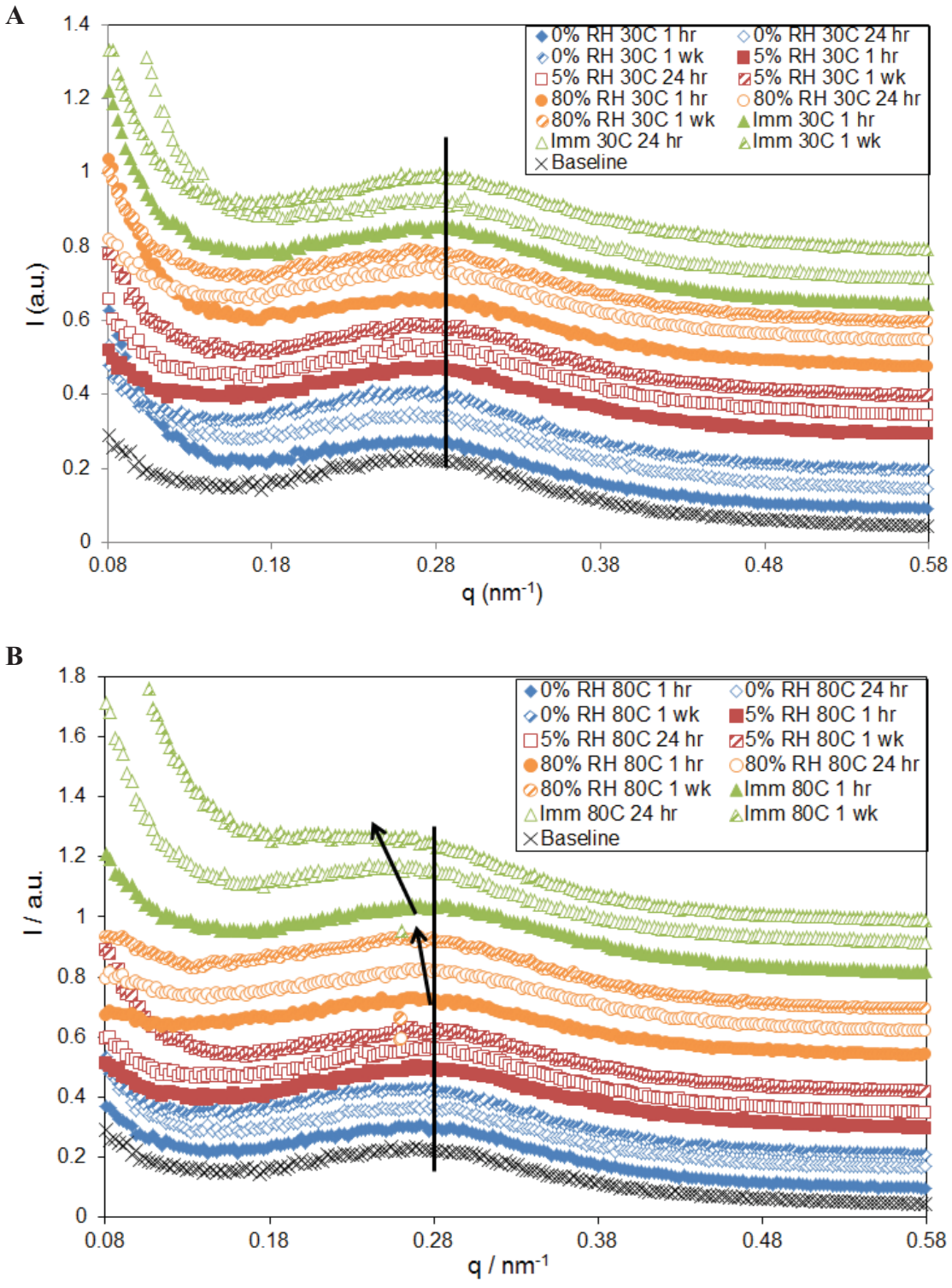

Figure 4.29. SAXS profiles of H^+ form PFCB/KF samples conditioned at **(A)** 30°C and **(B)** 80°C.

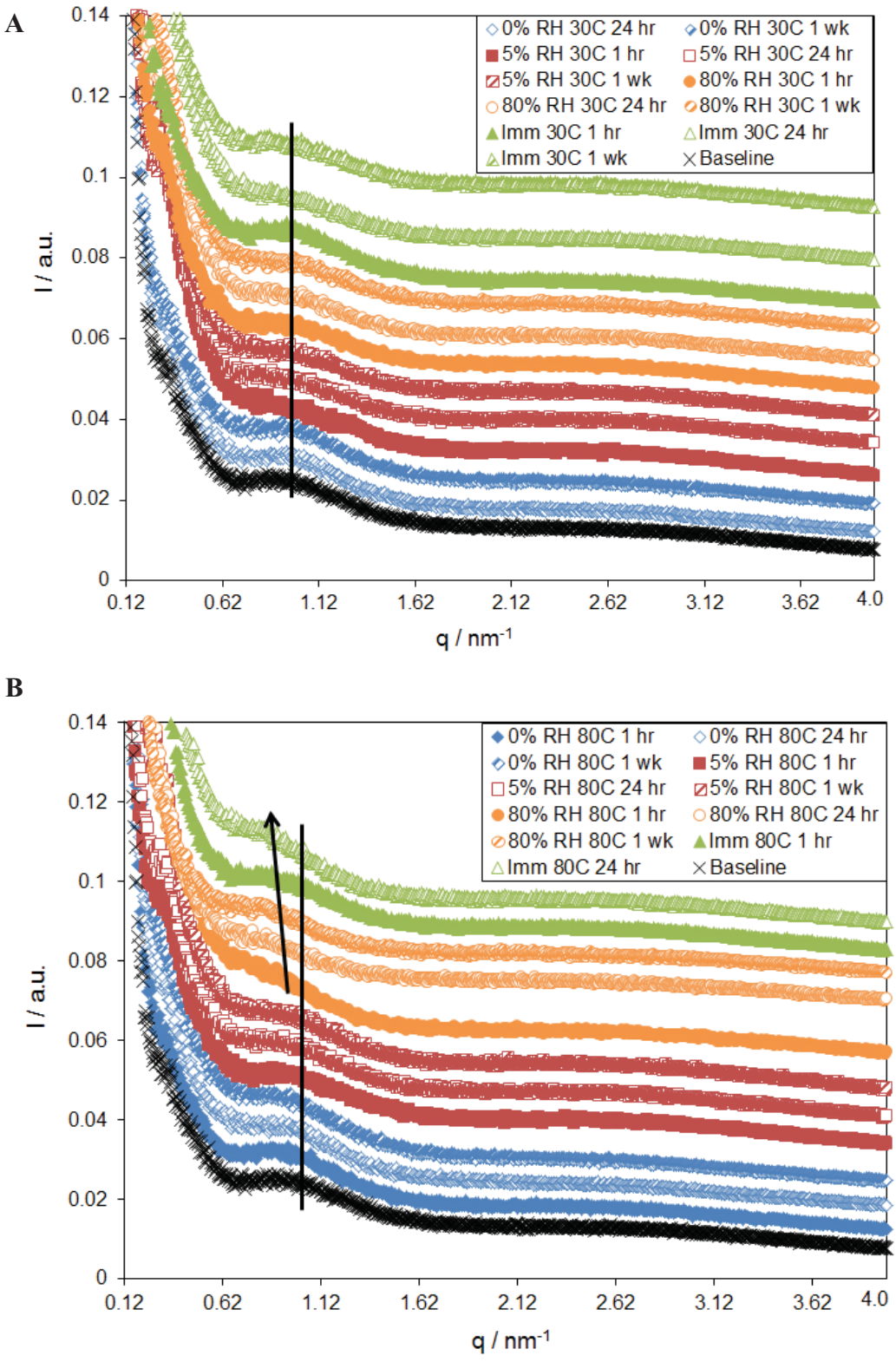

Figure 4.30. SAXS profiles of Na^+ form PFCB/KF samples conditioned at **(A)** 30°C and **(B)** 80°C.

4.3.2.5. Infrared Spectroscopy

Infrared spectroscopy was also performed to gain further understanding of molecular arrangements with different environmental exposures. The full spectrum scan performed using ATR-IR is provided in **Figure 4.31**. In addition to the PFCB/PVDF-HFP blend, scans of pure PVDF-HFP and pure sulfonated PFCB were also performed to help with the identification of peaks due solely to either component. Multiple peaks were identified, as noted in **Figure 4.31**, however only one was identified as being solely due to PVDF-HFP, a γ-form crystalline stretch, highlighted at approximately 880 Hz [65, 66]. Two peaks were identified as being solely due to the PFCB blend component, one at approximately 900 Hz corresponding to the ether linkage, and one at approximately 1055 Hz corresponding to the sulfonate group.

When all three peaks were examined, only the sulfonate stretch showed a notable change, as highlighted in **Figure 4.32**. A shift to higher frequencies is observed only for samples conditioned at 80°C immersed in DI water, with a similar shift noted for samples conditioned for increasing amounts of time. Scans were performed in both ATR and transmission mode, and the shift of the sulfonate peak is quite large under the transmission mode, implying this is a bulk material change, and not simply a surface effect. Based on work completed by Cable et al. on PFSA materials, it is believed this shift of the sulfonate peak to higher frequencies indicates the sulfonate group is now in a more polar environment [67]. The increased polar environment would correspond to tighter ionic aggregates, and less of a network throughout the membrane, which correlates well with the decrease in proton conductivity observed in samples aged at 80°C immersed in DI water. Therefore, the increased chain mobility at high temperatures and moisture contents not only results in a decrease in material strength over extended times, but also a decrease in proton conductivity, reducing fuel cell efficiency and lifetime.

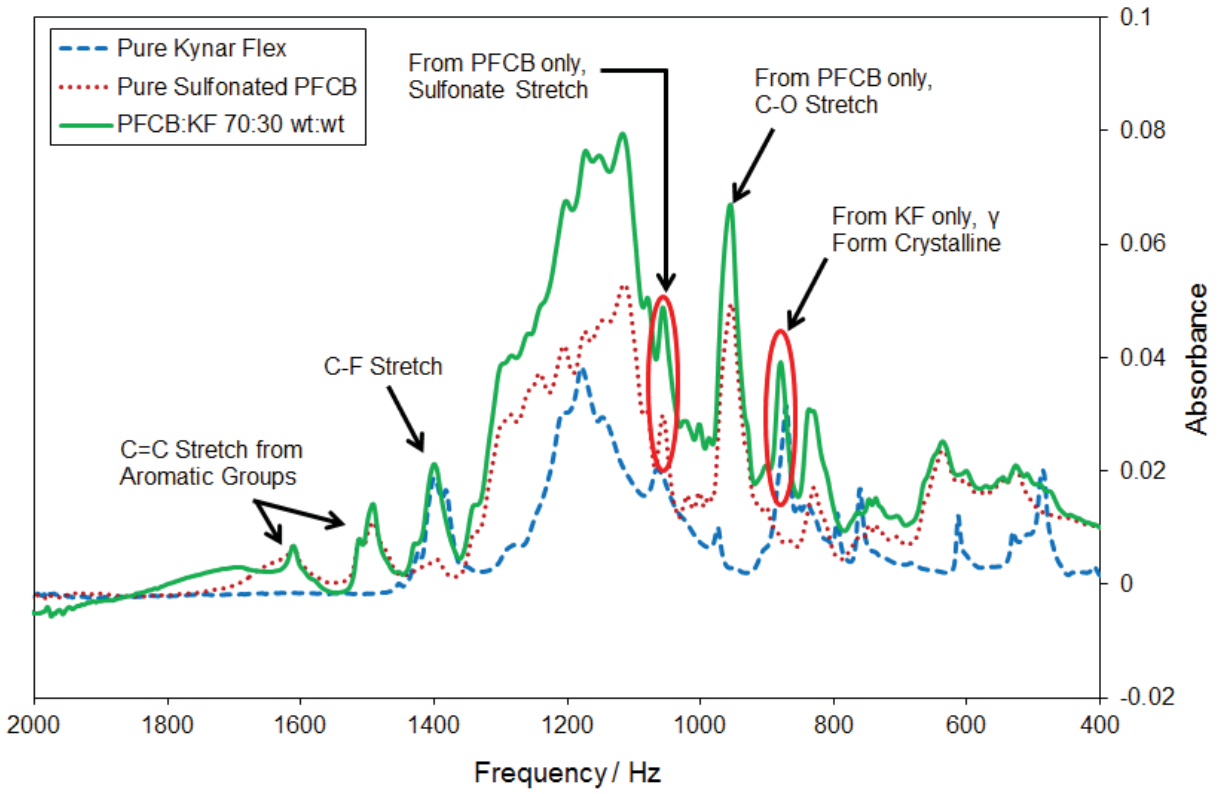

Figure 4.31. ATR scan of pure kynar flex, pure sulfonated PFCB, and solvent exchanged PFCB/KF.

A

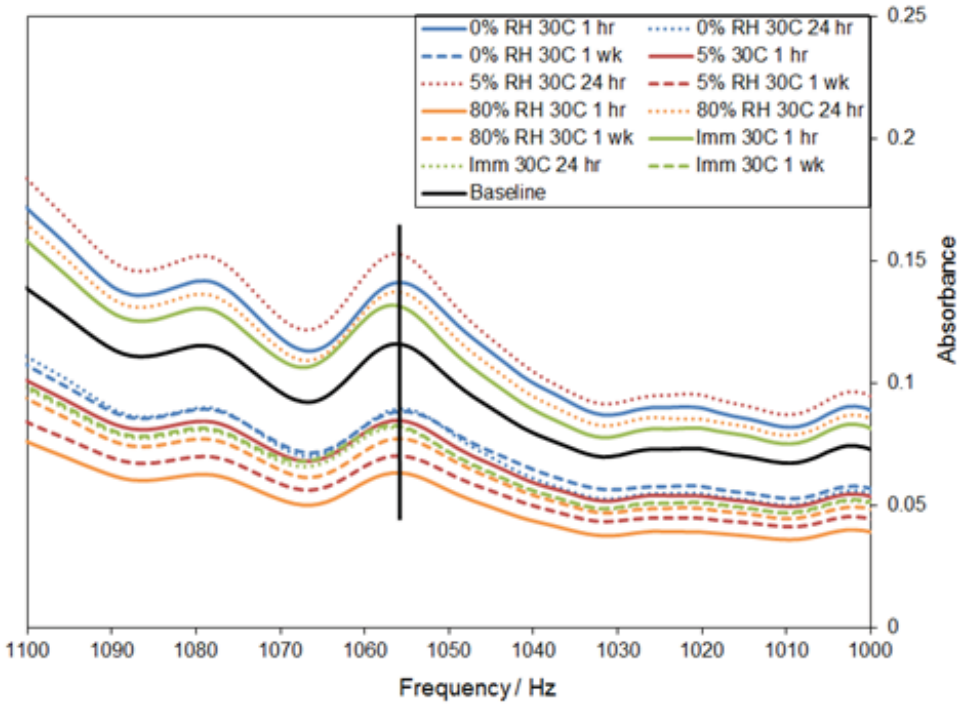
0% RH 30C 1 hr
0% RH 30C 24 hr
0% RH 30C 1 wk
5% 30C 1 hr
5% RH 30C 24 hr
5% RH 30C 1 wk
80% RH 30C 1 hr
80% RH 30C 24 hr
80% RH 30C 1 wk
Imm 30C 1 hr
Imm 30C 24 hr
Imm 30C 1 wk
Baseline
0.25
0.2
0.15
0.1
0.05
0
Absorbance
1100
1090
1080
1070
1060
1050
1040
1030
1020
1010
1000
Frequency / Hz

B

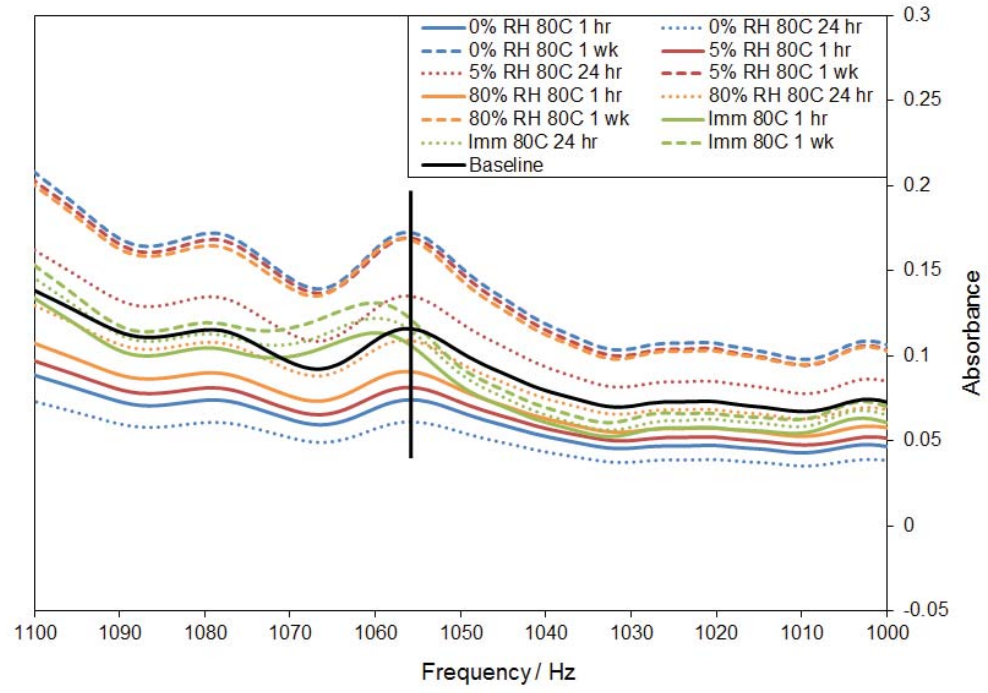
0% RH 80C 1 hr
0% RH 80C 24 hr
0% RH 80C 1 wk
5% RH 80C 1 hr
5% RH 80C 24 hr
5% RH 80C 1 wk
80% RH 80C 1 hr
80% RH 80C 24 hr
80% RH 80C 1 wk
Imm 80C 1 hr
Imm 80C 24 hr
Imm 80C 1 wk
Baseline
0.3
0.25
0.2
0.15
0.1
0.05
0
-0.05
Absorbance
1100
1090
1080
1070
1060
1050
1040
1030
1020
1010
1000
Frequency / Hz

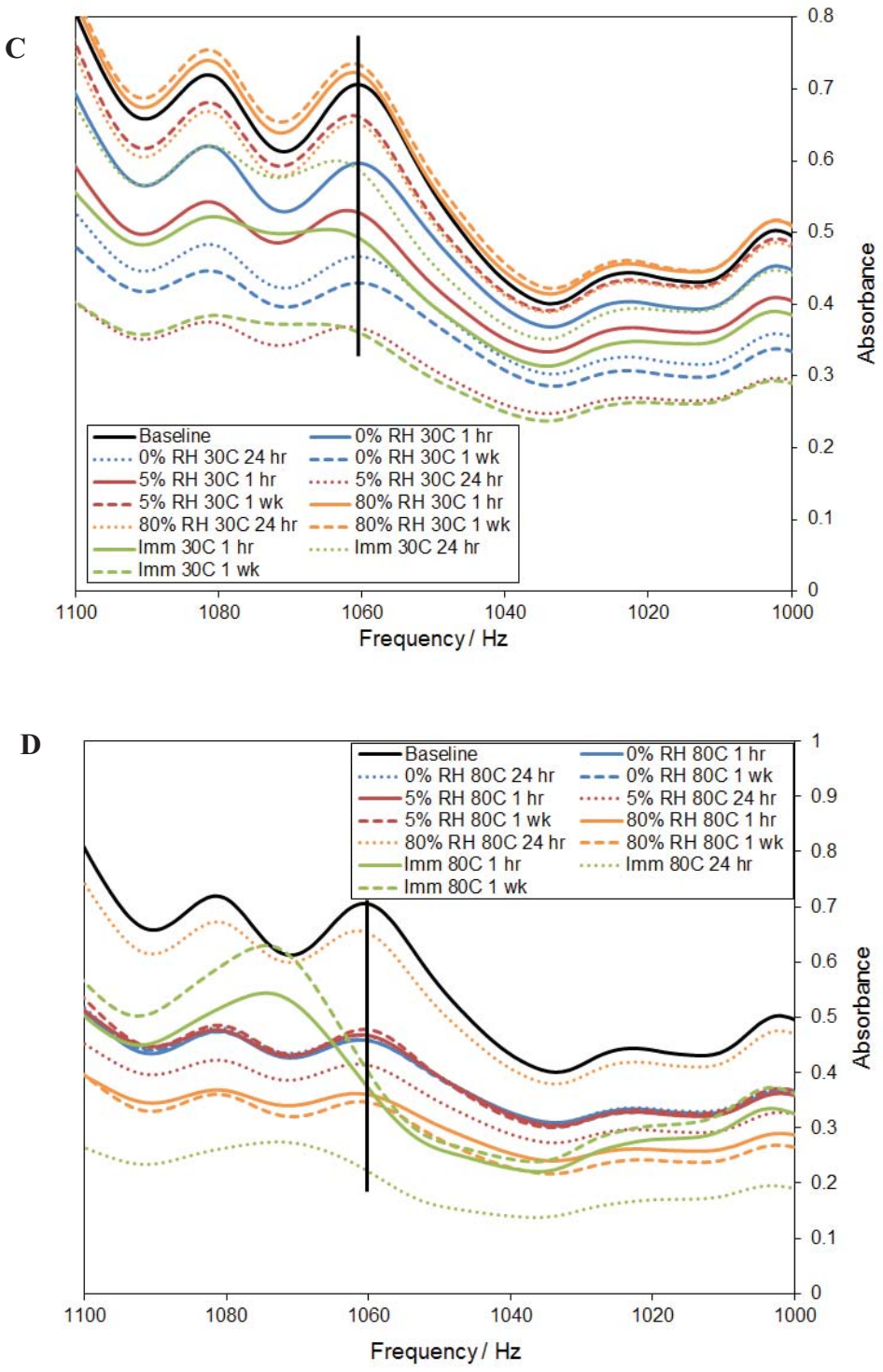

Figure 4.32. ATR IR of samples conditioned at **(A)** 30°C and **(B)** 80°C, and transmission IR of samples conditioned at **(C)** 30°C and **(D)** 80°C, focused on region highlighting the symmetric sulfonate stretch, showing the shift of this peak to higher frequency for samples conditioned immersed in DI water.

4.3.3. Detailed Study on the Effect of Immersion on Mechanical and Morphological Properties of PFCB/PVDF-HFP Membranes

4.3.3.1 Proton Conductivity

Previous proton conductivity testing showed a large decrease in the conductivity for samples conditioned at 80°C immersed in DI water (**Figure 4.28D**). To attempt to capture this decrease in conductivity in real time, a solvent exchanged sample was immersed at 80°C in the proton conductivity fixture and voltage scans were performed each minute for the first hour, and every five minutes for the following two hours, as shown in solid blue diamonds in **Figure 4.33**. As shown, the conductivity begins to decrease after about 10 minutes, and continues to decline over the entirety of the test period, resulting in a 31% reduction in the conductivity over three hours. To emulate a fuel cell cycle, the sample was then removed from the 80°C water and stored at ambient conditions overnight. The sample was then re-immersed at 80°C the following day and voltage scans were repeated for three hours. Upon reimmersion, the proton conductivity had decreased an additional 20% after exposure at ambient conditions, however the conductivity only declined slightly over the following three hours. It should be noted that the oscillations in the data are due to the heaters in the hot plate turning on and off, as evidenced by **Figure 4.34** in which the conductivity measured at 60°C is compared with the temperature profile of the DI water.

To examine the temperature dependence of this proton conductivity decline, the same testing protocol was repeated at 60, 70, and 90°C, also shown in **Figure 4.33**. Data collected at 60°C appears stable over the three hour test, and only shows a 9% reduction in conductivity after storage at ambient conditions. Increasing the temperature to 70°C shows a slight decline after approximately 60 min, resulting in about a 9% reduction in conductivity after three hours.

However, after storage at ambient conditions there is effectively no change from the final conductivity measured the previous day. It is therefore assumed that when the sample is immersed at lower temperatures that large changes in the conductivity do not occur over long time periods and after cycling to lower temperatures and moisture contents. On the contrary, immersing the sample at 90°C shows a steep decline in the conductivity after 7 minutes, and plateaus after approximately 90 minutes, resulting in a 63% decrease in conductivity. After storage at ambient conditions the conductivity decreased an additional 35%, but appeared to remain stable over the three hour test period. Clearly, immersion at 90°C is a more severe condition for the PFCB/PVDF-HFP material, resulting in a severe reduction in the proton conductivity. For comparison purposes, NRE 211 membranes were also tested under this same protocol at 80°C as shown in **Figure 4.33**, and this PFSA material does not show any decrease in conductivity over the initial three hour test period or after storage at ambient conditions.

This implies the decrease in conductivity is a material specific property such as PVDF-HFP blooming to the surface, phase separation of the PFCB from the PVDF-HFP, or a decrease in the electrostatic network. Previous data collected via ATR-IR and transmission IR suggests that when samples are immersed at 80°C the sulfonate groups form tighter aggregates and less of a network exists, corresponding well with a decrease in conductivity. In addition, work done previously on a similar material suggests that aging at high temperature and high moisture conditions causes the PVDF-HFP to bloom to the surface, again consistent with a decrease in proton conductivity [47, 48].

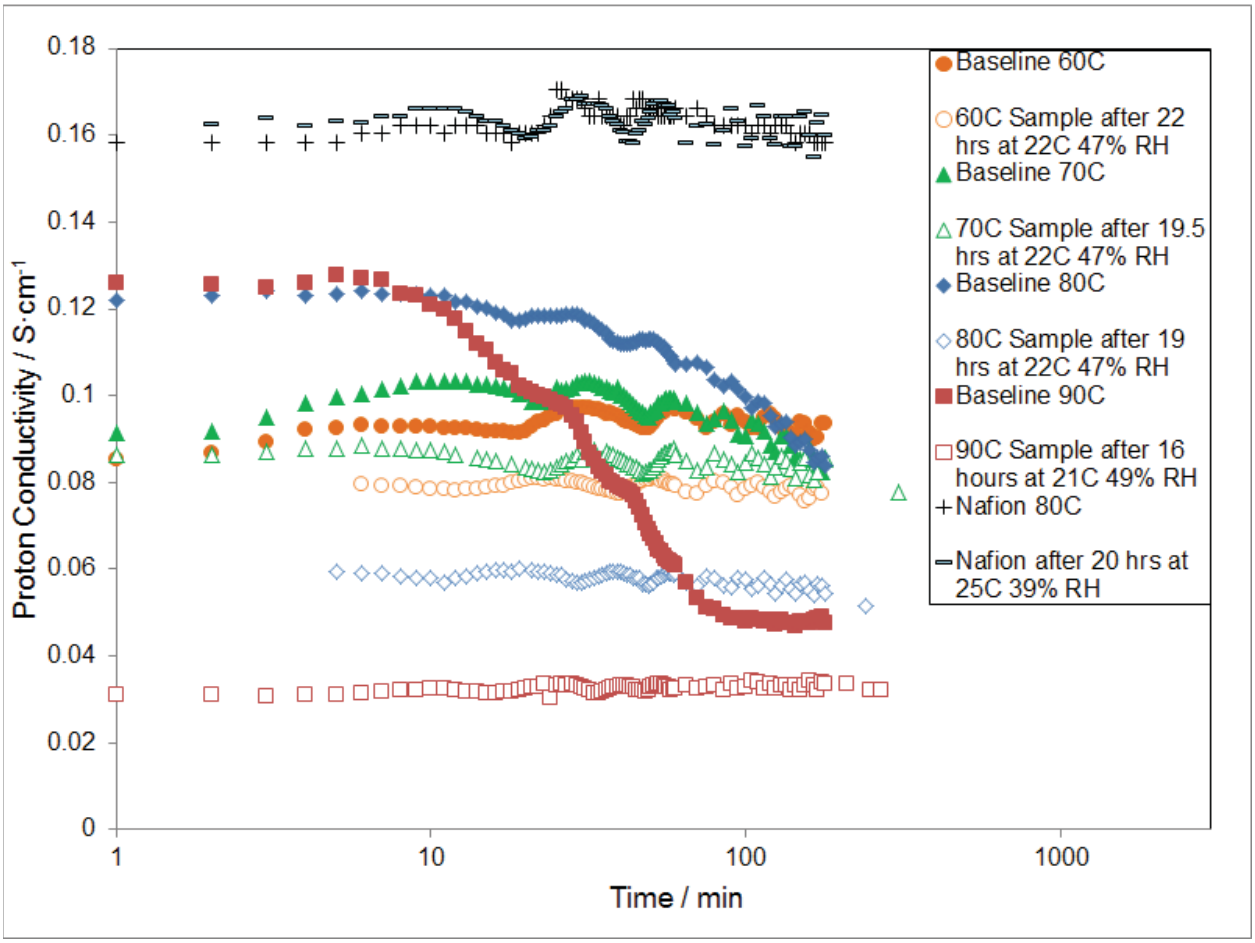

Figure 4.33. Proton conductivity measured over three hours immersed at temperatures from 60-90°C, and again after storing the sample at ambient conditions overnight, as noted in the legend.

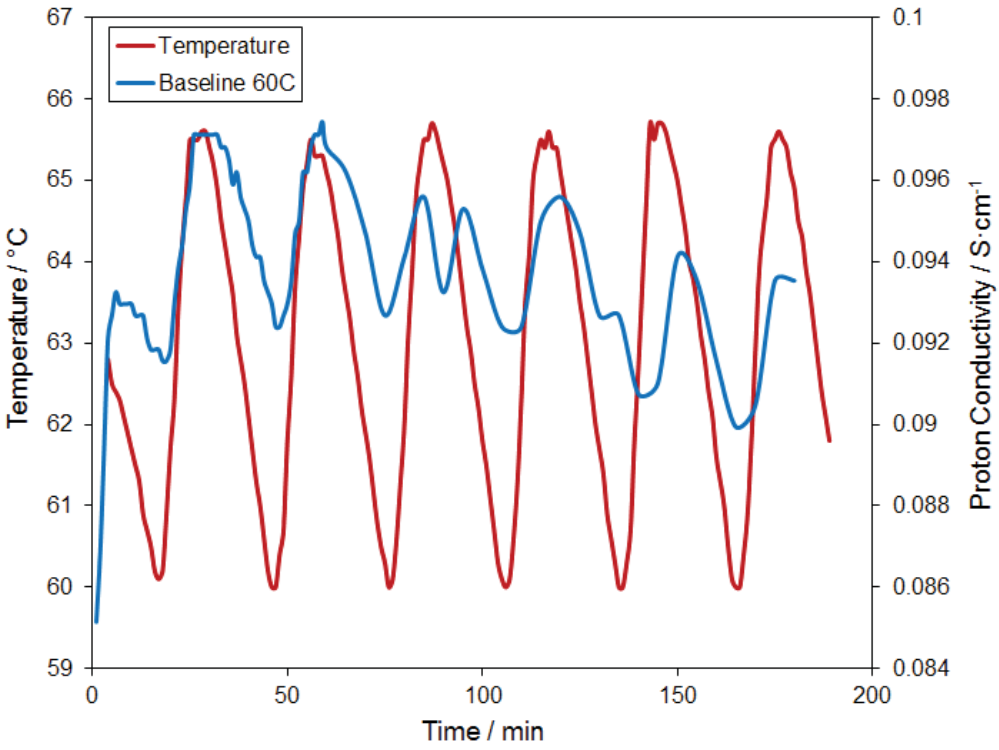

Figure 4.34. Comparison of proton conductivity oscillations with temperature oscillations.

To determine if this decline in conductivity was a bulk or surface effect, a sample 5 times as long was tested at 80°C immersed in DI water. This was accomplished by measuring conductivity on the two outer probes of the proton conductivity test cell shown in **Figure 4.2**, rather than the inner two as done for all other testing. The results of the longer sample are compared with those of the shorter sample in **Figure 4.35**. The initial conductivity of the longer sample is larger than that of the shorter sample due to the larger amount of material tested. The onset of the decline in the proton conductivity in the longer sample also occurs around 10 min, and the loss in conductivity over the three hour test period is about 29%, slightly less than that of the shorter sample. After storage at ambient conditions the conductivity decreased an additional 27%, and over the following three hours it declined another 29%, both values larger than those observed in the shorter sample. The smaller initial decrease could be indicative that the decline

in conductivity is due to a surface effect, such as PVDF-HFP blooming to the surface, however the larger decrease after re-immersion implies that a change in the bulk of the material is the cause.

To help understand these differences further, the surface resistance was separated from the bulk resistance (**Figure 4.36**). This was done by assuming the surface and bulk resistance were equivalent to a circuit with three resistors in series, two corresponding to the surface and one corresponding to the bulk, with only the bulk resistance proportional to the length of the sample. As expected, the bulk resistance is larger than the surface resistance, however it is clear from **Figure 4.36** that the surface resistance changes very little over the course of the testing period, while the bulk resistance increases almost linearly over the initial three hour test period, and almost exponentially over the second three hour test period. This indicates that the observed decline in proton conductivity is caused by changes in the bulk of the sample rather than changes at the surface, indicating PVDF-HFP blooming to the surface is likely not the cause of the decrease in conductivity.

In a fuel cell, 80-90°C is a common operating temperature range, and the cathode is frequently flooded due to electro-osmotic drag. Therefore it is highly likely a membrane would see these conditions during operation and if the conductivity is decreasing over a short time, it is highly likely the cell would no longer be a functional power source prior to the expected cell lifetime of 5000 hours. Thus to further understand why the conductivity is changing in these materials, IR spectroscopy, SAXS, DSC, and TEM imaging were employed.

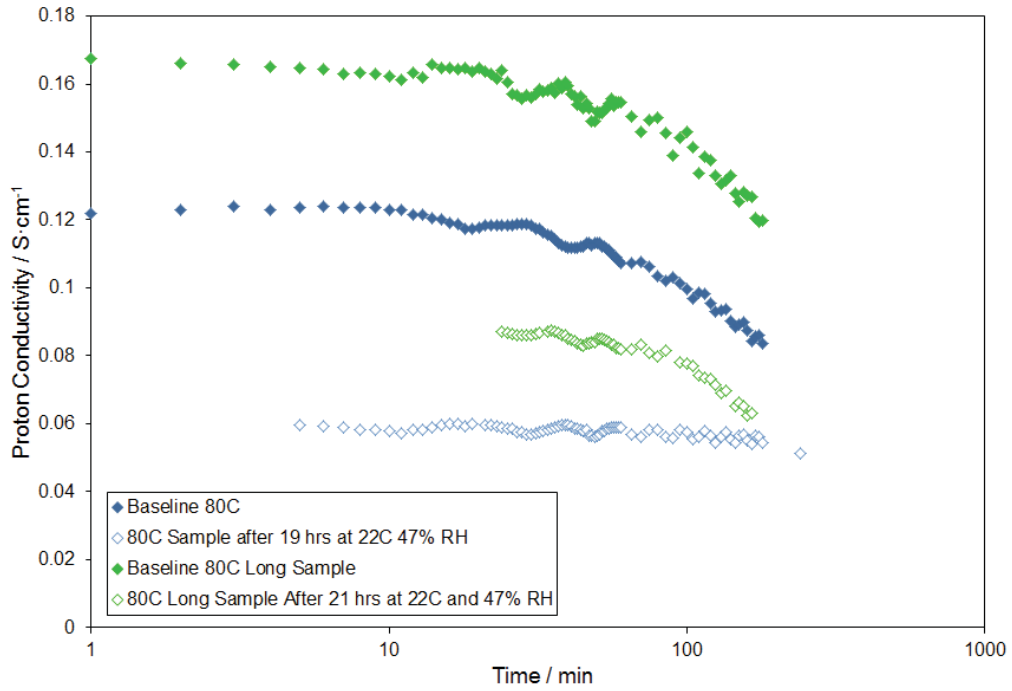

Figure 4.35. Comparison of proton conductivity measured over three hours for a short and long length sample, and again after storage at ambient conditions overnight as noted in the legend.

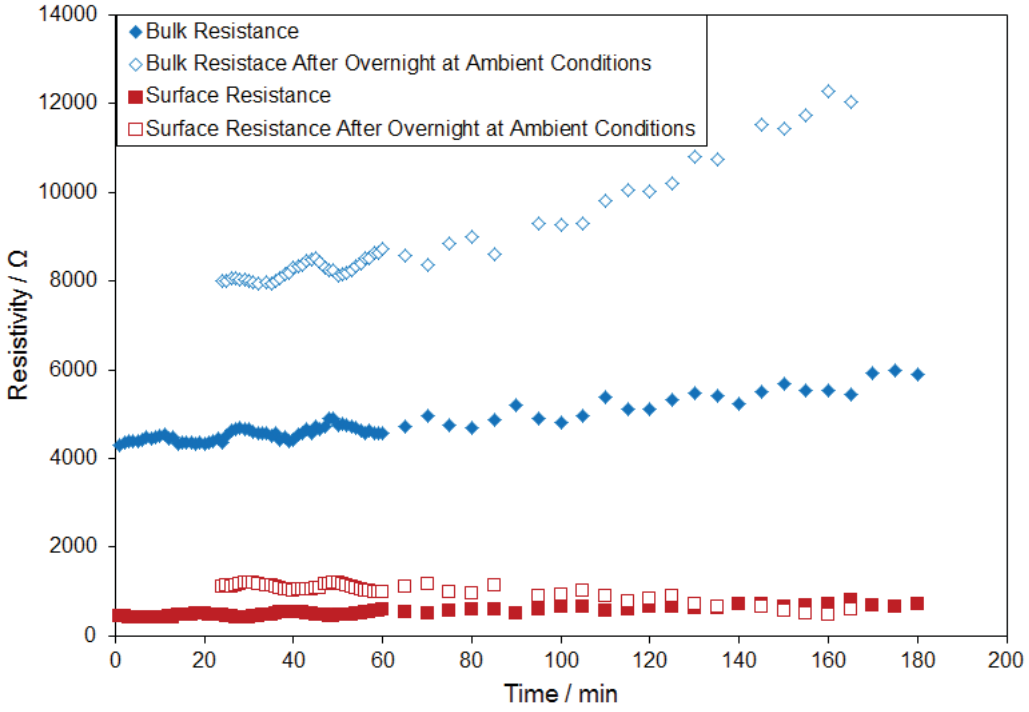

Figure 4.36. Calculated surface and bulk resistance based on electrical impedance measurements of short and long samples, before and after storage at ambient conditions.

4.3.3.2. Infrared Spectroscopy

To examine how the bulk and surface of the PFCB/PVDF-HFP material are changing ATR-IR was performed over time utilizing different temperature and moisture cycles. The peaks focused on in this investigation correspond to the sulfonate stretch at approximately 1055 Hz to examine if the sulfonic acid network is changing, and the PVDF-HFP γ-crystalline stretch at ~880 Hz to examine if PVDF-HFP was blooming to the surface. Three test cycles were utilized, as described in the experimental section, and to ensure that changes observed during the 30°C immersed or 80°C dry steps was due to the cycling of temperature or moisture, a sample was initially scanned every five minutes at 30°C immersed for six hours, and another sample at 80°C dry for three hours as shown in **Figure 4.37** and **Figure 4.38**. As can be seen, there is no shift in the sulfonate peak under these conditions, implying any changes noted during cycling are due to time spent at 80°C immersed in DI water.

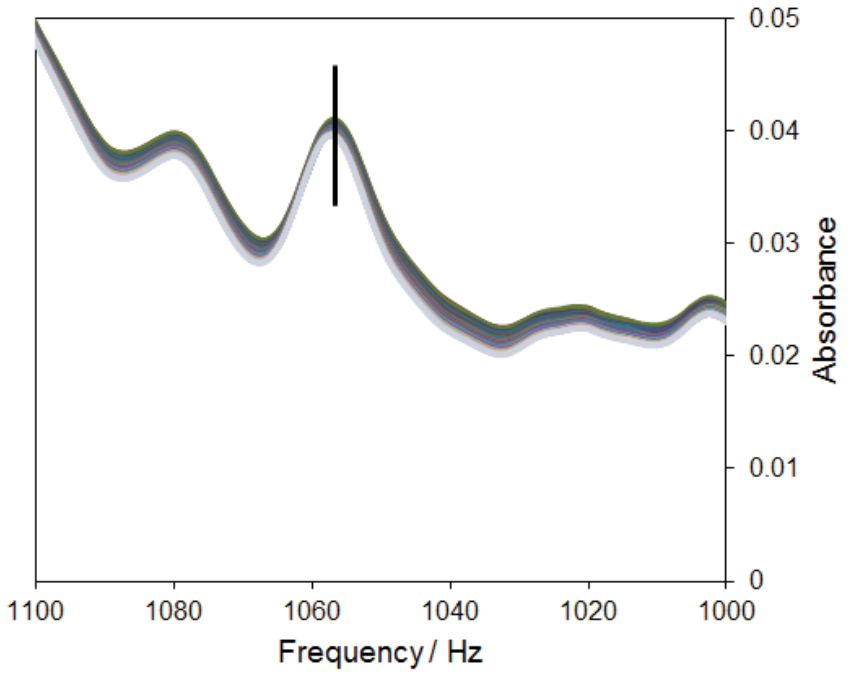

Figure 4.37. ATR-IR scans of a sample immersed at room temperature, measured every 5 minutes over 6 hours, focused on the symmetric sulfonate peak at ~1055 Hz.

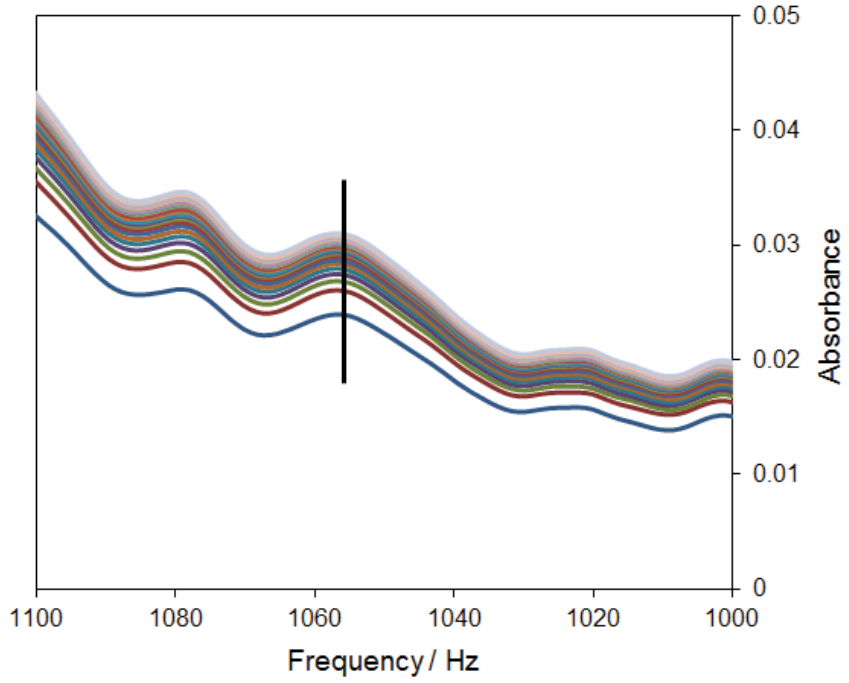

Figure 4.38. ATR-IR scans of a sample at 80°C, measured every 5 minutes over 3 hours, focused on the symmetric sulfonate peak at ~1055 Hz.

An example of the shift in the sulfonate peak from test cycle 1 is provided in **Figure 4.39**, where it can be clearly seen that the peak shifts to higher frequencies over the initial immersion at 80°C, and continues to shift further after reducing the temperature to 30°C. It is again pointed out that this shift to higher frequencies corresponds to the sulfonate group moving into a more polar environment. This would correspond to tighter aggregates forming, and a decrease in the ionic network in the material, ultimately resulting in a decrease in proton conductivity.

To more easily compare the shift of the sulfonate peak for all three test cycles, the frequency corresponding to the maximum of the sulfonate peak was plotted against time as shown in **Figure 4.40**. All three test cycles show a shift to higher frequencies over the initial 3 hour 80°C immersion step. This would correspond well with the decline in the proton conductivity noted over the first 3 hours. Based on cycles 1 and 2, reducing the temperature, whether immersed or dry, appears to have the same effect on how far the sulfonate peak shifts, however drying the sample at 80°C appears to induce a much larger shift in the sulfonate peak. This would imply that at dry conditions at high temperatures there is less of an ionic network in the material, which would result in a decrease in proton conductivity. However, in all three test cycles, when the samples are rehydrated at 80°C the sulfonate peak shifts to lower frequencies, beginning at the last peak location from the initial 3 hour hold. This implies the large shift incurred due to reduction in temperature and/or moisture is reversible, however the shift induced under 80°C immersed conditions is not. In addition, over the 1 hour hold at 80°C immersed in DI water, the sulfonate peak continues to shift to higher frequencies, implying that continued aging at this condition would result in further shifting of the sulfonate peak. Finally, when the temperature and/or moisture level is decreased a second time, in all three cycles the sulfonate

peak again shifts to higher values similar to the values observed from the first temperature and/or moisture decrease, except at dry 80°C conditions, the peak appears to have shifted to even higher frequencies.

The third test cycle could have very poor implications for use of this blend material in an operating fuel cell, as the cathode is frequently flooded due to electro-osmotic drag, which can also cause the anode to dry out. Therefore, one side of the membrane would see 80°C dry conditions while the other would be immersed or at a high humidity level at 80°C. This would likely result in a very poor ionic network across the membrane, causing a reduction in proton conductivity and thus electrical output. Therefore, when employing this membrane, it is important to maintain a high moisture content at the anode to also maintain a better ionic network in the material. While this will not prevent the formation of tighter aggregates over time, it will at least allow better conductivity and thus electrical output and power generation for a greater amount of time.

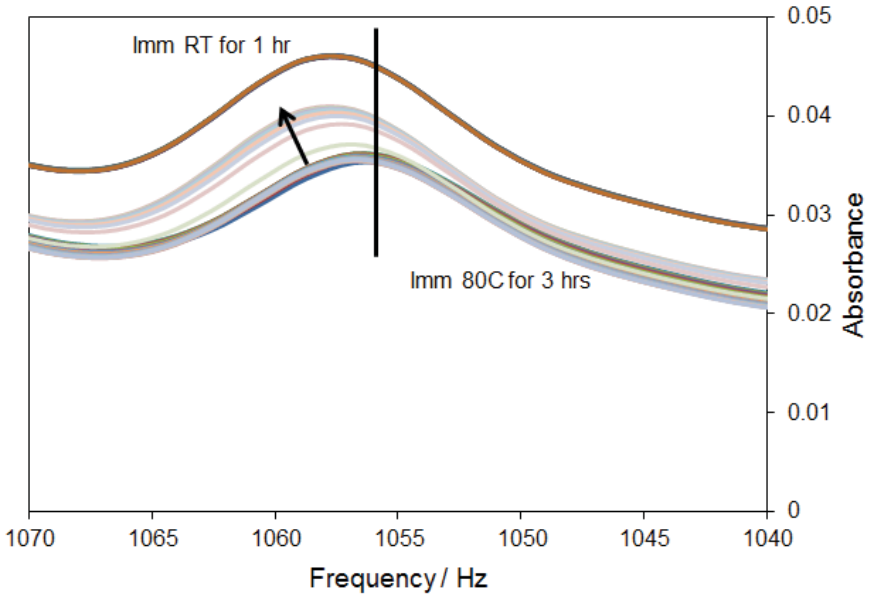

Figure 4.39. Example ATR-IR scans of samples cycled through temperature and moisture conditions, displaying the shift of the symmetric sulfonate peak from ~1055 Hz.

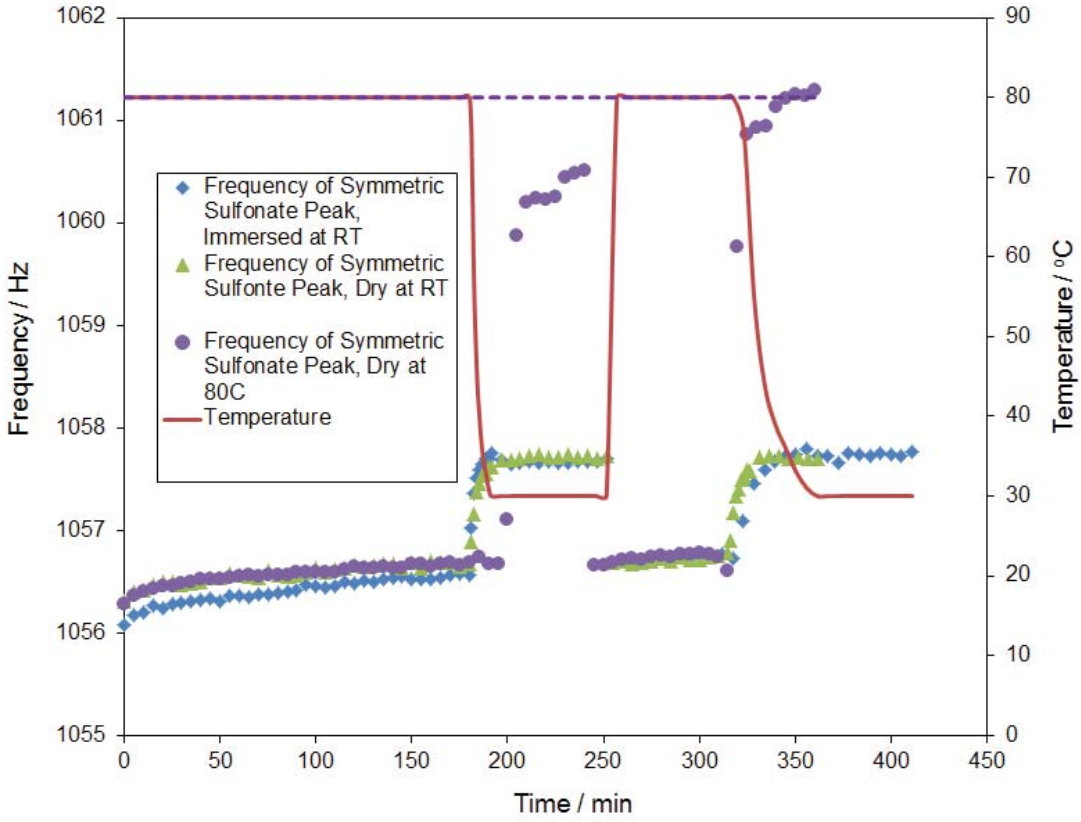

Figure 4.40. Shift of the symmetric sulfonate peak with time when temperature and/or moisture content is cycled.

In addition to changes in the sulfonate peak, it is possible that PVDF-HFP blooms to the surface, and thus also contributing to a decline in the proton conductivity. Therefore, the absorbance of the γ-form crystalline stretch of PVDF-HFP was examined for all three test cycles, as shown in **Figure 4.41A-E**. Because these measurements were performed via ATR-IR, an increase in the absorbance would imply an increase in that functional group at the surface of the material. In this case, because the γ-form crystalline is found in the PVDF-HFP and not the PFCB, this implies that PVDF-HFP is blooming to the surface. In addition, these IR scans have not been normalized, therefore a change in the peak shape such that a vertical shift would not allow alignment must be observed to indicate increased PVDF-HFP content at the surface of the membrane. For the first two test cycles, shown in **Figure 4.41A-D** when the temperature is reduced to 30°C, an increase in absorbance of the γ-form crystalline peak is not observed. Therefore it is highly unlikely that PVDF-HFP is blooming to the surface when the temperature is reduced. This could be due to restricted chain motion due to entanglements at these lower temperatures, even when immersed. However, when the γ-form crystalline peak is investigated for test cycle 3, as shown in **Figure 4.41E** and **F**, a clear change in peak shape is observed, corresponding to an increase in PVDF-HFP at the surface of the membrane when dried at 80°C, from an immersed condition. It should be noted that when the sample is re-immersed at 80°C, the γ-form crystalline peak returns to its original peak shape and absorbance, implying the PVDF-HFP blooming is a reversible phenomenon. In this case, it may correspond to the polarity switch noted in Nafion® materials, in which under dry conditions the surface appears to be highly fluorinated, and when immersed, the surface appears highly sulfonated [68]. This is in contrast to results found by Osborn et al. on a similar material, which showed gross phase separation, and a corresponding decrease in the proton conductivity when conditioned at high

temperatures and moisture conditions [47, 48]. Therefore, in agreement with the long vs. short proton conductivity samples, it appears that PVDF-HFP at the surface is not a large contribution to the reduction in proton conductivity. However, as noted with the shift in the sulfonate peak, if the cathode is flooded and the anode is dry, proton conductivity could be reduced due to the PVDF-HFP at the surface of the anode side. This increase in PVDF-HFP combined with a decrease in the ionic network, could cause an even larger decline in the conductivity, again emphasizing the importance of keeping the anode humidified to abate the contributions of PVDF-HFP at the surface.

A

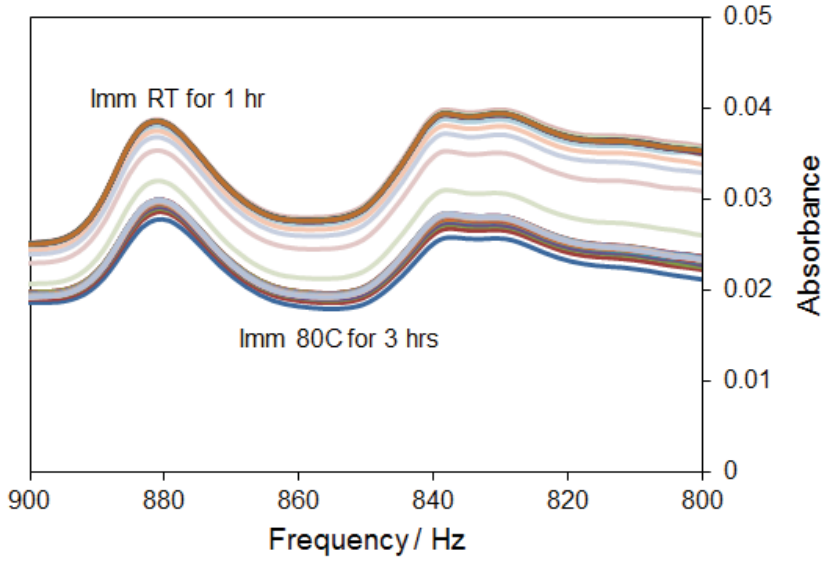
1mm RT for 1 hr
1mm 80C for 3 hrs
0.05
0.04
0.03
0.02
0.01
0
Absorbance
900
880
860
840
820
800
Frequency / Hz

B

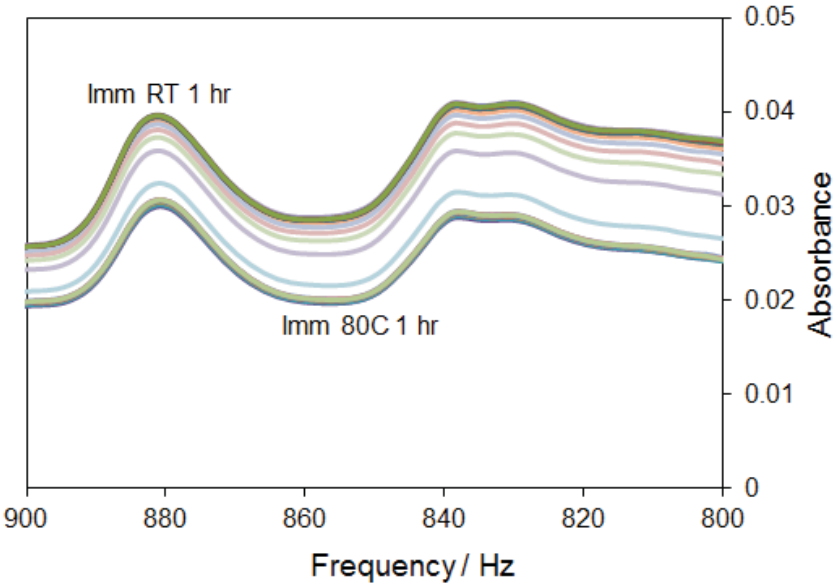
1mm RT 1 hr
1mm 80C 1 hr
0.05
0.04
0.03
0.02
0.01
0
Absorbance
900
880
860
840
820
800
Frequency / Hz

C

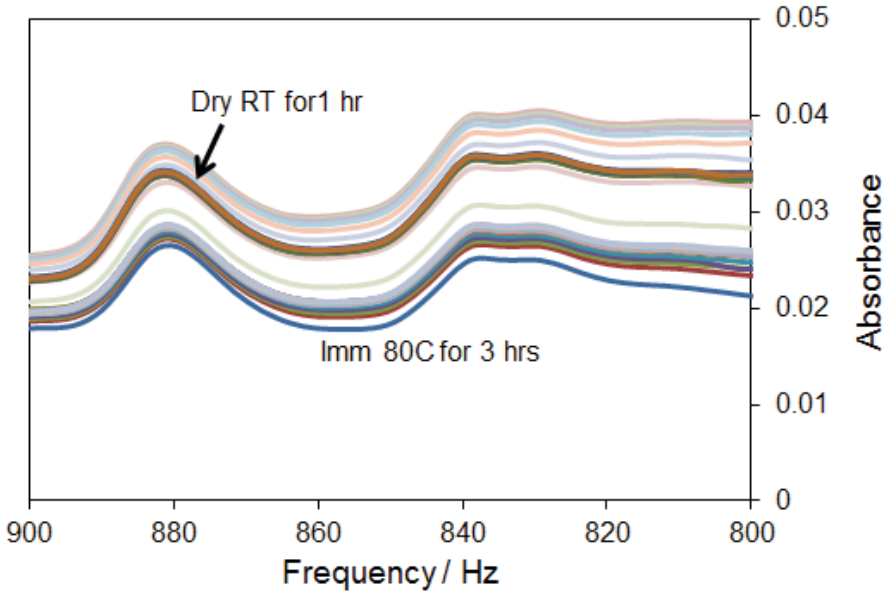
Dry RT for1 hr
Imm 80C for 3 hrs
0.05
0.04
0.03
0.02
0.01
0
Absorbance
900
880
860
840
820
800
Frequency / Hz

D

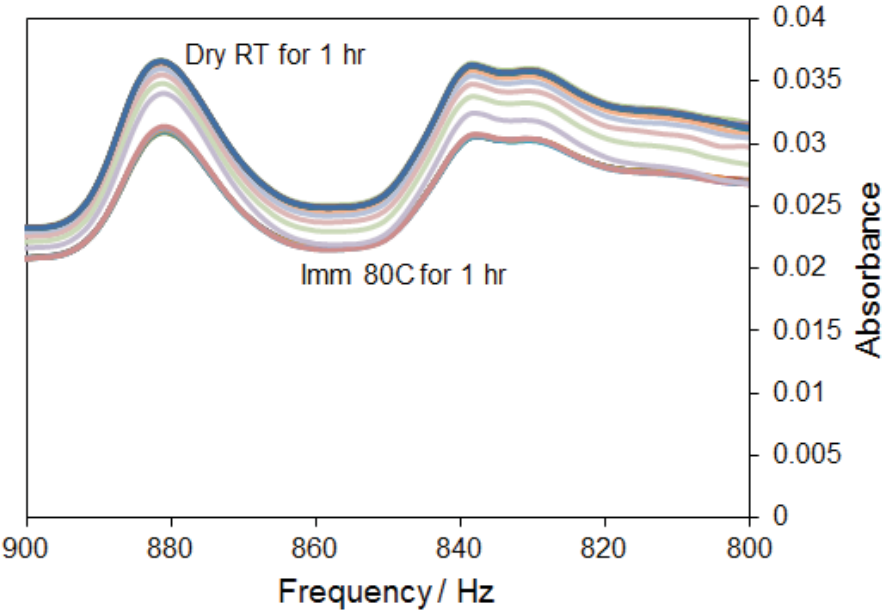
Dry RT for 1 hr
Imm 80C for 1 hr
0.04
0.035
0.03
0.025
0.02
0.015
0.01
0.005
0
Absorbance
900
880
860
840
820
800
Frequency / Hz

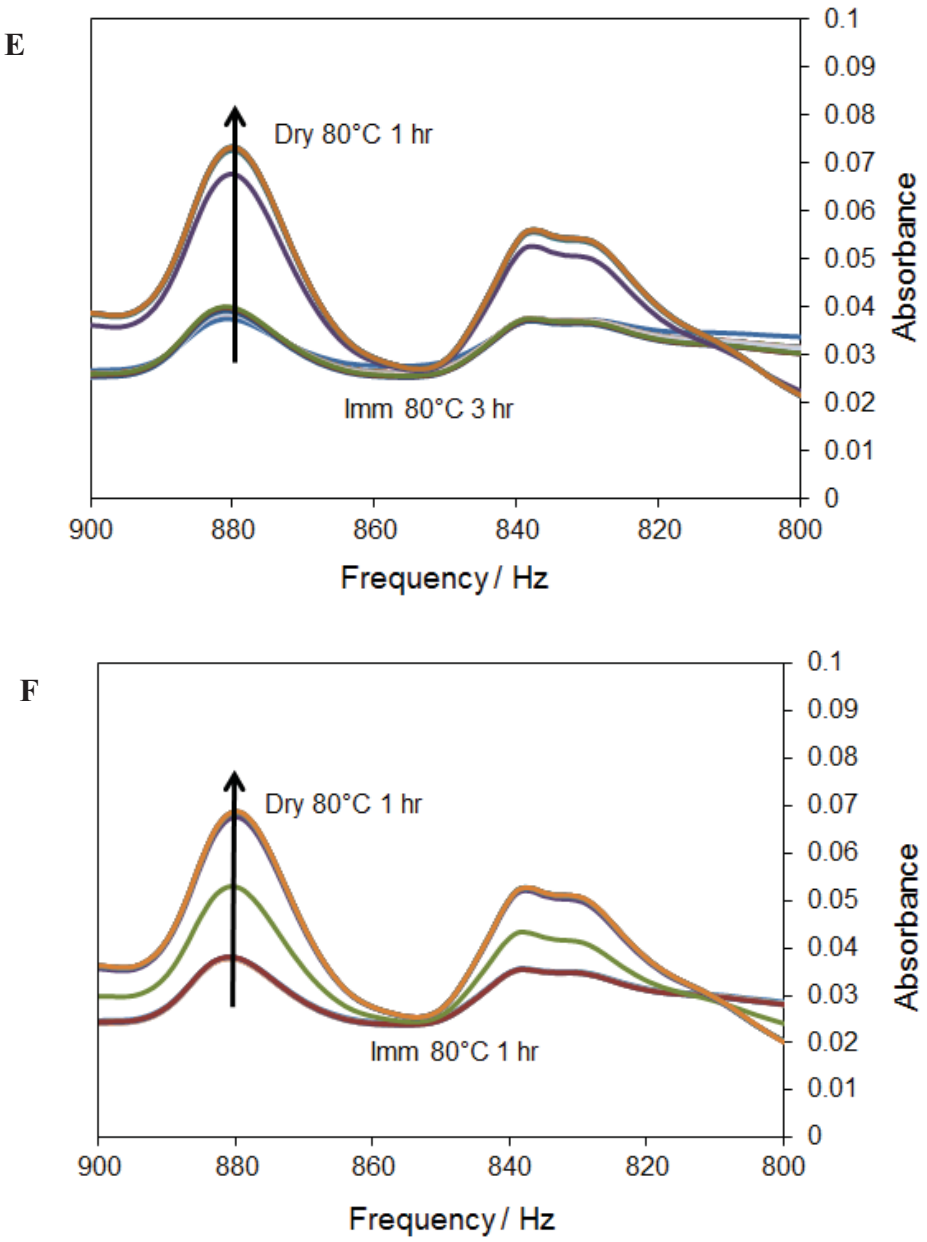

Figure 4.41. Examination of intensity change of the PVDF-HFP γ-form crystal stretch at ~880 Hz for a **(A)** sample immersed at 80°C for 3 hours followed by immersion at room temperature for 1 hr and **(B)** immersing the same sample at 80°C for 1 hr, and a final hour immersed at room temperature, a **(C)** sample immersed at 80°C for 3 hours followed by a dry isotherm at room temperature for 1 hr and **(D)** immersing the same sample at 80°C for 1 hr, and a final dry isotherm at room temperature for 1 hr, and a **(E)** sample immersed at 80°C for 3 hours followed by a dry isotherm at 80°C for 1 hr and **(F)** immersing the same sample at 80°C for 1 hr, and a final dry isotherm at 80°C for 1 hr.

4.3.3.3. SAXS

SAXS scans were performed on Cs+ form samples that were aged at 70, 80, or 90°C immersed in DI water for 1, 3, 8, 24 hrs, or 1 wk, as provided in **Figure 4.42A-D** and **Figure 4.43A-C**. While ATR-IR and proton conductivity can be performed over time to monitor changes with changes in temperature or moisture conditions, SAXS cannot because it is performed under vacuum. Therefore it was necessary to prepare samples aged for different amounts of time at different temperatures to compare with the previously collected proton conductivity and IR data. Cs+ form samples were utilized in an attempt to increase the contrast of the ionic aggregates even further than the Na+ form utilized previously, allowing for observation of the corresponding peak, unlike what is seen in the proton form of these membranes [62]. Unfortunately, the ionic peak is still obscured in the scans shown herein, therefore focus is placed on the block copolymer phase separation peak (**Figure 4.42A-D**) and the PVDF-HFP crystalline order peak (**Figure 4.43A-C**).

Examination of the block copolymer phase separation peak shows a shift to smaller q spacings with increased time of exposure for all three temperatures, indicating an increase in the degree of phase separation of the PFCB block copolymer, corresponding to larger spacing between the two blocks of the copolymer with increased aging time. In addition, the q spacing corresponding with the maximum of each block copolymer peak at each temperature is plotted in **Figure 4.42D**. This allows for easy comparison of the degree of the peak shift with increasing temperature. As can be seen, the shift of samples aged at 70 and 80°C is quite similar, while the samples aged at 90°C appear to shift to smaller q spacings. Therefore is appears that aging at 90°C results in a slightly greater degree of phase separation than aging at lower temperatures.

For all temperatures, an increase in the degree of phase separation correlates well with a decrease in the electrostatic network of the membrane, as increased phase separation would allow tighter aggregates to form, rather than being dispersed throughout the material.

The PVDF-HFP crystalline order peak is much subtler than the block copolymer phase separation peak. However, it can be observed to shift to lower q spacings with increased aging time for all three aging temperatures. In addition, it appears that the shift is greater with increasing temperature. This indicates that the spacing between crystallites is increasing, which could correspond to a reduction in the number of crystallites as larger crystallites are formed, correlating well with increased chain mobility at higher temperatures. The combination of increased crystalline order, increased block copolymer phase separation, and a decrease in the ionic network all correlate well with the decrease noted in the proton conductivity with increasing temperature and time.

A

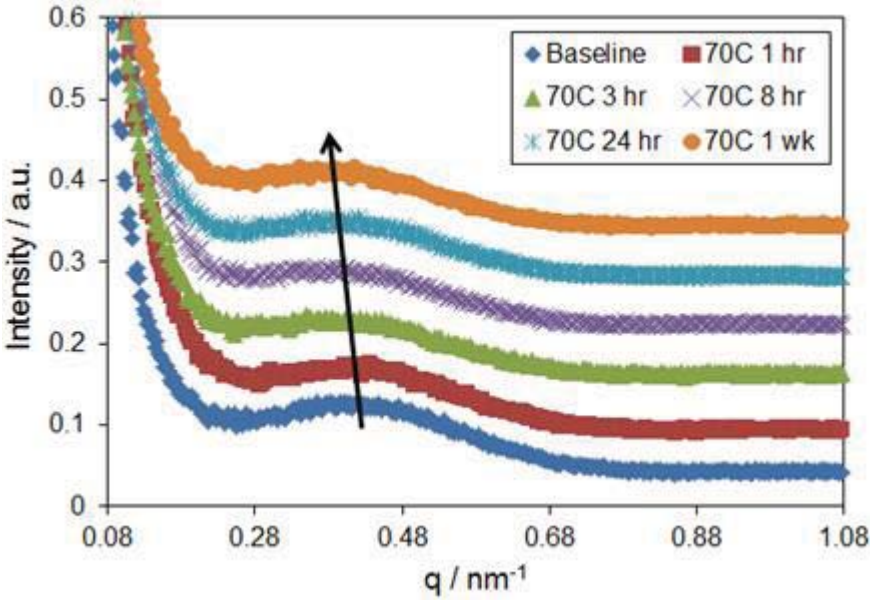
Baseline
70C 1 hr
70C 3 hr
70C 8 hr
70C 24 hr
70C 1 wk
Intensity / a.u.
0
0.1
0.2
0.3
0.4
0.5
0.6
0.08
0.28
0.48
0.68
0.88
1.08
q / nm-1

B

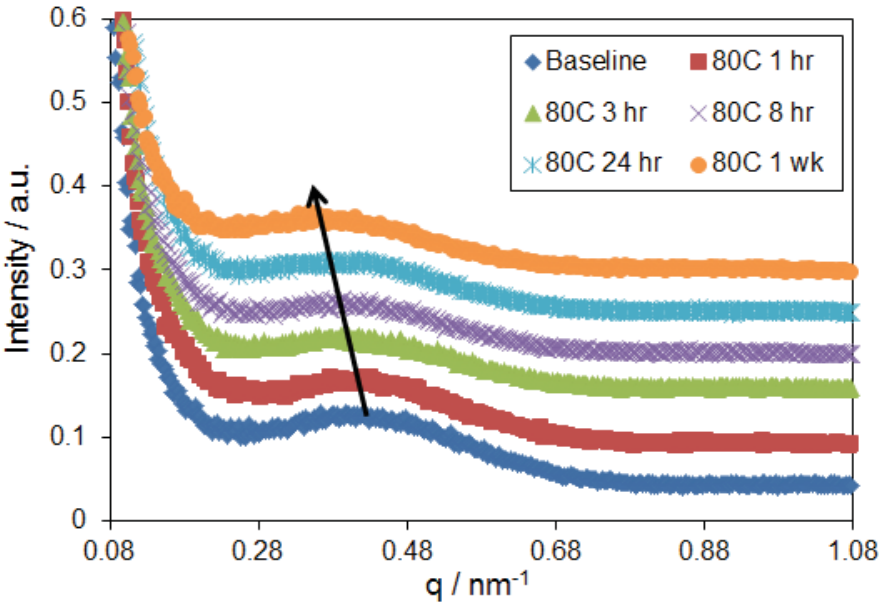
Baseline
80C 1 hr
80C 3 hr
80C 8 hr
80C 24 hr
80C 1 wk
Intensity / a.u.
0
0.1
0.2
0.3
0.4
0.5
0.6
0.08
0.28
0.48
0.68
0.88
1.08
q / nm-1

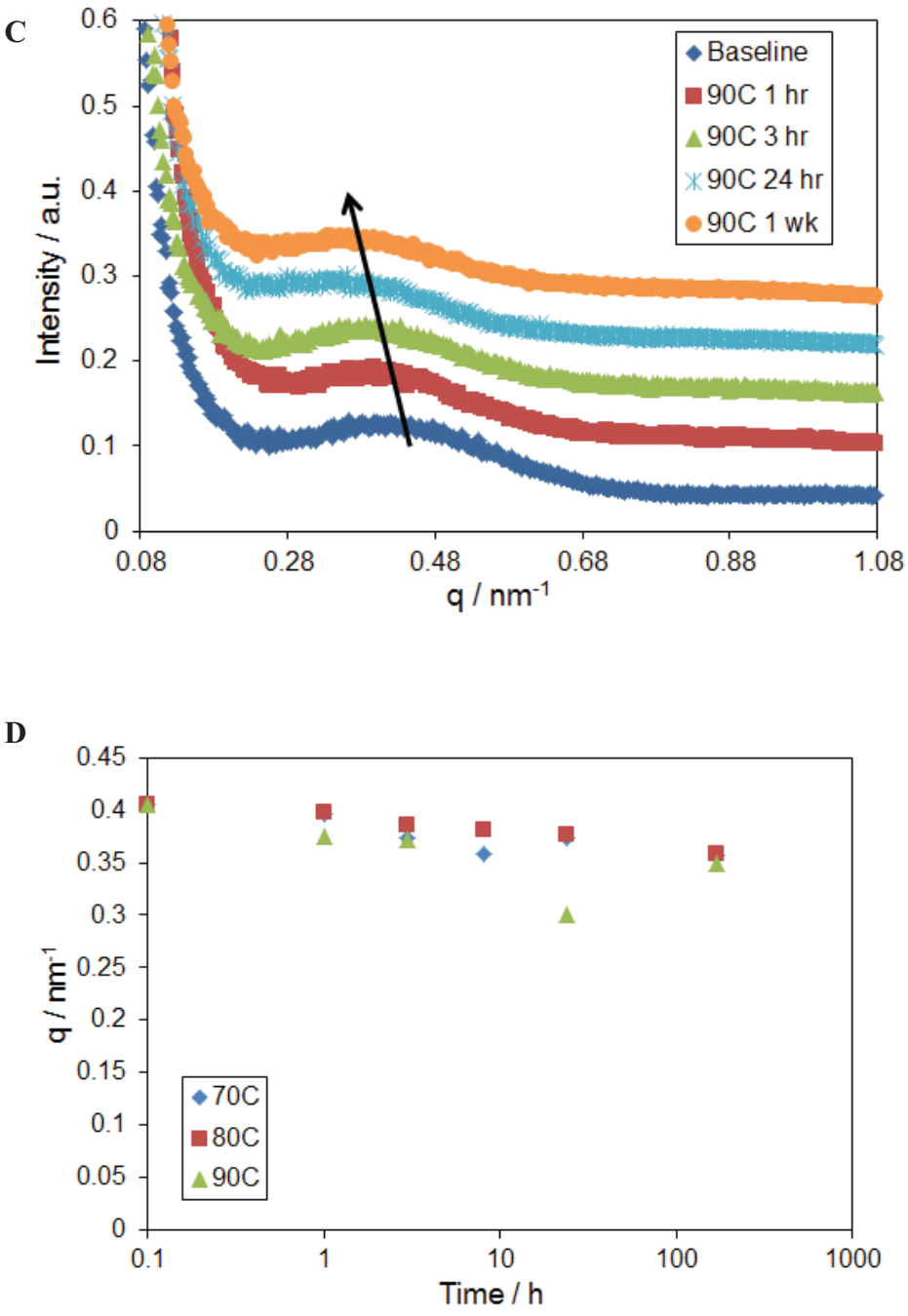

Figure 4.42. SAXS scattering profiles focused on the block copolymer phase separation peak for samples annealed immersed at **(A)** 70°C, **(B)** 80°, **(C)** 90°C, and **(D)** the change in peak position with respect to annealing time and temperature.

A

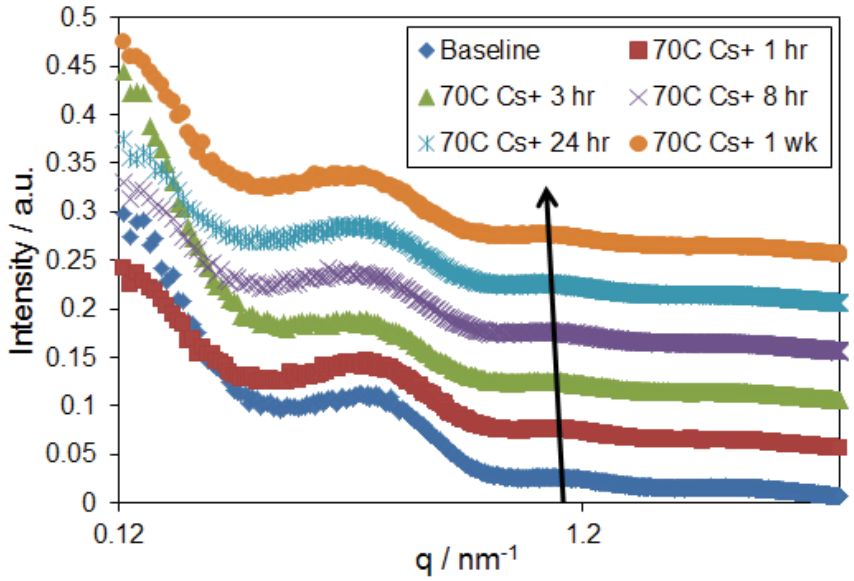
Baseline
70C Cs+ 1 hr
70C Cs+ 3 hr
70C Cs+ 8 hr
70C Cs+ 24 hr
70C Cs+ 1 wk
Intensity / a.u.
0.5
0.45
0.4
0.35
0.3
0.25
0.2
0.15
0.1
0.05
0
0.12
1.2
q / nm-1

B

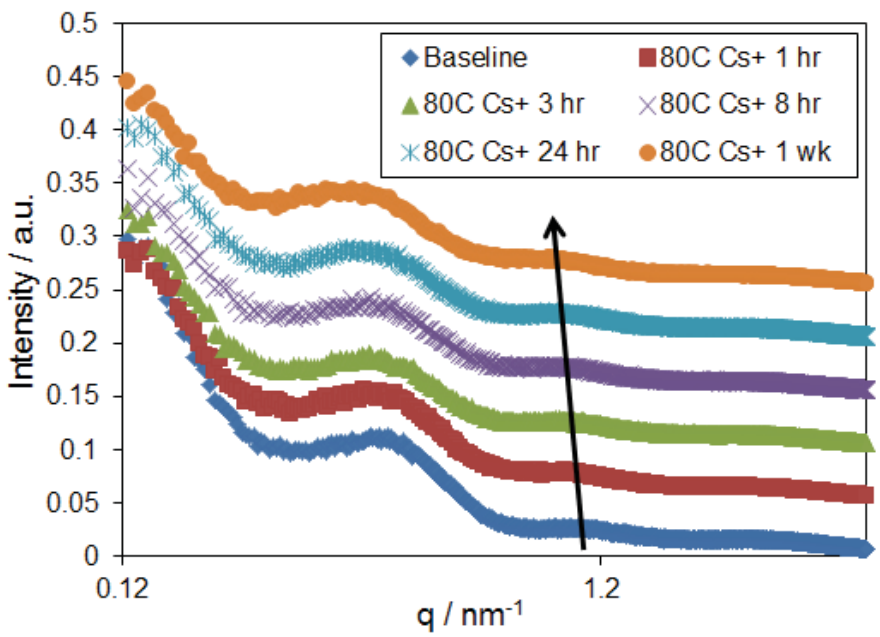
Baseline
80C Cs+ 1 hr
80C Cs+ 3 hr
80C Cs+ 8 hr
80C Cs+ 24 hr
80C Cs+ 1 wk
Intensity / a.u.
0.5
0.45
0.4
0.35
0.3
0.25
0.2
0.15
0.1
0.05
0
0.12
1.2
q / nm-1

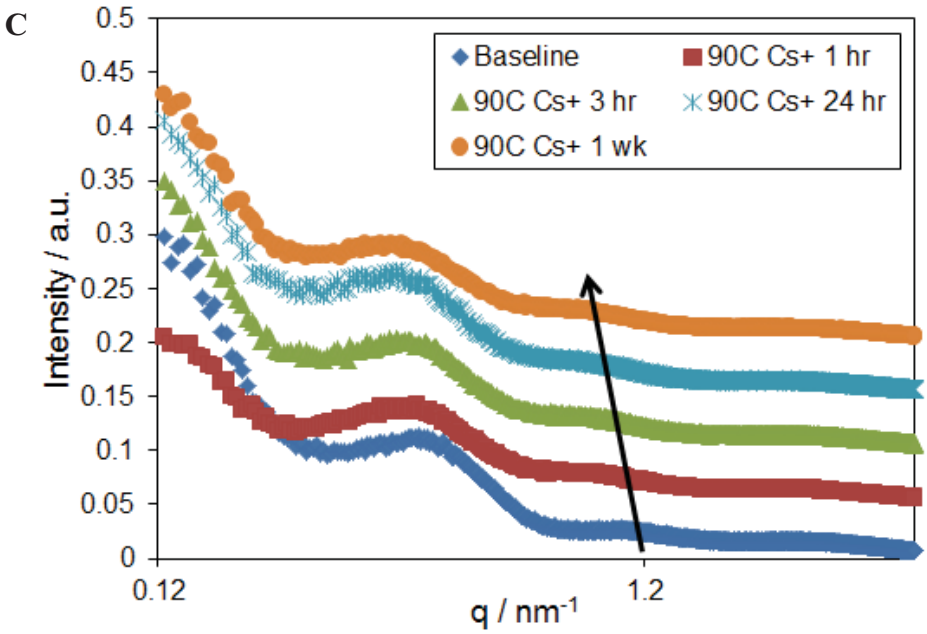

Figure 4.43. SAXS scattering profiles focused on the Kynar Flex crystalline order peak for samples annealed immersed at **(A)** 70°C, **(B)** 80°C, and **(C)** 90°C.

4.3.3.4. DSC

To further examine the crystalline order of aged samples, DSC was performed. The percent crystallinity of PVDF-HFP for each sample was calculated and plotted against aging time, as shown in **Figure 4.44A**, and the percent crystallinity of the entire PFCB/PVDF-HFP blend in **Figure 4.44B**. As compared with the non-aged sample, shown as a black X on the Y-abscissa, the samples aged at 70 and 80°C have a similar amount of crystallinity, with those aged at 80°C having a slightly greater amount. However, the samples aged at 90°C show a noticeable increase in the amount of PVDF-HFP crystallinity. This implies that with increasing temperature PVDF-HFP crystallinity increases, in agreement with the SAXS data as well as greater chain mobility at higher temperatures. It should be noted that the amount of time at each aging temperature appears to have a minimal effect on the amount of crystallinity, indicating that most of the crystallinity has formed within the first hour of exposure time.

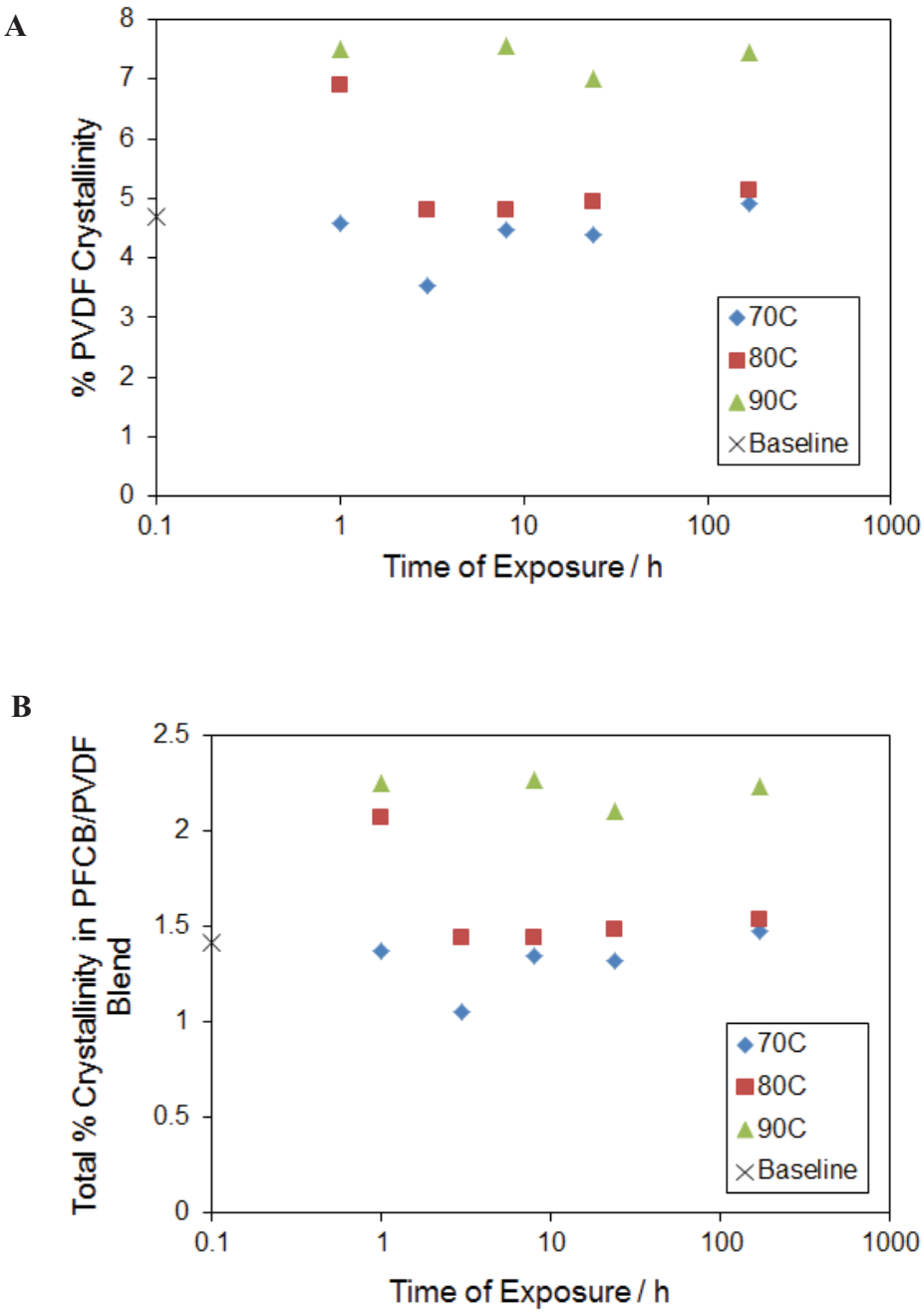

Figure 4.44. Percent crystallinity of **(A)** PVDF-HFP and **(B)** total crystallinity in the PFCB/PVDF-HFP blend, with respect to annealing temperature and time.

4.3.3.5. TEM Imaging

While ATR-IR, SAXS, and DSC data have all provided excellent evidence as to the morphological causes behind the decline in proton conductivity over time, TEM imaging provides a visual representation of these morphological explanations. As with SAXS, TEM imaging is performed under vacuum, and as such aged samples at 70, 80, and 90°C were examined. TEM imaging is a through-thickness technique, allowing for observation of the material bulk, rather than the surface as with SEM or AFM. In addition, areas with increasing electron density will show up darker, with the most electron dense regions appearing the darkest. Therefore, because the samples for TEM were stained with the heavy metal complex which associates strongly with the ionic regions, the darkest areas in the TEM images should correspond to the ionic aggregates of the sulfonated block of the PFCB block copolymer. It is likely the lightest regions correspond with the PVDF-HFP, however the electron density between the PVDF-HFP and the non-sulfonated block of the PFCB are likely very similar, and thus discerning between these two blend components in TEM may be quite difficult. Therefore, the main observations in these images will correspond to the ionic aggregates, rather than attempting to deconvolute the PVDF-HFP and non-sulfonated block of the PFCB.

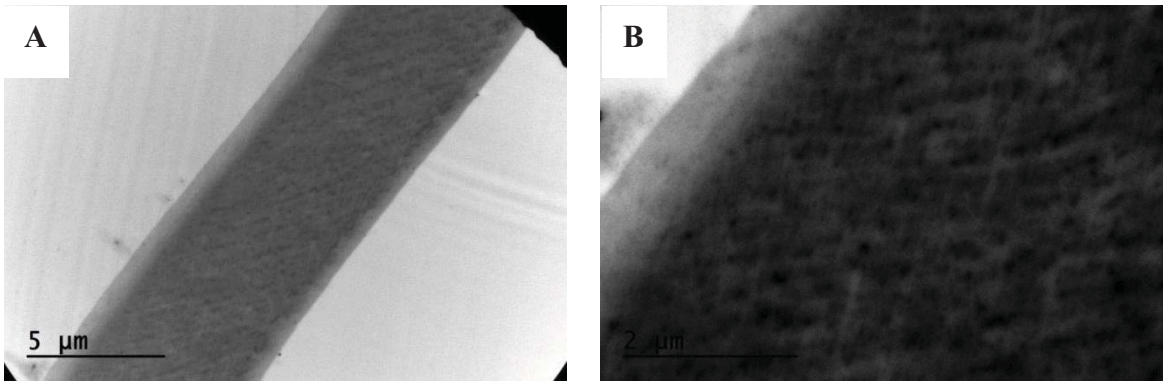

Figure 4.45. TEM images of solvent exchanged samples at **(A)** 10,000 and **(B)** 30,000 magnification.

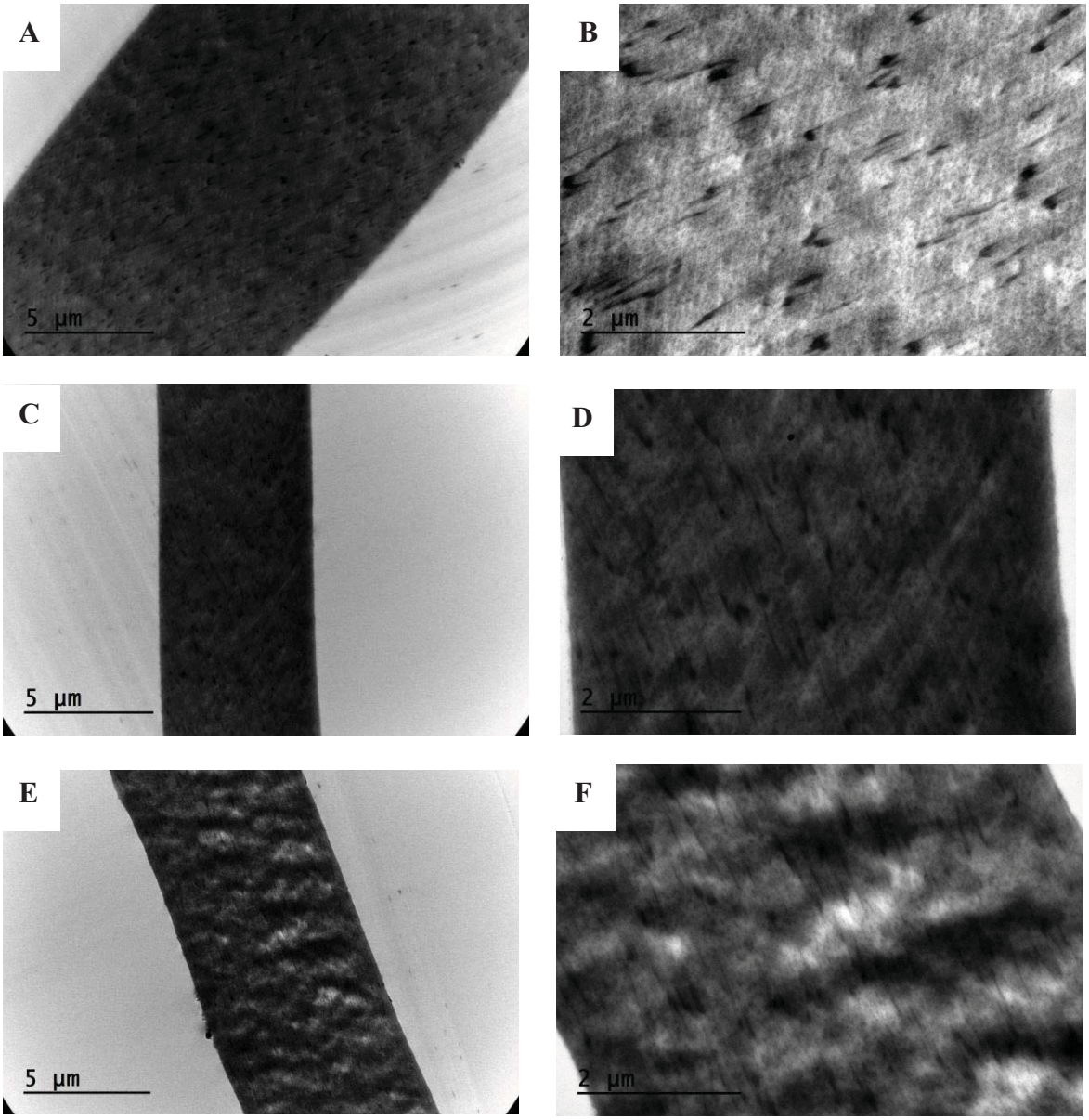

Figure 4.46. TEM images of samples immersed at 70°C for **(A)** 1 hr at 10,000 magnification, **(B)** 1 hr at 30,000 magnification, **(C)** and **(E)** 1 wk at 10,000 magnification, and **(D)** and **(F)** 1 wk at 30,000 magnification.

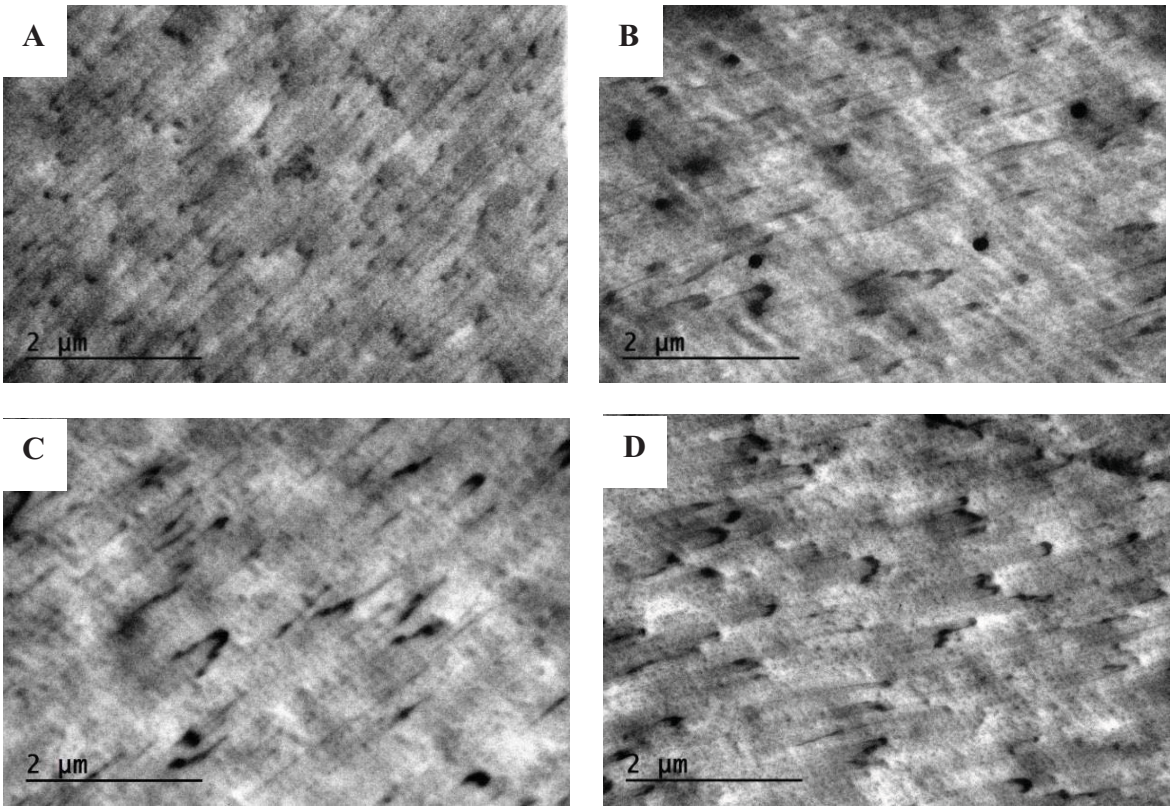

Figure 4.47. TEM images with 30,000 magnification of samples immersed at 80°C for **(A)** 1 hr, **(B)** 8 hr, **(C)** 24 hr, **(D)** and 1 wk.

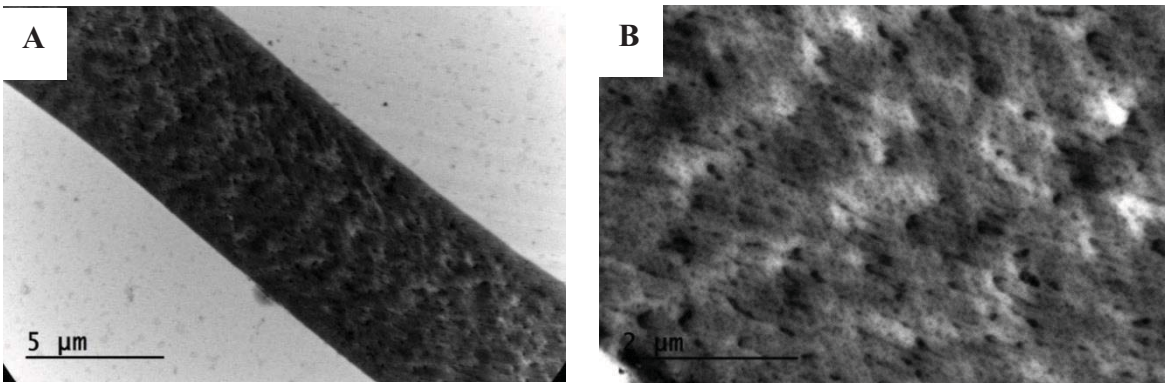

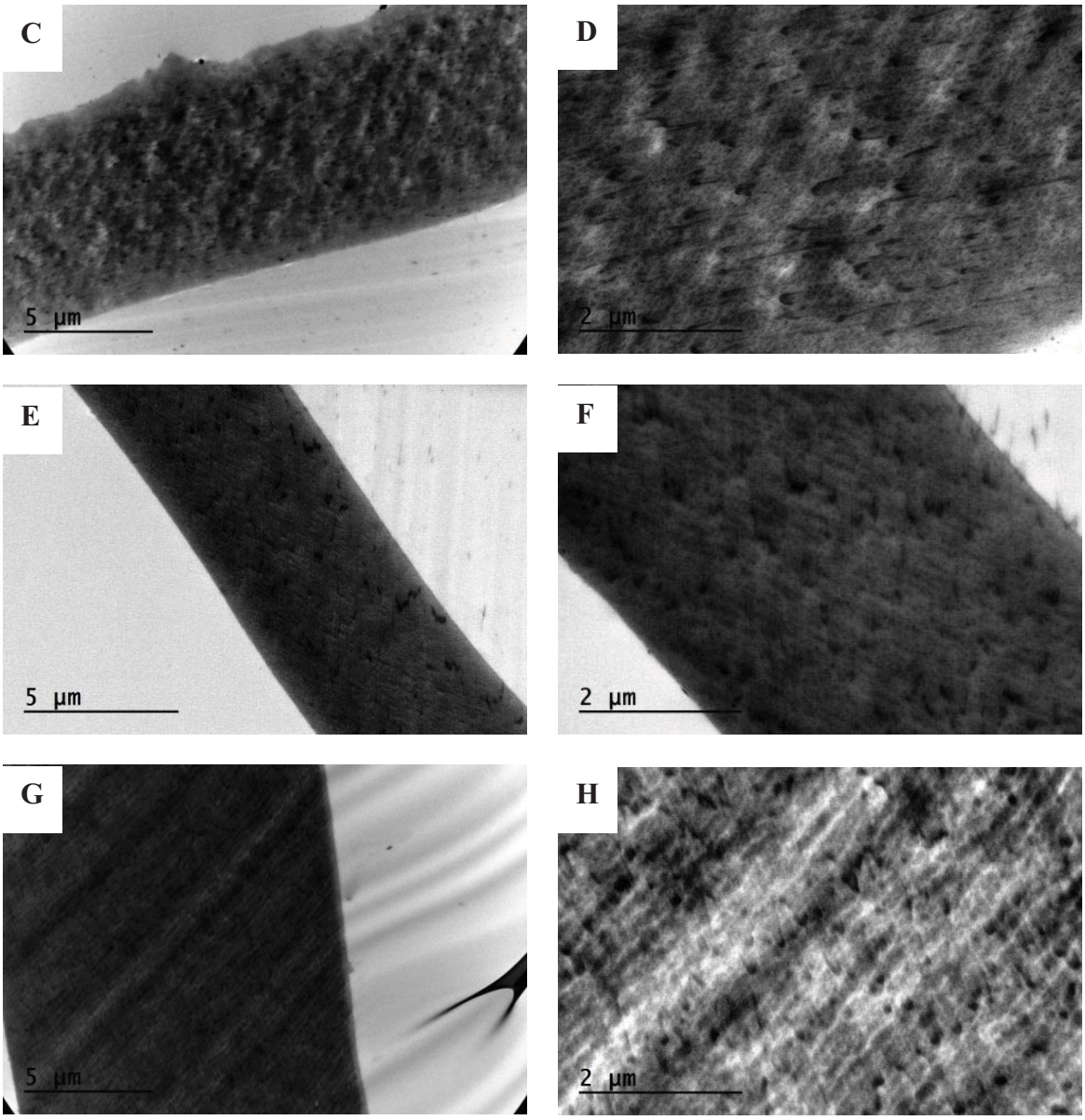

Figure 4.48. TEM images of samples immersed at 90°C for **(A)** 1 hr at 10,000 magnification, **(B)** 1 hr at 30,000 magnification, **(C)** 3 hrs at 10,000 magnification **(D)** 3 hrs at 30,000 magnification, **(E)** 8 hrs at 10,000 magnification, **(F)** 8 hrs at 30,000 magnification, **(G)** 1 wk at 10,000 magnification, and **(H)** 1 wk at 30,000 magnification.

Imaging of the baseline materials is provided in **Figure 4.45A** and **B** at two different magnifications. It can be seen that the ionic aggregates are small and evenly distributed throughout the sample, however it does appear that there is a PVDF-HFP edge on the sample. This edge does not appear in aged samples, and may be an anomaly of this particular sample as it

is not believed that PVDF-HFP blooms to the surface significantly in these blend materials. Imaging of samples aged at 70°C is provided in **Figure 4.46A-F**. Samples aged for 1 hr appear very similar to the baseline material, in that the ionic aggregates are very small and appear to be well distributed. This is in good agreement with the proton conductivity data in which no noticeable decline was measured after 1 hr. Four different images of a sample aged for 1 wk are provided because a variety of morphology was noted across the sample. After 1 wk the ionic aggregates were slightly larger than after 1 hr, but in one area these aggregates appeared to be fairly evenly distributed, while in another separation of the ionomer from the PVDF-HFP appeared to be occurring. This partially separated region appears similar to the sample aged at 90°C for 1 hr (**Figure 4.48A** and **B**) which is believed to also be in good agreement with the proton conductivity data as the conductivity of the 70°C sample is only beginning to decline after 3 hrs. It is therefore plausible that if the conductivity were measured over a week, it would be similar to that of a sample at 90°C after 1 hr.

Imaging of samples aged at 80°C is provided in **Figure 4.47A-D.** It can be seen that after 1 hr of aging the ionic aggregates are fairly small and evenly dispersed throughout the sample. However, as the aging time is increase, the ionic regions become larger and spaced further apart, corresponding well with the shift noted in the sulfonate peak in ATR-IR as well as the increased phase separation of the block copolymer noted in SAXS. This change in ionic aggregate spacing with increased aging time provides a strong visual to support the corresponding morphological data as well as provide a visual reason for the decrease in proton conductivity.

Imaging of samples aged at 90°C is provided in **Figure 4.48A-H**. It is clear after 1 hr of aging that these samples already show separation of the ionic region from the PVDF-HFP, as well as larger ionic aggregates. This is in excellent agreement with the proton conductivity,

SAXS, and DSC data accounting for the severe decline in conductivity, increase in the PFCB block copolymer phase separation, and increase in PVDF-HFP cyrstallinity. This behavior is continued at 3 and 8 hrs as further separation and larger aggregates can be noted. Finally, it is clear in the samples aged for 1 wk that the ionomer is separating from the PVDF-HFP and forming a layered structure. This layered structure would be very detrimental to fuel cell operation if the layers are parallel to the membrane plane as conductivity would be severely reduced. However, if it were possible to control the orientation of this morphological development, and force this layered structure to form perpendicular to the membrane plane, proton conductivity could be greatly increased, similar to behaviors noted with block copolymer membranes [69].

Additional imaging was performed to examine the ionic aggregates at higher magnification, with an example shown from the sample aged at 80°C for 8 hrs in **Figure 4.49A-C**. It should be noted that this ionic aggregate pattern was noted in multiple samples, and this sample was chosen purely as an example. In this case it is believed the dark regions still correspond with the ionic regions of the block copolymer, however the light area within the ionic aggregate is believed to be the non-sulfonated block of the PFCB copolymer. Based upon this image, it appears the sulfonated portion of the block copolymer is the major component of the aggregate and appears to contain the non-sulfonated portion of the block copolymer. This is in partial agreement with the morphology previously theorized by May, in which the ionic portion of the block copolymer is surrounded by the non-ionic portion, which is then mixed with the PVDF-HFP, as shown schematically in **Figure 4.16** [62]. This morphology was proposed based on the similarity of the PVDF-HFP and the non-sulfonated block of the PFCB, whereas the strongly polar sulfonated block would prefer to interact with itself, as compared with the other

non-polar components. Because there isn't a hard interface noted at the edges of the ionic aggregate, it is believed the aggregate is surrounded by the non-sulfonated block of the copolymer, however a large amount of this non-sulfonated block is also incorporated into the aggregate itself. In addition, this aggregate is about 400 nm in size, and with the sulfonated portion making up the majority, a large amount of ionic material is no longer available as part of the electrostatic network. This correlates well with the large irreversible decrease in proton conductivity observed at these conditions, and also implies fuel cell output would be severely reduced over a relatively short time.

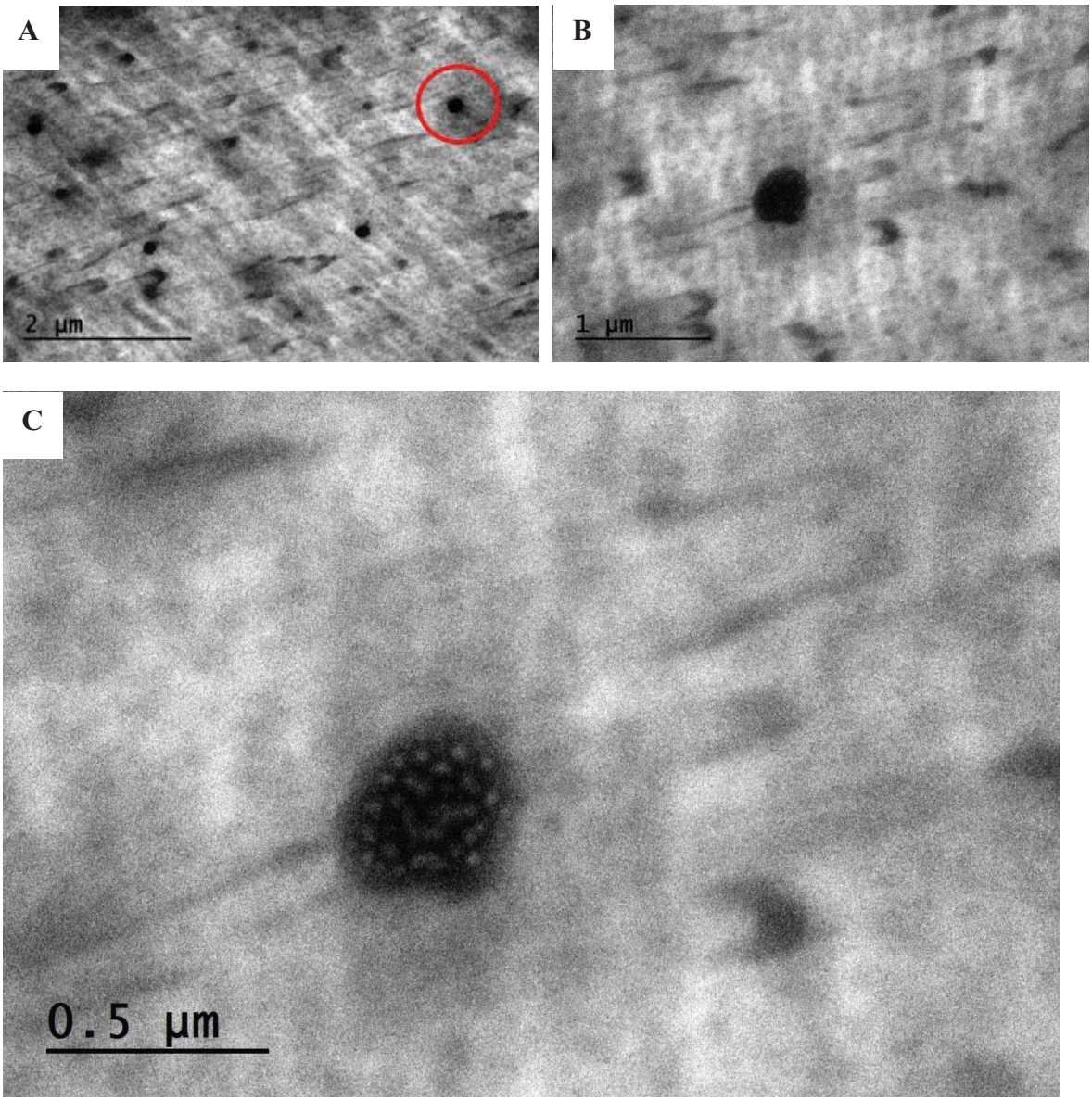

Figure 4.49. TEM images of an ionic aggregate in a sample immersed at 80°C for 8 hrs at **(A)** 30,000 magnification, **(B)** 50,000 magnification, and **(C)** 80,000 magnification.

Although evidence has been presented to explain the observed changes in proton conductivity over time while immersed at high temperature, fuel cell testing at General Motors has not specifically shown this proton conductivity behavior. One possibility is that the catalyst and gas diffusion media provide protection to the membrane, allowing for more controlled exposure to the high temperature and high moisture environment. In addition, it is also possible

this decline in proton conductivity could be related to hydrolysis of the sulfonic acid groups. However, it is possible the highly acidic environment of an operating fuel cell replenishes the sulfonic acid groups, and thus reduces the formation of tighter, more physically crosslinked aggregates. If these sulfonic acid groups are constantly re-protonated it is possible the electrostatic network would be maintained over the lifetime of the material. This theory could be tested by performing the three hour conductivity test immersed at 80 or 90°C, removing the sample and placing it in a concentrated acid, such as HCl, for one hour, and then beginning the three hour conductivity test again. If the conductivity returned to its initial value prior to extended exposure at high temperatures and moisture levels, this would be indicative that a highly acidic environment can reverse the reduction of the electrostatic network and possibly explain why this material change is not observed in an operating fuel cell.

4.3.3.6. Examination of Samples Annealed at 140°C for 4 Hours

It was previously noted by General Motors that annealing samples at 140°C for 4 hours increased the biaxial strength of the material. Further investigation into this pre-test treatment by May showed annealed samples no longer went into solution, indicating the materials had formed strong physical or chemical crosslinks, although the cause was never determined [62]. Based on work by Bi et al., who blended crosslinked sulfonated poly(arylene ether sulfone) with sulfonated polyimides, it was thought the additional crosslinking induced by the 140°C 4 hr anneal may reduce or prevent the decline in the proton conductivity [35]. Therefore, material was annealed at 140°C for 4 hrs, and the proton conductivity was measured immersed at 80°C for three hours, and again after storage at ambient conditions as described previously. This data is compared with an unannealed sample in **Figure 4.50**. As can be seen, the proton conductivity of the annealed sample is stable over the initial three hour test period, and declines slightly after

storage at ambient conditions, resulting in an 8% decline over the second three hour test period, compared with the 20+% reduction for the unannealed sample. Therefore, the annealed sample behaves more similarly to an unannealed sample at 60 or 70°C, and may provide a solution for stabilizing the electrostatic network.

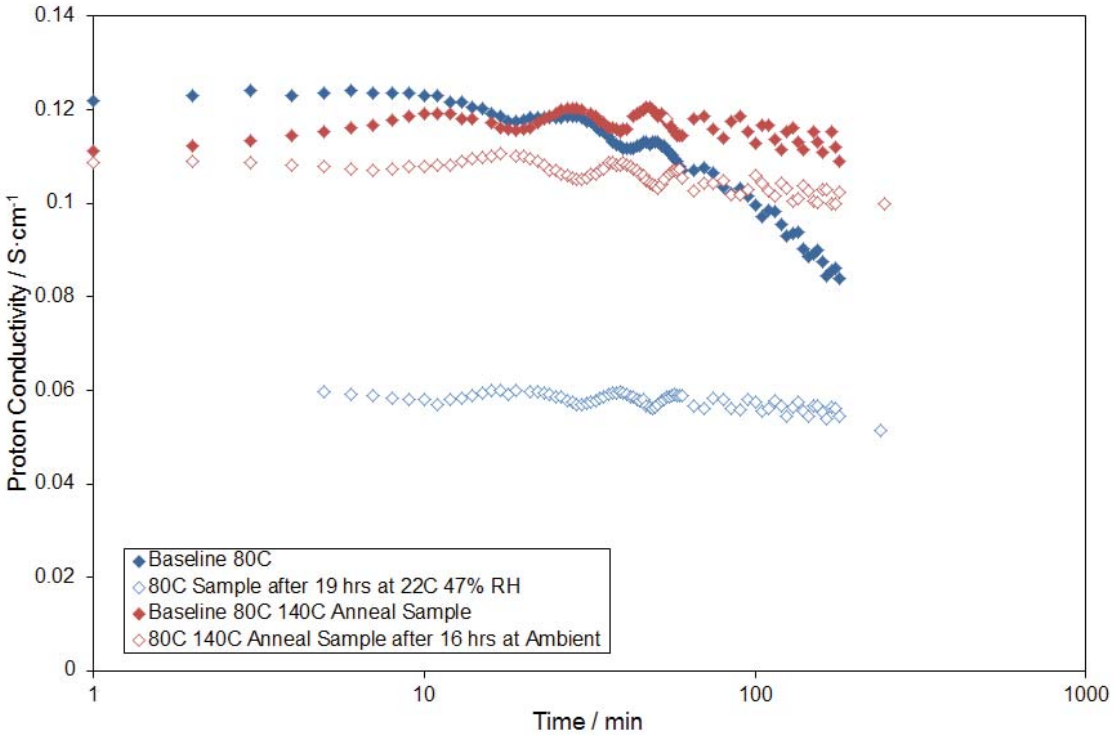

Figure 4.50. Comparison of proton conductivity measured over three hours for an untreated and 140°C 4 hr annealed sample, and again after storage at ambient conditions overnight as noted in the legend.

To investigate changes in the annealed membrane, ATR-IR was again performed and compared with that of an unannealed membrane, focusing on cycle 3 since this appeared to draw the most drastic response from the membrane. As shown in **Figure 4.51**, the annealed sample shows a smaller shift in the sulfonate peak over the first three hours immersed at 80°C. The annealed sample does not appear to show any difference from the unannealed sample when dried

at 80°C, with both membranes displaying a large shift to higher frequencies. However, when the sample is reimmersed at 80°C, both samples return to the last peak position from the previous three hours immersed at 80°C, and the difference between the annealed and unannealed sample can again be noted. A final dry out at 80°C again results in both samples showing a large shift to higher frequencies, with the annealed sample shifting further than the unannealed. The decrease in the sulfonate shift in the annealed sample is consistent with the more stable proton conductivity measured, implying a better electrostatic network is maintained over the testing period. However, annealing does not appear to prevent the large shift noted when the sample is dried at 80°C. Therefore, annealed samples will still require good hydration be maintained at the anode side of a fuel cell to avoid a decline in proton conductivity.

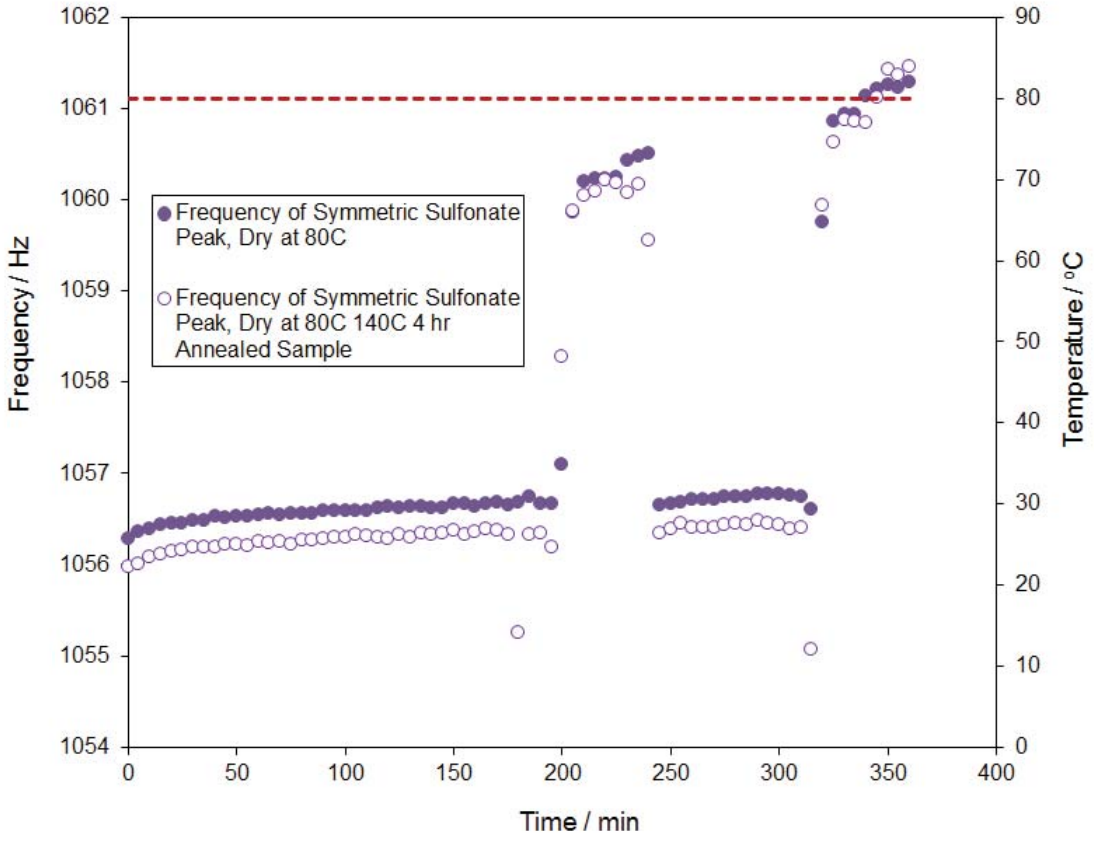

Figure 4.51. Shift of the symmetric sulfonate peak with time when temperature and/or moisture content is cycled.

In addition to the changes noted in the mobility of the sulfonate groups, changes in PVDF-HFP crystallinity with annealing were examined using DSC, as an increase in crystallinity would likely indicate a reduction in PVDF-HFP blooming due to restricted chain motions. As shown in **Figure 4.52A** and **B**, the PVDF-HFP crystallinity approximately doubles. In addition, the melting temperature increases to 138°C after annealing at 140°C, as compared with the ~120°C melting temperature observed for non-annealed samples (**Figure 4.53**). The increase in melting temperature corresponds with the formation of purer, denser, and larger PVDF-HFP crystallites, which would correlate well with an increase in the physical crosslinks in the PFCB/PVDF-HFP material and thus a likely reduction in the PVDF-HFP blooming effect during membrane dry-out [70]. Therefore annealing does appear to increase the physical network of the membrane likely resulting in a reduction in the polarity switch that occurs at high temperatures, which would be of help during fuel cell operation if the anode dries out.

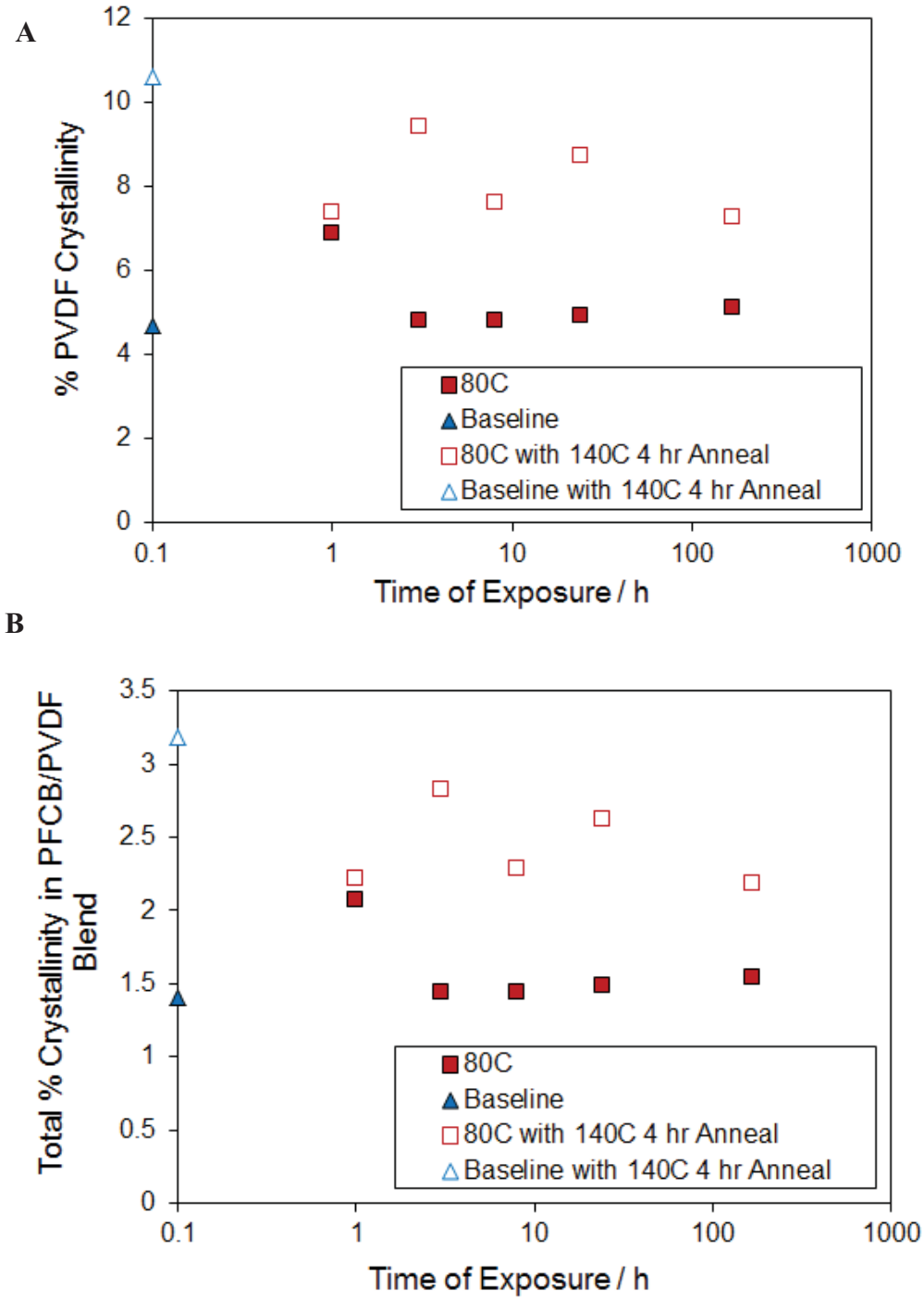

Figure 4.52. Percent crystallinity of **(A)** PVDF-HFP and **(B)** total crystallinity in the PFCB/PVDF-HFP blend, comparing 140°C annealed and non-annealed samples.

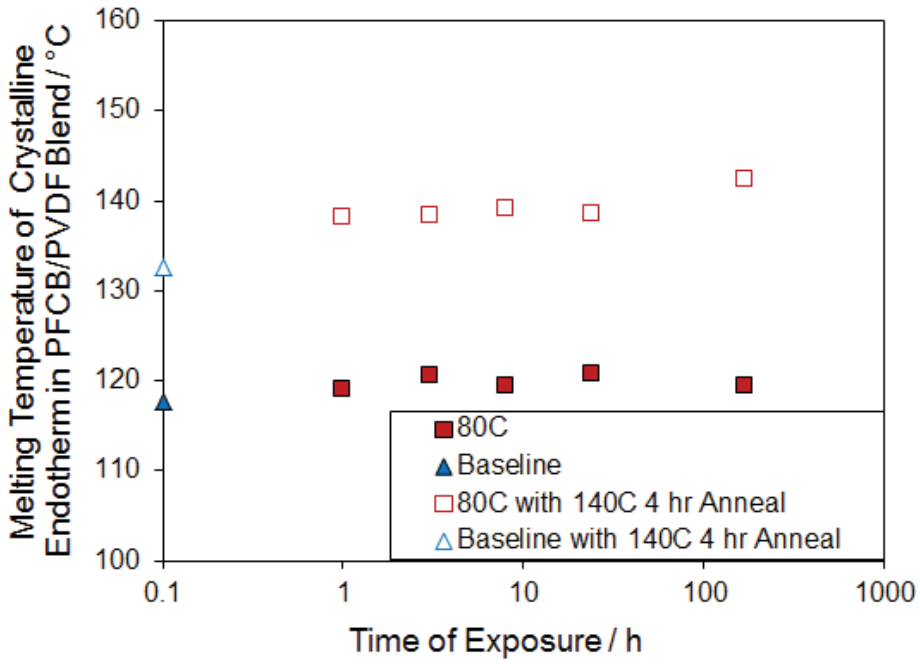

Figure 4.53. Melting temperature of PVDF-HFP crystalline endotherms in PFCB/PVDF-HFP comparing 140°C annealed and non-annealed samples.

The increase in the physical network, especially within the PVDF component, could contribute to better phase stability, however, based on previous work completed by May and Siuta, it is likely that chemical crosslinks are forming [49, 62]. To investigate this possibility further, an H^+ form unannealed PFCB/PVDF-HFP sample, a 140°C annealed H^+ sample, and a 140°C annealed Cs^+ sample were examined. As seen in **Figure 4.54** the 140°C annealed H^+ sample shows darkening as compared with the nonannealed H^+ sample and the 140°C annealed Cs^+ sample which both appear to have similar coloration. This darkening of the 140°C annealed H^+ sample is indicative of the degradation of sulfonate groups. It is believed that the 140°C annealed Cs^+ sample does not show any color change because the Cs^+ counterion stabilizes the sulfonate group, and therefore degradation does not occur until higher temperatures [71].

Furthermore, ion exchange capacity measurements performed on the nonannealed H^+ sample and the 140°C annealed H^+ sample show a decrease in the equivalent weight from ~1500 to ~1200 g PFCB/mol SO_3^-. This indicates a reduction in the number of sulfonate groups available in the PFCB, correlating well with the color change noted in the annealed H^+ sample. However, it should be noted that typically a reduction in the equivalent weight would result in a reduction in the proton conductivity. While there is an initial reduction in the proton conductivity of annealed samples, as shown in **Figure 4.50**, it is only approximately a 10% reduction, and the conductivity remains stable over the entirety of the test period.

To determine if chemical crosslinks were formed during the annealing process, the H^+ form unannealed PFCB/PVDF-HFP sample, 140°C annealed H^+ sample, and 140°C annealed Cs^+ sample were placed in DMAc such that a 0.5 wt% solution would be created. As shown in **Figure 4.55**, the 140°C annealed H^+ sample does not dissolve, and forms a gel-like substance, whereas both the H^+ form unannealed PFCB/PVDF-HFP sample and the 140°C annealed Cs^+ sample dissolved quickly and formed clear solutions with the DMAc. Therefore, it is believed that chemical crosslinks were formed in the 140°C annealed H^+ sample but not in the 140°C annealed Cs^+ sample. Because the Cs^+ counterion stabilizes the sulfonate group such that degradation does not occur and chemical crosslinks are not formed in this sample, it is thought that the chemical crosslinking mechanism is related to the degradation of the sufonate groups, as found in the 140°C annealed H^+ sample.

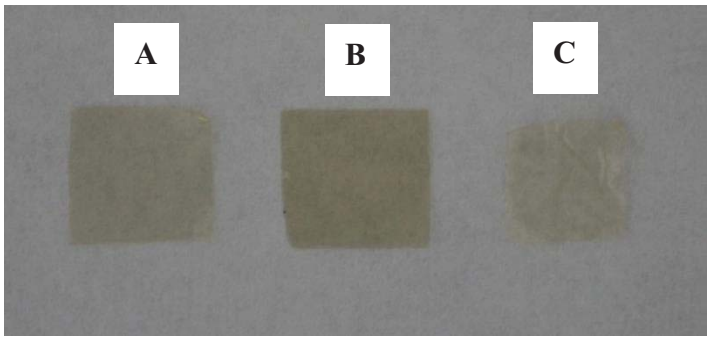

Figure 4.54. Comparison of **(A)** unannealed H^+ form PFCB/PVDF-HFP sample, **(B)** 140°C annealed H^+ form PFCB/PVDF-HFP sample, and **(C)** 140°C annealed Cs^+ form PFCB/PVDF-HFP sample

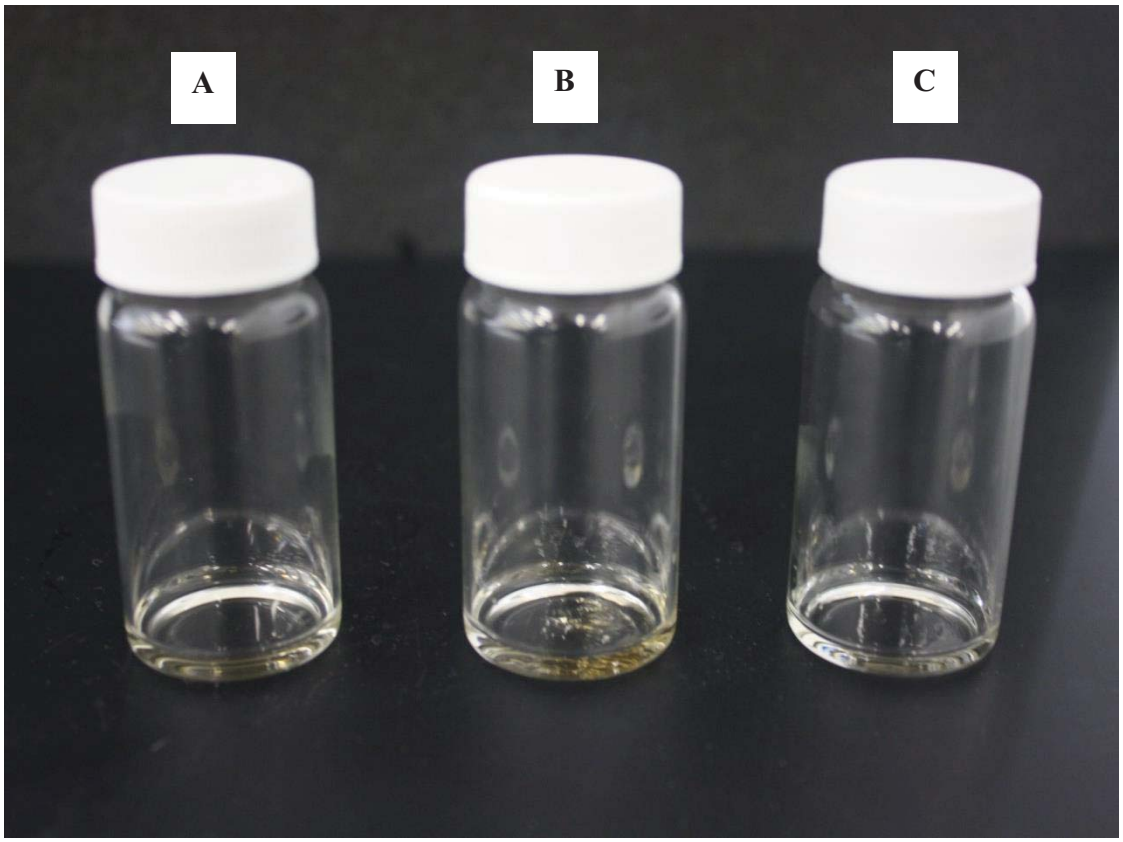

Figure 4.55. Comparison of **(A)** unannealed H^+ form PFCB/PVDF-HFP sample, **(B)** 140°C annealed H^+ form PFCB/PVDF-HFP sample, and **(C)** 140°C annealed Cs^+ form PFCB/PVDF-HFP sample, in DMAc.

To examine the possible chemical crosslinking mechanism further, the structure of the sulfonated PFCB block copolymer must be examined to understand the chemical make-up of the sulfonated substituents (**Figure 4.56**). It should be noted that in **Figure 4.56** the perfluorovinyl ether side chain is shown with a K^+ ion, which is the form the material is cast in. An ion exchange is later performed to place the material in the acid form. Therefore, all discussion will relate to the acid form of this material. Based on **Figure 4.56**, it is clear the perfluorovinyl ether side chain is very similar to that of Nafion®. Thus, it is highly likely it would undergo thermal degradation in a similar manner to Nafion®.

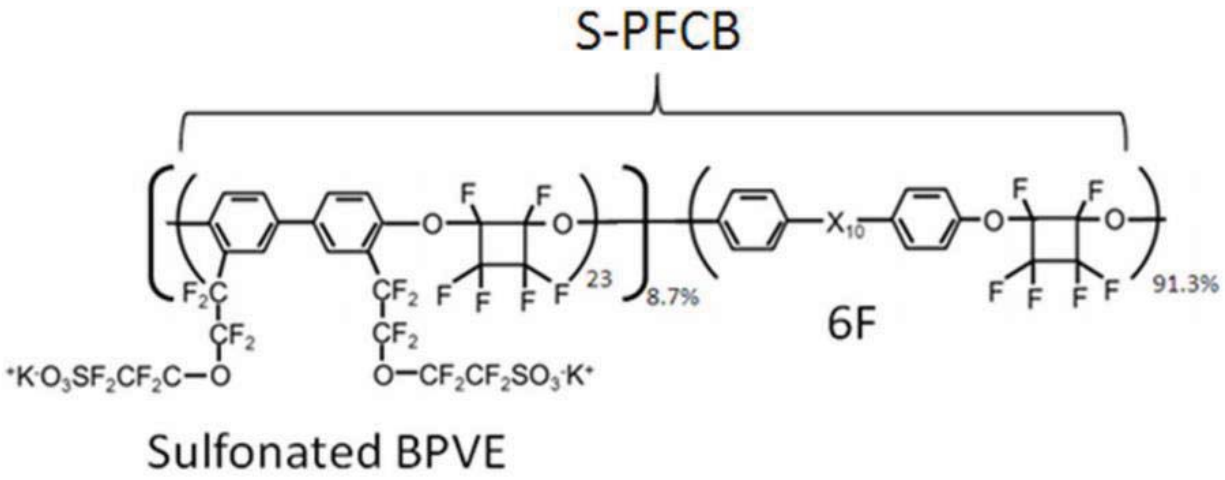

Figure 4.56. Structure of sulfonated PFCB block copolymer, displaying the structure of the sulfonated side substituents.

In **Scheme 4.1** the degradation of the S-O bond results in the creation of a hydroxy radical and a sulfone radical as proposed by Wilkie et al., Samms et al., and Deng et al. for Nafion® materials using TGA coupled with FTIR [71-73]. It is likely the hydroxyl radical would then extract the acidic proton from another sulfonate group, producing water, and a sulfonate radical. It is then possible that the sulfone radical and the sulfonate radical would combine, creating a disulfone ester, and thus chemically linking two different perfluorovinyl

ether side chains. This reaction mechanism provides a possible route for chemical crosslinking to occur due to the formation of a radical during thermal degradation, while **Scheme 4.2** provides a similar route for chemical crosslinking, but now based on hydrolysis of the sulfonate group. In **Scheme 4.2** a water molecule in the membrane extracts a proton from the sulfonate group, resulting in the formation of a sulfonate anion and a hydronium ion. The hydronium ion may then revert to a water molecule and a hydrogen cation. The hydroxyl group of the sulfonate can then interact with the hydrogen cation, resulting in the formation of another water molecule, and a sulfone cation. The sulfone cation and the sulfonate anion may then interact to form a disulfone ester, resulting in the chemical linking of two different perfluorovinyl ether side chains.

It is highly likely that the chemical crosslinks formed due to thermal degradation in the PFCB block copolymer provide better blend phase stability, and help decrease the mobility of the sulfonate groups as noted with ATR-IR measurements in **Figure 4.51**. Therefore, it is recommended that these PFCB/PVDF-HFP materials be annealed prior to use, as this will induce a small amount of chemical crosslinking, and likely extend the productive lifetime of the membrane. It should be noted that annealing for longer times or at higher temperatures may result in a greater degree of sulfonate degradation which could negatively impact the proton conductivity. Further work should be completed to determine the optimum annealing time and temperature, although this study is currently outside the scope of this research.

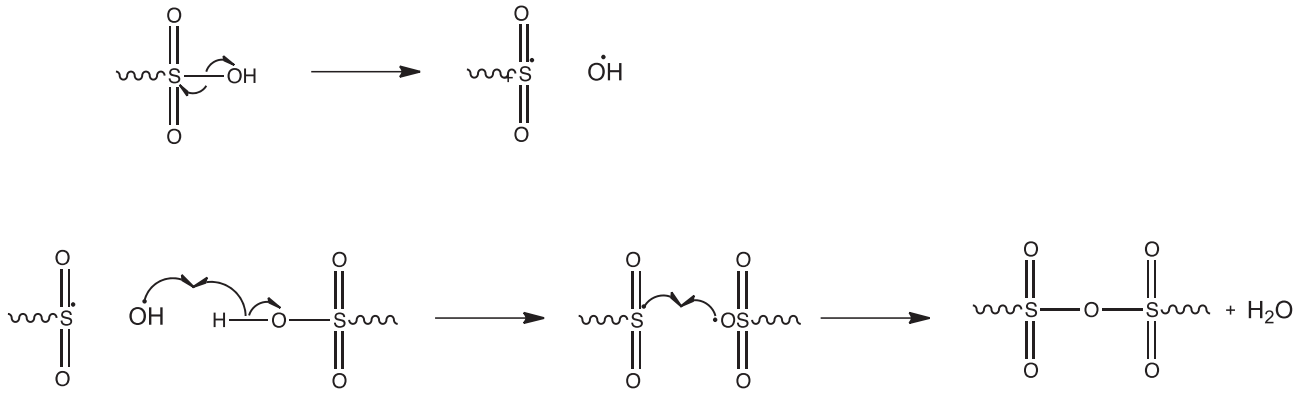

Scheme 4.1. Thermal degradation of the S-O bond, resulting in the creation of a disulfone ester, and the crosslinking of two side chains.

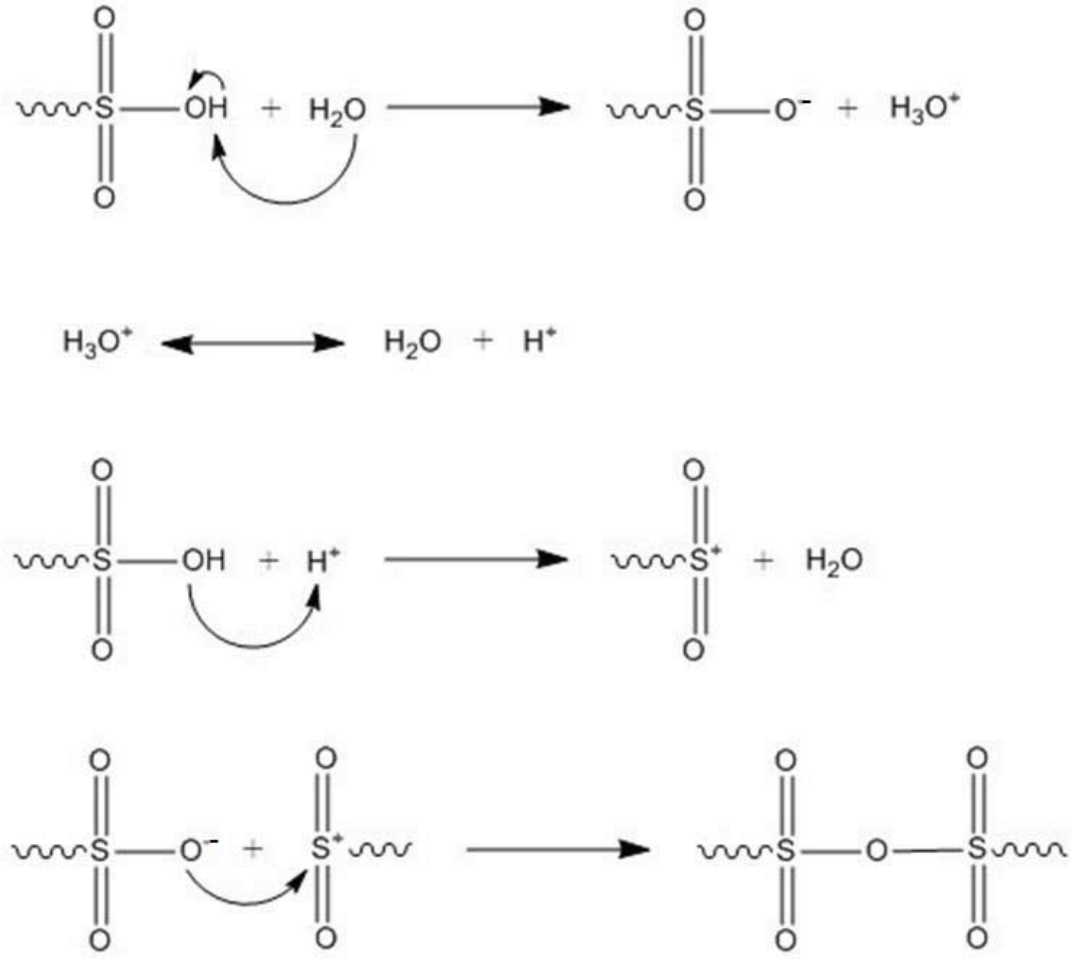

Scheme 4.2. Hydrolysis of the sulfonate group, resulting in the creation of a disulfone ester and the crosslinking of two side chains.

4.4. Conclusions

It was initially noted that the stress relaxation modulus stiffens with increased exposure time at increased temperature and moisture conditions. While this behavior appeared similar to mechanical conditioning used in fiber reinforced composites, additional investigations showed a decrease in the mass uptake and proton diffusion, as well as an increase in the phase separation of the PFCB block copolymer and PVDF-HFP crystalline order. This preliminary investigation indicated that exposure at increased moisture and temperature conditions resulted in a stiffening of the membrane, corresponding with molecules pinned in different domains due to increased phase separation.

To further understand how the material changes under more common fuel cell operating conditions, a more detailed analysis was performed on membranes aged at multiple temperature and moisture levels. It was noted that minimal changes occurred for all samples aged at 30°C, while samples aged at 80% RH or immersed in DI water showed a delay in the relaxation mechanism. In addition, immersed samples showed an increase in the biaxial strength after 1 and 24 hrs, and a decrease after 1 wk of conditioning. Based on small angle x-ray scattering, these materials conditioned at high temperature and moisture conditions showed an increase in the degree of phase separation and PVDF-HFP crystallite spacing with increasing time and moisture content. This is consistent with the preliminary study, as well as the mechanical constitutive data. Increased phase separation and crystallite spacing would pin the polymer chains in different domains, increasing entanglements, resulting in a delay in the relaxation mechanism and an increase in the biaxial strength. As the entanglements increase further, as noted with the sample immersed at 80°C for 1 wk, it is possible the chains are no longer able to

disentangle easily, resulting in an embrittlement of the material and an apparent reduction in the strength. Proton conductivity was also measured, noting a large decrease in the conductivity of samples immersed at 80°C. Based on IR measurements, this decline in conductivity could be attributed to the formation of tighter ionic aggregates, and less of an electrostatic network throughout the material.

Because the proton conductivity decreased so severely after 1 hr immersed at 80°C, further investigation of samples exposed to immersed conditions was completed. Proton conductivity measurements performed over three hours showed a large decline in the conductivity for samples immersed at 80 and 90°C. A further decline in conductivity was noted for these samples after storage at ambient conditions overnight. IR scans showed a shift in the sulfonate peak with time for samples immersed at 80°C, implying the ionic aggregates are becoming tighter, and less of an electrostatic network exists throughout the membrane, consistent with a decline in conductivity. In addition, IR scans also show PVDF-HFP does not bloom to the surface of the membrane unless it is dried at 80°C, however this phenomenon appears to be reversible when the sample is reimmersed similar to polarity changes noted in Nafion®. Small angle x-ray scattering is also consistent with the IR and proton conductivity data, showing an increase in the degree of phase separation and crystallite spacing with increased temperature and time at temperature. Increased phase separation would correspond well with the formation of tighter ionic aggregates, and thus a reduction in proton conductivity. In addition, DSC data shows an increase in the degree of crystallinity in samples conditioned at higher temperatures, consistent with the SAXS data, and also consistent with a reduction in proton conductivity. Finally, TEM imaging was performed, providing a visual of the formation of tighter ionic aggregates and the decrease of the electrostatic network with increased time at temperature.

Therefore, this blend membrane may be quite problematic in an operating fuel cell, as a decrease in conductivity would result in a decrease in power output and efficiency and likely lead to early failure of the cell.

However, a possible solution to prevent the decline in proton conductivity, increased phase separation, and decreased electrostatic network, is to anneal the sample at 140°C for 4 hrs. Based on DSC data it is clear there is not only increased crystallinity, but larger, denser, purper crystals, resulting in increased physical crosslinking. In addition, dissolution studies show that a small number of sulfonic acid groups are degrading and forming chemical crosslinks via condensation, but does not appear to negatively impact proton conductivity at this level of crosslinking. The combination of increased physical crosslinks and the addition of chemical crosslinking allows for better blend phase stability, and appears to mitigate the decline in the proton conductivity, even after storage at ambient conditions. Finally, IR data measured over time also shows less of a shift of the sulfonate group to a more polar environment, indicating a stabilization of the electrostatic network. Therefore, if possible, these blend membranes should be exposed to this annealing process prior to use to prevent early failure of the membrane, and thus extend the fuel cell lifetime.

4.5. References

[1] O.o.B.E.S. US Department of Energy, in: U. DOE (Ed.), Washington DC, 2004.
[2] Y.-H. Lai, D.A. Dillard, Mechanical Durability Characterization and Modeling of Ionomeric Membranes, in: W. Vielstich, H. Yokokawa, H. Gasteiger, A. (Eds.) Handbook of Fuel Cells - Fundamentals, Technology and Applications, John Wiley & Sons, New York, 2009.
[3] W.K. Liu, S.J.C. Cleghorn, B.E. Delaney, M. Crum, Chemical and Mechanical Membrane Degradation, in: W. Vielstich, H. Yokokawa, H. Gasteiger, A. (Eds.) Handbook of Fuel Cells - Fundamentals, Technology and Applications, John Wiley & Sons Ltd., New York, 2009, pp. 385-402.

[4] R. O'Hayre, S.-W. Cha, W. Colella, F.B. Prinz, Fuel Cell Fundamentals, 2nd ed., Wiley, New York, NY, 2009.
[5] Y. Li, D.A. Dillard, Y.-H. Lai, S. Case, W., M.W. Ellis, M.K. Budinski, C.S. Gittleman, Journal of the Electrochemical Society, 159 (2012) B173-B184.
[6] C.S. Gittleman, Y.-H. Lai, C. Lewis, D.P. Miller, in: AIChE, Cincinnati, OH, 2005.
[7] Y.-H. Lai, C.K. Mittelsteadt, C.S. Gittleman, Journal of Fuel Cell Science and Technology, 6 (2009) 021002/021001-021002/021013.
[8] Y.-H. Lai, C.K. Mittelsteadt, C.S. Gittleman, D.A. Dillard, in: Third International Conference on Fuel Cell Science, Engineering and Technology, Ypsilanti, Michigan, 2005.
[9] W. Liu, K. Ruth, R. Greg, Journal of New Materials for Electrochemical Systems, 4 (2001) 227-231.
[10] V. Stanic, in: 4th International Symposium on Proton Conducting Membrane Fuel Cells, 2004.
[11] A.Z. Weber, J. Newman, AIChE Journal, 50 (2004) 3215-3226.
[12] D. Liu, S. Case, Journal of Power Sources, 162 (2006) 521-531.
[13] S. Kundu, L.C. Simon, M. Fowler, S. Grot, Polymer, 46 (2005) 11707-11715.
[14] M. Marrony, R. Barrera, S. Quenet, S. Ginoccio, L. Montelatici, A. Alsanides, Journal of Power Sources, 182 (2008) 469-475.
[15] Y.P. Patil, W.L. Jarett, K.A. Mauritz, Journal of Membrane Science, 356 (2010) 7-13.
[16] T. Kyu, A. Eisenberg, Journal of Polymer Science, Symposia, 71 (1984) 203-219.
[17] A. Kusoglu, Y. Tang, M. Lugo, A. Karlsson, M., M. Santare, H., S. Cleghorn, W. Johnson, B., Journal of Power Sources, 195 (2010) 483-492.
[18] S.T. Iacono, S.M. Budy, J. Jin, D. Smith, Jr, Journal of Polymer Science Part A: Polymer Chemistry, 45 (2007) 5705-5721.
[19] S.T. Iacono, D. Ewald, A. Sankhe, A. Rettenbacher, D.W. Smith, Jr, High Performance polymers, 19 (2007) 581-591.
[20] B.-J. Chang, D.-J. Kim, J.-H. Kim, S.-B. Lee, H.-J. Joo, Journal of Membrane Science, 325 (2008) 989-996.
[21] DuPont, in, 2009, pp. 4.
[22] D.-J. Kim, B.-J. Chang, J.-H. Kim, S.-B. Lee, H.-J. Joo, Journal of Membrane Science, 325 (2008) 217-222.
[23] S.S. Mao, K.A. Lewinski, D.A. Ylitalo, in: U.S.P. Office (Ed.), 3M Innovative Properties Company, United States, 2003.
[24] D.A. Babb, B.R. Ezzell, K.S. Clement, W.F. Richey, A.P. Kennedy, Journal of Polymer Science Part A: Polymer Chemistry, 31 (1993) 3465-3477.
[25] A.P. Kennedy, L.D. Bratton, Z. Jezic, R.E. Lane, D.J. Perettie, W.F. Richey, D.A. Babb, K.S. Clement, in: U.S.P. Office (Ed.), The Dow Chemical Company, United States, 1995.
[26] H.-C. Liou, P.S. Ho, A. McKerrow, Journal of Polymer Science, Part B: Polymer Physics, 36 (1998) 1383-1392.
[27] J. Kerres, W. Cui, M. Junginger, Journal of Membrane Science, 139 (1998) 227-241.
[28] J. Kerres, A. Ullrich, T. Haring, M. Baldauf, U. Gebhardt, W. Preidel, Journal of New Materials for Electrochemical Systems, 3 (2000) 229-239.
[29] J. Kerres, A. Ullrich, F. Meier, T. Haring, Solid State Ionics, 125 (1999) 243-249.
[30] N. Gourdoupi, J.K. Kallitsis, S. Neophytides, Journal of Power Sources, 195 (2010) 170-174.

[31] A. Linares, J.L. Acosta, S. Rodriguez, Journal of Applied Polymer Science, 100 (2006) 3473-3482.
[32] M. Arigonda, A.P. Deshpande, S. Varughese, Journal of Applied Polymer Science, (2012).
[33] E. Sgreccia, M. Khadhraoui, C. de Bonis, S. Licoccia, M.L. Di Vona, P. Knauth, Journal of Power Sources, 178 (2008) 667-670.
[34] P. Bhavani, D. Sangeetha, Journal of Polymer Research, 19 (2012) 1-10.
[35] H. Bi, J. Wang, S. Chen, Z. Hu, Z. Gao, L. Wang, K.-i. Okamoto, journal of Membrane Science, 350 (2010) 109-116.
[36] T. Inan, H. Dogan, E.E. Unveren, E. Eker, International Journal of Energy and Environment, 35 (2010) 12038-11053.
[37] P. Zapata, P. Basak, J.C. Meredith, Electrochimica Acta, 54 (2009) 3899-3909.
[38] P. Zapata, J.-H. Lee, J.C. Meredith, Journal of Applied Polymer Science, 124 (2012) E241-E250.
[39] P. Zapata, D. Mountz, J.C. Meredith, Macromolecules, 43 (2010) 7625-7636.
[40] T. Zhang, W. He, J. Goldbach, D. Mountz, J. Yi, Journal of Power Sources, 196 (2011) 1687.
[41] P. Piboonsatsanasakul, J. Wootthikanokkhan, S. Thanawan, Journal of Applied Polymer Science, 107 (2008) 1325-1336.
[42] P. Bhavani, D. Sangeetha, Chinese Journal of Polymer Science, 30 (2012) 548-560.
[43] A. Mokrini, M.A. Huneault, Journal of Power Sources, 154 (2006) 51-58.
[44] N. Seeponkai, J. Wootthikanokkhan, Journal of Applied Polymer Science, 117 (2010) 393-399.
[45] A.R. Gordon, M.W. Ellis, D.A. Dillard, S.W. Case, R.B. Moore, Y. Li, Y.-H. Lai, C.S. Gittleman, in: ASME 6th International Conference on Energy Sustainability & 10th Fuel Cell Science, ASME, San Diego, CA, 2012.
[46] A.R. Gordon, M.W. Ellis, D.A. Dillard, S.W. Case, R.B. Moore, Y. Li, Y.-H. Lai, C.S. Gittleman, (In Preparation).
[47] A.M. Osborn, in: Macromolecular Science and Engineering, Virginia Polytechnic Institute and State University, Blacksburg, VA, 2010, pp. 501.
[48] A.M. Osborn, R.B. Moore, D.A. Dillard, S.W. Case, M.W. Ellis, T.J. Fuller, S.M. MacKinnon, C.S. Gittleman, Y.-H. Lai, in: 239th National American Chemical Society Meeting and Exposition, American Chemical Society, San Francisco, CA, 2010, pp. 55-56.
[49] C.M. Siuta, in: Engineering Science and Mechanics, Virginia Polytechnic Institute and State University, 2011, pp. 73.
[50] Y. Li, in, 2010.
[51] R. Christensen, M., Theory of Viscoelasticity: An Introduction, 2nd ed., Academic Press, New York NY, 1982.
[52] J.R. Grohs, Y. Li, D.A. Dillard, S.W. Case, M.W. Ellis, Y.-H. Lai, C.S. Gittleman, Journal of Power Sources, 195 (2010) 527-531.
[53] Y. Li, D. Dillard, A., S. Case, W., M. Ellis, W., Y.-H. Lai, C. Gittleman, S., D.P. Miller, Journal of Power Sources, 194 (2009) 873-879.
[54] J. Li, K.G. Wilmsmeye, L.A. Madsen, Macromolecules, 42 (2009) 255-262.
[55] J.-H. Cao, B.-K. Zhu, Y.-Y. Xu, Journal of Membrane Science, 281 (2006) 446-453.
[56] M. Tazaki, R. Wada, M. Okabe, T. Homma, Journal of Applied Polymer Science, 65 (1997) 1517-1524.

[57] L. Yan, D. Dillard, A., R.L. West, L.D. Lower, G.V. Gordon, Journal of Polymer Science Part B: Polymer Physics, 48 (2010) 2207-2214.
[58] L.C.E. Struik, Physical Aging in Amorphous Polymers and Other Materials, Elsevier Science, 1980.
[59] J. Hou, J. Li, L.A. Madsen, Macromolecules, 43 (2010) 347-353.
[60] W.S. Price, Concepts in Magnetic Resonance, 9 (1997) 299-336.
[61] W.S. Price, Concepts in Magnetic Resonance, 10 (1998) 197-237.
[62] N. May, in: Materials Science and Engineering, Virginia Polytechnic Institute and State University, Blacksburg, VA, 2011, pp. 101.
[63] M. Zhang, R.B. Moore, in, 2012.
[64] D.A. Dillard, Y. Li, J.R. Grohs, S.W. Case, M.W. Ellis, Y.-H. Lai, M.K. Budinski, C.S. Gittleman, Journal of Fuel Cell Science and Technology, 6 (2009) 031014/031011-021014/031018.
[65] S. Abbrent, J. Plestil, D. Hlavata, J. Lindgren, J. Tegenfeldt, A. Wendsjo, Polymer, 42 (2001) 1407-1416.
[66] X. Tian, X. Jiang, Journal of Hazardous Materials, 153 (2008) 128-135.
[67] K. Cable, M., K.A. Mauritz, R.B. Moore, Journal of Polymer Science Part B: Polymer Physics, 33 (1995) 1065-1072.
[68] T. Zawodzinski, A., S. Gottesfeld, S. Shoichet, T.J. McCarthy, Journal of Applied Electrochemistry, 23 (1993) 86-88.
[69] Y. Fan, M. Zhang, R.B. Moore, H.-S. Lee, J.E. McGrath, C.J. Cornelius, Polymer, 52 (2011) 3963-3969.
[70] J.M. Schultz, Polymer Crystallization The Development of Crystalline Order in Thermoplastic Polymers, Oxford University Press and American Chemical Society, New York, New York, 2001.
[71] C.A. Wilkie, J.R. Thomsen, M.L. Mittleman, Journal of Applied Polymer Science, 42 (1991) 901-909.
[72] Q. Deng, C.A. Wilkie, R.B. Moore, K.A. Mauritz, Polymer, 39 (1998) 5961-5972.
[73] S.R. Samms, S. Wasmus, R.F. Savinell, Journal of the Electrochemical Society, 143 (1996) 1498-1504.

Chapter 5 : Future Work: Analysis of PFCB/PVDF-HFP Membranes Under Immersed Conditions

5.1 Introduction

Previous work has been completed to examine the properties of PFCB/PVDF-HFP membrane under dry and humidified conditions. This included stress relaxation, hygral and thermal expansion, and mass uptake measurements. Additional measurements were taken after exposing material to different environmental conditions corresponding to conditions frequently found in operating fuel cells. While these latter measurements included membranes conditioned under an immersed environment, previous characterization did not include samples under immersed conditions. Therefore, to update the stress model presented in Chapter 3 to fully describe membrane properties over the entirety of fuel cell operating conditions, additional characterization should be completed. The work presented herein is the beginning of this additional characterization, including in- and out-of-plane hygral expansion, and buckling induced during hydration of a constrained membrane.

5.2 Experimental

5.2.1 Materials

Cast membranes, approximately 12 μm thick, of 70:30 wt:wt PFCB and PVDF-HFP (Kynar Flex® from Arkema) were received from the General Motors Electrochemical Energy Research Laboratory. The casting solution was created by dissolving 0.10000 kg of PFCB ionomer from Tetramer Technologies and 0.04286 kg of Kynar Flex® 2751 from Arkema in 0.7143 kg of *N,N*-dimethylacetamide (DMAc). The solution was roll milled for 1 week in a 1-L

jar with a Teflon® screw cap, and pressure filtered through a 5-μm Mitex® Millipore filter. Several coating solutions were then combined and diluted with DMAc, resulting in a 15 wt% solids solution, in order to create smoother coatings.

The solution was then cast using a coating line consisting of a knife over roll, reverse roll coater onto a polypropylene coated blue paper backer. A coating width of 203 mm and a gap of 0.050 mm were utilized with varying speeds to obtain the targeted membrane coating thickness. After laying the solution down on the backing material, the solution was passed through a 24.4-m drier. The first 12.2 m utilized convection heating, and the second 12.4, IR heating both at temperatures less than 100°C. Rolls of membranes were created at the intended thickness of 14-16 μm, however the actual thickness after casting was ~12 μm as measured by a drop gauge micrometer.

A pre-test treatment was deemed necessary to remove excess DMAc as the excess solvent appeared to be creating a softer, lower modulus, and lower strength material [1]. Therefore, all membranes received from GM underwent a solvent exchange in 50°C water for 1 h, while biaxially constrained in a 11.4 x 11.4 cm^2 polytetrafluoroethylene (PTFE) frame. The membranes were then stored in the PTFE frame overnight inside a desiccator to remove excess moisture. As the membrane dries in the frame, it becomes taut, producing locked in strains in the material. Therefore, immediately prior to testing and after removal from the PTFE frame, each membrane underwent a 100°C 2 h isotherm at 0% RH to remove the locked in strains.

For comparison purposes Dupont™ Nafion® NRE 211 (NRE 211) membranes, approximately 25 μm thick, produced reportedly from a casting process, were also characterized. These membranes were not subjected to the one hour 50°C solvent exchange because it was not

performed for prior characterization, but for consistency in membrane water content, samples were subjected to the two hour 100^{o}C isotherm prior to testing.

5.2.2. Dynamic Mechanical Analysis

Measurements were obtained using a tension immersion clamp with the TA Instruments Q800 DMA on PFCB/PVDF-HFP and NRE 211. The sample dimensions are defined by the clamp, and as such each sample is only 6mm wide with a single slit down the middle, and 15 mm in length. These samples were cut using a rule die into 50 x 9mm samples, with two 20mm slits creating three 3mm sections, however one section was then cut off using a scalpel to create the 6-mm wide samples. The PFCB/PVDF-HFP samples were double layered, as is done in all DMA testing, to create a larger thickness (24 μm) and therefore a higher stiffness and allow for the collection of cleaner data. NRE 211 samples were only a single layer due to their larger thickness (25 μm). Dynamic temperature scans were performed after immersing the sample in room temperature water for 3 hrs to allow for sample equilibration. The temperature was then ramped at 0.25°C/min to 80°C with a 0.5% strain and 3 mN static force applied, and a force track of 125%. The applied strain and force track were chosen based on the samples behaving more like a rubbery material, as noted by Kusoglu previously for NRE 211 [2].

Additional temperature sweeps were performed in a in a TA Instruments DMA Q800 in conjunction with a TA Instruments Relative Humidity Accessory. This was done to obtain the dynamic mechanical properties under a 0% RH atmosphere for comparison with the immersed data. These samples were cut using a rule die into 50 x 9mm samples, with two 20mm slits creating three 3mm sections, and mounted with a 15mm gage length.

5.2.3. In-Plane Hygral Expansion

In-plane swelling was performed using a Nikon Eclipse LV100 optical microscope. Samples were prepared by removing the membrane from the backing in the direction of casting and stored in a desiccator to ensure maximum swelling occurred during testing. To measure swelling, each sample was placed between two glass slides and surrounded with room temperature deionized water through capillary action. This method is assumed to not constrain the membrane in the XY plane because there is water above and below the membrane. The membrane is therefore floating between the layers of water and has the ability to expand freely.

Initial measurements were performed on small circular pieces of membrane, however it was determined that squares were easier to cut and measure. Therefore, the rectangular gage part of a small dogbone punch was used to cut even squares. Images were taken every minute for the first ten minutes, every 5 minutes for the first hour, and every hour for the first five hours. Thereafter, images were taken every 24 hours until the swelling had plateaued, indicating the membrane had reached a maximum in swelling. Each image taken is measured across the diagonal using the Nikon NIS-Elements™ BR 3.10 software, from the same two points on each subsequent image of the same sample. The resolution of the measurements is 0.97μm/pixel. To ensure the membrane stays immersed between daily readings the samples are kept in an enclosed 100% relative humidity environment.

Additional long term in-plane swelling tests were performed using a the same Nikon Eclipse LV100 optical microscope. Samples were prepared by removing the membrane from the backing in the direction of casting and cutting irregular quadrilateral shapes approximately 1.6 x 1.6 mm in size. All cut samples were stored in a desiccator to capture swelling over a wider

range of hydration levels. To conduct a test, a sample was placed between two glass slides and surrounded with deionized water through capillary action and monitored for three days utilizing the time-lapse feature of the microscope software. To ensure the sample stayed immersed over the course of the measurement, it was enclosed in a petri-dish containing liquid water and sealed with Teflon tape. Following the swelling time period, the images taken by the microscope were analyzed by taking the coordinates of each corner of the sample and calculating the total strain.

Additional in-plane swelling measurements were performed using a tension immersion clamp with the TA Instruments Q800 DMA on PFCB/PVDF-HFP and NRE 211. The sample dimensions are defined by the clamp, and as such each sample is only 6mm wide with a single slit down the middle, and 15 mm in length. The PFCB/PVDF-HFP samples are double layered, as is done in all DMA testing, to create a larger thickness (24 μm) and therefore a higher stiffness and allow for the collection of cleaner data. NRE 211 samples are only a single layer due to their larger thickness (25 μm). Measurements were performed using room temperature water and without the use of the DMA furnace. This was done so that data recording could begin prior to the addition of water, thus allowing for capture of membrane swelling when initially immersed. The length of the specimens, nominally loaded in uniaxial tension at very small stress levels, was monitored for three days and the corresponding thermal or hygral expansion was calculated.

5.2.4. Out-of-Plane Hygral Expansion

Out-of-plane hygral expansion was attempted utilizing the Nikon microscope. Samples were dotted on the top and bottom with red and black air brush ink and placed between two glass slides. The samples were then surrounded by deionized water through capillary action and the

focal point of the red and black dots was determined. The difference between the focal points was taken to be the out-of-plane hygral swelling of the membrane.

It is assumed the membrane is not constrained in-plane between the glass slides because there is water above and below the membrane. The membrane is therefore floating between the layers of water and has the ability to expand freely. A force calculation was completed to ensure the glass plate would not constrain the membrane in the Z direction. As calculated (shown below), the upward force applied as a result of membrane hygral expansion is 400 N for this experimental set-up using values from NRE 211, while the downward force of the glass plate on the membrane due to gravity is 0.045N. Therefore, during expansion the upward force of the membrane would be greater than that of the downward force of the plate, and thus it is believed there is insignificant constraint on the membrane in the through thickness direction.

Force of Glass Plate Down:

$m = 4.624g = 0.004624kg$

$F = (0.004624) * (9.8) = 0.045315N$

Force of Swelling Up: (Values from NRE 211 used)

$$\sigma = \frac{F}{A} = \frac{E}{\varepsilon}$$

$$F = \frac{EA}{\varepsilon}$$

$E = 10x10^{6} Pa$

$A = 8x10^{-6} m^{2}$

$\varepsilon = 0.2$

$$F = \frac{\left(10x10^{6}\right) * \left(8x10^{-6}\right)}{0.2} = 400N$$

5.2.5. Membrane Buckling Characterization

The Nikon optical microscope was also employed to examine the buckling, or wrinkling of the membranes when constrained between two glass microscope slides and secured with

binder clips at the narrow ends of the slides. Initially, membrane samples were cut into 19.05 mm wide strips, equivalent to the width of a glass slide, placed between the glass slides and clamped with the binder clips, and immersed in deionized water for 30 minutes. Examination under the microscope revealed an intriguing biaxial buckling pattern, however the biaxial nature made it difficult to discern a standard buckling pattern. Therefore to lessen the biaxial constraint of the membrane, further membrane samples were cut into 3.17 mm wide strips, yielding a more uniform buckling pattern and imposing a primarily uniaxial constraint. The Nikon microscope software program was used to measure the width of the buckles. The depth of the buckles was assessed in a similar manner to the out-of-plane expansion.

Additional buckling experiments were performed to examine how buckling occurs when a membrane is constrained in a set-up similar to a bipolar plate, however in these preliminary experiments no diffusion media was employed. In this case, glass slides were cut into thin strips and glued to two in-tact glass slides, as shown schematically in **Figure 5.1A** and **B**, creating two effective bipolar plates made of glass. Glass was chosen to maintain optical clarity such that the buckling pattern could be viewed using the Nikon optical microscope. Membrane samples were cut to the same size as the glass plates and placed between the plates such that the glass lands aligned. Binder clips were then used to clamp the glass bipolar plates around the entirety of the edges, to emulate clamping found in fuel cells. The entire sample set up was then submerged in deionized water for 30 minutes and then viewed using the Nikon optical microscope. Images were taken such that a view of just the land, just the channel, the edge of a land/channel, and a panoramic image across multiple lands and channels were obtained, as shown by red outlines in **Figure 5.1B**. All images were taken utilizing the large scan feature with manual focus of the Nikon software. The sample was then reimmersed for 5 days and viewed again to monitor any

changes in the buckling pattern over this time. Finally, the sample was allowed to dry, and viewed under the microscope, followed by disassembly and further photographs taken with a Canon Rebel XL DSLR camera.

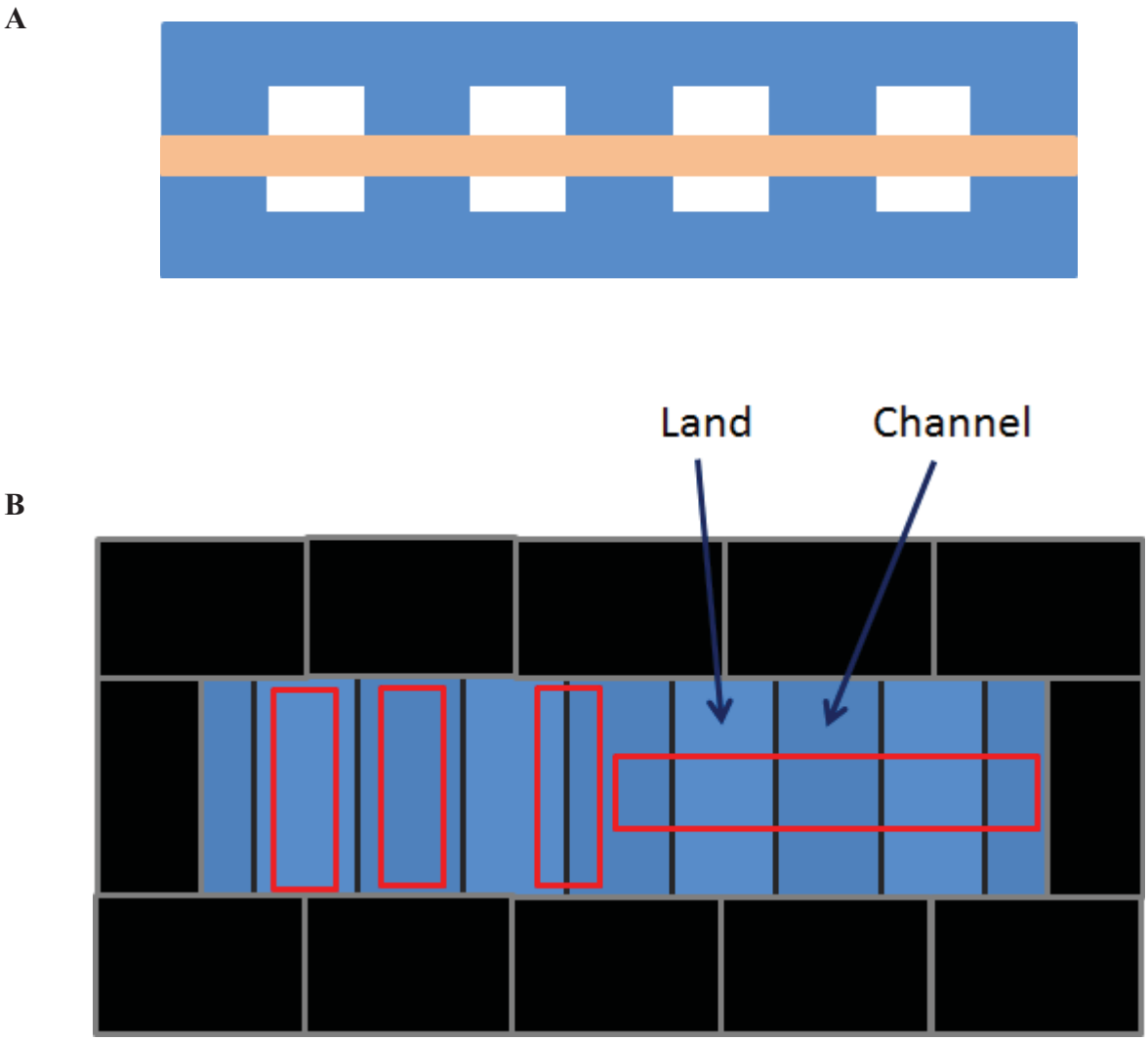

Figure 5.1. Schematics of glass bi-polar plate set up as viewed from **(A)** the side, and **(B)** the top, with the top view also showing the constraint provided by binder clips, as well as typical imaging areas outlined in red.

5.3 Results and Discussion

5.3.1. Dynamic Mechanical Analysis

The temperature sweeps of the immersed PFCB/PVDF-HFP and 0% RH PFCB/PVDF-HFP are compared in **Figure 5.2**. The storage modulus of the nominally dry material is about a half a decade larger than the immersed material, and does not significantly decrease over the temperature range tested. Comparing the tan δ scans it is easily seen that a transition occurs in the immersed material, centered around 75°C, whereas the nominally dry material is only just starting to enter a transition at 90°C. This implies that the transition observed at high temperatures in dry material has shifted to a lower temperature, in agreement with the kink noted in the thermal shift factors obtained for the hydrated thermal master curves as presented in **Chapter 2**.

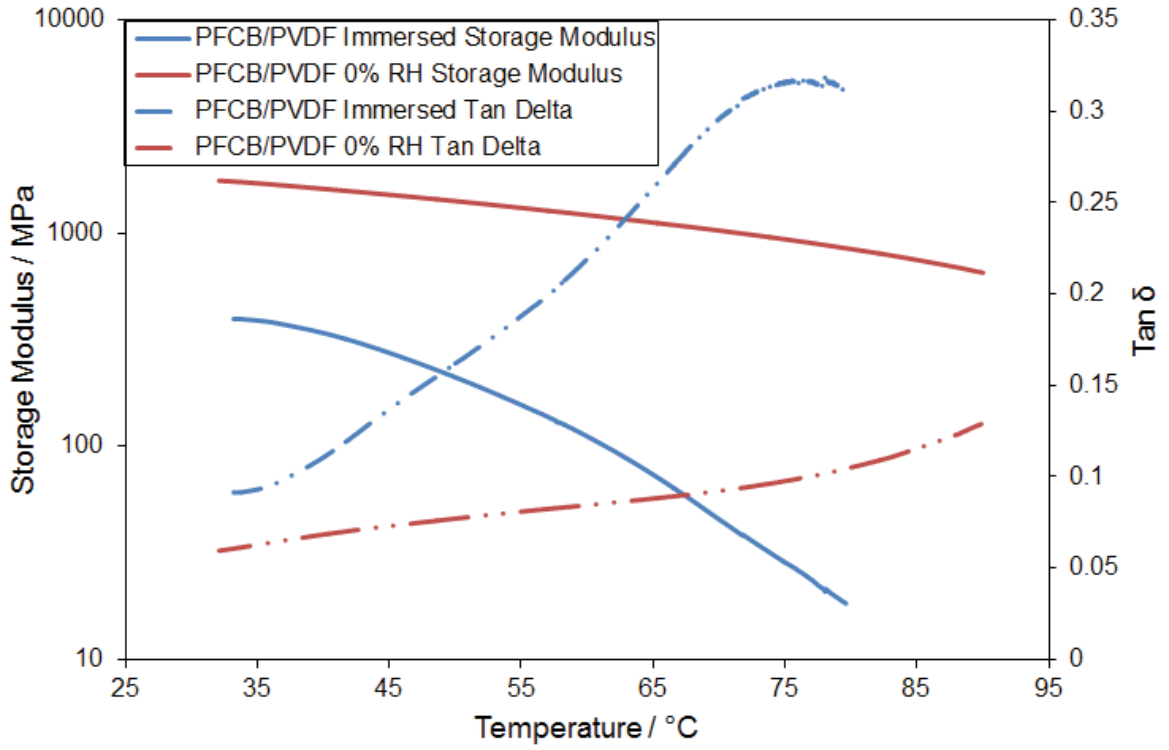

Figure 5.2. Storage modulus (solid lines) and Tan δ (dashed lines) of Immersed (blue lines) and 0% RH (red lines) temperature sweeps for PFCB/PVDF-HFP.

Temperature sweeps of immersed NRE 211 are compared with PFCB/PVDF-HFP in **Figure 5.3**. Although the scales are quite different, the Tan δ curves of both NRE 211 and PFCB/PVDF-HFP show a transition centered around 75°C. In addition, the PFCB/PVDF-HFP storage modulus is stiffer than NRE 211 at low temperatures, and softer at high temperatures, indicating that PFCB/PVDF-HFP is more sensitive to changes in temperature when hydrated than NRE 211.

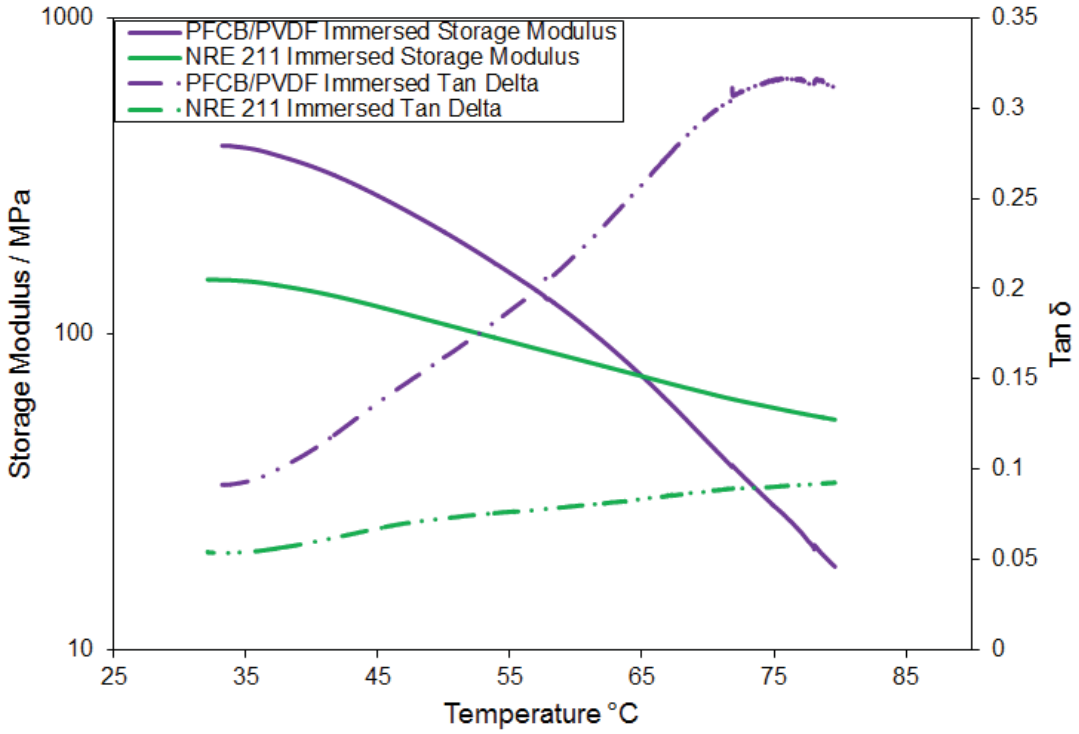

Figure 5.3. Storage modulus (solid lines) and Tan δ (dashed lines) of Immersed Nafion NRE 211 (green lines) and WBAN BM7646 (purple lines) temperature sweeps.

5.3.2. In-Plane Swelling

Preliminary testing was completed on the 2nd generation of PFCB/PVDF-HFP (60:40) on membranes stored at ambient conditions (20.9°C, 47.4% relative humidity) which therefore had

an original unmeasured water content due to the relative humidity of the room. Initial testing was completed using circular samples cut with a punch. Each sample was placed between two glass slides and water was dropped onto the sample before placing the glass slides together. Measurements were taken across the diameter of the sample using the same two points over a half hour. As can be seen in **Figure 5.4** a circular sample showed approximately 10% hygral expansion after 30 min. Other than the data taken at 9 min, this method appears to produce very clean data, sets showing promise for this visual observation of in-plane swelling.

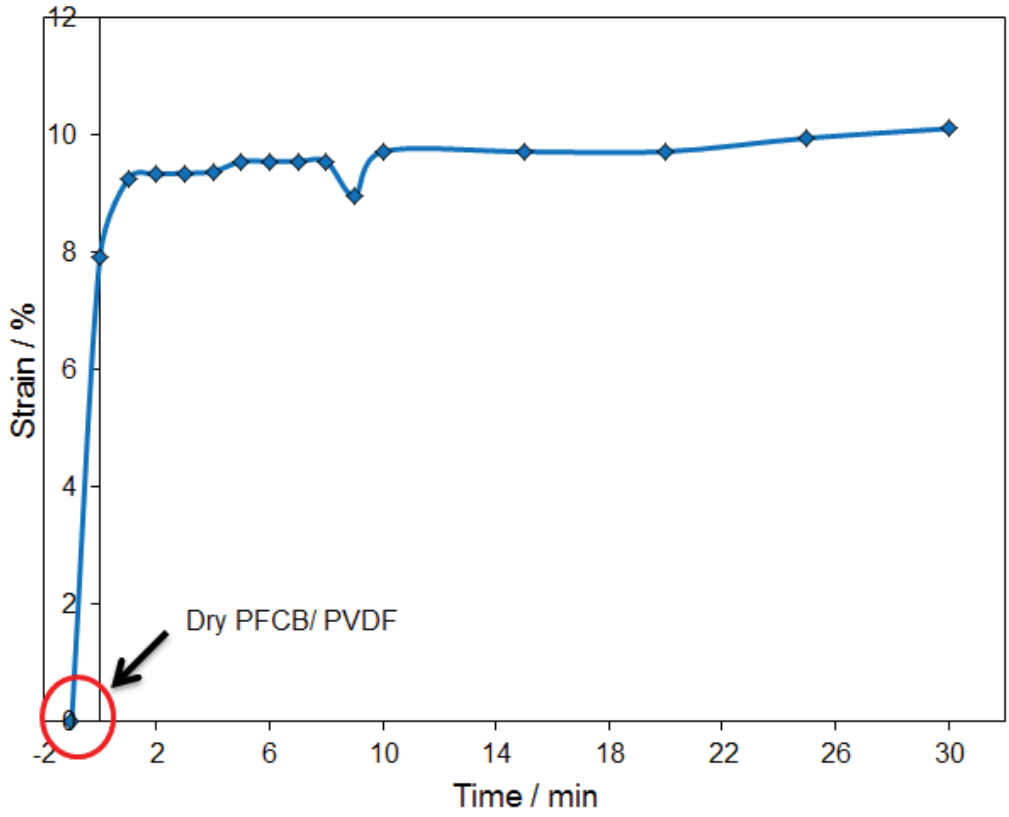

Figure 5.4. Initial swelling data measured on circular samples. Data measured on a dry membrane is shown at -1.

In further testing it was decided square samples would be easier to use rather than trying to punch perfect circles, also providing defined corners for measurement, and thus the rectangular gage portion of a small dogbone punch was used to cut even squares. In addition, two different techniques were examined for introducing water to the pieces of membrane. The first was the capillary method, introducing water as described in Section x. The second is the drop method, where a drop of water is placed on the glass slide without the membrane, and a drop is then applied to the membrane on the other glass slide on top of the microscope stage. The glass slide without the membrane is then quickly placed on top of the other glass slide, effectively sandwiching the membrane between layers of water. Images from the capillary method are provided in **Figure 5.5**, and the drop method in **Figure 5.6.**

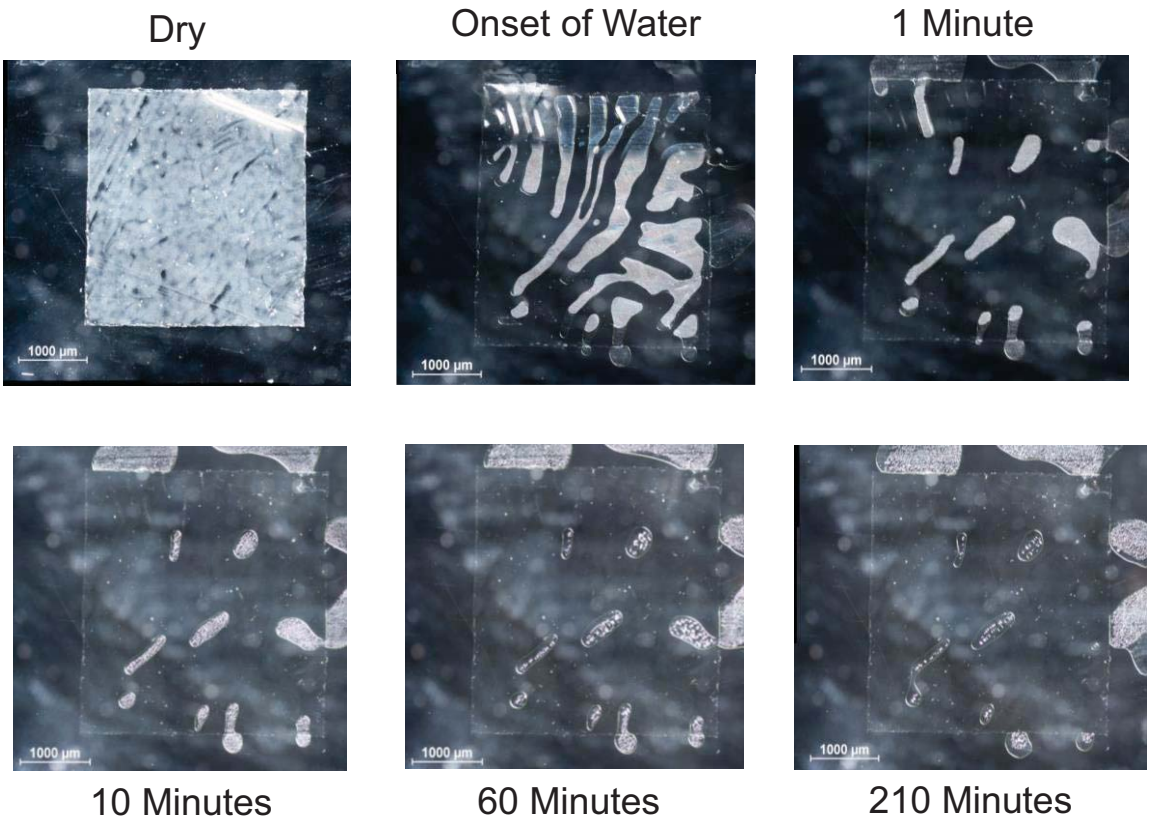

Figure 5.5. Images of membrane over time immersed in water using the capillary method.

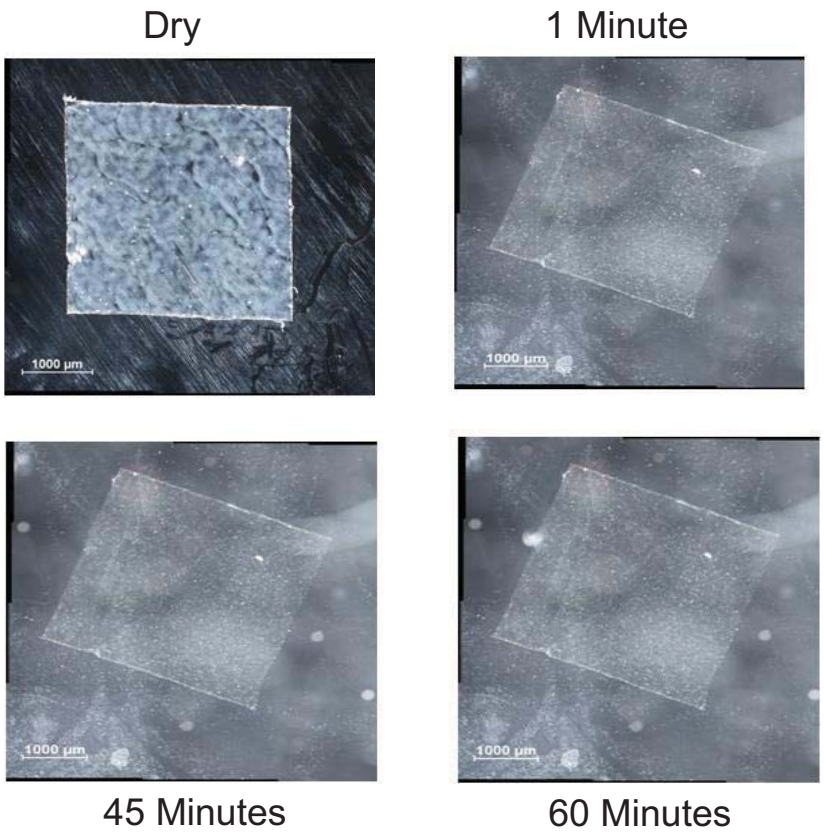

Figure 5.6. Images of membrane over time immersed in water using the drop method.

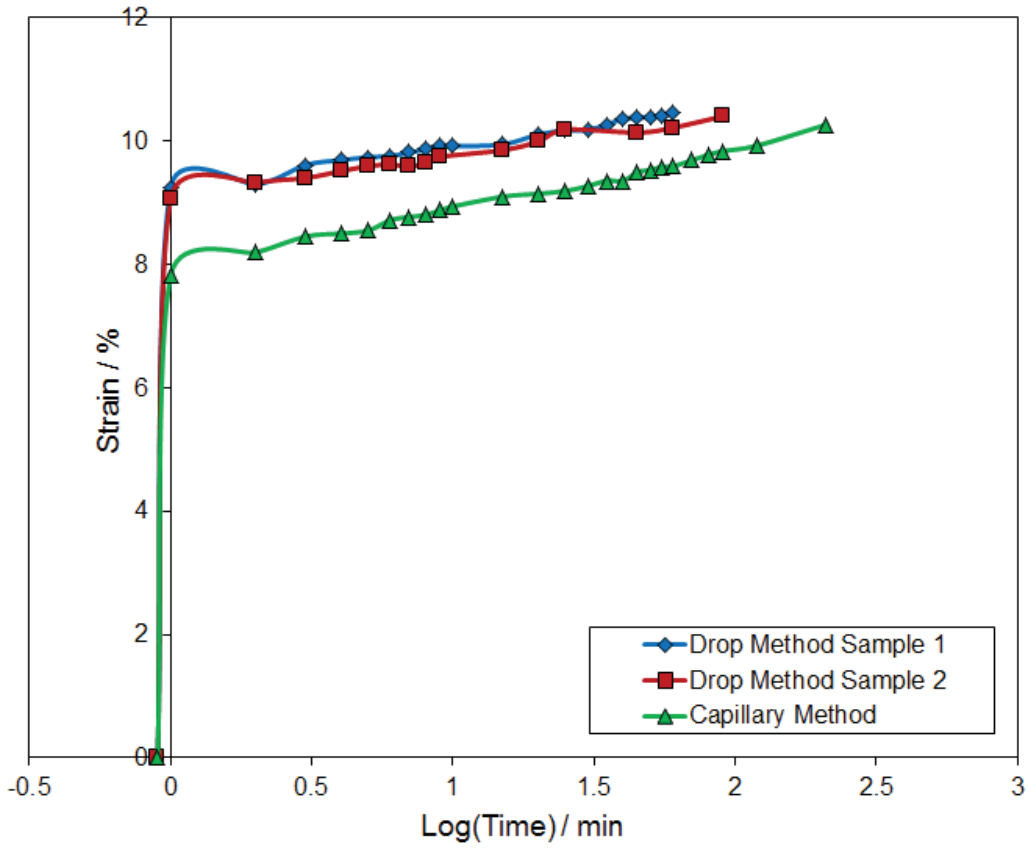

Figure 5.7. Swelling data taken via the drop and capillary method across the diagonal of the sample. Data shown in negative log time represents measurements taken on dry samples.

In these experiments, measurements were performed across the diagonal because the membrane wet using the drop method would rotate within the field of view due to the "sandwiching" process. The difference in swelling between data taken by the drop and capillary method, as noted in **Figure 5.7**, is due to the variation in which water is introduced to the sample. Water is rapidly introduced to the membrane in the drop method, allowing swelling to occur more quickly. However, water must travel across the glass slides in the capillary method, and as shown in the images does not immerse the membrane completely immediately. Therefore, it is expected swelling would occur at a slower rate using the capillary method, agreeing well with the differences shown in **Figure 5.7**. In addition, the two samples wet using

the drop method show excellent agreement in their swelling behavior, implying good repeatability can be obtained utilizing this test method.

An additional long term study was completed with irregular quadrilateral shapes over three days. To ensure the sample stayed immersed over the course of the measurement it was enclosed in a petri-dish with liquid water and sealed with Teflon tape. The total strain of the four sides of a PFCB/PVDF-HFP sample, as labeled in **Figure 5.8**, calculated using coordinate locations of the sample corners, is provided in **Figure 5.9**.

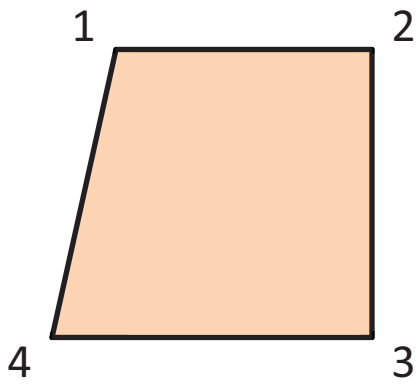

Figure 5.8. PFCB/PVDF-HFP swelling sample with corners labeled to provide the orientation of sides 1-2, 2-3, 3-4, and 4-1.

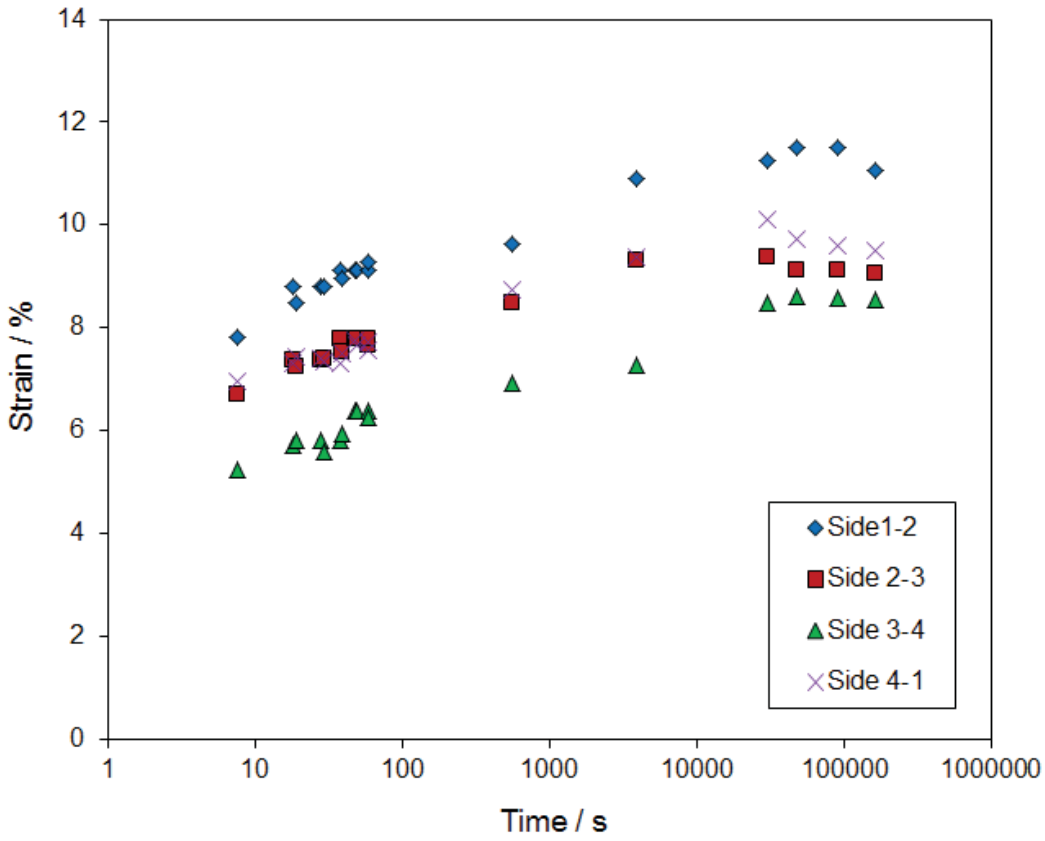

Figure 5.9. Total strain calculated for PFCB/PVDF-HFP with sides as referenced in **Figure 5.8.**

The overall swelling behavior shows a maximum of ~10% reached between 24 and 48 hours, after which the swelling reduced to ~9%. It should be noted that sides 2-3 and 4-1 swelled similarly, as seen in **Figure 5.9**, but sides 1-2 and 3-4 swelled very differently from each other. One possible explanation for this behavior is that the sample was tilted between the glass plates. However, there is only a ~40 µm gap between the glass slides including the water layers, and a 12 µm thick 1600 x 1600 µm sample. Therefore it is unlikely the sample is tilted enough to cause the large difference in measurements as seen between sides 1-2 and 3-4 in **Figure 5.9**. An alternative, and more likely explanation, for the difference between sides 1-2 and 3-4 is wrinkles that occur in the sample due to either rapid expansion of the sample, or air bubbles originating during the initial introduction of water through capillary action (**Figure 5.10**).

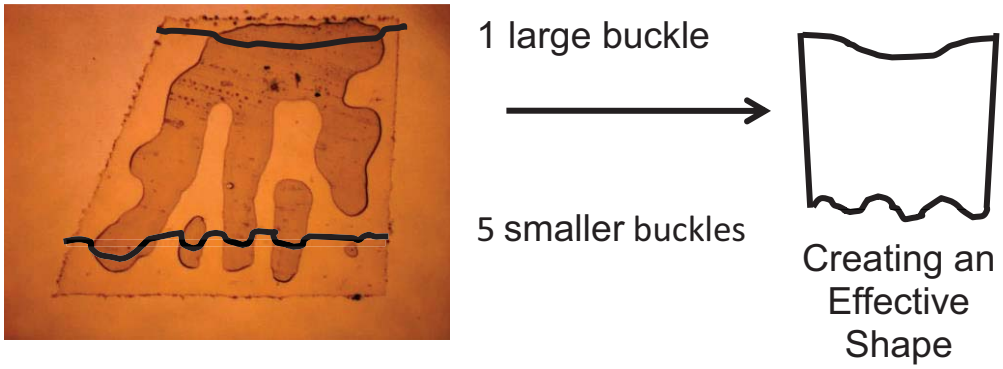

Figure 5.10. Image of PFCB/PVDF-HFP with air bubbles after the introduction of liquid water, and marked to show the effect of buckling.

As shown in **Figure 5.10**, there is one large air bubble near side 1-2, and five smaller air bubbles near side 3-4. This creates an effect such that side 3-4 is "shorter" than side 1-2 during the swelling process, thus producing the difference in swelling between sides 1-2 and 3-4. This explanation also applies to sides 2-3 and 4-1, which are both near one large bubble. Therefore sides 2-3 and 4-1 would swell similarly as seen in **Figure 5.9**. To avoid buckling arising from the presence of air bubbles, water either needs to be introduced differently, or the glass slides need to be manipulated to remove the air bubbles after water has been introduced. The capillary method of water introduction is convenient because it allows for easy focus on the sample and for the capture of swelling at the onset of water immersion. Other options for introduction of liquid water are increasing the gap between the glass slides or dropping water directly onto the membrane, as described previously. However, both of these methods require locating the membrane after water is introduced and as such tethering the membrane would be required to capture the first ten minutes of swelling. Therefore, while this visual method of hygral expansion shows promise, further work needs to be completed to determine the best method that

allows for repeatable results. While only room temperature DI water was used in these experiments, it is possible higher temperatures could be employed if a heated stage was employed with the microscope and glass slides. In addition, it may be possible to create a fixture that would allow for viewing expansion under humidified conditions, however it would be important to keep the viewing window heated to avoid condensation problems.

Additional hygral expansion measurements were performed using the DMA. A comparison of hygral expansion measured immersed in DI water at room temperature over 3 days for PFCB/PVDF-HFP and NRE 211 is provided in **Figure 5.11**. The NRE 211 hygral expansion rises quickly to about 10% strain, and changes very little, if any, over the three day time period. However, while PFCB/PVDF-HFP hygral expansion also rises quickly to about 10% strain, the PFCB/PVDF-HFP sample then continues to slowly expand to about 12% strain over the three day time period. This indicates that NRE 211 reaches an equilibrium in immersed water much more quickly than PFCB/PVDF-HFP, and full equilibration times for PFCB/PVDF-HFP are greater than three days. The greater equilibration time of PFCB/PVDF-HFP could be related to the increased moisture dependence of this material as compared with NRE 211. The hygrothermal shift factors of PFCB/PVDF-HFP span four decades while those of NRE 211 only span about a half of a decade. Therefore it is likely the viscoelastic rearrangements that occur due to moisture in PFCB/PVDF-HFP are greater than those in NRE 211, and thus may require more time to complete. This continued increase in the PFCB/PVDF-HFP sample could be due to creep in the sample caused by the small force applied to the sample to keep it taut. Therefore further studies should be investigated at lower applied force levels to determine if the slow increase over time is a true material behavior or a result of the testing method. Finally, testing was again only performed at room temperature, but it should be possible to capture hygral

expansion of immersed samples at higher temperatures by preheating water to the desired test temperature and applying blanket heaters to the DMA immersion fixture.

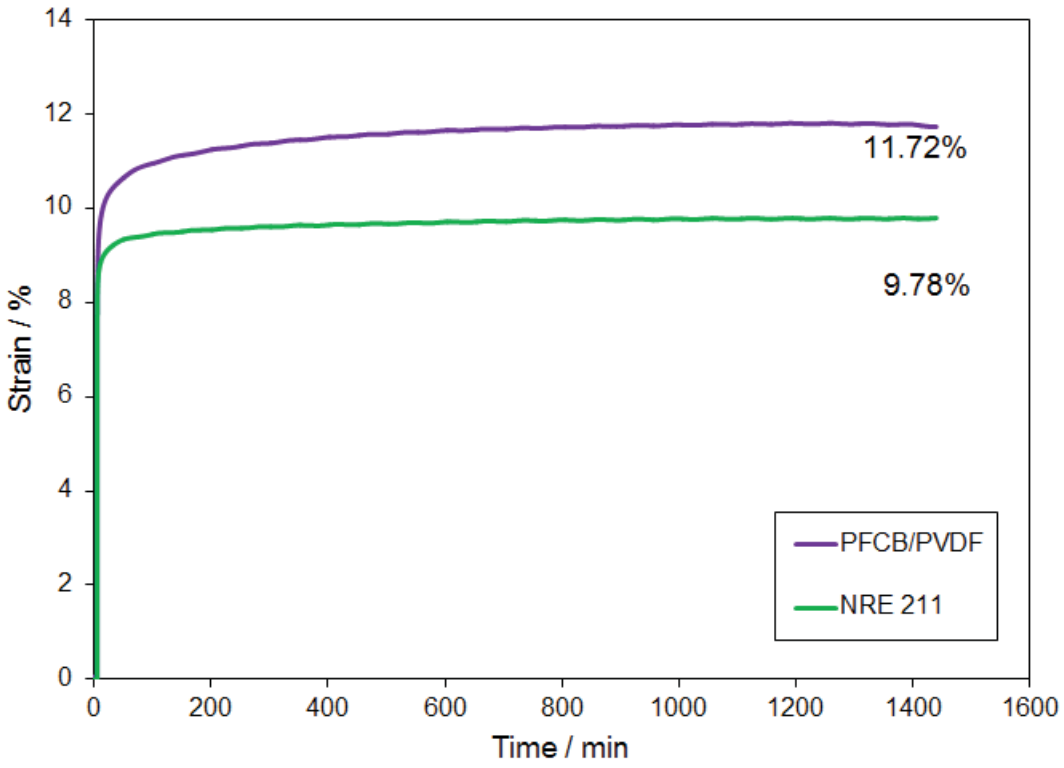

Figure 5.11. Hygral expansion at room temperature for PFCB/PVDF-HFP and NRE 211 over a 3 day period.

5.3.3. Out-of-Plane Swelling

Two out-of-plane expansion experiments were performed, as shown in **Figure 5.12A** and **B**. The swelling trend shown in **Figure 5.12A** does not show wide variation, unlike the swelling results shown in **Figure 5.12B**. Additionally, the results of **Figure 5.12A** indicate the membrane swells over 400% in the through-thickness direction, while the results of **Figure 5.12B** only reach ~250% swelling. While the values differ, the results from both through-thickness experiments show a large amount of swelling occurs compared to the 10% observed for in-plane

swelling. Due to the large variation in the results of **Figure 5.12B** and the large difference between the results of **Figure 5.12A** and **B**, a piece of swollen membrane was measured using a drop micrometer after being immersed for 30 minutes. This mechanical measurement showed through-thickness swelling of 169%, indicating the results of **Figure 5.12B** may be more accurate than those of **Figure 5.12A**, and that gross swelling in the through-thickness direction does occur. However, this large amount of swelling is in large contrast to the expected behavior of the membrane, and with the large variations observed and disagreement between samples, it is unlikely this is an accurate method for measuring out-of-plane expansion.

A

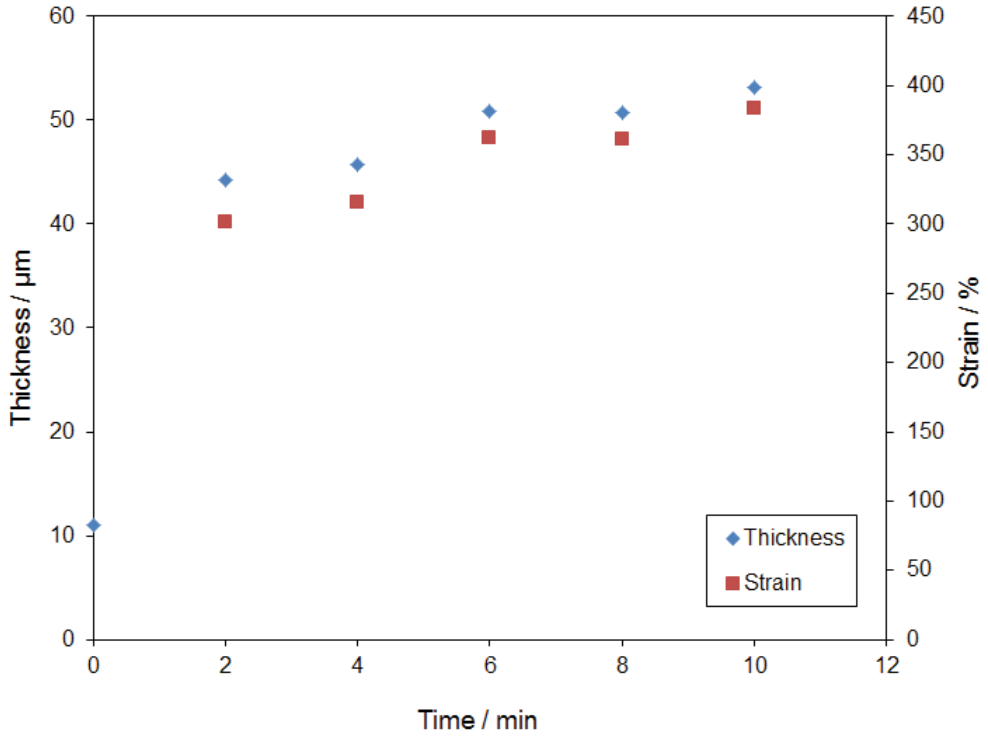

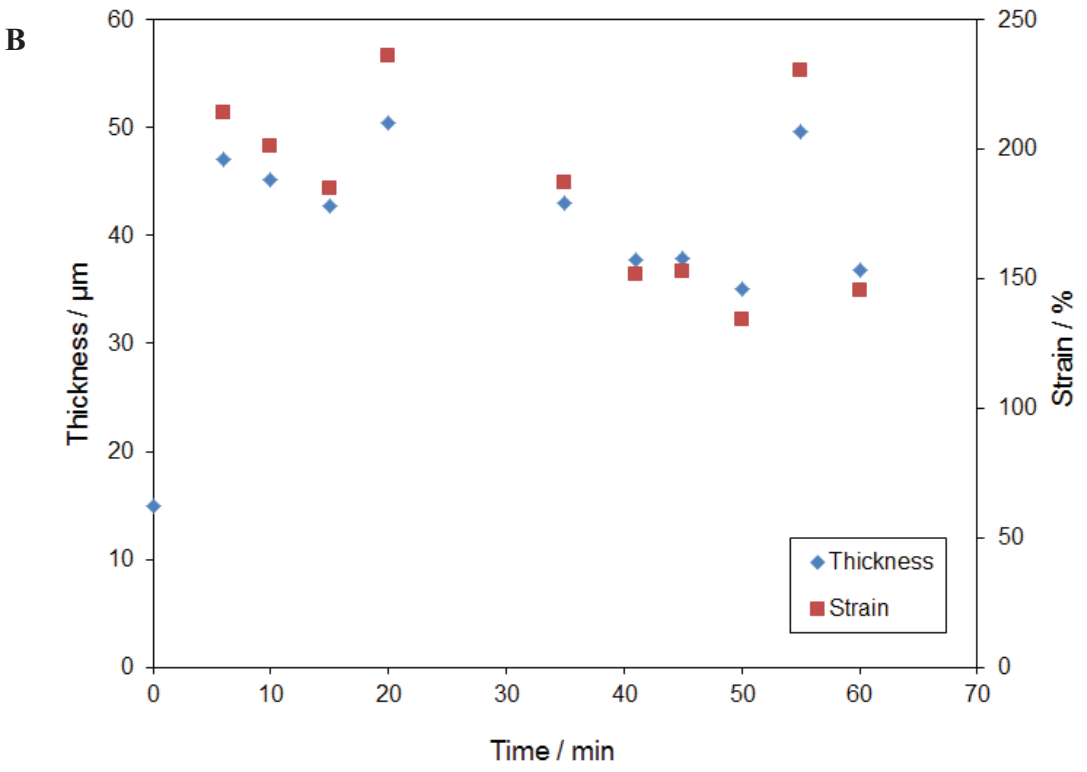

Figure 5.12. Results of through-thickness swelling on two different samples **(A)** and **(B)** of PFCB/PVDF-HFP.

Therefore, further investigation into out-of-plane hygral expansion was performed and a company called Filmetrics was found that produces instruments designed specifically for through-plane film thickness measurements. The Filmetrics instruments operate using spectral reflectance, which measures the amount of light reflected from an incident light perpendicular to the sample surface of a thin film using a range of wavelengths. The electromagnetic field, *E*, that describes light propagating through a material at a constant time is given by:

$$E = A \cdot \cos\left(n\frac{2\pi}{\Lambda}x\right) \cdot \exp\left(-k\frac{2\pi}{\Lambda}x\right) \qquad \textbf{[5.1]}$$

where x is the distance, Λ is the wavelength of incident light, n is the material's refractive index, and k is the material's extinction coefficient. The refractive index of a material is the ratio of the speed of light in a vacuum to the speed of light traveling through the material. The extinction coefficient is defined as a measure of how much light is absorbed in a material. For light reflected off of a material in air, the fraction of light reflected, R, by the surface is determined by the discontinuity of n and k:

$$R = \frac{(n-1)^2 + k^2}{(n+1)^2 + k^2} \qquad \textbf{[5.2]}$$

The total amount of reflected light is the sum of the reflection of the top and bottom of a material, or thin film. The phase relationship of the two reflections is determined by the difference in their optical path lengths which in turn is determined by the thickness of the film, the film's optical constants, and the wavelength of the incident light.

The reflectance of a thin film varies periodically with $1/\Lambda$, as seen by

$$R \approx A + B\cos\left(\frac{4\pi}{\Lambda} nd\right) \qquad \textbf{[5.3]}$$

In particular, for an incident light that is perpendicular to the material, the reflections add constructively when the reflections are out of phase by one integral multiple of light, $2nd = i\Lambda$ where d is the thickness of the film and i is an integer. Reflections add destructively when the reflections are out of phase by one half of a wavelength,

$$2nd = \left(i + \frac{1}{2}\right)\Lambda \qquad \textbf{[5.4]}$$

Thicker films will have a greater number of oscillations over a given range of light wavelengths and therefore thinner films will have a smaller number of oscillations over the same range of light wavelengths. To determine a film's properties a frequency sweep is performed on the sample (example in Figure 8), and the reflectance spectra is calculated using trial values of the thickness and *n* and *k* parameters and adjusting these values until the calculated values match the measured reflectance values. There are numerous mathematical models available in the software of the instrument used to calculate reflectance matches, and a chosen model should be able to describe *n* and *k* accurately over the desired wavelength range using as few parameters as possible to avoid non-distinct answers. If only a film thickness is desired the minimum single-film thickness is 10-300Å, but if optical constants are also needed, the minimum thickness increases to 100-2000Å.

After contacting Filmetrics for further literature on their instruments, the company offered to take sample measurements, and a small piece of NRE 211 was provided to the company. Three screenshots of the data collection were sent to Virginia Tech, and are provided below in **Figure 5.13-Figure 5.15**.

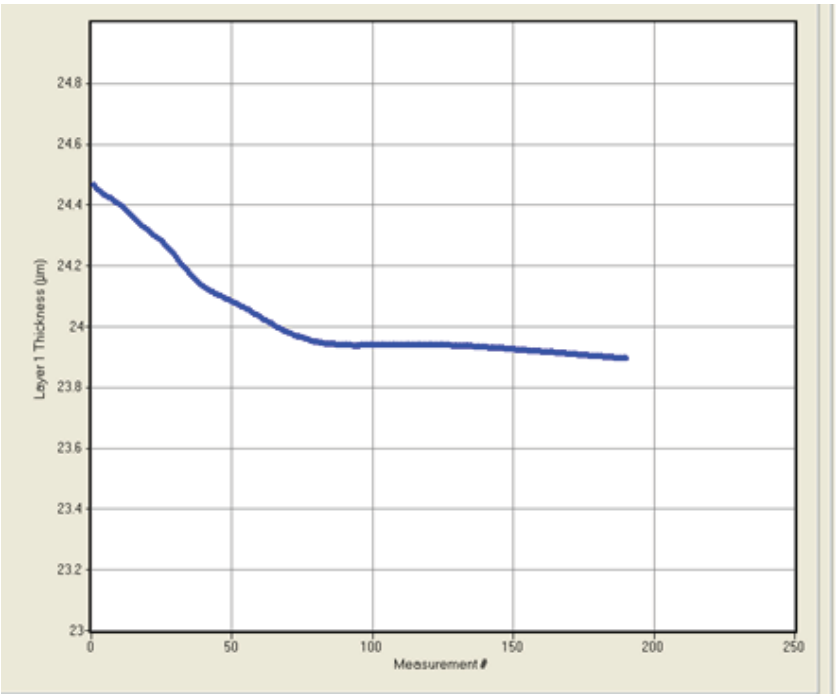

Figure 5.13. Screen shot of data taken using a Filmetrics Instrument on a piece of NRE 211 that was immersed in water, and then dried on the instrument stage.

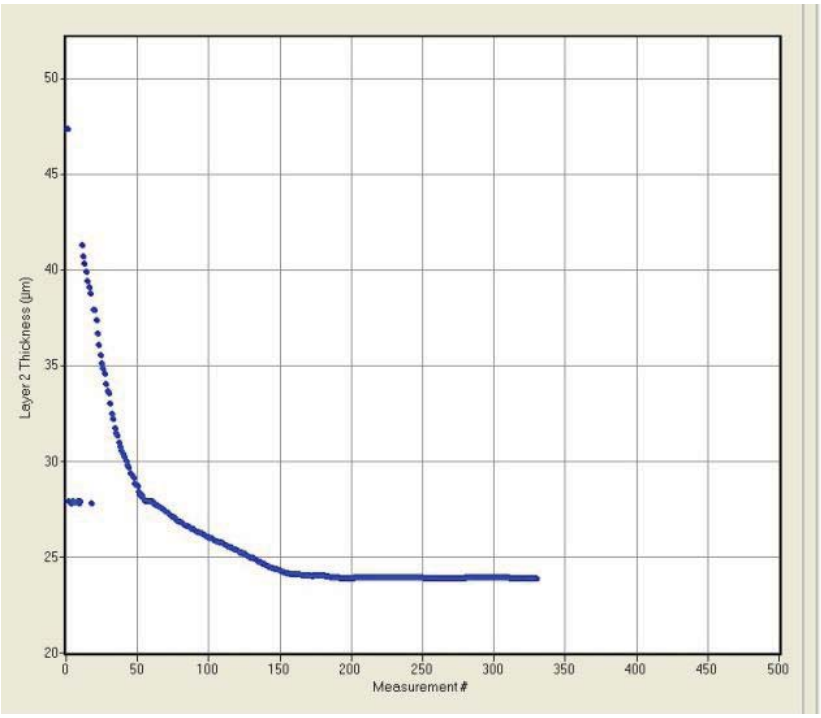

Figure 5.14. Screen shot of data taken using a Filmetrics Instrument on a piece of NRE 211 that was under a glass slide, immersed in water through capillary action, and the swelling and drying was monitored on the instrument stage.

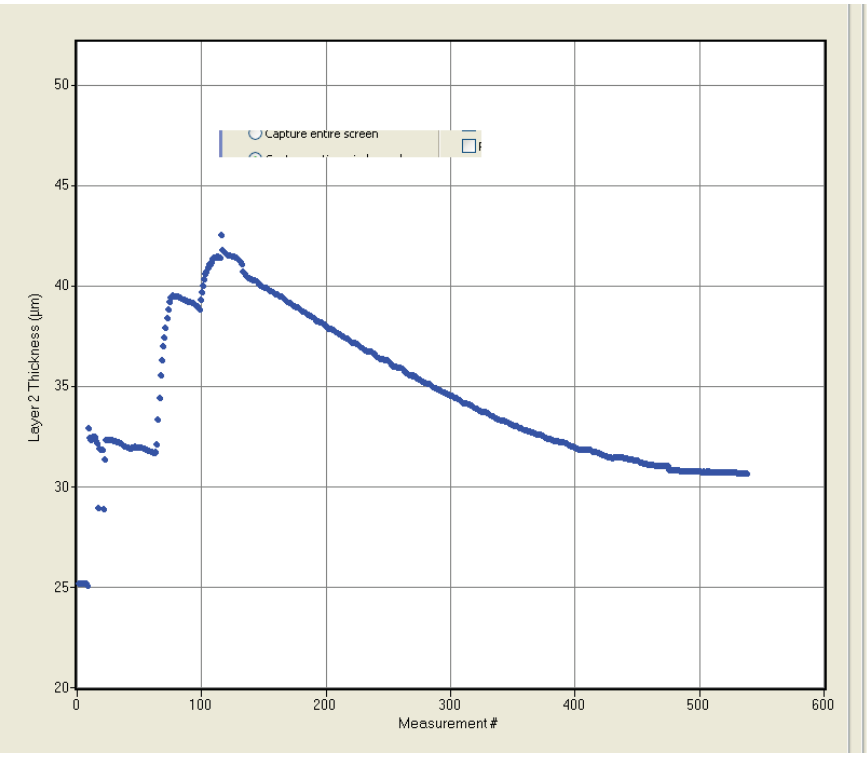

Figure 5.15. Screen shot of data taken using a Filmetrics Instrument on a piece of Nafion that was under a glass slide, immersed in water through capillary action, and the swelling and drying was monitored on the instrument stage.

The data provided by Filmetrics provides a very clear picture of the swelling and dehydration of the Nafion along with quantitative data that can be used in long term durability modeling. The sensors in the instrument can also be removed and used in different temperature and humidity conditions, resulting in a powerful measurement technique as the film can be free standing and does not need to be mounted on a substrate.

One limitation of this instrument is that it can only take measurements on smooth surfaces because it is measuring the reflection of the light. A rough surface would cause diffraction of the light, instead of a pure reflection, reducing or possibly eliminating the detection

signal used for calculations. When speaking with the representative from Filmetrics, he stated that he was having difficulty with the wrinkles, or cockles, that occurred in NRE 211 when immersed in water under a glass slide. Therefore, either a small sample size that does not wrinkle, or a special fixture would be needed to keep the sample from wrinkling during examination. This could be problematic if a large sample is desired, however, previous hygral expansion measurements were performed on very small pieces. Because the spot sizes are no larger than 200 μm, is believed that wrinkles due to immersion would not be a problem for thickness measurements with this instrument if focused on the sample correctly. Additionally, this measurement technique should be robust in multiple environments as it is simply shining a beam of light and then recording the reflected signal. Thus, if the environment does not disturb the impinging beam of light, or the reflecting beam, this instrument should be able to collect experimentally sound data. Finally, as mentioned previously, the instrument has a thickness limitation. A film that is very thin will only allow a few oscillations of light inside the material, before the light is reflected back. This could create a situation where multiple values of n and k could solve a mathematical model, creating non-unique solutions. Therefore, a minimum film thickness is required to obtain accurate results, which the 10 μm PFCB/PVDF-HFP samples are well above.

5.3.4. Membrane Buckling

Initial buckling measurements were performed on strips of PFCB/PVDF-HFP (60:40 wt:wt) membrane 19.05 mm wide. An image showing the interesting biaxial buckling pattern that formed after immersion in liquid water at room temperature is shown in **Figure 5.16**.

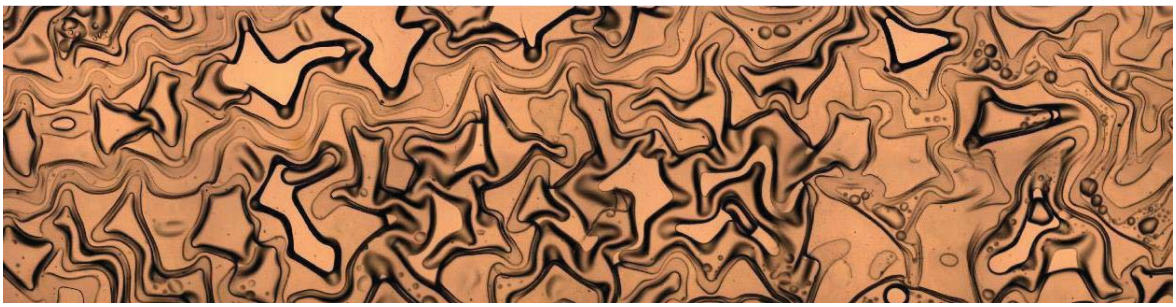

Figure 5.16. Buckling pattern of 19.05 mm wide PFCB/PVDF-HFP constrained biaxially between two glass slides held with binder clips after immersion in liquid water.

As can be seen in **Figure 5.16**, a uniform biaxial buckling pattern is obtained using this wide sample, however, it is therefore difficult to obtain a standard buckling width. Further samples were reduced in size to 3.17 mm wide, to reduce the biaxial constraint and obtain a better uniaxial buckling pattern, as shown in **Figure 5.17**.

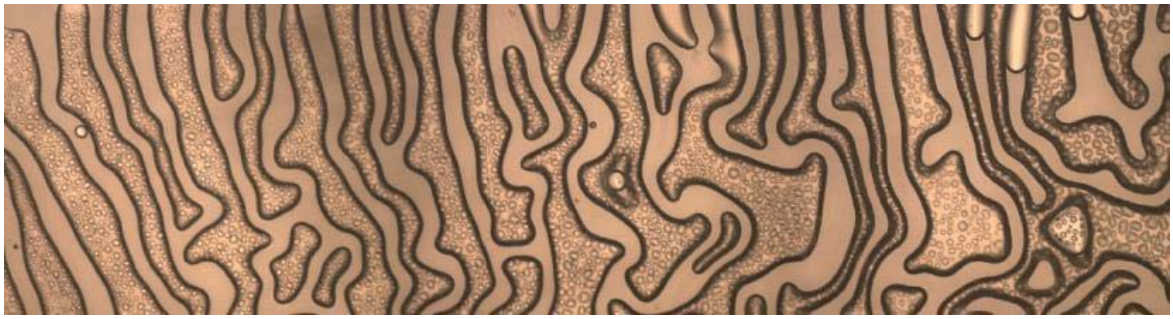

Figure 5.17. Buckling pattern of 3.17 mm wide PFCB/PVDF-HFP constrained primarily uniaxially between two glass slides held with binder clips after immersion in liquid water.

Although the pattern in **Figure 5.17** is more uniaxially uniform than that seen in **Figure 5.16**, variation is still seen in the buckling width as measured using the Nikon microscope software (**Figure 5.18**). Nonetheless, the buckling width range is about a factor of two, which is reminiscent of this classic phenomenon that occurs in the fragmentation length of fibers in

composite materials [3, 4], the parking of cars on unmarked curbs [5, 6], and other sequential event problems.

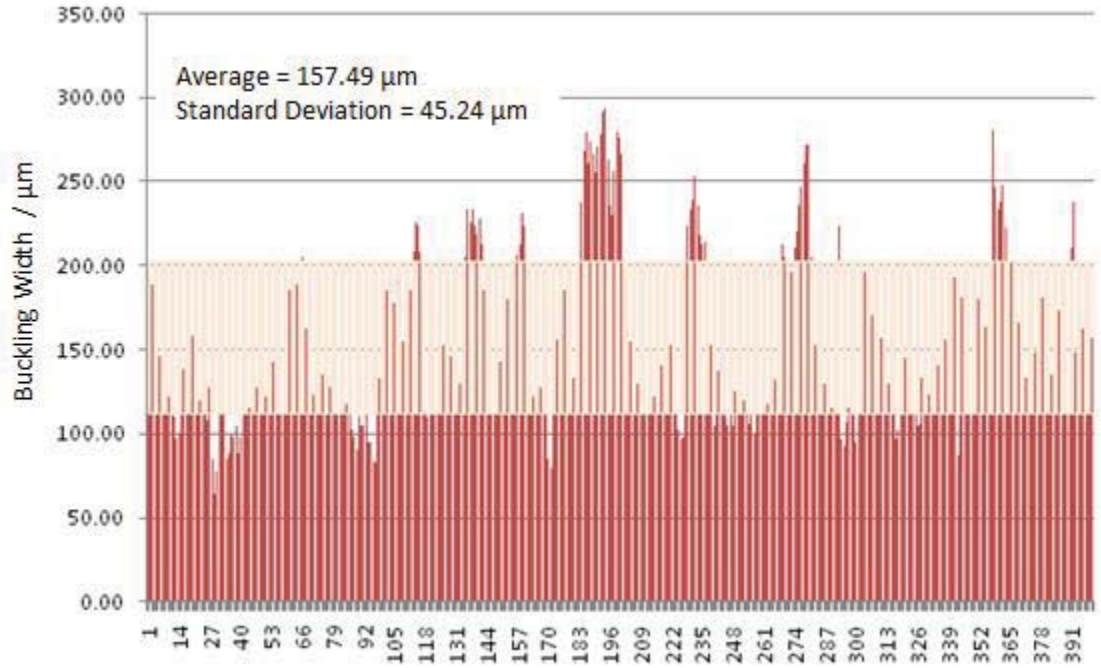

Figure 5.18. Buckling width measurements taken from **Figure 5.17** of 3.17 mm wide PFCB/PVDF-HFP constrained between two glass slides held by binder clips.

From **Figure 5.18**, the average width of the buckles in **Figure 5.17** is 157.5 µm with a standard deviation of 45.2 µm. A determination of the depth of the buckles has also been attempted, using a method similar to that used for characterizing through-thickness swelling with the Nikon microscope. The membrane was painted on opposite sides with thin red and black lines using waterproof air brush ink. After immersion in liquid water at room conditions, the membrane was examined under the Nikon microscope using the 120x objective. The focal point for the red and black lines was then found, and the difference between the two focal points was taken to be the height of the measured buckle. Due to the low thickness (11 µm) of these

membranes, there was difficulty in obtaining accurate results, and as such depth measurements were not very accurate, as seen with the out-of-plane swelling experiments.

To further understand the out-of-plane deformations that might occur within MEAs and UEAs suspended within the channel region of a fuel cell, membrane constrained by glass bipolar plates was examined. As shown in **Figure 5.19**, there were no wrinkles, buckles, or other deformities in the membrane upon assembly. Therefore, all changes shown occur due to the swelling and deformation of the membrane when immersed and constrained in a bipolar plate set-up. It should be noted that the gridlines observed in many images are due to the large image scan feature and stitching multiple images together, these gridlines are not a part of the glass or membrane.

Figure 5.19. Large image scan of membrane in glass bipolar plate fixture after assembly, prior to immersion.

After immersing the sample for 30 min in DI water, the images shown in **Figure 5.20** were captured. Under the land it is clear the sample is not fully hydrated due to the imposed constraint, while under the channel large buckles traversing the distance between the top and bottom of the channel have formed. It should be noted these buckles are likely larger than those observed in an actual fuel cell as there is no gas diffusion layer (GDL) included in this bipolar plate set-up, but future testing is planned to include an overhead projector sheet to emulate the constraint of the GDL. The sample was then reimmersed in DI water for 5 days, and reexamined

under the microscope for possible changes in the buckling pattern, as shown in **Figure 5.21**. It appears the buckling pattern has changed over this long immersion period, with the characteristic pattern disappearing, and the formation of large buckles extending across the entire depth of the channel, while the membrane under the land still appears flat and undeformed.

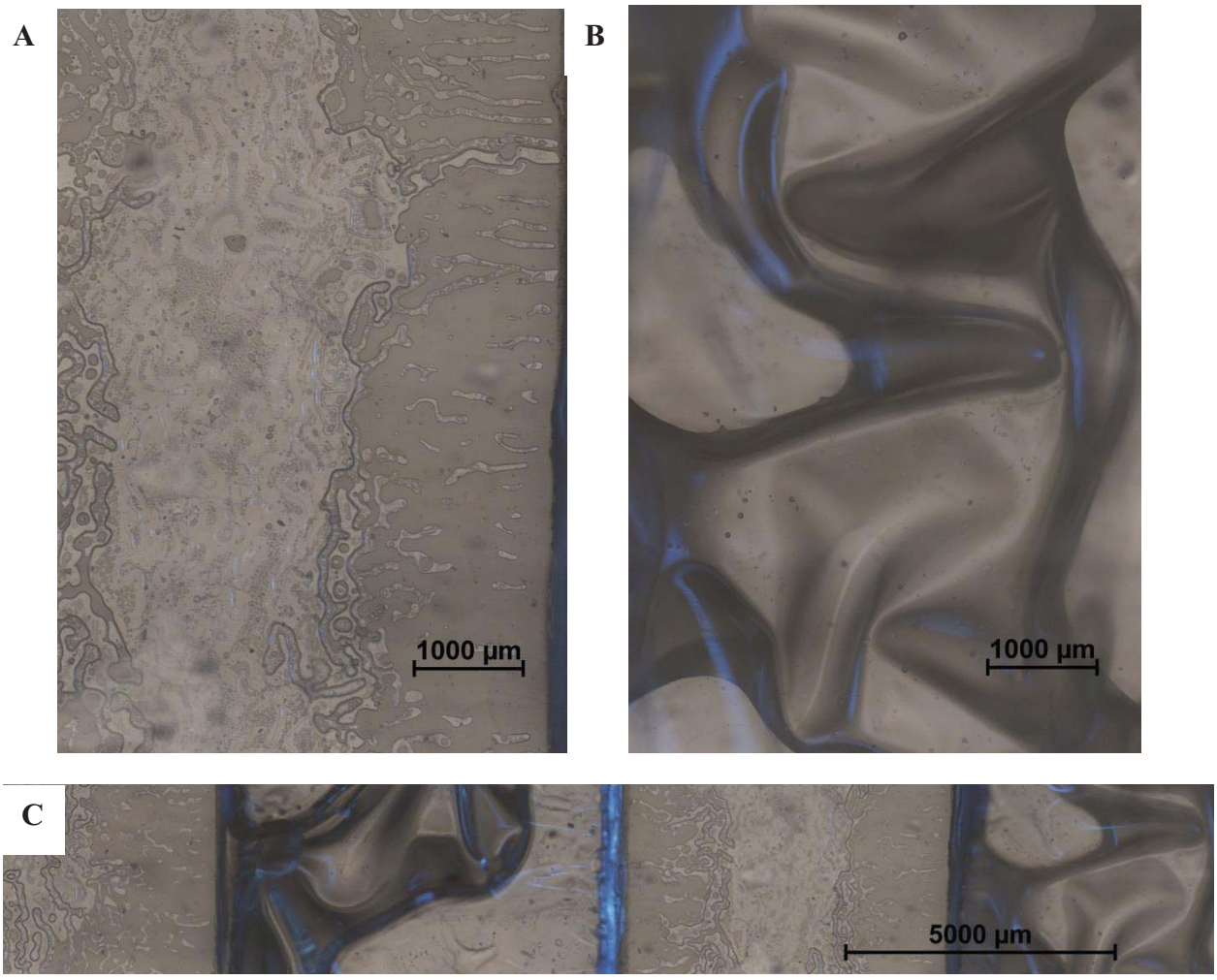

Figure 5.20. Images of membrane constrained in glass bipolar plate after 30 min immersed in DI water in the **(A)** land, **(B)** channel, and **(C)** panoramic image across multiple lands and channels.

Figure 5.21. Images of membrane constrained in glass bipolar plate after 5 days immersed in DI water across multiple lands and channels.

Finally, the sample was allowed to dry out over night at ambient conditions, after which it was reimaged with the Nikon microscope, as shown in **Figure 5.22A-C**. As can be seen, the membrane under the lands is still flat and undeformed, while the membrane in the channel shows wrinkles that have formed due to tensioning of the membrane while it dried. This corresponds well with the stress model predictions that a hydrated membrane is under compressive stresses, as noted by the buckling pattern, while a sample dried after hydration is under tensile stresses, as noted by the wrinkling pattern. Additional images were taken with a Canon DSLR camera after the glass bipolar plate fixture had been taken apart, as shown in **Figure 5.23**. These images show the material on the lands appears to be adhered, while the material in the channels shows tensioning, as evidenced by the wrinkling pattern of X's that exist in each channel. These wrinkles occur because the constrained sample is under a biaxial stress state, and the material buckles to relieve the in-plane strain incompatibility formed due to the Poisson effect [7]. In this case X's were formed corresponding well with the formation of in-plane shear stresses, likely due to the geometry of the bipolar plate set up in which of the channel is larger than the length, and the thickness of the membrane is significantly less than both. If a uniform wrinkling pattern

forms due to tensioning after drying, it could be used to estimate the tensile stresses, *T*, as described by **Eqn [5.5]**:

$$T = \frac{16\pi^2 L^2 B}{\lambda^4} \qquad \textbf{[5.5]}$$

where *L* is the length of the sample, λ is the wavelength of wrinkles, and *B* is the flexural rigidity which can be defined as:

$$B = \frac{Et^3}{12\left(1-\nu^2\right)} \qquad \textbf{[5.6]}$$

where *E* is the material modulus, *t* is the material thickness, and *v* is the material Poisson's ratio [7].

This test method allows for viewing the formation of buckles due to hydration and wrinkles due to membrane tensioning while the membrane is in the bipolar plate set up. Previous characterization of membrane buckling was performed after the fuel cell had been disassembled, showing characteristic patterns across the entirety of the sample [8]. Based on the images taken thus far, it is believed this pattern is truly confined to the channel regions, and further investigations are planned with more realistic bipolar plate set ups. This includes 1 and 2 mm land and channel widths, with a 0.5 mm channel depth. Clear cellulose film will be used to form the serpentine channel pattern, and cut using a laser cutter to ensure accuracy. The cellulose will then be adhered to glass plates, creating the clear bipolar plate set up. Finally, imaging will be performed with a DSLR camera at 50 frames per second to allow the time lapse capture of the formation of the buckles and wrinkles. Both NRE 211 and PFCB/PVDF-HFP will

be utilized, allowing for the first imaging of a fuel cell membrane in a fuel cell set-up when hydrated and dehydrated.

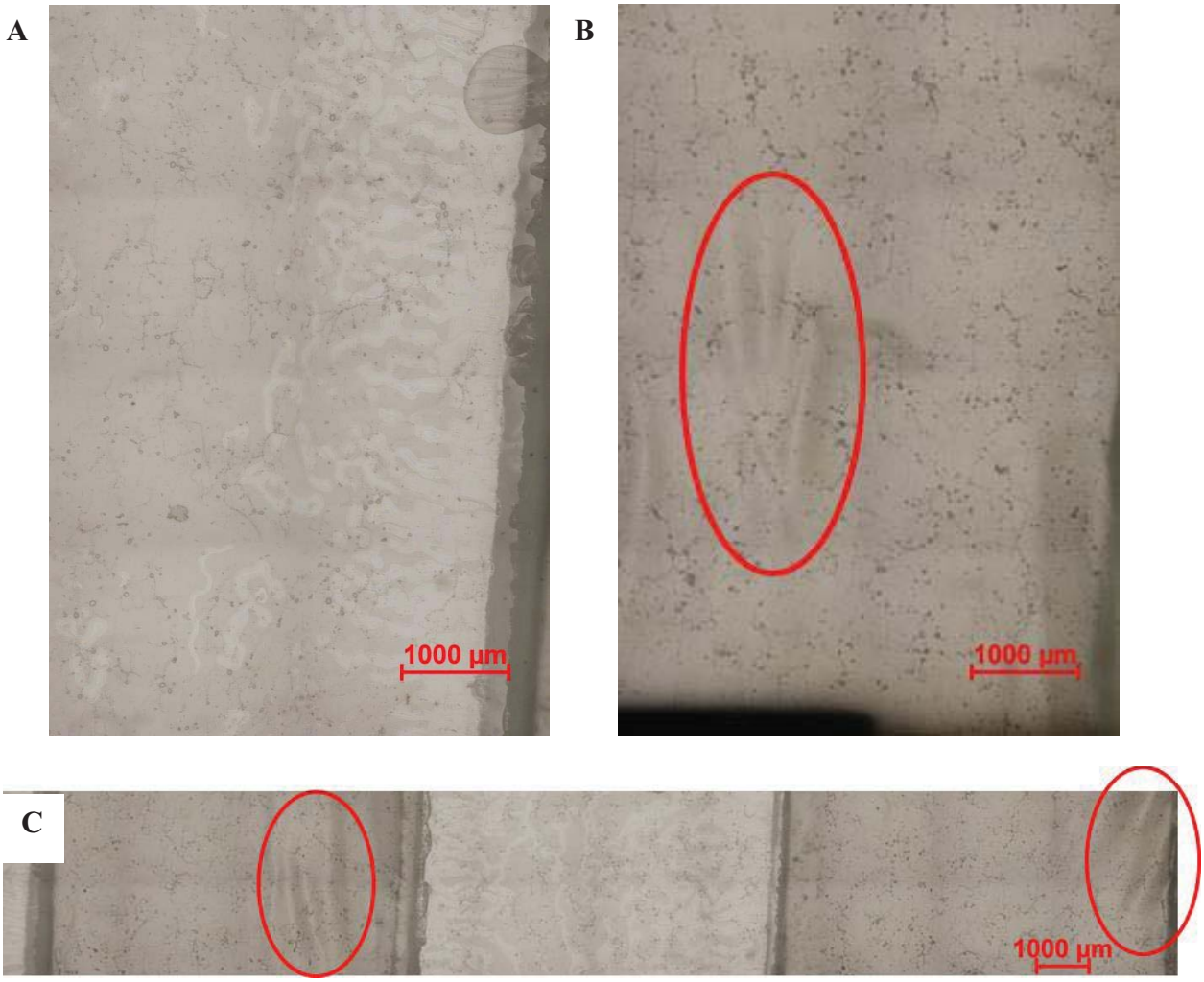

Figure 5.22. Images of membrane constrained in glass bipolar plate after drying out overnight at ambient conditions after immersion in the **(A)** land, **(B)** channel, and **(C)** panoramic image across multiple lands and channels.

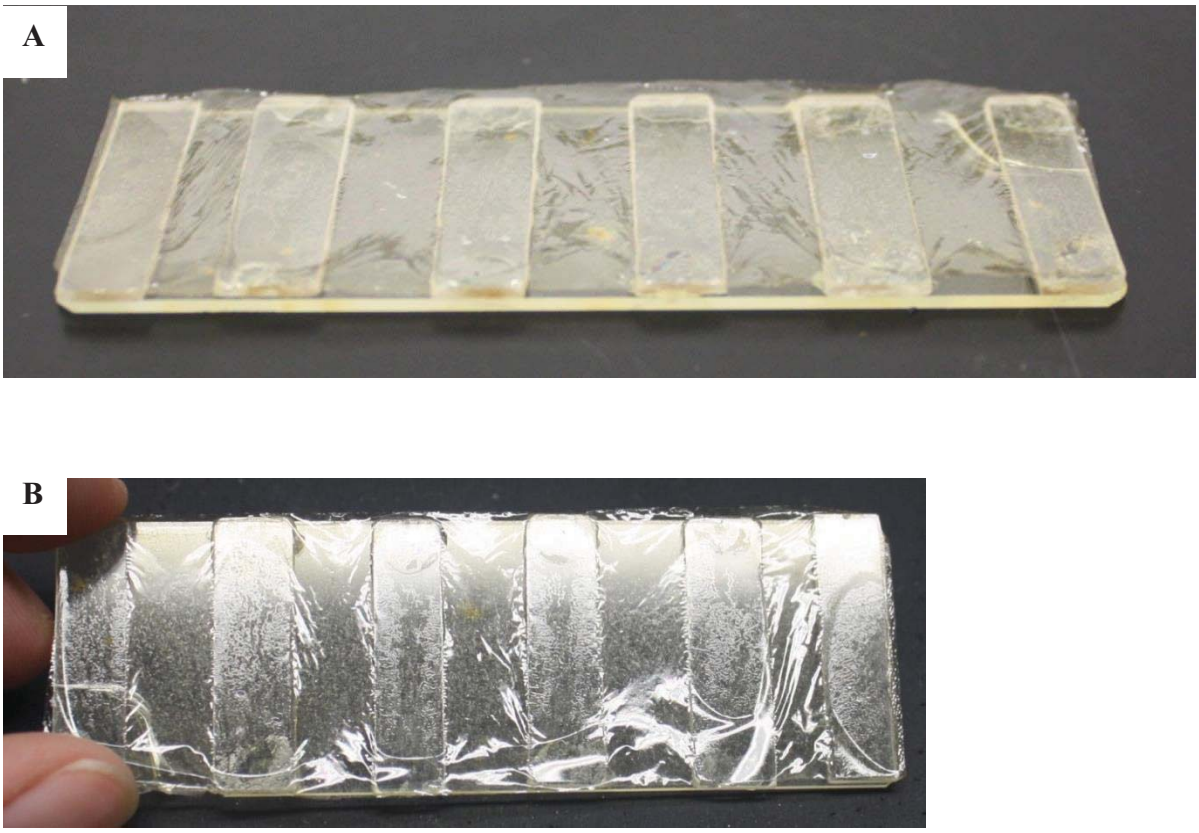

Figure 5.23. Images of membrane after disassembly of glass bipolar plate fixture using the Canon DSLR camera to highlight the wrinkles formed due to tensioning of the membrane during dry-out.

5.4 Conclusions and Recommendations

In-plane swelling measurements performed with the Nikon optical microscope showed promise, especially if water is introduced via the drop method or a wider gap between glass plates is used, avoiding the buckling problem created by air bubbles when water is introduced using the capillary method. If a small fixture were created, this method of in-plane swelling measurements could be performed at multiple temperatures and even possibly multiple humidities. However, out-of-plane swelling measurements utilizing the Nikon optical microscope were unsuccessful, and further experiments should be performed with the Filmetrics

optical instrument. There are many possibilities for using this instrument including immersion at multiple temperatures, as well as imaging at different relative humidities and temperatures.

Buckling of fuel cell membranes is an interesting area of research. Based on the imaging performed here, it is clear the samples buckle significantly in the channels, but not under the constraint of the land. Of even more interest are the wrinkles that form due to tensioning of the membrane as it dries. Therefore, it would be of great import to capture both the buckling and wrinkling under time lapse conditions. This would allow for measurements and calculations to be performed to better understand the forces and stresses developed by a membrane during hydration and dehydration cycles. This would provide better insight into membrane deformation under fuel cell operating constraints, and even conditions if temperature and moisture cycling were controlled, that would be very useful in updating models for the durability and lifetime of these membranes.

5.5 References

[1] Y. Li, in, 2010.
[2] A. Kusoglu, Y. Tang, M. Lugo, A. Karlsson, M., M. Santare, H., S. Cleghorn, W. Johnson, B., Journal of Power Sources, 195 (2010) 483-492.
[3] H. Ho, L.T. Drzal, Compos Eng, 5 (1995) 1231-1244.
[4] H. Ho, L.T. Drzal, Compos Eng, 5 (1995) 1245-1259.
[5] W.A. Curtin, J Mater Sci, 26 (1991) 5239-5253.
[6] W.A. Curtin, Appl Phys Lett, 58 (1991) 1155-1157.
[7] E. Cerda, L. Mahadevan, Physical Review Letters, 90 (2003) 074302-074301 - 074302-074304.
[8] T. Uchiyama, M. Kato, T. Yoshida, Journal of Power Sources, 206 (2012) 37-46.

Appendix A : Stress Relaxation Testing Method Development

Prior to creating the master curve provided in **Section 2.3.3.2**, testing was completed to determine the most appropriate test mode and parameters for characterizing PFCB/PVDF-HFP. Initially, PFCB/PVDF-HFP modulus data was taken utilizing the dynamic test mode in the same DMA-RH used for thermal and hygral expansion measurements. Testing was performed under 2, 10, 30, 55, and 80% RH, over a temperature range of 30 – 100^{o}C, using frequencies from 0.1 – 32.16 Hz. Under the dynamic mode, the applied deformation can be input utilizing two different methods, by defining the applied displacement amplitude of oscillation, or defining the applied strain amplitude of the oscillation. Initial testing was performed by defining the applied amplitude as 10 μm, approximately equivalent to 0.067% strain for the 15-mm gage length sample. This low strain level was originally chosen for PFCB due to problems with breakage at higher strain levels. Higher frequencies were not employed because the instrument cannot perform high frequency tests on low stiffness materials, as this leads to inaccurate data. The same dynamic testing was performed on NRE 211, and compared with previous stress relaxation data taken by Patankar et al. under the stress relaxation mode of the DMA at 0.5% strain, utilizing the in-house RH unit [1]. Under the assumption that data taken in the linear viscoelastic region should match, neither the strain level or test method employed should affect the data. As such the dynamic data was converted to stress relaxation using a Prony series approximation of the dynamic data. However, it was found that when the two data sets were charted together they differed by an order of magnitude, as shown in **Figure A.1**. This would imply that NRE 211 is dependent on the applied strain level, and therefore would be considered in the nonlinear viscoelastic region, however this is inconsistent with the softening type nonlinearity observed with Nafion®. Based on previous work by Patankar et al. and the

inconsistency with previously observed behavior, it is not believed the material is truly in the nonlinear viscoelastic region, and further studies were employed to determine the cause.

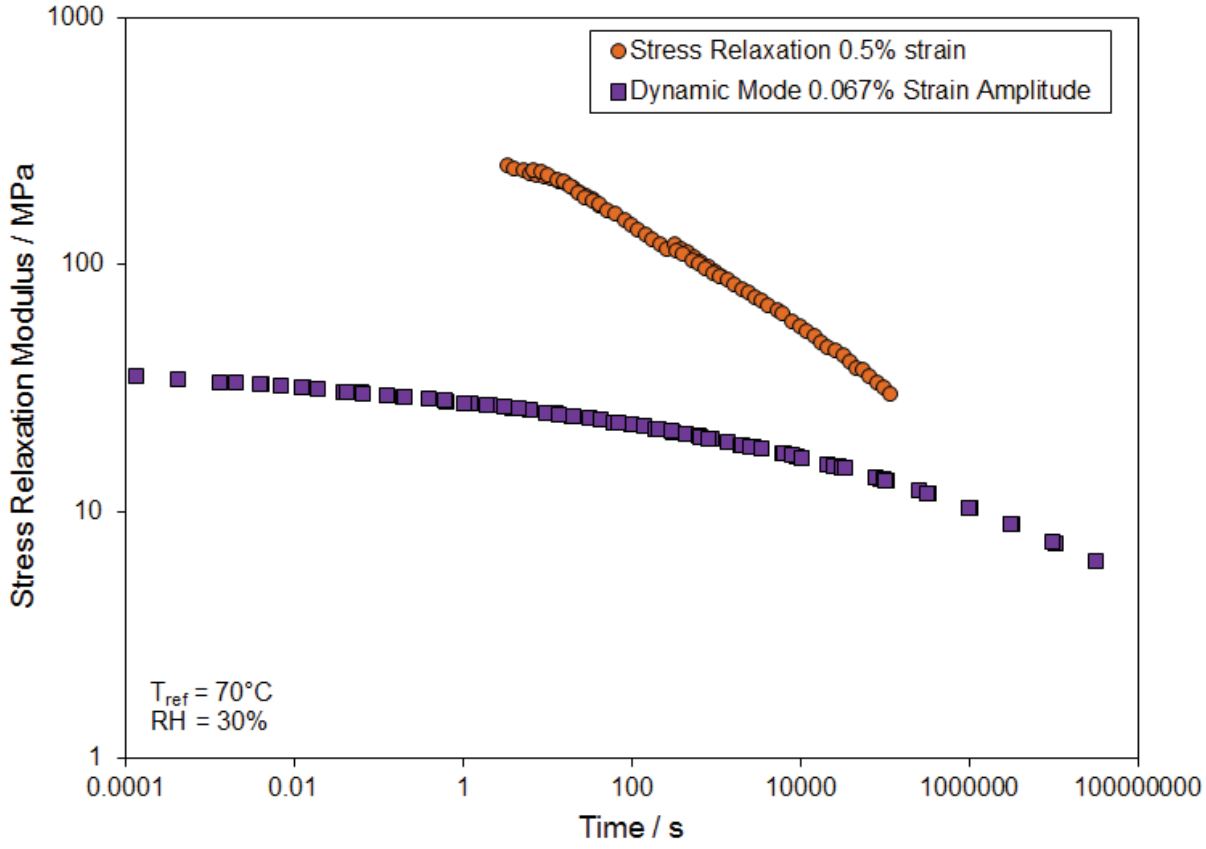

Figure A.1. Stress relaxation modulus master curves for NRE211 taken at different strain levels under dynamic or stress relaxation modes.

Due to the implications of the NRE 211 data, a similar comparison was performed on the PFCB/PVDF-HFP material to examine the validity of the master curve created using data collected under the dynamic mode with a 10-μm amplitude oscillation input (**Figure A.2**). It was found that a stress relaxation test performed at 0.1% applied strain amplitude input did not match well with the original master curve collected with a 10-μm amplitude oscillation input, equivalent to an approximate 0.067% applied strain amplitude. In addition, dynamic testing

performed with a 0.1% applied strain amplitude has a slightly larger modulus than the 10-μm amplitude oscillation input and also relaxes approximately 4 decades later. To examine the possible effects of a non-uniform applied strain level, a dynamic test was completed at 0.067% applied strain amplitude input. As mentioned previously, this strain level is similar to that of a 10-μm amplitude oscillation input, but by defining a strain amplitude rather than a displacement amplitude, the strain remained constant over the entirety of the test as the sample changed length. The modulus from the 0.067% applied strain amplitude input matches well with the modulus obtained from the original 10-μm amplitude, implying a very small non-uniformity in strain does not cause gross error in the collected data. However, if the material is truly being tested in the linear viscoelastic region then there should be no significant differences in the data collected at different strain levels or via different test modes in both the modulus and the shift factors obtained from master curves. Therefore, it is believed that the different strain levels and test modes employed are not the cause of the discrepancies in the data, and investigations into the effects of poor conversion, sample misalignment, hygral expansion, and instrumental limitations were conducted.

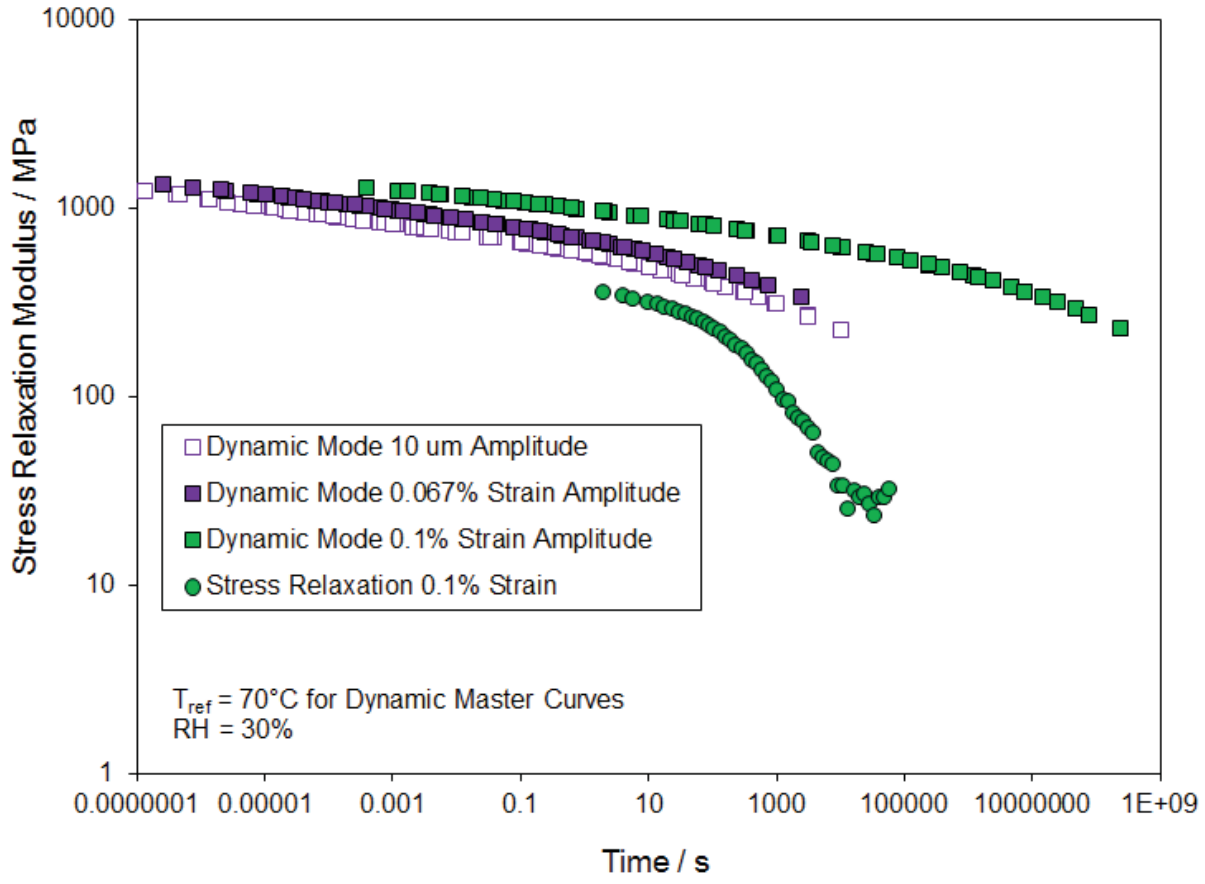

Figure A.2. Stress relaxation master curve moduli of PFCB/PVDF-HFP at 30% RH referenced to 70°C, taken at different strain levels under dynamic mode, compared with the stress relaxation modulus measured under the stress relaxation mode at 0.1% strain.

To avoid the complexities of the ionomeric materials while investigating the ability to properly convert a storage modulus to a stress relaxation modulus, polystyrene was examined in the glassy regime. Two separate samples were tested, one at 0.1% strain in both dynamic and stress relaxation modes and another at 0.2 and 0.3% strain in dynamic mode. Each storage modulus was converted to a stress relaxation modulus using a Prony series as done previously for both NRE211 and PFCB/PVDF-HFP. The data taken at 0.1% strain in both dynamic and stress relaxation modes match well, implying the conversion technique employed was used

correctly. The data taken at 0.2 and 0.3% strain matches well also, implying linear viscoelasticity can be measured in dynamic mode in the DMA, for simple polymeric systems.

To understand the effects of specimen misalignment, two NRE 211 samples were tested, one perfectly aligned and one purposely misaligned. This misalignment was set such that the 9 mm width of each sample was still contained entirely in the grips, but the sample was angled, rather than straight between the grips as shown in **Figure A.3**. Each sample was subjected to four tests at 0.1% strain, a dynamic test, followed by a stress relaxation test, an eight hour rest, and an additional dynamic and stress relaxation test. The first dynamic test performed on the misaligned sample produced data that was unshiftable, but the second dynamic test worked well. All three sets of dynamic data agree perfectly, implying that alignment does not have a large effect on dynamic testing. However, alignment does appear to have an impact on stress relaxation data. The stress relaxation data collected on the perfectly aligned sample does not quite match the dynamic data, but the two tests do show good agreement with each other. The stress relaxation data collected on the misaligned sample does not agree with the perfectly aligned stress relaxation data, and also disagrees with the dynamic data to a larger extent than the perfectly aligned samples. While this phenomenon is not completely understood, it does emphasize the need for good alignment during testing to ensure better data agreement between different test modes.

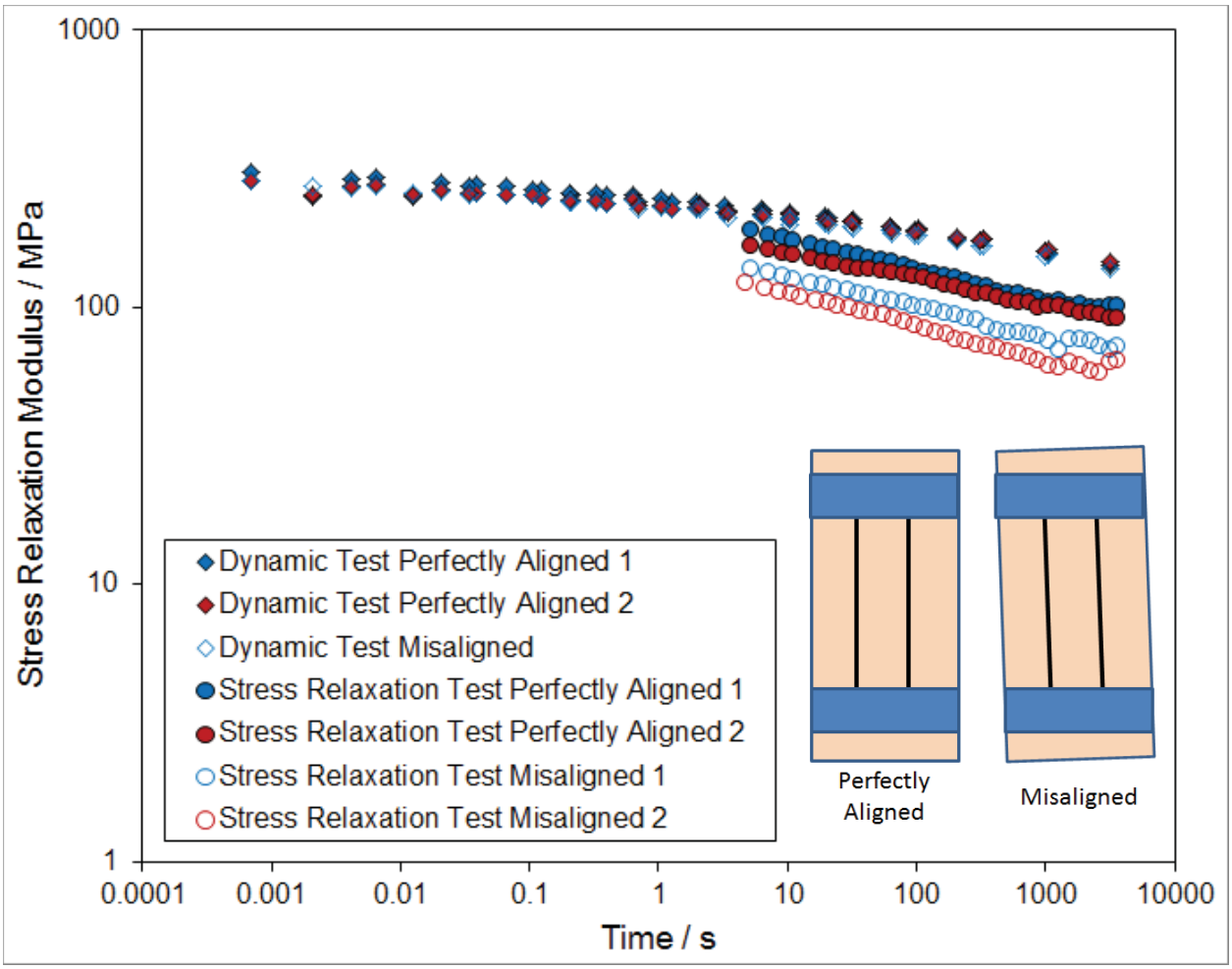

Figure A.3. Stress relaxation modulus of Nafion NRE 211 taken at 0.1% strain in dynamic and stress relaxation mode, used to study the effects of misalignment.

Due to the high moisture sensitivity of ionomeric materials, it is important to understand the experimental accuracy of the TA RH unit. TA Instruments reports an RH accuracy of ± 2%, and as such hygral shift factors and the strain from hygral expansion were predicted at 28% and 32% RH based on previously collected dynamic data, as shown in **Figure A.4**. The hygral shift factors would correspond to a horizontal shift, possibly explaining the differences in the 0.067% and 0.1% strain dynamic tests for the PFCB. The hygral strain would correspond to a vertical shift, because a higher or lower strain level would decrease or increase the modulus respectively.

The hygral shift factors for PFCB were found to be, $a_H(28\%) = -0.070$ and $a_H(32\%) = +0.068$, and the hygral strain was found to be $\varepsilon_H(28\%) = -0.083\%$ and $\varepsilon_H(32\%) = +0.088\%$.

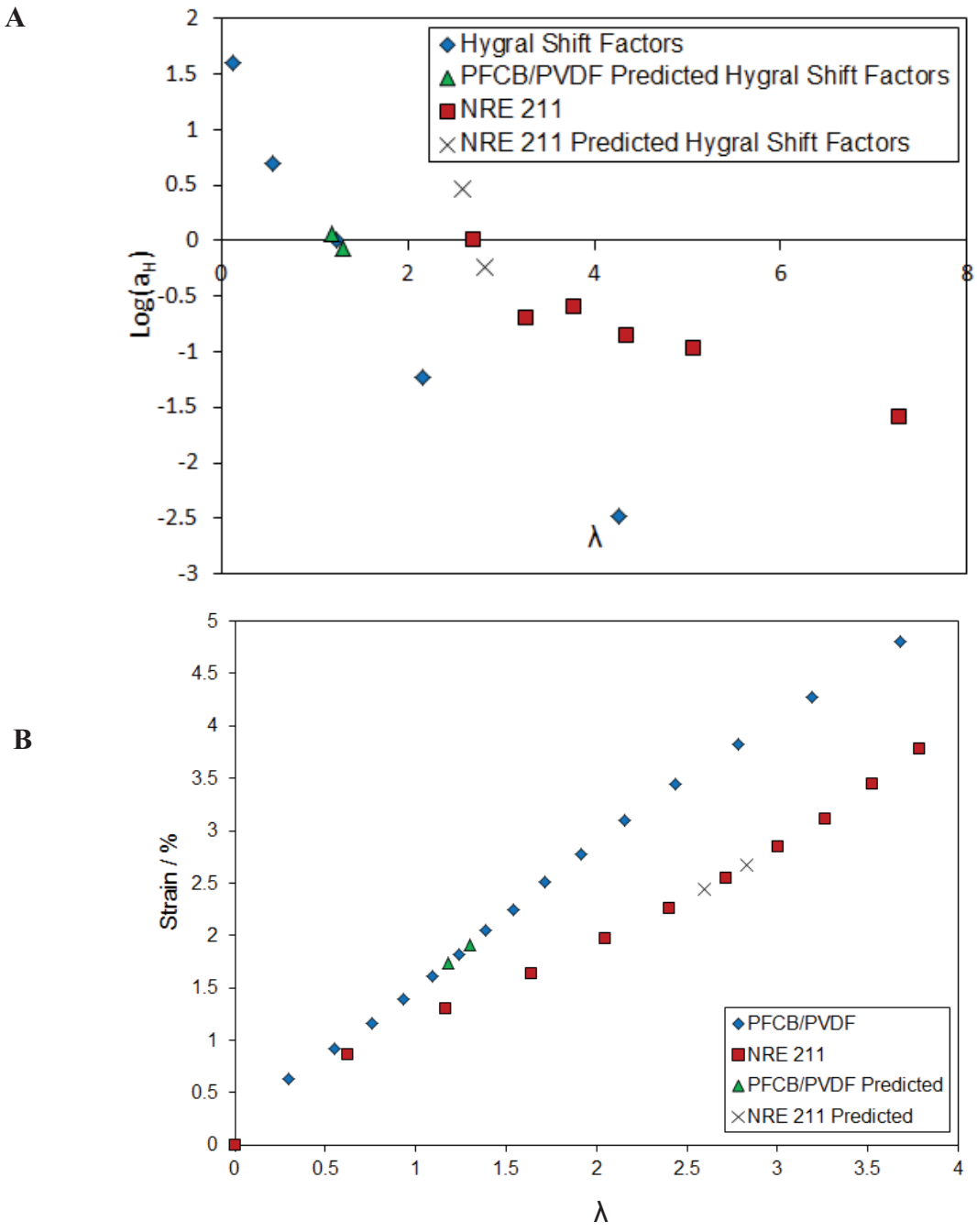

Figure A.4. **(A)** Predicted hygral shift factors for PFCB/PVDF-HFP (green triangles) and NRE 211 NRE 211 (black X's) at 28 and 32% RH. **(B)** Predicted hygral strain for PFCB/PVDF-HFP (green triangles) and NRE 211 (black X's) at 70°C for 28 and 32% RH.

Using these values, storage moduli for PFCB were predicted for 28 and 32% RH and plotted with the original 30% RH dynamic data in **Figure A.5**. These predicted curves would be the maximum difference expected from RH error, and could be seen as horizontal and vertical error bars. As can be seen in **Figure A.5**, the horizontal shift from the hygral shift factor had little effect on the predicted modulus, however the vertical shift from the hygral strain created a large effect. Decreasing the relative humidity by 2% increased the modulus by 268%, and increasing the relative humidity by 2% decreased the modulus by 42%. The asymmetric response seen corresponds to the WLF like behavior seen in the RH shift factors in **Figure A.4**. Removing 2% RH at a 30% RH level has a greater effect on the modulus than adding 2% RH, as seen over the entire humidity range. Adding a small amount of moisture at low humidity levels has a much greater effect on the material than adding a small amount of moisture at high humidity levels. This vertical shift due to hygral strain could easily account for the observed differences in the magnitude of the modulus, however because data taken at the same strain level appears to be repeatable, hygral expansion alone does not account for differences in data taken at different strain levels.

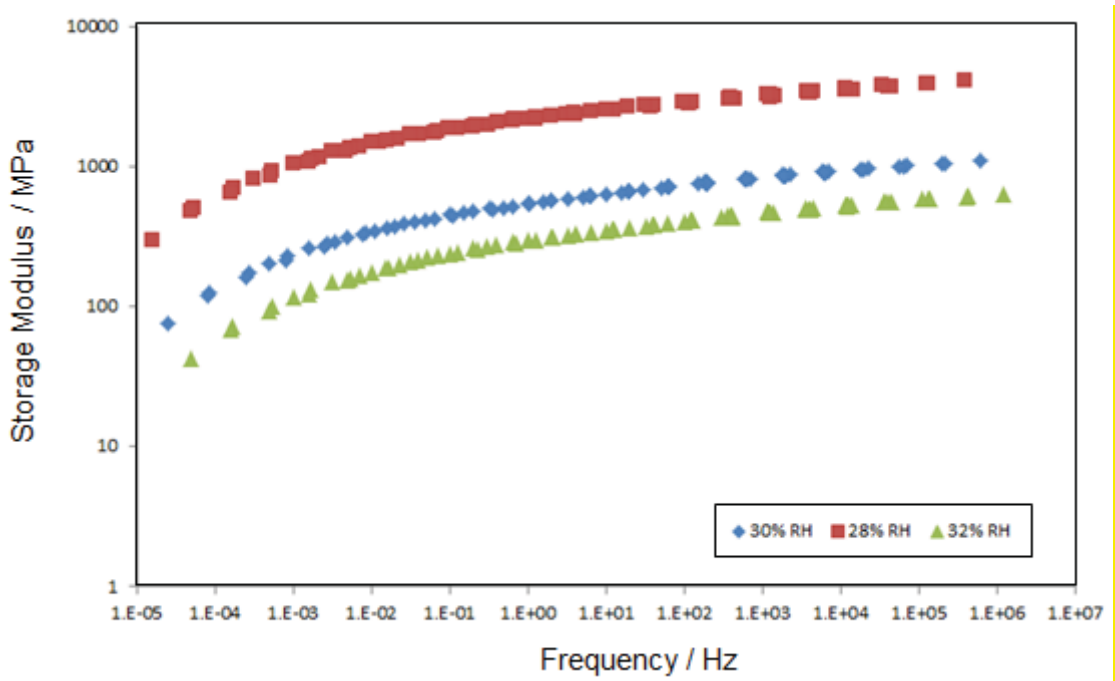

Figure A.5. Predicted storage modulus for PFCB at 28 (red squares) and 32% RH (green triangles), compared with the measured modulus at 30% RH (blue diamonds).

Therefore, it was thought that the differences in strain caused by the moisture sensitivity of the material combined with the low force used during measurement could be within the noise limits of the instrument. As such, multiple strain levels were tested on a single piece of NRE 211 and PFCB/PVDF-HFP to see if the measurements stabilized above a certain strain. The testing was completed by first applying the dynamic mode with a single frequency of 0.10 Hz at 70°C and 30% RH, over 6 applied strain amplitude levels of 0.067, 0.1, 0.2, 0.3, 0.4, and 0.5% tested in series on a single sample. At the end of the strain sequence the 0.067% test was repeated to check for changes in material response after testing higher strain levels. After the completion of the dynamic testing, stress relaxation was performed using the same sample and strain sequence at 70°C and 30% RH. It should be noted that the 0.067% strain level was not used during the NRE 211 test, and as such the 0.1% strain test was repeated at the end of each test sequence. The results of these strain tests are shown in **Figure A.6A** and **B** for NRE 211 and PFCB/PVDF-

HFP respectively. The dynamic results were plotted as stress relaxation using the frequency conversion $\omega = \frac{2\pi}{t}$.

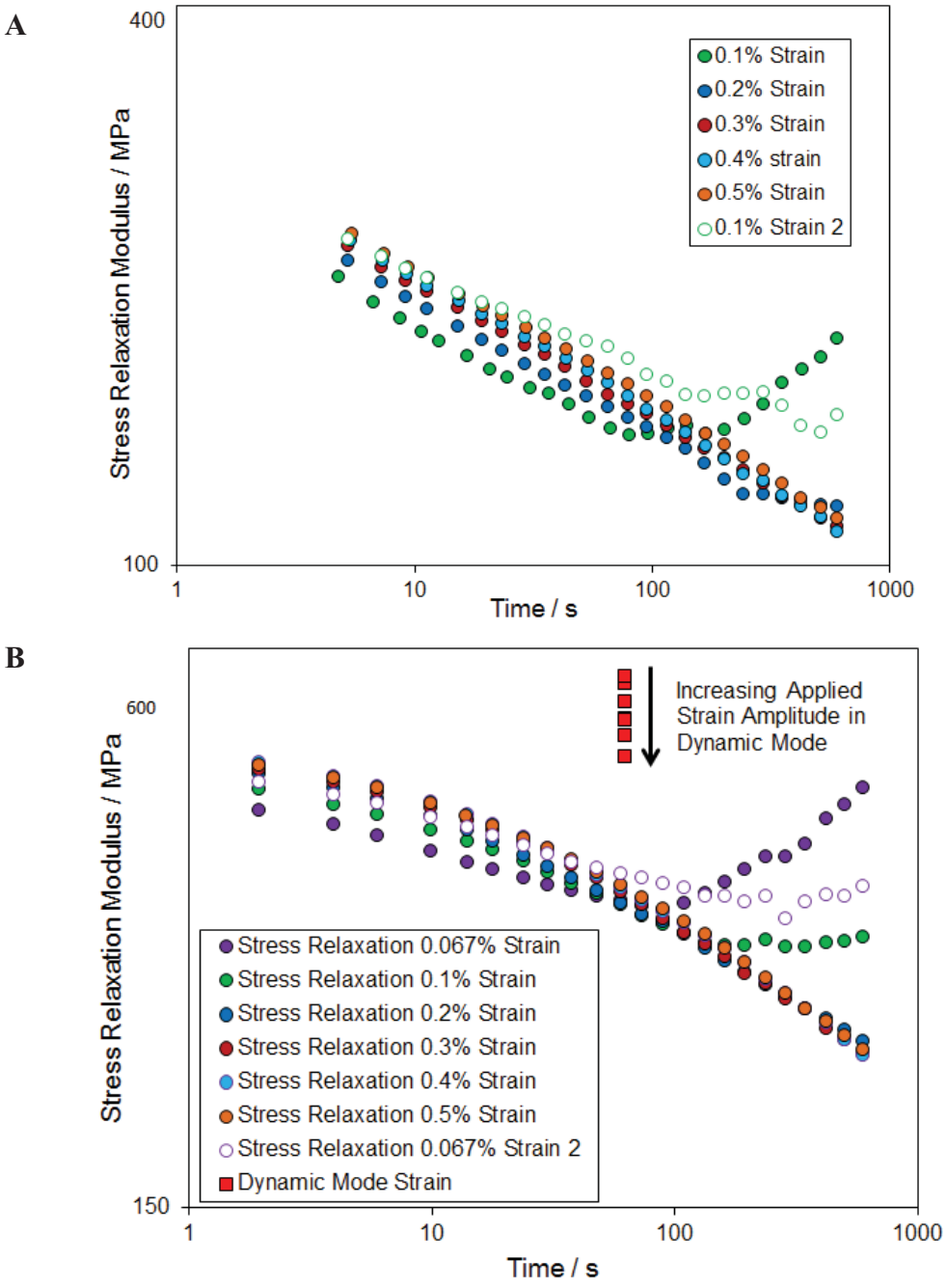

Figure A.6. **(A)** NRE 211 strain level comparisons in dynamic and stress relaxation test modes, at 70°C and 30% RH. **(B)** PFCB/PVDF-HFP strain level comparisons in dynamic and stress relaxation test modes, at 70°C and 30% RH.

The NRE 211 data provided in **Figure A.6A**, shows excellent agreement between the 0.3 – 0.5% strain level stress relaxation tests, while the 0.1 and 0.2% data sets show differing behavior. In addition, the 0.1% dynamic data point is highly separated from the rest of the measured dynamic data points, suggesting that 0.1% is within a noise range of the instrument. Because the 0.2% strain level stress relaxation also shows odd behavior, it is suggested that all subsequent testing of NRE 211 be performed at 0.3% strain and above, although previous testing was performed at 0.5% strain, as mentioned previously, and may be easier to use for consistency. These results explain why the magnitude of the dynamic testing at low strain levels did not match. As long as dynamic test values remain close to stress relaxation test values for strain levels above 0.3%, it is thought that dynamic data is valid, although stress relaxation data may provide a more accurate representation of the material.

Similar to the NRE 211, the PFCB/PVDF-HFP stress relaxation data, provided in **Figure A.6B**, shows good agreement at strain levels above 0.3% and odd behavior at low strain levels. However, the dynamic data shows a typical nonlinear response of a decreasing modulus with increasing strain level. In addition, the moduli measured with the dynamic mode are much larger than the measured stress relaxation moduli, as seen previously for PFCB/PVDF-HFP in **Figure A.2** however it is unclear why this was not observed in **Figure A.1**. The typical nonlinear response of dynamic data observed with PFCB/PVDF-HFP materials implies that dynamic testing may not be suitable for the PFCB/PVDF-HFP material system, due to the apparent strain dependence, however stress relaxation testing above 0.3% strain should provide accurate data. As such, a PFCB/PVDF-HFP hygrothermal master curve created using stress relaxation data was determined to be more appropriate.

To determine an appropriate strain level to perform these stress relaxation tests to characterize PFCB/PVDF-HFP, an isochronal plot was made to ensure a higher strain level could be employed for testing while remaining within the linear viscoelastic region. These plots were constructed using creep tests taken at 70^{o}C and 30% RH, and using applied stresses of 0.1, 0.2. 0.3, 0.4, 0.5, 1, 2, 3, and 4 MPa. It was also noted during testing that differences existed in the strain response in the material parallel and transverse to the casting direction. Therefore, two separate isochronal plots, **Figure A.7A** and **B** parallel and transverse to the casting direction respectively, were created to examine the anisotropy of the material further.

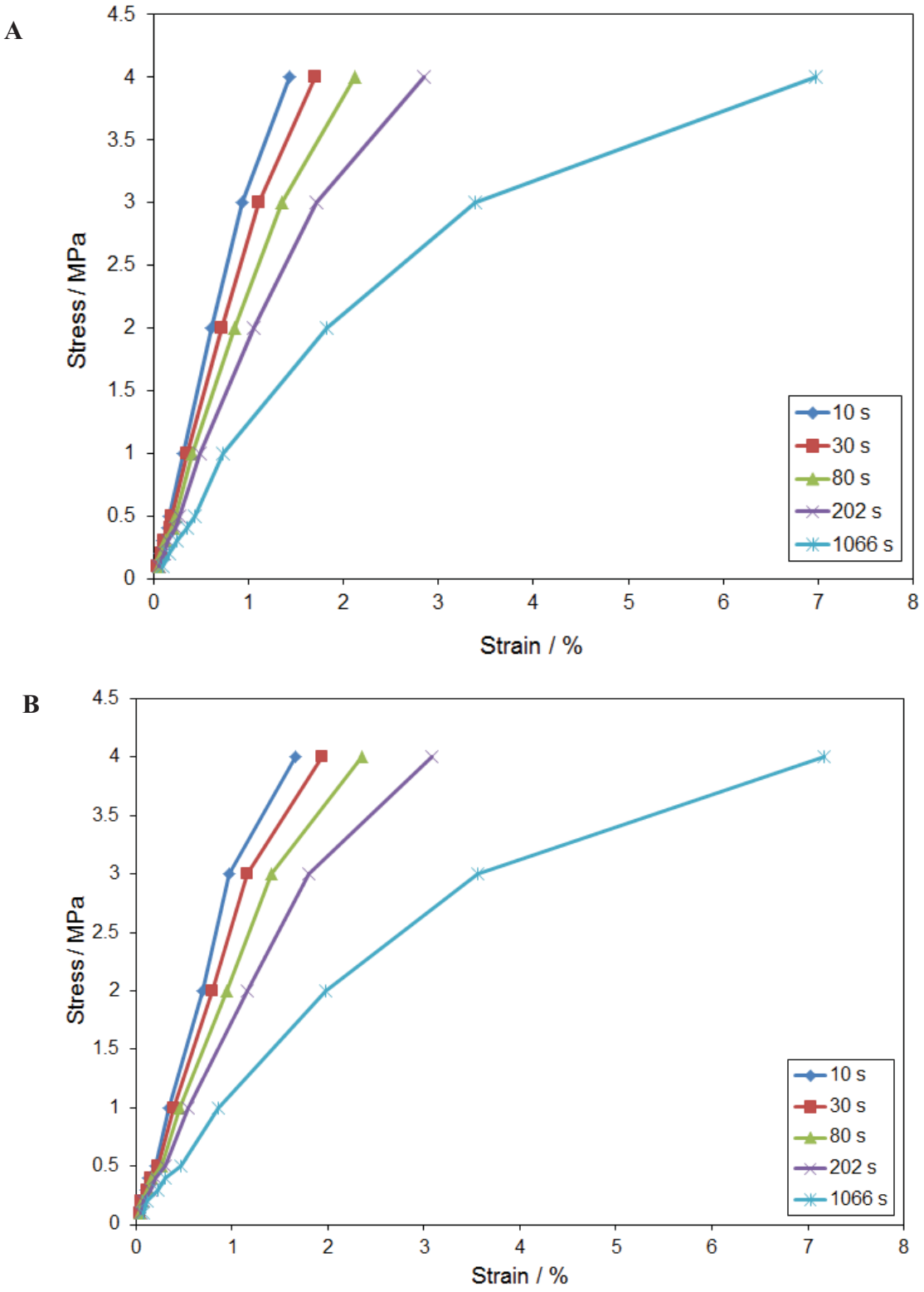

Figure A.7. (A) Isochronal creep plot for PFCB/PVDF-HFP parallel to the casting direction, taken at 70°C and 30% RH. **(B)** Isochronal creep plot for PFCB/PVDF-HFP transverse to the casting direction, taken at 70°C and 30% RH.

Figure A.7A and **B** both show similar envelopes for the linear viscoelastic region, below 3 MPa and 2% strain. It is likely that the linear viscoelastic region is not sharply defined by this stress and strain limit rather, that a curved envelope exists. However further tests would need to be performed to obtain the full curve of this envelope and therefore an approximate region is defined below the 3 MPa and 2% strain limits. Based on these limits, a strain of 0.5% for stress relaxation testing was chosen to ensure testing is completed outside the noise range of the instrument and well within the linear viscoelastic region.

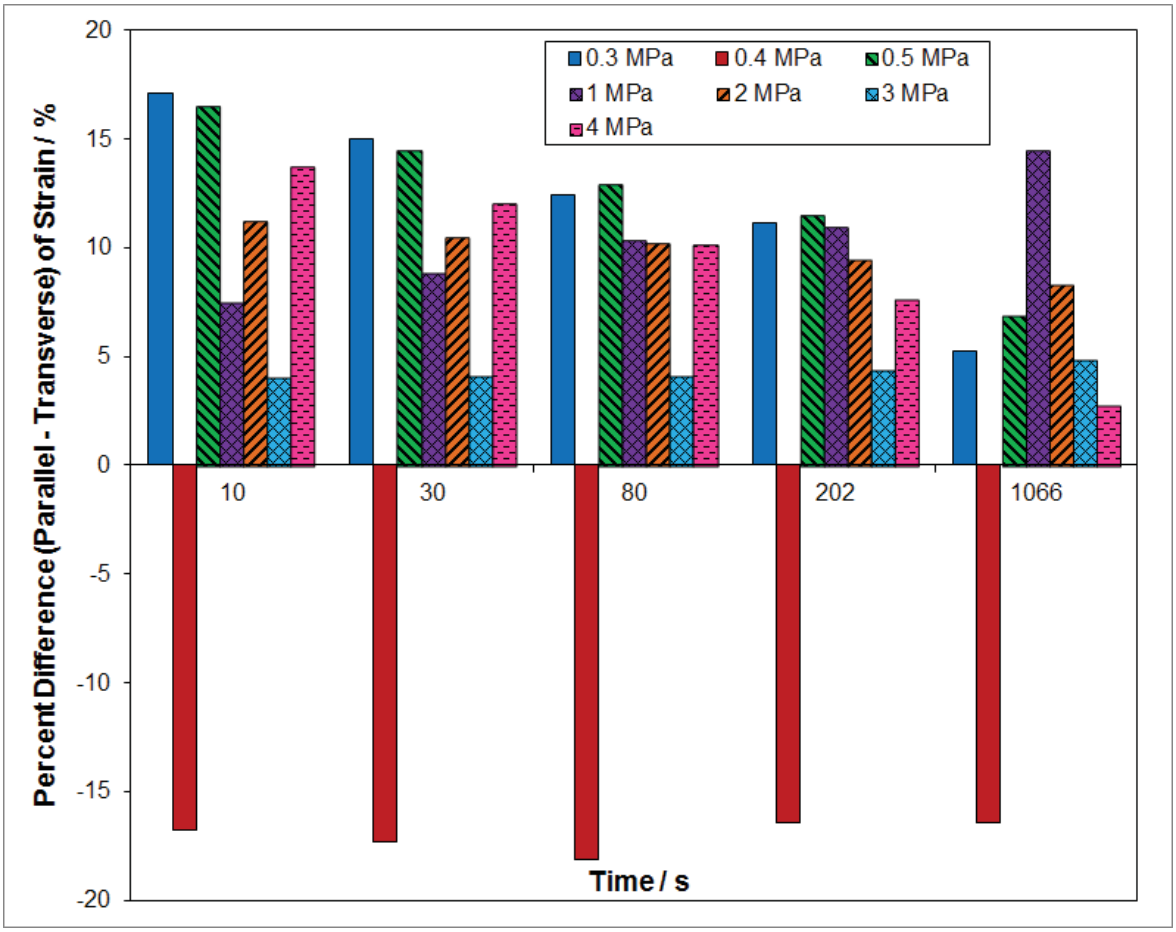

Figure A.8. Comparison of the differences in strain obtained during creep tests for the parallel and transverse direction to casting for PFCB/PVDF-HFP.

A further plot was created comparing the differences in the percent strain obtained in the parallel and transverse to casting directions, as shown in **Figure A.8**. It is important to note that the transverse strain was always higher than the parallel strain, except at 0.4 MPa, as shown in **Figure A.8**. Other than the 0.4 MPa anomaly, it is expected for the material to stretch further in the transverse direction. This is because in the parallel direction the strain is being applied parallel to the polymer chains, and therefore attempting to lengthen the chains themselves. Whereas in the transverse direction, the strain is being applied perpendicular to the chains, and thus acting to separate the chains from one another rather than pull on the chemical bonds of each chain. Because it is easier to separate chains than stretch a chemical bond, the strain in the transverse direction to casting should be higher than in the parallel direction. Although the membrane thickness, 10-12 μm, is quite large in terms of molecular length scales, the force of drawing applied to the viscous solution causes the molecules to orient parallel to the drawing direction. Over the entire testing period there was as much as 17% difference between the two directions, indicating that it is important to know the material direction for all uniaxial testing. Because the parallel to casting direction strains less than the transverse direction, all stress relaxation testing for the creation of a hygrothermal master curve was performed in the parallel to casting direction so the material with the highest stiffness was characterized. Transverse material could also be used, as long as all testing is consistent with the chosen casting direction.

Based on this body of testing, the stress relaxation test mode was chosen, with a 0.5% strain, using materials all cut parallel to the casting direction. The final test method utilized is described in **Section 2.2.4.1**.

References

[1] K.A. Patankar, D.A. Dillard, S.W. Case, M.W. Ellis, Y.-H. Lai, M.K. Budinski, C.S. Gittleman, Fuel Cells, (Accepted).

Appendix B : Comparison of Analysis Performed Utilizing Giner Mass Uptake Data and VT Mass Uptake Data

As discussed in **Section 2.3.1**, mass uptake taken at Virginia Tech differs from that taken at Giner, and as such the analysis performed in **Chapter 3** was examined utilizing both the λ relationship developed by Giner and by VT. This appendix will compare the results of the two analyses side by side, and show why the VT mass uptake data is possibly more appropriate to use for stress modeling of PFCB/PVDF-HFP.

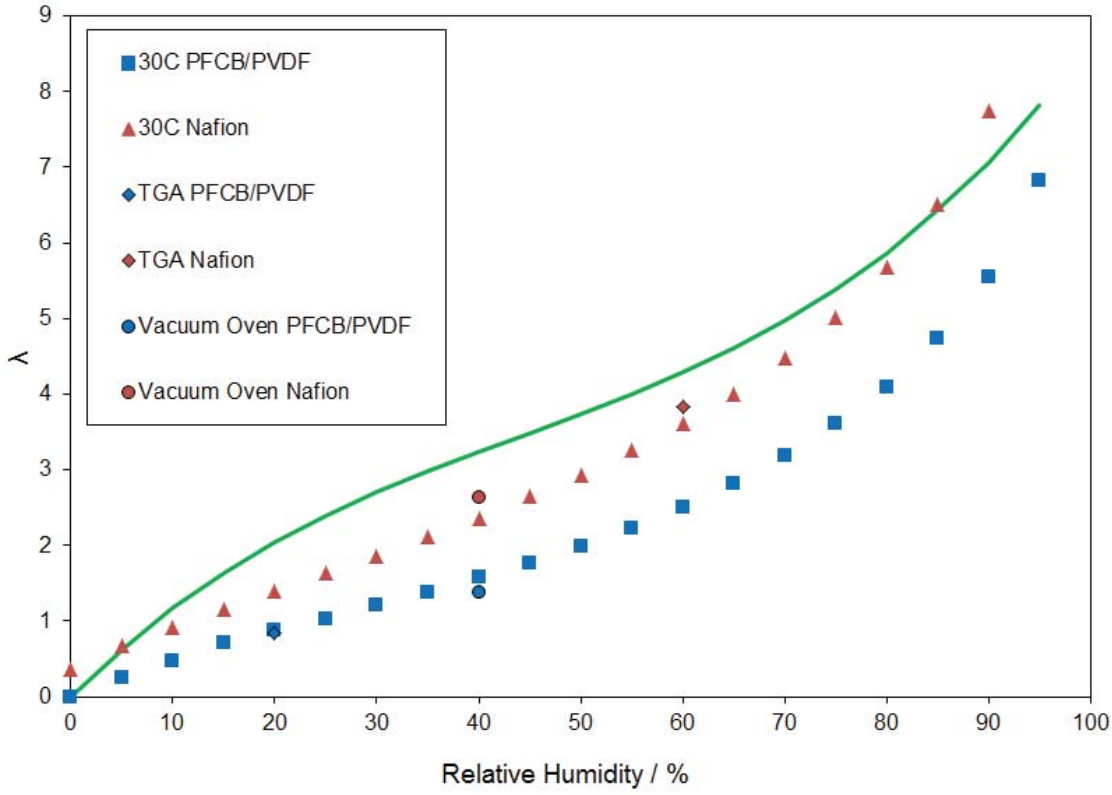

Figure B.1. Comparison of mass uptake data collected at Virginia Tech and compared with the Giner λ equation at 30°C.

The hygral expansion was calculated first for both λ expressions. This was done to ensure subsequent analysis was performed consistently. Therefore, analysis performed with the

Giner λ expression utilizes the corresponding variables calculated with the Giner λ expression, and similar for analysis performed with the Virginia Tech λ expression. As shown in **Figure B.2**, the regions of interest are over different λ regions, corresponding to 35-90% RH. The calculated coefficients of hygral expansion are 1.24%/λ using Giner's λ relationship, and 1.32%/λ using VT's λ relationship.

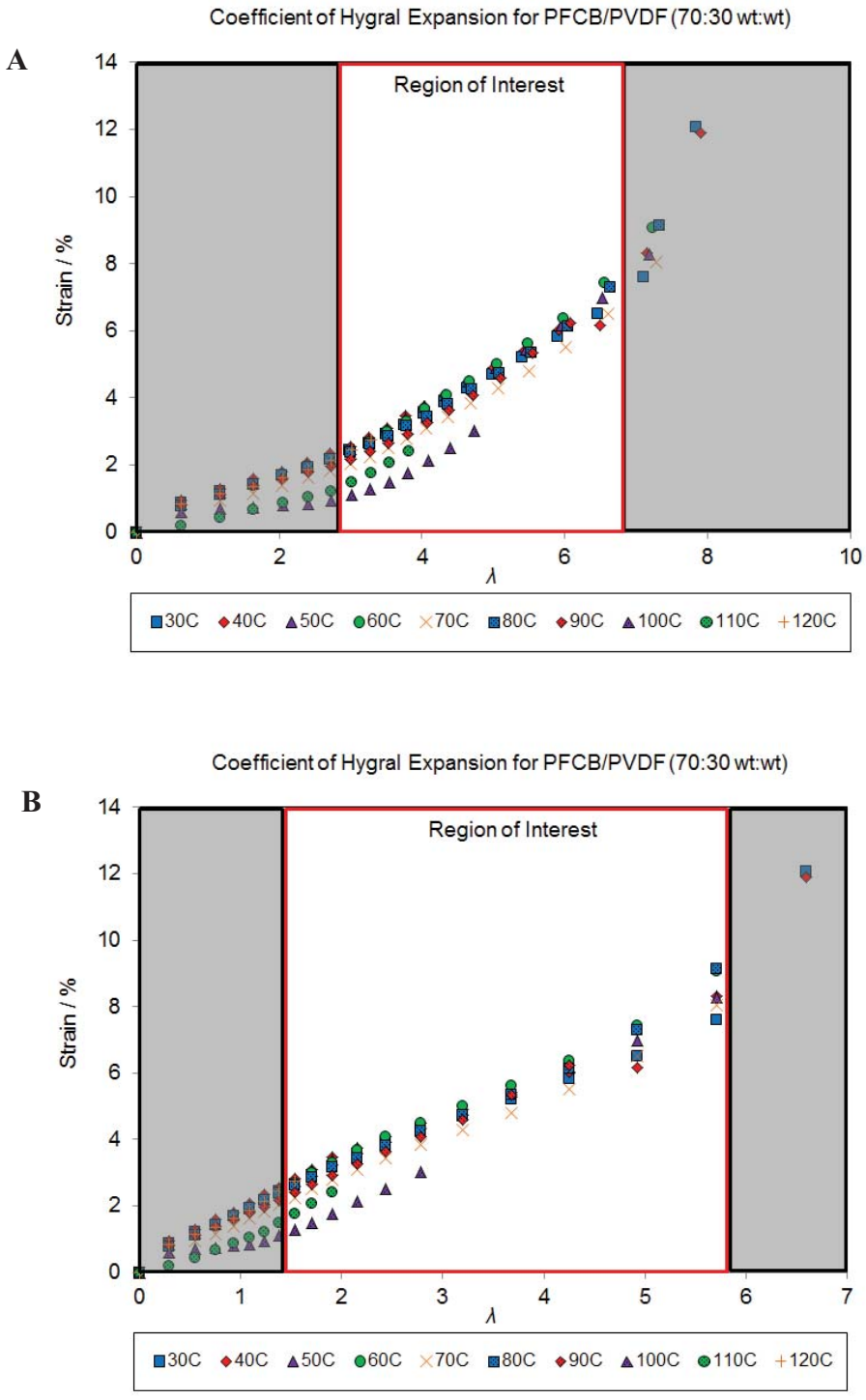

Figure B.2. Hygral expansion measured from 0-95% RH over 30-120°C utilizing **(A)** Giner's λ relationship and **(B)** VT's λ relationship.

After calculating the coefficient of hygral expansion, the hygrothermal shift factors developed for the hygrothermal stress relaxation master curve were fit, as shown in **Figure B.3**. As described in Section **3.3,** a combined Arrhenius and free volume fit was performed over the entire temperature and λ range (**Eqn [B.1]**). The hygrothermal shift factors plotted against the VT λ require a two-equation fit (**Eqns [3.18]** and **[B.3**]) to account for the different activation energies above and below 70°C as seen in the approximate thermal shift factors provided in **Figure B.4C**, whereas the shift factors plotted against the Giner λ require a four equation fit (**Eqns [B.4**]**-[B.7**]). The extra equations using the Giner λ are required to describe two different regions of hygral expansion of the free volume. These two regions can be observed if the efficiency of swelling is examined.

The efficiency of swelling is defined as the degree of expansion of the membrane compared with the volume of water sorbed by the membrane, assuming it was in the liquid state. This efficiency of swelling can be examined by plotting the volume of water uptake vs. the volume of membrane expansion, and observing the slope. If perfect swelling efficiency were observed the slope would be unity, as each water molecule would contribute to the expansion of the membrane as if it were in the liquid state. The volume of water uptake was calculated by dividing the mass measured via water uptake, by the density of water, taken to be 1 g/cm^3. The volume of membrane expansion was calculated by assuming isotropic swelling, and therefore multiplying the measured hygral expansion by 3. The efficiency of swelling for both the Giner λ and the VT λ is provided in **Figure B.4A** and **B**. Over the λ region used for fitting the hygrothermal shift factors, shown in **Figure B.4D,** a kink in the efficiency of swelling at a λ of ~3.4 is observed when employing the Giner λ, whereas a single line is observed when using the VT λ. Therefore, the two regions of hygral expansion noted with the Giner λ must be accounted

for with two hygral expansion of free volume values, whereas only one is required when using the VT λ. Therefore, a simpler fit is achieved when using the VT λ, which is advantageous for programming purposes. However, a simpler fit is not enough to say the VT λ relationship is more accurate than the Giner λ relationship and further analysis was performed.

$$\log a_{TH} = \frac{-\frac{B}{2.303}\alpha_f \Delta T - \frac{B}{2.303}\beta_f \Delta\lambda}{f_o{}^2 + f_o\alpha_f \Delta T + f_o\beta_f \Delta\lambda} - \frac{2.303R}{E_a}\Delta T \qquad \textbf{[B.1]}$$

$\alpha_f = 0.000145/^{\circ}\mathrm{C}, f_o = 0.051$

$\mathrm{T_{ref}} = 343K, \lambda_{ref} = 1.24$

$T \le 70^o C$:

$$\log a_{TH} = \frac{\frac{1}{2.303}\alpha_f \Delta T + \frac{1}{2.303}(0.007)\Delta\lambda}{0.051^2 + 0.051\alpha_f \Delta T + 0.051(0.007)\Delta\lambda} + 0.0319\Delta T \qquad \textbf{[B.2]}$$

$T > 70^o C$:

$$\log a_{TH} = \frac{\frac{1}{2.303}\alpha_f \Delta T + \frac{1}{2.303}(0.007)\Delta\lambda}{0.051^2 + 0.051\alpha_f \Delta T + 0.051(0.007)\Delta\lambda} + 0.0993\Delta T \qquad \textbf{[B.3]}$$

$\alpha_f = 0.000145/^{\circ}\mathrm{C},\ f_o = 0.043$

$\mathrm{T}_{\mathrm{ref}} = 343K, \lambda_{ref} = 2.775$

$\mathrm{T} \le 70^{\circ}\mathrm{C}, \lambda \le 3.46$:

$$\log a_{TH} = \frac{.43\alpha_f \Delta T + .43(0.0025)\Delta\lambda}{0.043^2 + 0.043\alpha_f \Delta T + 0.043(0.0025)\Delta\lambda} + 0.013\Delta T \quad \textbf{[B.4]}$$

$\mathrm{T} \le 70^{\circ}\mathrm{C}, \lambda > 3.46$:

$$\log a_{TH} = \frac{.43\alpha_f \Delta T + .43(0.0031)\Delta\lambda}{0.043^2 + 0.043\alpha_f \Delta T + 0.043(0.0031)\Delta\lambda} + 0.013\Delta T \quad \textbf{[B.5]}$$

$T > 70^{o}C, \lambda \le 3.46$:

$$\log a_{TH} = \frac{.43\alpha_f \Delta T + .43(0.0025)\Delta\lambda}{0.043^2 + 0.043\alpha_f \Delta T + 0.043(0.0025)\Delta\lambda} + 0.085\Delta T \quad \textbf{[B.6]}$$

$T > 70^{o}C, \lambda > 3.46$:

$$\log a_{TH} = \frac{.43\alpha_f \Delta T + .43(0.0031)\Delta\lambda}{0.043^2 + 0.043\alpha_f \Delta T + 0.043(0.0031)\Delta\lambda} + 0.085\Delta T \quad \textbf{[B.7]}$$

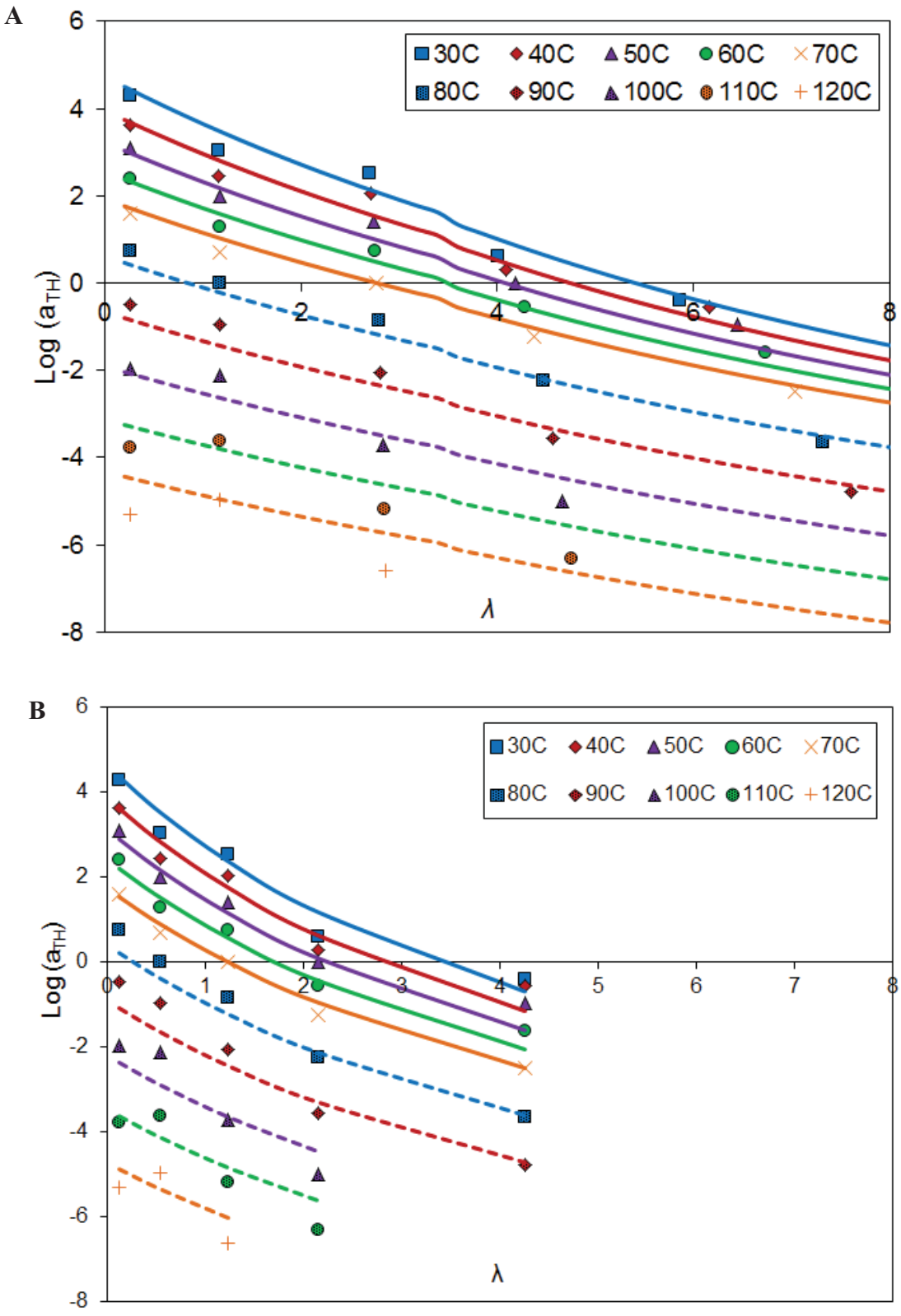

Figure B.3. Hygrothermal shift factors fit utilizing **(A)** Giner's λ relationship and **(B)** VT's λ relationship.

A

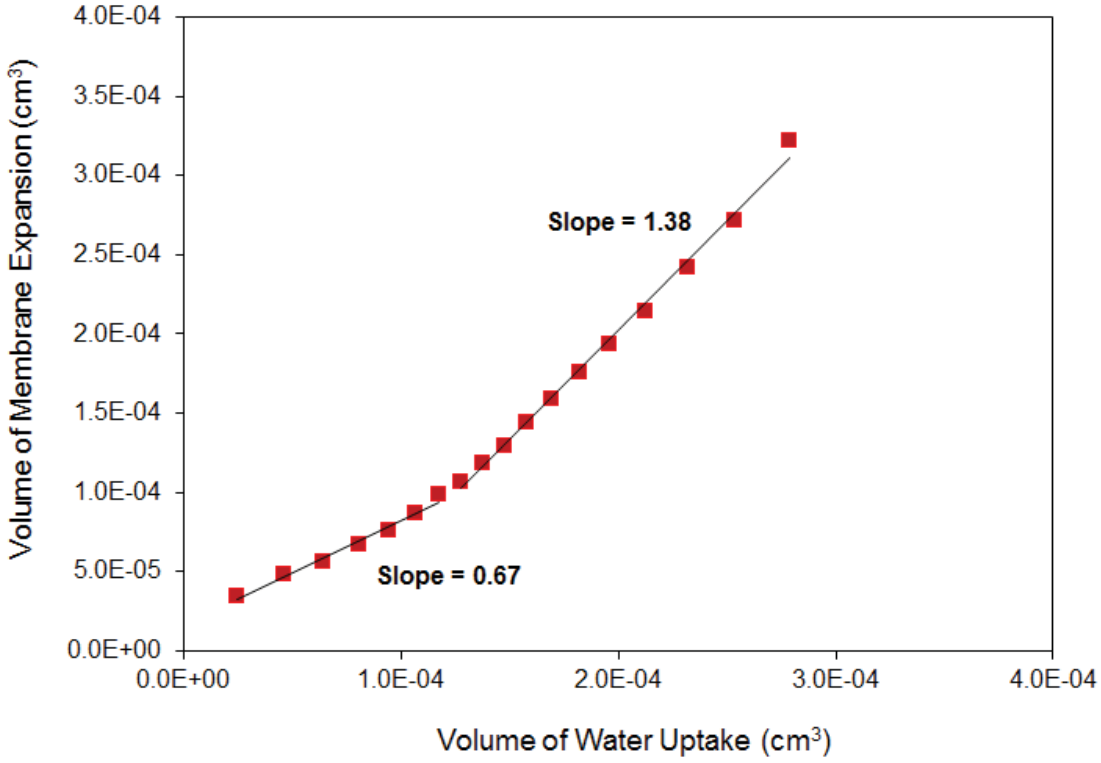
4.0E-04
3.5E-04
3.0E-04
2.5E-04
2.0E-04
1.5E-04
1.0E-04
5.0E-05
0.0E+00
Volume of Membrane Expansion (cm3)
Slope = 1.38
Slope = 0.67
0.0E+00
1.0E-04
2.0E-04
3.0E-04
4.0E-04
Volume of Water Uptake (cm3)

B

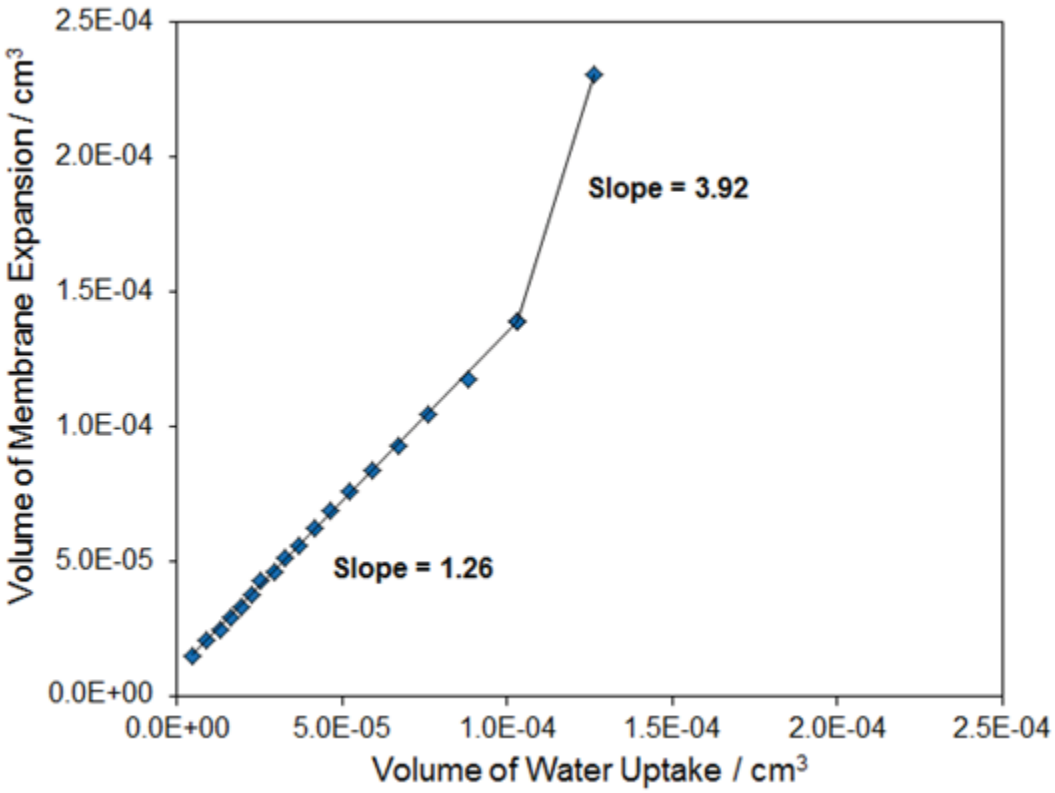
2.5E-04
2.0E-04
1.5E-04
1.0E-04
5.0E-05
0.0E+00
Volume of Membrane Expansion / cm3
Slope = 3.92
Slope = 1.26
0.0E+00
5.0E-05
1.0E-04
1.5E-04
2.0E-04
2.5E-04
Volume of Water Uptake / cm3

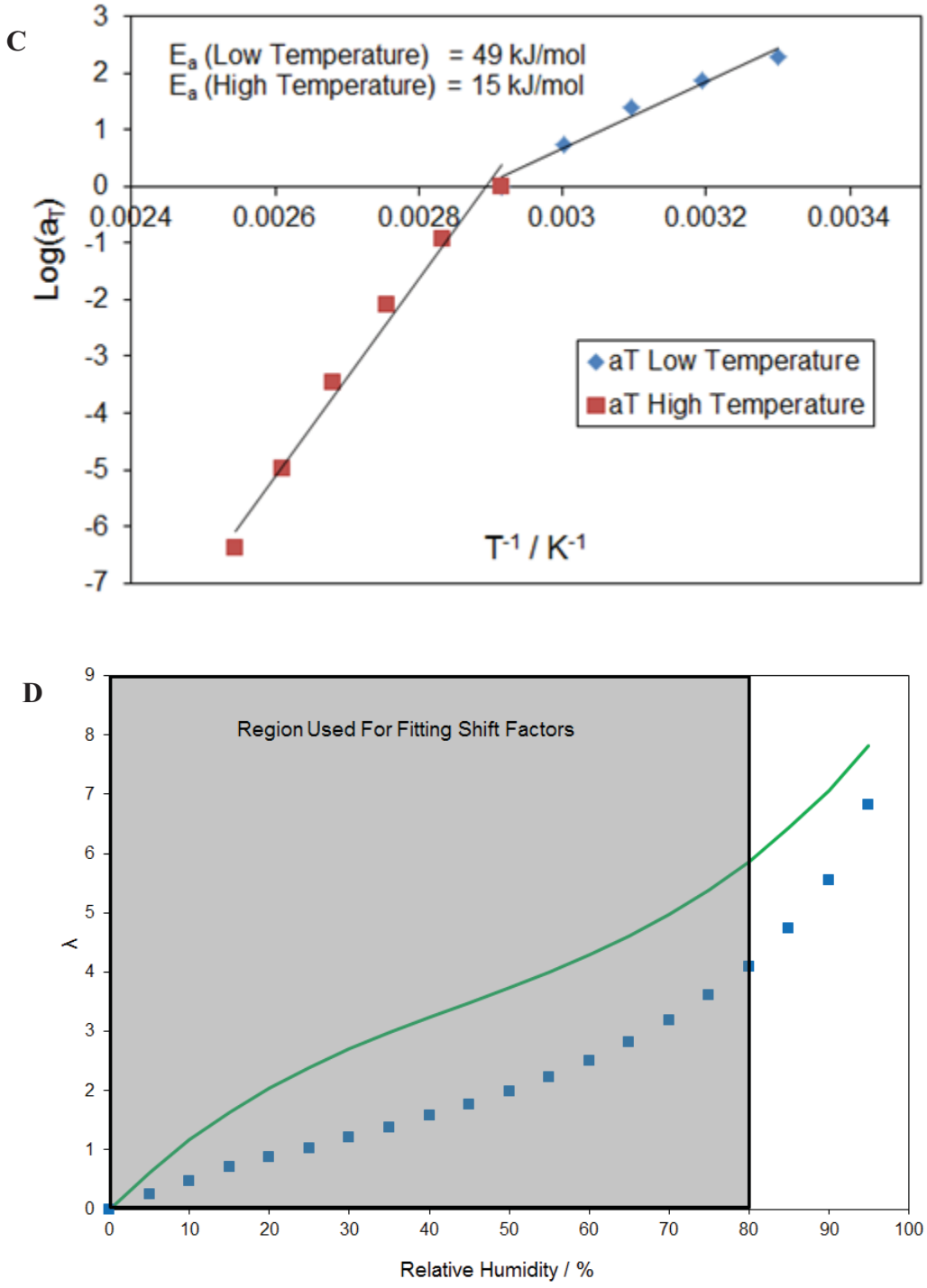

Figure B.4. **(A)** Efficiency of swelling calculated using Giner's λ relationship, **(B)** efficiency of swelling calculated using VT's λ relationship, **(C)** approximate thermal shift factors for PFCB/PVDF-HFP from the hygrothermal master curve, **(D)** highlighted region of λ relationships used for fitting the hygrothermal shift factors.

Using the hygrothermal shift factor fits provided in **Eqns [3.18]** and **[B.3**] using the VT λ expression, and **Eqns [B.4**]**-[B.7**] using the Giner λ expression, as well as the Prony series presented in **Section 3.4.1**, an analytical model was created with **Eqn 3.15**. To ensure the model was coded correctly for both λ analyses, a self-prediction of the Prony series at 70°C and 30% RH was performed, as shown by the red line and the purple X's in **Figure B**.**5A** and **B**. After successfully completing the self-prediction, the model was verified by predicting the approximate thermal master curves at 2, 10, 55, and 80% RH as shown with black lines in **Figure B**.**5A** and **B**. Both λ expressions show excellent agreement with the approximate thermal master curves, and based on the model verification either λ expression appears to describe the material behavior well.

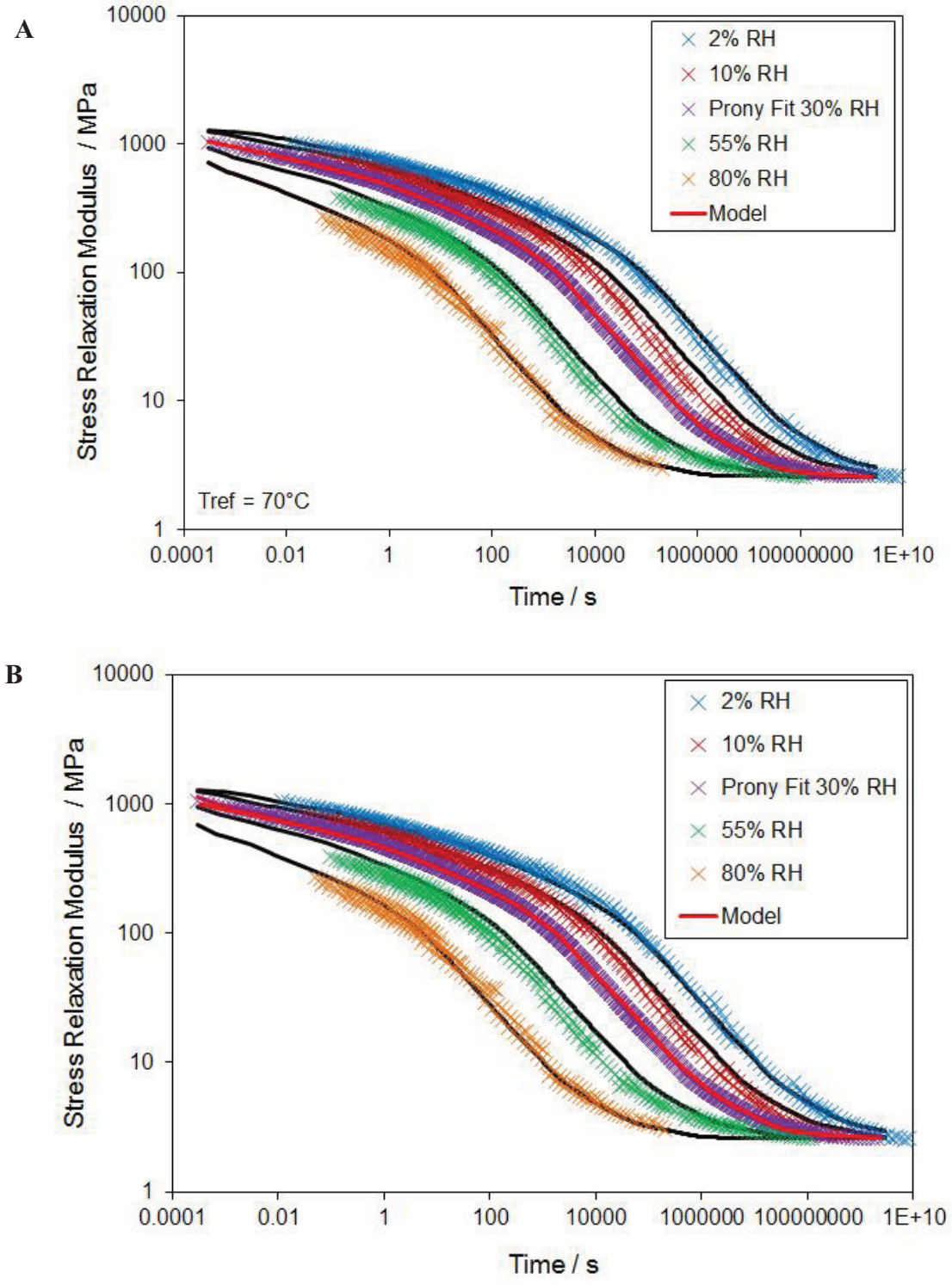

Figure B.5. Analytical model predictions of approximate thermal master curves utilizing **(A)** Giner's λ relationship and **(B)** VT's λ relationship.

To further assess the differences between the two λ relationships, each was used to predict the uniaxial hygrothermal strain of PFCB/PVDF-HFP exposed to four different RH cycles, and compared with strains measured using the TA Instruments Q800 Dynamic Mechanical Analyzer (DMA), as shown in **Figure B.6A-D**. Strain data was measured utilizing the creep mode, with a 9-mm wide sample, slit into three 3-mm sections, allowing for a stronger signal to noise ratio. The gage length was approximately 15 mm to maintain a 5:1 aspect ratio which approximates a uniaxial stress state. A small 3 mN load was applied during testing to hold the sample taut without causing significant creep in the sample. This applied load was an order of magnitude larger than the lower force limits of the instrument, and therefore outside the noise range of the instrument. Four tests were completed, two at 80°C and two at 90°C. At each temperature two different humidity cycles were performed. The first RH profile cycled from 80% RH to 0% RH four times, and the second RH profile cycled from 80% RH to 50% RH. For all tests the sample was initially equilibrated at 30% RH. In **Figure B.6A-D** the strain measured with the DMA is shown as red squares, the predictions made using Giner's λ relationship are shown as green lines, and the predictions using VT's λ relationship are shown as blue lines. As seen, the VT λ strain predictions match the tensile DMA data very well and mildly under predict the compressive strains. However, the Giner λ strain predictions over predict the tensile and compressive strains when cycling between 0 and 80% RH, and over predict the tensile and under predict the compressive strains when cycling between 50 and 80% RH. The Giner λ strain predictions are off by as much as 2%, which could easily translate to large over predictions of the stress, resulting in an under prediction of membrane lifetime. Based on these strain predictions, the VT λ appears to capture the material response to moisture more accurately.

A

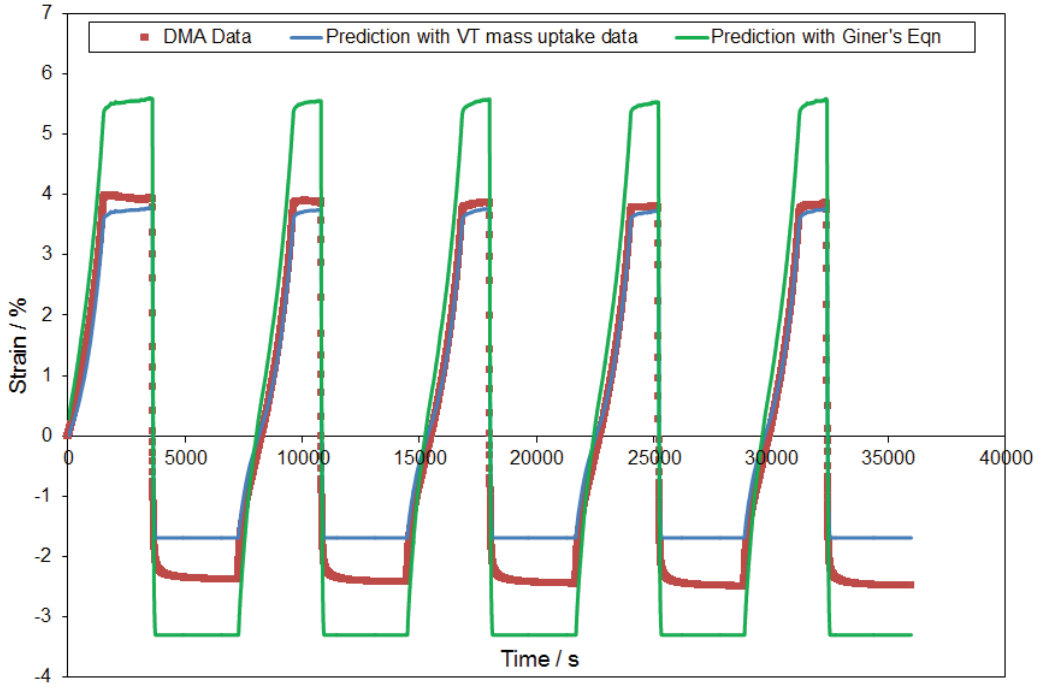
DMA Data
Prediction with VT mass uptake data
Prediction with Giner's Eqn
Strain / %
Time / s
7
6
5
4
3
2
1
0
-1
-2
-3
-4
0
5000
10000
15000
20000
25000
30000
35000
40000

B

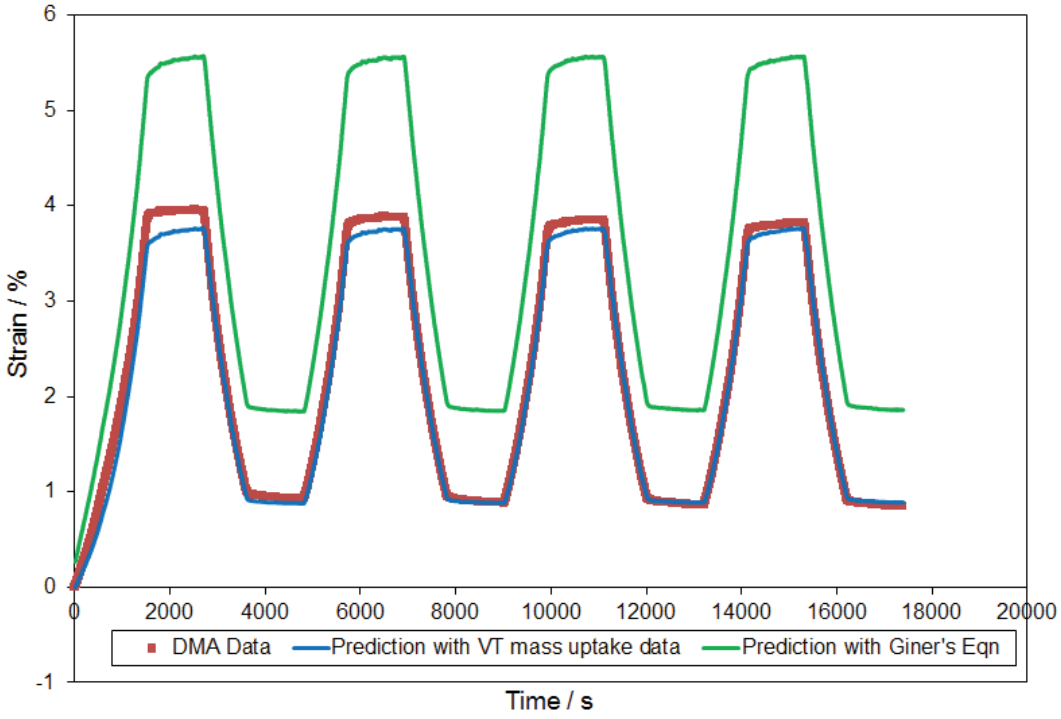
Strain / %
Time / s
6
5
4
3
2
1
0
-1
0
2000
4000
6000
8000
10000
12000
14000
16000
18000
20000
DMA Data
Prediction with VT mass uptake data
Prediction with Giner's Eqn

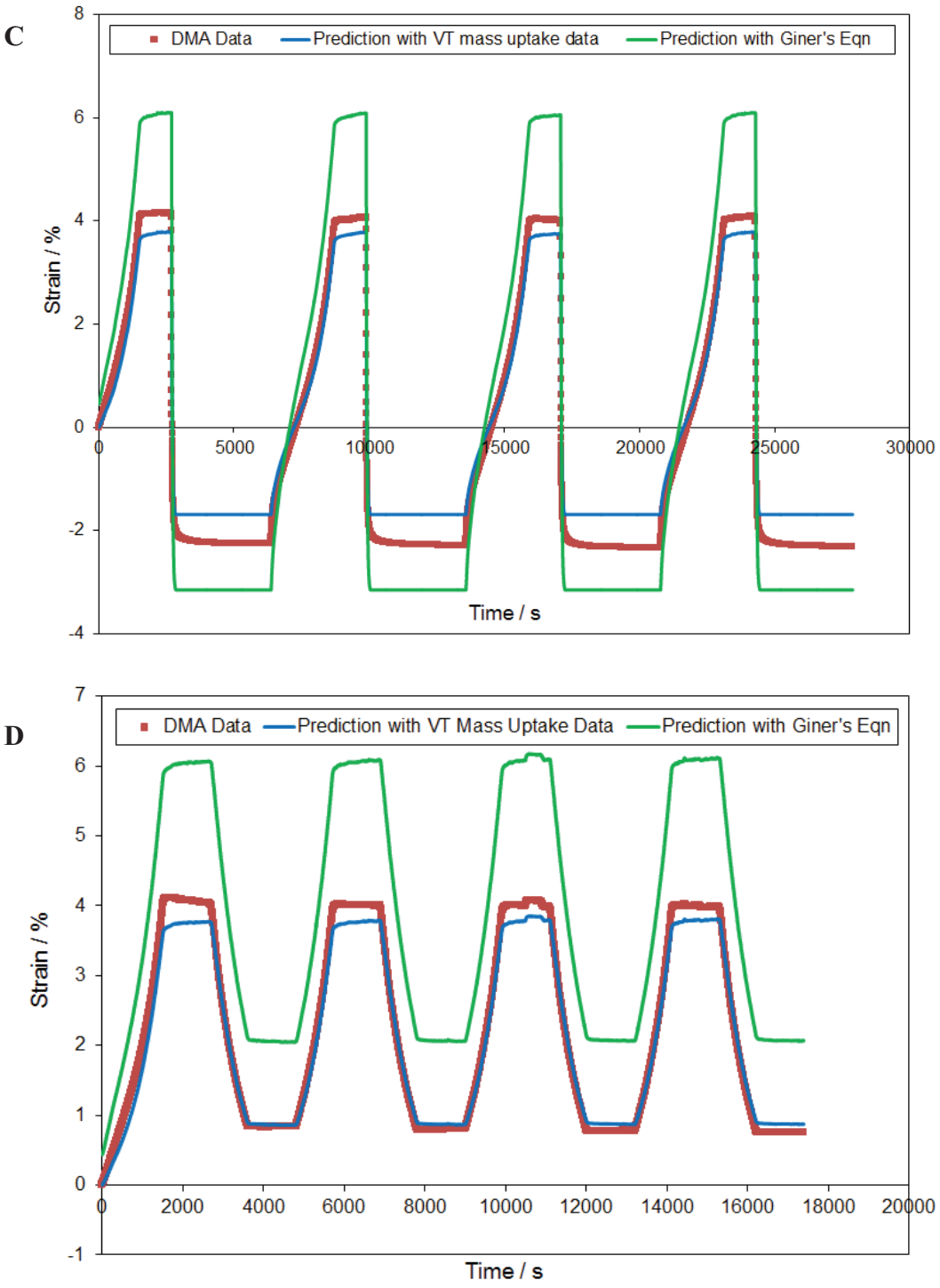

Figure B.6. Strain predictions utilizing Giner's λ relationship and VT's λ relationship, compared with different RH cycles performed at **(A)** 80°C 0-80% RH, **(B)** 90°C 0-80% RH, **(C)** 80°C 50-80% RH, and **(D)** 90°C 50-80% RH.

To examine the impact of the differing strain predictions, stress predictions based on both λ relationships were completed utilizing an RH cycle from 0 to 100%, as shown in **Figure B.7A** and **B**, with close-ups provided in **Figure B.7C** and **D**. The tensile stresses predicted using the Giner λ relationship are approximately 21 MPa, while the tensile stresses predicted using the VT λ relationship are approximately 11 MPa. It should be assumed that these stresses are over predicted because nonlinearity is not accounted for, however the 21 MPa prediction using Giner's λ relationship is much larger than expected. The stress predicted for PFCB/PVDF-HFP should be higher than PFSA materials due to the increased stiffness of PFCB/PVDF-HFP, however three times larger is extreme. The large stresses predicted by the Giner λ relationship are likely due to the over prediction of the strains shown previously in **Figure B.6**. Therefore, it is believed that the VT λ relationship, showing a maximum tensile stress less than two times greater than PFSA materials, provides a more accurate stress prediction.

A

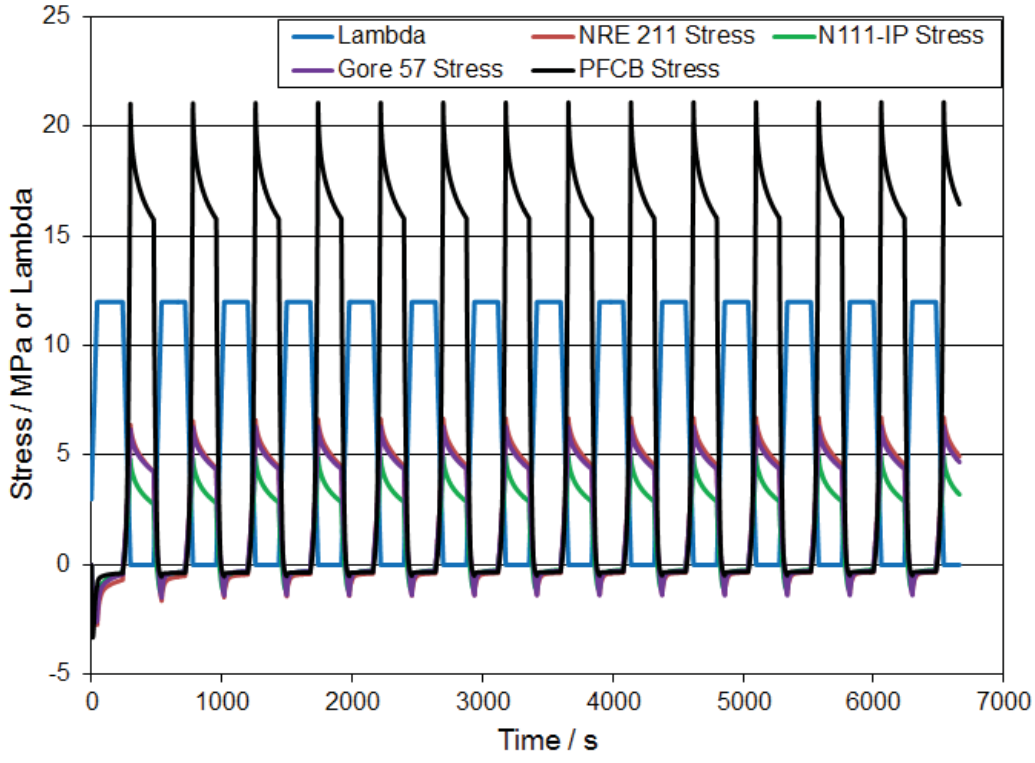
Lambda
NRE 211 Stress
N111-IP Stress
Gore 57 Stress
PFCB Stress
Stress / MPa or Lambda
Time / s
25
20
15
10
5
0
-5
0
1000
2000
3000
4000
5000
6000
7000

B

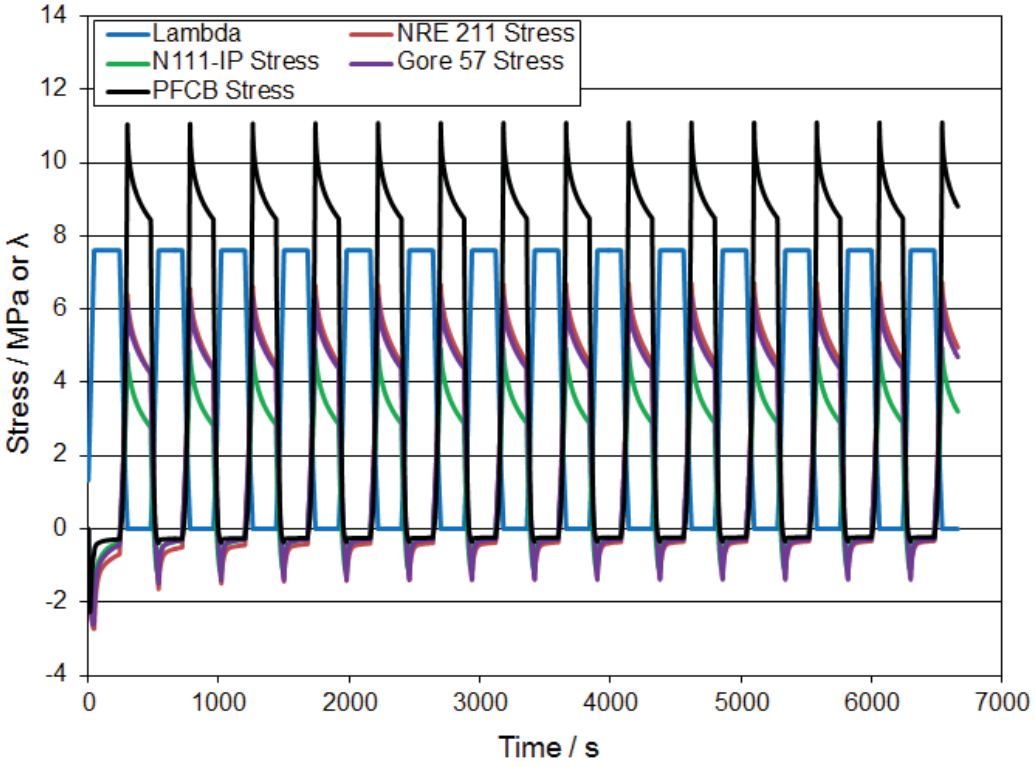
Lambda
NRE 211 Stress
N111-IP Stress
Gore 57 Stress
PFCB Stress
Stress / MPa or λ
Time / s
14
12
10
8
6
4
2
0
-2
-4
0
1000
2000
3000
4000
5000
6000
7000

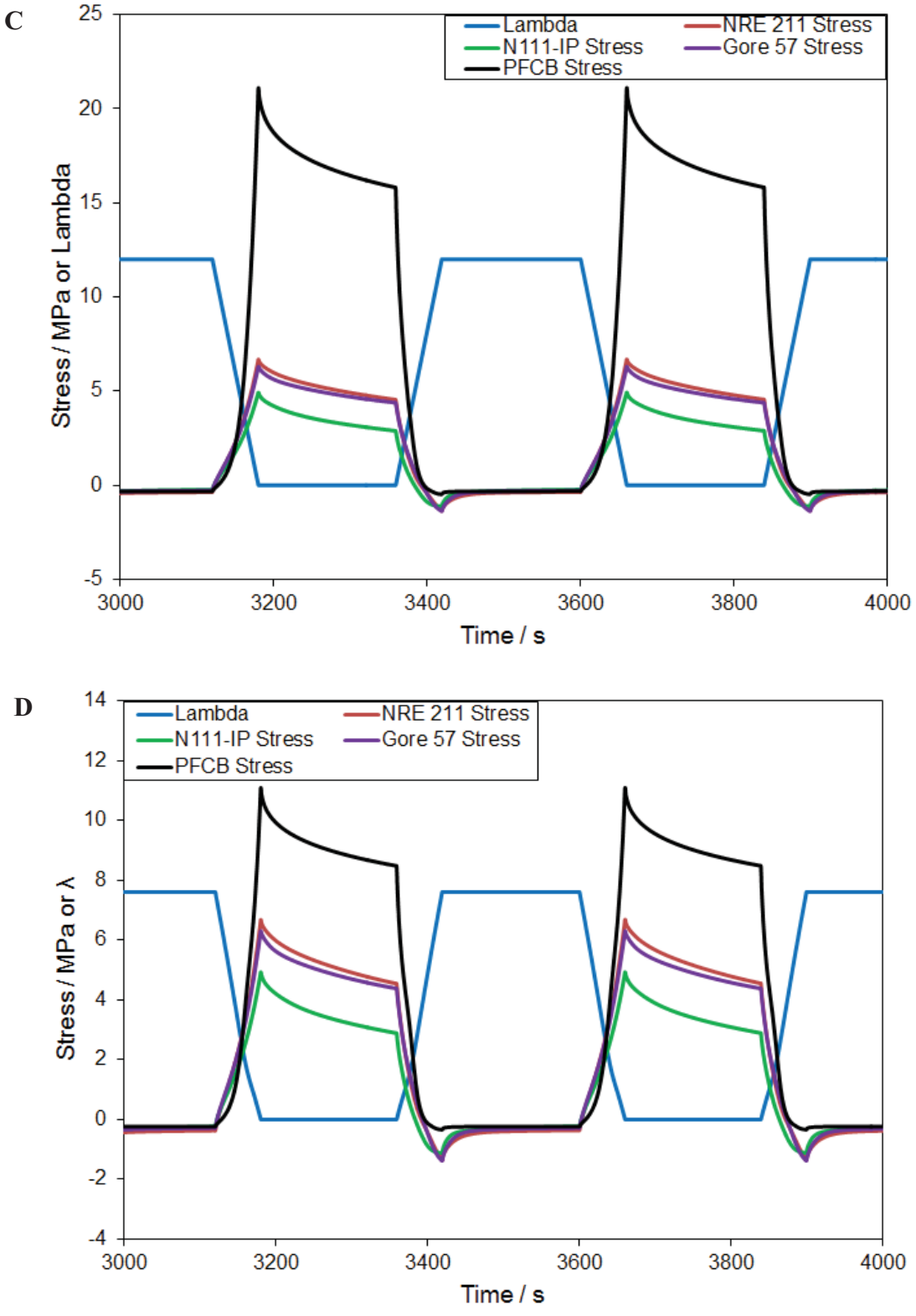

Figure B.7. Stress predictions performed utilizing **(A)** and **(C)** Giner's λ relationship and **(B)** and **(D)** VT's λ relationship.

To further investigate the validity of the VT λ relationship, a stress life prediction was performed based on data collected at General Motors. To perform the stress life prediction, the coefficient of hygral expansion was recalculated based on out-of-plane expansion data (**Figure B.8)** collected at GM using in-situ measurements in an in-house developed fixture. In this case the coefficient of hygral expansion was calculated by performing a linear fit of the expansion data, and dividing the slope by 54. The 54 value comes from 18 to account for the volume of water, and 3 to convert from volumetric swelling to linear expansion. The volumetric hygral expansion coefficient calculated using Giner's λ relationship is 1.06 %/λ, and 1.56 %/λ at 80°C and 1.67 %/λ at 88°C for VT's λ relationship. After obtaining the new hygral expansion coefficients, stress predictions were calculated for different RH cycles with different sized RH swings, corresponding with RH cycling performed at General Motors, as shown in **Figure B.9**. Again it should be noted that the stresses predicted using the Giner λ relationship are much higher than those predicted using the VT λ relationship, despite the larger coefficient of expansion calculated using the VT λ.

To examine the lifetime of a membrane at a given biaxial stress level, a biaxial stress lifetime plot was created. The stress was taken as the highest biaxial tensile stress the material sees during RH cycling, for example, ~5.5 MPa for a sample cycled from 50-150% RH at 88°C and calculated using the VT λ relationship. The lifetime was taken as the number of cycles measured during RH cycling, as shown in Figure 3.14, multiplied by 120 seconds, the time the membrane is under a tensile load. Only the tensile loading is used for lifetime predictions because the compressive stresses are negligible in PFCB/PVDF-HFP membranes, and it is thusly believed it is the tensile stresses that lead to membrane failure. In addition, to create a stress lifetime master curve, the data points are shifted hygrothermally using the shift factors provided

in **Figure B.3** and the corresponding fits provided by **Eqns [3.18]** and **[3.19**], and referenced to 80°C, 10% RH. The RH levels chosen for shifting each data point correspond to the low humidity level utilized during RH cycling, thus either 10, 30 or 50% RH, where the maximum biaxial tensile stress occurs. The resulting biaxial stress lifetime master curve is provided in **Figure B.10**. When the Giner λ relationship is employed, the shift factors determined from the stress relaxation hygrothermal master curve do not shift the stress lifetime data to form a single stress lifetime master curve. However, when the VT λ relationship is employed, the shift factors do create a single stress lifetime master curve. It is encouraging that the shift factors determined for stress relaxation data appear to shift the stress lifetime data well when using the VT λ relationship, implying the validity of TTMSP. Finally, if predictions were made based off of the stress lifetime master curve created using the VT λ relationship for RH cycle lifetime at 70°C, and compared with RH cycle test measurements performed at General Motors it would be clear if the VT λ relationship provides a better prediction of stress lifetime. Based on the data presented it is believed that the VT λ relationship provides a better description of the PFCB/PVDF-HFP material behavior than the Giner λ relationship. However if the 70°C RH cycle test could be performed it would provide further validity as to which λ relationship should be employed during analysis.

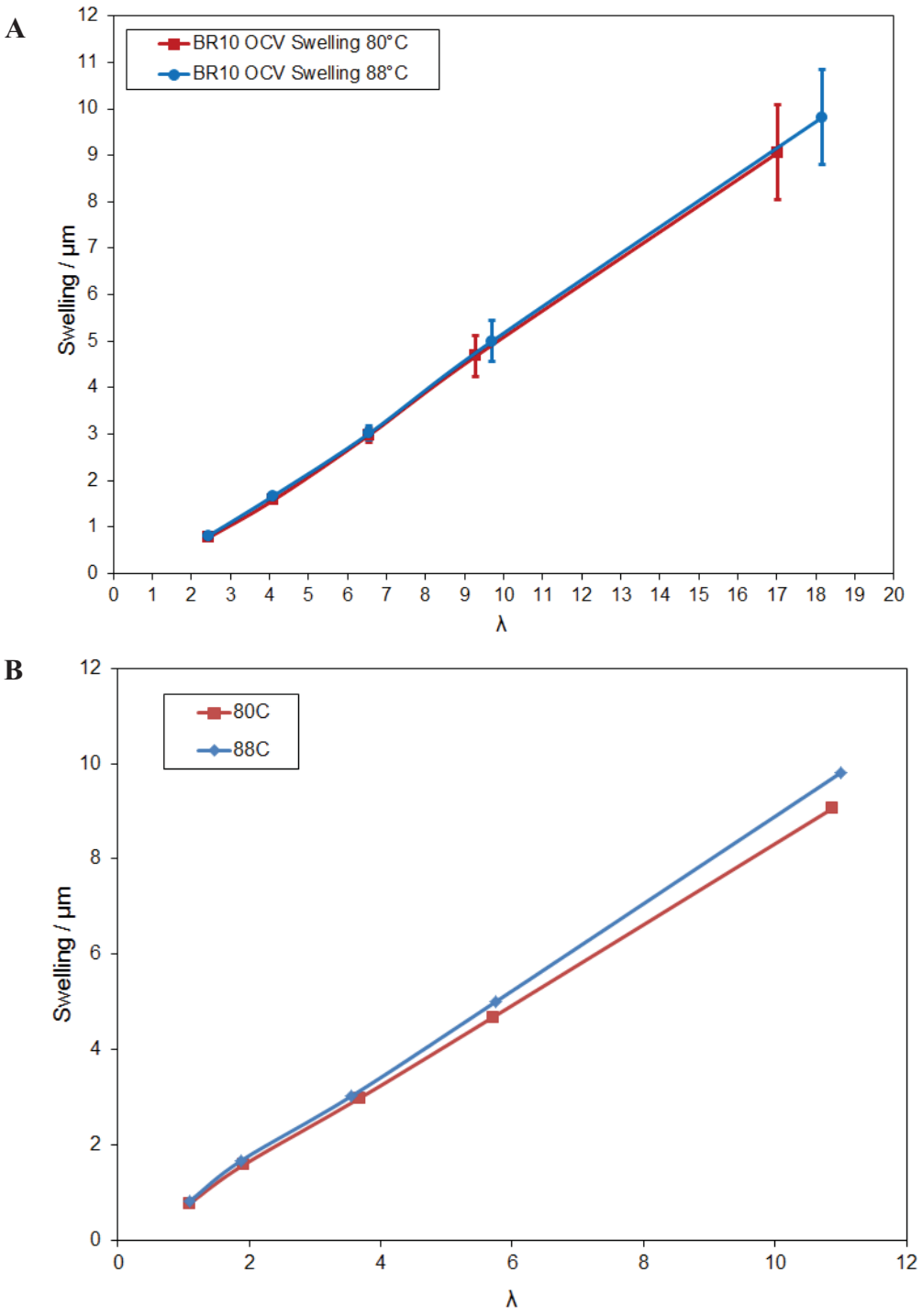

Figure B.8. Swelling ratios calculated using out-of-plane expansion data collected at General Motors utilizing **(A)** Giner's λ relationship and **(B)** VT's λ relationship.

A

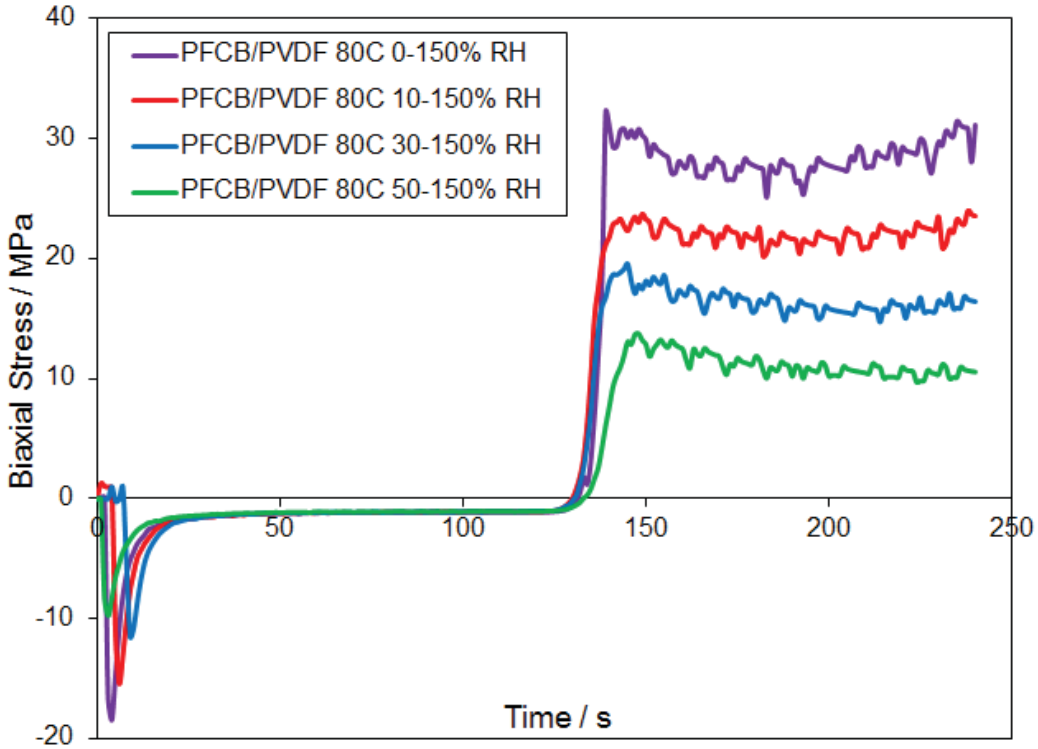
PFCB/PVDF 80C 0-150% RH
PFCB/PVDF 80C 10-150% RH
PFCB/PVDF 80C 30-150% RH
PFCB/PVDF 80C 50-150% RH
Biaxial Stress / MPa
Time / s
40
30
20
10
0
-10
-20
0
50
100
150
200
250

B

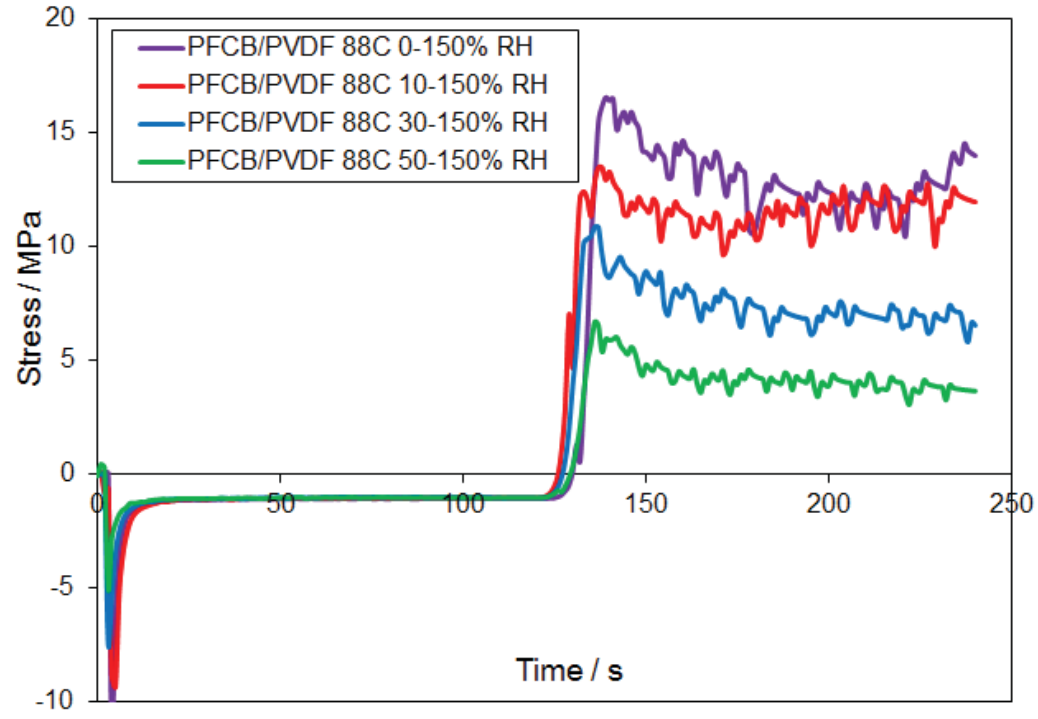
PFCB/PVDF 88C 0-150% RH
PFCB/PVDF 88C 10-150% RH
PFCB/PVDF 88C 30-150% RH
PFCB/PVDF 88C 50-150% RH
Stress / MPa
Time / s
20
15
10
5
0
-5
-10
0
50
100
150
200
250

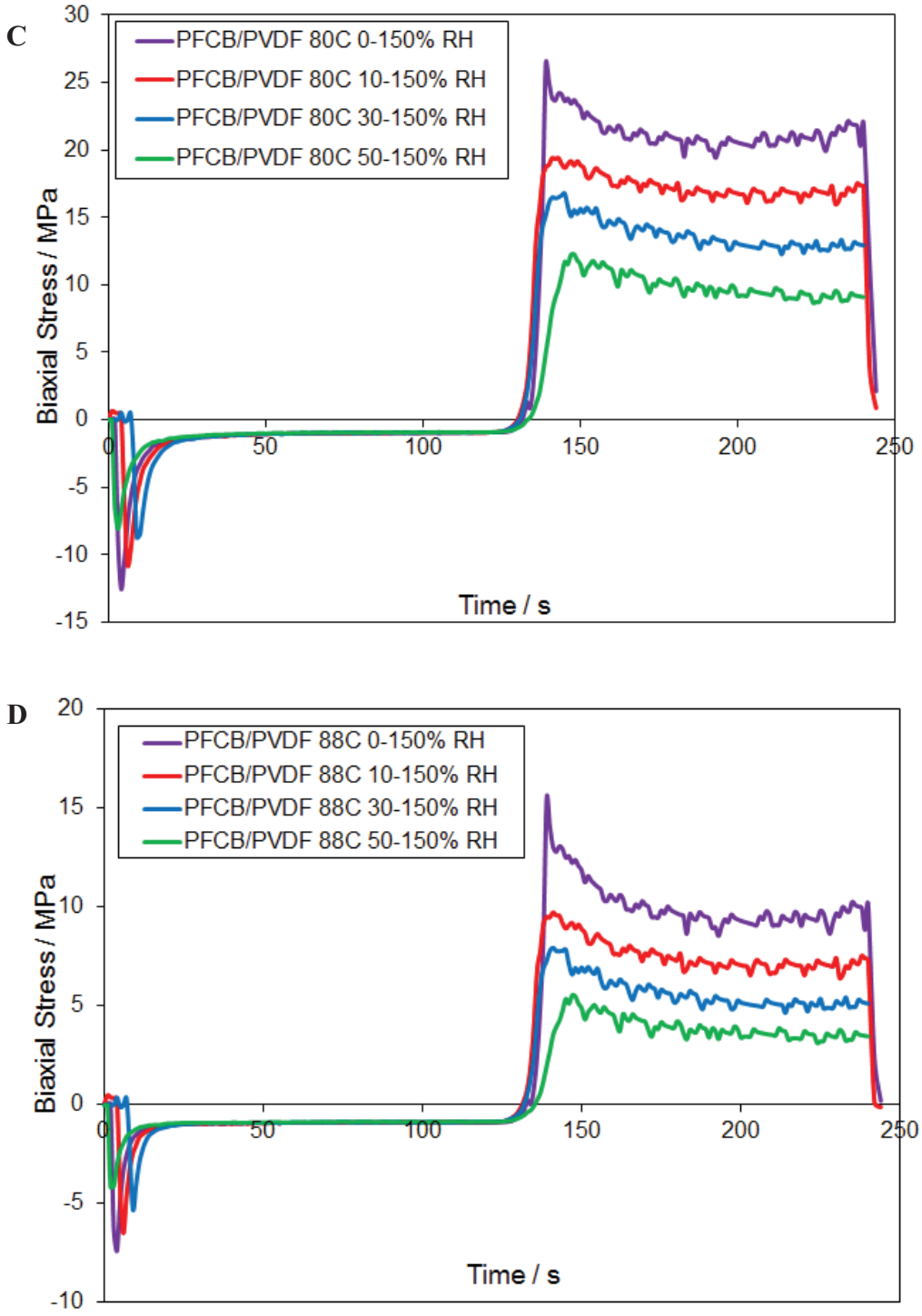

Figure B.9. Stresses predicted from RH cycles with differing low RH levels utilizing Giner's λ relationship at **(A)** 80°C and **(B)** 88°C and VT's λ relationship at **(C)** 80°C and **(D)** 88°C.

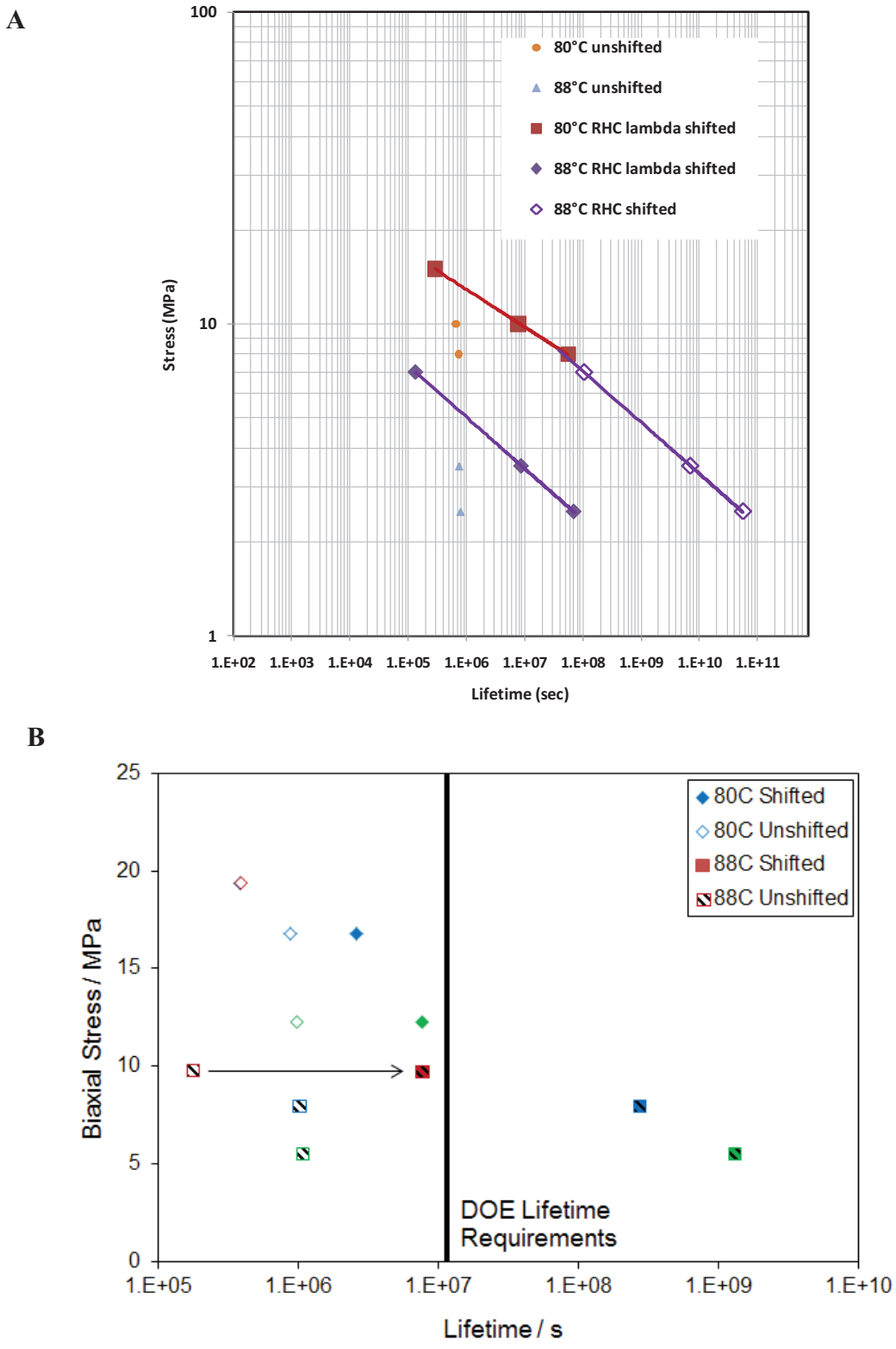

Figure B.10. Stress lifetime master curves referenced to 80°C and 10% RH utilizing **(A)** Giner's λ relationship and **(B)** VT's λ relationship.